Springer Series on Chemical Sensors and Biosensors 16
Series Editor: G. Urban

Michael J. Schöning · Arshak Poghossian
Editors

Label-Free Biosensing

Advanced Materials, Devices and Applications

Springer

16
Springer Series on Chemical Sensors and Biosensors

Methods and Applications

Series Editor: G. Urban

More information about this series at http://www.springer.com/series/5346

Label-Free Biosensing

Advanced Materials, Devices and Applications

Volume Editors:
Michael J. Schöning
Arshak Poghossian

With contributions by

N. Abramova · S. Badhulika · A. Bratov · S. Brosel-Oliu · V. Cimalla · T. J. Cleij · H. Dong · K. Eersels · M. E. Gracheva · J. Halámek · L. Halámková · S. Ingebrandt · K. J. Jetzschmann · C. Jungmann · E. Katz · H.-J. Krause · S. Krause · F. Lisdat · P. A. Lieberzeit · D. Mayer · D. V. Melnikov · K.-i. Miyamoto · V. M. Mirsky · A. Mulchandani · S. Nizamov · D. A. Oliveira · O. N. Oliveira, Jr. · V. Pachauri · M. Peeters · A. Poghossian · D. Rani · M. Riedel · P. Rinklin · F. W. Scheller ·V. Scherbahn · M. J. Schöning · R. Sha · J. R. Siqueira, Jr. · B. van Grinsven · P. Wagner · T. Wagner · J. Wang · C. C. Wells · C. F. Werner · B. Wolfrum · U. Wollenberger · A. Yarman · T. Yoshinobu · X. Zhang

Springer

Editors
Michael J. Schöning
Institute of Nano- and Biotechnologies
Aachen University of Applied Sciences
Jülich, Germany

Arshak Poghossian
Institute of Nano- and Biotechnologies
Aachen University of Applied Sciences
Jülich, Germany

ISSN 1612-7617
Springer Series on Chemical Sensors and Biosensor
ISBN 978-3-319-75219-8 ISBN 978-3-319-75220-4 (eBook)
https://doi/org/10.1007/978-3-319-75220-4

Library of Congress Control Number: 2018944624

Printed on acid-free paper

This Springer imprint is published by the registered company Springer International Publishing AG part of Springer Nature.
The registered company address is: Gewerbestrasse 11, 6330 Cham, Switzerland

Series Editor

Prof. Dr. Gerald Urban
IMTEK - Laboratory for Sensors
Institute for Microsystems Engineering
Albert-Ludwigs-University
Georges-Köhler-Allee 103
79110 Freiburg
Germany
urban@imtek.de

Aims and Scope

Chemical sensors and biosensors are becoming more and more indispensable tools in life science, medicine, chemistry and biotechnology. The series covers exciting sensor-related aspects of chemistry, biochemistry, thin film and interface techniques, physics, including opto-electronics, measurement sciences and signal processing. The single volumes of the series focus on selected topics and will be edited by selected volume editors. The *Springer Series on Chemical Sensors and Biosensors* aims to publish state-of-the-art articles that can serve as invaluable tools for both practitioners and researchers active in this highly interdisciplinary field. The carefully edited collection of papers in each volume will give continuous inspiration for new research and will point to existing new trends and brand new applications.

Preface

The last decades have seen unprecedented activities in the development of biosensors and other miniaturized analytical devices for the detection, quantification, and monitoring of numerous chemical and biological compounds. A biosensor generally consists of at least two functional components: a molecular recognition element (receptor) that selectively interacts with its target analyte (e.g., ions, DNA, antibodies, cells, and microorganisms) and a physicochemical transducer. The latter converts the bio-recognition information into a measurable quantity, being an electrochemical, electrical, optical, magnetic, mass-sensitive, or thermal signal.

Due to the fact that biological analytes are often hard to detect purely on basis of their intrinsic physical properties, biosensors often require labels such as enzymes and fluorescent or radioactive molecules attached to the targeted analyte. As a result, the final sensor signal corresponds to the amount of labels, representing the number of bound target molecules. As a drawback, label-based technologies are often labor- and cost-intensive as well as time-consuming. In addition, labeling of biomolecules can block active binding sites and alter the binding properties. Altogether, this may adversely affect the affinity-based interaction between the recognition elements and the target molecules.

In contrast, label-free biosensing technologies, by definition, do not require the use of labels to facilitate measurements. Instead, they utilize intrinsic physical properties of the analytes, such as molecular weight, size, charge, electrical impedance, dielectric permittivity, or refractive index, to detect their presence in a sample. Label-free biosensing methods have made enormous progress in recent years due to their ability for rapid and inexpensive bio-detection in small reaction volumes. Moreover, they lend themselves for integration into lab-on-chip platforms and allow monitoring the concentration of target analytes in real time.

The book *Label-Free Biosensing – Advanced Materials, Devices and Applications* addresses state-of-the-art technologies and emerging developments in the field of label-free biosensing and the underlying transducer principles, materials, device fabrication, and applications. It is intended to give both the expert user and the curious reader a view into the "world" of label-free technologies. It provides

graduate students, academic researchers, and industry professionals with a comprehensive source for key advancements and future trends in label-free biosensing.

This volume consists of 16 chapters, which cover a broad range of label-free biosensors based on a variety of transducer principles and advanced nanomaterials. To start with, the first chapters address semiconductor field-effect biosensors, which are a subclass of the electrochemical transducers. The selected examples include capacitive electrolyte–insulator–semiconductor structures (chapter "Nanomaterial-Modified Capacitive Field-Effect Biosensors"), silicon- nanowire transistors (chapter "Silicon Nanowire Field-Effect Biosensors"), III-nitride semiconductor devices (chapter "Label-Free Biosensors Based on III-Nitride Semiconductors"), and light-addressable potentiometric sensors [chapter "(Bio-)chemical Sensing and Imaging by LAPS and SPIM"].

The next group of chapters is devoted to several other types of electrochemical transducers such as impedimetric biosensors with planar and three-dimensional electrodes (chapters "Biosensorial Application of Impedance Spectroscopy with Focus on DNA Detection" and "Label-Free Impedimetric Biosensing Using 3D Interdigitated Electrodes"), electrochemical nanocavities (chapter "Electrochemical Nanocavity Devices"), and solid-state nanopore devices (chapter "Computational Modeling of Biomolecule Sensing with a Solid-State Membrane"). Chapter "Amperometric Sensors Based on Carbon Nanotubes in Layer-by-Layer Films" discusses amperometric sensors utilizing electrodes modified with carbon nanotubes, while chapter "Graphene-Based Biosensors and Their Applications in Biomedical and Environmental Monitoring" deals with graphene and graphene oxide as next-generation electrode materials for biosensing in a medical and environmental context.

Chapter "Label-Free MIP-Sensors for Protein Biomarkers" provides a survey on biosensors based on molecularly imprinted polymer receptors and their application on clinically relevant biomarkers, while biomimetic sensors based on acoustic signal transduction are reviewed in chapter "Biomimetic Recognition for Acoustic Sensing in Liquids". Next, in chapter "Enzyme Logic Systems – Biomedical and Forensic Biosensor Applications", the readers will find a comprehensive overview on enzyme logic systems and digital biosensors based on the biocomputing concept for biomedical and forensic applications. The heat-transfer method as a novel transducer principle for label-free biosensing is introduced in chapter "Heat Transfer as a New Sensing Technique for the Label-Fee Detection of Biomolecules". Finally, chapter "Towards Ultrasensitive Surface Plasmon Resonance Sensors" summarizes ultrasensitive biosensors based on surface plasmon resonance, and chapter "Biomagnetic Sensing" describes magnetic biosensors and magnetic imaging devices.

Given the considerable research efforts into label-free biosensing in recent years, we are now getting to the point at which label-free technologies find their way to real-life applications including drug discovery, environmental monitoring, medical diagnostics, and life sciences. From a commercial perspective, the global label-free detection market is expected to grow with an annual growth rate of about 8.8% from 2017 to reach 2.29 billion $ by 2022. We believe that this book can contribute in

stimulating and generating new ideas for further development of label-free biosensing technologies.

The editors would like to thank all authors of this volume for their high-quality contributions as well as A. Schlitzberger and G. Urban for their helpful advice and patience.

Jülich, Germany Michael J. Schöning
Jülich, Germany Arshak Poghossian

Contents

Nanomaterial-Modified Capacitive Field-Effect Biosensors

Arshak Poghossian and Michael J. Schöning

Abstract The coupling of charged molecules, nanoparticles, and more generally, inorganic/organic nanohybrids with semiconductor field-effect devices based on an electrolyte–insulator–semiconductor (EIS) system represents a very promising strategy for the active tuning of electrochemical properties of these devices and, thus, opening new opportunities for label-free biosensing by the intrinsic charge of molecules. The simplest field-effect sensor is a capacitive EIS sensor, which represents a (bio-)chemically sensitive capacitor. In this chapter, selected examples of recent developments in the field of label-free biosensing using nanomaterial-modified capacitive EIS sensors are summarized. In the first part, we present applications of EIS sensors modified with negatively charged gold nanoparticles for the label-free electrostatic detection of positively charged small proteins and macromolecules, for monitoring the layer-by-layer formation of oppositely charged polyelectrolyte (PE) multilayers as well as for the development of an enzyme-based biomolecular logic gate. In the second part, examples of a label-free detection by means of EIS sensors modified with a positively charged weak PE layer are demonstrated. These include electrical detection of on-chip and in-solution hybridized DNA (deoxyribonucleic acid) as well as an EIS sensor with pH-responsive weak PE/enzyme multilayers for enhanced field-effect biosensing.

Keywords Biomolecular logic gate, DNA, Enzyme biosensor, Field-effect sensor, Gold nanoparticle, Polyelectrolyte

A. Poghossian (✉) and M. J. Schöning (✉)
Institute of Nano- and Biotechnologies, FH Aachen, Campus Jülich Heinrich-Mußmannstr. 1, 52428 Jülich, Germany
e-mail: a.poghossian@fz-juelich.de; schoening@fh-aachen.de

M. J. Schöning, A. Poghossian (eds.), *Label-Free Biosensing: Advanced Materials, Devices and Applications*, Springer Series on Chemical Sensors and Biosensors (2018) 16: 1–26
DOI 10.1007/5346_2017_2, © Springer International Publishing AG 2017,
Published online: 17 May 2017

Contents

1 Introduction

The construction of nanoscale electronic devices utilizing single molecules and nanoobjects (e.g., metal, oxide and semiconductor nanoparticles, carbon nanotubes, etc.) as building blocks represents an exciting and promising approach to realize future electronics beyond the current semiconductor technologies, as electronic devices are becoming progressively smaller and silicon technology is reaching its limit. In the past decade, a number of nanoelectronic and molecular devices (e.g., single-electron transistors [1, 2], molecular transistors [3, 4]) have been proposed, which are based on unique properties of individual molecules or nanoobjects as well as new physical phenomena in the nano-world. In spite of enormous efforts devoted in the research field of molecular electronic devices, nevertheless, the replacement of Si with "molecule-only" or "nanoobject-only" technologies in the near future is considered to be a challenging task [5]. It has been widely discussed that an integration of nanoobject/biomolecule inorganic/organic functional hybrid systems with a macroscopic electronic transducer (hybrid device concept) might be a more realistic approach for a new generation of (bio-)chemical sensors, sensor arrays, and multifunctional biochips. The combination of nano- and biomaterials within a hybrid system allows an enhancement of their functional properties and often leads to new synergistic effects originating from the components of the hybrid system [6–8].

In this context, the coupling of charged molecules, nanoobjects, and inorganic/organic nanohybrids with semiconductor field-effect devices (FEDs) based on an electrolyte–insulator–semiconductor (EIS) system represents a very promising strategy for the active tuning of electrochemical properties of FEDs and, therefore, can open new opportunities for label-free biosensing with direct electrical readout [5, 9–11]. Currently, FEDs based on an EIS system represent one of the key structural elements for chemical and biological sensing (see, e.g., reviews

[12–18]). Ion-sensitive field-effect transistors (ISFET), capacitive EIS sensors, light-addressable potentiometric sensors (LAPS), and silicon nanowire transistors (SiNW) are typical examples of (bio-)chemically sensitive FEDs. These devices provide a lot of potential advantages such as small size and weight, fast response time, compatibility with advanced micro- and nanofabrication technology, the possibility of on-chip integration of multiple sensors (arrays), and signal processing circuits.

The capacitive EIS sensor is the simplest field-effect sensor and represents a (bio-) chemically sensitive capacitor. Since field-effect EIS sensors are charge-sensitive devices, in principle, they are able to detect any kind of charge (or potential) changes at or nearby the gate insulator–electrolyte interface induced by (bio-)chemical reactions or molecular interactions, in particular, adsorption and binding of molecules. In previous experiments, EIS sensors have been applied for the measurement of various (bio-)chemical quantities in liquids, like pH value, ion and analyte concentrations [19–22]. In addition, during the last few years, label-free sensing of charged molecules and nanoobjects (e.g., nanoparticles, carbon nanotubes) has become one of the most reported applications for capacitive EIS sensors [5, 11, 23–26]. The present chapter summarizes selected examples of recent developments and current research activities in the field of label-free biosensing using nanomaterial-modified capacitive field-effect sensors. These include:

1. EIS sensors modified with negatively charged gold nanoparticles (AuNP) for the label-free electrostatic detection of positively charged small proteins and macromolecules, for monitoring the layer-by-layer (LbL) formation of oppositely charged polyelectrolyte (PE) multilayers, as well as for the development of an enzyme-based molecular logic gate
2. EIS sensors modified with (a) positively charged weak PE layer for the label-free electrical detection of DNA (deoxyribonucleic acid) immobilization and hybridization by its intrinsic molecular charge and (b) weak PE/enzyme multilayer for enhanced field-effect biosensing

2 Capacitive EIS Sensors Modified with AuNP/Molecule Hybrids

Assemblies of AuNPs on a macroscopic transducer surface are an emerging and highly attractive class of chemically and electrically tunable functional materials. Due to the unique electrical, electrochemical, catalytic, and optical properties of AuNPs, different from those of bulk Au, they have been extensively applied in both fundamental research (e.g., catalysis, adsorption and binding of molecules, biotechnology, electron transport phenomena in nanoscale materials with 1D, 2D, or 3D dimensionalities) [27–29] and various application-oriented fields (optical and electronic devices, chemical sensors and biosensors, molecular logic gates, drug delivery systems, etc.) [1, 2, 5–7, 20, 30–36].

Since the surface of AuNPs can be easily modified with variously charged shell molecules and because the vast majority of biomolecules or PE macromolecules are charged under physiological conditions, AuNP-modified EIS sensors can provide a universal and efficient platform for label-free electrical detection of a wide variety of molecules by their intrinsic molecular charge. The EIS sensor detects the charge changes in those AuNP/molecule inorganic/organic hybrids induced by the molecular adsorption or binding events. Below, the feasibility of this approach is demonstrated on the examples of AuNP-modified capacitive EIS sensors for the electrostatic detection of positively charged cytochrome c (CytC) and poly-D-lysine (PDL) molecules as well as the formation of PE multilayers consisting of poly(allylamine hydrochloride) (PAH)/poly(sodium 4-styrenesulfonate) (PSS) system, representing typical model examples of detecting small proteins and macromolecules and the consecutive adsorption of positively/negatively charged PE molecules, respectively. In addition, the results of interfacing of an enzyme-based **AND–Reset** logic gate (that mimics the operation of electronic logic gates) with such EIS sensor functionalized with pH-responsive AuNPs are presented.

2.1 Preparation of AuNP-Modified EIS Sensors and Measurement Setup

The EIS sensors consisting of an Al–p-Si–SiO_2 structure (30 nm thermally grown SiO_2; 300 nm Al as rear-side contact layer) with chip sizes of 10 mm × 10 mm were prepared from a p-Si wafer (specific resistivity, 5–10 Ω cm). Before deposition of AuNPs, the SiO_2 surface was silanized with 3-mercaptopropyl trimethoxysilane (MPTMS). It is a bifunctional molecule that contains both thiol and silane functional groups and serves as a coupling agent between the AuNPs and SiO_2 [37]. The negatively charged citrate-capped AuNPs were prepared from a water solution using the well-established chloroauric acid ($HAuCl_4$) reduction method [38, 39]. For deposition of AuNPs on the MPTMS-modified SiO_2 surface, the sensor was immersed in a water solution of citrate-stabilized AuNPs for 12 h. The surface of the AuNP-modified EIS sensors was characterized by scanning electron microscopy (SEM) and atomic force microscopy (AFM) (see Fig. 1). The average diameter and density of AuNPs evaluated from several SEM images were approximately 18 ± 2 nm and $N = (0.8–1.2) \times 10^{11}$ AuNPs/cm^2, respectively. The negatively charged citrate surface provides a convenient scaffold to attach positively charged molecules. For details of surface silanization, AuNP preparation, and deposition steps, see [5].

The capacitance–voltage (C–V) and constant–capacitance (ConCap) modes are the most convenient methods for the electrochemical characterization of capacitive field-effect sensors [40]. The C–V and ConCap curves were recorded before and after surface modification or molecular adsorption process using an impedance analyzer (see Fig. 2a). In the ConCap mode, the capacitance of the EIS sensor at the

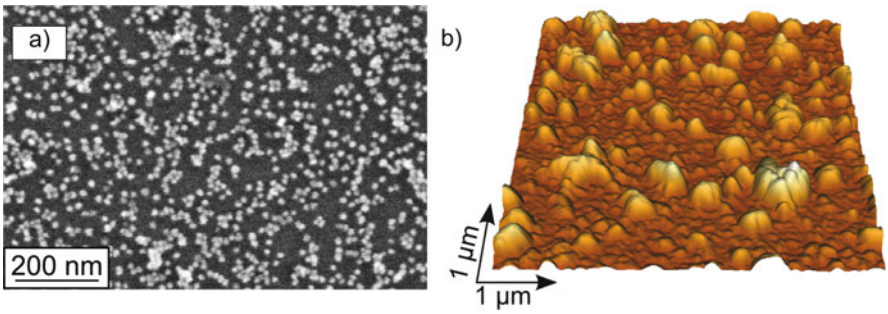

Fig. 1 SEM (**a**) and tapping-mode AFM (**b**) images of an AuNP-modified EIS sensor surface. Reproduced from [5] with permission of the Royal Society of Chemistry

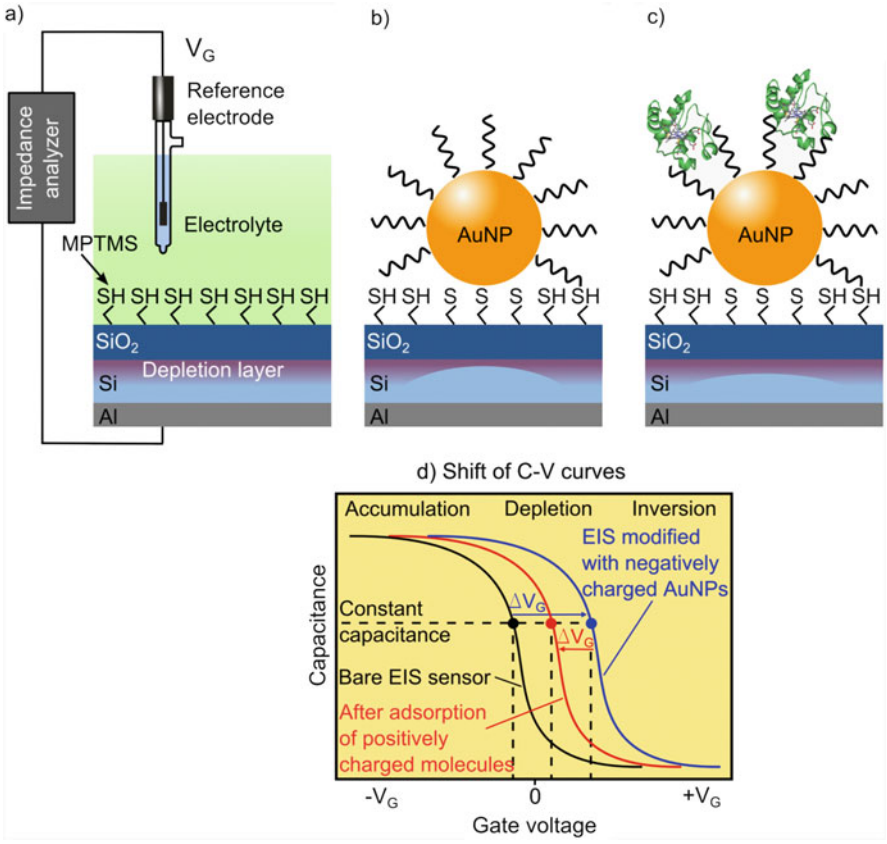

Fig. 2 Schematic cross section of the capacitive field-effect Al–p-Si–SiO_2 EIS sensor after silanization (**a**), deposition of negatively charged citrate-capped AuNPs (**b**), adsorption of positively charged molecules on the AuNPs (**c**), and the corresponding *C–V* curves with typical accumulation, depletion, and inversion regions (**d**). Local changes in the width of the depletion layer are shown, too. Reproduced from [5] with permission of the Royal Society of Chemistry

working point (which is usually chosen within the linear range of the depletion region of the *C–V* curve) is kept constant by using a feedback control circuit, and potential changes at the gate surface, induced by the molecular adsorption or binding event, are recorded directly. For operation, a DC (direct current) polarization voltage is applied to the gate via the reference electrode (conventional Ag/AgCl liquid-junction electrode) to set the working point and a small superimposed AC (alternating current) voltage (20 mV) with a frequency of 100 Hz is applied to the system to measure the capacitance of the sensor. The contact area of the EIS sensor with the solution was about 0.4 cm^2. All potential values are referred to the reference electrode.

2.2 *Functioning of EIS Sensors Modified with AuNP/ Molecule Hybrids*

Figure 2 schematically shows the simplified measurement setup and cross section of the capacitive Al–p-Si–SiO_2 sensor structure after silanization of the SiO_2 surface (a), deposition of negatively charged citrate-capped AuNPs (b), adsorption of positively charged molecules on the AuNPs (c), and the expected shift of a high-frequency *C–V* curve of the bare EIS sensor after these surface modification steps (d).

In such a device, the ligand-stabilized AuNPs have a dual role: they provide a simple way for the attachment/binding of a wide variety of charged biomolecules on their surface; at the same time, AuNPs act as additional quasi-spherical metal gates, whose potential can be tuned by the intrinsic charge of attached molecules, resulting in local changes in the width of the depletion layer, as shown in Fig. 2b, c. In a simplified electrical equivalent circuit model, the total capacitance of the EIS structure, C, is usually represented as a series connection of the insulator capacitance (C_i), and the variable capacitance of the space-charge or depletion region in the semiconductor (C_{sc}) (the electrochemical double-layer capacitance is assumed to be much greater than C_i and C_{sc} and can, thus, be neglected) [40, 41]:

$$C = \frac{C_i C_{sc}}{C_i + C_{sc}} = \frac{C_i}{1 + C_i/C_{sc}} \tag{1}$$

In Eq. (1), for a given insulator thickness, the value of C_i is constant, while C_{sc} is determined by the width of the space-charge region in the semiconductor, which depends, among others, on the voltage applied to the gate, V_G, and the potential at the gate insulator/electrolyte interface. Dependent on the magnitude and polarity of the applied gate voltage, V_G, three regions in the *C–V* curve can be distinguished: accumulation, depletion, and inversion. In the accumulation region, $C_i \ll C_{sc}$, the total capacitance of the EIS structure is determined by the geometrical capacitance of the insulator, $C = C_i$, and corresponds to the maximum capacitance of the system (Fig. 2d).

The binding of charged species to the AuNPs is analogous to the effect of applying an additional voltage to the gate. Therefore, for the investigation of charge effects induced in a capacitive EIS structure by the adsorption or binding of charged molecules or nanoobjects, more important is the shift of the *C–V* curves along the voltage axis (ΔV_G) in the depletion region. The direction of these potential shifts depends on the sign of the charge of adsorbed molecules. The binding of negatively charged citrate-capped AuNPs to the silanized SiO_2 surface will decrease the width of the depletion layer (Fig. 2b) and increase the depletion capacitance (C_{sc}) in the Si within regions under surface areas covered with AuNPs. This will result in an increase of the total capacitance of the sensor and in a shift of the *C–V* curve in the direction of more positive (or less negative) gate voltages. In contrast, the electrostatic adsorption or binding of positively charged molecules to the negatively charged citrate-capped AuNPs will modulate the charge of the AuNP/molecule hybrids and, thus, will lead to a local increase of the width of the depletion layer (Fig. 2c) and decrease of the space-charge capacitance. As a consequence, the total capacitance of the modified EIS sensor will also decrease, resulting in a shift of the *C–V* curve in the direction of more negative (or less positive) gate voltages (see Fig. 2d). The amplitude of potential shifts (ΔV_G) depends on the surface coverage of the AuNPs, number of attached molecules, and their intrinsic charge and is given by [5]

$$\Delta V_G = \frac{nN_{NP}N_M Q_M}{C_d} \tag{2}$$

where N_{NP} is the surface density of the citrate-capped AuNPs, n is the AuNP-coated fraction (coverage) of the gate surface, N_M is the number of adsorbed molecules per AuNP, Q_M is the effective charge of the adsorbed molecule, and C_d is the double-layer capacitance.

Equation (2) is obtained by assuming that (a) the surface potential can be considered as the average mixed potential of the silanized SiO_2/solution and AuNP hybrid/solution interfaces; (b) the double-layer capacitance, C_d, is similar at the AuNP hybrid/solution and silanized SiO_2/solution interface; and (c) screening of the charge of AuNP hybrids by counterions in the solution can be neglected. It is worth noting that due to the counterion-screening effect, the effective charge of molecules and, therefore, the potential shift will depend on the ionic strength of the measurement solution. Equation (2) clearly indicates the possibility of gating field-effect EIS sensors by the charge of nanoparticle/molecule hybrids. In addition, it allows to estimate potential changes induced by the adsorption or binding of charged molecules onto AuNP-modified sensor surfaces. The large sensor signal can be expected by a high surface coverage of AuNPs, a large number of highly charged, adsorbed molecules per AuNP, and by measurements in low ionic strength solutions (i.e., by a reduced counterion-screening effect and a small double-layer capacitance).

2.3 Detection of Cytochrome c

CytC is an essential component of the electron transport chain in mitochondria. It is a small, nearly spherical protein with a size of 2.6 nm × 3.2 nm × 3.0 nm [42]. Since the isoelectric point of CytC is around pH 10 [43], it is sufficiently positively charged at neutral pH value; the net positive charge of CytC in pH 7 solution is approximately +9*e* (*e* is the elementary charge, 1.6×10^{-19} C) [44]. CytC rapidly binds to an AuNP due to electrostatic interactions between the positively charged CytC and negatively charged citrate-capped AuNP. Figure 3 shows an example of the label-free electrical detection of CytC molecules by means of the EIS sensor modified with citrate-capped AuNPs. As can be seen, after the CytC adsorption, a large shift of the *C*–*V* curve of about 328 mV in the direction to more negative voltages has been observed in the depletion region that can be attributed to the presence of positively charged CytC molecules on/close to the negatively charged citrate-capped AuNPs. Both the direction and amplitude of potential shifts can directly be determined from the dynamic ConCap-mode measurements. The number of adsorbed CytC molecules per AuNP calculated from Eq. (2) using the experimentally observed potential change of $\Delta V_G = 330$ mV (evaluated from the ConCap curve in Fig. 3) amounted to be approximately $N_M = 46$ [5].

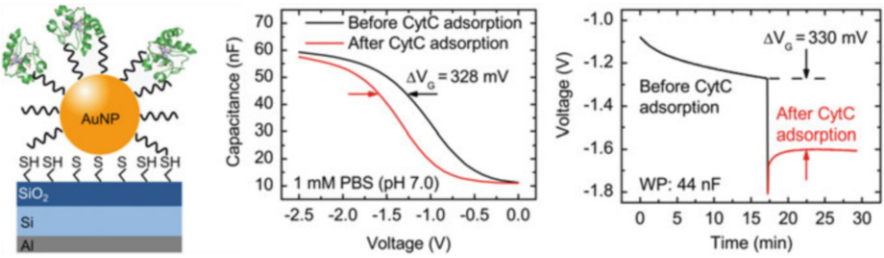

Fig. 3 Label-free electrical detection of positively charged CytC molecules by means of the EIS sensor modified with negatively charged citrate-capped AuNPs (*left*). The *C*–*V* curves (*middle*) and the ConCap response (*right*) were recorded in 1 mM phosphate buffer solution (PBS) of pH 7 before and after the adsorption of CytC molecules. For the CytC adsorption, the sensor was exposed to 1 mM PBS (pH 7) containing 50 µM CytC for 10 min. The *C*–*V* curves exhibit a typical high-frequency shape with the usual accumulation ($V_G < -2$ V), depletion (-1.7 V $< V_G < -0.75$ V), and inversion ($V_G > -0.6$ V) regions. *WP* working point. Reproduced from [5] with permission of the Royal Society of Chemistry

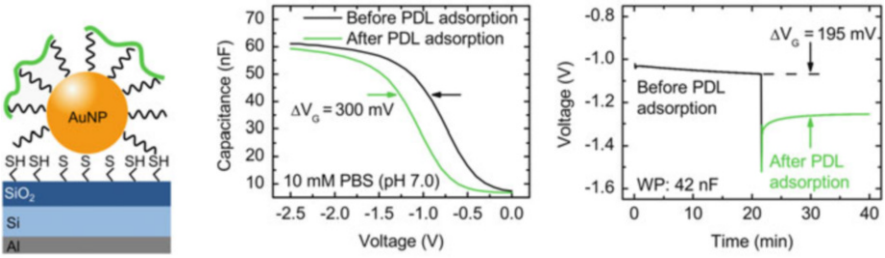

Fig. 4 Label-free detection of PDL molecules by means of a capacitive EIS sensor modified with citrate-capped AuNPs (*left*). The *C–V* curves (*middle*) and the ConCap response (*right*) of the EIS sensors were recorded before and after adsorption of positively charged PDL molecules. For PDL adsorption, the AuNP-modified EIS sensor was exposed to 10 mM PBS, pH 7, containing 10 mg/mL PDL for 15 min. Reproduced from [5] with permission of the Royal Society of Chemistry

2.4 Detection of Poly-D-lysine

A sketch of the EIS sensor modified with AuNP/PDL hybrids is depicted in Fig. 4 (left). PDL is a synthetic amino acid chain that is positively charged and widely used as a coating to enhance cell attachment and adhesion to surfaces. In weakly acidic to weakly alkaline solutions (pH 5–9), a strong electrostatic interaction exists between polycationic chains of PDL and citrate-capped AuNPs, which is a result of direct coupling of positive NH_3^+ groups of PDL with negative COO^- groups of the citrate-capped AuNPs [45, 46]. The single AuNP can serve as docking site for multiple PDL chain adsorptions. On the other hand, the PDL macromolecule can bind to multiple AuNPs.

An example for label-free electrical detection of PDL with the AuNP-modified EIS sensor is demonstrated in Fig. 4. The potential shifts detected after the adsorption of PDL molecules evaluated from the *C–V* curves and the ConCap response of three sensors were between 195 and 300 mV.

2.5 Detection of LbL Adsorption of Oppositely Charged PE Macromolecules and Multilayer Formation

Polyelectrolytes are macromolecules carrying a large number of charged or chargeable groups when dissolved in solution. LbL deposition of PE multilayers from solutions provides a simple, low-cost, and efficient method for the preparation of ultrathin films as well as complex heterostructures with a well-defined composition and multiple functionalities, whereby ultrathin films are assembled electrostatically from the repetitive, sequential adsorption of polyions with alternating charge [47, 48].

Recent experiments on the detection of PE macromolecules using capacitive EIS sensors [40, 49, 50], silicon thin-film resistors [51], field-effect transistors [52],

nanowire transistors [53], and metal–insulator–semiconductor devices [54] as transducer have demonstrated that the semiconductor field-effect platform represents a powerful tool for real-time, in-situ electrical monitoring of PE multilayer formation. The feasibility of an AuNP-modified capacitive EIS sensor for the label-free detection of consecutive adsorption of polyelectrolytes has recently been demonstrated using cationic weak PE PAH and anionic strong PE PSS as a model system [5].

Figure 5 presents a schematic of the LbL formation of PAH/PSS multilayers on the surface of AuNPs (a) as well as zoomed *C–V* curves in the depletion region and a ConCap response of the AuNP-modified EIS sensor after the consecutive adsorption of each cationic PAH and anionic PSS layer from the respective PE solution (50 μM PAH or PSS, adjusted with 100 mM NaCl, pH 5.4) (b). At this pH value, both the PSS and the PAH molecules are fully charged [55]. As the citrate-capped AuNPs are negatively charged, the PE multilayer formation was started with the positively charged PAH macromolecules.

The consecutive adsorption of oppositely charged PE layers leads to alternating shifts of the *C–V* curve and ConCap signal of the AuNP-modified EIS sensor along

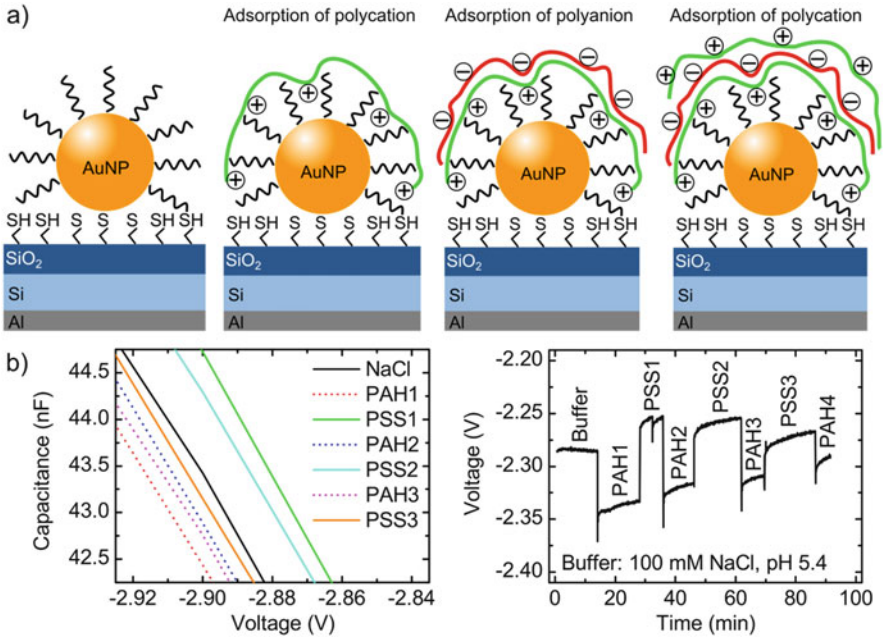

Fig. 5 Schematic of LbL formation of PAH/PSS multilayer on a surface of AuNPs (**a**) as well as zoomed *C–V* curves in the depletion region (*left*) and ConCap response (*right*) of the AuNP-modified EIS sensor after the consecutive adsorption of cationic PAH and anionic PSS macromolecules (**b**). In this experiment, the EIS sensor was consecutively exposed to the respective PE solution for about 10 min (the time necessary for depositing a single monolayer), followed by recording of the *C–V* curve and ConCap response. These procedures were repeated until the desired number of layers was achieved (in this study, 6–7 layers). Reproduced from [5] with permission of the Royal Society of Chemistry

the voltage axis. The direction of the signal changes correlates with the charge sign of the outermost PE layer that is in good agreement with previous studies on PE detection with various types of field-effect devices [40, 49–51, 53]. It is assumed that the charge of the outermost layer overcompensates the charge of the underlying layer and, thus, enables the adsorption of the next layer. Due to the reversal of the charge of the outermost layer, the potential shifts show a "zigzag"-like behavior. When the multilayer is terminated with the PAH layer, the sensor signal shifts toward the direction corresponding to a more positively charged gate surface. In contrast, the adsorption of a negatively charged PSS layer shifts the sensor signal to less negative gate voltages.

As can be seen from the ConCap response in Fig. 5b, the magnitude of potential shifts has a tendency to decrease with increasing the number of adsorbed PE layers. For example, the ConCap signal decreases from ~80 to ~40 mV after the formation of the first and third bilayers of PAH/PSS, respectively. A similar effect was observed for field-effect thin-film resistors and capacitive EIS sensors without AuNPs [40, 51]. To explain the impact of the number of adsorbed PE layers on the signal behavior of the capacitive EIS sensor, a simplified theoretical model that describes, among others, the influence of the distance of the outermost PE layer from the gate surface has been developed in [40]. The electrostatic coupling between the PE charge and the gate surface will drop with increasing the distance between the outermost PE layer and the sensor surface. As a consequence, the potential changes at the gate surface induced upon the PE adsorption will decrease with increasing the number of PE layers and thickness of multilayer that, in fact, has been observed in the experiment.

2.6 Enzyme Logic Gates Based on an AuNP-Modified EIS Sensor

The idea creating a biocomputer using different biomolecules (e.g., proteins, DNA, or enzymes) has attracted significant interest. Therefore, in the past decade, a large variety of biochemical Boolean logic gates (**AND**, **NAND**, **OR**, **XOR**, **NOR**, **INHIB**, etc.) and some more complex devices have been realized (see e.g., recent reviews [56–61]). However, most of developments on molecular logic gates and circuits represent elegant proof-of-concept experiments mimicking the operation of their electronic analogues but are not able to compete with electronic computers [57, 59, 60]. It is widely discussed that future of molecular logic elements is strongly connected with the successful transfer of biomolecular logic principles to solid substrates and integration with an electronic transducer as well as with the possibility of their addressing and switching on/off externally [57, 62]. A coupling of biomolecular logic systems with electronic transducers and stimuli-responsive materials might enable the creation of novel digital biosensors with qualitative binary output signals in a YES/NO format, logically triggered actuators for

substance- or drug-release systems [57, 59, 63–65] and even closed-loop intelligent sense/act/treat systems [66], opening a new research avenue in advanced personalized medicine and theranostics.

In this context, an integration of biomolecular logic gates with field-effect devices based on an EIS system – an electrochemical analog of the basic element of conventional electronic logic gates and computing – is considered as one of the most attractive and promising approaches for the transformation of molecular logic outputs into electrical signals. The feasibility of this approach has recently been demonstrated by realizing enzyme-based **AND–Reset** and **OR–Reset** gates using capacitive field-effect EIS sensors consisting of an Al–p-Si–SiO_2 structure functionalized with AuNPs [35] and an Al–p-Si–SiO_2–Ta_2O_5 structure modified with a multienzyme membrane [62, 67], where analytes were used as chemical input. In the following, the functioning of a field-effect-based enzyme logic gate is explained in case of an **AND–Reset** logic gate interfaced with an Al–p-Si–SiO_2 EIS sensor modified with pH-responsive AuNPs, which have thiolated shell molecules containing carboxylic groups [35]. In aqueous solution, carboxylic groups deprotonate to carboxylate anions (COO^-), yielding in AuNPs with a negatively charged shell. In contrast to [35, 62, 67], the enzymes have been used as biochemical input signal.

Before the logic gate experiments, the pH sensitivity of the bare and AuNP-modified EIS sensors has been proven in standard buffer solutions from pH 4 to pH 9. The EIS sensors with a SiO_2 gate insulator showed a pH sensitivity of about 38–42 mV/pH that is in good accordance to values typically reported for a SiO_2 layer [68]. A slightly higher pH sensitivity of 46 mV/pH was found for EIS sensors modified with AuNPs.

The schematic of the **AND–Reset** logic gate is shown in Fig. 6a. It consists of three enzymes, glucose oxidase (GOD), invertase, and urease, added into the solution containing sucrose and dissolved oxygen. The absence of the respective enzymes is considered as the input signal **0**, while addition of enzymes is used as the input signal **1**. The operation of the enzyme logic gates is based on the cascade of enzymatic reactions. The **AND** gate was activated by invertase and GOD, while urease was used to realize the **Reset** function. The hydrolytic conversion of sucrose to glucose and fructose catalyzed by invertase was followed by glucose oxidation catalyzed by GOD in the presence of dissolved O_2. Final product of these biochemical reactions is gluconic acid, thus lowering the pH value of the solution. As a result of the pH-induced charge changes associated with the protonation/deprotonation of both the carboxylic groups of pH-responsive shells on the immobilized AuNPs and the silanol groups on the SiO_2 surface areas not covered with AuNPs, the EIS sensor generates an electronic signal (changes in the capacitance of the depletion layer in the semiconductor) corresponding to the logic output produced by the enzymes. The logic output signal has been read out by means of the *C–V* method. As can be seen from Fig. 6b, only if both enzymes (invertase and GOD) are present in the solution (input **1**,**1**), the cascade of enzymatic reactions is completed, resulting in a pH decrease and a large shift (about 118 mV) of the *C–V* curve toward more negative voltage values. The reaction cascade cannot start if

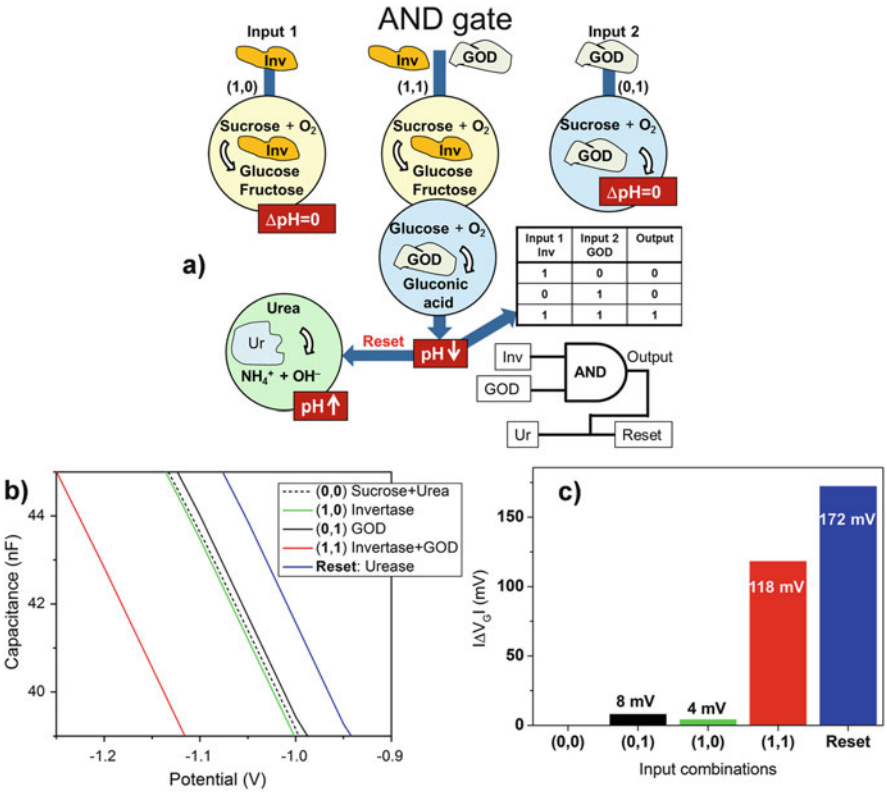

Fig. 6 Schematic of the **AND–Reset** logic gate (**a**), zoomed *C–V* curves in the depletion region for the AuNP-modified EIS sensor recorded by **AND** and **Reset** operations (**b**), and corresponding potential shifts induced by different chemical input combinations (**0**,**0**, **1**,**0**, **0**,**1,** or **1**,**1**) (**c**). *Inv* invertase, *Ur* urease

invertase is missing (input signal **1**,**0**) or it cannot be completed if GOD is missing (input signal **0**,**1**). The potential shifts by different chemical input combinations are depicted in Fig. 6c.

In order to provide the reversible operation of the **AND** gate, the pH value should be increased again [67]. This has been achieved via activation of the **Reset** function by adding the enzyme urease in the solution containing urea (10 mM). This results in a pH increase and a rapid change in the sensor signal for about 172 mV in the direction of less negative voltage values.

These experiments demonstrate an example of the successful interfacing of enzyme logic principles with the field-effect transducer. Since EIS field-effect devices are capable for detection of any kind of charge changes at the gate insulator–electrolyte interface induced by molecular interactions or (bio-)chemical reactions, in the future, the realization of a large class of EIS-based chemical and biomolecular single logic gates and even an array of concatenated logic gates could be possible by applying this transducer principle.

3 Polyelectrolyte-Modified EIS Sensors

3.1 Label-Free Detection of DNA with PAH-Modified EIS Sensor

DNA biosensors and microarrays are considered as a powerful tool in many fields of applications ranging from pathogen identification and diagnosis of genetic diseases over drug and food industry to forensic testing or detection of biowarfare agents [15, 69–72]. Most of the DNA detection techniques are based on a highly specific DNA hybridization reaction by which a single-stranded probe DNA (ssDNA) binds to a complementary single-stranded target DNA (cDNA), forming a double-stranded DNA (dsDNA) with a well-known helix structure. For a signal readout and sensitivity enhancement, these techniques often require labeling of either the target or probe DNA molecules using various markers (e.g., fluorescence, redox, enzymatic, radiochemical) that make them time-consuming, complicated, and expensive [69, 73]. For the creation of inexpensive and simple genosensors or DNA chips, label-free detection principles are preferred. Therefore, considerable research efforts have been invested toward the label-free electrical detection of DNA by its intrinsic molecular charge using various kinds of FEDs (see, e.g., recent reviews [15, 16, 24, 74]). Examples are detection of DNA immobilization, hybridization, and denaturation [25, 75, 76], identification of single nucleotide polymorphism [77], monitoring of DNA extension reaction and sequencing [78, 79], as well as verification of DNA amplification by polymerase chain reaction (PCR) [80, 81]. In these devices, the binding/adsorption of negatively charged DNA molecules on the gate surface of the FED effectively changes the charge applied to the gate, resulting in a modulation of the flat band or threshold voltage and the output signal of the FED.

The major disadvantage of electrostatic DNA detection is the screening of the negative charge of DNA molecules by mobile ions in the surrounding solution that could significantly reduce the sensor signal, especially in high ionic strength solutions. FEDs are able to detect the charge changes that occur directly at the gate surface or within the order of the Debye screening length from the surface. The Debye length defines the distance at which the electrostatic potential drops 1/e; it is inversely proportional to the ionic strength of the solution and amounts to be, for instance, ~1 nm for a 0.1 M solution of monovalent 1:1 salt. As a consequence, the electrostatic coupling between the charged DNA molecule and the FED strongly depends on the ionic strength of the solution, the distance between the charge of the molecule and the gate surface, and, therefore, on the orientation of DNA molecules to the gate surface. For example, if the DNA molecules are tethered to the gate surface via linker molecules or a spacer, the fraction of DNA charge that remains in the double layer and, thus, the FED signal induced by the DNA hybridization will strongly drop with increasing length of linker molecules. These problems can be overcome by immobilizing DNA molecules flat to the FED surface as well as by signal readout in a low ionic strength solution.

Direct electrostatic adsorption of DNA molecules onto typically used gate insulator (e.g., SiO_2, Ta_2O_5, Si_3N_4) surfaces is, in general, impossible, because both are negatively charged in a wide pH range. Therefore, recently, we proposed a strategy for the electrostatic detection of ssDNA adsorption and subsequent DNA hybridization on the gate surface of an EIS sensor modified with a positively charged weak polyelectrolyte layer of PAH [82–84]. Generally, a modification of the sensor surface by means of LbL electrostatic adsorption of a cationic polyelectrolyte/DNA bilayer becomes more popular in DNA biosensor design based on the field-effect platform [85, 86]. It has been discussed that in the presence of a positively charged polyelectrolyte layer, the electrostatically adsorbed DNA molecules will form preferentially flat-oriented elongated structures on the sensor surface with the molecular charges positioned near the gate surface within the Debye length, yielding a higher detection signal [82, 83]. Moreover, in contrast to often applied covalent immobilization methods that require time-consuming, cost-intensive procedures and complicated chemistry for functionalization of the gate surface and/or DNA molecules, the LbL adsorption technique is easy, fast, and cost-effective.

In the following, we present results of an application of PAH-modified Al–p-Si–SiO_2 EIS sensors for the label-free detection of a so-called on-chip and in-solution hybridization of DNA molecules, schematically shown in Fig. 7. In case of the on-chip hybridization, probe ssDNA molecules of known sequences were immobilized onto the PAH-modified FED surface, and the subsequent hybridization event was either detected in-situ by monitoring the sensor signal during the hybridization process or ex-situ by measuring the sensor signal before and after hybridization reaction. In contrast, by in-solution hybridization, the EIS sensor directly detects the electrostatic adsorption of dsDNA molecules formed after hybridization reaction occurred in the solution. In some cases, this could offer several advantages over detection by on-chip hybridization, especially, when the field-effect sensor is used for the detection of DNA amplification by PCR [80, 81]. By direct dsDNA detection, the surface modification procedure can be significantly simplified, because no probe ssDNA molecules have to be immobilized onto the sensor surface that could reduce both the detection time and costs.

Figure 7 demonstrates an example of detection of on-chip (a) and in-solution (b) hybridized DNA molecules with PAH-modified EIS sensors. In this experiment, the ConCap response has been recorded before and after each surface modification step: PAH adsorption, probe ssDNA immobilization on the PAH layer, and subsequent hybridization with complementary target cDNA as well as dsDNA adsorption on the PAH layer. The PAH layer (with thickness of about 2 nm) was prepared by exposing the Al–p-Si–SiO_2 EIS sensor to 50 μM PAH solution (pH 5.4) for 10 min. As it has been discussed in [82], at pH 5.4, both the SiO_2 surface and PAH molecules can be considered to be sufficiently charged to provide a successful electrostatic adsorption of positively charged PAH molecules onto the negatively charged SiO_2 surface. For probe ssDNA immobilization, the PAH-modified chip surface was exposed to 5 μM ssDNA solution for 1 h. For hybridization, the chip

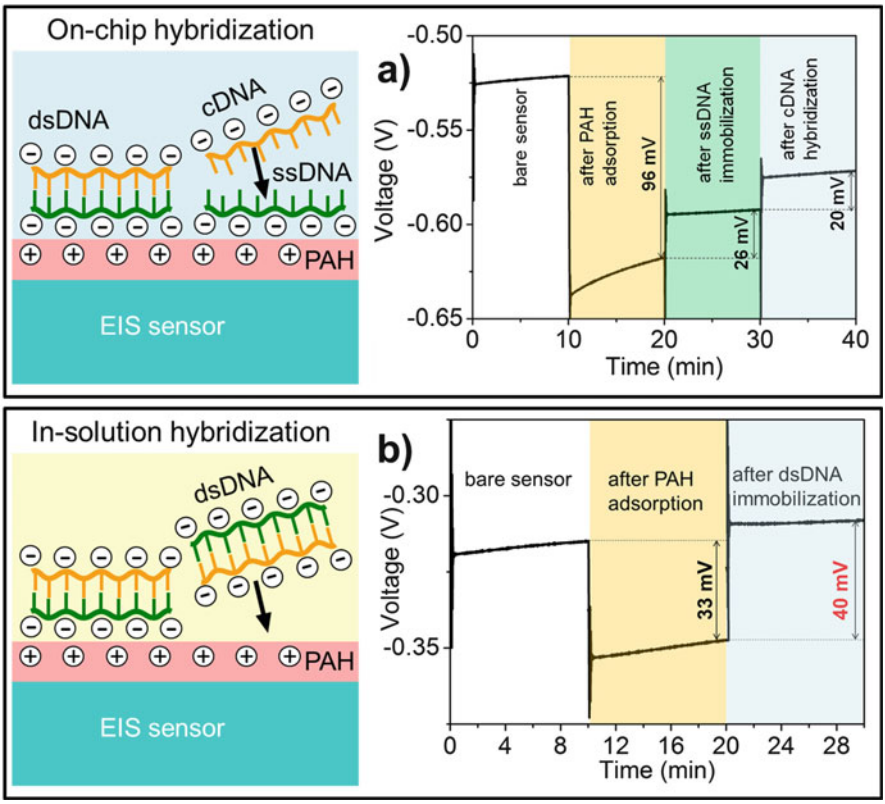

Fig. 7 Label-free detection of an on-chip (**a**) and in-solution (**b**) hybridization of 40-mer probe ssDNA with 20-mer cDNA molecules. To reduce the charge-screening effect and, thus, to enhance the sensitivity of the EIS sensor to the molecular charge, all measurements were performed in a low ionic strength solution (0.33 mM PBS buffer, pH 7, 5 mM NaCl)

surface covered with the PAH/ssDNA bilayer was incubated with target cDNA solution (5 μM cDNA) for 40 min at room temperature. For dsDNA adsorption, the PAH-modified SiO_2 surface was exposed to a solution containing in-solution hybridized dsDNA molecules for 1 h. The in-solution hybridization was achieved by mixing the solutions containing 5 μM probe ssDNA (40-mer) and 5 μM complementary target cDNA (20-mer) for 1 h. For the experimental details, see [82–84].

The consecutive adsorption of oppositely charged PAH and probe ssDNA layers leads to alternating potential shifts of about 96 and 26 mV, respectively (Fig. 7a). As it has been discussed in Sect. 2.2, the direction of these potential shifts depends on the sign of the charge of the adsorbed outermost layer, while the amplitude reflects the amount of adsorbed charge. If a positively charged PAH layer is adsorbed onto the negatively charged SiO_2 surface, one needs to apply a more negative gate voltage to compensate for this positive charge and to keep the capacitance constant. In contrast, the adsorption of negatively charged probe

ssDNA molecules shifts the sensor signal toward the direction of more positive (or less negative) bias voltages. After the hybridization process, the negative charge of the dsDNA molecules is increased, resulting in an additional potential shift (hybridization signal) of 20 mV in the direction of less negative voltages.

The average potential shift of about 40 mV was achieved after the adsorption of in-solution hybridized dsDNA molecules onto the PAH-modified EIS sensor surface (Fig. 7b). The lower detection limit evaluated from measurements in LAPS setup [84] was ~0.1 nM dsDNA that is in good agreement with results reported previously for DNA sensors based on silicon nanowires [87]. It is worth to note that the PAH-modified EIS-based DNA sensors, generally, exhibited better operating characteristics than EIS sensors modified with poly-L-lysine layer reported in [26].

3.2 Biosensors Based on an EIS Sensor Modified with a PAH/Enzyme Multilayer

At present, a lot of field-effect enzyme biosensors for the detection of various analytes (glucose, lactose, creatinine, penicillin, urea, organophosphorus pesticides, etc.) have been developed using different immobilization methods (see, e.g., [13, 88, 89]). These include, for instance, physical adsorption, covalent binding, cross-linking, entrapment within polymeric membranes, etc. The working characteristics (sensitivity, detection limit, response time, lifetime) of enzyme biosensors are strongly affected by the method of enzyme immobilization onto the transducer surface. With the aim to enhance biosensor performance, a completely different enzyme immobilization strategy has been proposed in [90], which is based on a modification of the EIS sensor surface with a pH-responsive weak PE/enzyme multilayer. Such modified EIS biosensor is capable for sensing not only local pH changes on the gate surface induced by the enzymatic reaction but also pH-induced changes in the charge of the weak PE macromolecules. In the following, the proposed concept is described in detail, taking the example of a penicillin biosensor prepared via modification of a SiO_2 gate EIS structure with a PAH/penicillinase multilayer (see Fig. 8).

The working principle of the field-effect penicillin biosensor is based on the detection of H^+ ions, which are produced during the hydrolysis of penicillin catalyzed by the enzyme penicillinase [91]. The resulting local pH decrease near the surface of the gate insulator (here, SiO_2) will change the surface charge of the SiO_2 and, thus, will shift the *C–V* curve of the field-effect sensor along the voltage axis (see, Fig. 8). The magnitude of this shift (ΔV_s) depends on the local pH change (ΔpH) and, therefore, on the penicillin concentration in the solution. On the other hand, if the enzyme penicillinase is embedded within the multilayer of a weak PE of PAH exhibiting pH-responsive ionizable groups [92], the local pH changes induced by the enzymatic reaction will also alter the effective molecular charge of the polyelectrolyte and charge density within the multilayer. This will cause an

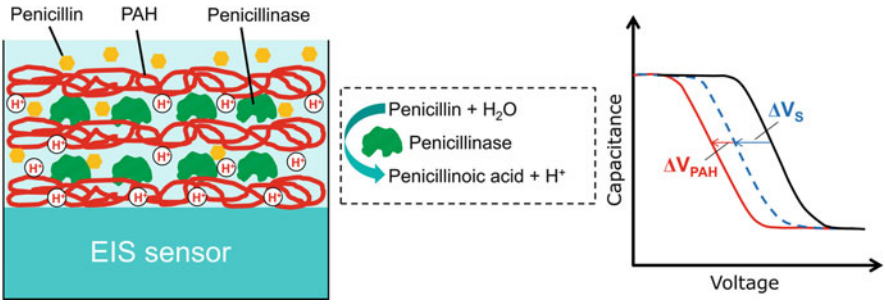

Fig. 8 Functioning principle of a penicillin-sensitive EIS biosensor modified with a pH-responsive weak PE/enzyme multilayer: schematic structure (*left*); enzymatic reaction of catalyzed hydrolysis of penicillin by the enzyme penicillinase (*middle*); expected shift of the *C–V* curves of the EIS sensor (*right*)

additional shift of the *C–V* curve along the voltage axis (ΔV_{PAH}). Consequently, for the EIS sensor modified with a weak PE/enzyme multilayer, a large sensor signal and a higher sensitivity should be expected.

In order to prove the described detection mechanism, the pH and penicillin sensitivity of an Al–p-Si–SiO_2–$(PAH/penicillinase)_3$–PAH structure with LbL-prepared three bilayers of PAH/penicillinase and PAH as outermost layer has been studied [90]. For comparison, penicillin sensitivity of an Al–p-Si–SiO_2–penicillinase structure with adsorptively immobilized penicillinase has been tested, too. The pH sensitivity of the EIS sensor modified with the PAH/penicillinase multilayer was higher (52 mV/pH in the range from pH 5 to 8) than that of a bare SiO_2 gate EIS sensor (38 mV/pH). As it has been reported in [92, 93], the ionization degree and, therefore, the molecular charge of weak PE in the embedded layer changes with both the pH of the surrounding solution and the net charge of the outermost layer. Thus, the higher pH sensitivity of the modified EIS sensor can be explained by assuming that both the underlying SiO_2 gate insulator and the effective molecular charge of the PAH multilayer contribute to the pH-dependent sensor response.

As expected, the higher penicillin sensitivity (around 100 mV/decade in the linear range of 0.25–2.5 mM penicillin G) has been obtained for the Al–p-Si–SiO_2–$(PAH/penicillinase)_3$–PAH sensor (for comparison, penicillin sensitivity of the Al–p-Si–SiO_2 sensor with adsorptively immobilized penicillinase was ~45 mV/decade [90, 91]). The lower and upper detection limit was around 0.02 and 10 mM, respectively. The 90% response time was about 1 min. Long-term measurements show that even after 2 months, the loss of the original penicillin sensitivity was only around 10–12% [90].

Taking together, an incorporation of enzymes in a weak PE multilayer provides high analyte sensitivity, reduces enzyme leaching effects, and, thus, enhances the operation stability and lifetime of the biosensor. Moreover, an entrapment of enzymes within a polyelectrolyte multilayer could provide a larger amount of

enzymes immobilized per sensor area [90]. Finally, the described strategy could be extended to further enzyme-based field-effect biosensors.

4 Summary and Outlook

During the last few years, label-free biosensing has become one of the most reported research fields for nanomaterial-modified capacitive EIS sensors. In this chapter, we presented selected examples of recent developments on EIS sensors modified with ligand-stabilized AuNPs or a weak PE layer for the electrostatic detection of charged molecules. The AuNP-modified EIS sensor detects charge changes in AuNP/ligand inorganic/organic hybrids induced by molecular adsorption or binding events. Since the vast majority of biomolecules are charged under physiological conditions and because the surface of AuNPs can be easily modified with different charged (positively/negatively) shell molecules, AuNP-modified EIS sensors represent a powerful and universal platform for label-free electrical detection of a wide variety of biomolecules by their intrinsic molecular charge. The feasibility of this approach has been demonstrated on examples of EIS sensors modified with citrate-stabilized negatively charged AuNPs for the electrostatic detection of positively charged CytC and PDL, representing typical model examples of detecting small proteins and PE macromolecules. In addition, AuNP-modified EIS sensors were successfully applied for the monitoring of a LbL buildup of PE multilayers of PAH/PSS as well as for the realization of enzyme logic gates. Furthermore, a label-free DNA sensor and enzyme-based biosensor with enhanced performance have been realized using EIS structures modified with a weak PE of PAH.

The presented approach can be extended to other FEDs as well as other charged molecules and even biological entities, e.g., virus particles. Nowadays, viruses are considered not only as disease-causing agents but also as highly promising smart materials for bio- and nanotechnology applications [94] as well as for biosensing [95]. The *tobacco mosaic virus* (TMV) is one of the most extensively studied plant viruses [94], which is nonpathogenic for mammals. TMV particles have a tubelike shape (with a typical length of about 300 nm, an outer diameter of 18 nm, and an inner channel diameter of 4 nm). The outer surface of the TMV nanotubes possesses thousands of regularly spaced sites that can be used for selective binding of molecules (see Fig. 9). For instance, recently, we successfully applied TMV nanotubes as enzyme nanocarriers for the development of an amperometric glucose biosensor [96]. The presence of TMV nanotubes on the sensor surface allows binding of a high amount of precisely positioned enzymes without substantial loss of their activity and may also ensure accessibility of their active centers for analyte molecules. We believe that the integration of virus particles, in particular TMV nanotubes with FEDs (Fig. 9), will open new strategies in advanced label-free biosensing technology.

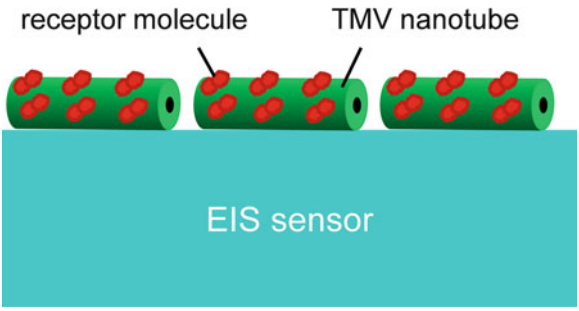

Fig. 9 Schematic of the EIS sensor modified with TMV nanotubes functionalized with receptor molecules

It is worth mentioning that in spite of successful experiments with nanomaterial-modified FEDs, the label-free electrostatic detection of charged biomolecules in real samples, especially in biological samples such as blood, urine, or saliva, remains still a major challenge. Biological samples are very complex mixtures of proteins, ions, and other chemical species. A possible nonspecific adsorption of proteins and other charged molecules onto the sensor surface could generate false background signals in addition to the signals from analytes of interest. Therefore, reduction of nonspecific adsorption of biomolecules is evident in label-free biosensor development and commercialization. Various blocking agents, like bovine serum albumin or polyethylene glycol, have been used to reduce nonspecific adsorption on biosensor surfaces. The problem of nonspecific response can also be reduced by pre-filtering/purifying the complex biological liquids or by applying differential-mode measurements.

Acknowledgments The authors thank M. Bäcker, D. Mayer, M. Weil, and E. Katz for valuable discussion and H. Iken, T.S. Bronder, S. Scheja, P. Mehndiratta, and M. Jablonski for technical support.

References

1. Noguchi Y, Yamamoto M, Ishii H, Ueda R, Terui T, Imazu K, Tamada K, Sakano T, Matsuda K (2013) Photoresponses in gold nanoparticle single-electron transistors with molecular floating gates. Jpn J Appl Phys 52:110102
2. Khondaker SI, Luo K, Yao Z (2010) The fabrication of single-electron transistors using dielectrophoretic trapping of individual gold nanoparticles. Nanotechnology 21:095204
3. Diez-Perez I, Li Z, Guo S, Madden C, Huang H, Che Y, Yang X, Zang L, Tao N (2012) Ambipolar transport in an electrochemically gated single-molecule field-effect transistor. ACS Nano 6:7044–7052
4. Chen YS, Hong MY, Huang GS (2012) A protein transistor made of an antibody molecule and two gold nanoparticles. Nat Nanotechnol 7:197–203
5. Poghossian A, Bäcker M, Mayer D, Schöning MJ (2015) Gating capacitive field-effect sensors by the charge of nanoparticle/molecule hybrids. Nanoscale 7:1023–1031
6. Samanta A, Medintz IL (2016) Nanoparticles and DNA – a powerful and growing functional combination in bionanotechnology. Nanoscale 8:9037–9095

7. Willner I, Baron R, Willner B (2007) Integrated nanoparticle-biomolecule systems for biosensing and bioelectronics. Biosens Bioelectron 22:1841–1852
8. Mehrabani S, Maker AJ, Armani AM (2014) Hybrid integrated label-free chemical and biological sensors. Sensors 14:5890–5928
9. Boettcher SW, Strandwitz NC, Schierhorn M, Lock N, Lonergan MC, Stucky GD (2007) Tunable electronic interfaces between bulk semiconductors and ligand-stabilised inorganic nanoparticle assemblies. Nat Mater 6:592–596
10. Gun J, Gutkin V, Lev O, Boyen HG, Saitner M, Wagner P, D'Olieslaeger M, Abouzar MH, Poghossian A, Schöning MJ (2011) Tracing gold nanoparticle charge by electrolyte-insulator-semiconductor devices. J Phys Chem C 115:4439–4445
11. Siqueira Jr JR, Abouzar MH, Bäcker M, Zucolotto V, Poghossian A, Oliveira Jr ON, Schöning MJ (2009) Carbon nanotubes in nanostructured films: potential application as amperometric and potentiometric field-effect (bio-)chemical sensors. Phys Status Solidi A 206:462–467
12. Jimenez-Jorquera C, Orozco J, Baldi A (2010) ISFET based microsensors for environmental monitoring. Sensors 10:61–83
13. Lee CS, Kim SK, Kim M (2009) Ion-sensitive field-effect transistor for biological sensing. Sensors 9:7111–7131
14. Nakazato K (2009) An integrated ISFET sensor array. Sensors 9:8831–8851
15. Poghossian A, Schöning MJ (2014) Label-free sensing of biomolecules with field-effect devices for clinical applications. Electroanalysis 26:1197–1213
16. Pachauri V, Ingebrandt S (2016) Biologically sensitive field-effect transistors: from ISFETs to NanoFETs. Essays Biochem 60:81–90
17. Zhou W, Dai X, Lieber CM (2017) Advances in nanowire bioelectronics. Rep Prog Phys 80:016701
18. Zhang A, Lieber CM (2016) Nano-bioelectronics. Chem Rev 116:215–257
19. Rolka D, Poghossian A, Schöning MJ (2004) Integration of a capacitive EIS sensor into a FIA system for pH and penicillin determination. Sensors 4:84–94
20. Gun J, Rizkov D, Lev O, Abouzar MH, Poghossian A, Schöning MJ (2009) Oxygen plasma-treated gold nanoparticle-based field-effect devices as transducer structures for (bio-)chemical sensing. Microchim Acta 164:395–404
21. Beyer M, Menzel C, Quack R, Scheper T, Schügerl K, Treichel W, Voigt H, Ullrich M, Ferretti R (1994) Development and application of a new enzyme sensor type based on the EIS capacitance structure for bioprocess control. Biosens Bioelectron 9:17–21
22. Menzel C, Lerch T, Scheper T, Schügerl K (1995) Development of biosensors based on an electrolyte insulator semiconductor (EIS) capacitor structure and their application for process monitoring. Anal Chim Acta 317:259–264
23. Poghossian A, Ingebrandt S, Abouzar MH, Schöning MJ (2007) Label-free detection of charged macromolecules by using a field-effect-based sensor platform: experiments and possible mechanisms of signal generation. Appl Phys A Mater Sci Process 87:517–524
24. Kataoka-Hamai C, Miyahara Y (2011) Label-free detection of DNA by field-effect devices. IEEE Sensors J 11:3153–3160
25. Abouzar MH, Poghossian A, Cherstvy AG, Pedraza AM, Ingebrandt S, Schöning MJ (2012) Label-free electrical detection of DNA by means of field-effect nanoplate capacitors: experiments and modeling. Phys Status Solidi A 209:925–934
26. Hou CSJ, Milovic N, Godin M, Russo PR, Chakrabarti R, Manalis SR (2006) Label-free microelectronic PCR quantification. Anal Chem 78:2526–2531
27. Tiwari PM, Vig K, Dennis VA, Singh SR (2011) Functionalized gold nanoparticles and their biomedical applications. Nano 1:31–63
28. Pelaz B, Jaber S, Jimenez de Aberasturi D, Wulf V, Aida T, de la Fuente JM, Feldmann J, Gaub JHE, Josephson L, Kagan CR, Kotov NA, Liz-Marzán LM, Mattoussi H, Mulvaney P, Murray CB, Rogach AL, Weiss PS, Willner I, Parak W (2012) The state of nanoparticle-based nanoscience and biotechnology: progress, promises, and challenges. ACS Nano 6:8468–8483

29. Zabet-Khosousi A, Dhirani A (2008) Charge transport in nanoparticle assemblies. Chem Rev 108:4072–4124
30. Luo X, Morrin A, Killard AJ, Smyth MR (2006) Application of nanoparticles in electrochemical sensors and biosensors. Electroanalysis 18:319–326
31. Giljohann DA, Seferos DS, Daniel WL, Massich MD, Patel PC, Mirkin CA (2010) Gold nanoparticles for biology and medicine. Angew Chem Int Ed 49:3280–3294
32. Yeh YC, Creran B, Rotello VM (2012) Gold nanoparticles: preparation, properties, and applications in bionanotechnology. Nanoscale 4:1871–1880
33. Gun J, Schöning MJ, Abouzar MH, Poghossian A, Katz E (2008) Field-effect nanoparticle-based glucose sensor on a chip: amplification effect of coimmobilized redox species. Electroanalysis 20:1748–1753
34. Pita M, Krämer M, Zhou J, Poghossian A, Schöning MJ, Fernandez VM, Katz E (2008) Optoelectronic properties of nanostructured ensembles controlled by biomolecular logic systems. ACS Nano 2:2160–2166
35. Krämer M, Pita M, Zhou J, Ornatska M, Poghossian A, Schöning MJ, Katz E (2009) Coupling of biocomputing systems with electronic chips: electronic interface for transduction of biochemical information. J Phys Chem C 113:2573–2579
36. Ghosh P, Han G, De M, Kim CK, Rotello VM (2008) Gold nanoparticles in delivery applications. Adv Drug Deliv Rev 60:1307–1315
37. Fu Y, Yuan R, Xu L, Chai Y, Zhong X, Tang D (2005) Indicator-free DNA hybridization detection via EIS based on self-assembled gold nanoparticles and bilayer two-dimensional 3-mercaptopropyltrimethoxysilane onto a gold substrate. Biochem Eng J 23:37–44
38. Kruglenko I, Shirshov Y, Burlachenko J, Savchenko A, Kukla O, Belyaev O (2012) Sensor for detection of water presence in gaseous mixtures based on gold nanoparticles stabilized by sodium citrate. Sensors Actuators B Chem 170:109–114
39. Polavarapu L, Xu QH (2009) A simple method for large scale synthesis of highly monodisperse gold nanoparticles at room temperature and their electron relaxation properties. Nanotechnology 20:185606
40. Poghossian A, Weil M, Cherstvy AG, Schöning MJ (2013) Electrical monitoring of polyelectrolyte multilayer formation by means of capacitive field-effect devices. Anal Bioanal Chem 405:6425–6436
41. Bergveld P (1991) A critical evaluation of direct electrical protein detection methods. Biosens Bioelectron 6:55–72
42. Vinu A, Murugesan V, Tangermann O, Hartmann M (2004) Adsorption of cytochrome c on mesoporous molecular sieves: influence of pH, pore diameter, and aluminum incorporation. Chem Mater 16:3056–3065
43. Bonk SM, Lisdat F (2009) Layer-by-layer assembly of electro-active gold nanoparticle/cytochrome c multilayers. Biosens Bioelectron 25:739–744
44. Imabayashi S, Mita T, Kakiuchi T (2005) Effect of the electrostatic interaction on the redox reaction of positively charged cytochrome c adsorbed on the negatively charged surfaces of acid-terminated alkanethiol monolayers on a Au(111) electrode. Langmuir 21:1470–1474
45. Stobiecka M, Hepel M (2011) Double-shell gold nanoparticle-based DNA carriers with poly-L-lysine binding surface. Biomaterials 32:3312–3321
46. Murthy VS, Cha JN, Stucky GD, Wong MS (2004) Charge-driven flocculation of poly (L-lysine)-gold nanoparticle assemblies leading to hollow microspheres. J Am Chem Soc 126:5292–5299
47. Decher G, Eckle M, Schmitt J, Struth B (1998) Layer-by-layer assembled multicomposite films. Curr Opin Colloid Interface Sci 3:32–39
48. Schönhoff M, Ball V, Bausch AR, Dejugnat C, Delorme N, Glinel K, Klitzing R, Steitz R (2007) Hydration and internal properties of polyelectrolyte multilayers. Colloids Surf A Physicochem Eng Asp 303:14–29

49. Abouzar MH, Poghossian A, Pedraza AM, Gandhi D, Ingebrandt S, Moritz W, Schöning MJ (2011) An array of field-effect nanoplate SOI capacitors for (bio-)chemical sensing. Biosens Bioelectron 26:3023–3028
50. Garyfallou GZ, de Smet LCPM, Sudhölter EJR (2012) Characteristics of electrolyte-oxide-silicon sensors: pH sensing and polyelectrolyte adsorption. Sensors Actuators B Chem 168:207–213
51. Neff PA, Wunderlich BK, Klitzing R, Bausch AR (2007) Formation and dielectric properties of polyelectrolyte multilayers studied by a silicon-on-insulator based thin film resistor. Langmuir 23:4048–4052
52. Poghossian A, Abouzar MH, Sakkari M, Kassab T, Han Y, Ingebrandt S, Offenhäusser A, Schöning MJ (2006) Field-effect sensors for monitoring the layer-by-layer adsorption of charged macromolecules. Sensors Actuators B Chem 11:163–170
53. Vu XT, Stockmann R, Wolfrum B, Offenhäusser A, Ingebrandt S (2010) Fabrication and application of a microfluidic-embedded silicon nanowire biosensor chip. Phys Status Solidi A 207:850–857
54. Gorin DA, Yashchenok AM, Manturov AO, Kolesnikova TA, Möhwald H (2009) Effect of layer-by-layer electrostatic assemblies on the surface potential and current voltage characteristic of metal−insulator−semiconductor structures. Langmuir 25:12529–12534
55. Smith RN, McCormick M, Barrett CJ, Reven L, Spiess HW (2004) NMR studies of PAH/PSS polyelectrolyte multilayers adsorbed onto silica. Macromolecules 37:4830–4838
56. Andreasson J, Pischel U (2015) Molecules with a sense of logic: a progress report. Chem Soc Rev 44:1053–1069
57. Pischel U, Andreasson J, Gust D, Pais VF (2013) Information processing with molecules – quo vadis? ChemPhysChem 14:28–46
58. Katz E, Privman V (2010) Enzyme-based logic systems for information processing. Chem Soc Rev 39:1835–1857
59. Wang J, Katz E (2010) Digital biosensors with built-in logic for biomedical applications – biosensors based on a biocomputing concept. Anal Bioanal Chem 398:1591–1603
60. Katz E, Poghossian A, Schöning MJ (2017) Enzyme-based logic gates and circuits – analytical applications and interfacing with electronics. Anal Bioanal Chem 409:81–94
61. Lai YH, Sun SC, Chuang MC (2014) Biosensors with built-in biomolecular logic gates for practical applications. Biosensors 4:273–300
62. Poghossian A, Malzahn K, Abouzar MH, Mehndiratta P, Katz E, Schöning MJ (2011) Integration of biomolecular logic gates with field-effect transducers. Electrochim Acta 56:9661–9665
63. Molinnus D, Sorich M, Bartz A, Siegert P, Willenberg HS, Lisdat F, Poghossian A, Keusgen M, Schöning MJ (2016) Towards an adrenaline biosensor based on substrate recycling amplification in combination with an enzyme logic gate. Sensors Actuators B Chem 237:190–195
64. Liu J, Zhou H, Xu JJ, Chen HY (2013) Dual-biomarker-based logic-controlled electrochemical diagnosis for prostate cancers. Electrochem Commun 32:27–30
65. Katz E, Minko S (2015) Enzyme-based logic systems interfaced with signal-responsive materials and electrodes. Chem Commun 51:3493–3500
66. Molinnus D, Bäcker M, Iken H, Poghossian A, Keusgen M, Schöning MJ (2015) Concept for a biomolecular logic chip with an integrated sensor and actuator function. Phys Status Solidi A 212:1382–1388
67. Poghossian A, Katz E, Schöning MJ (2015) Enzyme logic AND-Reset and OR-Reset gates based on a field-effect electronic transducer modified with multi-enzyme membrane. Chem Commun 51:6564–6567
68. Cane C, Gracia I, Merlos A (1997) Microtechnologies for pH ISFET chemical sensors. Microelectron J 28:389–405
69. Sassolas A, Leca-Bouvier BD, Blum LJ (2008) DNA biosensors and microarrays. Chem Rev 108:109–139

70. Wei F, Lillehoj PB, Ho CM (2010) DNA diagnostics: nanotechnology-enhanced electrochemical detection of nucleic acids. Pediatr Res 67:458–468
71. Choi S, Goryll M, Sin LYM, Wong PK, Chae J (2011) Microfluidic-based biosensors toward point-of-care detection of nucleic acids and proteins. Microfluid Nanofluid 10:231–247
72. Palecek E, Bartosik M (2012) Electrochemistry of nucleic acids. Chem Rev 112:3427–3481
73. Javanmard M, Davis RW (2011) A microfluidic platform for electrical detection of DNA hybridization. Sensors Actuators B Chem 154:22–27
74. Veigas B, Fortunato E, Baptista PV (2015) Field effect sensors for nucleic acid detection: recent advances and future perspectives. Sensors 15:10380–10398
75. Wu C, Bronder T, Poghossian A, Werner CF, Bäcker M, Schöning MJ (2014) Label-free electrical detection of DNA with a multi-spot LAPS: first step towards light-addressable DNA chips. Phys Status Solidi A 211:1423–1428
76. Lu N, Gao A, Dai P, Li T, Wang Y, Gao X, Song S, Fan C, Wang Y (2013) Ultra-sensitive nucleic acids detection with electrical nanosensors based on CMOS-compatible silicon nanowire field-effect transistors. Methods 63:212–218
77. Ingebrandt S, Han Y, Nakamura F, Poghossian A, Schöning MJ, Offenhäusser A (2007) Label-free detection of single nucleotide polymorphisms utilizing the differential transfer function of field-effect transistors. Biosens Bioelectron 22:2834–2840
78. Kamahori M, Ishige Y, Shimoda M (2008) Detection of DNA hybridization and extension reactions by an extended-gate field-effect transistor: characterizations of immobilized DNA–probes and role of applying a superimposed high-frequency voltage onto a reference electrode. Biosens Bioelectron 23:1046–1054
79. Sakata T, Miyahara Y (2006) DNA sequencing based on intrinsic molecular charges. Angew Chem Int Ed 45:2225–2228
80. Hou CSJ, Godin M, Payer K, Chakrabarti R, Manalis SR (2007) Integrated microelectronic device for label-free nucleic acid amplification and detection. Lab Chip 7:347–354
81. Veigas B, Branquinho R, Pinto JV, Wojcik PJ, Martins R, Fortunato E, Baptista PV (2014) Ion sensing (EIS) real-time quantitative monitorization of isothermal DNA amplification. Biosens Bioelectron 52:50–55
82. CS W, Bronder T, Poghossian A, Werner CF, Schöning MJ (2015) Label-free detection of DNA using a light-addressable potentiometric sensor modified with a positively charged polyelectrolyte layer. Nanoscale 7:6143–6150
83. Bronder TS, Poghossian A, Scheja S, Wu C, Keusgen M, Mewes D, Schöning MJ (2015) DNA immobilization and hybridization detection by the intrinsic molecular charge using capacitive field-effect sensors modified with a charged weak polyelectrolyte layer. ACS Appl Mater Interfaces 7:20068–20075
84. Wu C, Poghossian A, Bronder TS, Schöning MJ (2016) Sensing of double-stranded DNA molecules by their intrinsic molecular charge using the light-addressable potentiometric sensor. Sensors Actuators B Chem 229:506–512
85. Braeken D, Reekmans G, Zhou C, van Meerbergen B, Callewaert G, Borghs G, Bartic C (2008) Electronic DNA hybridisation detection in low-ionic strength solutions. J Exp Nanosci 3:157–169
86. Wang J, Zhou YL, Watkinson M, Gautrot J, Krause S (2015) High-sensitivity light-addressable potentiometric sensors using silicon on sapphire functionalized with self-assembled organic monolayers. Sensors Actuators B Chem 209:230–236
87. Adam T, Hashim U (2015) Highly sensitive silicon nanowire biosensor with novel liquid gate control for detection of specific single-stranded DNA molecules. Biosens Bioelectron 67:656–661
88. Dzyadevych SV, Soldatkin AP, El'skaya AV, Martelet C, Jaffrezic-Renault N (2006) Enzyme biosensors based on ion-selective field-effect transistors. Anal Chim Acta 568:248–258
89. Schöning MJ, Poghossian A (2006) Bio FEDs (field-effect devices): state-of-the-art and new directions. Electroanalysis 18:1893–1900

90. Abouzar MH, Poghossian A, Siqueira Jr JR, Oliveira Jr ON, Moritz W, Schöning MJ (2010) Capacitive electrolyte–insulator–semiconductor structures functionalised with a polyelectrolyte/enzyme multilayer: new strategy for enhanced field-effect biosensing. Phys Status Solidi A 207:884–890
91. Beging S, Leinhos M, Jablonski M, Poghossian A, Schöning MJ (2015) Studying the spatially resolved immobilisation of enzymes on a capacitive field-effect structure by means of nanospotting. Phys Status Solidi A 212:1353–1358
92. Mauser T, Dejugnat C, Sukhorukov GB (2004) Reversible pH-dependent properties of multilayer microcapsules made of weak polyelectrolytes. Macromol Rapid Commun 25:1781–1785
93. Xie AF, Gramick S (2002) Local electrostatics within a polyelectrolyte multilayer with embedded weak polyelectrolyte. Macromolecules 35:1805–1813
94. Culver JN, Brown AD, Zang F, Gnerlich M, Gerasopoulos K, Ghodssi R (2015) Plant virus directed fabrication of nanoscale materials and devices. Virology 479–480:200–212
95. Fan XZ, Pomerantseva E, Gnerlich M, Brown AD, Gerasopoulos K, McCarthy M, Culver JN, Ghodssi R (2013) Tobacco mosaic virus: a biological building block for micro/nano/bio systems. J Vac Sci Technol A 31:050815
96. Bäcker M, Koch C, Eiben S, Geiger F, Eber F, Gliemann H, Poghossian A, Wege C, Schöning MJ (2016) Tobacco mosaic virus as enzyme nanocarrier for electrochemical biosensors. Sensors Actuators B Chem 238:716–722

Silicon Nanowire Field-Effect Biosensors

Dipti Rani, Vivek Pachauri, and Sven Ingebrandt

Abstract Silicon (Si), still by far the most important semiconductor material in this day and age, is dominating the microelectronic industry for decades. Due to well-studied and firmly established processing methods, Si also serves as a robust technology platform for the development of new devices in different scientific areas such as optics, photovoltaics and sensor applications. One-dimensional forms of Si such as Si nanowires (SiNW), due to their high surface-to-volume ratio, well-controlled material properties and surfaces, are at the forefront of miniaturized sensor devices. In the recent years, many bottom-up and top-down methods of SiNW fabrication were established and utilized for state-of-the-art sensor platforms towards emerging sensor applications. In this chapter, we will discuss the evolution of the classical ion-sensitive field-effect transistor (ISFET) concept into its nano-scale versions. Firstly, we describe the basis of the ISFET operation and different readout methods for sensing of biomolecules of different sizes and surface charges. Then, we focus on SiNW sensor platforms that were used for the detection of various chemicals and biomolecules. Significant advances were made towards realizing single-cell assays as well as novel applications such as organ-on-a-chip. We discuss these new developments and the different detection methods utilized for SiNW sensors. Differences in bottom-up and top-down fabrication methods are summarized in brief. Further, the intrinsic limitations associated with SiNW sensors so far hindering their commercialization are discussed. In the end, other competing technologies and future prospects for the application of SiNW sensors are discussed.

D. Rani and V. Pachauri
Biomedical Signalling Group, Informatics and Microsystem Technology, University of Applied Sciences Kaiserslautern, Zweibrücken, Germany

S. Ingebrandt (✉)
Biomedical Signalling Group, Informatics and Microsystem Technology, University of Applied Sciences Kaiserslautern, Zweibrücken, Germany

Institute of Materials in Electrical Engineering 1, RWTH Aachen University, Aachen, Germany
e-mail: sven.ingebrandt@hs-kl.de; ingebrandt@iwe1.rwth-aachen.de

M. J. Schöning, A. Poghossian (eds.), *Label-Free Biosensing: Advanced Materials, Devices and Applications*, Springer Series on Chemical Sensors and Biosensors (2018) 16: 27–58
DOI 10.1007/5346_2017_19,
Published online: 10 April 2018

Keywords Electrical double layer, Ion-sensitive field-effect transistors, Silicon nanowires, Surface potential, Threshold voltage

Contents

1 Introduction: Ion-Sensitive Field-Effect Transistors

Piet Bergveld is considered as the pioneer in using silicon field-effect transistor (FET) devices for sensing applications in liquid environments. He demonstrated the use of a surface-modified FET for the detection of ions in an electrolyte solution by monitoring the changes in the current flow through the device at varying pH values of the solution. He named these devices ion-sensitive field-effect transistors (ISFETs) [1]. In the decades following this invention, ISFETs, due to their small sizes and easiness of operation, became one of the best candidates for ion-sensing applications in general. The sensing mechanism of an ISFET is governed by the electrical properties of the transistor and the electrical potential at the solid-liquid interface of the gate oxide surface, which are detailed in this chapter.

An ISFET is a classical metal-oxide-semiconductor field-effect transistor (MOSFET), where the typical metal/polysilicon gate electrode is replaced by an electrolyte solution in direct contact to the gate insulator and electronically contacted by a reference electrode. Similar to the classical MOSFET, an ISFET consists of three terminals – source, drain and electrochemical gate electrode. A schematic of a special form of a *p*-type Si ISFET is shown in Fig. 1. This special device is realized on a silicon-on-insulator (SOI) wafer having the top layer Si separated from the handle Si wafer by a buried oxide. The top Si works as the transducer material, acting as a channel between the *p*-doped source and drain contacts, which are further metallized and contacted to the outside. The Si channel is covered by a thin gate oxide (e.g. 7–10 nm SiO_2 in the case of this SOI ISFET), which is in contact to the electrolyte solution. Usually, the gate oxide thickness is scaled with transistor size, like in semiconductor industry with values of several 100 nm for large ISFETs down to a limit of roughly 5–7 nm for nanoscale ISFETs. An electrical double layer (EDL) is spontaneously formed at the solid-liquid interface. The potential at the gate oxide surface is called the surface potential

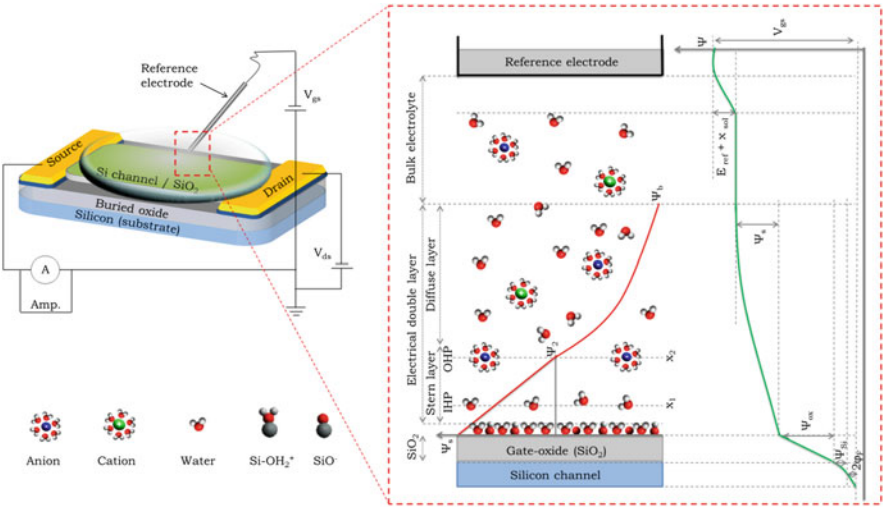

Fig. 1 A Si ISFET is shown in the schematic (left) with a detailed illustration of the solid-liquid interface (inset): (Left) The Si ISFET is realized on an SOI substrate and consists of three terminals – source and drain electrodes connecting the Si channel, which is covered by a thin gate oxide (SiO_2). Drain-source voltage V_{ds} and gate-source voltage V_{gs} are applied, and the drain-source current I_{ds} is measured by a current amplifier (Amp.). The gate-source voltage is applied to a reference electrode suspended in electrolyte solution over the gate oxide. (Right) Schematic of the Gouy-Chapman-Stern model of the electrical double layer composed of the Stern layer and the diffuse layer. Inside the Stern layer the inner Helmholtz plane (IHP at x_1) and the outer Helmholtz plane (OHP at x_2) are defined as explained in the text. The surface potential Ψ_s drops linearly inside the Stern layer and exponentially in the diffuse layer. The potential at this plane is called the Zeta-potential Ψ_2. Two solid-liquid interfaces are included at the gate oxide SiO_2/electrolyte interface (bottom) and at the reference electrode/electrolyte interface (top). The schematic is also showing the potential distribution within the ISFET – the applied V_{gs} drops at the reference electrode/electrolyte interface ($E_{ref} + \chi_{sol}$), within the electrical double layer near the oxide/electrolyte interface (Ψ_s), within the insulator (Ψ_{ox}) and due to depletion of charge carriers also within the Si (Ψ_{Si}). All terms are described in the text

(Ψ_s). The surface potential depends on chemical reactions at the gate oxide surface and is given in a first approximation by the ratio of the net surface-charge density (σ_s) and the differential capacitance (C_d) of the EDL, $\Psi_s = \sigma_s/C_d$. A surface reaction or binding event of ions or charged molecules to the gate oxide surface results in a change in Ψ_s, which can be directly detected as a change in the threshold voltage (V_{th}) of the ISFET. In a Si ISFET, the surface hydroxyl groups (Si-OH for SiO_2 as gate oxide) can undergo protonation or deprotonation depending on the pH value of the electrolyte solution. This protonation/deprotonation leads to a rearrangement of ionic constituents of the electrolyte and results in the formation of an EDL up to a certain distance from the interface as shown in Fig. 1. The formation of the EDL can be explained by sophisticated models such as the Gouy-Chapman-Stern theory. The EDL enforces a build-up of a surface potential Ψ_s at the oxide surface, which is then the basis behind the pH-sensing mechanism of an ISFET. The surface potential Ψ_s

is a function of the pH value of the electrolyte solution, $\Psi_s = f(\text{pH})$ [2]. It is known from the site-binding model that the acid/base reactions take place between the gate oxide surface hydroxyl groups (Si-OH) and the hydrogen ions (H^+) in the electrolyte solution, which can be described by two dissociation constants K_a and K_b as follows:

$$\text{Si} - \text{OH}_2^+ \rightleftharpoons \text{Si} - \text{OH} + \text{H}^+, \quad \text{with } K_b = \frac{[\text{Si} - \text{OH}][\text{H}^+]_s}{[\text{Si} - \text{OH}_2^+]} \tag{1}$$

$$\text{Si} - \text{OH} \rightleftharpoons \text{SiO}^- + \text{H}^+, \text{with } K_a = \frac{[\text{SiO}^-][\text{H}^+]_s}{[\text{Si} - \text{OH}]} \tag{2}$$

where $[H^+]_s$ (also called the activity of the H^+ ions at the surface) is the surface concentration of H^+ ions and the other quantities in the square brackets represent the number of surface sites per unit area.

The potential at the solid-liquid interface is governed by the charges and its strength decays away from the surface with zero potential in the bulk of the solution as depicted in Fig. 1 (right, red curve). Due to the protonation/deprotonation of hydroxyl groups at the oxide surface, there is difference in H^+ ion concentration at the solid-liquid interface and in the bulk electrolyte solution [3]. The concentration of H^+ ions at the surface ($[H^+]_s$) can be related with the bulk H^+ ions concentration ($[H^+]_b$) by the Boltzmann distribution:

$$[\text{H}^+]_s = [\text{H}^+]_b \exp\left(-\frac{q\Psi_s}{kT}\right) \tag{3}$$

$$\text{pH}_s = \text{pH}_b + \frac{q\Psi_s}{2.3kT}, \tag{4}$$

with

$$\text{pH}_s = -\log_{10}[\text{H}^+]_s, \quad \text{pH}_b = -\log_{10}[\text{H}^+]_b \tag{5}$$

where q is the elementary charge, k is the Boltzmann constant and T is the absolute temperature.

The total density of surface sites (N_s) at the gate oxide is given by

$$N_s = [\text{Si} - \text{OH}] + [\text{SiO}^-] + [\text{Si} - \text{OH}_2^+] \tag{6}$$

The parameters K_a, K_b and N_s depend strongly on the type of gate insulator.

The surface-charge density σ_s is given by the difference in the number of positively charged groups and negatively charged groups per unit area [4]:

$$\sigma_s = q\left([\text{Si} - \text{OH}_2^+] - [\text{SiO}^-]\right) = qN_s\left(\frac{[\text{H}^+]_s^2 - K_aK_b}{K_aK_b + K_b[\text{H}^+]_s + [\text{H}^+]_s^2}\right) = -q[B] \tag{7}$$

At the point of zero charge ($pH_{pzc} = \frac{pK_a + pK_b}{2}$), the number of positively charged groups equals the number of negatively charged groups giving a zero net charge, $[B] = \sigma_s = 0$. For instance in case of SiO_2 as gate oxide, the point of zero charge is $pH_{pzc} = 2$.

Dividing Eq. (7) with pH_s and differentiating gives

$$\frac{\delta\sigma_s}{\delta pH_s} = -q\frac{\delta[B]}{\delta pH_s} = -q\beta_{int} \tag{8}$$

where β_{int} is the intrinsic buffer capacity, i.e. a measure of the charging capability of the oxide surface with changes in the pH value of the solution. It depends only on the intrinsic properties of the surface, i.e. N_s, K_a and K_b.

At the EDL, an equal amount of charge density σ_{EDL} with opposite polarity appears on the electrolyte side of the layer due to the charge-neutrality condition. According to the Gouy-Chapman-Stern model, the electrolyte side of the EDL is composed of several layers depending on the distribution of ionic constituents of the electrolyte – called the Helmholtz or Stern layer and the diffuse layer (DL) [3]. In the very inner layer, some surface adsorbate ions and molecules may get close to the gate oxide. An imaginary plane passing through the loci of the electrical centres of these adsorbed ions is called the inner Helmholtz plane (IHP) – which is at a distance of x_1 from the gate oxide (Fig. 1). The surface-charge density σ_s on the gate oxide is counterbalanced by the solvated ions, which can approach the oxide surface only to a distance x_2. The imaginary space between the IHP and the loci of nearest available solvated ions is called the outer Helmholtz plane (OHP). The concentration of the solvated counterions decreases from the OHP to the bulk of the electrolyte, forming a DL. Since the interaction between the surface charge and the solvated counterions is via electrostatic force, a thinner DL is related to a higher ionic strength electrolyte due to a stronger screening effect. As the distance from the gate oxide surface towards the electrolyte solution increases, the potential drops in roughly linear inside the Stern layer. After this the potential decreases exponentially into the DL and, finally, approaches zero in the bulk solution (Ψ_b) (Fig. 1 right, red curve). The potential, which is present at the interface between the immobile ions of the Stern layer and the mobile ions of the DL, is called Zeta-potential (Fig. 1, Ψ_2). The distance from the oxide surface in the electrolyte solution, where the potential drops to 1/e of its value at the gate oxide, is called the Debye length (λ_D). For a given electrolyte solution, λ_D can be calculated by

$$\lambda_D = \sqrt{\frac{\in_0 \in_r kT}{2q^2 P}} \quad \text{where } P = \frac{1}{2}\sum c_i z_i^2 \tag{9}$$

where ε_0 is the vacuum permittivity, ε_r is the dielectric constant of the electrolyte solution, P is the ionic strength of the electrolyte and c_i and z_i are the concentration and valence of the ions in the electrolyte solution.

The surface-charge density σ_s is balanced by charges in the electrolyte side of EDL (σ_{EDL}) with no counterions in the IHP (as shown in Fig. 1) [3]:

$$\sigma_s = -\sigma_{\mathrm{EDL}} = \sigma_{\mathrm{OHP}} + \sigma_{\mathrm{DL}} \tag{10}$$

where σ_{OHP} and σ_{DL} represent the charge densities in the OHP and DL, respectively.

Alternatively, the double-layer charge can be related to the double-layer capacitance (C_{EDL}) by

$$\sigma_s \approx C_{\mathrm{EDL}} \Psi_s \tag{11}$$

$$\frac{\delta\sigma_s}{\delta\Psi_s} \approx C_d \tag{12}$$

with C_d the double-layer capacitance. Combining Eqs. (8) and (12), the dependence of Ψ_s on the pH_b can be obtained as

$$\frac{\delta\Psi_s}{\delta \mathrm{pH}_b} = -2.3\frac{kT}{q}\alpha, \text{and } \alpha = \frac{1}{1 + 2.3\frac{kTC_d}{q^2\beta_{\mathrm{int}}}} \tag{13}$$

where α is a dimensionless sensitivity parameter with a value varying between 0 and 1. For high β_{int} with low C_d values, α will be close to 1, and highest pH sensitivity can be expected. From this equation, the upper limit of the pH sensitivity of a Si ISFET, called the Nernst limit, can be calculated as 59.2 mV/pH at 25°C with $\alpha = 1$. For Si ISFET pH sensors, the best gate insulator is tantalum oxide as its β_{int} value is highest known for dielectrics. It gives nearly ideal pH response, and it is inert to changes in the ionic strength of the solution.

In a Si ISFET shown in Fig. 1, the reference electrode in contact with the electrolyte solution is used to modulate the charge-carrier density in the transducer channel by applying a gate voltage (V_{gs}). As shown in the inset in Fig. 1 (right side), the V_{gs} successively drops at the reference electrode/electrolyte interface, the EDL near the gate oxide/electrolyte interface, the gate-oxide layer and at the Si layer under the gate oxide [5]. The individual potential drops at the different interfaces depend on the type of reference electrode, the electrolyte-solution conductance, the gate-oxide charges and the doping level of the Si layer below the gate oxide [2]. The gate-oxide charges include fixed charges in the oxide (Q_{ox}), at the oxide-Si interface (Q_{ss}) and the depletion charges in the Si (Q_B), respectively. Additionally, the doping level of the Si layer defines the Si work function (Ψ_{Si}) and the change in potential at the Si surface ($2\Phi_F$) that is required to initiate the inversion of charge carriers (see Fig. 1, right). In our particular device example, Φ_F is the difference in Fermi level of the intrinsic Si channel and the *p*-doped Si layer in the source and drain regions.

As an example, Fig. 2 illustrates a scanning electron microscopy (SEM) image of a SiNW device that consists of eight individually addressable SiNWs with a common source and individual drain contacts. The device was realized on an SOI

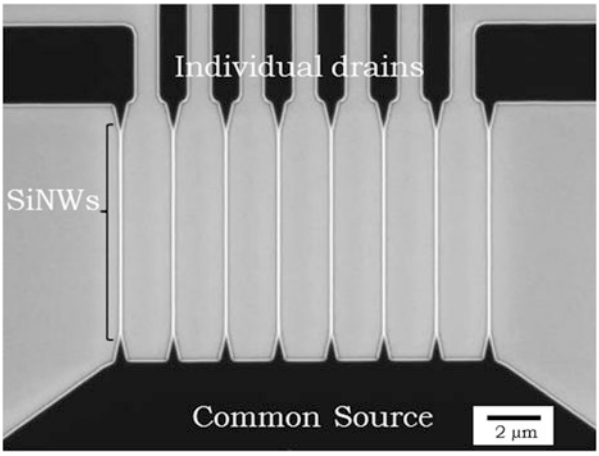

Fig. 2 SiNW device with eight nanowires (SEM image): The nanowires were realized on an SOI wafer and etched out of the top silicon layer similar to the schematics shown in Fig. 1 (dark areas are the silicon structures). Eight individually addressable nanowires are shown with eight drain contacts (from top) sharing a common source contact (bottom). Nanowires are 8 µm long having a spacing of 2 µm and a width of 100 nm [6]

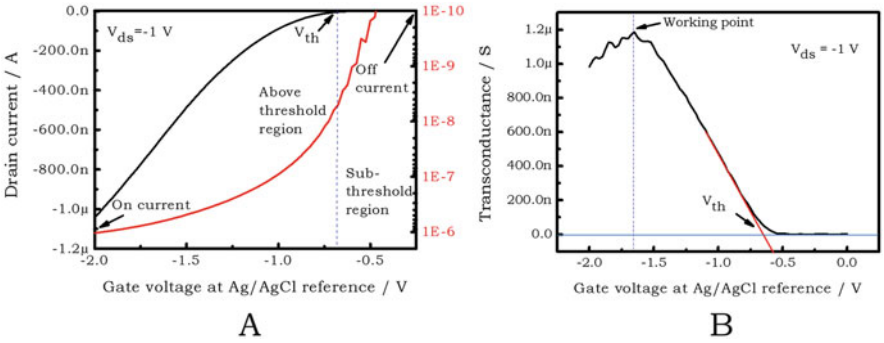

Fig. 3 Operation of a SiNW ISFET for sensing in liquids: (**a**) The graph displays the drain-source current I_{ds} values against the voltage applied at the reference electrode (V_{gs}) in linear (black curve) and in log scale (red curve). It is named the transfer characteristics of this typical *p*-type, enhancement-mode SiNW ISFET. (**b**) The transconductance curve can be numerically derived from the transfer characteristics of the SiNW ISFET. For sensing experiments, the working point of the SiNW ISFET is chosen at the highest transconductance value as shown by the vertical, dashed line

wafer using a top-down nanolithography process, which is described in brief in the next sections [6].

Figure 3a shows a typical transfer-characteristic curve for this *p*-type, enhancement-mode SiNW ISFET, where the black and red curves of the graph represent the drain current (I_{ds}) values against V_{gs} in a linear and a log scale,

respectively. Here, the drain-source current I_{ds} was measured as a function of V_{gs} ranging between 0 to −2 V and at a fixed drain-source bias $V_{ds} = -1$ V. The SiNW device behaves like a long-channel FET device. One can see that for this *p*-type SiNW ISFET, there is no current flow in the channel at $V_{gs} = 0$. This is caused by the fully depleted area in the SiNW channel, and the situation is called the "off state" of the device. The decrease of V_{gs} results in an increase of the charge-carrier density in the nanowire. At a certain front-gate voltage V_{gs}, the charge carriers can flow through the channel, and this point is characterized as the threshold voltage (V_{th}) marking the onset of the drain-source current I_{ds} similar to a typical Si ISFET. There are various methods to define the V_{th} from an actual measurement of a Si ISFET [7]. The V_{th} of a Si ISFET is theoretically given by the following (Eq. (2)):

$$V_{th} = E_{ref} - \Psi_s + \chi_{sol} - \frac{\Psi_{Si}}{q} - \frac{(Q_{ox} + Q_{ss})}{C_{ox}} - \frac{Q_B}{C_{ox}} + 2\Phi_F \tag{14}$$

where χ_{sol} defines the surface-dipole potential of the electrolyte, which is assumed to be constant, and C_{ox} represents the capacitance of the gate-oxide layer.

All other components are also approximated to be constant in Eq. (12), with Ψ_s the only variable. The V_{th} of a Si ISFET depends on the change in surface potential ($\Delta\Psi_s$), only when the potential at the reference electrode (E_{ref}) is stable. For this purpose, typically an Ag/AgCl reference electrode can be used, which possesses an electrode reaction given as [8]

$$AgCl(s) + \bar{e} \rightleftharpoons Ag(s) + Cl^-(aq) \tag{15}$$

with (*s*) referring to the solid form and (aq) referring to the solvated form. An Ag/AgCl reference electrode usually contains an internal filling of 3M potassium chloride solution with a small addition of silver nitrate ($AgNO_3$), which provides an electrochemically stable interface with the reference electrode via a well-defined redox reaction between the silver metal (Ag) and its salt (AgCl). The highly concentrated KCl solution ensures a minimum dependency of the electrode from eventual chloride concentration changes in the test solution and is usually in contact with this solution via an ion conductor bridge.

Before using the Si ISFETs in sensing applications, the characterization of V_{th} is very crucial, since it represents the change in surface charge or the effective charge-carrier density of the device. The shift in V_{th} can be taken as an indicator for changes happening at the transducer surface. For example, binding of biomolecules or ions from the electrolyte solution onto the transducer surface will result in a change in the net surface-charge density on the transducer surface, which in turn will influence the V_{th} of the Si ISFET.

When V_{gs} is higher than the threshold voltage, i.e. $V_{gs} > V_{th}$, the transistor is weakly inverted. The subthreshold current is in this case diffusion-limited and

increases exponentially with V_{gs} as shown in Fig. 3a. Here, the drain-source current I_{ds} is defined as

$$I_{ds} \propto e^{2.3\frac{V_{gs}-V_{th}}{SS}} \tag{16}$$

where SS is the subthreshold slope (also called subthreshold swing, $SS = \left(\frac{\partial V_{gs}}{\partial \log I_{ds}}\right)$) of the Si ISFET. A small SS is desirable as it implies that the device can switch rapidly from the "off state" to the "on state" with a small change in gate potential. When the transistor is operated in its subthreshold region, the current sensitivity is higher, i.e. $\Delta I_{ds}/I_{ds}$ as the drain current depends exponentially on V_{gs}.

For an enhancement-mode, *p*-type Si ISFET, when $V_{gs} < V_{th}$ and for small V_{ds} (where $|V_{ds}| \ll 2(|V_{gs} - V_{th}|)$), the drain-source current I_{ds} is

$$I_{ds} = \frac{W}{L}\mu_p C_{ox}\left(V_{gs} - V_{th}\right)V_{ds} \tag{17}$$

where W and L are the width and length of the semiconducting channel and μ_p is the hole mobility. Therefore, for small drain-source voltages V_{ds}, the current-voltage relation is linear for a given gate-source voltage V_{gs}, and the transistor behaves as a resistor.

The ratio of change in drain current as a function of gate voltage, i.e. the efficiency of the gating effect or amplification, is termed as the transconductance g_m of the Si ISFET, which is given by

$$g_m = \frac{\partial I_{ds}\left(V_{gs}\right)}{\partial V_{gs}}\Bigg]_{V_{ds}=\text{constant}} \tag{18}$$

As a first-order numerical derivative of the transfer characteristic curve shown in Fig. 3a, the g_m of the same device is plotted in Fig. 3b. A higher g_m value reflects a higher sensitivity of the transistor as it reflects a larger change in I_{ds} for a given change in V_{gs} [9]. The g_m can be calculated from the first derivative of the transfer-characteristic curve, and in our works the V_{gs} at the maximum g_m value is typically chosen as the working point of the Si ISFETs. This sensitivity to gate-potential changes should not be confused with the sensitivity of the biosensor, since many other aspects such as the biological receptor layer play an important role.

2 Sensor Operation and Readout Strategies

From the above discussion, it is obvious that Si ISFETs can be used for the detection of chemical events taking place at the transducer surface. The same concept can be applied to detect biological molecules, where a receptor layer on top of the transducer surface enables a specific binding of target-analyte biomolecules from a test solution. This selective binding has been so far exploited for

virtually all biomolecular recognition types such as deoxyribonucleic acids (DNAs), aptamers, proteins, enzymes, living cells, etc. [10–15]. The efficiency of the sensor platform for analyte detection depends on the capability of the receptor-analyte pairs to induce a change in the surface-charge density on the transducer layer. There are mainly two alternative approaches to explain the changes in surface potential upon binding of charged biomolecules. A direct effect of modulating the surface-charge density of an oxide-liquid interface upon binding of charged molecules can be described by the Poisson-Boltzmann theory considering a charged biomolecular layer on top of the sensor surface [16–19]. An alternative approach is an indirect effect, where the ionic cloud composed of counterions surrounding the charged biomolecules at the surface is detected by the oxide surface. The binding of charged biomolecules changes the composition of this cloud and thereby modulates the ion concentration near the surface. With this the surface potential is indirectly modulated, which, however, leads to very similar sensing effects [20]. With the latter theory, one could also explain why the detection of larger biomolecules – clearly larger than the Debye length λ_D – could still be possible by the potentiometric or direct current (DC) readout method. In either case the recording of the V_{th} shift of a Si ISFET can determine the binding of biomolecules to the sensor surface, but recordings will be different for different types of analyte biomolecules depending on the size, charge, arrangement, distance and the composition of the surrounding electrolyte solution in terms of ionic strength and pH value. Usually, for small, charged molecules with sizes in the range of the thickness of the EDL, a DC-readout approach displays a very strong electrical effect. For this, short DNA molecules eventually captured by neutrally charged, peptide nucleic acid molecules (PNA) are showing the largest responses. However, for larger biomolecules the DC-readout methods exhibit limited efficiency and require additional measures to detect the binding events occurring at much farther distance in the bulk – away from the solid-liquid interface. This effect is called the Debye limitation and it is a major issue in all biosensor concepts using ISFET devices. In the following, we will discuss two fundamental readout methods of Si ISFETs for the detection of biomolecules – potentiometric and impedimetric readout [9].

2.1 Surface-Charge Sensing

The detection of small molecules carrying a charge can be explained by a similar model as for the pH sensing, just with an addition of the charge-screening effect by the surrounding counterion cloud. In case of pH sensing, the reactive groups (–OH) lie very close to the solid-liquid interface, i.e. clearly within the Debye length, which for physiological buffers or biological fluids such as human blood serum is below 1 nm. Therefore, the choice of an appropriate receptor molecule is essential for surface charge-based detection strategies. The biorecognition layer should be as thin as possible to locate the receptor-analyte binding events into close vicinity of the gate-oxide surface at best within the Debye length λ_D. Smaller receptor

molecules such as nucleic acids and aptamers are an ideal choice for this surface charge-based, potentiometric readout as explained in Fig. 4a. When short, single-stranded DNA (ssDNA) was used as a receptor layer on the transducer surface, some nucleotides lie well within λ_D even in physiological buffer concentrations [21]. In such DNA assays the negative charges of the phosphate backbone of the DNA molecules are sensed. An analyte-DNA binding to this receptor layer can therefore alter the surface-charge density on the gate-oxide interface of the transducer and is resulting in a detectable shift in V_{th} of the Si ISFET. However, the signal strength to the analyte-DNA binding depends strongly on its distance from the transducer surfaces [22]. It has been shown that in diluted buffers, when the charge-screening effect is minimized and λ_D is extended to more than 10 nm, the shifts become much larger. However, in such diluted buffer solutions, the stabilization of the solutions' pH value and also the control of the solution potential by the Ag/AgCl reference electrode are difficult. Even minute changes of the ionic composition might cause unstable and unreliable sensor responses – especially in the impedimetric readout mode as discussed below. In the case of larger biomolecules such as proteins, which consist of sequences of charged amino acids conformed into different parts of the proteins, the situation is much less clear compared to DNA molecules. The net charge of such larger molecules and the distribution of the charges along their entire surface depend on various factors such as the type of amino acids, on the amino acid sequence, on their three-dimensional conformation and on the ionic strength and pH value of the electrolyte solution. Most of the volume of larger molecules such as antibodies (Fig. 4) is expanded beyond λ_D. It can therefore be assumed that in physiological solutions, the surface charges on the

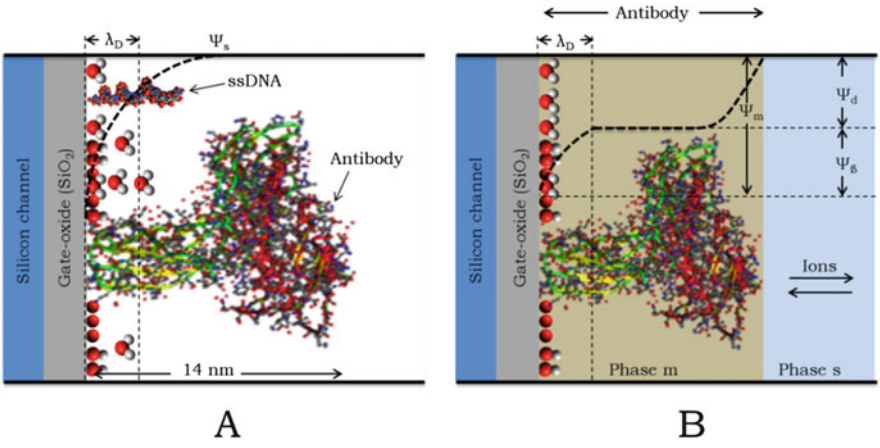

Fig. 4 Representation of the bio-functionalized layers on a Si ISFET, the electrical readout method and its limitations: (**a**) A simplistic picture of surface-potential change caused by the binding of the molecules small and large in size as compared to the Debye length. (**b**) Schematic explaining the change of the surface-potential drop over the solid-liquid interface and the bio-immobilized layers made of large molecules leading to the Donnan potential. All the terms are described in the text

antibodies (with sizes of about 10 nm) would be completely shielded by counter-ions. The direct detection in physiological fluids with a small Debye length of less than 1 nm is then extremely challenging. However, in some works published in the field, ISFETs do show responses also to larger molecules such as antibodies in DC-readout mode of the sensors. It can be anticipated that eventually secondary effects of the change of the surface-near ionic composition upon biomolecules binding play a role [20, 23]. In any case, the detection of proteins by the above-mentioned DC-readout method is complicated, and one can only assume that due to the protein receptor-analyte binding, there are some other factors influencing the net surface-charges change ($\Delta\sigma_s$) on the gate oxide, resulting in a detectable surface-potential change ($\Delta\Psi_s$). It is generally difficult to determine the exact charge of protein molecules bound on the gate-oxide surface due to the difference in pH at the surface and in the bulk of the electrolyte solution (as it was described above and given by Eq. (3)) [24]. Here, various effects were proposed to explain the changes observed in the electronic signals upon binding of proteins. A notable effect called Donnan potential has been proposed to explain an additional potential change caused by the binding of proteins. The protein receptors are considered as a membrane layer that is deposited onto the gate oxide and is in a Donnan equilibrium. As shown in Fig. 4b, the phase "m" represents the protein membrane and phase "s" the solution.

Due to the presence of fixed charges in the protein layer, there would be a diffusion of ions between the two phases, which gives rise to a potential drop across the interface Donnan potential Ψ_d. In an equilibrium condition, the electrochemical potential of ions in phase "m" and "s" should be equal, and Ψ_d can be given by

$$\Psi_d = \Psi_m - \Psi_\beta = \frac{kT}{q} \ln \frac{\sqrt{4c_s^2 + c_x^2} + c_x}{2c_s} \tag{19}$$

where Ψ_m and Ψ_β represent the electrical potentials in phase "m" and "s", respectively. The value c_s represents the concentration of salt in the electrolyte and c_x the effective, fixed charge concentration inside the protein membrane [24].

The value of c_x changes upon binding of the analyte proteins to the receptor proteins on the gate-oxide surface leading to a change in the Donnan potential. Therefore, the change in V_{th} of a Si ISFET during protein binding can be regarded as the result of the change in Donnan potential ($\Delta\Psi_d$) at the protein membrane/solution interface and the change in surface potential ($\Delta\Psi_s$) at the oxide/protein membrane interface due to change of the pH value in phase m (as given by Eq. (13)). This finally results in a total change of the threshold voltage:

$$\Delta V_{\text{th}} = (1 - \alpha)\Delta\Psi_d \tag{20}$$

where α is the same dimensionless sensitivity parameter with a value varying between 0 and 1 as was discussed in Eq. (13).

Thus, there is a total change in V_{th} upon binding of proteins at the gate oxide only under the condition of a nonideal Nernst response ($\alpha < 1$) of the gate-oxide

material. This condition is in contrast to the situation when the ISFET device should be optimized for ideal pH sensing. The condition for a large influence of the Donnan effect is for sure fulfilled when SiO_2 is used as a gate oxide on SiNW devices, which is the typical case for most of the devices presented in literature. More recently, it was demonstrated that even analyte proteins located clearly outside the Debye length λ_D may also influence changes in V_{th} [25].

Although potentiometric readout methods were reported for sensitive detection of versatile molecular species such as nucleic acids, proteins, macromolecules, bacteria, viruses and living cells and even mapping of neural circuits, etc., the use of this potentiometric readout mode alone remains elusive for real applications in biological fluids concerning the detection of large molecules, cells and larger living systems [12–14, 26–29]. This detection strategy is highly influenced by changes in side parameters such as temperature, ionic strength and pH value of the test solution and conformation of the bioreceptor layer and/or the analyte molecules. Therefore, it is very important to control these side parameters as precisely as possible during detection. In this field of biosensor research, it is a common approach that sensor arrays are used, where a differential readout of electronically identical sensor spots on a chip is done. Typically the sensor spots are coated with different types of receptor molecules to realize a specific capture of analyte molecules. With this approach side effects can be minimized, by assuming that each sensor spot reacts similarly to side parameters such as pH, ionic strength and temperature changes and by further assuming that the unspecific binding of background molecules is similar to each spot as well. Under such idealized circumstances, more specific biomolecule detection can be done. Another strategy in the field of biosensing is to use multiple transducer principles, which have different receptiveness for influences of a particular side parameter. Then, a combinatorial data analysis can be applied leading to hopefully more specific, reliable and robust biosensor recordings.

2.2 Beyond Surface-Charge Sensing

In the previous section, we learned that potentiometric readout methods for Si ISFETs are limited in their sensor performance by the requirement that the biomolecular binding events should happen within the Debye length λ_D. This limitation can be overcome by an alternating current (AC) or impedimetric detection mode as an alternative readout method. In impedimetric detection, the overall impedance of a Si ISFET is tested, while an AC signal is applied to the reference electrode. The response of the Si ISFET to this AC signal applied to the gate input depends on the frequency of the applied signal. The binding of biomolecules onto the solid-liquid interface results in a change in input impedance of the device leading to a change in the frequency response of the Si ISFET output characteristics such as impedance or g_m [9]. A Si ISFET with a physically bound membrane (e.g. proteins or DNA) on top of a gate insulator can be represented by an equivalent electronic circuit as shown in Fig. 5a [30]. In this circuit, the membrane impedance can be divided into

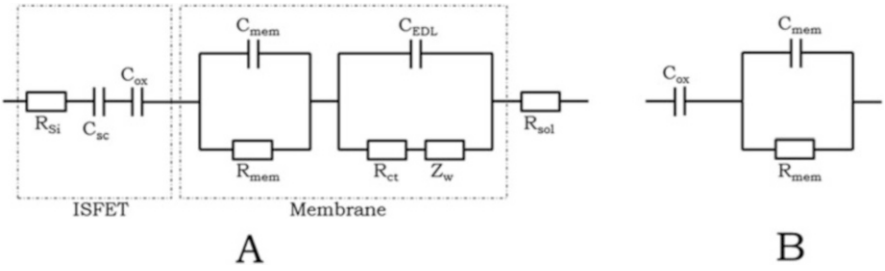

Fig. 5 Implementation of an impedimetric readout with Si ISFETs: (**a**) Equivalent circuit of a Si ISFET having gate oxide covered with a membrane. (**b**) Simplified equivalent electronic circuit of a Si ISFET with a bio-functionalized layer or a membrane

two parts: the biological membrane impedance in series with the interfacial (membrane/electrolyte) impedance. The biological membrane impedance can be described by a combination of a resistance (R_{mem}) and a capacitance (C_{mem}) in parallel. The membrane/electrolyte interfacial impedance is described by the double-layer capacitance (C_{EDL}) in parallel with a series combination of the charge-transfer resistance (R_{ct}) at the interface and the Warburg impedance (Z_w) due to the limited diffusion of ions. The Si ISFET contributes to the whole impedance by the Si-electrode resistance (R_{Si}) in series with a space-charge capacitance (C_{sc}) and the capacitance of the gate oxide (C_{ox}). At higher frequencies $\geq$5 Hz, this electronic circuit can be simplified by a configuration as shown in Fig. 5b, where the circuit consists of a series combination of C_{ox} with an element consisting of C_{mem} and R_{mem} in parallel. This simplified circuit can be characterized by a transfer function, $H(\text{j}\omega)$, which is the mathematical relation between the input and the output signals of a frequency-dependent system. When a DC voltage is applied between gate and source electrodes (V_{gs}), there is a flow of current (I_{ds}) between the drain and source electrodes. When this gate voltage is superimposed with a small sinusoidal voltage δV_{gs}, it leads to a frequency-dependent drain current δI_{ds}, which in turn results in a frequency dependence of the transconductance, $g_m = \delta I_{\text{ds}}/\delta V_{\text{gs}}$ [30, 31]. The output voltage, V_{out}, of the operational amplifier is related to I_{ds}, g_m and V_{gs} by

$$V_{\text{out}} = -R_f I_{\text{ds}} = -R_f g_m V_{\text{gs}} \tag{21}$$

where R_f is the feedback resistance of the operational amplifier.

When a biological membrane (e.g. proteins or DNA) is deposited on the gate-oxide surface, the applied gate-source voltage drops at the membrane and the gate oxide. Therefore, the applied V_{gs} is larger than the effective potential difference

between the gate and source, and a frequency-dependent component, the transfer function, $H(j\omega)$, needs to be included as a multiplication factor of V_{gs}:

$$V_{out} = -R_f g_m H(j\omega) V_{gs} \tag{22}$$

$$H(j\omega) = \frac{1 + j\omega R_{mem} C_{mem}}{1 + j\omega R_{mem}(C_{mem} + C_{ox})} \tag{23}$$

for this simplified model.

Thus, with the impedimetric readout of Si ISFETs, it is possible to complement the potentiometric readout with an alternative transducer approach. As discussed above, the potentiometric readout is generally influenced by side parameters such as pH, temperature and ionic composition of the test solution, leading to direct effects on V_{th}. The impedimetric readout is largely dependent on the ionic strength of the solution but less influenced by surface-charge changes originating from pH changes in the solution. The combination of both procedures might be beneficial to overcome limitations of the potentiometric methods [32, 33].

It has to be noted here that the simplified circuit shown in Fig. 5 does not include parasitic components of the chip design and the recording circuit. A complete description of the recorded impedance spectra is challenging and clearly beyond the scope of this book chapter. In a recent work, an analytical model for the adhesion of a single tumour cell to the gate surface of a micro-sized Si ISFET was presented. This method can be utilized for the detection of cell adhesion on an individual cell level and to detect influences of anti-cancer drugs to the cells on a Si ISFET. For the analytical modelling of the recorded impedance spectra most importantly also the parasitic contributions of contact-line impedance and capacitance, amplifier bandwidth and reference-electrode type and position need to be included [34, 35]. For a more detailed discussion of the method and the models to explain the impedance readout with ISFET or SiNW devices, interested readers should consult the references [30, 31, 34, 35].

3 Silicon Nanowire Ion-Sensitive Field-Effect Transistors

With the introduction of scalable nanofabrication methods in Si technology, miniaturization of ISFETs became predominant for the development of electronic sensor platforms for chemical and biosensor applications. In comparison to conventional ISFETs, the use of nanoscale sensors provides distinct advantages such as increased packaging density and possibility to integrate with lab-on-a-chip (LoC) concepts for the development of a next generation of sensor devices. The electrical biosensor concept based on the use of SiNWs was firstly introduced by Cui et al. [36]. The first devices were extremely promising for their excellent electronic and physical properties and easy surface functionalization with chemical linkers [36–41]. The use of SiNWs provides a very high surface-to-volume ratio for the transducer compared to their classical, micro-scale counterparts. With such device

types, this scaling effect was taken as the reason for the achievement of higher sensitivities and lower detection limits for various applications. However, the obtained recordings were highly unstable and largely influenced by side parameters such as temperature, pH and ionic strength of the test solutions. In particular, the bottom-up fabricated SiNW devices of diameters less than 10 nm showed remarkable sensitivities, but also very low reproducibility. The advantages and disadvantages of this approach are controversially discussed in the scientific literature, but to date a robust and commercially viable technology platform is not established with the bottom-up grown devices.

The scaling effect (i.e. the increase in sensitivity with decrease of the NW dimensions) for a SiNW device can be in a first approximation explained as follows. The electrostatic gate coupling of the charge carriers inside the SiNW transducers is more efficient due to a dimensional effect (i.e. nanoscale SiNW channels can be gated from all sides acting as a three-dimensional device and thus, the electrostatic control of the channel is better resulting in steeper SS in the subthreshold region). As a result, the charge-carrier density can also be modulated by biomolecules more efficiently, resulting in an ultrahigh sensitivity of the SiNW sensor platform. The charge sensitivity (S) of a SiNW-based sensor can be given as follows:

$$S = \frac{G - G_0}{G_0} = \frac{\Delta G}{G_0} = \frac{4\Delta\sigma_s}{qdN_D} \tag{24}$$

where G_0 and G are the conductances of the SiNW before and after the binding of biomolecules on the SiNW surface, respectively. Other parameters are the diameter d, the uniform doping density N_D and the change in surface-charge density of a cylindrical SiNW after the biomolecule binding $\Delta\sigma_s$ [42].

From Eq. (24), the sensitivity of a SiNW is inversely proportional to its diameter and doping level. This predicts a higher sensitivity of SiNWs (with finite d) than that of planar ISFETs for a comparable surface area (with d (diameter i.e. channel width) approaching infinity). It also predicts that ultrathin SiNWs can exhibit ultrahigh sensitivity. Further, the detection with thinner wires may offer reduced detection times due better, three-dimensional diffusion kinetics of the target biomolecules. In addition, SiNWs need fewer molecules to generate a notable change compared to their microscale counterparts [9, 43]. It should also be noted that low-doping levels of Si are also beneficial for sensor applications, as the sensitivity is expected to increase with decreasing dopant concentration [13, 44–46]. Although Eq. (24) is often used to design and interpret the fabrication procedure and the experimental data, it has some limitations to accurately describe SINW biosensor devices. Most importantly it neglects the effect of the fluidic environment on the performance of SiNW ISFETs. Also the effects of the electrostatic screening of biomolecules due to other ions present in the sample solution are not accounted for. It also does not differentiate between accumulation- and depletion-mode operation of SiNWs [46].

In order to determine the detection limit of the sensor, it is important to investigate its signal-to-noise ratio (SNR). A device with higher SNR relates to a

lower detection limit. SNR depends upon the intrinsic electronic properties of the SiNW devices (e.g. utilized fabrication methods), and it is independent of the electrolyte concentration, composition and pH value [47]. The SNR of a SiNW sensor is approximated as (neglecting the external instrument and environmental noise)

$$\mathrm{SNR} \propto \frac{\Delta Q}{\sqrt{A}} \tag{25}$$

where ΔQ defines the total change in charge bound to the device surface and A gives the device surface area.

From Eq. (25), the SNR is higher for devices with larger surface area if ΔQ is also scaling with A. In contrast to that, the SNR is higher for devices with smaller area if ΔQ is constant. In biosensor applications, where the analyte concentration needs to be quantified, nanoribbons/nanoplates are preferred since the probability of analyte binding increases linearly with the surface area available. Further, for single molecule-detection studies, single-molecule binding on a small nanowire is preferred, where the gate length is identified as the predominant factor [43, 48]. In the above description, the Si/SiO_2 interface-trap density is assumed to be constant, which is regarded as the main factor for the typical $1/f$-noise present in these FET devices. Therefore, the detection limit depends on the total device noise. It also depends on the system characteristics such as the rate of diffusion of analytes to the surface and the affinity of the analyte-receptor interaction.

Demonstration of label-free detection of trace concentrations of biomarkers using SiNW sensors continuously attracts attention for their eventual application in diagnostics and disease control [26, 49, 50]. Compared to existing state-of-the-art technologies used for biomedical diagnostics, fast and portable electrical detection offered by such sensor platforms may revolutionize modern healthcare [15, 43, 48, 51, 52]. SiNW sensors, depending on their targeted applications, can be produced in a scalable nanofabrication method leading to suitable device configurations with advanced functionalities such as differential readout and multiplexing. Therefore, such concepts are deployable to perform more complex bioassays in order to collect meaningful information in a statistical manner, which is critically sought for the development of next generation treatment of many diseases [6, 53–57].

So far, different configurations of SiNW sensors were reported for the detection of diverse chemicals and biomolecules such as ions, enzymes, nucleic acids, proteins, cells, viruses and the mapping of neural circuits [12–14, 58]. A list of further examples of SiNW-based sensors is given in Table 1.

From these examples, it is apparent that SiNW sensors are versatile for many biosensor applications [11, 13, 14, 27, 72]. Single crystalline SiNWs are favourable compared to polysilicon NWs, as they have a higher conductivity and thus, a larger g_m in response to a given field [43, 51].

The mode of operation of SiNW sensors described above is not always in liquid gate configuration. The transistors can be operated in liquid gate and dry gate mode

Table 1 Examples of SiNW sensors for chemical and biomolecule sensing

Application	Examples	Performance	Reference
pH sensor/ chemical	• Highly reproducible SiNW ISFET arrays for pH-sensing applications	Sensitivity 43 mV/pH	[6]
	• Molecularly modified SiNW FETs for non-invasive and selective diagnosis of diseases such as lung cancer, gastric cancer, asthma and chronic obstructive pulmonary disease by using their breathprints and also for estimation of the disease stages		[59]
	• Transient electronic devices and sensors based on Si nanomembranes and nanoribbons on a biodegradable elastomer (poly (1,8-octanediol-co-citrate)) for sensing pH and skin-mounted monitors of electrophysiology		[60]
Protein detection	• Multiplexed label-free immunodetection of three cancer biomarkers (carcinoembryonic antigen, prostate-specific antigen and alpha-fetoprotein) using Si FETs	Limit of detection 0.2 ng/mL	[61]
	• Detection of cytokines such as tumour necrosis factor-alpha and interleukin-6 using SiNW devices	100 fg/mL	[62]
	• T-NW FET sensor incorporating two SiNW FETs, one for sensing and the other for amplification to detect cytokine interleukin-1 beta	10 fg/mL	[63]
	• SiNW FET arrays for multiplexed detection of cardiac biomarkers in serum via application-specific integrated circuit readout	100 fg/mL	[64]
DNA detection	• Sequence-specific detection of DNA using SiNW FETs	25 pM	[65]
	• Nanowire-nanopore sensors for local electrical detection of DNA		[66]
Virus detection	• Simultaneous electrical and optical measurements using fluorescently labelled influenza A to confirm the binding of a virus at the SiNW devices		[67]
Cell-signal detection	• Nanoscale axial *p-n* junction-embedded kinked SiNW FET for recording intracellular signals of cardiomyocytes		[68]
	• Highly sensitive detection, stimulation and inhibition of neuronal signal propagation using high-density SiNW transistor arrays		[28]
	• SiNW FETs-based nanoelectronic scaffolds for cardiac tissues to carry out action-potential mapping		[69]
Organ detection/ interface	• Simultaneous electrical recording and optical registration of flexible SiNW devices to heart surfaces in three-dimensional conformations		[70]
	• Syringe-injectable mesh electronics containing SiNW FETs towards neurons and neural circuits tracking applications		[71]

using the back-gate voltage as a control. A list of different modes of SiNW-based sensor operation is given in Table 2.

The most common mode of operation of SiNW sensors is via chemical or biomolecular gating [36]. Here, typically the conductance $\left(\frac{dI_{ds}}{dV_{ds}}\right)$ of the SiNW FETs is measured with a fixed bias voltage (equivalent to an application of a drain-source voltage V_{ds}), as a function of time as schematically illustrated in Fig. 6a. The receptor-functionalized SiNW surface is allowed to react with the analyte in a test solution, and the change in surface charge due to the receptor-analyte interaction at the SiNW surface is then detected as a change in wire conductance over time. However, this mode of operation has certain limitations, since the potential of the test solution is not fixed (or only fixed by a pseudo-reference system such as Ag/AgCl wires or even only noble metal wires as polarizable electrodes – like often described in literature). Therefore, the observed changes in conductance during real-time measurements could also be caused by

Table 2 Examples of different detection modes of SiNW sensor operation for chemical and biosensing applications

Application	Examples	Comments	Ref.
Chemical and biomolecule-gated SiNW FET	pH and biomolecule measurements using SiNW FETs	• Conductance ($\frac{dI_{ds}}{dV_{ds}}$) at constant V_{ds}, measured as a function of time and solution pH	[36]
		• Protonation/deprotonation of functional groups at the SiNW surface due to the buffer pH acts as a chemical gate for the SiNW	
Liquid-gated SiNW FET	Real-time pH measurements using highly reproducible SiNW ISFET arrays	• I_{ds} at a fixed V_{gs} and V_{ds} is measured as a function of time at different pH buffer	[6]
		• Change in I_{ds} is converted into change in V_{gs} using g_m	
Liquid-gated SiNW FET-AC mode	Electrical impedimetric investigation of the interfacial effects of rat adrenal pheochromocytoma cells on SiNW FETs	• Change in impedance parameters of SiNW FETs due to the cell growth and differentiation	[73]
SiNW FET dry-state operation	Dry-state operation of SiNW FETs, after the antibodies-antigen coupling over the SiNWs, to carry out the detection of the vascular endothelial growth factor	• Claimed no limitation on Debye screening	[74]
Back-gated SiNW FET	A comparison of wet and dry environment of SiNW FET biosensor operation, where the transistor was operated in back-gate configuration with floating liquid gate and dry-gate environment	• High sensitivity in dry environment in comparison to the wet environment	[75]
		• Sensitivity is very irregular and unstable due to the charged polymer layers, which were not chemically uniform in the dry environment	

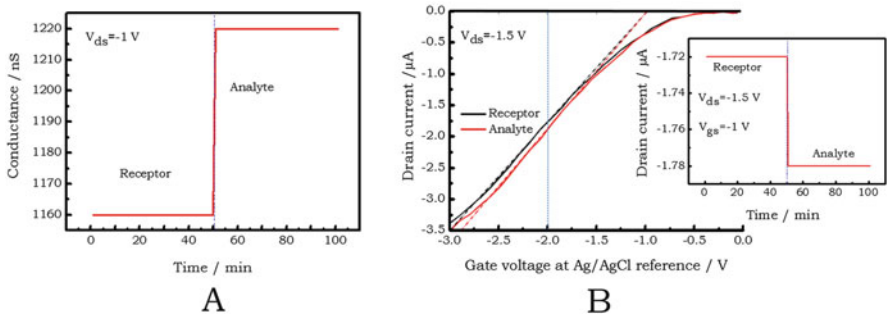

Fig. 6 Plots illustrating two different, time-dependent modes of bio/chemical detection with SiNW sensors: (**a**) Hypothetical conductance change in a SiNW, where the conductance would be measured as a function of time with a bias voltage of $V_{ds} = -1$ V applied between the ends of the nanowire. When the current I_{ds} changes by 60 nA (which is a typical value), a change in conductance of 60 nS would be obtained similarly to what is published in other works [36]. (**b**) Experimental data of a liquid-gated, enhancement-mode, *p*-type SiNW FET, where the transfer characteristics (with and without analyte) were measured to evaluate the best working point of the transistors (as described in Fig. 3). This experiment was presented in an earlier publication of our group [77]. In the left diagram at a working point of $V_{gs} = 0$ V, this enhancement-mode SiNW transistor would be in a normally off mode and would only show a very small conductance, which would also be highly influenced by the contact potential of the Ag/AgCl electrode to the solution depending on the ionic composition and chloride concentration. In a better working point suggested with the dotted line in the graph ($V_{ds} = -1.5$ V and $V_{gs} = -2$ V), the drain-source current change could be measured as a function of time (as exemplary shown in the right graph). The change in I_{ds} at this working point caused by the receptor-analyte interaction at the SiNW surface could then be correlated with the change in V_{gs} observed in the transfer characteristics. However, as it can be seen by the transfer characteristics, the selection of the working point strongly influences the result of a time-dependent experiment, since also the steepness of the SiNW transfer characteristics is changing [77].

fluctuations of the above-mentioned side parameters, like pH value, ionic strength and temperature of the liquid solution away from the surface. In addition, it was earlier described for carbon nanotube (CNT) FET devices that it is even possible that transfer-characteristic curves are crossing [76]. Nowadays, it is widely accepted in the field that the use of a reference electrode for fixation of the liquid potential is inevitable for stable sensor performance. However, not only the grounding of the liquid potential but also a thoughtful choice of the working point is necessary. As discussed above, SiNW devices can be regarded as long-channel FET devices, and their conductance value in the experiment is strongly dependent on this choice. A typical example is illustrated in Fig. 6b, where the transfer-characteristic curves after the analyte binding on the SiNW surface are shown. We discussed in an earlier publication that the binding of the charged molecules might not only cause a threshold voltage shift but also an additional effect of charge accumulation leading to a steeper characteristic curve [77].

This demonstrates that the magnitude of the conductance change during the real-time measurements for analyte binding depends strongly on the selection of the working point of the SiNW. For time-dependent measurements, a working point

can be selected by fixing V_{gs} and V_{ds}, and the change in I_{ds} of the SiNW ISFET can be measured as a function of time [6]. This is illustrated in the inset in Fig. 6b, where I_{ds} is measured at a fixed working point ($V_{gs} = -1$ V and $V_{ds} = -1.5$ V, respectively) and the analyte binding is monitored as a function of time (note that the binding curve in the inset of Fig. 6 represents only a hypothetical experiment). The receptor-analyte interactions at the SiNW surfaces are then detected as a change in I_{ds}. The absolute increase in I_{ds} shown in the inset is equivalent to the change in V_{gs} shown in the transfer-characteristic curves (Fig. 6b). It can be correlated back to the surface-potential change using the g_m value of the transistor. It is to be noted that the absolute change in I_{ds} is also in this case indicating an increase in wire conductance, but due to the typical convention of transistor classification, the current is plotted into the negative direction for a *p*-type FET.

Further, in a recent report, operation of SiNW FETs in a dry state was reported after the antibody-antigen binding onto the SiNW surface in order to overcome the Debye-screening limitation [74]. Nonetheless, when comparing the response of wet- and dry-state operation of SiNW FETs, it was found that the sensitivity in wet-state operation is more stable and regular. This was interpreted with a more uniform distribution of charged polymers in the wet environment [75]. Although there are many publications reporting very high sensitivities achieved with SiNWs, the optimum detection mechanism is still under debate. In far too many of these publications stability and reproducibility issues are not addressed at all.

In the future, the SiNW platforms are expected to be integrated into advanced wearable sensors for continuous readout applications not only for biomolecules but also to perform sensor recordings on living systems such as cells and tissues. Although the first works with SiNW sensors were already published 16 years ago, clinical applications and robust sensor platforms for the biomedical industry are yet to come. The most challenging part of this technology is the robust and industrially scalable fabrication of the devices and their stable readout using multi-parametric and combinatorial methods to exclude side effects and false readings from the recordings.

3.1 Fabrication of SiNW ISFETs

The fabrication of SiNW FETs can be done by both "top-down" and "bottom-up" approaches, and the recent efforts in these nanofabrication methods are discussed here in the following. The bottom-up approaches for the fabrication of SiNWs start from individual atoms aggregating into clusters and assembling further into the form of nanostructures. Common "bottom-up" approaches include chemical vapour deposition (CVD), vapour-liquid-solid, solid-liquid-solid, oxide-assisted growth and thermal evaporation methods for the synthesis of high-quality SiNWs of very small diameters [58, 78]. The as-synthesized SiNWs need to be assembled afterwards by various methods such as the Langmuir-Blodgett transfer technique or polydimethylsiloxane (PDMS) transfer, followed by electrode patterning or

capillary-assisted di-electrophoresis on conventional, lithographically patterned electrodes on desired substrates [10, 36, 78]. However, intrinsic limitations of these methods including device-integration challenges and limited reproducibility have made these fabrication routes less favourable for mass production of biosensor devices [10, 15]. Issues related to "bottom-up" approaches can be mitigated to a certain extent by combining them with classical "top-down" approaches, where device-to-device reproducibility can be achieved using conventional lithography and well-controlled wafer-etching methods [44, 51, 79–81].

The "top-down" approaches, on the other hand, start with a planar substrate (e.g. a single crystalline Si wafer), which is then micro-/nano-patterned using state-of-the-art lithography methods such as ultraviolet (UV) or deep-ultraviolet photolithography combined with electron-beam lithography (EBL) or focussed ion beam (FIB) etching or atomic force microscope nanolithography followed by wet or dry etching steps [82]. Nanopatterning techniques such as EBL and FIB are less favourable for industry application since they are very expensive and time-consuming but widely used in the research community for their flexibility of operation. More recently, nanoimprint lithography (NIL) for nanopatterning of planar substrates has gained momentum, since it offers cost-effectiveness, easy operation, high reproducibility at wafer-scale fabrication and a much faster process compared to all other techniques. Thermal or UV-assisted NIL in combination with anisotropic wet-etching provides a very suitable "top-down" approach for the fabrication of SiNW FETs on wafer scale [6, 82–85].

3.2 Limitations of SiNW-based ISFETs

Despite the popularity of SiNW ISFETs, there are certain issues such as the low-frequency noise (LFN) and current stress, reproducibility, multiplexing capability, detection in physiological solutions, low-cost fabrication and portability of the readout systems that need to be solved before SiNW sensors can be commercialized. Some of these limitations are described in the following.

3.2.1 Downscaling of ISFETs

When the dimensions of SiNW FETs are decreased, issues such as the increase in LFN and in the current stress come into play, eventually resulting in false-positive readings [27, 86]. LFN increases due to the decrease in the number of charge carriers, which leads to an increase in surface contributions to the total electrical noise. Additionally, the current stress is related to the drift in the signal with no change on the sensing membrane. The above two issues are strongly related to the choice of the gate potential [37]. In the subthreshold regime of operation, the current stress can be suppressed, but the signal-to-noise ratio is generally lower than in the linear regime [87]. In contrast to this, in the linear regime, the

conductance response of the SiNW varies linearly with the gate voltage, but screening of charge carriers inside the SiNW occurs. Another possible solution in order to overcome issues related to down-scaling of the devices for reliable recordings is to implement both *p*-type and *n*-type SiNWs devices on a single platform [10, 88]. The opposite effect upon binding of a charge type (e.g. negative charge for DNA assays) can increase the reliability of such platforms and avoid false-positive recordings of side effects.

3.2.2 Surface Functionalization

Several surface-modification methods for covalent linkage of receptors at the surface of SiO_2 were reported, where silanization using two different silane types (3-aminopropyltriethoxysilane, glycidyloxypropyltrimethoxysilane) is mostly preferred [89]. This normally results in receptor immobilization over the entire chip surface unless localized immobilization techniques such as microspotting are used. Immobilization of the receptors on the entire chip results in binding of a large quantity of analyte on the surrounding surface of the SiNWs (instead onto the SiNWs itself) and thus, results in a decrease in sensitivity of the devices. However, other methods such as electric-field alignment of surface-probe molecules or functionalization via nanoscale joule heating can enhance the nanowire-sensing capability [90, 91].

3.2.3 Gate Oxide and Sensor Configuration

For stable sensor operation in constant buffer solutions (constant pH value and concentration), the surface of the SiNWs is usually coated with a thin layer of gate dielectrics (e.g. 7–10 nm of SiO_2), and it should be chemically inert to the detection buffer [89]. However, SiO_2 as the traditional, straightforward gate material on SiNWs has many disadvantages in chemical and biochemical applications such as low pH buffer capacity, susceptibility to leakage current due to ion incorporation in the presence of fluids and electrochemical etching in saline solutions [13, 43]. These effects result in severe long-term drift in the signal of SiO_2 SiNW devices [92, 93]. Other gate materials with high relative dielectric constant such as aluminium oxide, hafnium oxide and tantalum oxide, mainly fabricated by atomic layer deposition, allow a reduction in leakage current maintaining a high gate-oxide capacitance. The higher *k*-values allow a larger physical thickness of the dielectric material, which can supress leakage currents without compromising the sensitivity to the surface charge.

In a conventional, “top-down”-fabricated SiNW biosensor, the nanowires are attached to the substrate. Therefore, the transport of analytes to the surface of the SiNW is limited resulting in a decrease of sensitivity and an increase in detection time. This can be overcome by suspending the SiNWs, which increases the sensing area and hence, also increases the sensitivity and reduces the response time

[94]. This is then, however, bought in by a reduced mechanical robustness of the sensors.

Moreover, a robust surface passivation of the sensors, and in particular that of the contact lines, is required to minimize the leakage current and to isolate from the external environment. For the passivation of the sensor surface, methods based on the usage of silicon oxide or silicon nitride grown by different CVD procedures or polymer layers such as SU-8 resist or Parylene-C are reported in the literature [45, 95].

3.2.4 Sensing in Physiological Solutions

For biomolecule detection in physiological solutions such as human serum or whole blood with SiNW sensors, as for many other affinity-binding-based biosensor assays, the non-specific binding of analytes is a major issue. It readily degrades the small active surface of the devices reducing the probability of capturing the analyte of interest and leading to false-positive results [11, 38, 96]. In order to avoid this non-specific adsorption, various blocking agents such as bovine serum albumin, ethylene glycol and OH-terminated, self-assembled monolayers were used.

Moreover, the sensing with SiNW ISFETs is limited by the Debye-screening effect as explained above [97]. Thus, low-concentration buffers are required for label-free detection of analytes based on their charge. There are several other methods reported to overcome this charge-screening effect, for instance (see Sect. 2.1) using smaller receptor molecules such as aptamers, glycans, etc. [53, 98–102]. In order to overcome the limitations of charge-based sensing, impedance readout was developed, where the change in impedance during binding of biological analytes is studied [103–105].

4 Competing Platforms and New Concepts

Several hybrid devices based on SiNWs or other nanomaterials such as carbon nanotubes (CNTs), graphene and conducting polymer FETs were reported for biosensor applications and are shortly described in the following.

4.1 New Materials and Nanowire Hybrids

CNT devices are promising candidates for biosensing applications, because of their high sensitivity, selectivity, label-free readout and real-time response [106, 107]. Because of several limitations in fabrication, the application of CNT FETs and conducting polymer devices are limited compared to SiNW FETs [58, 108]. Various material hybrid platforms were reported for biosensor applications as well [109–111]. For instance, a method of transferring highly ordered SiNWs arrays

from SOI wafers to plastic substrates using PDMS was reported [70, 112]. This method has attracted attention due to its biocompatibility, flexibility, light weight and shock resistance. Electronic devices based on these substrates are very promising for future handheld consumer electronics.

4.2 Microfluidic Integration

Microfluidic devices normally consist of channels of several ten to hundred micrometres in width, where small quantities of reagents can be manipulated with high flexibility and controllability. Because of the miniaturization, all reagent manipulation steps can be performed very rapidly at very low cost [26, 113, 114]. Microfluidic manipulation methods offer to overcome the limitations of conventional diagnostic strategies and can offer rapid and simple assays for biomarker separation and enrichment [113, 114]. Such sample separation platforms can be ideally combined with these ultrasensitive SiNW sensors in order to accomplish typical diagnostic tasks such as the detection of DNA or micro-ribonucleic acids (mRNA) from patient samples [114, 115]. The small size of the SiNWs enables the integration of several sensors into a microfluidic channel of typical dimensions. However, the success of this miniaturization effort depends on the type of the sensing device and also on integrating a stable and reliable reference electrode [79]. This issue is an unsolved problem for a long time in the field of ISFET biosensing, and it is still the same or even a more complicated technological challenge, when ISFETs are scaled down to SiNWs.

5 Conclusions

Over the past decades – due to the advancement in nanofabrication techniques – new nanoelectronic biosensor platforms were developed. SiNW ISFETs are very attractive for miniaturization to create high-density sensor arrays and to integrate them into microfluidic chips for advanced LoC systems. In the field of biosensing, SiNW ISFETs are very popular because of their exceptional electronic properties, high sensitivity and selectivity and their potential for label-free and fast real-time detection. These device types have shown favourable performance compared to competing platforms such as CNT FETs and conducting polymer devices. The main reasons for the widespread usage of the SiNW variant are their commercial viability, potential for mass production and the ability to tune their electrical properties by controlling the dopant concentration, gate oxides and the SiNW diameter. These process steps are already well-controlled in the silicon industry down to few nm feature sizes, but in many approaches of the scientific community not fully applied or adapted. Still many technological challenges need to be overcome, which are exactly the same, like already discussed many decades ago

with classical ISFETs. Nowadays, based on the miniaturization into nanoscale regimes, these challenges are even stronger than in the ISFET age, since devices are smaller, currents are much smaller, gate oxides are much thinner, etc. In the future, especially the industry, process-compatible fabrication techniques for robust and reliable SiNW sensors have a high potential for commercialization in the fields of biosensing and biomedicine.

References

1. Bergveld P (1970) Development of an ion-sensitive solid-state device for neurophysiological measurements. IEEE Trans Biomed Eng 17:70–71
2. Bergveld P (2003) Thirty years of ISFETOLOGY: what happened in the past 30 years and what may happen in the next 30 years. Sensors Actuators B Chem 88:1–20
3. van Hal REG, Eijkel JCT, Bergveld P (1996) A general model to describe the electrostatic potential at electrolyte oxide interfaces. Adv Colloid Interf Sci 69:31–62
4. Afrasiabi R (2016) Silicon nanoribbon FET sensors: fabrication, surface modification and microfluidic integration. Dissertation, KTH Royal Institute of Technology, Stockholm, Sweden
5. Shinwari MW, Deen MJ, Landheer D (2007) Study of the electrolyte-insulator-semiconductor field-effect transistor (EISFET) with applications in biosensor design. Microelectron Reliab 47:2025–2057
6. Rani D, Pachauri V, Mueller A, Vu XT, Nguyen TC, Ingebrandt S (2016) On the use of scalable nanoISFET arrays of silicon with highly reproducible sensor performance for biosensor applications. ACS Omega 1:84–92
7. Ortiz-Conde A, García-Sánchez FJ, Muci J, Barrios AT, Liou JJ, Ho C-S (2013) Revisiting MOSFET threshold voltage extraction methods. Microelectron Reliab 53:90–104
8. Skoog DA, West DM, Holler FJ, Crouch SR (2013) Fundamentals of analytical chemistry, 9th edn. Brooks/Cole Cengage Learning, Belmont
9. Vu XT (2011) Silicon nanowire transistor arrays for biomolecular detection. Dissertation, RWTH Aachen University, Aachen, Germany
10. Zheng G, Patolsky F, Cui Y, Wang WU, Lieber CM (2005) Multiplexed electrical detection of cancer markers with nanowire sensor arrays. Nat Biotechnol 23:1294–1301
11. Stern E, Vacic A, Rajan NK, Criscione JM, Park J, Ilic BR, Mooney DJ, Reed MA (2009) Label-free biomarker detection from whole blood. Nat Nanotechnol 5:138–142
12. Lin S-P, Pan C-Y, Tseng K-C, Lin M-C, Chen C-D, Tsai C-C, Yu S-H, Sun Y-C, Lin T-W, Chen Y-T (2009) A reversible surface functionalized nanowire transistor to study protein–protein interactions. Nano Today 4:235–243
13. Noor MO, Krull UJ (2014) Silicon nanowires as field-effect transducers for biosensor development: a review. Anal Chim Acta 825:1–25
14. Li B-R, Chen C-C, Kumar UR, Chen Y-T (2014) Advances in nanowire transistors for biological analysis and cellular investigation. Analyst 139:1589–1608
15. Kim A, Ah CS, Yu HY, Yang J-H, Baek I-B, Ahn C-G, Park CW, Jun MS, Lee S (2007) Ultrasensitive, label-free, and real-time immunodetection using silicon field-effect transistors. Appl Phys Lett 91:103901
16. Landheer D, Aers G, McKinnon WR, Deen MJ, Ranuarez JC (2005) Model for the field-effect from layers of biological macromolecules on the gates of metal-oxide-semiconductor transistors. J Appl Phys 98:044701

17. Landheer D, McKinnon WR, Aers G, Jiang W, Deen MJ, Shinwari MW (2007) Calculation of the response of field-effect transistors to charged biological molecules. IEEE Sensors J 7:1233–1242
18. Landheer D, McKinnon WR, Jiang WH, Aers G (2008) Effect of screening on the sensitivity of field-effect devices used to detect oligonucleotides. Appl Phys Lett 92:253901
19. McKinnon WR, Landheer D (2006) Sensitivity of a field-effect transistor in detecting DNA hybridization, calculated from the cylindrical Poisson-Boltzmann equation. J Appl Phys 100:054703
20. Poghossian A, Cherstvy A, Ingebrandt S, Offenhäusser A, Schöning MJ (2005) Possibilities and limitations of label-free detection of DNA hybridization with field-effect-based devices. Sensors Actuators B Chem 111–112:470–480
21. Schöning MJ, Poghossian A (2002) Recent advances in biologically sensitive field-effect transistors (BioFETs). Analyst 127:1137–1151
22. Zhang G-J, Zhang G, Chua JH, Chee R-E, Wong EH, Agarwal A, Buddharaju KD, Singh N, Gao Z, Balasubramanian N (2008) DNA sensing by silicon nanowire: charge layer distance dependence. Nano Lett 8:1066–1070
23. Huang W, Diallo AK, Dailey JL, Besar K, Katz HE (2015) Electrochemical processes and mechanistic aspects of field-effect sensors for biomolecules. J Mater Chem C 3:6445–6470
24. Schasfoort RBM, Bergveld P, Kooyman RPH, Greve J (1990) Possibilities and limitations of direct detection of protein charges by means of an immunological field-effect transistor. Anal Chim Acta 238:323–329
25. De Vico L, Iversen L, Sorensen MH, Brandbyge M, Nygard J, Martinez KL, Jensen JH (2011) Predicting and rationalizing the effect of surface charge distribution and orientation on nanowire based FET bio-sensors. Nanoscale 3:3635–3640
26. Eicher D, Merten CA (2011) Microfluidic devices for diagnostic applications. Expert Rev Mol Diagn 11:505–519
27. Rim T, Meyyappan M, Baek C-K (2014) Optimized operation of silicon nanowire field effect transistor sensors. Nanotechnology 25:505501
28. Patolsky F, Timko BP, Yu G, Fang Y, Greytak AB, Zheng G, Lieber CM (2006) Detection, stimulation, and inhibition of neuronal signals with high-density nanowire transistor arrays. Science 313:1100–1104
29. Maedler C, Kim D, Spanjaard RA, Hong M, Erramilli S, Mohanty P (2016) Sensing of the melanoma biomarker TROY using silicon nanowire field-effect transistors. ACS Sens 1:696–701
30. Antonisse MMG, Snellink-Ruël BHM, Lugtenberg RJW, Engbersen JFJ, van den Berg A, Reinhoudt DN (2000) Membrane characterization of anion-selective CHEMFETs by impedance spectroscopy. Anal Chem 72:343–348
31. Kharitonov AB, Wasserman J, Katz E, Willner I (2001) The use of impedance spectroscopy for the characterization of protein-modified ISFET devices: application of the method for the analysis of biorecognition processes. J Phys Chem B 105:4205–4213
32. Laborde C, Pittino F, Verhoeven HA, Lemay SG, Selmi L, Jongsma MA, Widdershoven FP (2015) Real-time imaging of microparticles and living cells with CMOS nanocapacitor arrays. Nat Nanotechnol 10:791–795
33. Ingebrandt S (2015) Bioelectronics: sensing beyond the limit. Nat Nanotechnol 10:734–735
34. Susloparova A, Koppenhofer D, Law JKY, Vu XT, Ingebrandt S (2015) Electrical cell-substrate impedance sensing with field-effect transistors is able to unravel cellular adhesion and detachment processes on a single cell level. Lab Chip 15:668–679
35. Nguyen TC, Vu XT, Freyler M, Ingebrandt S (2013) PSPICE model for silicon nanowire field-effect transistor biosensors in impedimetric measurement mode. Phys Status Solidi A 210:870–876
36. Cui Y, Wei Q, Park H, Lieber CM (2001) Nanowire nanosensors for highly sensitive and selective detection of biological and chemical species. Science 293:1289–1292

37. Hsu C-C, Yang CY, Lai C-J, Dai C-L (2014) Optimization of reusable polysilicon nanowire sensor for salt concentration measurement. Jpn J Appl Phys 53:06JE04
38. Krivitsky V, Zverzhinetsky M, Patolsky F (2016) Antigen-dissociation from antibody-modified nanotransistor sensor arrays as a direct biomarker detection method in unprocessed biosamples. Nano Lett 16:6272–6281
39. Salhi B, Hossain MK, Mukhaimer AW, Al-Sulaiman FA (2016) Nanowires: a new pathway to nanotechnology-based applications. J Electroceram 37:34–49
40. Stoop RL, Wipf M, Müller S, Bedner K, Wright IA, Martin CJ, Constable EC, Fu W, Tarasov A, Calame M, Schönenberger C (2015) Competing surface reactions limiting the performance of ion-sensitive field-effect transistors. Sensors Actuators B Chem 220:500–507
41. Amato M, Rurali R (2016) Surface physics of semiconducting nanowires. Prog Surf Sci 91:1–28
42. Chen S (2013) Electronic sensors based on nanostructured field-effect devices. Dissertation, Uppsala University, Uppsala, Sweden
43. Luye M, Ye C, Sawtelle SD, Wipf M, Xuexin D, Reed MA (2015) Silicon nanowire field-effect transistors – a versatile class of potentiometric nanobiosensors. IEEE 3:287–302
44. Trivedi K, Yuk H, Floresca HC, Kim MJ, Hu W (2011) Quantum confinement induced performance enhancement in sub-5-nm lithographic Si nanowire transistors. Nano Lett 11:1412–1417
45. Zeimpekis I, Sun K, Hu C, Thomas O, de Planque MRR, Chong HMH, Morgan H, Ashburn P (2015) Study of parasitic resistance effects in nanowire and nanoribbon biosensors. Nanoscale Res Lett 10:79
46. Nair PR, Alam MA (2007) Design considerations of silicon nanowire biosensors. IEEE Trans Electron Dev 54:3400–3408
47. Rajan NK, Routenberg DA, Reed MA (2011) Optimal signal-to-noise ratio for silicon nanowire biochemical sensors. Appl Phys Lett 98:264107
48. Carmignani C, Rozeau O, Scheiblin P, Thuaire A, Reynaud P, Barraud S, Ernst T, Cheramy S, Vinet M (2016) Fine charge sensing using a silicon nanowire for biodetection. In: 2016 international symposium on VLSI technology, systems and application (VLSI-TSA), Hsinchu, 2016, pp 1–2
49. Abdul Rashid JI, Abdullah J, Yusof NA, Hajian R (2013) The development of silicon nanowire as sensing material and its applications. J Nanomater 2013:16
50. Adam T, Hashim U (2015) Highly sensitive silicon nanowire biosensor with novel liquid gate control for detection of specific single-stranded DNA molecules. Biosens Bioelectron 67:656–661
51. Pui T-S, Agarwal A, Ye F, Tou Z-Q, Huang Y, Chen P (2009) Ultra-sensitive detection of adipocytokines with CMOS-compatible silicon nanowire arrays. Nanoscale 1:159–163
52. Lu N, Gao A, Zhou H, Wang Y, Yang X, Wang Y, Li T (2016) Progress in Silicon nanowire-based field-effect transistor biosensors for label-free detection of DNA. Chin J Chem 34:308–316
53. Li B-R, Hsieh Y-J, Chen Y-X, Chung Y-T, Pan C-Y, Chen Y-T (2013) An ultrasensitive nanowire-transistor biosensor for detecting dopamine release from living PC12 cells under hypoxic stimulation. J Am Chem Soc 135:16034–16037
54. Shen S-H, Cheng H, Kao T-Y, Chen M-J, Lin C-T (2014) Silicon-based multi-nanowire biosensor with high-k dielectric and stacked oxide sensing membrane for cardiac troponin I detection. Proc Eng 87:648–651
55. Xiaofeng G, Rui Z, Xiaomei Y (2015) High sensitive detections of norovirus DNA and IgG by using multi-SiNW-FET biosensors. 2015 Transducers – 2015 18th international conference on solid-state sensors, actuators and microsystems (TRANSDUCERS), Anchorage, AK, 2015, pp 1537–1540
56. Zheng G, Lieber CM (2009) Nanowire biosensors for label-free, real-time, ultrasensitive protein detection. Methods Mol Biol 790:223–237

57. Regonda S, Tian R, Gao J, Greene S, Ding J, Hu W (2013) Silicon multi-nanochannel FETs to improve device uniformity/stability and femtomolar detection of insulin in serum. Biosens Bioelectron 45:245–251
58. Zhang A, Lieber CM (2016) Nano-bioelectronics. Chem Rev 116:215–257
59. Shehada N, Cancilla JC, Torrecilla JS, Pariente ES, Brönstrup G, Christiansen S, Johnson DW, Leja M, Davies MPA, Liran O, Peled N, Haick H (2016) Silicon nanowire sensors enable diagnosis of patients via exhaled breath. ACS Nano 10:7047–7057
60. Hwang S-W, Lee CH, Cheng H, Jeong J-W, Kang S-K, Kim J-H, Shin J, Yang J, Liu Z, Ameer GA, Huang Y, Rogers JA (2015) Biodegradable elastomers and Silicon nanomembranes/nanoribbons for stretchable, transient electronics, and biosensors. Nano Lett 15:2801–2808
61. Kim A, Ah CS, Park CW, Yang J-H, Kim T, Ahn C-G, Park SH, Sung GY (2010) Direct label-free electrical immunodetection in human serum using a flow-through-apparatus approach with integrated field-effect transistors. Biosens Bioelectron 25:1767–1773
62. Pui T-S, Agarwal A, Ye F, Huang Y, Chen P (2011) Nanoelectronic detection of triggered secretion of pro-inflammatory cytokines using CMOS compatible silicon nanowires. Biosens Bioelectron 26:2746–2750
63. Mao Y, Shin K-S, Wang X, Ji Z, Meng H, Chui CO (2016) Semiconductor electronic label-free assay for predictive toxicology. Sci Rep 6:24982
64. Zhang G-J, Chai KTC, Luo HZH, Huang JM, Tay IGK, Lim AE-J, Je M (2012) Multiplexed detection of cardiac biomarkers in serum with nanowire arrays using readout ASIC. Biosens Bioelectron 35:218–223
65. Li Z, Chen Y, Li X, Kamins TI, Nauka K, Williams RS (2004) Sequence-specific label-free DNA sensors based on silicon nanowires. Nano Lett 4:245–247
66. Xie P, Xiong Q, Fang Y, Qing Q, Lieber CM (2011) Local electrical potential detection of DNA by nanowire–nanopore sensors. Nat Nanotechnol 7:119–125
67. Patolsky F, Zheng G, Hayden O, Lakadamyali M, Zhuang X, Lieber CM (2004) Electrical detection of single viruses. Proc Natl Acad Sci U S A 101:14017–14022
68. Qing Q, Jiang Z, Xu L, Gao R, Mai L, Lieber CM (2014) Free-standing kinked nanowire transistor probes for targeted intracellular recording in three dimensions. Nat Nanotechnol 9:142–147
69. Dai X, Zhou W, Gao T, Liu J, Lieber CM (2016) Three-dimensional mapping and regulation of action potential propagation in nanoelectronics-innervated tissues. Nat Nanotechnol 11:776–782
70. Timko BP, Cohen-Karni T, Yu G, Qing Q, Tian B, Lieber CM (2009) Electrical recording from hearts with flexible nanowire device arrays. Nano Lett 9:914–918
71. Schuhmann TG, Yao J, Hong G, Fu T-M, Lieber CM (2017) Syringe-injectable electronics with a plug-and-play input/output interface. Nano Lett 17:5836–5842. https://doi.org/10.1021/acs.nanolett.7b03081
72. Zhou W, Dai X, Lieber CM (2017) Advances in nanowire bioelectronics. Rep Prog Phys 80:016701
73. Lin S-P, Vinzons LU, Kang Y-S, Lai T-Y (2015) Non-faradaic electrical impedimetric investigation of the interfacial effects of neuronal cell growth and differentiation on silicon nanowire transistors. ACS Appl Mater Interfaces 7:9866–9878
74. Puppo F, Traversa FL, Di Ventra M, De Micheli G, Carrara S (2016) Surface trap mediated electronic transport in biofunctionalized silicon nanowires. Nanotechnology 27:345503
75. Choi HM, Shin DJ, Lee JH, Mo H-S, Park TJ, Park B-G, Kim DM, Choi S-J, Kim DH, Park J (2016) The analysis of characteristics in dry and wet environments of silicon nanowire-biosensor. J Nanosci Nanotechnol 16:4901–4905
76. Heller I, Janssens AM, Männik J, Minot ED, Lemay SG, Dekker C (2008) Identifying the mechanism of biosensing with carbon nanotube transistors. Nano Lett 8:591–595

77. Schwartz M, Nguyen TC, Vu XT, Weil M, Wilhelm J, Wagner P, Thoelen R, Ingebrandt S (2016) DNA detection with top–down fabricated silicon nanowire transistor arrays in linear operation regime. Phys Status Solidi A 213:1510–1519
78. Namdari P, Daraee H, Eatemadi A (2016) Recent advances in silicon nanowire biosensors: synthesis methods, properties, and applications. Nanoscale Res Lett 11:406
79. Kim S, Rim T, Kim K, Lee U, Baek E, Lee H, Baek C-K, Meyyappan M, Deen MJ, Lee J-S (2011) Silicon nanowire ion-sensitive field-effect transistor with integrated Ag/AgCl electrode: pH sensing and noise characteristics. Analyst 136:5012–5016
80. Dehzangi A, Larki F, Naseri MG, Navasery M, Majlis BY, Wee MFR, Halimah MK, Islam MS, Ali SHM, Saion E (2015) Fabrication and simulation of single crystal p-type Si nanowire using SOI technology. Appl Surf Sci 334:87–93
81. Nuzaihan MMN, Hashim U, Ruslinda AR, Arshad MK, Baharin MHA (2015) Fabrication of silicon nanowires array using E-beam lithography integrated with microfluidic channel for pH sensing. Curr Nanosci 11:239–244
82. Tong HD, Chen S, van der Wiel WG, Carlen ET, van den Berg A (2009) Novel top-down wafer-scale fabrication of single crystal Silicon nanowires. Nano Lett 9:1015–1022
83. Balla T, Spearing SM, Monk A (2008) An assessment of the process capabilities of nanoimprint lithography. J Phys D Appl Phys 41:174001
84. Stern E, Klemic JF, Routenberg DA, Wyrembak PN, Turner-Evans DB, Hamilton AD, LaVan DA, Fahmy TM, Reed MA (2007) Label-free immunodetection with CMOS-compatible semiconducting nanowires. Nature 445:519–522
85. Gao A, Lu N, Dai P, Li T, Pei H, Gao X (2011) Silicon nanowire-based CMOS-compatible field-effect transistor nanosensors for ultrasensitive electrical detection of nucleic acids. Nano Lett 11:3974–3978
86. Li J, Pud S, Petrychuk M, Offenhäusser A, Vitusevich S (2014) Sensitivity enhancement of Si nanowire field-effect transistor biosensors using single trap phenomena. Nano Lett 14:3504–3509
87. Gao XPA, Zheng G, Lieber CM (2010) Subthreshold regime has the optimal sensitivity for nanowire FET biosensors. Nano Lett 10:547–552
88. Gao A, Lu N, Wang Y, Li T (2016) Robust ultrasensitive tunneling-FET biosensor for point-of-care diagnostics. Sci Rep 6:22554
89. Li B-R, Chen C-W, Yang W-L, Lin T-Y, Pan C-Y, Chen Y-T (2013) Biomolecular recognition with a sensitivity-enhanced nanowire transistor biosensor. Biosens Bioelectron 45:252–259
90. Chu C-J, Yeh C-S, Liao C-K, Tsai L-C, Huang C-M, Lin H-Y, Shyue J-J, Chen Y-T, Chen C-D (2013) Improving nanowire sensing capability by electrical field alignment of surface probing molecules. Nano Lett 13:2564–2569
91. Park I, Li Z, Pisano AP, Williams RS (2007) Selective surface functionalization of silicon nanowires via nanoscale Joule heating. Nano Lett 7:3106–3111
92. Bergveld P (1996) The future of biosensors. Sensors Actuators A Phys 56:65–73
93. Morrison SR, Madou MJ, Frese KW (1980) Imperfections in and ion diffusion through oxide layers on silicon. Appl Surf Sci 6:138–148
94. Zhou W, Dai X, Fu TM, Xie C, Liu J, Lieber CM (2014) Long term stability of nanowire nanoelectronics in physiological environments. Nano Lett 14:1614–1619
95. Liu J, Xie C, Dai X, Jin L, Zhou W, Lieber CM (2013) Multifunctional three-dimensional macroporous nanoelectronic networks for smart materials. Proc Natl Acad Sci 110:6694–6699
96. Poghossian A, Schöning MJ (2014) Label-free sensing of biomolecules with field-effect devices for clinical spplications. Electroanalysis 26:1197–1213
97. Huang Y-W, Wu C-S, Chuang C-K, Pang S-T, Pan T-M, Yang Y-S, Ko F-H (2013) Real-time and label-free detection of the prostate-specific antigen in human serum by a polycrystalline silicon nanowire field-effect transistor biosensor. Anal Chem 85:7912–7918
98. Cheng S, Hotani K, Hideshima S, Kuroiwa S, Nakanishi T, Hashimoto M, Mori Y, Osaka T (2014) Field-effect transistor biosensor using antigen binding fragment for detecting tumor marker in human serum. Materials 7:2490–2500

99. Kim KS, Lee H-S, Yang J-A, Jo M-H, Han S-K (2009) The fabrication, characterization and application of aptamer-functionalized Si-nanowire FET biosensors. Nanotechnology 20:235501
100. Presnova G, Presnov D, Krupenin V, Grigorenko V, Trifonov A, Andreeva I, Ignatenkoa O, Egorova A, Rubtsovaa M (2017) Biosensor based on a silicon nanowire field-effect transistor functionalized by gold nanoparticles for the highly sensitive determination of prostate specific antigen. Biosens Bioelectron 88:283–289
101. Elnathan R, Kwiat M, Pevzner A, Engel Y, Burstein L, Khatchtourints A, Lichtenstein A, Kantaev R, Patolsky F (2012) Biorecognition layer engineering: overcoming screening limitations of nanowire-based FET devices. Nano Lett 12:5245–5254
102. Gao N, Zhou W, Jiang X, Hong G, Fu T-M, Lieber CM (2015) General strategy for biodetection in high ionic strength solutions using transistor-based nanoelectronic sensors. Nano Lett 15:2143–2148
103. Ingebrandt S, Han Y, Nakamura F, Poghossian A, Schöning MJ, Offenhäusser A (2007) Label-free detection of single nucleotide polymorphisms utilizing the differential transfer function of field-effect transistors. Biosens Bioelectron 22:2834–2840
104. Susloparova A, Koppenhöfer D, Vu XT, Weil M, Ingebrandt S (2013) Impedance spectroscopy with field-effect transistor arrays for the analysis of anti-cancer drug action on individual cells. Biosens Bioelectron 40:50–56
105. Pandya HJ, Kim HT, Roy R, Chen W, Cong L, Zhong H, Foran DJ, Desai JP (2014) Towards an automated MEMS-based characterization of benign and cancerous breast tissue using bioimpedance measurements. Sensors Actuators B Chem 199:259–268
106. Balasubramanian K, Kern K (2014) 25th anniversary article: label-free electrical biodetection using carbon nanostructures. Adv Mater 26:1154–1175
107. Jariwala D, Sangwan VK, Lauhon LJ, Marks TJ, Hersam MC (2014) Emerging device applications for semiconducting two-dimensional transition metal dichalcogenides. ACS Nano 8:1102–1120
108. Khung YL, Narducci D (2013) Synergizing nucleic acid aptamers with 1-dimensional nanostructures as label-free field-effect transistor biosensors. Biosens Bioelectron 50:278–293
109. Lin T-Y, Li B-R, Tsai S-T, Chen C-W, Chen C-H, Chen Y-T, Pan C-Y (2012) Improved silicon nanowire field-effect transistors for fast protein-protein interaction screening. Lab Chip 13:676–684
110. Krivitsky V, Hsiung L-C, Lichtenstein A, Brudnik B, Kantaev R, Elnathan R, Pevzner A, Khatchtourints A, Patolsky F (2012) Si nanowires forest-based on-chip biomolecular filtering, separation and preconcentration devices: nanowires do it all. Nano Lett 12:4748–4756
111. Tsai C-C, Chiang P-L, Sun C-J, Lin T-W, Tsai M-H, Chang Y-C, Chen Y-T (2011) Surface potential variations on a silicon nanowire transistor in biomolecular modification and detection. Nanotechnology 22:135503
112. McAlpine MC, Ahmad H, Wang D, Heath JR (2007) Highly ordered nanowire arrays on plastic substrates for ultrasensitive flexible chemical sensors. Nat Mater 6:379–384
113. Hoffman JM, Stayton PS, Hoffman AS, Lai JJ (2015) Stimuli-responsive reagent system for enabling microfluidic immunoassays with biomarker purification and enrichment. Bioconjug Chem 26:29–38
114. Xie Y, Yang S, Mao Z, Li P, Zhao C, Cohick Z, Huang P-H, Huang TJ (2014) In situ fabrication of 3D Ag@ZnO nanostructures for microfluidic surface-enhanced raman scattering systems. ACS Nano 8:12175–12184
115. Kuan D-H, Wang IS, Lin J-R, Yang C-H, Huang C-H, Lin Y-H, Lin C-T, Huang N-T (2016) A microfluidic device integrating dual CMOS polysilicon nanowire sensors for on-chip whole blood processing and simultaneous detection of multiple analytes. Lab Chip 16:3105–3113

Label-Free Biosensors Based on III-Nitride Semiconductors

Volker Cimalla

Abstract Chip-based biosensor devices received an increased attention for medical and pharmaceutical screening as well as for environmental monitoring. Most semiconductor devices such as the highly developed Si-based ISFET are, however, not sufficiently stable up to date. Due to their superior chemical stability in electrolytes and their biocompatibility, group III-nitrides emerged as promising electronic transducer material for biosensors. Moreover, their transparency for visible light enables the simultaneous application of optical measurements, which are standard in biology and medicine. In this chapter, fabrication and properties of group III-nitride electronic biosensors are discussed with a main focus on AlGaN/GaN field-effect transistors. Using appropriate designs and functionalization, highly sensitive group III-nitride-based biosensors can be realized for a large variety of applications including detection of ions, biomolecules, toxins, deoxyribonucleic acid (DNA), proteins, and even explosives. In addition, other sensor concepts employing other members of the group III-nitride family (InN, AlN, and solid solutions) as well as alternative transducer concepts (optical, mechanical) are discussed shortly. Finally, the possibilities for the integration of such biosensors are addressed.

Keywords Biosensor, Field-effect transistor, Group III-nitrides, High-electron-mobility transistor, Semiconductor

Contents

V. Cimalla (✉)
Fraunhofer Institute for Applied Solid State Physics, Freiburg, Germany
e-mail: Volker.cimalla@iaf.fraunhofer.de

M. J. Schöning, A. Poghossian (eds.), *Label-Free Biosensing: Advanced Materials, Devices and Applications*, Springer Series on Chemical Sensors and Biosensors (2018) 16: 59–102
DOI 10.1007/5346_2017_20, © Springer International Publishing AG 2017,
Published online: 30 December 2017

1 Introduction

The progress in all fields of research continuously increases the number of data, which are collected, monitored, and analyzed. Chemical sensors are surely part of this development and found increasing attention to guarantee a healthy environment. Such applications include medical and environmental monitoring as well as food safety or security issues and should include the analysis of biological media in order to detect desired target species with high specificity and sensitivity. As a part of it, the identification and quantification of biological materials, such as DNA or proteins, are important targets [1, 2]. Conventional detection methods can fulfill the requirements in terms of reliability, sensitivity, and selectivity. As an example, polymerase chain reaction (PCR) or gel electrophoresis combined with fluorescent labels is a common technique to analyze DNA profiles. Enzyme-linked immunosorbent assay (ELISA) is the most common method to detect antigens with labeled antibodies. Further methods include mass spectrometry, electrochemical impedance measurements, resonant micromechanical devices, gas or ion chromatography, magnetic biosensors, etc.

As a major drawback, those methods are usually time-consuming and require laboratories with expensive equipment. Considering the increasing use of smart phones also for sensing applications as well as the trend for ambulant medical monitoring, decentralized solutions are of growing importance. In addition, to reduce the required quantity of biological samples and to accelerate the analysis due to faster reactions and enhanced separation efficiency and sensitivity, the analysis in smaller volumes, portability, and easy handling is favorable. Meanwhile, miniaturized

analysis systems, like μTAS (micro total analysis system) and lab-on-a-chip, have been proposed to enable fast "point-of-care" diagnostic close to the patient [3], easy environmental surveillance measurements in field applications [4, 5], or accelerated analysis cycles in pharmaceutical drug development [6]. Despite their reliability, those techniques may not fulfill the needs for those new developments or for handheld biosensors.

The research efforts in the field of biosensors have increased over the last decade. The IUPAC *Compendium of Chemical Terminology* ("gold book") defines a biosensor [7] as "a device that uses specific biochemical reactions mediated by isolated enzymes, immune systems, tissues, organelles or whole cells to detect chemical compounds usually by electrical, thermal or optical signals." It is, thus, a hybrid sensor concept, which combines a biological component with a physicochemical transducer in serial connection. According to the definition, biomolecules such as enzymes, antibodies, or nucleic acids as well as organelles, cells, or tissues can serve as the biological element. It is responsible for the reaction with the analytes and transforms parameters from the biochemical domain, e.g., analyte concentrations, into chemical or physical quantities, e.g., ions, heat, or light. The following transducer transforms those quantities into an electrical signal. Depending on the transducer, the transformation may include amplification or signal processing.

In 1962, Clark and Lyons [8] demonstrated the first biosensor by immobilization of an enzyme on an amperometric oxygen electrode. In the following years, the progress in bio- and electrochemistry, solid-state and surface physics, bioengineering, integrated circuit Si technology, and data processing stimulated the development of highly specific, sensitive, selective, and reliable micro (bio)chemical sensors and sensor arrays [9, 10]. However, receptor molecules immobilized on metal surfaces, which are necessary for biosensing, are degrading in time. In 1970, Bergveld demonstrated the ion-sensitive field-effect transistor (ISFET), which evolved as one of the most attractive transducer concepts for miniaturized electrochemical biosensors [11]. Despite very promising demonstrations of Si ISFET-based biosensors [12] and outstanding opportunities for mass production, their moderate chemical long-term stability in biological aqueous environments [13, 14] limits the areas of application.

Those stability issues triggered the search for new functional materials for biosensors with chemical inertness as well as the ability of functionalizing the surface with a biological recognition element. Wide bandgap semiconducting materials such as diamond, silicon carbide, metal oxides, and the group III-nitrides were demonstrated to fulfill those requirements. Among these materials, the group III-nitrides, in particular gallium nitride (GaN), aluminum nitride (AlN), and their solid solutions (AlGaN), are especially interesting. The material properties enable the fabrication of electronic, microwave, optoelectronic, and electroacoustic devices – all of them can be employed as transducer material in biosensors.

This chapter concentrates on biosensors where the media to be analyzed are in direct contact with a group III-nitride surface. Most investigated are sensors based on field-effect transistors, which will be discussed in the main part of the chapter including their cleaning, preparation, and functionalization. Further transducer principles for group III-nitride-based biosensors, which employ very similar treatments and biofunctionalization procedures, will be discussed shortly as well.

2 Group III-Nitrides

2.1 Basic Properties

The III-nitride system is built by the compounds AlN, GaN, InN, and BN as well as their solid solutions. Especially, GaN and its ternary and quaternary solid solutions with Al and In are nowadays considered as one of the most important semiconductors after Si with various applications, notably in optoelectronics and electronics [15]. The growth of single crystalline GaN was described already 50 years ago [16]; the breakthrough for applications, however, was the discovery of p-type doping by magnesium and subsequent thermal treatment [17]. This improvement leads to increasing research activities on group III-nitrides and their commercial breakthrough in 1994 with the introduction of the blue GaN-based light-emitting diode (LED) [18]. Meanwhile, group III-nitrides can be synthesized with well-defined electronic properties.

As a first prominent feature of group III-nitrides, the bandgap can be tuned over a wide range from 0.7 eV for InN [19] to 6.2 eV for AlN [20] covering the near-infrared, the visible, and the ultraviolet spectra (Fig. 1), which is reasonably important for the design of light-emitting devices such as LEDs, laser diodes, as well as solar-blind photodetectors [21]. On the other hand, however, solid solutions of GaN (3.4 eV [22]) and AlN are fully transparent in the visible range of the spectra.

Group III-nitrides usually crystallize in hexagonal (wurtzite) or in cubic (zinc blende) polytypes, and the wurtzite structure as the thermodynamically stable form is the commonly employed one. Due to the high bond strength, these compounds exhibit high stability in aggressive environment and are, in turn, nontoxic; this is an important precondition for their use in biosensors [23]. In an early stage of biosensor research, group III-nitrides were usually grown epitaxially by plasma-

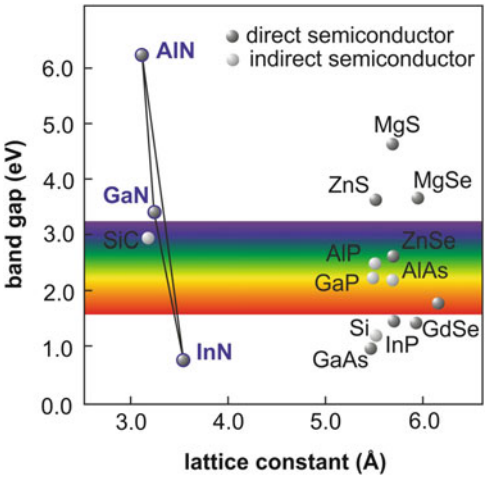

Fig. 1 Bandgap and lattice constants of group III-nitrides and other selected semiconductors

induced molecular beam epitaxy (PIMBE) [24–26]. Due to the better structural quality, thus chemical stability, most groups switched to metal-organic chemical vapor deposition (MOCVD) [27–29]. Common substrates are sapphire, SiC, or Si substrates. While for electronic applications the scalable Si substrate receives increasing attention, the inertness of sapphire and SiC favors those substrates for applications in harsh environment including sensors. In heteroepitaxial growth, dislocations cannot be avoided; thus, the active surface has usually defect densities in the order of 10^8–10^9 cm^{-2}. Despite the high stability of the group III-nitrides, such defects can be locally attacked, e.g., in alkaline solutions. Only recently, native GaN and AlN bulk substrates became available [30], where dislocation densities in the range of 10^3–10^5 cm^{-2} can be achieved. In addition to the improved electronic properties, also enhanced chemical stability can be expected.

2.2 Polarization in Group III-Nitrides

As the wurtzite structure is noncentrosymmetric, two different stacking sequences are possible, finally resulting in a polarity along the [0001] axis. In this direction, double layers of Ga and nitrogen are formed. If Ga is on top of this double layer (called Ga-face), the spontaneous polarization is orientated toward the substrate, whereas in the opposite case (N-face), it is orientated toward the surface [31]. The spontaneous and piezoelectric polarization of III-nitrides is up to ten times larger in comparison with other III-V and II-IV semiconductors. The piezoelectric properties were exploited for the realization of surface acoustic wave (SAW) and further electro-acoustic devices [32].

The spontaneous polarization, however, becomes very important in heterostructures oriented along the [0001] axis. The discontinuity of the spontaneous polarization P_{SP} and a piezoelectric polarization P_{PE} due to strain in the thin films induces fixed charges σ_P at the interface. Depending on their polarity, these charges are partially compensated by free carriers, i.e., electrons or holes.

In the case of common metal-polar AlGaN/GaN heterostructures, a negative charge is generated at the surface and a positive charge at the AlGaN-GaN interface. An additional piezoelectric polarization is generated by the tensile strain in the barrier due to the lattice mismatch of GaN and AlGaN. This piezoelectrically induced charge σ_{PE} increases the polarization of the AlGaN barrier. The resulting charges $\sigma_{P,\ AlGaN}$ and $\sigma_{P,\ GaN}$ are shown in Fig. 2. To maintain charge neutrality, free electrons accumulate near the interface in the GaN buffer and generate the two-dimensional electron gas (2DEG) on the order of 10^{12}–10^{13} cm^{-2} [31] and finally, the conductive channel of a high-electron-mobility transistor (HEMT) [33]. These channels can be adjusted by the composition of the solid solutions in the heterostructures without any doping and are employed for high-power high-frequency amplifiers [34].

The channel formed by the surface-near 2DEG is confined in a fully epitaxial structure about 10–30 nm below the surface, which allows an effective modulation of the charge density through electric fields. Any additional charges on the surface will

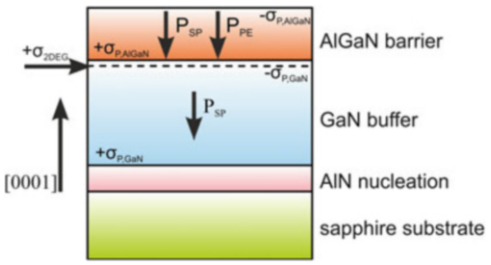

Fig. 2 Schematic drawing of an AlGaN/GaN heterostructure (Ga-face) with spontaneous and piezoelectric polarization field and induced charges

compensate or amplify the field inside the AlGaN barrier; thus, positive or negative charges on the surface increase or decrease the electron concentration of the 2DEG, respectively. Such changes can be induced by ions or polar molecules interacting with the surface of the AlGaN/GaN heterostructure. This basic principle is employed for sensing of gases, ions, and (bio)molecules and the determination of pH in solutions.

A very attractive feature of those HEMTs employing a 2DEG is the principal operation with gain and thus, the potentially higher sensitivity than a bulk material. Moreover, the same heterostructure can be used for the fabrication of amplifying HEMTs as well as passive surface acoustic wave devices, which principally enables monolithic integration of both sensor functions and analog as well as digital data processing and transmission. Although such concepts will not replace Si electronics for data processing, it is a possible route to realize integrated devices with multifunctional sensors, on-chip amplification and computation capability, and even remote wireless readout.

2.3 *Indium Nitride*

InN as the representative with lowest bandgap behaves differently to the other members of the group III-nitride family. For most of the semiconductors, the Fermi level at the surface tends to be within the forbidden gap, which results in a surface depletion zone (see GaN in Fig. 3). In InN, however, the Fermi stabilization energy is in the conduction band. As a consequence, native defects of InN act as donors. These properties result in a remarkable accumulation of electrons at the InN surface (Fig. 3), which can be considered as a large defect in the crystal, and are also the reason for the strong n-type conductivity of InN [35]. This high affinity of the surface for electrons has consequences in the adsorption behavior of polar or charged species and, thus, on the properties as chemical sensor.

2.4 *Summary of Features Relevant for Biosensors*

The employed optical and electronic properties of group III-nitride-based micro- and nanostructures, however, have been proven to be extremely sensitive to any

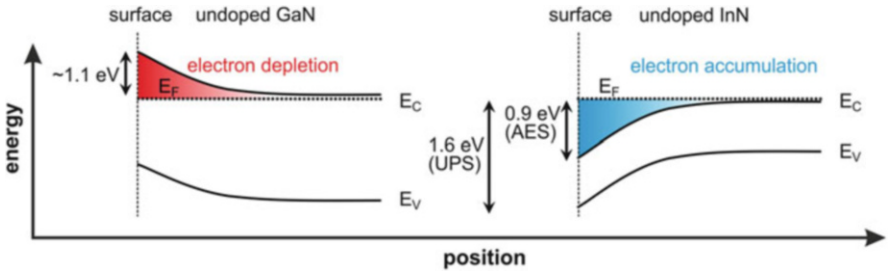

Fig. 3 Schematic band diagram for the surface-near region on undoped GaN (left) and InN (right) (E_F, Fermi level; E_C, conduction band minimum; and E_V, valence band maximum). Values for the band bending are obtained by Auger electron spectroscopy (AES) and ultraviolet photoelectron spectroscopy (UPS) (after [36])

manipulation of surface charges. Already the exposure of unpassivated AlGaN/GaN HEMTs to water vapor is causing depletion of the 2DEG. Similarly, electrons and ions on the surface of InGaN/GaN-LEDs modulate the band profile, thus altering the wavelength and the intensity of the emitted light.

These observations stimulated the research on GaN-based heterostructures to sense those effects. Meanwhile various sensing principles have been proposed [37–40], and most of them can be adapted for biosensors. The advantages and possibilities of the group III-nitrides for biosensing are summarized as follows.

1. The outstanding chemical inertness [41] results in

   high (bio)chemical stability and
   biocompatibility [23, 42].

2. The wide bandgap enables

   devices with low electronic noise [27] and
   transparency in the visible range of light
   (possibility to combine well-established methods in biology) and
   light-addressable potentiometric sensors (LAPS) [43].

3. Due to the direct band transition,

   light-emitting devices can be fabricated (LEDs, laser); thus,
   integration of spectroscopic methods [44] is possible.

4. The high spontaneous polarization [31] can be used in

   single-crystalline field-effect transistors
   without further dielectrics such as gate oxides
   (resulting in enhanced chemical stability).

5. The piezoelectric properties facilitate

   electroacoustic devices such as SAW devices [45] and
   further microelectromechanical systems (MEMS).

Expectedly, those properties resulted in the proposal of various transducer principles, which are categorized in the following.

2.5 *Overview on Nitride-Based Biosensors*

Biosensors could be classified according to their transducer principle or to the employed receptor. Using the transducer as the criterion, most sensors can be categorized as electronic, optical, or mechanical [46].

1. Electronic biosensors are the most attractive type of sensors due to the easy data collection and processing capabilities. The simplest configuration employs bulk GaN and was demonstrated for ion sensing applications. Potentiometric measurements revealed a pronounced sensitivity to anions, which was found to be reversible though not selective [47]. GaN nanowires were also suggested due to their high surface area to volume ratio [48]. Most of the reported biochemical sensors based on group III-nitrides, however, employ HEMT devices derived from AlGaN/GaN heterostructures, which will cover the major part of the following discussion.
2. Systems, which detect biomolecules or cells by measuring their interaction with light, are optical biosensors. The employment of techniques such as reflection, transmission, or Raman spectroscopy could be considered as optical biosensors as well. Although the direct semiconductor system with tunable bandgap offers interesting possibilities for spectroscopic analysis, this will not be the target here. Only optoelectronic devices, where the light emission is directly affected by adsorbed biological species, are considered here.
3. Finally, mechanical biosensors usually employ resonators and the frequency shift upon adsorption.

More specific, Schöning and Poghossian [49] classified Si-based BioFETs using the function of the biorecognition element for the detection as main criterion, which easily can be adapted for group III-nitride-based BioFETs (Fig. 4). These types of biosensors have been realized by employing an HEMT as transducer element, which will be described in the following paragraph.

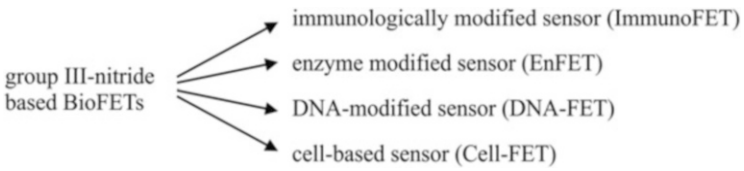

Fig. 4 Classification of AlGaN/GaN-based BioFETs

3 High-Electron-Mobility Transistor Sensors

3.1 Sensor Structure and Technology

The simplest configuration to use a 2DEG-containing AlGaN/GaN heterostructure is a planar open-gate HEMT (Fig. 5). To enhance the chemical stability, the heterostructures are terminated by a thin 2–3 nm GaN layer. There is no principle difference in the use of N-polar or Ga-polar heterostructures [50], due to the superior crystal quality and chemical stability; however, usually Ga-face heterostructures are employed. The size of the active sensor area can be a few millimeters [51] for single devices or scaled down to a few micrometers for sensor arrays [27] or for integrated structures. Usually, a mesa etching is required to isolate the device [23]. Alternately, ion implantation [52] or UV laser cuts [53] can be used to isolate the 2DEG channels of the active sensor area. Conventional Ti-/Al-/Au-based metallization used for the HEMT technology [54] is forming the ohmic contacts for source and drain. The active area is confined, and the contacts are passivated by additional insulating layers as SiN_x or Sc_2O_3 [28], which is often used for high-performance radio-frequency (rf)-HEMT passivation [54], CF_x [26], SiO_2 [29], silicone rubber [24], polyimide [25], epoxy [27], polymethyl methacrylate [55], or other materials depending on the actual sensing application. Finally, the active gate might be modified or coated to activate it or to achieve certain selectivity.

3.2 pH Sensors

In an early study, Neuberger et al. demonstrated a high sensitivity of GaN/$Al_{0.3}Ga_{0.7}N$/GaN heterostructures with open gate to ions provided by plasma spray ionizer and concluded that effectively for each negative ion on the surface one electron is lost in the 2DEG [50]. From such high sensitivity of AlGaN/GaN-based sensors to ions in air, a response to ions in electrolytic solutions can be expected as well. In ISFETs or electrolyte-gated field-effect transistors (EGFETs), the open-gate area is exposed

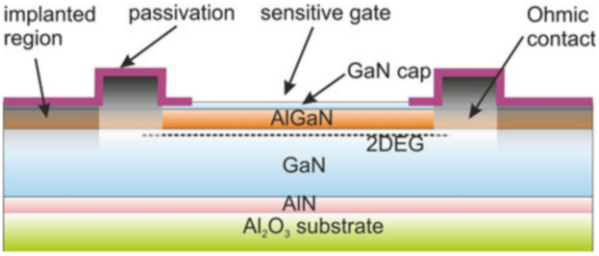

Fig. 5 Schematic cross section of the basic AlGaN/GaN heterostructure with insulation by ion implantation

directly to an electrolyte, whose concentration of specific ions shall be determined. This EGFET is the basic element of all AlGaN/GaN-based biosensors. Instead of the fixed gate, a reference potential V_{ref} is applied to the electrolyte-oxide-semiconductor system via a reference electrode, which is dipped into the electrolyte (Fig. 6) and defines the potential of the solution. It should be noted that some investigations performed by Kang et al. [55–57] and Podolska et al. [58] are carried out without a reference electrode measuring I_D at constant drain-source voltage V_{DS}. This configuration, however, is very susceptible to electrostatic interference, and the reproducibility is therefore limited.

The chemical response of an EGFET to changes in the electrolyte composition can be monitored by recording of the drain-source current I_{DS} at a fixed V_{ref} or by adjusting the gate voltage via the Ag/AgCl reference electrode (Fig. 6) in order to keep I_{DS} constant.

Reproducible and quantitative results for an electrochemical AlGaN/GaN pH sensor are first reported in 2003 by Steinhoff et al. [59]. They achieved a linear response of 56 mV/pH with a resolution better than 0.05 pH close to the Nernstian limit of 58.7 mV/pH at 23°C. Similar results were demonstrated also by other groups (57.0 mV/pH [60], 57.5 mV/pH [25]), and no qualitative differences of the pH response are reported for ISFET structures with GaN cap layers [59] compared to bare AlGaN surfaces [29]. Furthermore, Steinhoff et al. compared different transistor structures with respect to their pH response and found that even the thin surface oxide layer forming upon exposure to atmosphere is sufficient for a linear response in the range from pH 2 to pH 12. X-ray photoelectron spectroscopy (XPS) analysis of as-deposited GaN revealed the almost immediate formation of a thin oxide film at the surface [60]. Surfaces with native oxide and thermally oxidized samples showed almost no difference in sensitivity. Thus, in contrast to the established Si-based ISFETs, neither thermal oxidation nor specific pH-sensitive oxide layers, e.g., Ta_2O_5 or Al_2O_3, are needed.

The influence of the ions on the surface potential of an oxidized GaN surface can be explained with the site-binding model [61]. It proposes that atoms in the surface are acting as amphoteres, when they are in contact with an electrolyte (Fig. 7). In the case of a high concentration of H_3O^+ ions (low pH, Fig. 7b), the Ga-OH groups tend to accept a proton, and the oxide surface becomes positively charged. In contrast, if

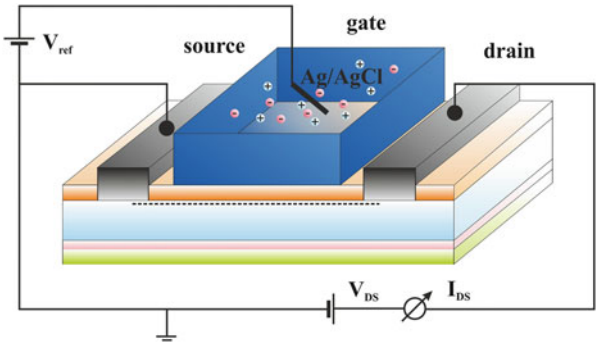

Fig. 6 Schematic view of an AlGaN/GaN EGFET. The metal gate is replaced by an electrolyte bath chamber contacted with an Ag/AgCl reference electrode

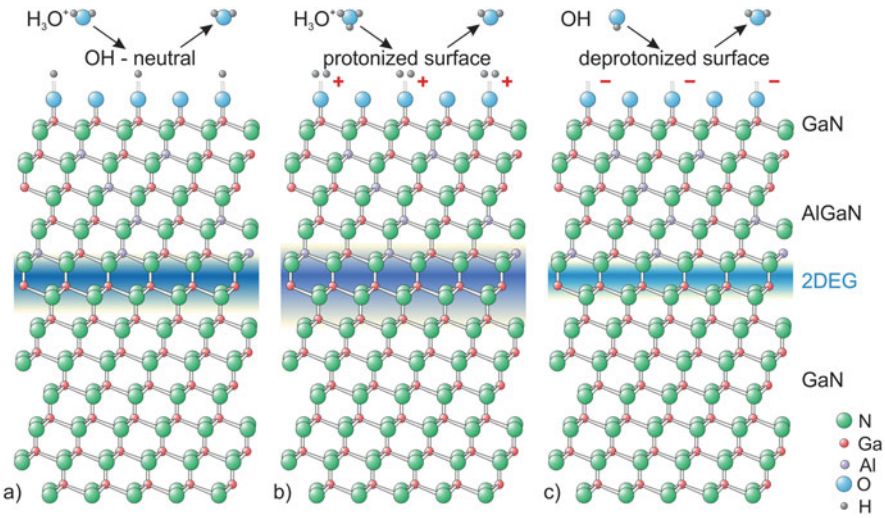

Fig. 7 (**a**) Model for the oxidized AlGaN surface in water and the reaction with (**b**) positive H_3O^+ and (**c**) negative OH^- ions and the impact on the 2DEG sheet carrier density

the concentration of H_3O^+ ions is low, i.e., the concentration of OH^- ions is high (high pH, Fig. 7c), most of the Ga-OH groups release a proton, and the surface charge becomes negative. These changes in surface charge due to the change of pH in the electrolyte directly affect the surface potential and consequently the sheet carrier density of the 2DEG [59]. A theoretical study [62] employing this model and the Poisson-Boltzmann equation is in good agreement with the reported experimental results.

The selectivity to specific ions can be achieved by functionalization of the gate area. In the simplest case, it was achieved by a thin Au film [63], which resulted in a slightly increased response on halide ions. Due to the high affinity to electrons, InN selectively reacts with anions. Higher selectivity can be achieved by covering the active gate area with polymeric membranes. This technique was successfully employed for the selective sensing of potassium, ammonium, sodium, and nitrate [64]. Other techniques could be the use of selective ion channels in lipid membranes as proposed by Steinhoff et al. [65] and Kang et al. [38] or ion-selective chalcogenide glasses [66].

The employment of HEMTs for chemical sensors is not limited to AlGaN/GaN heterostructures. InAlN barriers have been developed, which are lattice-matched to GaN for indium compositions of 16–18%. The reduced strain is expected to increase the lifetime and, thus, the long-term reliability. Moreover, due to the higher spontaneous polarization compared to AlGaN solutions, the barrier thickness can be decreased. With a channel closer to the surface, the current response of a sensor increases [67].

3.3 Monitoring Biochemical Reactions

Although pH sensors are not biosensors in the sense of the definition by IUPAC [7], they can be employed in medical applications or to monitor biochemical reactions, which will be described in the following exemplarily.

Lübbers realized a micro-blood pH analyzer for fetal blood sampling in order to minimize the volume of the blood sample (Fig. 8) [68]. The heart of the system is a fluidic module with AlGaN/GaN pH sensor, reference electrode, and an optical detection system for gas bubbles in the sample fluid. The shown measurements in the blood demonstrate the usability of AlGaN/GaN-based sensors in a biologically relevant environment.

On the other hand, many biochemical reactions are accompanied by changes of the pH value. A qualitative monitoring of biochemical reactions was demonstrated for an enzyme assay in a volume of 35 µl [69]. The catalytic splitting of 4-nitrophenyl caprylate by the enzyme lipase resulted in a pH change due to the release of caprylic acid, which was detected by an AlGaN/GaN ISFET (Fig. 9a). Faster reaction was

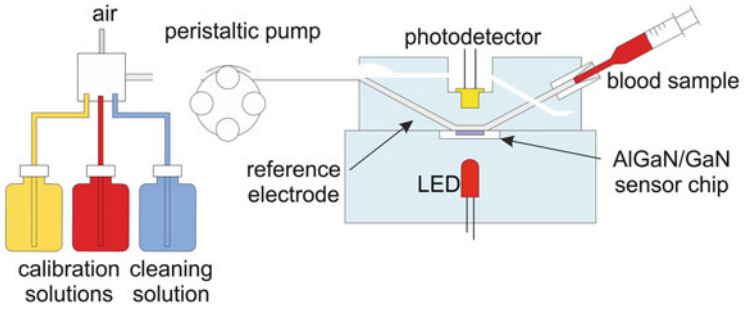

Fig. 8 Scheme of the fluidic circuitry of the micro-blood pH measurement setup (adapted from [68])

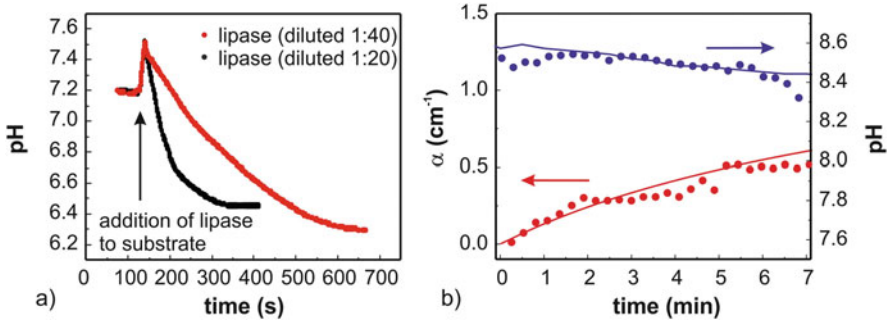

Fig. 9 (**a**) Monitoring of the catalytic splitting of 4-nitrophenyl caprylate with an AlGaN/GaN ISFET for different concentrations of lipase [69]. (**b**) Simultaneous determination of changes in the absorption coefficient α and pH value induced by the enzyme reaction. Compared are the opto-electrochemical analysis utilizing an AlGaN/GaN ISFET in a droplet volume of 700 nl (circles) and consecutive measurements with a pH meter and spectrophotometer in a volume of 700 µl (solid line) (adapted from [68])

observed for higher enzyme concentrations, and a good reproducibility was achieved with a measurement error of ±0.022 pH. Interestingly, the reaction products additionally cause a change in the light adsorption, which was monitored simultaneously (Fig. 9b).

4 Surface Treatment and Stability

Despite the high stability of the group III-nitrides, electronic and optoelectronic devices require a careful surface passivation in order to stabilize their performance and block any influence from the environment. In contrast, for biosensors, the interaction of the environment with the surface is an essential precondition. Thus, for a reproducible operation, the surface needs to be stabilized or functionalized. Various sensing principles have been investigated up to date, see the reviews and the references therein [14, 37–40], and most of the demonstrators exhibited an excellent stability at laboratory conditions. Nevertheless, reliability and stability issues at practical conditions are rarely addressed.

The ideal case of clean group III-nitride surfaces will be altered by any subsequent treatment, and even the exposure to air results in immediate adsorption of oxygen, carbon, and hydrogen [23], which will influence the sensing behavior. For example, Chaniotakis et al. [70] explained the pH response of a clean GaN surface immediately after growth with an electron transfer with anions, while Steinhoff et al. [59] used the above described site-binding model on an oxidized GaN surface. In addition, every processing step that is involved in the fabrication of the devices causes different adsorbed species [23] as well as significant changes of the surface potential [31]. Both effects have important influence on the stability of group III-nitride-based biosensors. Since a clean group III-nitride surface cannot be maintained, an alternative stabilization needs to be employed, for example, an oxidized or otherwise functionalized surface.

4.1 Oxidation

Oxidation of the GaN surface is one of the most basic functionalization methods for AlGaN/GaN ISFETs. According to the site-binding model, it is essential for the pH response of the group III-nitrides [59, 71], supports covalent binding of functionalizing molecules through hydroxyl groups [72], and promotes a stable attachment of lipid membranes as well as living cells [65]. Silicon oxide has a major drawback in applications as gate dielectric in biosensors due to the low stability in electrolytic solutions [73]. In contrast, metal oxide surfaces such as Ta_2O_5 and Al_2O_3 have shown operation with superior long-term stability in physiological environment.

Exposure to air results already in the formation of a thin oxide layer as confirmed by XPS [26, 60, 74, 75]. It enables already the operation of AlGaN/GaN sensors as

ion detectors. On Ga-polar GaN, this native oxide can have a thickness of one monolayer or even less, while an enhanced formation of native oxide on the surface with N-face polarity was shown by XPS [75]. Due to the low thickness, which might be altered during the operation as a sensor exposed to a liquid, it is assumed that it is responsible for long-term instabilities. Moreover, Ga_xO_y is attacked in alkaline solutions which would impair the stable operation over a wide pH range [74]. The observed hysteresis effects after repeated exposure to alkaline and acidic solutions as well as the deviations from a linear response of the sensors at pH $\geq$10 [64] indeed support the existence of a degraded surface oxide. The influence on a biosensor working at lower pH (<pH 9), however, is not known.

On the other hand, stoichiometric Ga_2O_3 can be etched only in hot acids [76]; thus, intentional oxidation may stabilize the performance of AlGaN/GaN sensors. Thermal oxidation of the surface was investigated by Steinhoff et al. [65]. Based on contact angle measurements, the best oxide layers were obtained at 650°C. At this temperature, however, the heterostructure degrades, demonstrated by a reduction of the sheet carrier concentration in the 2DEG of about 50%. To avoid such degradation, rapid thermal processing can be employed at slightly increased temperatures of about 700°C [26]. In all cases, with increasing oxidation temperature, the oxygen concentration at the outermost surface decreases slightly, whereas a considerably higher amount is detected in the bulk, which is finally responsible for the degradation of an AlGaN/GaN transistor at higher oxidation temperatures. Consequently, there is only a small process window as a compromise between oxidation temperature and time and the degradation of the electronic properties of the sensor. Also plasma oxidation in O_2 or N_2O was shown to result in substantial degradation of the electronic properties [77]. On the other hand, soft fluorine plasma treatment can form a metallic surface phase as observed by XPS [23]. When exposed to ambient conditions, these surfaces are directly oxidized due to the high reactivity of metallic gallium, resulting in the formation of gallium oxide on the sensor surface. In contrast to the direct plasma oxidation, this method can have even positive effect on the electronic properties of the AlGaN/GaN heterostructure [23, 51, 78].

Oxides up to 3 nm can be formed by exposure to H_2O_2 [79], and it was shown that this oxide film improves the performance of a pH sensor in terms of drift and hysteresis effects. Wetting experiments have shown that thermal oxidation results only in slightly improved properties. Finally, electrochemical oxidation was demonstrated to result in homogeneous oxides with flat sharp interfaces [80]. Such chemical, electrochemical, or photo-assisted chemical oxidation methods at low temperatures appear to be promising for the stabilization of the sensor surfaces.

4.2 Stability in Water

As a very first precondition for the operation as biosensors, the material has to be stable in water and different aqueous solutions. Here, group III-nitrides turned out to be superior to Si as well as other III-V compound semiconductors. In a basic study,

Foster et al. demonstrated the stability of both N- and Ga-polar GaN in deionized water, at pH 5 and pH 9, and in H_2O_2 solutions [81]. After immersion for 7 days, the amount of gallium leached from the surface was measured by inductively coupled plasma mass spectrometry of the solutions. The study confirmed a higher stability for the Ga-polar material. Furthermore, acidic and neutral solutions have less impact on the surfaces than alkaline solutions. Stability to extreme pH values is necessary only if aggressive cleaning or sterilization treatments are required. The reduced stability in alkaline solutions might be caused by the abovementioned properties of the gallium oxide on the GaN surface, which is stable in acidic and neutral solutions, while it is attacked in alkaline environment [74]. This effect needs to be investigated further since many of the physiological solutions relevant also for biosensing are slightly alkaline.

4.3 Cleaning of GaN Surfaces

The cleaning of the sensor surfaces has to be performed for the two major purposes: (1) the cleaning during processing and (2) cleaning or sterilization during the use of the sensors.

Cleaning procedures during device processing are out of the scope of this chapter; for a review see Refs. [82, 83]. In the following, however, their impact on the functionality of a biosensor is summarized. Common treatments in organic solvents (acetone, methanol, ethylene) and DI water are used to remove contaminations such as particles, dirt, and to a less extent organic species. Exposure to HF and HCl solutions are standard cleaning procedures resulting in low coverage of oxygen and carbon on GaN sensor surface. After cleaning, however, residues of fluorine and chlorine, respectively, have been detected by XPS [23]. It has been shown that none of those treatments have negative impact on the biocompatibility of the sensor surface, ensuring freedom to select proper cleaning procedures among the available and well-studied variants.

Effective removal of oxide from group III-nitride surfaces was also demonstrated by immersing them in ammonium sulfide $(NH_4)_2S$ [84]. It should be noted that the method exchanges oxygen by sulfur. The impact on biosensors or biocompatibility is not known. Sulfur, however, might be beneficial for alternative routes in biofunctionalization of the surface.

For biological applications, the sensors have to be carefully sterilized. Cleaning in polar and nonpolar solvents is not effective to remove the organic material stemming from the cells as well as the various components of the cell media completely. A treatment in steam at elevated temperatures was shown to not affect the sensor properties [23]. In contrast, the treatment in NaOH at 80°C tends to attack both the passivation layers and crystal defects such as dislocations, which degrades the sensor performance or even destroys the structure [60]. Appropriate passivation layers to be integrated into the sensor, which withstand the abovementioned treatments, are multi-stacks of silicon oxide and nitride as well as the implementation of

thin diamond films [85]. MOCVD-grown sensors have generally shown higher stability than heterostructures grown by PIMBE [60]. It is generally improved by a thin GaN cap layer of 2–3 nm. The preferential etching of defects of GaN and AlGaN layers results in local etch pits at the surface, typically in hexagonal shape. Such pits can short-cut the 2DEG to the active surface resulting in a drastic decay of the sensor performance.

4.4 Wetting Behavior

Most of the investigated treatments change the wetting behavior of the surface, which can be used as indicator for the state of the sensor surface [23]. A summary for selected processing steps is given in Fig. 10a, while Fig. 10b displays the influence of the contact of cell media or living cells with the sensor surface. A significant decrease of the contact angle was observed after the SF_6 plasma etching due to the formation of a thin surface oxide as described before. A similar but less pronounced effect was observed after immersion in HF. In contrast, autoclave treatment enhances the carbon contamination with negative impact on the sensor properties and increased contact angle to water. For all other treatments, the contact angle recaptures a stable value of about 50 $\pm$ 5° after exposure to air or water droplets for some hours due to contamination by hydrocarbons. Oxidation processes generally improve the wetting behavior. Also, increased Al content in AlGaN as well as N-polar material was observed to lead to lower wetting angles [65]. After contact with culture media, an angle of about 50° was always measured. After cell adhesion, the contact angle was slightly higher (about 55°), most probably due to the enhanced carbon concentration compared to the hydrocarbons in the case of the untreated sensors.

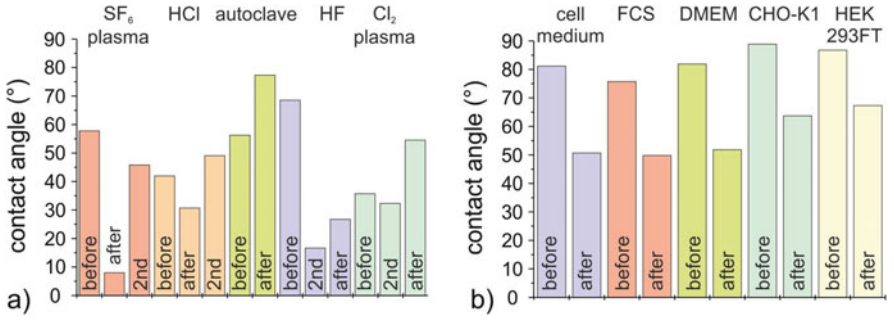

Fig. 10 Contact angle to water before and after (**a**) different processing treatments and (**b**) cell adhesion on GaN surfaces. The second represents a measurement after 24 h. Cell growth and cell media exposure have been performed after autoclaving (*FCS* fetal calf serum, *DMEM* Dulbecco's modified Eagle's medium-high glucose, *CHO-K1* Chinese hamster ovary cells, *HEK 293FT* human embryonal kidney cells) (adapted from [23])

To obtain a high wetting angle of about 100°, the deposition of fluorocarbon coating can be employed. In combination with oxidation, the confinement of droplets on the hydrophilic active area of the sensor within a hydrophobic environment can be achieved. It was realized for the measurements in droplets [26, 53]; it is, however, also a route to control the growth of living cells or the selective absorption of proteins [86].

4.5 Impact of Device Processing

In addition to typical sensor devices in planar configuration (e.g., HEMTs), free-standing three-dimensional (3D) structures (e.g., MEMS) and further configurations can be employed for biosensors. The processing of such devices includes different steps, like metallization, passivation, wet chemical etching, and lithography, as well as fluorine- and chlorine-based dry etching and cleaning procedures. Consequently, each fabrication step for semiconductor devices involves various kinds of impacts on the surface including high-temperature and high-energy treatments, which can disorder the chemical composition and introduce defects on the surface [87, 88], and thus may influence the electrical properties of the devices as well as the biocompatibility and wetting behavior of the surfaces, which are important factors for biosensors [26, 65].

The impact of the treatments can be summarized [23, 51]:

- Fluorine- and chlorine-based plasma dry etching processes alter the surface morphologies and the electrical properties due to the formation of a thin oxide layer and contaminate the surface with F^-- and Cl^--ions.
- Soft fluorine-based etching has a positive impact on the electrical performance of the sensor, while heavy fluorine-based etching leads to degradation.
- The established cleaning procedure with HCl and HF indeed decreases the surface concentration of oxygen and carbon. The remaining traces of chlorine and fluorine have no measurable effect on the sensor properties.
- KOH and NaOH at 70° C etch the GaN layer anisotropically at defects, which degrades the electronic performance of the device.
- Most of the investigated treatments change the contact angle. After a few hours at environmental conditions, however, the starting value of about 50° is recovered.
- The contact to cells and cell media contaminates the surface with carbon and metal ions (mainly Zn), and a nondestructive procedure for their complete removal is not available at present. Its influence on the sensing behavior is not known up to now.
- The exposure of the heterostructure to different biological materials in medium is not changing the electrical performance of the sensor.
- The sterilization by autoclaving, which is very commonly used in working with cell cultures, contaminates the surface with carbon-containing species. Consequently, a modified sterilization method has to be developed for the AlGaN/GaN sensor surface, e.g., additional purification with surfactants or alcoholic derivatives.

Finally, the electrical performance of an AlGaN/GaN sensor degrades after the first use due to surface oxidation and, however, stabilizes thereafter. This phenomenon has to be taken into account for the calibration procedure of the sensors (and for repetitive use of the expensive sensor material in future biomedical applications).

5 Biofunctionalization of the Surfaces

The clean gate surface of an HEMT is sensitive to every type of charges. To achieve selectivity toward specific analytes, the HEMT surface needs to be modified. As discussed before, the pH sensing is achieved by an oxidized surface. Biosensing, however, requires the binding of receptors, which interact with specific analytes. Figure 11 gives an overview about principle possibilities to functionalize AlGaN/GaN sensors for biochemical applications. The upper row represents biosensors according to the definition of IUPAC [7], while the lower row shows further possibilities for biochemical sensing, which will not be discussed further in this chapter.

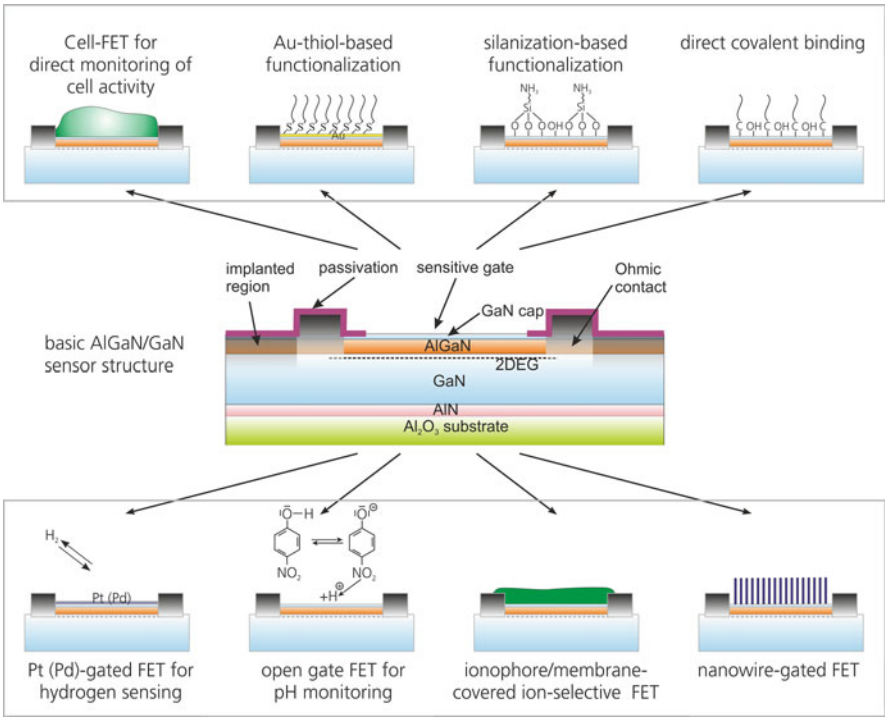

Fig. 11 Schematic overview illustrating the surface functionalization and possible applications of the AlGaN/GaN heterostructure for biosensors (upper row) and (bio)chemical sensors (lower row) (adapted from [89, 90])

The functionalization with living cells will be discussed in the context of Cell-FETs. The functionalization by a thin gold film represents a classic approach for immobilization of organic molecules. Employing the well-established thiol chemistry, Kang et al. reported label-free detection of DNA hybridization [55]. Alternatively, a HEMT sensor can be also used to monitor the reaction of biomolecules on functionalized particles, which were spread over the open gate [91]. This approach was also used to detect explosive 2,4,6-trinitrotoluene (TNT) [92].

The functionalization of GaN surfaces with organic molecules was first performed by Bermudez [93, 94], who analyzed the absorption and bonding of organic molecules, such as aniline ($C_6H_5NH_2$) and 3-pyrroline (C_4H_6NH) on reconstructed GaN by electron spectroscopy in ultrahigh vacuum. These fundamental investigations demonstrate that organic amines are easily adsorbed on GaN and they can be used to attach functional groups at the surface. The physisorption of single-stranded DNA (ssDNA) directly onto AlGaN surfaces was demonstrated, which could be performed by simple printing techniques without the need for cross-linking agents or complex surface pre-functionalization procedures [95].

Higher stability, however, is expected by covalent binding of organic molecules to the group III-nitride surface. Silanization (Fig. 12a) was demonstrated by covering the surface with organosilanes such as aminopropyltriethoxysilane (APTES) [56], octadecyltrimethoxysilane (ODTMS) [72], aminopropyltrimethoxysilane (APTMS) [48], or mercaptopropyltrimethoxysilane (MPTMS) [96], and the linkage was proven by XPS. The attachment is achieved by bonding on surface oxygen. Similarly, phosphonic acid (Fig. 12b) was attached to the nitride surface via oxygen bonds [97]. Strong differences were found in the case of APTES for growth n- and p-GaN surfaces [98]. Arisio et al. [99], however, concluded on a low stability of organosilanes in water and attributed this observation to dissolution of the interfacial gallium oxide.

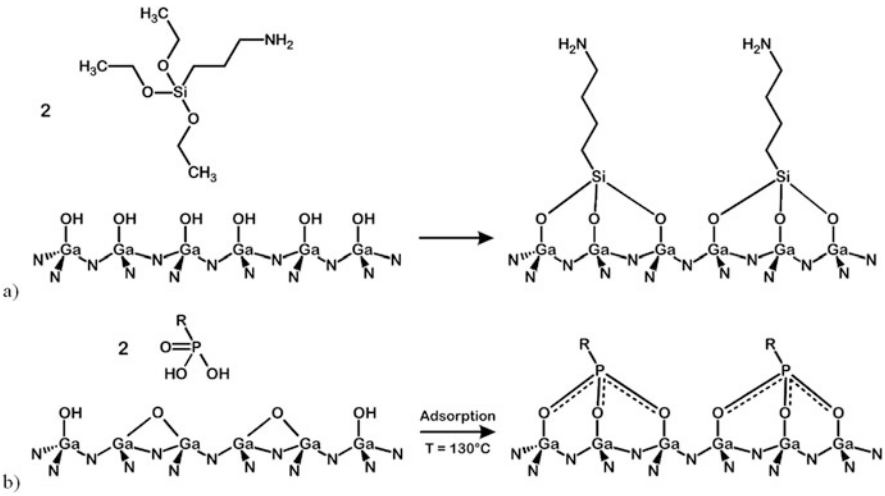

Fig. 12 Examples for the attachment of biomolecules by bonding to surface oxygen: (**a**) organosilane (APTES) [56] and (**b**) phosphonic acid [97] (taken from [100])

Other approaches claimed to bond organic molecules directly to GaN such as peptides [101] or amines [102]; however, peptides also bond via surface oxygen [103]. Nevertheless, high stability in water over several days was observed. Thus, the stability of the functionalized surfaces still requires further research. Direct covalent bonding was also proposed by photo-assisted attachment of n-alkenes with different carbon chain lengths, such as 10-aminodec-1-ene protected with trifluoroacetamide (TFAAD) [104], allylamine protected with trifluoroacetamide (TFAAA) [105], and 5-bromo-1-pentene [106]. A study by electron spectroscopy, however, revealed that also this attachment proceeds rather by bonding to surface oxygen than directly to gallium [107]. On the example of TFAAD, the full chain of biofunctionalization of an AlGaN/GaN HEMT to serve as DNA sensor [108] is shown in Fig. 13.

A direct comparison between the functionalization of GaN and GaP by phosphonic acid revealed no fundamental difference in the bonding and stability. GaN, however, had shown less leaching in solutions demonstrating the increased stability [109].

AlN, which could be interesting for mechanical biosensors due to the good piezoelectric properties, and InN can be functionalized using the same principles as described for the HEMTs above. Examples that are described in the literature have been organosilanes [72, 110] as well as peptides [111] on AlN and organosilanes on InN [112, 113]. A physisorption study of amino acids on InGaN solid solutions demonstrated that with increasing indium content, the adsorption is enhanced. The effect was assigned to the surface oxide, which is more developed in indium rich solid solutions [114].

These few observations show that no fundamental differences should be expected for the different members of the group III-nitride family.

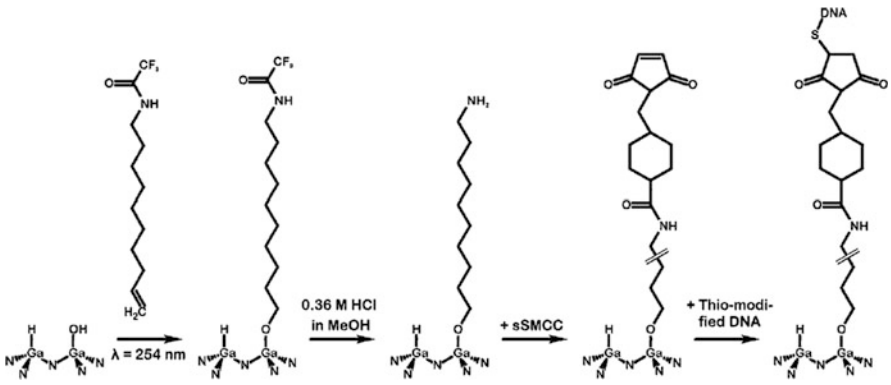

Fig. 13 Surface functionalization process for an AlGaN/GaN-based BioFET: TFAAD is linked to the GaN surface in a photochemical process. In subsequent steps, the protective CF_3 group is removed, the cross-linker sulfosuccinimidyl-4-[*N*-maleimidomethyl]cyclohexane-1-carboxylate (sSMCC), and finally the probe DNA is attached (taken from [100])

6 BioFETs (Detection of Biomarkers)

6.1 Enzyme-Modified Sensor: EnFET

Enzymes enhance biochemical reactions and are highly specific in the binding to educts or substrates. The first biosensor by Clark and Lyons [8] employed such catalyzed reaction by immobilizing glucose oxidase to an amperometric oxygen electrode, in order to determine the glucose level in the blood. Also the first demonstrated BioFET had immobilized enzymes on the gate of a field-effect transistor [106]. These EnFETs often employ the generation of acids by the reaction of the immobilized enzymes with a specific substrate, and the resulting change of the pH value of the electrolyte in the vicinity of the sensor surface is detected.

The first AlGaN/GaN EnFET was reported by Baur et al. to detect penicillin G [115]. The authors compared immobilization of the enzymes by covalent immobilization (c-EnFETs) and physisorption (p-EnFET) and demonstrated strong degradation for the p-EnFET, while c-EnFETs were highly reproducible after several measurements cycles. Long-term exposure accompanied by kinetic modeling has shown the stability of covalently bonded enzymes and the sequential loss of physisorbed enzymes [116]. A linear response of 152 ± 8 μV/μM was found between 10 μM and 300 μM of penicillin G due to the acidification in the vicinity of the gate area. Detection limit has been 2 μM, while at 3 mM penicillin, the EnFET saturates, which is comparable to Si-based EnFETs. In addition, the capability of such EnFETs for the detection of penicillin in μl droplets was demonstrated [44].

A different approach for EnFETs has been used by Chu et al. [117] and Kang et al. [118] for the enzymatic detection of lactic acid and glucose, respectively. In their case, the AlGaN/GaN HEMT gate area was functionalized with ZnO nanorods, and enzymes are linked to those nanorods. Alternatively, Makowski et al. [119] proposed the enzymatic detection of kinase employing functionalized gold particles, which are physiosorbed on the gate.

6.2 Immunologically Based Sensor: ImmunoFET

As part of the immune system, antibody response is defined as the interaction between antibodies and antigens. Antibodies are proteins, and the recognition mechanism between antibodies and antigens is highly specific, enabling highly selective biosensors. The enzyme-linked immunosorbent assay (ELISA) is a well-known example for a bioanalytical tool employing this principle of antigen-antibody reaction.

First approaches toward AlGaN/GaN ImmunoFETs were demonstrated by Kang et al. using APTES [56] as well as Au-thiol-functionalized gate surfaces [57] for the detection of streptavidin and prostate-specific antigen (PSA), respectively. Further demonstrated possibilities are summarized in Table 1, for example, the detection of toxins [120] and cancer antigens [57, 121] or the separation between human and

Table 1 Demonstrated BioFETs based on AlGaN/GaN heterostructures

Target	Functionalization	Receptor	Detection limit	Reference
ENFET				
Penicillin G	APTES	Penicillinase	2 μM	[115]
Lactic acid	ZnO nanorods	Lactate oxidase	167 nM	[117]
Glucose	ZnO nanorods	Glucose oxidase	0.5 nM	[118]
Glucose	ZnO nanorods	Glucose oxidase	1 μM	[128]
SRC kinase	Au nanoparticles	Kinase inhibitor	1 pM	[119]
ImmunoFET				
Streptavidin	APTES	Biotin		[56]
Streptavidin	APTES	Biotin	4.7 pM	[129]
Streptavidin	APTES	Biotin		[130]
Peptides	Au-gated FET		10 pM	[131]
Prostate-specific antigen	Au-gated FET	PSA antibody	1 μg/ml–10 pg/ml	[57]
Prostate-specific antigen	APTES	PSA antibody	0.1 pg/ml	[132]
Monokine induced by interferon gamma	Au-gated FET	MIG, CXCL9 antibody		[133]
Monokine induced by interferon gamma	APTES	MIG, CXCL9 antibody	0.4 μM	[134]
Vitellogenin	Au-gated FET	Vitellogenin antibody	2 μM/ml	[135]
MCP-1	TFAAD	MCP-1 antibody		[122]
Botulinum toxin	Au-gated FET	Antibody	1 ng/ml	[120]
Hg^{2+}	Au-gated FET	Thioglycolic acid	15 nM	[123]
Kidney injury molecule-1	Au-gated FET	KIM-1 antibody	1 ng/ml	[136]
Traumatic brain injury	Au-gated FET	Antibody	10 μM/ml	[137]
Breast cancer antigen		c-erB antibody	0.25 μg/ml	[121]
C-reactive protein	Au-gated FET	CRP antibody	10 ng/ml	[138]
DNA-FET				
DNA	Au-gated FET	ssDNA	0.1 M	[55]
DNA	Au-gated FET	ssDNA		[139]
DNA	11-Mercaptound-ecanoic acid SAM	ssDNA	1 μM	[125]
DNA	TFAAD	ssDNA	10^{-9}–10^{-14} M	[140]
DNA	Au nanoparticles	ssDNA		[91]
DNA	–	Physisorption of ssDNA		[141]

mouse MCP-1 proteins [122]. In a wider sense, ions such as Hg^{2+} ions [123] are detected with a functionalized HEMT. It should be noted that the large size of the proteins and their complicated structure allow static measurements only in diluted solutions, where the Debye length is sufficiently large to avoid the screening of the charges by mobile ions [124].

6.3 DNA-Modified Sensor: DNA-FET

DNA is the nucleic acid that contains the genetic instructions for development and functioning of all known living organisms. The DNA hybridization process is the most applied method for detecting DNA. It identifies unknown single-stranded DNA (ssDNA) by formation of a double-stranded DNA (dsDNA) with the complementary counterpart. The DNA-FET employs a layer of complementary ssDNA immobilized on the gate surface and detects the hybridization event through the additional charge that is introduced by the binding of the target ssDNA. Despite the limitations due to charge shielding in an electrolyte by counter ions, direct detection was demonstrated due to a positively charged transducer surface which attracts the negatively charged sugar-phosphate backbone of the immobilized ssDNA. The hybridization alters this attraction which influences the charge distribution [49].

Similar to their realization of an ImmunoFET, Kang et al. [55] used thiol-modified oligonucleotides to covalently bind ssDNA with 15 base pairs (bp) to the Au-coated surface of an AlGaN/GaN ISFET. They demonstrated repeatability even after denaturation as well as the absence of nonspecific reactions. Repeatability for several cycles was also observed for TFAAD-functionalized AlGaN/GaN HEMTs [100]. Comparing, however, directly the functionalization via Au-thiol and bonding on a self-assembled monolayer (SAM) of mercaptoundecanoic acid, Thapa et al. showed better specificity on SAMs [125]. Further improvement could be demonstrated by dynamic measurements [126] or impedance spectroscopy [127] taking benefit of the reduced diffusivity through a dense functionalized sensor surface.

6.4 Advanced Measurement Schemes

The following chapter shall shortly summarize trends to improve the sensitivity of biosensors by enhanced measurement schemes. Although not specific for AlGaN/GaN-based BioFETs, they have demonstrated already their potential.

6.4.1 Subthreshold Operation

The channel current in a field-effect transistor is linearly and exponentially dependent on the gate voltage above and below the threshold voltage, respectively. Thus, above the threshold voltage, the channel current follows the surface potential shift, in the case of pH sensing according to the Nernstian limit. If the gate voltage is controlled by a gate to be below the threshold voltage, the exponential dependence leads to sensitivities exceeding the Nernstian limit [142]. Higher sensitivity in the subthreshold regime has been demonstrated also employing an AlGaN/GaN BioFET for the detection of proteins [129]. It should be noted, however, that most of the instabilities arise from the surface and, thus, from surface potential changes. Consequently, the subthreshold operation amplifies also these fluctuation and drift phenomena.

6.4.2 Impedance Spectroscopy

As highlighted by Schöning and Poghossian [49], the development of BioFETs still faces multiple theoretical and practical problems. Especially, the distance of the charge that shall be detected to the responding surface in physiological solutions is generally larger than the Debye length, and consequently, the charges would be shielded by counter ions [124]. To circumvent this problem, several dynamic methods have been suggested including impedance spectroscopy [143]. For interpretation of the experimental results, however, usually a model in form of an equivalent circuit is necessary.

For example, the impedance spectra of an AlGaN/GaN sensor in an electrolyte can be modeled by a serial connection of the capacitance of the AlGaN barrier C_{ins}, the double-layer capacitance C_{dl}, and the electrolyte resistor R_{e} (Fig. 14, left). The functionalization with DNA can be considered as a membrane and modeled with an extended capacitance C_{dl} in parallel to a Warburg element Z_w and a transfer resistance R_{ct} [127] (Fig. 14, right). The Warburg element represents the diffusion of ions through the DNA layer. If the functionalization is sufficiently dense, the hybridization of the ssDNA will reduce the diffusivity for ions, which can be measured if the gate voltage is superimposed by an alternating current with small amplitude. Thus, in contrast to the static measurements, which rely on the detection of changes in charge distribution within the Debye length, impedance spectroscopy can employ indirect mechanisms, which are independent of the double-layer thickness and could enhance the sensitivity.

Similarly, impedance spectroscopy can be used in Cell-FETs to obtain additional information on occupancy and cell expansion or movement, which are not accessible by static measurements [144].

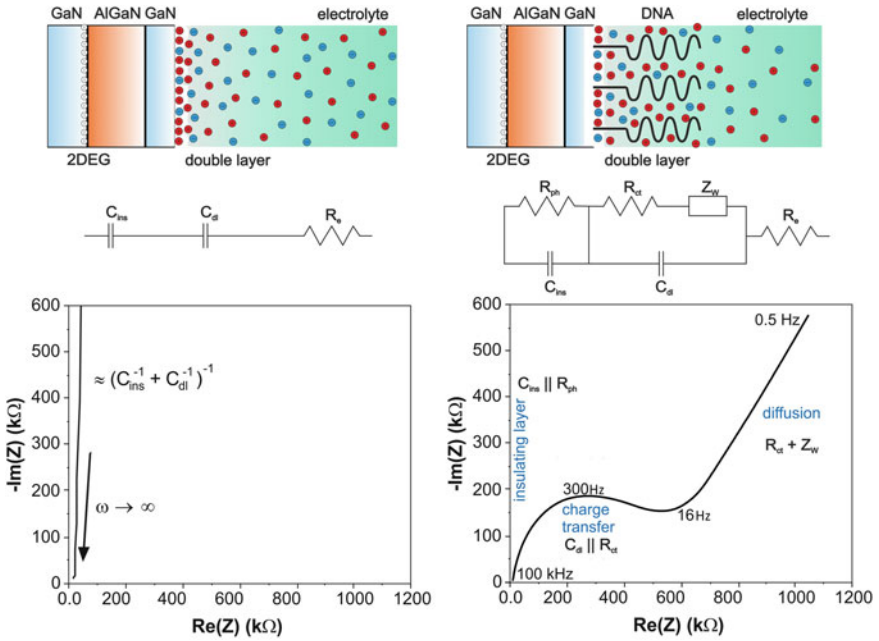

Fig. 14 Scheme of the insulator/electrolyte interface and Nyquist plot (*left*) prior to and (*right*) after functionalization. After functionalization, few pinholes appeared in the passivation (R_{ph}) without affecting sensor performance. At intermediate frequencies, R_{ct} and C_{dl} (double-layer capacitor) in parallel are dominant (semicircle). C_{ins} is insulator capacitance [122]

6.4.3 Dynamic Measurements

The abovementioned model of altered diffusivity can be used for a modified measurement scheme. Instead of an alternating current (ac) voltage, bipolar step input could be applied on the gate [126] within the linear regime of the transistor transfer characteristics. The channel current follows with an exponential dependence, and in the case of perfect matching of target and probe DNA, the corresponding time constants for the response current on both positive τ_p and negative input pulses τ_n were proportional to the logarithm of target concentration until saturation at 10^{-7} mol/L (Fig. 15). Those methods allowed a remarkable increase in the sensitivity compared to static measurements.

7 Cell Proliferation

For the biocompatibility of a material, several definitions are known. In this chapter, biocompatibility is assigned to the ability of a material to be in contact with a biological material without affecting it negatively. More specific for biosensing

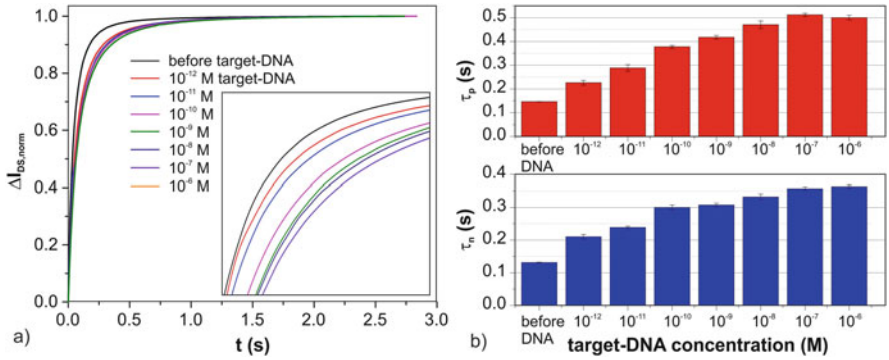

Fig. 15 (**a**) Normalized change of the drain-source current $\Delta I_{\mathrm{DS,norm}}$ for positive input. Insert: Magnification of the range with most prominent changes. (**b**) τ_n and τ_p in dependence on the target concentration [122]

applications, a biocompatible material should allow living cells to grow on top of the biosensor surface. Most of the compound semiconductors such as arsenides, phosphides, and antimonides as well as compounds containing cadmium or tellurium have negative impact on biological host materials and require passivation (e.g., GaAs [145]). In contrast, the biocompatibility of GaN and AlGaN was demonstrated in several publications including a survival of living cells on those materials over long periods [23, 146–150].

The ability to grow cells on top of active sensors is plausibly a critical issue for the realization of cell-on-chip concepts. As shown before, group III-nitride-based ISFETs are chemically inert and stable under physiological conditions. The attachment phase of cell adhesion proceeds rapidly and involves physicochemical linkages between cells and the material surface. Diminished cell adhesion can be used as a measure of toxicity, if first the initial attachment of cells is investigated [151]. First studies with rat fibroblasts (3T3 cells) have demonstrated good adhesion properties of the group III-nitrides independent of the aluminum concentration in the $Al_xGa_{1-x}N$ solid solution ($x = 0, 0.22, 1$) and slightly improved behavior after a pretreatment by oxidation [27, 65]. Podolska et al. [148] observed with more sensitive HEK 293FT cells a slightly decreased survival rate on AlGaN with increasing Al concentration up to 35%. They concluded that a thin GaN capping layer on top of AlGaN supports the proliferation of cells. This and further investigations [27, 149] clearly demonstrated that adhesion and growth of living cells on GaN are superior to Si. Furthermore, Young et al. demonstrated the cultivation of neuronal cells on GaN surfaces [42] and found no fundamental differences on p-type and n-type GaN. Jewett et al. [146] investigated the proliferation of PC12 cells, which is a widely used cell line for studying neuronal differentiation on etched and on functionalized GaN. The cultivation on etched GaN surface confirmed the good adhesion properties of pure GaN. In a control experiment on Si, the cell density decreases over time and eventually reaches zero. For GaN surfaces, which were functionalized with peptides, however, the cell density slightly increased further. Thus, biofunctionalization of the GaN surface could promote the biocompatibility to specific cells.

It should be noted that contrary to ISFETs based on Si, no complex modifications are needed to promote the adhesion and proliferation of cells on AlGaN/GaN ISFETs. Nevertheless modification with fibronectin might be beneficial to enhance the proliferation of cells on AlGaN surfaces [152]. Furthermore, Hofstetter et al. could show by comparing living cells on AlGaN/GaN and on glass after X-ray radiation that the GaN surface has no negative impact on cell repair mechanisms [153].

For the investigation of the influence of surface contamination on the biocompatibility of AlGaN/GaN sensors, mammalian cell cultures HEK 293FT and CHO-K1 were employed (Fig. 16) [23]. A surface contamination by carbon, hydrocarbons, and metal ions slightly decreases the cell proliferation. There is evidence that the human HEK 293FT cells are more sensitive since they show a reduced growth. Nevertheless, the study revealed that typical cleaning and etching procedures, which are used in the fabrication of AlGaN/GaN sensors and in the functionalization of the sensor surface (i.e., KOH, HCl, HF wet chemical etching, SF_6 and Cl plasma etching), have very small influence on the biocompatibility. Even remaining ionic contamination such as Cl from HCl or K from KOH with a concentration that allows detection by X-ray photoelectron spectroscopy had no significant influence. According to this observation, a variety of surface cleaning and functionalization treatments for GaN can be employed without negative impact on the biocompatibility, which gives a high degree of freedom for the transfer of well-established techniques to the fabrication and reuse of GaN-based biosensors.

Leaving the sensors in water, algae [155] (in lake water) or bacteria [156] (in open-cell media) grow on top of it, forming biofilms. These processes of biofilm formation can be monitored with the AlGaN/GaN sensor. In the case of algae (Fig. 17), the growth of a biofilm was observed on the sensor under illumination. It was accompanied by a continuous increasing of the channel current. In contrast, in dark environment, no algae appeared and the sensor signal was constant with some fluctuations due to temperature and light variations.

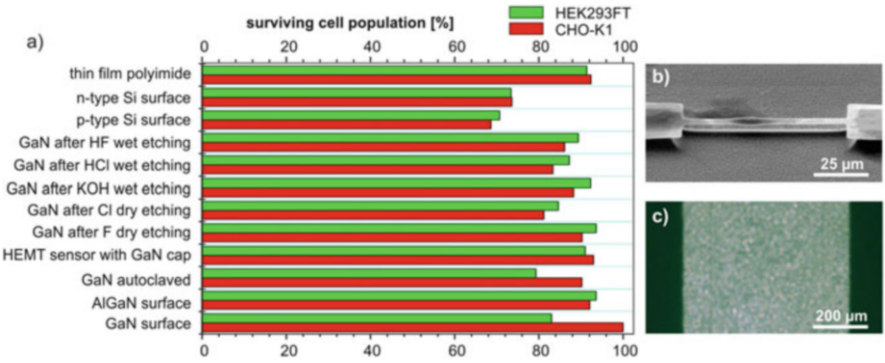

Fig. 16 (**a**) Cell population after 2 days on differently treated AlGaN/GaN heterostructures and comparison to a bare AlGaN surface, to Si, and to polyimide, which is used for passivation of the sensor metallization. Upper (green) and lower (red) bars represent the HEK 293FT and the CHO-K1 cell lines, respectively [154]. (**b**) CHO-K1 cells on MEMS sensor and (**c**) HEK 293FT cells on the active area of a planar AlGaN/GaN sensor

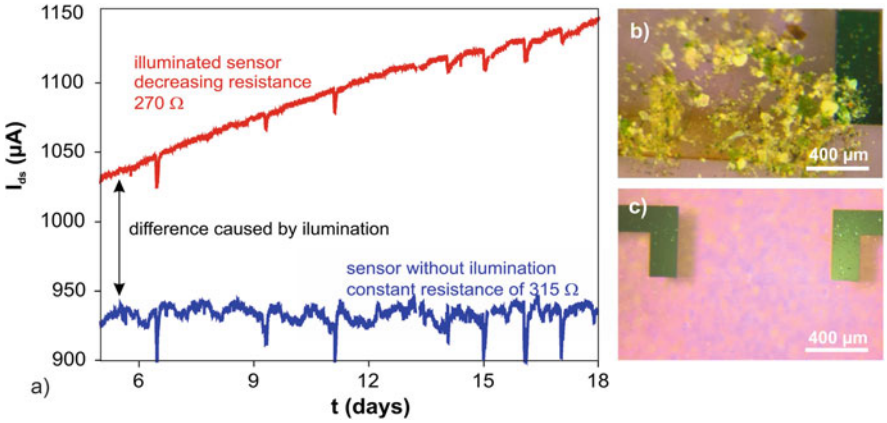

Fig. 17 (**a**) Channel current of an AlGaN/GaN sensor in light, where algae were growing (red line) and in dark environment (blue line) and corresponding photograph (**b**) in light and (**c**) in dark environment [155]

Table 2 Demonstrated hybrids of living cells and (Al)GaN surfaces

Cells/cell line	Substrate	Treatment	Reference
Rat fibroblasts (3T3 cells)	$Al_xGa_{1-x}N$ ($x = 0$, 0.22, 1)		[27]
Cerebellar granule neurons prepared from 7-day-old Wistar rats	GaN	Alcohol, autoclave	[42]
PC12	GaN GaN/peptide	Piranha/HCl/NH_4F	[158]
SaOS-2 human osteoblast-like cells	AlGaN/GaN	Organic solvents/UV light	[152]
HEK 293FT	AlGaN/GaN	Organic solvents	[148]
HEK 293FT	GaN, AlGaN/GaN	Organic solvents, autoclave	[23]
CHO-K1	GaN, AlGaN/GaN	Organic solvents, autoclave	[23]
Nerve cell line NG108-15 (mouse neuroblastoma × rat glioma hybrid)	AlGaN/GaN	Organic solvents, autoclave	[149]
Algae	AlGaN/GaN	Organic solvents	[155]
Bacteria	AlGaN/GaN	Organic solvents	[156]

The abovementioned examples, which are summarized in Table 2, demonstrate that there are no serious restrictions to build hybrids of a GaN-based sensor element with cells, showing also the high stability of the sensors over several days under non-optimized conditions.

Finally, it should be mentioned that the growth of PC12 cells on AlN required a surface functionalization such as peptides [157], which is in contrast to good proliferation of CHO-K1 cells on AlN microstructures (Fig. 16b [154]).

8 Cell-FETs (Monitoring Living Cells)

Surely, the most interesting but also most complex biosensor is constructed coupling whole cells as a biorecognition element with a transducer device. It offers the possibility to study the effect of drugs or environmental influences on the cell metabolism directly by measuring, e.g., extracellular acidification, intra- and extracellular potentials, or simply the adhesion properties.

The interaction in hybrids between living cells and an AlGaN/GaN HEMT was first demonstrated with cardiac myocyte cells of embryonic Wistar rats on HEMT arrays [27]. After 5 days of cultivating, a monolayer of cells developed, which spontaneously contracted with stable frequency, and the extracellular potential of about 70 µV was recorded with high signal-to-noise ratio.

The monitoring of the condition of living cells could be employed to obtain information about the environment relevant for living species with high impact in environmental protection, toxicology, and drug development. Firstly, the growth of cells on the sensor (Fig. 17) [155] or the acidification as a result of the cell metabolism [90] can be analyzed using AlGaN/GaN HEMTs.

A more detailed study on the electrically detectable stimulation of NG108-15 neuronal cells has been performed by Cimalla et al. [159] and Gebinoga et al. [160, 161]. The used substances diisopropyl fluorophosphate (DFP) and phenylmethanesulfonyl fluoride (PMSF) are inhibitors for acetylcholinesterase (AChE). In addition to PMSF, amiloride was used to block Na^+ and Ca^{2+} channels. The extracellular activity of the same cell field was recorded over long time, and the device has shown stable operation under physiological conditions and a very good signal resolution. As an example, the reaction of the Cell-FET on dosing of DFP is shown in Fig. 18. The current in the AlGaN/GaN HEMT decreases due to a decreasing number of positive ions (Na^+) in the cleft. A summary of the observed reactions is given in

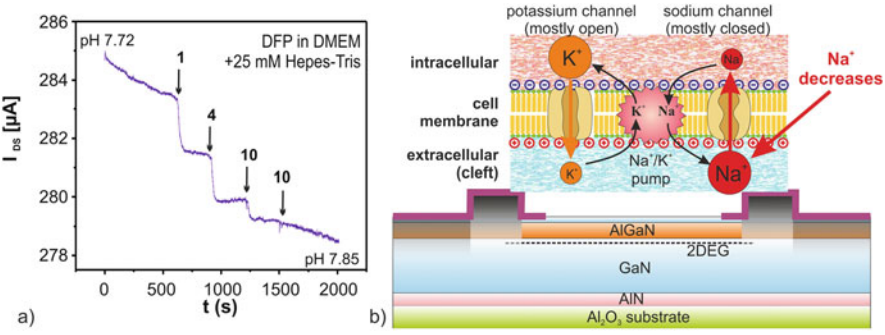

Fig. 18 (**a**) The recorded NG108-15 cell reaction to different concentrations of the neuroinhibitors DFP in DMEM with 25 mM HEPES-Tris (4-(2-hydroxyethyl)-1-piperazineethanesulfonic acid) buffer solution as cell medium (dosing by titration; numbers correspond to added concentrations in the solution in units of µM; pH is measured at the beginning and the end of the experiments by glass electrode). (**b**) Corresponding model for the reaction of the hybrid (adapted from [90])

Table 3, in particular, the possibility to monitor the reaction on inhibitors and ion channel blockers.

Further studies [152] combined the patch-clamp technique with AlGaN/GaN ISFETs in order to detect the reaction of SaOS-2 human osteoblast-like cells to different concentrations of quaternary ammonium ion and tetrodotoxin, which block K^+ and Na^+ channels, respectively. Ca^{2+}-ion channel inhibitors as well as activators have been dosed in HEK 293FT cells [150] demonstrating the possibility for Ca^{2+} sensing. The experimental observations so far are summarized in Table 4. From the experimental details, it can be concluded that AlGaN/GaN ISFETs are well suited for the construction of Cell-FETs owing to the inherent properties of III-nitrides like

Table 3 Summary of observed sensor response on the cell reaction on different treatments [90, 159]

Experiment	Cell reaction	Sensor response	Underlying effect
Alkalization	Consumption of H_3O^+ and diffusion of CO_2 into the atmosphere	I_D decreases	Increase of OH^- ions
Breathing	Decreasing CO_2 concentration in the cell medium, creating non-equilibrium of membrane potential	I_D oscillates	Alternating HCO_3^- concentration in the cell medium
Dosing of DFP	Inhibition of AChE, thus, keeping the Na^+ channels open	I_D decreases	Depletion of positive ions in the cleft (Na^+) due to equilibration of the concentration gradient
Dosing of amiloride	Blocking of Na^+ channels	I_D increases	Accumulation of positive ions in the cleft (Na^+, K^+)
Dosing of PMSF	Inhibition of AChE, thus, keeping the Na^+ channels open	I_D decreases	Depletion of positive ions in the cleft (Na^+) due to equilibration of the concentration gradient

Table 4 Summary of reported Cell-FETs with AlGaN/GaN HEMTs

Cells	Reaction	Reference
Cardiac myocyte cells of embryonic Wistar rats	Spontaneously beating cardiac myocyte cells	[27]
P19 cells (embryonic mouse-teratocarcinoma stem cell)	Acidification as a result of cell metabolism	[90]
Algae	Growth of a biofilm	[155]
Nerve cells NG108-15	Inhibitor DFP, PMSF Na^+ ion channel blocker amiloride	[159]
SaOS-2 human osteoblast-like cells	K^+ ion channel blocker TEA Na^+ ion channel blocker TTX	[152]
HEK 293FT	Ca^{2+} as well as Ca^{2+} blocker as activators	[150]
Physarum polycephalum	Cell metabolism	[144]
Yeast (*Saccharomyces carlsbergensis*)	Cell metabolism	[162]

chemical stability and low noise. Clear response signals to inhibitors illustrate the applicability for drug development, although their interpretation remains an inherently complex issue.

Finally, two slightly different approaches shall underline the versatility of the AlGaN/GaN HEMTs for BioFETs. In addition to biomolecules, virus and bacteria can be detected employing site-specific reactions. For example, Wang et al. demonstrated the detection of *Perkinsus marinus* [163] in high concentrated electrolyte simulating the conditions of seawater and could distinguish between infected and healthy environment, while Kang et al. immobilized human immunodeficiency virus (HIV) [164].

9 Further Biosensors

As listed in Sect. 2.5, there is a high number of possible transducer principles for group III-nitrides, which can be electrical as in the case of nanowires or based on other phenomena. Such transducer possibilities are described shortly in the following section.

9.1 Electrical Biosensors: Nanowires

Nanowires represent miniaturized field-effect transistors, where the conductive channel is confined in two dimensions. It exhibits a higher surface-to-volume ratio than planar FETs, which is expected to increase the sensitivity. The dimensions of the nanowires can be in the range of the target molecules, which principally enables single-molecule detection. Furthermore, absorption of proteins as well the growth of living cells can be controlled by wettability of the surfaces. On GaN nanowires it was shown to switch from superhydrophobic to superhydrophilic behavior via radiation by ultraviolet light [86]. It is assumed that the high surface-to-volume ratio serves as amplifier of those effects resulting in very large changes of contact angle between 155° and ~0°. Finally, due to the small sizes, increased packaging density and integration in microfluidic systems such as lab-on-a-chip concepts are possible. Functionalization can be achieved similarly to the planar structures via oxygen on the hydroxylated GaN surface employing the organosilanes APTMS [48], MTPMS [165, 166], APTES [167], or 1,10-decanedicarboxylic acid and poly(amidoamine)dendrimer as linker [168]. While the first GaN nanowires were analyzed by luminescence [48] and electrochemical impedance spectroscopy [165], DNA-FET operation was demonstrated in Refs. [166, 168] and DNA concentrations as low as 0.1 aM could be detected [168]. Although high aspect ratios are usually disturbing cell growth, living cells were demonstrated to grow on nanowires as well as on planar or porous GaN [158].

9.2 Mechanical Biosensors: Electroacoustic Resonators

SAW devices generate and detect acoustic waves on the surface of a piezoelectric material. The acoustic wave is confined at the surface, which makes such waves very sensitive toward any change at the surface such as mass loading or viscosity changes. SAW devices can be used for different sensing applications, which enable integrated sensor concepts. For example, a passivated SAW device measures temperature, while a functionalized SAW device detects with high-precision protein molecules, ultra-small cells, or DNA [169]. While first attempts to realize biosensors relied on functionalization via Au film (e.g., on $LiNbO_3$, detection of DNA and cells [170]), for piezoelectric AlN films, the organosilane functionalization can be used to immobilize ssDNA and to detect the hybridization [171]. An interesting feature of group III-nitride-based SAW devices is the possibility to fabricate them from the same AlGaN/GaN heterostructure as a BioFET [172]. Such devices demonstrated already good sensing properties for gases [173]; a biosensor, however, was not demonstrated yet.

Biosensors, however, usually should operate in liquid environment. SAW devices in liquids are highly damped since the displacement of the SAW is directed into the liquid. In another type of acoustoelectric resonators, Lamb waves propagate in solid plates. The wave velocity of the Lamb waves can be much smaller than the corresponding waves in liquids, which permits operation in liquids with reduced damping. The main drawback of Lamb wave biosensors, however, is the necessary employment of thin membranes due to a decreased sensitivity with increasing membrane thickness, which makes the devices more fragile. First group III-nitride-based Lamb wave sensors were demonstrated on AlN by Duhamel et al. [174].

Furthermore, there are no restrictions to employ different kinds of bulk acoustic wave (BAW) devices [32]. BAW sensors have been already demonstrated for the detection of thin organic films [175]. A more detailed review on AlN for fluidic and biosensing applications is given in Ref. [176].

9.3 Optical Biosensors

As mentioned in the classification in Sect. 2.5, sensors relying on spectroscopic or similar methods are not considered here. Instead, the described functionalized surfaces and their electronic sensing mechanisms in BioFETs can be also used to modify the emission characteristics of optoelectronic devices.

If a close packed ssDNA-functionalized surface is exposed to a matching target DNA, the hybridization leads to compressive stress, which induces a piezoelectric polarization in wurtzite group III-nitrides. This polarization modification will modify the field within the quantum well close to the surface. As a result, the wavelength of the emitted light will shift. Such kind of biosensor was demonstrated by Shih et al. [177] employing $In_{0.22}Ga_{0.78}N$/GaN multiple quantum wells functionalized with Au and ssDNA. Instead of piezoelectric effects, the band bending of the surface upon

adsorption of molecules can be employed as well [178]. Also, the photoluminescence (PL) in lateral polarity heterostructures, where periodically the polarity of the wurtzite material is reversed, was shown to be altered on peptide-functionalized AlGaN [179]. A major advantage of these concepts is the pure optical readout of electronic surface effects via photoluminescence, which avoids any electrical connections to the sensing surface or electrical currents within the analyzed media.

The effect will be more pronounced in nanostructures, where the band bending affects the major part of the material. In stacked GaN/AlN quantum dots, it resulted in a strong response of the PL intensity on hydrogen [180] and increased in InGaN quantum dots in GaN nanowires [181], which can be integrated in small compact micro-optical systems [182]. In solutions, however, their potential was stabilized by an $Ag/AgCl_3$ reference electrode and pH values were measured by PL. Based on this principle, the operation as biosensor was demonstrated detecting photocatalytic oxidation of nicotinamide adenine dinucleotide [183].

10 Multiparameter Systems

Due to the transparency of the material system for visible light, nearly each optical analysis technique can be performed simultaneously in addition to electrical measurements. For example, cell-based approaches benefit from a careful monitoring of cell vitality, adhesion, coverage, and count during on-chip cultivation through standard inverse optical microscopy [39, 43]. Moreover, this opens up a huge field for innovative multiparameter analysis approaches where optical and electrical parameters are easily accessible, complementing each other to produce a more complete picture of the bioreaction in question. Combining InGaN-based laser diode and band-selective photodetector allows for absorption measurements in droplets positioned on an AlGaN/GaN ISFET [53]. In this configuration, the laser diode emits light with specific wavelength about 410–420 nm. At this wavelength, the AlGaN/GaN sensor is completely transparent. An InGaN detector with tailored spectral selectivity records the transmitted light for colorimetric measurements of the droplet simultaneously to the electrical measurements with the sensor. The concept has been demonstrated for the monitoring of enzymatic reactions and of cell activities.

There is a variety of further concepts for integrated sensing possible taking benefit of the well-developed technologies for light emitters (LEDs, laser) and rf power devices (HEMTs). A straightforward solution is the employment of differently functionalized biosensors including pH or further ion-selective devices. Optical methods could be integrated by combining AlGaN/GaN BioFETs with a light-emitting diode, which was demonstrated even monolithically [184], and employing of the transparent sapphire substrate as micro-optical platform on the base of planar diffractive optical elements [185]. Also electroacoustic devices can be implemented and integrated if the same AlGaN/GaN heterostructure is used for BioFETs and SAW devices to measure further physical parameters [172].

11 Conclusions

The development of biosensors based on group III-nitrides gained increased interest within the last decade and remarkable progress has been made. Benefiting from the development of Si-based BioFETs, biosensors employing enzymes, DNA, antibodies, and whole cells have been realized. The large bandgap and strong bond strength in group III-nitrides allow operating devices in harsh environments and aggressive solutions and guarantee the excellent chemical stability and biocompatibility. Several biofunctionalization schemes are available, and especially schemes employing covalent bonding to the surface have shown to be stable and applicable in reusable biosensors. On the other hand, no functionalization is required for the adhesion and proliferation of cells on the surface. Such semiconductor-cell hybrids are highly prospective for drug screening and as broadband toxicity sensors.

The majority of group III-nitride-based biosensors employ the high-electron-mobility transistor on an AlGaN/GaN heterostructure, where a well-developed technology for the transducer is available. The possibilities for integration of BioFETs with electronic, optoelectronic, or SAW devices for data processing and contactless readout are further attractive features. Fundamental challenges and problems, however, are still to be tackled. Further investigations are required to understand phenomena related to sensing, passivation, and especially interface stability. In addition to that, it is well known, though mostly omitted in the publications concerning AlGaN/GaN ISFETs, that a persistent photocurrent is induced even at sub-bandgap photon energies due to lattice defects and impurities. To overcome this limitation, crystal quality has to be optimized and new approaches have to be investigated.

Finally, it shall be noted that despite the extraordinary properties, InN has been rarely used in biosensors as well as for sensing applications at all. The high surface affinity to electrons creates a conductive channel directly on the surface, and anion selectivity can be achieved [186]. An interesting feature, however, is the high work function, which enables an adaptation to the lowest unoccupied molecular orbital band of a large number of organic molecules. The wide tunability of the group III-nitrides allows realizing tailored surfaces for the specific bonding of selected molecules to realize biofunctionalization [187]. These opportunities are by far not understood and exploited.

References

1. Calladine CR, Drew H, Luisi BF, Travers AA (2004) Understanding DNA: the molecule and how it works. Elsevier Academic Press, San Diego
2. Zourob M, Elwary S, Turner APF (eds) (2008) Principles of bacterial detection: biosensors, recognition receptors and microsystems. Springer Science & Business Media LLC, New York
3. Tüdos AJ, Besselink GAJ, Schasfoort RBM (2001) Trends in miniaturized total analysis systems for point-of-care testing in clinical chemistry. Lab Chip 1:83–95

4. Rodriguez-Mozaz S, de Lopez Alda M, Barceló D (2006) Biosensors as useful tools for environmental analysis and monitoring. Anal Bioanal Chem 386:1025–1041
5. LaGier MJ, Fell JW, Goodwin KD (2007) Electrochemical detection of harmful algae and other microbial contaminants in coastal waters using hand-held biosensors. Mar Pollut Bull 54:757–770
6. Yu D, Blankert B, Viré JC, Kauffmann JM (2005) Biosensors in drug discovery and drug analysis. Anal Lett 38:1687–1701
7. Nic M, Jirat J, Kosata B (2016) IUPAC Compendium of Chemical Terminology. http://goldbook.iupac.org/html/B/B00663.html. Accessed 02 Nov 2016
8. Clark LC, Lyons C (1962) Electrode systems for continuous monitoring in cardiovascular surgery. Ann N Y Acad Sci 102:29–45
9. Bashir R (2004) BioMEMS: state-of-the-art in detection, opportunities and prospects. Adv Drug Deliv Rev 56:1565–1586
10. Gooding J (2006) Biosensor technology for detecting biological warfare agents: recent progress and future trends. Anal Chim Acta 559:137–151
11. Bergveld P (1970) Development of an ion-sensitive solid-state device for neurophysiological measurements. IEEE Trans Biomed Eng 17:70–71
12. Madou MJ (1989) Chemical sensing with solid state devices. Academic Press, Boston
13. Chaniotakis N, Sofikiti N (2008) Novel semiconductor materials for the development of chemical sensors and biosensors: a review. Anal Chim Acta 615:1–9
14. Pearton SJ, Ren F, Wang YL, Chu BH, Chen KH, Chen KH, Chang CY, Lim W, Lin J, Norton DP (2010) Recent advances in wide bandgap semiconductor biological and gas sensors. Prog Mater Sci 55:1–59
15. Gil B (ed) (1998) Group III nitride semiconductor compounds: physics and applications. Clarendon Press, Oxford
16. Maruska HP, Tietjen JJ (1969) The preparation and properties of vapor-deposited single-crystal-line GaN. Appl Phys Lett 15:327–329
17. Nakamura S, Mukai T, Senoh M, Iwasa N (1992) Thermal annealing effects on p-type Mg-doped GaN films. Jpn J Appl Phys Part 2 31:L139–L142
18. Nakamura S, Mukai T, Senoh M (1994) Candela-class high-brightness InGaN/AlGaN double-heterostructure blue-light-emitting diodes. Appl Phys Lett 64:1687–1689
19. Wu J, Walukiewicz W, KM Y, Ager III JW, Haller EE, Lu H, Schaff WJ, Saito Y, Nanishi Y (2002) Unusual properties of the fundamental band gap of InN. Appl Phys Lett 80:3967–3969
20. Yoshida S, Misawa S, Gonda S (1982) Properties of $Al_xGa_{1-x}N$ films prepared by reactive molecular beam epitaxy. J Appl Phys 53:6844–6848
21. Lebedev V, Cimalla I, Cimalla V, Wagner R, Kaiser U, Ambacher O (2005) Defect related absorption and emission in AlGaN solar-blind UV photodetectors. Phys Status Solidi C 2:1360–1365
22. Monemar B (1974) Fundamental energy gap of GaN from photoluminescence excitation spectra. Phys Rev B 10:676–681
23. Cimalla I, Will F, Tonisch K, Niebelschütz M, Cimalla V, Lebedev V, Kittler G, Himmerlich M, Krischok S, Schaefer JA, Gebinoga M, Schober A, Friedrich T, Ambacher O (2007) AlGaN/GaN biosensor – effect of device processing steps on the surface properties and biocompatibility. Sensors Actuators B 123:740–748
24. Neuberger A, Müller G, Ambacher O, Stutzmann M (2001) High-electron-mobility AlGaN/GaN transistors (HEMTs) for fluid monitoring applications. Phys Status Solidi A 185:85–89
25. Alifragis Y, Georgakilas A, Konstantinidis G, Iliopoulos E, Kostopoulos A, Chaniotakis NA (2005) Response to anions of AlGaN/GaN high-electron-mobility transistors. Appl Phys Lett 87:253507
26. Buchheim C, Kittler G, Cimalla V, Lebedev V, Fischer M, Krischok S, Yanev V, Himmerlich M, Ecke G, Schaefer JA, Ambacher O (2006) Tuning of surface properties of AlGaN/GaN sensors for nano- and picodroplets. IEEE Sensors J 6:881–886

27. Steinhoff G, Baur B, Wrobel G, Ingebrandt S, Offenhäusser A, Dadgar A, Krost A, Stutzmann M, Eickhoff M (2005) Recording of cell action potentials with AlGaN/GaN field-effect transistors. Appl Phys Lett 86:033901
28. Kang BS, Mehandru R, Kim S, Ren F, Fitch RC, Gillespie JK, Moser N, Jessen G, Jenkins T, Dettmer R, Via D, Crespo A, Gila BP, Abernathy CR, Pearton SJ (2004) Hydrogen-induced reversible changes in drain current in Sc_2O_3/AlGaN/GaN high electron mobility transistors. Appl Phys Lett 84:46354637
29. Kokawa T, Sato T, Hasegawa H, Hashizume T (2006) Liquid-phase sensors using open-gate AlGaN/GaN high electron mobility transistor structure. J Vac Sci Technol B 24:1972–1976
30. Hartmann C, Dittmar A, Wollweber J, Bickermann M (2014) Bulk AlN growth by physical vapour transport. Semicond Sci Technol 29:084002
31. Ambacher O (1998) Growth and applications of group III-nitrides. J Phys D Appl Phys 31:2653–2710
32. Cimalla V, Pezoldt J, Ambacher O (2007) Group III nitride and SiC based MEMS and NEMS: materials properties, technology and applications. J Phys D Appl Phys 40:6386–6434
33. Ibbetson JP, Fini PT, Ness KD, DenBaars SP, Speck JS, Mishra UK (2000) Polarization effects, surface states, and the source of electrons in AlGaN/GaN heterostructure field effect transistors. Appl Phys Lett 77:250–252
34. Flack TJ, Pushpakaran BN, Bayne AB (2016) GaN technology for power electronic applications: a review. J Electron Mater 45:2673–2682
35. Mahboob I, Veal TD, Piper LFJ, McConville CF, Lu H, Schaff WJ, Furthmüller J, Bechstedt F (2004) Origin of electron accumulation at wurtzite InN surfaces. Phys Rev B 69:R201307
36. Cimalla V, Niebelschütz M, Ecke G, Lebedev V, Ambacher O, Himmerlich M, Krischok S, Schaefer JA, Lu H, Schaff WJ (2006) Surface band bending at nominally undoped and Mg-doped InN by Auger Electron Spectroscopy. Phys Status Solidi A 203:59–65
37. Eickhoff M, Schalwig J, Steinhoff G, Weidemann O, Görgens L, Neuberger R, Hermann M, Baur B, Müller G, Ambacher O, Stutzmann M (2003) Electronics and sensors based on pyroelectric AlGaN/GaN heterostructures. Phys Status Solidi C 0:1908–1918
38. Pearton SJ, Kang BS, Kim S, Ren F, Gila BP, Abernathy CR, Lin J, Chu SNG (2004) GaN-based diodes and transistors for chemical, gas, biological and pressure sensing. J Phys Condens Matter 16:R961–R994
39. Ambacher O, Cimalla V (2008) Polarization induced effects in GaN-based heterostructures and novel sensors. In: Wood C, Jena D (eds) Polarization effects in semiconductors: from ab initio to device application. Springer, New York, pp 27–109
40. Cimalla I, Lübbers B, Cimalla V, Gebinoga M, Schober A, Ambacher O (2009) Group III-nitride based sensors – advances towards a new generation of biosensors. In: Ho-Young C (ed) Advanced semiconductor materials and devices research: III-nitrides and SiC. Transworld Research Network, Trivandrum, pp 341–374
41. Pearton SJ, Zolper JC, Shul RJ, Ren F (1999) GaN: processing, defects, and devices. J Appl Phys 86:1–78
42. Young TH, Chen CR (2006) Assessment of GaN chips for culturing cerebellar granule neurons. Biomaterials 27:3361–3367
43. Das A, Das A, Chang LB, Lai CS, Lin RM, Chu FC, Lin YH, Chow L, Jeng MJ (2013) GaN thin film based light addressable potentiometric sensor for pH sensing application. Appl Phys Express 6:036601
44. Lübbers B, Kittler G, Ort P, Linkohr S, Wegener D, Baur B, Gebinoga M, Weise F, Eickhoff M, Maroldt S, Schober A, Ambacher O (2008) A novel GaN-based multiparameter sensor system for biochemical analysis. Phys Status Solidi C 5:2361–2363
45. Wong KY, Tang W, Lau KM, Chen KJ (2007) Surface acoustic wave device on AlGaN/GaN heterostructure using two-dimensional electron gas interdigital transducers. Appl Phys Lett 90:213506
46. Sang S, Wang Y, Feng Q, Wei Y, Ji J, Zhang W (2016) Progress of new label-free techniques for biosensors: a review. Crit Rev Biotechnol 36:465–468

47. Chaniotakis NA, Alifragis Y, Konstantinidis G, Georgakilas A (2004) Gallium nitride-based potentiometric anion sensor. Anal Chem 76:5552–5556
48. Simpkins B, McCoy K, Whitman L, Pehrsson P (2007) Fabrication and characterization of DNA-functionalized GaN nanowires. Nanotechnology 18:355301
49. Schöning MJ, Poghossian A (2002) Recent advances in biologically sensitive field-effect transistors (BioFETs). Analyst 127:1137–1151
50. Neuberger R, Müller G, Eickhoff M, Ambacher O, Stutzmann M (2002) Observation of ion-induced changes in the channel current of high electron mobility AlGaN/GaN transistors (HEMT). Mater Sci Eng B 93:143–146
51. Linkohr S, Pletschen W, Polyakov V, Himmerlich M, Lorenz P, Krischok S, Kirste L, Müller S, Ambacher O, Cimalla V (2012) Influence of plasma treatments on the properties of GaN/AlGaN/GaN HEMT structures. Phys Status Solidi C 9:1096–1098
52. Binari SC, Dietrich HB, Kelner G, Rowland LB, Doverspike K, Wickenden DK (1995) H, He, and N implant isolation of n-type GaN. J Appl Phys 78:3008–3011
53. Schober A, Kittler G, Buchheim C, Majdeddin A, Cimalla V, Fischer M, Yanev V, Himmerlich M, Krischok S, Schaefer JA, Romanus H, Sändig T, Burgold J, Weise F, Wurmus H, Drüe KH, Hintz M, Thust H, Gebinoga M, Kittler M, Spitznas A, Gottwald E, Weibezahn KF, Wegener D, Schwienhorst A, Ambacher O (2005) A novel class of sensors for system integrative concepts in biotechnological applications. In: Technical Proceedings of the 2005 NSTI Nanotechnology Conference and Trade Show, vol 1, pp 489–495
54. Fan Z, Mohammand SN, Kim W, Aktas O, Botchkarev AE, Morkoc H (1996) Very low resistance multilayer Ohmic contact to n-GaN. Appl Phys Lett 68:16721674
55. Kang BS, Pearton SJ, Chen JJ, Ren F, Johnson JW, Therrin RJ, Rajagopal P, Roberts JC, Piner EL, Linthicum KJ (2006) Electrical detection of deoxyribonucleic acid hybridization with AlGaN/GaN high electron mobility transistors. Appl Phys Lett 89:122102
56. Kang BS, Ren F, Wang L, Lofton C, Tan WW, Pearton SJ, Dabiran A, Osinsky A, Chow PP (2005) Electrical detection of immobilized proteins with ungated AlGaN/GaN high-electron-mobility transistors. Appl Phys Lett 87:023508
57. Kang BS, Wang HT, Lele TP, Tseng Y, Ren F, Pearton SJ, Johnson JW, Rajagopal P, Roberts JC, Piner EL, Linthicum KJ (2007) Prostate specific antigen detection using AlGaN/GaN high electron mobility transistors. Appl Phys Lett 91:112106
58. Podolska A, Kocan M, Cabezas AMG, Wilson TD, Umana-Membreno GA, Nener BD, Parish G, Keller S, Mishra UK (2010) Ion versus pH sensitivity of ungated AlGaN/GaN heterostructure-based devices. Appl Phys Lett 97:012108
59. Steinhoff G, Hermann M, Schaff WJ, Eastman LF, Stutzmann M, Eickhoff M (2003) pH response of GaN surfaces and its application for pH-sensitive field-effect-transistors. Appl Phys Lett 83:177–179
60. Kittler G (2007) GaN-basierte pH-Sensoren: Empfindlichkeit, Drift und Passivierungstechnologien. Thesis, TU Ilmenau. urn:nbn:de:gbv:ilm1-2008000012
61. Yates DE, Levine S, Healy TW (1974) Site-binding model of the electrical double layer at the oxide/water interface. J Chem Soc Faraday Trans 1:1807–1818
62. Bayer M, Uhl C, Vogl P (2005) Theoretical study of electrolyte gate AlGaN/GaN field effect transistors. J Appl Phys 97:33703
63. Kang BS, Ren F, Kang MC, Lofton C, Ran W, Pearton SJ, Dabiran A, Osinsky A, Chow PP (2005) Detection of halide ions with AlGaN/GaN high electron mobility transistors. Appl Phys Lett 86:173502
64. Alifragis Y, Volosirakis A, Chaniotakis NA, Konstantinidis G, Adikimenakis A, Georgakilas A (2007) Potassium selective chemically modified field effect transistors based on AlGaN/GaN two-dimensional electron gas heterostructures. Biosens Bioelectron 22:2796–2801
65. Steinhoff G, Purrucker O, Tanaka M, Stutzmann M, Eickhoff M (2003) $Al_xGa_{1-x}N$ – a new material for biosensors. Adv Funct Mater 13:841–846
66. Mourzina YG, Schubert J, Zander W, Legin A, Vlasov YG, Lüth H, Schöning MJ (2001) Development of multisensor systems based on chalcogenide thin film chemical sensors for

the simultaneous multicomponent analysis of metal ions in complex solutions. Electrochim Acta 47:251–258
67. Brazzini T, Bengoechea-Encabo A, Sánchez-García MA, Calle F (2013) Investigation of AlInN barrier ISFET structures with GaN capping for pH detection. Sensors Actuators B 176:704–707
68. Lübbers B (2012) AlGaN-based pH-sensors. Impedance characterisation, optimisation and application for foetal blood sampling. Thesis, TU Ilmenau. urn:nbn:de:gbv:ilm1-2012000298
69. Kittler G, Spitznas A, Lübbers B, Lebedev V, Wegener D, Gebinoga M, Weise F, Schober A, Ambacher O (2007) Advances in III-V nitride semiconductor materials and devices. In: Materials Research Society Symposium Proceedings, Warrendale, PA I14-03
70. Chaniotakis NA, Alifragis Y, Georgakilas A, Konstantinidis G (2005) GaN-based anion selective sensor: probing the origin of the induced electrochemical potential. Appl Phys Lett 86:164103
71. Kang BS, Wang HT, Ren F, Hlad M, Gila BP, Abernathy CR, Pearton SJ, Li C, Low ZN, Lin J, Johnson JW, Rajagopal P, Roberts JC, Piner EL, Linthicum KJ (2008) Role of gate oxide in AlGaN/GaN high-electron-mobility transistor pH sensors. J Electron Mater 37:550–553
72. Baur B, Steinhoff G, Hernando J, Purrucker O, Tanaka M, Nickel B, Stutzmann M, Eickhoff M (2005) Chemical functionalization of GaN and AlN surfaces. Appl Phys Lett 87:263901
73. Abe H, Esashi M, Matsuo T (1979) ISFET's using inorganic gate films. IEEE Trans Electron Dev 26:1939–1944
74. Prabhakaran K, Andersson T, Nozawa K (1996) Nature of native oxide on GaN surface and its reaction with Al. Appl Phys Lett 69:3212–3214
75. Eickhoff M, Neuberger R, Steinhoff G, Ambacher O, Müller G, Stutzmann M (2001) Wetting behaviour of GaN surfaces with Ga- or N-face polarity. Phys Status Solidi B 228:519–522
76. Lide DR (2003) CRC handbook of chemistry and physics.84th edn. CRC Press, Boca Raton
77. Tajima M, Kotani J, Hashizume T (2009) Effects of surface oxidation of AlGaN on dc characteristics of AlGaN/GaN high-electron-mobility transistors. Jpn J Appl Phys 48:020203
78. Linkohr S, Pletschen W, Kirste L, Himmerlich M, Lorenz P, Krischok S, Polyakov V, Müller S, Ambacher O, Cimalla V (2012) Plasma affected 2DEG properties on GaN/AlGaN/GaN HEMTs. Phys Status Solidi C 9:938–941
79. Chen CC, Chen HI, Liu HY, Chou PC, Liou JK, Liu WC (2015) On a GaN-based ion sensitive field-effect transistor (ISFET) with a hydrogen peroxide surface treatment. Sensors Actuators B 209:658–663
80. Harada N, Hori Y, Azumaishi N, Ohi K, Hashizume T (2011) Formation of recessed-oxide gate for normally-off AlGaN/GaN high electron mobility transistors using selective electrochemical oxidation. Appl Phys Express 4:021002
81. Foster CM, Collazo R, Sitar Z, Ivanisevic A (2012) Aqueous stability of Ga- and N-polar gallium nitride. Langmuir 29:216–220
82. King SW, Barnak JP, Bremser MD, Tracy KM, Ronning C, Davis RF, Nemanich RJ (1998) Cleaning of AlN and GaN surfaces. J Appl Phys 84:5248–5260
83. Lee KN, Donovan SM, Gila B, Overberg M, Mackenzie JD, Abernathy CR, Wilson RG (2000) Surface chemical treatment for the cleaning of AlN and GaN surfaces. J Electrochem Soc 147:3087–3090
84. Huh C, Kim SW, Kim HS, Lee IH, Park SJ (2000) Effective sulfur passivation of an n-type GaN surface by an alcohol-based sulfide solution. J Appl Phys 87:4591–4593
85. Linkohr S, Pletschen W, Schwarz SU, Anzt J, Cimalla V, Ambacher O (2013) CIP (cleaning-in-place) stability of AlGaN/GaN pH sensors. J Biotechnol 163:354–361
86. Li J, Han Q, Zhang Y, Zhang W, Dong M, Besenbacher F, Yang R, Wang C (2013) Optical regulation of protein adsorption and cell adhesion by photoresponsive GaN nanowires. ACS Appl Mater Interfaces 5:9816–9822
87. Hashizume T, Hasegawa H (2004) Effects of nitrogen deficiency on electronic properties of AlGaN surfaces subjected to thermal and plasma processes. Appl Surf Sci 234:387–394

88. Kim HS, Lee YH, Yeom GY, Lee JW, Kim TI (1997) Effects of inductively coupled plasma conditions on the etch properties of GaN and ohmic contact formations. Mater Sci Eng B 50:82–87
89. Cimalla V, Lebedev V, Linkohr S, Cimalla I, Lübbers B, Tonisch K, Brückner K, Niebelschütz F, Hein M, Ambacher O (2008) Nitride based sensors. In: Proceedings of the 17th European Workshop on Heterostructure Technology HETECH, Venice, Italy, 3–5 November, pp 33–40
90. Cimalla I (2011) AlGaN/GaN sensors for direct monitoring of fluids and bioreactions. Universitätsverlag Ilmenau, Ilmenau
91. Makowski MS, Kim S, Gaillard M, Janes D, Manfra MJ, Bryan I, Sitar Z, Arellano C, Xie J, Collazo R, Ivanisevic A (2013) Physisorption of functionalized gold nanoparticles on AlGaN/GaN high electron mobility transistors for sensing applications. Appl Phys Lett 102:074102
92. Guo Y, Wang X, Miao B, Li Y, Yao W, Xie Y, Li J, Wu D, Pei R (2015) An AuNPs-functionalized AlGaN/GaN high electron mobility transistor sensor for ultrasensitive detection of TNT. RSC Adv 5:98724–98729
93. Bermudez V (2002) Functionalizing the GaN(0001)-(1×1) surface I. The chemisorption of aniline. Surf Sci 499:109–124
94. Bermudez V (2002) Functionalizing the GaN(0001)-(1×1) surface II. Chemisorption of 3-pyrroline. Surf Sci 499:124–134
95. Xu X, Jindal V, Shahedipour-Sandvik F, Bergkvist M, Cady NC (2009) Direct immobilization and hybridization of DNA on group III nitride semiconductors. Appl Surf Sci 255:5905–5909
96. Yakimova R, Steinhoff G, Petoral RMJR, Vahlberg C, Khranovskyy V, Yazdi GR, Uvdal K, Lloyd Spetz A (2007) Novel material concepts of transducers for chemical and biosensors. Biosens Bioelectron 22:2780–2785
97. Kim H, Colavita PE, Paoprasert P, Gopalan P, Kuech TF, Hamers RJ (2008) Grafting of molecular layers to oxidized gallium nitride surfaces via phosphonic acid linkages. Surf Sci 602:2382–2388
98. Arranz A, Palacio C, García-Fresnadillo D, Orellana G, Navarro A, Munoz E (2008) Influence of surface hydroxylation on 3-aminopropyltriethoxysilane growth mode during chemical functionalization of GaN surfaces: an angle-resolved x-ray photoelectron spectroscopy study. Langmuir 24:8667–8671
99. Arisio C, Cassou CA, Lieberman M (2013) Loss of siloxane monolayers from GaN surfaces in water. Langmuir 29:5145–5149
100. Schwarz SU (2013) Biofunktionalisierung und -sensorik mit AlGaN/GaN-Feldeffekttransistoren. Thesis, Albert-Ludwigs-Universität Freiburg URN: urn:nbn:de:bsz:25-opus-93594
101. Rohrbaugh N, Bryan I, Bryan Z, Arellano C, Collazo R, Ivanisevic A (2014) AlGaN/GaN field effect transistors functionalized with recognition peptides. Appl Phys Lett 105:134103
102. Stine R, Simpkins BS, Mulvaney SP, Whitman LJ, Tamanaha CR (2010) Formation of amine groups on the surface of GaN: a method for direct biofunctionalization. Appl Surf Sci 256:4171–4175
103. Berg NG, Nolan M, Paskova T, Ivanisevic A (2014) Characterization of gallium nitride modified with peptides before and after exposure to ionizing radiation. Langmuir 30:15477–15485
104. Kim H, Colavita PE, Metz KM, Nichols BM, Sun B, Uhlrich J, Wang X, Kuech TF, Hamers RJ (2006) Photochemical functionalization of gallium nitride thin films with molecular and biomolecular layers. Langmuir 22(19):8121–8126
105. Wang C, Zhuang H, Huang N, Heuser S, Schlemper C, Zhai Z, Liu B, Staedler T, Jiang X (2016) Photochemical modification of single crystalline GaN film using n-alkene with different carbon chain lengths as biolinker. Langmuir 32:5731–5737
106. Caras S, Janata J (1980) Field effect transistor sensitive to penicillin. Anal Chem 52:1935–1937

107. Linkohr S, Schwarz SU, Krischok S, Lorenz P, Nakamura T, Polyakov V, Cimalla V, Nebel CE, Ambacher O (2010) A novel functionalization of AlGaN/GaN-pH-Sensors for DNA-sensors. Mater Res Soc Symp Proc 1202:I06–I02
108. Schwarz SU, Linkohr S, Lorenz P, Krischok S, Nakamura T, Cimalla V, Nebel CE, Ambacher O (2011) DNA-sensor based on AlGaN/GaN high electron mobility transistor. Phys Status Solidi A 208:1626–1629
109. Wilkins SJ, Paskova T, Reynolds Jr CL, Ivanisevic A (2015) Comparison of the stability of functionalized GaN and GaP. ChemPhysChem 16:1687–1694
110. Chiu CS, Lee HM, Gwo S (2010) Site-selective biofunctionalization of aluminum nitride surfaces using patterned organosilane self-assembled monolayers. Langmuir 26:2969–2974
111. Chan EHM (2015) Surface functionalization of piezoelectric aluminum nitride with selected amino acid and peptides. Thesis, University of Toronto
112. Chen CF, CL W, Gwo S (2006) Organosilane functionalization of InN surface. Appl Phys Lett 89:252109
113. Kao KW, Su YW, Lu YS, Yao DJ, Gwo S, Yeh JA (2012) Calcium ions detection using miniaturized InN-based sensor. In: Proceedings of MEMS, Paris, France, 29 January, pp 781–783
114. Bain LE, Jewett SA, Mukund AH, Bedair SM, Paskova TM, Ivanisevic A (2013) Biomolecular gradients via semiconductor gradients: characterization of amino acid adsorption to $In_xGa_{1-x}N$ surfaces. ACS Appl Mater Interfaces 5:7236–7243
115. Baur B, Howgate J, von Ribbeck HG, Gawlina Y, Bandalo V, Steinhoff G, Stutzmann M, Eickhoff M (2006) Catalytic activity of enzymes immobilized on AlGaN/GaN solution gate field-effect transistors. Appl Phys Lett 89:183901
116. Müntze GM, Baur B, Schäfer W, Sasse A, Howgate J, Röth K, Eickhoff M (2015) Quantitative analysis of immobilized penicillinase using enzyme-modified AlGaN/GaN field-effect transistors. Biosens Bioelectron 64:605–610
117. Chu BH, Kang BS, Ren F, Chang CY, Wang YL, Pearton SJ, Glushakov AV, Dennis DM, Johnson JW, Rajagopal P, Roberts JC, Piner EL, Linthicum KJ (2008) Enzyme-based lactic acid detection using AlGaN/GaN high electron mobility transistors with ZnO nanorods grown on the gate region. Appl Phys Lett 93:042114
118. Kang BS, Wang HT, Ren F, Pearton SJ, Morey LTE, Dennis DM, Johnson JW, Rajagopal P, Roberts JC, Piner EL, Linthicum KJ (2007) Enzymatic glucose detection using ZnO nanorods on the gate region of AlGaN/GaN high electron mobility transistors. Appl Phys Lett 91:252103
119. Makowski MS, Bryan I, Sitar Z, Arellano C, Xie JQ, Collazo R, Ivanisevic A (2013) Kinase detection with gallium nitride based high electron mobility transistors. Appl Phys Lett 103:013701
120. Wang YL, Chu BH, Chen KH, Chang CY, Lele TP, Tseng Y, Pearton SJ, Ramage J, Hooten D, Dabiran A, Chow PP, Ren F (2008) Botulinum toxin detection using AlGaN/GaN high electron mobility transistors. Appl Phys Lett 93:262101
121. Chen KH, Kang BS, Wang HT, Lele TP, Ren F, Wang YL, Chang CY, Pearton SJ, Dennis DM, Johnson JW, Rajagopal P, Roberts JC, Piner EL, Linthicum KJ (2008) c-erbB-2 sensing using AlGaN/GaN high electron mobility transistors for breast cancer detection. Appl Phys Lett 92:192103
122. Espinosa N (2016) Dynamic detection of target-DNA with AlGaN/GaN high electron mobility transistors. Thesis, Albert-Ludwigs-Universität Freiburg. https://doi.org/10.6094/UNIFR/11557
123. Chen KH, Wang HW, Kang BS, Chang CY, Wang YL, Lele TP, Ren F, Pearton SJ, Dabiran A, Osinsky A, Chow PP (2008) Low Hg(II) ion concentration electrical detection with AlGaN/GaN high electron mobility transistors. Sens Actuators B 134:386–389
124. Bergveld P (1996) The future of biosensors. Sens Actuators A Phys 56:65–73

125. Thapa R, Alur S, Kim K, Tong F, Sharma Y, Kim M, Ahyi C, Dai J, Hong JW, Bozack M, Williams J, Son A, Dabiran A, Park M (2012) Biofunctionalized AlGaN/GaN high electron mobility transistor for DNA hybridization detection. Appl Phys Lett 100:232109
126. Espinosa N, Schwarz SU, Cimalla V, Podolska A, Ambacher O (2015) Dynamic detection of target-DNA with AlGaN/GaN high electron mobility transistors. Proc Eng 120:908–911
127. Espinosa N, Schwarz SU, Cimalla V, Podolska A, Ambacher O (2015) Impedance characterization of DNA-functionalization layers on AlGaN/GaN high electron mobility transistors. Proc Eng 120:912–915
128. Zeggai O, Ould-Abbas A, Bouchaour M, Zeggai H, Sahouane N, Madani M, Trari D, Boukais M, Chabane-Sari NE (2014) Biological detection by high electron mobility transistor (HEMT) based AlGaN/GaN. Phys Status Solidi C 11:274–279
129. Wen XJ, Gupta S, Wang YJ, Nicholson TR, Lee SC, Lu W (2011) High sensitivity AlGaN/GaN field effect transistor protein sensors operated in the subthreshold regime by a control gate electrode. Appl Phys Lett 99:043701
130. Gupta S, Elias M, Wen X, Shapiro J, Brillson L, Lu W, Lee SC (2008) Detection of clinically relevant levels of protein analyte under physiologic buffer using planar field effect transistors. Biosens Bioelectron 24:505–511
131. Huang CC, Lee GY, Chyi JI, Cheng HT, Hsu CP, Hsu YR, Hsu CH, Huang YF, Sun YC, Chen CC, Li SS, Yeh JA, Yao DJ, Ren F, Wang YL (2013) AlGaN/GaN high electron mobility transistors for protein-peptide binding affinity study. Biosens Bioelectron 41:717–722
132. Li JD, Cheng JJ, Miao B, Wei XW, Xie J, Zhang JC, Zhang ZQ, DM W (2014) Detection of prostate-specific antigen with biomolecule-gated AlGaN/GaN high electron mobility transistors. J Micromech Microeng 24:075023
133. Huq HF, Trevino IIH, Castillo J (2016) Characteristics of AlGaN/GaN HEMTs for detection of MIG. J Mod Phys 7:1712–1724
134. Casal P, Wen XJ, Gupta S, Nicholson T, Wang YJ, Theiss A, Bhushan B, Brillson L, Lu W, Lee SC (2012) Immuno FET feasibility in physiological salt environments. Phil Trans R Soc A 370:2474–2488
135. Chu BH, Chang CY, Kroll K, Denslow N, Wang YL, Pearton SJ, Dabiran AM, Wowchak AM, Cui B, Chow PP, Ren F (2010) Detection of an endocrine disrupter biomarker, vitellogenin, in largemouth bass serum using AlGaN/GaN high electron mobility transistors. Appl Phys Lett 96:013701
136. Wang HT, Kang BS, Ren F, Pearton SJ, Johnson JW, Wang HT, Kang BS, Ren F, Pearton SJ, Johnson JW, Rajagopal P, Roberts JC, Piner EL, Linthicum KJ (2007) Electrical detection of kidney injury molecule-1 with AlGaN/GaN high electron mobility transistors. Appl Phys Lett 91:222101
137. Ren F, Pearton SJ, Kang BS, Chu BW (2011) AlGaN/GaN high electron mobility transistor based sensors for bio-applications. In: Serra PA (ed) Biosensors for health, environment and biosecurity. InTech, Rijeka, ISBN: 978-953-307-443-6
138. Lee HH, Bae M, Jo SH, Shin JK, Son DH, Won CH, Jeong HM, Lee JH, Kang SW (2015) AlGaN/GaN high electron mobility transistor-based biosensor for the detection of C-reactive protein. Sensors 15:18416–18426
139. Wang Y, Lu W (2011) AlGaN/GaN FET for DNA hybridization detection. Phys Status Solidi A 208:1623–1625
140. Espinosa N, Schwarz SU, Cimalla V, Ambacher O (2015) Detection of different target-DNA concentrations with highly sensitive AlGaN/GaN high electron mobility transistors. Sens Actuators B 210:633–639
141. Fahrenkopf NM, Shahedipour-Sandvik F, Tokranova N, Bergkvist M, Cady NC (2010) Direct attachment or DNA to semiconducting surfaces for biosensor applications. J Biotechnol 150:312–314
142. Gao XPA, Zheng G, Lieber CM (2010) Subthreshold regime has the optimal sensitivity for nanowire biosensors. Nano Lett 10:547–552

143. Ingebrandt S, Han Y, Nakamura F, Poghossian A, Schöning MJ, Offenhäusser A (2007) Label-free detection of single nucleotide polymorphisms utilizing the differential transfer function of field-effect transistors. Biosens Bioelectron 22:2834–2840
144. Witte H, Lippelt T, Warnke C, Dadgar A, Hauser MJB, Krost A (2014) High-frequency detection of cell activity of Physarum polycephalum by a planar open gate AlGaN/GaN HEMT. J Phys D Appl Phys 47:425401
145. Ozasa K, Nemoto S, Hara M, Maeda M (2006) Modification/oxidation of GaAs surface in electrolytes for cell-culture bio-sensing devices. Phys Status Solidi A 203:2287–2293
146. Jewett SA, Makowski MS, Andrews B, Manfra MJ, Ivanisevic A (2012) Gallium nitride is biocompatible and non-toxic before and after functionalization with peptides. Acta Biomater 8:728–733
147. Foster CM, Collazo R, Sitar Z, Ivanisevic A (2013) Cell behavior on gallium nitride surfaces: peptide affinity attachment versus covalent functionalization. Langmuir 29:837783–837784
148. Podolska A, Tham S, Hart RD, Seeber RM, Kocan M, Kocan M, Mishra UK, Pfleger KDG, Parish G, Nener PD (2012) Biocompatibility of semiconducting AlGaN/GaN material with living cells. Sens Actuators B 169:401–406
149. Gebinoga M, Cimalla I, Silveira L, Klett M, Lebedev V, Tonisch K, Will F, Ambacher O, Schober A (2009) Response of nerve cell to inhibitor recorded by aluminum-gallium-nitride FET. In: Baraton MI (ed) Sensors for environment, health and security: advanced materials and technologies. Springer, New York, pp 311–318
150. Podolska A, Hool LC, Pfleger KDG, Mishra UK, Parish G, Nener BD (2013) AlGaN/GaN-based biosensor for label-free detection of biological activity. Sens Actuators B 177:577–582
151. Kumari TV, Vasudev U, Anil K, Menon B (2002) Cell surface interaction in the study of biocompatibility. Trends Biomater Artif Organs 15:37–41
152. Yu J, Jha SK, Xiao L, Liu Q, Wang P, Surya C, Yang M (2007) AlGaN/GaN heterostructures for non-invasive cell electrophysiological measurements. Biosens Bioelectron 23:513–519
153. Hofstetter M, Howgate J, Schmid M, Schoell S, Sachsenhauser M, Adigüzel D, Stutzmann M, Sharp ID, Thalhammer S (2012) In vitro bio-functionality of gallium nitride sensors for radiation biophysics. Biochem Biophys Res Commun 424:348–353
154. Cimalla V, Niebelschutz F, Tonisch K, Foerster C, Brueckner K, Cimalla I, Friedrich T, Pezoldt J, Stephan R, Hein M, Ambacher O (2007) Nanoelectromechanical devices for sensing applications. Sens Actuators B 126:24–34
155. Linkohr S (2011) AlGaN/GaN-basierte-pH-Sensoren für biochemische Anwendungen. Thesis, Albert Ludwig Universität Freiburg. URN: urn:nbn:de:bsz:25-opus-84035
156. Anzt J, unpublished results
157. Berg NG, Paskova T, Ivanisevic A (2017) Tuning the biocompatibility of aluminum nitride. Mater Lett 189:1–4
158. Bain LE, Collazo R, Hsu SH, Pfiester LN, Manfra MJ, Ivanisevic A (2014) Surface topography and chemistry shape cellular behavior on wide band-gap semiconductors. Acta Biomater 10:2455–2462
159. Cimalla I, Gebinoga M, Schober A, Polyakov V, Lebedev V, Cimalla V (2011) AlGaN/GaN sensors for direct monitoring of nerve cell response to inhibitors. In: Ren F, Pearton SJ (eds) Semiconductor device-based sensors for gas, chemical, and biomedical applications. CRC Press, Boca Raton, pp 1–43
160. Gebinoga M, Mai P, Donahue M, Kittler M, Cimalla I, Lübbers B, Klett M, Lebedev V, Silveira L, Singh S, Schober A (2012) Nerve cell response to inhibitors recorded with an aluminum-galliumnitride/galliumnitride field-effect transistor. J Neurosci Methods 206:195–199
161. Gebinoga M, Silveira L, Cimalla I, Dumitrescu A, Kittler M, Lübbers B, Becker A, Lebedev V, Schober A (2010) Nanosensors for label-free measurement of sodium ion fluxes of neuronal cells. Mater Sci Eng B 169:182–185
162. Warnke C, Witte H, Mair T, Hauser MJB, Dadgar A, Krost A (2010) Monitoring glycolytic oscillations using AlGaN/GaN high electron mobility transistors (HEMTs). Sens Actuators B 149:310–313

163. Wang YL, Chu BH, Chen KH, Chang CY, Lele TP, Papad G, Coleman JK, Sheppard BJ, Dungen CF, Pearton SJ, Johnson JW, Rajagopal P, Roberts JC, Piner EL, Linthicum KJ, Ren F (2009) Fast detection of a protozoan pathogen, Perkinsus marinus, using AlGaN/GaN high electron mobility transistors. Appl Phys Lett 94:243901
164. Kang YW, Lee GY, Chyi JI, Hsu CP, Hsu YR, Hsu CH, Huang YF, Sun YC, Chen CC, Hung SC, Ren F, Yeh JA, Wang YL (2013) Human immunodeficiency virus drug development assisted with AlGaN/GaN high electron mobility transistors and binding-site models. Appl Phys Lett 102:173704
165. Chen CP, Ganguly A, Wang CH, Hsu CW, Chattopadhyay S, Hsu YK, Chang YC, Chen KH, Chen LC (2009) Label-free dual sensing of DNA molecules using GaN nanowires. Anal Chem 81:36–42
166. Chen CP, Ganguly A, Lu CY, Chen TY, Kuo CC, Chen RS, Tu WH, Fischer WB, Chen KH, Chen LC (2011) Ultrasensitive in situ label-free DNA detection using a GaN nanowire-based extended-gate field-effect-transistor sensor. Anal Chem 83:1938–1943
167. Williams EH, Davydov AV, Oleshko VP, Steffens KL, Levin I, Lin NJ, Bertness KA, Manocchi AK, Schreifels JA, Rao MV (2014) Solution-based functionalization of gallium-nitride nanowires for protein sensor development. Surf Sci 627:23–28
168. Sahoo P, Suresh S, Dhara S, Saini G, Rangarajan S, Tyagi AK (2013) Direct label free ultrasensitive impedimetric DNA biosensor using dendrimer functionalized GaN nanowires. Biosens Bioelectron 44:164–170
169. Bo L, Xiao C, Hualin C, Mohammad MA, Xiangguang T, Luqi T, Yi Y, Tianling R (2016) Surface acoustic wave devices for sensor applications. J Semicond 37:021001
170. Cai HL, Yang Y, Chen X, Mohammad MA, Ye TX, Guo CR, Yi LT, Zhou CJ, Liu J, Ren TL (2015) A third-order mode high frequency biosensor with atomic resolution. Biosens Bioelectron 71:261–268
171. Chiu CS, Lee HM, Kuo CT, Gwo S (2008) Immobilization of DNA-Au nanoparticles on aminosilane-functionalized aluminum nitride epitaxial films for surface acoustic wave sensing. Appl Phys Lett 93:163106
172. Shigekawa N, Nishimura K, Yokoyama H, Hohkawa K (2008) Surface acoustic waves in reverse-biased AlGaN/GaN heterostructures. IEEE Trans Electron Dev 55:1585–1591
173. Lalinský T, Rýger I, Vanko G, Tomáška M, Kostic I, Haščíka Š, Vallo M (2010) AlGaN/GaN based SAW-HEMT structures for chemical gas sensors. Proc Eng 5:152–155
174. Duhamel R, Robert L, Jia H, Li F, Lardet-Vieudrin F, Manceau J-F, Bastien F (2006) Sensitivity of a Lamb wave sensor with 2 μm AlN membrane. Ultrasonics 44:e893–e897
175. Rey-Mermet S, Lanz R, Muralt P (2006) Bulk acoustic wave resonator operating at 8 GHz for gravimetric sensing of organic films. Sens Actuators B 114:681–686
176. YQ F, Cherng JS, Luo JK, Desmulliez MPY, Li Y, Walton AJ, Placido F (2010) Aluminium nitride thin film acoustic wave device for microfluidic and biosensing applications. In: Dissanayake DW (ed) Acoustic waves. Sciyo, Rijeka, pp 263–298
177. Shih HY, Chen TT, Wang CH, Chen KY, Chen YF (2008) Optical detection of deoxyribonucleic acid hybridization with InGaN/GaN multiple quantum wells. Appl Phys Lett 92:261910
178. Heinz D, Huber F, Spiess M, Asad M, Wu L, Rettig O, Wu D, Neuschl B, Bauer S, Wu Y, Chakrabortty S, Hibst N, Strehle S, Weil T, Thonke K, Scholz F (2017) GaInN quantum wells as optochemical transducers for chemical sensors and biosensors. IEEE J Sel Top Quantum Electron 23:1900109
179. Berg NG, Franke A, Kirste R, Collazo R, Ivanisevic A (2016) Photoluminescence changes of III-nitride lateral polarity structures after chemical functionalization. Mater Res Exp 3:125906
180. Weidemann O, Kandaswamy PK, Monroy E, Jegert G, Stutzmann M, Eickhoff M (2009) GaN quantum dots as optical transducers for chemical sensors. Appl Phys Lett 94:113108

181. Maier K, Helwig A, Müller G, Becker P, Hille P, Schörmann J, Teubert J, Eickhoff M (2014) Detection of oxidising gases using an optochemical sensor system based on GaN/InGaN nanowires. Sens Actuators B 197:87–94
182. Kleindienst R, Becker P, Cimalla V, Grewe A, Hille P, Krüger M, Schörmann J, Schwarz UT, Teubert J, Eickhoff M, Sinzinger S (2015) Integration of an opto-chemical detector based on group III-nitride nanowire heterostructures. Appl Opt 54:839–847
183. Riedel M, Hölzel S, Hille P, Schörmann J, Eickhoff M, Lisdat F (2017) InGaN/GaN nanowires as a new platform for photoelectrochemical sensors – detection of NADH. Biosens Bioelectron 94:298–304
184. Li Z, Waldron J, Detchprohm T, Wetzel C, Karlicek Jr RF, Chow TP (2013) Monolithic integration of light-emitting diodes and power metal-oxide-semiconductor channel high-electron-mobility transistors for light-emitting power integrated circuits in GaN on sapphire substrate. Appl Phys Lett 102:192107
185. Hofmann M, Hauguth-Frank S, Lebedev V, Ambacher O, Sinzinger S (2008) Sapphire-GaN-based planar integrated free-space optical system. Appl Opt 47:2950–2955
186. Lu YS, Ho CL, Yeh JA, Lin HW, Gwo S (2008) Anion detection using ultrathin InN ion selective field effect transistors. Appl Phys Lett 92:212102
187. Stutzmann M, Garrido JA, Eickhoff M, Brandt MS (2006) Direct biofunctionalization of semiconductors. A survey. Phys Status Solidi A 203:3424–3437

(Bio-)chemical Sensing and Imaging by LAPS and SPIM

Tatsuo Yoshinobu, Steffi Krause, Ko-ichiro Miyamoto, Carl Frederik Werner, Arshak Poghossian, Torsten Wagner, and Michael J. Schöning

Abstract The light-addressable potentiometric sensor (LAPS) and scanning photo-induced impedance microscopy (SPIM) are two closely related methods to visualise the distributions of chemical species and impedance, respectively, at the interface between the sensing surface and the sample solution. They both have the same field-effect structure based on a semiconductor, which allows spatially resolved and label-free measurement of chemical species and impedance in the form of a photocurrent signal generated by a scanning light beam. In this article, the principles and various operation modes of LAPS and SPIM, functionalisation of the sensing surface for measuring various species, LAPS-based chemical imaging and high-resolution sensors based on silicon-on-sapphire substrates are described and discussed, focusing on their technical details and prospective applications.

Keywords Chemical imaging, Field-effect device, Light-addressable potentiometric sensor, Potentiometry, Scanning photo-induced impedance microscopy

T. Yoshinobu (✉)
Department of Biomedical Engineering, Tohoku University, Sendai, Japan

Department of Electronic Engineering, Tohoku University, Sendai, Japan
e-mail: nov@ecei.tohoku.ac.jp

S. Krause
School of Engineering and Materials Science, Queen Mary University of London, London, UK

K.-i. Miyamoto and C. F. Werner
Department of Electronic Engineering, Tohoku University, Sendai, Japan

A. Poghossian, T. Wagner, and M. J. Schöning
Institute of Nano- and Biotechnologies, Aachen University of Applied Sciences, Jülich, Germany

Institute of Complex Systems (ICS-8), Forschungszentrum Jülich GmbH, Jülich, Germany

M. J. Schöning, A. Poghossian (eds.), *Label-Free Biosensing: Advanced Materials, Devices and Applications*, Springer Series on Chemical Sensors and Biosensors (2018) 16: 103–132
DOI 10.1007/5346_2017_22, © Springer International Publishing AG 2018,
Published online: 25 January 2018

Contents

1 Introduction

Potentiometry based on a semiconductor field-effect structure offers a method of label-free (bio-)chemical sensing. The ion-sensitive field-effect transistor (ISFET) [1] is the most well-known device of this kind, which has an electrolyte–insulator–semiconductor (EIS) structure, and the variation of the activity of the target ions in the sample solution is detected in the form of the drain current in a FET structure.

The light-addressable potentiometric sensor (LAPS) [2] has the same EIS structure, but it has no laterally patterned structures. The semiconductor layer is illuminated with a light beam to induce a photocurrent signal, which is dependent on the activity of the target ions. Here, the measured area is defined by the illuminated area, which realises spatially resolved measurements using a scanning light beam. By recording the photocurrent at respective locations, a photocurrent map is obtained, which is then converted into a chemical image or a map of the ion concentration on the sensing surface. A LAPS sensor plate can be fabricated at low cost without the need for microfabrication processes, which makes it advantageous for disposable uses.

Scanning photo-induced impedance microscopy (SPIM) [3] was devised as a method to visualise the lateral distribution of the electrochemical impedance at the interface between the solution and the sensing surface, based on the same sensor structure and measurement set-up as those of LAPS. As for the physics and technologies involved, these two methods, LAPS and SPIM, share much in common, and they offer complementary information of the analyte.

In this article, the principle of operation, technological developments for enhancement of the sensor performance such as spatial and temporal resolutions and various applications of (bio-)chemical sensing and imaging by LAPS and SPIM are summarised and discussed.

2 Principles of LAPS and SPIM

2.1 Measurement Set-Up

As shown in Fig. 1, a typical LAPS measurement set-up consists of a sandwich structure of an insulator material on top of a semiconductor substrate. Usually, the insulator consists of a high-quality SiO_2 layer and a transducer layer sensitive to a specific analyte, as this combination guarantees good electrical and chemical properties at the same time. On the rear side of the sensor plate, an ohmic contact is created by a suitable metal layer. Typical parameters for LAPS are silicon substrate with a resistivity of 1–10 Ωcm and a thickness between 100 and 400 µm, insulating layers consisting of 20–50 nm thermally oxidised SiO_2 and, e.g. 50–100 nm of Ta_2O_5 [4], Si_3N_4 [5] or Al_2O_3 [6]. The insulating layer stays in direct contact with the analyte solution, forming an EIS structure. A reference electrode (RE, typically Ag/AgCl) is used to apply a bias voltage between the analyte solution and the ohmic contact on the rear side of the sensor plate.

A light beam is utilised to define, in a spatially resolved manner, a measurement region within the above-described sensor set-up. If the intensity of the light beam is continuously modulated, an ac (alternating current) photocurrent can be generated from the sensor structure. Modulation frequencies in the range of 1–20 kHz are reported in the literature [7]. To avoid possible influences of the analyte solution (e.g. absorption of stray light), the light source is usually placed underneath the sensor plate. To generate an ac photocurrent, the photons emitted by the light source need to have an energy higher than the bandgap of the utilised semiconductor material. For silicon, light with a wavelength shorter than 1,100 nm and therefore within the visible up to the beginning of the near-infrared region will be sufficient. This allows a choice from a wide range of commercially available light sources. In the literature, conventional gas lasers, laser diodes and femtosecond lasers [8–10],

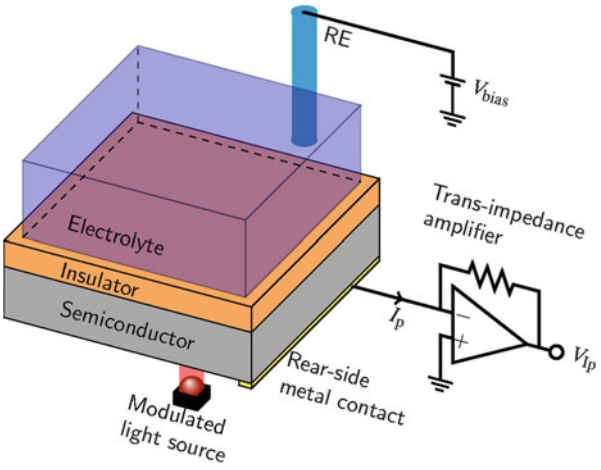

Fig. 1 Illustration of a typical measurement set-up for LAPS, consisting of a LAPS sensor plate in contact with a sample solution, biased with a dc voltage via a reference electrode, including the required intensity-modulated light source and the photocurrent readout circuit

light emitting diodes (LEDs) [11], organic LED displays [12, 13] and light sources based on digital micromirror devices (DMDs) [14] have been successfully utilised as light sources for LAPS-based devices.

A measurement electronic to detect the resulting external ac photocurrent is connected to the rear-side metal contact. Typically, the amplitude of the ac photocurrent is in the range of a few nanoamperes up to several microamperes. Therefore, usually the measurement electronic needs to amplify the photocurrent and converts it into a voltage in the order of several hundred millivolts to several volts by means of a trans-impedance amplifier stage. As the amplitude and phase values of the obtained ac signal represent the actual measurement information, this initial amplifying stage has to be designed carefully to avoid distortions of the measurement signals. Additional filtering techniques help to reject measurement noise. The obtained voltage is then either digitised by an analog-to-digital (AD) converter unit and further processed by digital filters or fed to an external filter circuitry to isolate the ac signal, e.g. by means of a lock-in amplifier circuit, before digitisation. The obtained amplitude and phase information is then stored for further data processing and analyses. Usually, this measurement cycle has to be repeated for different input parameters, and therefore, beside the ongoing photocurrent measurement task, the electronic circuitry and the software are often required to vary certain input parameters such as the geometry, position, intensity, modulation frequency and wavelength of the light spot as well as the applied dc bias voltage. The so obtained measurement data usually requires further data processing steps specific to applications, e.g. calibration, unit conversion, time-resolved analysis, image generation, etc., which are usually performed within the software.

2.2 *Generation of Photocurrent Dependent on Analyte Concentration*

Depending on the doping (*n*-type or *p*-type) of the semiconductor, applying a negative or positive dc (direct current) bias voltage with respect to the rear-side contact of the LAPS structure leads to formation of a space-charge region at the insulator–semiconductor interface (see Fig. 2a). The following discussion assumes the case of a *p*-type silicon; however, the same discussion will apply for an *n*-type silicon with opposite signs for the applied potentials. Varying this dc bias voltage from more negative towards more positive potential results in the typical capacitance vs. voltage characteristics, which is well-known for a metal–oxide–semiconductor (MOS) capacitor, depicting the accumulation, depletion and inversion states of the semiconductor. However, additional surface interactions at the transducer due to the electrolyte solution (e.g. the local pH value on a Ta_2O_5 surface) lead to the formation of a spatially distributed surface potential, which will be locally superimposed to the applied dc bias voltage. Hence, the thickness of the space-charge region varies depending on the local value of the surface potential.

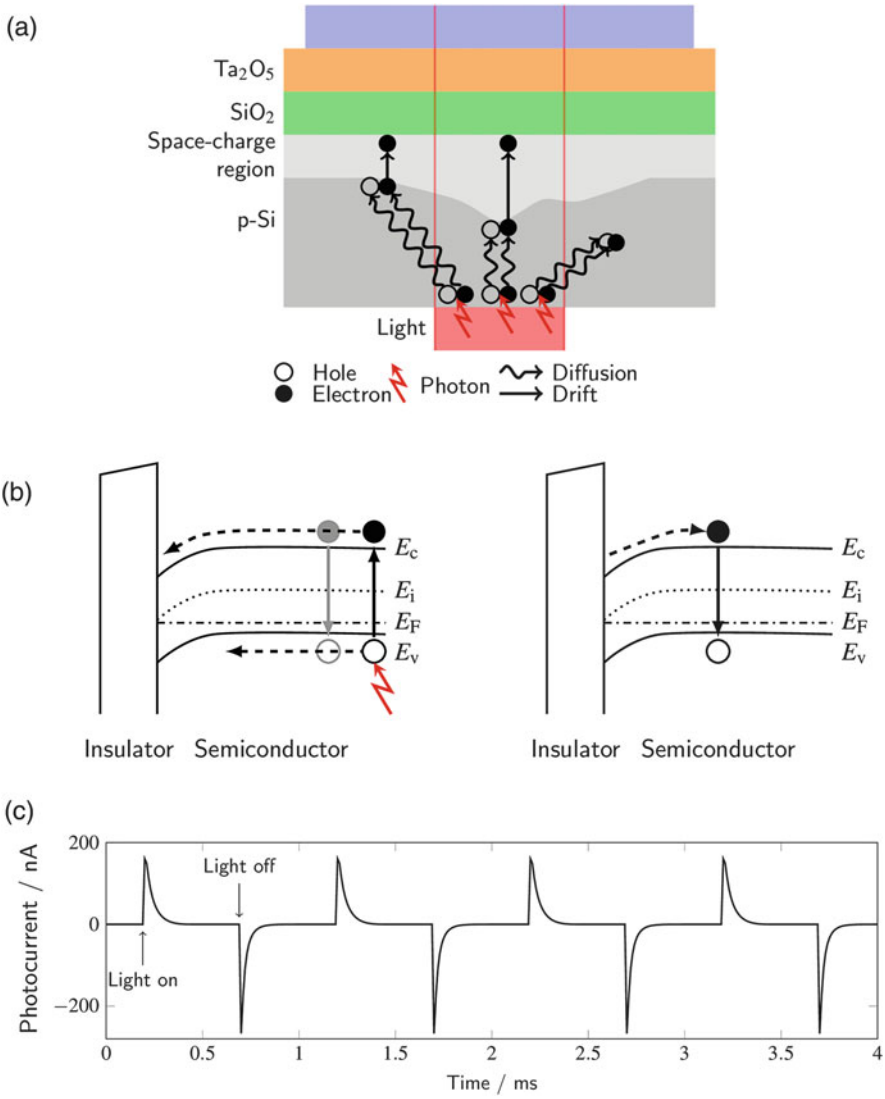

Fig. 2 (**a**) Schematic representation of the photocurrent generation. (**b**) Band diagrams illustrating photogeneration, diffusion, separation and recombination of electrons and holes after the light is turned on (left) and off (right), respectively. (**c**) An example of simulated photocurrent over time in the presence of modulated illumination. Simulation parameters are as follows: 100-µm-thick *n*-type Si substrate with a doping concentration of 10^{15} cm^{-3}, biased at −0.8 V, illuminated with a light beam with a wavelength of 950 nm and an intensity of 50 W/cm^2, modulated at 1 kHz

Illuminating a small area of the sensor by a light beam with an energy higher than the bandgap of the semiconductor will lead to generation of electron-hole pairs by the photoelectric effect, in which photons are absorbed and electrons are excited

from the valence band into the conduction band as shown in Fig. 2b, left. The so generated electron-hole pairs diffuse within the semiconductor bulk and eventually recombine. In the case of depletion or inversion, a small amount of the generated carriers will, however, reach the space-charge region, in which the electrons and holes are separated by the vertical electric field. The electrons will move towards the insulator interface, whereas the holes will be pushed back into the semiconductor bulk. This separation of charges will result in an externally measurable transient current that compensates for the occurring charging effect as shown in Fig. 2c. Under constant illumination, the charging effect would start to counteract against the charge separation and finally lead to an internal balance between the amount of electron-hole pairs separated and the charge-induced drift of electrons back into the bulk. At that point, the EIS system would be in an equilibrium state, and no more external current would be observable.

Switching the light off, the excess of electrons at the insulator–semiconductor interface will eventually move back into the semiconductor bulk and recombine as shown in Fig. 2b, right. This in turn requires compensation by a transient current in the reverse direction until a new point of equilibrium is reached.

To obtain a continuously measurable ac photocurrent, the intensity of the light source is usually modulated to repeat the charging–discharging cycles. The amplitude and phase of the external ac photocurrent depend on the thickness of the space-charge region, which is locally modified by the surface potential; an increase in the thickness of the space-charge region increases the amplitude and decreases the phase of the external ac photocurrent and vice versa. The measurement of the amplitude and phase of the external ac photocurrent therefore contains the information of the local surface potential of the area under illumination. Thus, with the help of a calibration step, the surface potential can be mapped into the distribution of the analyte concentration, and thus, LAPS can be used to read out the analyte concentration on the sensor surface in a spatially resolved manner.

2.3 Photocurrent–Voltage and Phase–Voltage Characteristics

When a single spot on the LAPS surface is illuminated, one can record the resulting ac photocurrent as a function of the dc bias voltage. Photocurrent–voltage characteristics and phase–voltage characteristics are obtained by plotting the amplitude and phase vs. the bias voltage as shown in Fig. 3. Under a negative bias voltage with respect to the rear-side contact, the semiconductor will be in the state of accumulation, where no space-charge region is formed, and hence, almost no external ac photocurrent is observable. With the increase of the bias voltage, a space-charge region appears as depletion occurs. The increase of the thickness of the space-charge region results in an increase of the ac photocurrent and decrease of the phase. Finally, at even more positive bias voltages, inversion will set in, and the thickness

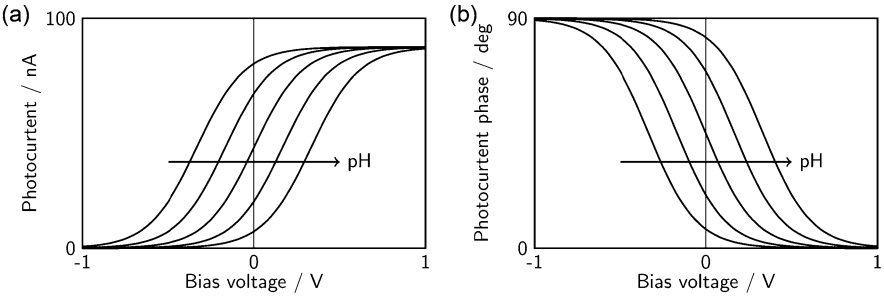

Fig. 3 Schematic representations of (**a**) photocurrent–voltage and (**b**) phase–voltage characteristics of a *p*-type LAPS for different pH values

of the space-charge region saturates at its maximum, resulting in the maximum photocurrent amplitude and minimum phase.

In the state of depletion, a change of the analyte concentration will change the surface potential resulting in a shift of the photocurrent–voltage curve along the bias voltage axis. For a change towards more positive charges (e.g. a decrease of the pH value), the resulting photocurrent at the same bias voltage will be higher, moving the photocurrent–voltage curve effectively to the left. For a more negative charge (e.g. an increase of the pH value), the amplitude of the photocurrent will be lower, moving the photocurrent–voltage curve to the right. Thus, the shift of the photocurrent–voltage curve can be correlated with the analyte concentration. In addition, the maximum amplitude of the photocurrent in the state of inversion depends on the overall impedance of the EIS system, which is utilised for impedance mapping in SPIM.

To accurately determine the shift of the photocurrent–voltage curve and impedance changes, various operation modes have been proposed for LAPS and SPIM as discussed in Sect. 2.5.

2.4 Equivalent Circuit of the LAPS

Figure 4a shows a simplified electrical equivalent circuit of the LAPS, which is usually applied to describe the measured photocurrent. Under low-intensity illumination, the resistance of the depletion layer (R_d) is relatively high [16], and if the impedance of the measurement circuit can be neglected, the circuit represents a capacitive divider. Then, the amplitude of the photocurrent (I_m), which is the quantity to be measured, is given by [16]:

$$I_m = I_p \frac{C_i}{C_i + C_d} \tag{1}$$

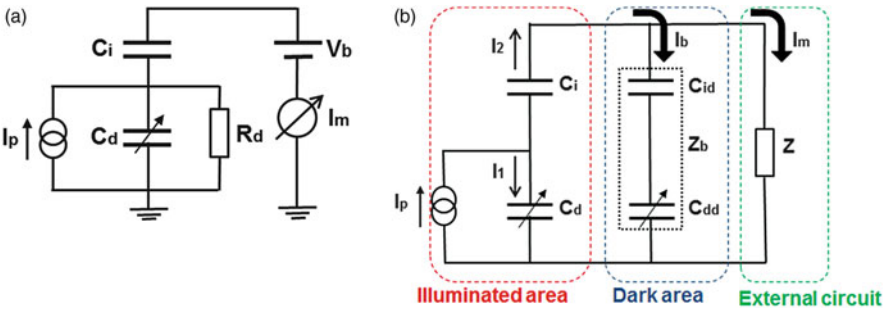

Fig. 4 (**a**) Simplified equivalent circuit of the LAPS and (**b**) extended equivalent circuit with the illuminated and dark surface areas. Adapted with permission from [15]. Copyright 2017, Elsevier

Here, I_p is the generated photocurrent; C_i and C_d are the insulator and depletion capacitances in the illuminated region. Equation (1) is valid if the global series impedance (Z, which includes, e.g. the resistances of bulk Si, contacts, electrolyte, reference electrode and impedance of the external readout circuit) is 0. However, since in real experiments $Z \neq 0$, the non-illuminated (dark) region can act as a shunting capacitor. The possible gate-surface potential changes in the non-illuminated region may induce to a certain extent a cross-talk effect during the signal detection in the illuminated region and thus, may also affect the measured photocurrent (I_m). In order to study the shunting effect of the non-illuminated area on the measured photocurrent and addressability of LAPS devices, recently, an extended equivalent circuit model of the LAPS with illuminated and non-illuminated (dark) surface areas has been proposed as shown in Fig. 4b [15]. In contrast to the equivalent circuit presented in Fig. 4a, in case of non-zero series impedance ($Z \neq 0$), a part of the photocurrent across C_i will flow through the bypass impedance (Z_b) of the non-illuminated region, thus reducing the measured photocurrent I_m as useful signal. From Fig. 4b, the relationship between the measured and generated photocurrents is given by [15]:

$$I_m = I_p \frac{C_i}{(C_i + C_d)\left(1 + \frac{Z}{Z_b}\right)} = I_{m\max} \frac{1}{1 + Z/Z_b} \tag{2}$$

$$Z_b = \frac{1}{j\omega C_{id}} + \frac{1}{j\omega C_{dd}} = \frac{C_{id} + C_{dd}}{j\omega C_{id} C_{dd}} \tag{3}$$

Here, C_{id} and C_{dd} are the insulator and depletion capacitances in the dark region, respectively, ω is the angular frequency of the intensity-modulated light, and $j = \sqrt{-1}$ represents the imaginary unit.

As can be seen from Eq. (2), the measured photocurrent depends on the ratio Z/Z_b, i.e. depends on the impedance of the dark region. Hence, the maximum measured photocurrent ($I_{m\max}$) can be achieved if $Z = 0$ or $Z_b >> Z$: From Eq. (2), by constant I_p and C_i, the maximum measured photocurrent depends only on C_d, which is affected by the local interfacial potential in the illuminated region and the bias

voltage. Thus, under assumption of $Z = 0$ or $Z_b >> Z$, the LAPS is addressable, i.e. the measured spot on the sensing surface is defined by the illumination area and the measured photocurrent will reflect a local analyte concentration. However, in real measuring systems, $Z \neq 0$, and therefore, the measured photocurrent will be determined not only by the local interfacial potential in the illuminated region but also by possible interfacial potential changes in the dark region, resulting in changes in the bypass impedance Z_b yielding a cross-talk effect. Thus, an impact of the non-illuminated region on the addressability of the LAPS and the measured photocurrent will be defined by the ratio of impedance magnitudes $|Z|/|Z_b|$. To minimise the impact (or cross-talk effect) of the non-illuminated region, most of the photocurrent must flow into the measurement circuit. These findings were supported by the experimental investigations of a penicillin-sensitive multi-spot LAPS and a metal–insulator–semiconductor LAPS as model systems [15].

2.5 *Operation Modes*

The effective voltage applied to the EIS system is the superposition of the externally applied bias and the Nernst potential on the sensing surface. The photocurrent–voltage curve shifts along the voltage axis in proportion to the logarithm of the activity of the target species as shown in Fig. 3a. The shift to be correlated with the analyte concentration can be determined, for example, at the inflection point of the curve [2]. This scheme is time-consuming, however, because a settling time is required to charge the EIS system at a new value, every time the bias is updated.

To meet different requirements of applications, various operation modes have been devised to extract the information of the sample from the photocurrent signal.

2.5.1 Constant-Bias Mode

In this mode, the external bias is fixed at a constant value within the transition region of the photocurrent–voltage curve, and the variation of the photocurrent is correlated to the analyte concentration. In most cases, the transition region is linearly approximated, so that a variation of the photocurrent is converted into the potential shift using the average slope of the transition region. This measurement mode is the most time-efficient and often used in LAPS-based chemical imaging [8]. The essential limitation of this mode is that the range of the photocurrent is restricted within the transition region. In case the variation of the analyte concentration is too large and either the minimum or the maximum of the photocurrent is reached by the corresponding shift of the photocurrent–voltage curve, the measurement will be out of range.

2.5.2 Constant-Current Mode

In this mode, the external bias is feedback-controlled, so that the amplitude of the photocurrent is maintained at a constant value selected within the transition region of the photocurrent–voltage curve [17]. The external bias is recorded as a function of time, which represents the temporal variation of the analyte concentration. Unlike in the case of the constant-bias mode, even a large shift of the curve can be followed.

2.5.3 Potential-Tracking Mode

The potential-tracking mode [18] acquires a reduced number of data points on the photocurrent–voltage curve, so that a wide range of bias can be scanned in a short time. The shift of the photocurrent–voltage curve is then determined by fitting the data points to a sigmoid curve or a logistic function, instead of calculating the inflection point based on the local curvature. This measurement mode can follow a large variation of analyte concentration while reducing the total measurement time by effectively using a reduced number of data points.

2.5.4 Phase Mode

If the determination of the analyte concentration relies on the absolute value of the photocurrent, variation of the height of the photocurrent–voltage curve results in an error. This is caused, for example, by fluctuation of the light intensity, non-uniformity of recombination rate in the semiconductor substrate due to defects and variation of the conductivity of the sample solution. It has been demonstrated that the phase of the photocurrent signal can be also correlated with the analyte concentration with much less sensitivity to such disturbances because the phase is not a quantity proportional to the number of charge carriers [19]. Figure 3b shows an example of phase–voltage curves for different pH values. In analogy to the photocurrent–voltage curve, the phase–voltage curve shifts along the voltage axis depending on the surface potential. Figure 5a, b compares the influence of the light intensity on the photocurrent–voltage curve and the phase–voltage curve. When the laser power decreases, the height of the photocurrent–voltage curve decreases accordingly, whereas the phase–voltage curve remains the same. It has been also demonstrated that the phase mode was insensitive to the non-uniform carrier recombination rate due to defects in a sensor plate [19].

2.5.5 SPIM Mode

Photocurrents measured at LAPS structures biased towards inversion are independent of the surface potential of the insulator and can be related to the local impedance

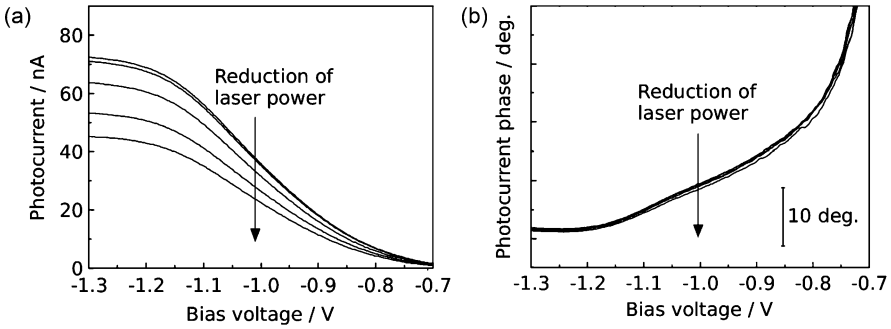

Fig. 5 Influence of the laser power on (**a**) the amplitude and (**b**) the phase of the photocurrent signal in a LAPS. Adapted with permission from [19]. Copyright 2014, Elsevier

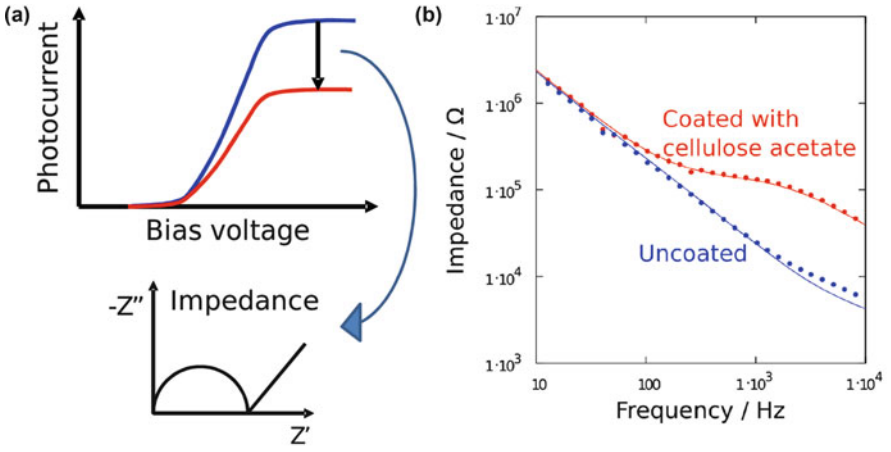

Fig. 6 (**a**) Principle of SPIM. Photocurrent changes measured in inversion are directly related to the local impedance of the sensor structure. Here, Z' and $-Z''$ represent the real part and the imaginary part of the electrochemical impedance. (**b**) Comparison of impedance spectra of an uncoated LAPS structure and a LAPS structure coated with cellulose acetate derived from photocurrent measurements in inversion (dots) and impedance spectra measured with an impedance analyser (lines). Reproduced with permission from [20]. Copyright 2006, Elsevier

of the structure. This measurement mode has been termed scanning photo-induced impedance microscopy (SPIM) [3]. Experiments with model systems have shown that the impedance data obtained from photocurrent measurements over a range of different modulation frequencies are in good agreement with those obtained with traditional ac impedance spectroscopy (Fig. 6) [20].

Similar measurements have also been carried out with amorphous hydrogenated silicon photodiode structures (a-Si:H n-i-p/SiO_2 structures) [21]. Amorphous silicon was chosen as the diffusion length of charge carriers in this material is relatively short, which was expected to improve the lateral resolution (also see Sect. 3.4), and a

photodiode structure would yield larger photocurrents than a field-effect capacitor. The structures were shown to be suitable for SPIM imaging. The resolution was strongly frequency-dependent due to the conductivity of the semiconductor layer closest to the SiO_2. To date, SPIM measurements with a-Si:H n-i-p/SiO_2 structures have been applied to the interrogation of biosensor arrays based on the degradation of thin polymer films [22].

3 LAPS-Based Sensing and Imaging

LAPS-based set-ups are widely used targeting different applications, including environmental monitoring, pharmaceutical and medical research, and material investigations. Those applications can be split into two categories. In the first category, LAPS is used as a sensor device with a single or multiple measurement spots defined on a single LAPS surface. The measurement spots are defined by the underlying light source, and the individual transducer layer can be further modified to detect different analyte species at different sensor spots, hence creating a multi-parameter sensor array on a single substrate. Usually, those set-ups focus on a fast and simplified readout procedure, a robust and miniaturised measurement set-up, and they are often designed for a specific application.

The second category utilises a light source to define a large array of small measurement spots, albeit the sensing mechanism remains the same throughout the entire LAPS structure. Thus, these set-ups can detect the spatial distribution of a single analyte above the sensor surface, and the distribution is represented as a chemical image similar to a thermal image obtained with a thermography camera. Usually, those set-ups are more complex and targeting many measurement spots ("pixels") with a high lateral resolution. The following sections will introduce both categories summarising typical examples found in the literature.

The LAPS measurement principle is applicable to a wide variety of analytes by modification of the transducer layer. As LAPS belongs to the family of sensors utilising the potentiometric principle, approaches and techniques developed for potentiometric sensors can usually be directly applicable to LAPS. Beside the detection of various ions, LAPS-based set-ups can be augmented with additional biological recognition elements to specifically detect biomolecules, including label-free detection of DNA hybridisation.

3.1 Detection of Various Ions

In the literature, different LAPS-based devices have been reported to detect the change of pH and other ion concentrations. To realise a specific sensitivity and selectivity towards an analyte, LAPS transducer layers have been replaced, modified or further functionalised. Thus, to make LAPS-based devices sensitive to different

ions, deposition of additional organic layers (e.g. PVC, polyvinyl chloride or photocurable polymers) including a specific ionophore on top of the LAPS transducer has been frequently reported [23–28]. This approach benefits from well-established standard techniques, like spin-coating or dip-coating, to deposit a polymer matrix including the ionophore on top of the LAPS surface. In addition, solid-state membranes have been developed over the years, providing specific sensitivity towards target ions [29–32]. They are usually deposited on the LAPS surface by conventional thin-film deposition techniques (e.g. sputtering, evaporation, pulsed laser deposition, etc.). For example, set-ups for the detection of heavy metal ions have been developed combining chalcogenide glasses with the LAPS measurement principle [33–36]. The ion exchange will result in a potential change at the LAPS surface resulting in a variation of the generated photocurrent. LAPS-based devices that have been used to detect various cations and anions are listed in Table 1.

3.2 Utilisation of Enzymes and Antibodies

An additional biological recognition element can be added to the LAPS surface to enable the detection of biological substances and organisms. There are two main forms of such biosensing functionalities: one relies on the detection of the concentration change of chemical species involved or produced in a biocatalytic reaction and the other relies on the specific affinity between the probe and the target resulting in variation of the charge on the sensor surface.

If the product of an enzymatic reaction is detectable by the transducer material of a LAPS, the catalysing enzyme can be used as a biological recognition element, which acts on its substrate molecule with a high specificity. For example, a LAPS with a pH-sensitive transducer layer can detect a pH change, which results from a variety of enzymatic reactions. Examples of target biomolecules of an enzyme LAPS include penicillin [39–42], glucose [39], urea [39, 43–46], butyrylcholine [46], ethanol [47] and acetylcholine [48]. Immobilisation of enzyme molecules onto the transducer surface can be realised either by physical adsorption or by chemical binding [4, 49, 50]; examples of the former technique include polymeric matrices and the layer-by-layer (LbL) technique, whereas examples of the latter technique include those based on aminosilanes and crosslinkers such as glutaraldehyde.

A specific binding between the probe on the LAPS surface and the target is recognisable, if the binding anchors charged molecules within the Debye length from the sensor surface. Immunosensors that rely on the specific binding of antigens and antibodies are the most typical examples of such affinity-based biosensors [51–59]. Enzyme-linked immunosorbent assay (ELISA) reactions are also extensively used in conjunction with LAPS. In addition, LAPS sensitive to adenosine triphosphate (ATP) [60], cancer cells [61] and tumour markers [62] have been also reported. Table 2 gives an overview on LAPS sensitive to various biological substances and organisms.

Table 1 Different types of ion-sensitive LAPS

Target ion	Ion-sensitive material or ionophore/membrane system		Sensitivity (mV/decade)	Lower detection limit (M)	Reference
	Type	Name			
Na^+	Oxide	HfO_2	31.8	–	[31]
K^+	Ionophore/PVC	Valinomycin	50	–	[23]
			57	–	[24]
			57	3×10^{-3}	[37]
		18-crown-6 ether	50	–	[23]
		bis-[(benzo-15-crown-5)-4′-ylmethyl]pimelat	57	6×10^{-6}	[37]
	Ionophore/PM	Valinomycin	58 ± 1	2×10^{-6}	[25]
Li^+	Ionophore/PVC	*N*,*N*-dicyclohexyl-*N*′,*N*′-diisobutyl-*cis*-cyclohexane-1,2-dicarbamide	59	8×10^{-5}	[37]
		6,6-dibenzyl-14-crown-4	56	1×10^{-4}	[37]
	Ionophore/PM	*N*,*N*-dicyclohexyl-*N*′,*N*′-diisobutyl-*cis*-cyclohexane-1,2-dicarbamide	59 ± 1	2×10^{-6}	[25]
Cs^+	Ionophore/PM	Cs ionophore I	57 ± 2	4×10^{-6}	[25]
NH_4^+	Oxide	CF_4 plasma-threated HfO_2	37	–	[38]
Ca^{2+}	Ionophore/PVC	*bis*-[di(*n*-octylphenyl)phosphato]calcium(II)	25	–	[23]
	Ionophore/PM	*t*-HDOPP-Ca	27 ± 2	7×10^{-6}	[25]
Mg^{2+}	Ionophore/PVC	*N*,*N*′-diheptyl-*N*,*N*′-dimethyl-1,4-butanediamide	19	–	[23]
	Ionophore/PM	Mg ionophore I	26 ± 1	5×10^{-6}	[25]
Pb^{2+}	Ionophore/PVC	*N*,*N*′-tetrabutyldipicolinediamide	29.3 ± 0.5	6.4×10^{-6}	[28]
	Chalcogenide glass	Pb–Ag–As–I–S	29 ± 1	1×10^{-6}	[33]
Cd^{2+}	Ionophore/PVC	*N*,*N*′-diethyl-*N*,*N*′-diphenyldiamide of 2,2′-dipyridyl-6,6′-dicarboxylic acid	28.7 ± 0.2	5.8×10^{-5}	[28]
	Chalcogenide glass	Cd–S–Ag–I–As–S	24.5	6×10^{-7}	[30]
Zn^{2+}	Ionophore	Zn sensor membrane cocktail	29.2 ± 0.3	6.6×10^{-6}	[28]
Hg^{2+}	Chalcogenide glass	Hg–Ag–I–S	–	3×10^{-6}	[35]
Fe^{3+}	Chalcogenide glass	Fe–Ge–Sb–Se	–	1×10^{-5}	[36]
Cl^-	Oxide	Sm_2O_3	36.17	–	[32]
F^-	Ionic crystal	LaF_3	49	–	[29]
NO_3^-	Organic IE	Tridodecylmethylammonium nitrate	58 ± 2	1×10^{-5}	[26]
SO_4^{2-}	Ionophore/PVC	1,3-[*bis*(3-phenylthioureidomethyl)]benzene	26 ± 1	1×10^{-6}	[26]

PVC polyvinylchloride, *PM* photocurable membrane, *IE* ion exchanger

Table 2 Different types of biosensing LAPS

Target analyte	Biological recognition element		Concentration range	Lower detection limit	Reference
	Type	Name			
Penicillin	Enzyme	Penicillinase	5–25 mM	–	[39]
			0.05–1 mM	50 μM	[40]
			0.1–10 mM	–	[41]
			0.5–5 mM	–	[42]
Glucose		Glucose oxidase	−4 mM	–	[39]
Urea		Urease	−15 mM	–	[39]
			0.3×10^{-3} to 1×10^{-1} M	–	[45]
			6.3×10^{-5} to 0.9 M	–	[46]
Butyrylcholine		Butyrylcholinesterase	2.5×10^{-4} to 2×10^{-1} M	–	[46]
Ethanol		Alcohol dehydrogenase	0.5–352 mM	–	[47]
Acetylcholine		Acetylcholine esterase	1–10 mM	–	[48]
Urease	Substrate	Urea	–	2.4×10^{-13} M	[43]
			–	2.5×10^{-10} M	[44]
Alcohol dehydrogenase		Ethanol	1.4×10^{-8} to 7.1×10^{-10} M	–	[47]
Mojave toxin (MoTX)	Antibody	Anti-MoTX antibody	0.3–2.5 ng	–	[51]
E. coli		Goat anti-*E. coli* O157:H7 antibody	–	7.1×10^{2} cells/mL (heat-killed cells) 2.5×10^{4} cells/mL (live cells)	[52]
Salmonella typhimurium		Rabbit anti-salmonella antibody	–	119 CFU	[53]
Newcastle disease virus (NDV)		Anti-NDV antibody	–	2 ng/mL	[54]
Venezuelan equine encephalitis virus		Biotinylated single chain fragment variable antibody (B-scFv)	–	0.29 μg/mL	[55]
		Biotinylated monoclonal antibody (B-mAb)	–	0.34 μg/mL	
Terbuthylazine		Monoclonal antibody (mAb)	1.5–10 μg/L	–	[56]
Human IgG		Goat antihuman IgG antibody	−150 μg/mL	0.15 μg/mL	[57]
Rabbit anti-mouse IgG	Antigen	Mouse IgG	−4 μg/mL	–	[58]
ATP	Aptamer	ATP-sensitive aptamer	1×10^{-8} to 1×10^{-4} M	2.6×10^{-8} M	[60]

IgG immunoglobulin, *ATP* adenosine triphosphate, *CFU* colony-forming unit

3.3 Detection of DNA

In spite of the popularity of LAPS in many chemical and biological applications (e.g. measurement of pH and ion concentration, enzymatic reactions, acidification rate of living cells), very little is known about LAPS-based biosensors for the label-free detection of DNA (deoxyribonucleic acid) molecules by their intrinsic molecular charge [63, 64]. It has been discussed [65–67] that the electrostatic coupling between charged DNA molecules and field-effect devices depends on the orientation of DNA molecules to the gate surface and strongly reduces with increasing the distance between the DNA charge and the gate surface (see also [68]). A high signal can be expected by the immobilisation of DNA molecules flat to the sensor surface. Therefore, recently, a new multi-spot LAPS-based DNA biosensor has been developed, where a simple LbL electrostatic adsorption is used for a rapid immobilisation of single- or double-stranded DNA molecules (ssDNA, dsDNA) onto the gate surface modified with a positively charged weak-polyelectrolyte layer of PAH (poly(allylamine hydrochloride)) [69, 70]. The LbL immobilisation of DNA usually results in the formation of preferentially flat orientation of DNA strands [71], a crucial factor to reduce the distance between the DNA charge and LAPS surface and thus, to enhance the sensitivity of the LAPS to the DNA charge. In addition, the positively charged PAH layer may reduce the electrostatic repulsion between probe ssDNA and complementary target DNA (cDNA) and thus, may accelerate the hybridisation process.

Figure 7 shows a schematic structure and measurement set-up of the multi-spot LAPS for DNA immobilisation and hybridisation detection (a) and a LAPS signal (mean potential shifts averaged over 16 measurement spots) before and after PAH adsorption, after probe ssDNA immobilisation, after non-specific adsorption of fully mismatched ssDNA molecules and after hybridisation of probe ssDNA with complementary target cDNA (b). As expected, PAH adsorption, probe ssDNA immobilisation and target cDNA hybridisation occurring on the gate surface of the LAPS effectively alter the charge applied to the gate, resulting in a shift of the photocurrent–voltage curve along the voltage axis. The high signals of 83 mV and 32 mV were registered after ssDNA immobilisation and hybridisation with cDNA, respectively. In contrast, non-specific adsorption of fully mismatched ssDNA (5 μM) induces only a small potential shift of less than 5 mV, which was similar to that observed after hybridisation of cDNA with a more than four orders of magnitude smaller concentration of 0.1 nM. This confirms that the developed LAPS is able to differentiate between complementary and mismatched DNA sequences. The obtained results demonstrate the potential of the LAPS in combination with the simple and rapid LbL immobilisation technique as a promising platform for the future development of multi-spot light-addressable label-free DNA chips with direct electrical readout.

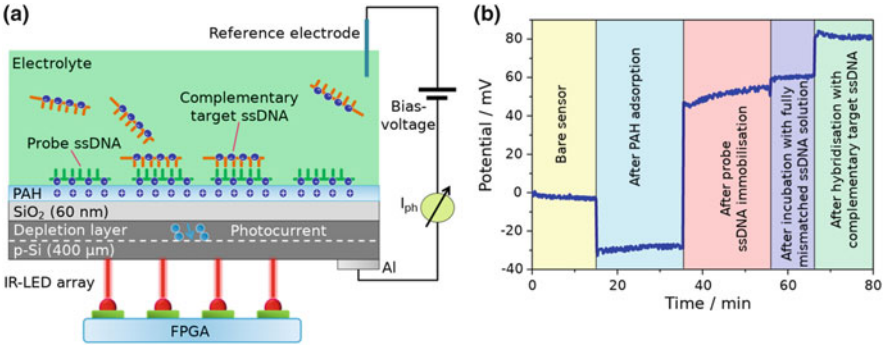

Fig. 7 (**a**) Schematic layer structure and measurement set-up of the multi-light LAPS (consisting of an Al–p–Si–SiO_2 structure) for DNA immobilisation and hybridisation detection and (**b**) a LAPS signal (mean potential shifts averaged over 16 measurement spots) before and after PAH adsorption, after probe ssDNA immobilisation, after non-specific adsorption of fully mismatched ssDNA molecules and after hybridisation of probe ssDNA with complementary target cDNA. For photocurrent generation, all 16 spots were illuminated in parallel by using an array of 4 × 4 infrared LEDs with different modulation frequencies (from 1 to 1.75 kHz). The mean potential shifts were evaluated from the inflection points of the respective photocurrent–voltage curves. To reduce the influence of the charge-screening effect, measurements were performed in a low ionic-strength solution (10 mM NaCl). *FPGA* field-programmable gate array, I_{ph} measured photocurrent. Reproduced from [69]. Copyright 2015, the Royal Society of Chemistry

3.4 LAPS-Based Chemical Imaging

The sensing area of a LAPS is not the entire surface in contact with the solution but is defined by a localised illumination [2]. This light-addressability facilitates application of a LAPS to imaging of spatially distributed chemical species [8, 27, 72, 73]. A LAPS-based chemical imaging system consists of a LAPS sensor plate, a scanning light beam and measurement electronics. The excitation light is typically a focused laser beam that raster-scans the rear surface of the sensor plate with the help of a mechanical stage [74, 75] or scanning mirrors [8, 76]. Another type of light source is a display device such as an organic LED display [12, 13] or DMD [77]; a selected pixel within the display area illuminates the rear surface of the sensor plate. The use of a display device eliminates the need for a scanning mechanism and, therefore, is advantageous in terms of miniaturisation, while the flexibility of pixel layout is limited. The LAPS-based chemical imaging sensor is usually operated in the constant-bias mode, in which a photocurrent image is obtained under a fixed bias and is converted through a calibration step into a chemical image or a concentration map of target species. In addition to pH images, distribution of various ions and molecules can be visualised by modifying the sensing surface with ion-selective membranes [27] or enzymes [74].

In the rest of this subsection, the spatial resolution, the temporal resolution and the applications of LAPS-based chemical imaging are summarised and discussed.

3.4.1 Spatial Resolution

The spatial resolution of LAPS-based chemical imaging is determined by the lateral diffusion of charge carriers [78–82]. When the light beam enters the semiconductor, the intensity decays as $e^{-\alpha z}$ by absorption, where α is the absorption coefficient and z is the depth. Charge carriers are generated at various depths and start diffusion. The number of minority carriers decays as $e^{-r/L}$ by recombination, where r is the travelling distance and L is the diffusion length of minority carriers. In case where the penetration depth $1/\alpha$ is much smaller than the thickness of the semiconductor layer d, most of charge carriers are generated at the illuminated point on the rear surface. The spatial resolution in this case is given by $\sqrt{L(L+2d)}$, assuming isotropic three-dimensional diffusion of charge carriers from a point source [72]. In the other extreme case where $1/\alpha$ is much larger than d, the diffusion becomes two-dimensional and the spatial resolution is given by L [81].

One straightforward approach to enhance the spatial resolution is, therefore, to use a sensor plate with a smaller d, which has been experimentally demonstrated [79]. In the case of crystalline Si, however, a sensor plate thinner than 100 μm is very fragile and difficult to handle, and therefore, a support structure such as silicon-on-sapphire (SOS) [83] is necessary. Another approach to enhance the spatial resolution is to use an infrared light beam with a smaller α that enters deeper into silicon and generates charge carriers near the depletion layer [80]. Yet another approach is to use a semiconductor material other than crystalline silicon with a smaller L, such as GaAs [84] or amorphous Si [85], which suppresses diffusion of minority carriers at the cost of reduction in the photocurrent signal.

More sophisticated techniques to enhance the spatial resolution have also been proposed. A ring-shaped illumination surrounding the excitation light was used to block the lateral diffusion of charge carriers by enhancement of recombination [86]. Time-resolved measurement of photocurrent response to a pulsed laser excitation was used to exclude the contribution of charge carriers that travelled a longer distance [87]. So far, the highest spatial resolution was obtained by the two-photon technique [10] (see Sect. 4.2).

3.4.2 Temporal Resolution

The temporal resolution or the measurement speed is another important factor that characterises the performance of a chemical imaging system. If a chemical image is acquired in a pixel-by-pixel manner, the acquisition time is the product of the measurement time per pixel and the number of pixels. The former is typically of the order of milliseconds, resulting in a total acquisition time of the order of minutes for a typical resolution of 128 × 128 or 256 × 256.

Various efforts have been made to achieve high-speed imaging. There exist, however, various trade-offs among the measurement speed, the signal-to-noise ratio and the spatial resolution, and therefore, a compromise must be made to meet the requirements

of applications. For example, an analog micromirror was employed for high-speed scanning, which reduced the measurement time per pixel down to 200 μs, corresponding to a pixel rate of 5,000 pixels/s, and acquired an image of 500 × 400 pixels in 40 s [76]. Another approach is to use a plurality of light beams to read out more than one pixels at one time [88]. The light beams are modulated at different frequencies, so that the photocurrent signals from corresponding locations are multiplexed in the frequency domain and extracted by Fourier analysis. An array of 8 × 8 light beams guided with an optical fibre bundle was employed to illuminate 64 different locations at the same time, and the photocurrent signals were extracted every 10 ms [89]. This system could record a low-resolution (64 pixels) but high-frame-rate (100 fps) movie of the spatiotemporal change of pH distribution in the sample solution.

3.4.3 Applications

As a label-free method of visualisation for pH and chemical species, the LAPS-based chemical imaging sensor has a wide range of potential applications, for example, in materials science, environmental science, biology and medicine. Applications in materials science include in-situ observation of a corroding surface of stainless steel [90]. In spite of the high resistance to corrosion, stainless steel is known to corrode when placed in a narrow gap of few micrometres, which is difficult to access for analysis. By forming a narrow gap between a test piece of stainless steel and the sensing surface of LAPS, variation of pH associated with corrosion was visualised. Applications in environmental science include characterisation of diffusivity in soils and study of the influence of acid rain on plant leaves [91].

Many studies have been directed towards biomedical application of LAPS. It has been applied to detection, quantification and visualisation of metabolic activities of cells and microorganisms [92–94], which can be further applied, for example, to plate counting of microbial colonies, investigation of efficacy and side effects of drugs in screening tests and so on. The LAPS-based chemical imaging has been also applied to the study of pH distribution in dentinal caries of human teeth [95, 96].

Combination of LAPS and microfluidics as illustrated in Fig. 8 is a prospective strategy for future applications [97]. Thanks to the flat sensing surface, it is easy to construct microfluidic channels on LAPS and to integrate multiple functions on a single chip. Light-addressability facilitates access to an arbitrary location inside the channel, and spatiotemporal recording allows monitoring at each step of reactions.

From the viewpoint of commercialisation, different approaches have been taken for a LAPS and for a LAPS-based chemical imaging system. The Cytosensor® Microphysiometer (Molecular Devices) focused on cell-based assays, in which a LAPS was used as a microfabricated pH sensor to monitor the acidification rate related to cell activities. On the other hand, the scanning chemical microscope, SCHEM™ (Horiba), was developed as a general-purpose pH imaging tool with a wide range of supposed application fields. Both examples have shown the importance of developing applications in gaining popularity of the method. After decades of technological developments, it is expected that the number of potential applications has drastically

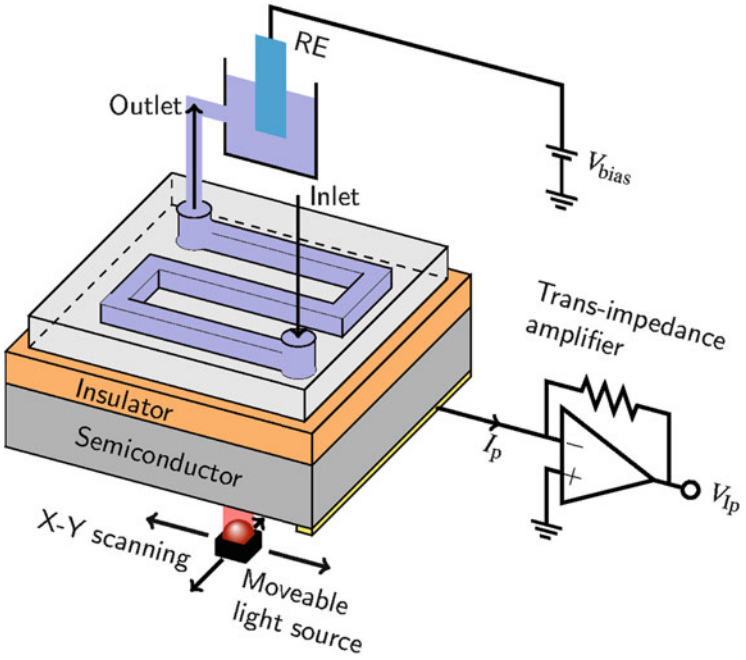

Fig. 8 Example of a microfluidic channel constructed on the sensing surface for spatiotemporal recording of chemical species

increased, for which developments of application-specific instrumentations and protocols are important.

4 High-Resolution SPIM and LAPS Imaging Based on SOS Substrates

Thinning silicon has been shown to be a very effective method for improving the resolution of LAPS and SPIM (see Sect. 3.4). SOS combines the advantages of ultrathin silicon with a mechanically stable, transparent substrate, which offers high flexibility in the wavelengths that can be employed for charge carrier generation. The diffusion length of minority charge carriers determined by measuring the decay of the photocurrent outside the gate area was 0.56 μm for a 1-μm-thick silicon layer on sapphire indicating the potential of the material for submicrometre resolution imaging [20]. SOS has therefore been adopted as the semiconductor substrate of choice for high-resolution SPIM and LAPS imaging.

4.1 Surface Functionalisation of SOS Substrates

Attempts to grow good-quality, thermal oxide on SOS failed, most likely due to a mismatch in the thermal expansion coefficients of silicon and sapphire. This problem was first solved with a 6.7-nm-thick anodic oxide grown in 0.1 M HCl, which could be produced at room temperature and stabilised with a short annealing process [10]. Later, the traditional insulator was replaced with oxide-free self-assembled organic monolayers by reacting hydrogen-terminated silicon (100) surfaces with alkenes [98] or alkynes [99] under mild conditions as illustrated in Fig. 9. The organic monolayers provide ultrathin insulators with low impedance and low interface state density resulting in high sensitivity for SPIM and good accuracy for LAPS measurements. Undecylenic acid monolayers on SOS displayed pH sensitivity similar to that of a traditional oxide insulator, but it was difficult to achieve oxide-free silicon surfaces [98]. Better results were obtained with 1,8-nonadiyne, which allowed assembly of oxide-free monolayers. Both methods are suitable for further functionalisation – acid-terminated monolayer with physical adsorption based on surface charge [98] or traditional coupling chemistry – and alkyne-terminated monolayers could conveniently be modified with a copper(I)-catalysed "click" cycloaddition illustrated in Fig. 9b [99]. Surface functionalisation allows adaptation of the surfaces to different applications in sensing or bioimaging. It was shown that both, physical absorption and "click" modification, can be coupled with microcontact printing (μCP) to create patterned surfaces and sensor arrays [98, 99].

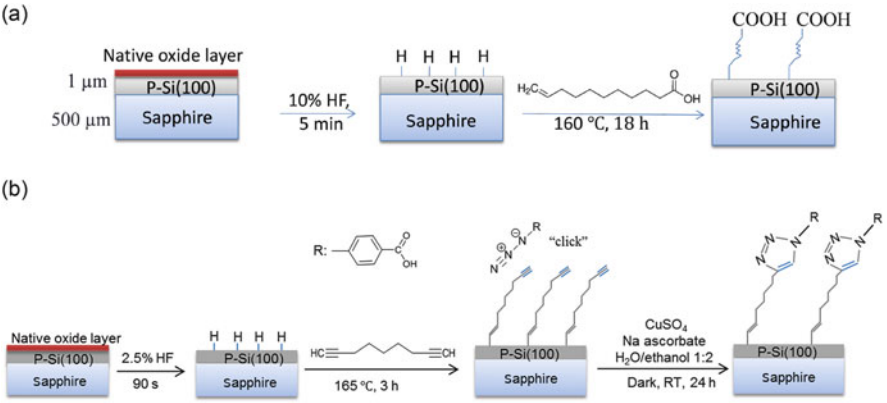

Fig. 9 Modification of hydrogen-terminated SOS with (**a**) undecylenic acid [98] and (**b**) 1;1,8-nonadiyne with subsequent functionalisation using a copper(I)-catalysed "click" cycloaddition between the terminal alkyne of the monolayer and an azide [99]. Figure (**a**) was adapted with permission from [98]. Copyright 2015, Elsevier. Figure (**b**) was adapted with permission from [99]. Copyright 2015, American Chemical Society

4.2 SPIM and LAPS Imaging

High-resolution SPIM and LAPS imaging has to date been carried out using traditional mechanical stages to move the sensor substrate with respect to a laser beam focused with a microscope objective onto the silicon layer through the back of the SOS substrate. As focusing light through a solid substrate such as sapphire can degrade the resolution substantially due to spherical aberration, a microscope objective with correction has to be used. The wavelength dependence of the spatial resolution has been investigated by imaging SU-8 photoresist patterns with backside illumination [10]. Scans of the laser beam from uncoated to coated parts of the substrate showed the expected improvement of the resolution with decreasing wavelength from 3 μm at 1,064 nm wavelength to 1.5 μm at 405 nm wavelength (Fig. 10b). This is in agreement with the Rayleigh criterion:

$$r = \frac{0.61\lambda}{\mathrm{NA}}, \tag{4}$$

where r is the resolution, λ the wavelength and NA the numerical aperture of the microscope objective used.

Two-photon absorption can be used for photocurrent excitation by employing a femtosecond laser with an energy smaller than the bandgap of silicon. The resulting non-linear absorption (Fig. 10a, 1,250 nm) leads to an improved effective laser beam profile and a resolution of 800 nm (Fig. 10b).

The feasibility of using photocurrent measurements at SOS substrates for bioimaging applications was first demonstrated by μCP a dot pattern of the positively charged PAH on an undecylenic acid-modified SOS surface [98]. Photocurrent images showed a clear contrast between the different surface charges of the unmodified carboxylate-terminated surface and the PAH-modified surface (Fig. 11a). Exposing the patterns to double-stranded DNA caused a change in the photocurrent contrast (Fig. 11b) and a shift of the local photocurrent–voltage curve to positive values due to

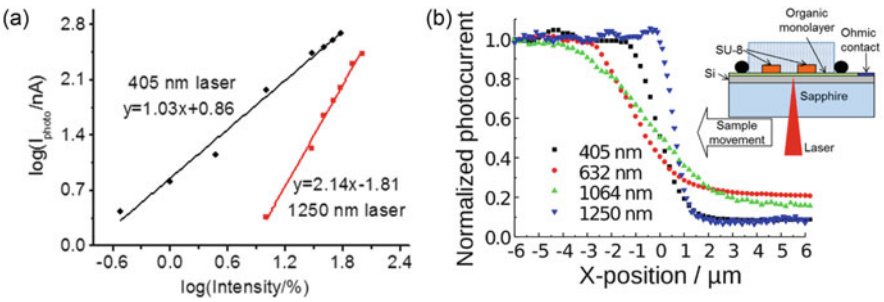

Fig. 10 (**a**) Intensity dependence of the photocurrent using a femtosecond laser with a wavelength of 1,250 nm (red squares) and a diode laser with a wavelength of 405 nm (black diamonds). (**b**) Photocurrent line scan across the edge of an SU-8 photoresist pattern at different wavelengths. Reproduced with permission from [98]. Copyright 2015, Elsevier

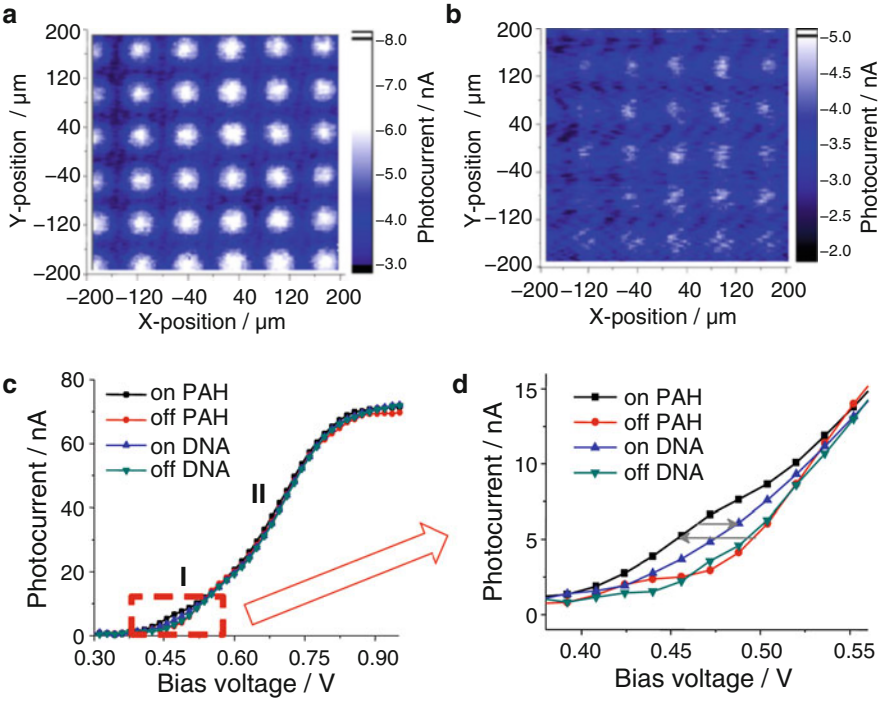

Fig. 11 (**a**) LAPS image of PAH dots printed on an undecylenic acid SAM; (**b**) LAPS image after adsorption of dsDNA on PAH dots; (**c**) *I–V* curves for PAH and PAH/dsDNA patterned on undecylenic acid-modified SOS substrate and (**d**) zoomed graph in the depletion region. Reproduced with permission from [98]. Copyright 2015, Elsevier

the adsorption of the negatively charged DNA on the positively charged PAH dots (Fig. 11c, d), clearly demonstrating the capability of the technique of interrogating biosensor arrays for label-free DNA sensing. Printing PAH onto the surface caused the appearance of a step in the photocurrent–voltage curve (Fig. 11c), which was attributed to incomplete coverage caused by the µCP process. It was suggested that this behaviour could be used to quantify coverage of surfaces with charged polymers, DNA and other charged biomolecules in the future.

LAPS and SPIM imaging with organic monolayer-modified SOS substrates has proven to be very sensitive to the contamination of the monolayers through various patterning processes, which are not easily detected by alternative techniques. The efficacy of chemical modification of 1,8-nonadiyne monolayers on SOS was reduced after exposure and development of photoresist [99]. An organic residue left behind by the photolithographic process could be visualised in LAPS images due to changes in the surface charge caused by the contaminants. Similarly, a copper(I) residue left behind in the monolayer after a combination of "click" modification and µCP that was not detectable by X-ray photoelectron spectroscopy (XPS) could be clearly seen in LAPS and SPIM images as copper(I) increased the positive surface charge and

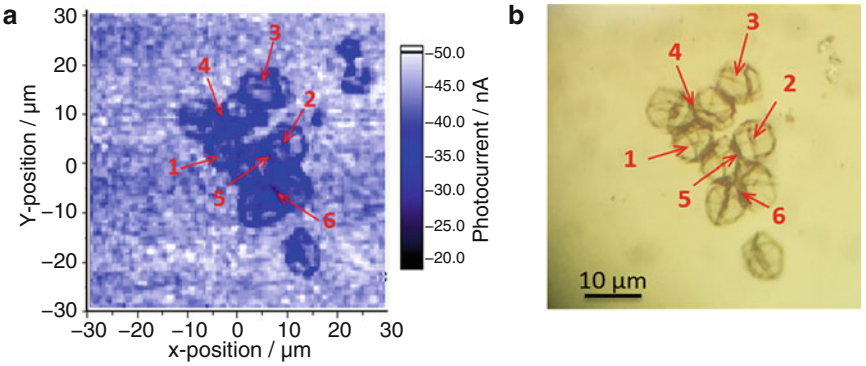

Fig. 12 (**a**) SPIM image of microcapsules attached on a COOH-terminated SOS substrate measured in inversion, (**b**) corresponding microscope image. Reproduced with permission from [101]. Copyright 2016, Elsevier

lowered the local impedance of the EIS structure [100]. After removal of the copper(I) residue, it was shown that SPIM is sensitive enough to determine the local impedance of a self-assembled organic monolayer.

Polyelectrolyte microcapsules have attracted considerable interest because of their potential uses in drug delivery, sensing and smart materials. Microcapsules have been modified with gold nanoparticles as a means to trigger release through light-induced local heating. SPIM images confirmed by conductive atomic force microscopy have shown that modification with gold nanoparticles increased the impedance of the capsules significantly more than expected from the increase in the capsule wall thickness introduced by a layer of gold nanoparticles [101]. High-resolution SPIM images show the impedance changes across the collapsed capsules in good detail (Fig. 12a) and are in good agreement with the corresponding microscope image of the same capsules (Fig. 12b).

SPIM and LAPS are prospective techniques for gaining information about processes in the surface attachment area of living cells. Zhang et al. [102] recently demonstrated that 1,8-nonandiyne-modified SOS is pH-insensitive and that SPIM and LAPS imaging can be used to gain information about cell surface charges and cell impedance of a colony of yeast cells immobilised by agarose gel. It is envisaged that the good lateral resolution and sensitivity of SPIM and LAPS can be utilised for single cell imaging in the future.

5 Summary

Since the first invention of LAPS in 1988, enormous efforts have been made to enhance its sensing capabilities and to add imaging capabilities to visualise the distributions of chemical species and impedance, today known as the chemical imaging sensor and SPIM, respectively. Various operation modes and measurement

set-ups have been proposed to meet different requirements such as high precision, high resolution, high speed and miniaturisation. Functionalisation of the sensing surface allowed sensing and imaging of various chemical species including biomolecules. The use of a two-photon effect realised submicron resolution. The LAPS-based chemical imaging sensor and SPIM are therefore expected as powerful and versatile tools of label-free sensing and imaging, to be applied in chemistry, materials science, biology and medicine.

References

1. Bergveld P (1970) Development of an ion-sensitive solid-state device for neurophysiological measurements. IEEE Trans Biomed Eng 17:70–71
2. Hafeman DG, Parce JW, McConnell HM (1988) Light-addressable potentiometric sensor for biochemical systems. Science 240:1182–1185
3. Krause S, Talabani H, Xu M, Moritz W, Griffiths J (2002) Scanning photo-induced impedance microscopy – an impedance based imaging technique. Electrochim Acta 47:2143–2148
4. Yoshinobu T, Ecken H, Poghossian A, Lüth H, Iwasaki H, Schöning MJ (2001) Alternative sensor materials for light-addressable potentiometric sensors. Sensors Actuators B Chem 76:388–392
5. Adami M, Alliata D, Del Carlo C, Martini M, Piras L, Sartore M, Nicolini C (1995) Characterization of silicon transducers with Si_3N_4 sensing surfaces by an AFM and a PAB system. Sensors Actuators B Chem 24–25:889–893
6. Ismail ABM, Harada T, Yoshinobu T, Iwasaki H, Schöning MJ, Lüth H (2000) Investigation of pulsed laser-deposited Al_2O_3 as a high pH-sensitive layer for LAPS-based biosensing applications. Sensors Actuators B Chem 71:169–172
7. Werner CF, Wagner T, Yoshinobu T, Keusgen M, Schöning MJ (2013) Frequency behaviour of light-addressable potentiometric sensors. Phys Status Solidi A 210:884–891
8. Nakao M, Yoshinobu T, Iwasaki H (1994) Scanning-laser-beam semiconductor pH-imaging sensor. Sensors Actuators B Chem 20:119–123
9. Wagner T, Werner CF, Miyamoto K, Schöning MJ, Yoshinobu T (2011) A high-density multi-point LAPS set-up using a VCSEL array and FPGA control. Sensors Actuators B Chem 154:124–128
10. Chen L, Zhou Y, Jiang S, Kunze J, Schmuki P, Krause S (2010) High resolution LAPS and SPIM. Electrochem Commun 12:758–760
11. Adami M, Sartore M, Nicolini C (1995) PAB: a newly designed potentiometric alternating biosensor system. Biosens Bioelectron 10:155–167
12. Miyamoto K, Kaneko K, Matsuo A, Wagner T, Kanoh S, Schöning MJ, Yoshinobu T (2012) Miniaturized chemical imaging sensor system using an OLED display panel. Sensors Actuators B Chem 170:82–87
13. Werner CF, Wagner T, Miyamoto K, Yoshinobu T, Schöning MJ (2012) High speed and high resolution chemical imaging based on a new type of OLED-LAPS set-up. Sensors Actuators B Chem 175:118–122
14. Wagner T, Miyamoto K, Werner CF, Schöning MJ, Yoshinobu T (2011) Utilising digital micro-mirror device (DMD) as scanning light source for light-addressable potentiometric sensors (LAPS). Sens Lett 9:812–815
15. Poghossian A, Werner CF, Buniatyan VV, Wagner T, Miamoto K, Yoshinobu T, Schöning MJ (2017) Towards addressability of light-addressable potentiometric sensors: shunting effect of non-illuminated region and cross-talk. Sensors Actuators B Chem 244:1071–1079

16. Bousse L, Mostarshed S, Hafeman D, Sartore M, Adami M, Nicolini C (1994) Investigation of carrier transport through silicon wafers by photocurrent measurements. J Appl Phys 75:4000–4008
17. Yoshinobu T, Ecken H, Poghossian A, Simonis A, Iwasaki H, Lüth H, Schöning MJ (2001) Constant-current-mode LAPS (CLAPS) for the detection of penicillin. Electroanalysis 13:733–736
18. Miyamoto K, Sakakita S, Yoshinobu T (2016) A novel data acquisition method for visualization of large pH changes by chemical imaging sensor. ISIJ Int 56:492–494
19. Miyamoto K, Wagner T, Yoshinobu T, Kanoh S, Schöning MJ (2011) Phase-mode LAPS and its application to chemical imaging. Sensors Actuators B Chem 154:28–32
20. Krause S, Moritz W, Talabani H, Xu M, Sabot A, Ensell G (2006) Scanning photo-induced impedance microscopy – resolution studies and polymer characterization. Electrochim Acta 51:1423–1430
21. Zhou Y, Chen L, Krause S, Chazalviel JN (2007) Scanning photoinduced impedance microscopy using amorphous silicon photodiode structures. Anal Chem 79:6208–6214
22. Zhou Y, Jiang S, Krause S, Chazalviel JN (2007) Biosensor arrays based on the degradation of thin polymer films interrogated by scanning photoinduced impedance microscopy. Anal Chem 79:8974–8978
23. Seki A, Motoya K, Watanabe S, Kubo I (1999) Novel sensors for potassium, calcium and magnesium ions based on a silicon transducer as a light-addressable potentiometric sensor. Anal Chim Acta 382:131–136
24. Wu Y, Wang P, Ye X, Zhang Q, Li R, Yan W, Zheng X (2001) A novel microphysiometer based on MLAPS for drugs screening. Biosens Bioelectron 16:277–286
25. Ermolenko YE, Yoshinobu T, Mourzina Y, Levichev S, Furuichi K, Vlasov YG, Schöning MJ, Iwasaki H (2002) Photocurable membranes for ion-selective light-addressable potentiometric sensor. Sensors Actuators B Chem 85:79–85
26. Mourzina YG, Ermolenko YE, Yoshinobu T, Vlasov YG, Iwasaki H, Schöning MJ (2003) Anion-selective light-addressable potentiometric sensors (LAPS) for the determination of nitrate and sulphate ions. Sensors Actuators B Chem 91:32–38
27. Yoshinobu T, Iwasaki H, Ui Y, Furuichi K, Ermolenko YE, Mourzina Y, Wagner T, Näther N, Schöning MJ (2005) The light-addressable potentiometric sensor for multi-ion sensing and imaging. Methods 37:94–102
28. Ha D, Hu N, Wu CX, Kirsanov D, Legin A, Khaydukova M, Wang P (2012) Novel structured light-addressable potentiometric sensor array based on PVC membrane for determination of heavy metals. Sensors Actuators B Chem 174:59–64
29. Ismail ABM, Furuichi K, Yoshinobu T, Iwasaki H (2002) Light-addressable potentiometric fluoride (F^-) sensor. Sensors Actuators B Chem 86:94–97
30. Kloock JP, Moreno L, Bratov A, Huachupoma S, Xu J, Wagner T, Yoshinobu T, Ermolenko YE, Vlasov YG, Schöning MJ (2006) PLD-prepared cadmium sensors based on chalcogenide glasses–ISFET, LAPS and μISE semiconductor structures. Sensors Actuators B Chem 118:149–155
31. Lue CE, Lai CS, Chen HY, Yang CM (2010) Light addressable potentiometric sensor with fluorine-terminated hafnium oxide layer for sodium detection. Jpn J Appl Phys 49:04DL05
32. Wang JC, Ye YR, Lin YH (2015) Light-addressable potentiometric sensor with nitrogen-incorporated ceramic Sm_2O_3 membrane for chloride ions detection. J Am Ceram Soc 98:443–447
33. Mourzina Y, Yoshinobu T, Schubert J, Lüth H, Iwasaki H, Schöning MJ (2001) Ion-selective light-addressable potentiometric sensor (LAPS) with chalcogenide thin film prepared by pulsed laser deposition. Sensors Actuators B Chem 80:136–140
34. Kloock JP, Mourzina YG, Ermolenko YE, Doll T, Schubert J, Schöning MJ (2004) Inorganic thin-film sensor membranes with PLD-prepared chalcogenide glasses: challenges and implementation. Sensors 4:156–162

35. Men H, Zou SF, Legin A, Wang P (2005) A novel mercury ion selective thin film sensor. Chin J Anal Chem 33:428–431
36. Hu W, Cai H, Fu J, Wang P, Yang G (2008) Line-scanning LAPS array for measurement of heavy metal ions with micro-lens array based on MEMS. Sensors Actuators B Chem 129:397–403
37. Ermolenko YE, Yoshinobu T, Mourzina YG, Vlasov YG, Schöning MJ, Iwasaki H (2004) Laser-scanned silicon transducer (LSST) as a multisensor system. Sensors Actuators B Chem 103:457–462
38. Yang JH, Lu TF, Wang JC, Yang CM, Pijanowska DG, Chin CH, Lue CE, Lai CS (2013) LAPS with nanoscaled and highly polarized HfO_2 by CF_4 plasma for NH_4^+ detection. Sensors Actuators B Chem 180:71–76
39. Seki A, Ikeda S, Kubo I, Karube I (1998) Biosensors based on light-addressable potentiometric sensors for urea, penicillin and glucose. Anal Chim Acta 373:9–13
40. Poghossian A, Yoshinobu T, Simonis A, Ecken H, Lüth H, Schöning MJ (2001) Penicillin detection by means of field-effect based sensors: EnFET, capacitive EIS sensor or LAPS? Sensors Actuators B Chem 78:237–242
41. Jang SW, Lee SY, Yuan H, Kim DE, Kwon DH, Kang SW (2007) High-sensitivity membranes of light addressable potentiometric sensor for penicillin detection. Sens Mater 18:115–124
42. Siqueira JR, Werner CF, Bäcker M, Poghossian A, Zucolotto V, Oliveira ON, Schöning MJ (2009) Layer-by-layer assembly of carbon nanotubes incorporated in light-addressable potentiometric sensors. J Phys Chem C 113:14765–14770
43. Bousse L, Kirk G, Sigal G (1990) Biosensors for detection of enzymes immobilized in microvolume reaction chambers. Sensors Actuators B Chem 1:555–560
44. Paddeu S, Fanigliulo A, Lanzi M, Dubrovsky T, Nicolini C (1995) LB-based PAB immunosystem: activity of an immobilized urease monolayer. Sensors Actuators B Chem 25:876–882
45. Miyamoto K, Yoshida M, Sakai T, Matsuzaka A, Wagner T, Kanoh S, Yoshinobu T, Schöning MJ (2011) Differential setup of light-addressable potentiometric sensor with an enzyme reactor in a flow channel. Jpn J Appl Phys 50:04DL08
46. Mourzina IG, Yoshinobu T, Ermolenko YE, Vlasov YG, Schöning MJ, Iwasaki H (2004) Immobilization of urease and cholinesterase on the surface of semiconductor transducer for the development of light-addressable potentiometric sensors. Microchim Acta 144:41–50
47. Adami M, Piras L, Lanzi M, Fanigliulo A, Vakula S, Nicoli C (1994) Monitoring of enzymatic activity and quantitative measurements of substrates by means of a newly designed silicon-based potentiometric sensor. Sensors Actuators B Chem 18:178–182
48. Werner CF, Takenaga S, Taki H, Sawada K, Schöning MJ (2013) Comparison of label-free ACh-imaging sensors based on CCD and LAPS. Sensors Actuators B Chem 177:745–752
49. Abouzar MH, Poghossian A, Siqueira JR, Oliveira ON, Moritz W, Schöning MJ (2010) Capacitive electrolyte – insulator – semiconductor structures functionalised with a polyelectrolyte/enzyme multilayer: new strategy for enhanced field-effect biosensing. Phys Status Solidi A 207:884–890
50. Sassolas A, Blum LJ, Leca-Bouvier BD (2012) Immobilization strategies to develop enzymatic biosensors. Biotechnol Adv 30:489–511
51. Colston JT, Kumar P, Rael ED, Tsin ATC, Valdes JJ, Chambers JP (1993) Detection of sub-nanogram quantities of Mojave toxin via enzyme immunoassay with light addressable potentiometric detector. Biosens Bioelectron 8:117–121
52. Gehring AG, Patterson DL, Tu SI (1998) Use of a light-addressable potentiometric sensor for the detection of *Escherichia coli* O157:H7. Anal Biochem 258:293–298
53. Dill K, Stanker LH, Young CR (1999) Detection of *salmonella* in poultry using a silicon chip-based biosensor. J Biochem Biophys Methods 41:61–67

54. Lee WE, Thompson HG, Hall JG, Bader DE (2000) Rapid detection and identification of biological and chemical agents by immunoassay, gene probe assay and enzyme inhibition using a silicon-based biosensor. Biosens Bioelectron 14:795–804
55. Hu WG, Thompson HG, Alvi AZ, Nagata LP, Suresh MR, Fulton RE (2004) Development of immunofiltration assay by light addressable potentiometric sensor with genetically biotinylated recombinant antibody for rapid identification of Venezuelan equine encephalitis virus. J Immunol Methods 289:27–35
56. Mosiello L, Laconi C, Del Gallo M, Ercole C, Lepidi A (2003) Development of a monoclonal antibody based potentiometric biosensor for terbuthylazine detection. Sensors Actuators B Chem 95:315–320
57. Liang J, Guan M, Huang G, Qiu H, Chen Z, Li G, Huang Y (2016) Highly sensitive covalently functionalized light-addressable potentiometric sensor for determination of biomarker. Mater Sci Eng C 63:185–191
58. Jia Y, Gao C, Feng D, Wu M, Liu Y, Chen X, Xing K, Feng X (2011) Bio-initiated light addressable potentiometric sensor for unlabeled biodetection and its MEDICI simulation. Analyst 136:4533–4538
59. Ercole C, Gallo MD, Mosiello L, Baccella S, Lepidi A (2003) *Escherichia coli* detection in vegetable food by a potentiometric biosensor. Sensors Actuators B Chem 91:163–168
60. Wu C, Du L, Zou L, Zhao L, Wang P (2012) An ATP sensitive light addressable biosensor for extracellular monitoring of single taste receptor cell. Biomed Microdevices 14:1047–1053
61. Jia Y, Qin M, Zhang H, Niu W, Li X, Wang L, Li X, Bai Y, Cao Y, Feng X (2007) Label-free biosensor: a novel phage-modified light addressable potentiometric sensor system for cancer cell monitoring. Biosens Bioelectron 22:3261–3266
62. Jia YF, Gao CY, He J, Feng DF, Xing KL, Wu M, Liu Y, Cai WS, Feng XZ (2012) Unlabeled multi tumor marker detection system based on bioinitiated light addressable potentiometric sensor. Analyst 137:3806–3813
63. Zong X, Wu C, Wu X, Lu Y, Wang P (2009) A non-labeled DNA biosensor based on light addressable potentiometric sensor modified with TiO_2 thin film. J Zhejiang Univ Sci B 10:860–866
64. Wu C, Bronder TS, Poghossian A, Werner CF, Bäcker M, Schöning MJ (2014) Label-free electrical detection of DNA with a multi-spot LAPS: first step towards light-addressable DNA chips. Phys Status Solidi A 211:1423–1428
65. Poghossian A, Schöning MJ (2014) Label-free sensing of biomolecules with field-effect devices for clinical applications. Electroanalysis 26:1197–1213
66. Bronder TS, Poghossian A, Scheja S, Wu C, Keusgen M, Mewes D, Schöning MJ (2015) DNA immobilization and hybridization detection by the intrinsic molecular charge using capacitive field-effect sensors modified with a charged weak polyelectrolyte layer. ACS Appl Mater Interfaces 7:20068–20075
67. Zhang GJ, Zhang G, Chua JH, Chee RE, Wong EH, Agarwal A, Buddharaju KD, Singh N, Gao Z, Balasubramanian N (2008) DNA sensing by silicon nanowire: charge layer distance dependence. Nano Lett 8:1066–1070
68. Poghossian A, Schöning MJ (2017) Nanomaterial-modified capacitive field-effect biosensors (Chapter 1). In: Springer series on chemical sensors and biosensors (Methods and applications). Springer, Heidelberg (this volume)
69. Wu C, Bronder TS, Poghossian A, Werner CF, Schoning MJ (2015) Label-free detection of DNA using a light-addressable potentiometric sensor modified with a positively charged polyelectrolyte layer. Nanoscale 7:6143–6150
70. Wu C, Poghossian A, Bronder TS, Schöning MJ (2016) Sensing of double-stranded DNA molecules by their intrinsic molecular charge using the light-addressable potentiometric sensor. Sensors Actuators B Chem 229:506–512
71. Evtugyn GA, Hianik T (2011) Layer-by-layer polyelectrolyte assembles involving DNA as a platform for DNA sensors. Curr Anal Chem 7:8–34
72. Yoshinobu T, Miyamoto K, Wagner T, Schöning MJ (2015) Recent developments of chemical imaging sensor systems based on the principle of the light-addressable potentiometric sensor. Sensors Actuators B Chem 207:926–932

73. Yoshinobu T, Miyamoto K, Werner CF, Poghossian A, Wagner T, Schöning MJ (2017) Light-addressable potentiometric sensors for quantitative spatial imaging of chemical species. Annu Rev Anal Chem 10:225–246
74. Inoue S, Nakao M, Yoshinobu T, Iwasaki H (1996) Chemical-imaging sensor using enzyme. Sensors Actuators B Chem 32:23–26
75. Uchida H, Zhang WY, Katsube T (1996) High-speed chemical image sensor with digital LAPS system. Sensors Actuators B Chem 34:446–449
76. Das A, Chen TC, Yang CM, Lai CS (2014) A high-speed, flexible-scanning chemical imaging system using a light-addressable potentiometric sensor integrated with an analog micromirror. Sensors Actuators B Chem 198:225–232
77. Wagner T, Werner CF, Miyamoto K, Schöning MJ, Yoshinobu T (2012) Development and characterisation of a compact light-addressable potentiometric sensor (LAPS) based on the digital light processing (DLP) technology for flexible chemical imaging. Sensors Actuators B Chem 170:34–39
78. Sartore M, Adami M, Nicolini C, Bousse L, Mostarshed S, Hafeman D (1992) Minority-carrier diffusion length effects on light-addressable potentiometric sensor (LAPS) devices. Sens Actuators A 32:431–436
79. Nakao M, Yoshinobu T, Iwasaki H (1994) Improvement of spatial-resolution of a laser-scanning pH-imaging sensor. Jpn J Appl Phys 33:L394–L397
80. Nakao M, Inoue S, Yoshinobu T, Iwasaki H (1996) High-resolution pH imaging sensor for microscopic observation of microorganisms. Sensors Actuators B Chem 34:234–239
81. Parak WJ, Hofmann UG, Gaub HE, Owicki JC (1997) Lateral resolution of light-addressable potentiometric sensors: an experimental and theoretical investigation. Sens Actuators A 63:47–57
82. George M, Parak WJ, Gerhardt I, Moritz W, Kaesen F, Geiger H, Eisele I, Gaub HE (2000) Investigation of the spatial resolution of the light-addressable potentiometric sensor. Sens Actuators A 86:187–196
83. Ito Y (1998) High-spatial resolution LAPS. Sensors Actuators B Chem 52:107–111
84. Moritz W, Gerhardt I, Roden D, Xu M, Krause S (2000) Photocurrent measurements for laterally resolved interface characterization. Fresenius J Anal Chem 367:329–333
85. Moritz W, Yoshinobu T, Finger F, Krause S, Martin-Fernandez M, Schöning MJ (2004) High resolution LAPS using amorphous silicon as the semiconductor material. Sensors Actuators B Chem 103:436–441
86. Guo Y, Seki K, Miyamoto K, Wagner T, Schöning MJ, Yoshinobu T (2014) Novel photoexcitation method for light-addressable potentiometric sensor with higher spatial resolution. Appl Phys Express 7:067301-1–067301-4
87. Werner CF, Miyamoto K, Wagner T, Schöning MJ, Yoshinobu T (2017) Lateral resolution enhancement of pulse-driven light-addressable potentiometric sensor. Sensors Actuators B Chem 248:961–965
88. Zhang Q, Wang P, Parak WJ, George M, Zhang G (2001) A novel design of multi-light LAPS based on digital compensation of frequency domain. Sensors Actuators B Chem 73:152–156
89. Miyamoto K, Itabashi A, Wagner T, Schöning MJ, Yoshinobu T (2014) High-speed chemical imaging inside a microfluidic channel. Sensors Actuators B Chem 194:521–527
90. Miyamoto K, Sakakita S, Wagner T, Schöning MJ, Yoshinobu T (2015) Application of chemical imaging sensor to in-situ pH imaging in the vicinity of a corroding metal surface. Electrochim Acta 183:137–142
91. Kohno Y, Matsuki R, Nomura S, Mitsunari K, Nakao M (2001) Neutralization of acid droplets on plant leaf surfaces. Water Air Soil Pollut 130:977–982
92. Nakao M, Inoue S, Oishi R, Yoshinobu T, Iwasaki H (1995) Observation of microorganism colonies using a scanning-laser-beam pH-sensing microscope. J Ferment Bioeng 79:163–166
93. Stein B, George M, Gaub HE, Behrends JC, Parak WJ (2003) Spatially resolved monitoring of cellular metabolic activity with a semiconductor-based biosensor. Biosens Bioelectron 18:31–41

94. Werner CF, Krumbe C, Schumacher K, Groebel S, Spelthahn H, Stellberg M, Wagner T, Yoshinobu T, Selmer T, Keusgen M, Baumann MEM, Schöning MJ (2011) Determination of the extracellular acidification of *Escherichia coli* by a light-addressable potentiometric sensor. Phys Status Solidi A 208:1340–1344
95. Hiraishi N, Kitasako Y, Nikaido T, Foxton RM, Tagami J, Nomura S (2003) Acidity of conventional luting cements and their diffusion through bovine dentine. Int Endod J 36:622–628
96. Murakami K, Kitasako Y, Burrow MF, Tagami J (2006) In vitro pH analysis of active and arrested dentinal caries in extracted human teeth using a micro pH sensor. Dent Mater J 25:423–429
97. Miyamoto K, Ichimura H, Wagner T, Schöning MJ, Yoshinobu T (2013) Chemical imaging of the concentration profile of ion diffusion in a microfluidic channel. Sensors Actuators B Chem 189:240–245
98. Wang J, Zhou Y, Watkinson M, Gautrot J, Krause S (2015) High-sensitivity light-addressable potentiometric sensors using silicon on sapphire functionalized with self-assembled organic monolayers. Sensors Actuators B Chem 209:230–236
99. Wang J, Wu F, Watkinson M, Zhu J, Krause S (2015) "Click" patterning of self-assembled monolayers on hydrogen-terminated silicon surfaces and their characterization using light-addressable potentiometric sensors. Langmuir 31:9646–9654
100. Wu F, Zhang DW, Wang J, Watkinson M, Krause S (2017) Copper contamination of self-assembled organic monolayer modified silicon surfaces following a 'click' reaction characterized with LAPS and SPIM. Langmuir 33:3170–3777
101. Wang J, Campos I, Wu F, Zhu J, Sukhorukov GB, Palma M, Watkinson M, Krause S (2016) The effect of gold nanoparticles on the impedance of microcapsules visualized by scanning photo-induced impedance microscopy. Electrochim Acta 208:39–46
102. Zhang DW, Wu F, Wang J, Watkinson M, Krause S (2016) Image detection of yeast *Saccharomyces cerevisiae* by light-addressable potentiometric sensors (LAPS). Electrochem Commun 72:41–45

Biosensorial Application of Impedance Spectroscopy with Focus on DNA Detection

M. Riedel and F. Lisdat

Abstract The chapter introduces the use of impedance spectroscopy for biosensing. It gives an overview on biocatalytic and bioaffinity-based systems. Special attention is devoted to the detection of DNA and DNA-binding molecules.

Keywords Antibodies, DNA, Enzymes, Hybridization, Impedance spectroscopy, Label-free, Sensor

Contents

1 Impedance Spectroscopy and Biosensors

In bioanalysis impedance spectroscopy is applied to monitor both the different fabrication steps of sensing surfaces and the biosensorial recognition process itself. Applications have been demonstrated for all types of (bio)analytes such as proteins,

M. Riedel and F. Lisdat (✉)
Biosystems Technology, Institute of Applied Life Sciences, Technical University of Applied Sciences Wildau, Wildau, Germany
e-mail: flisdat@th-wildau.de

M. J. Schöning, A. Poghossian (eds.), *Label-Free Biosensing: Advanced Materials, Devices and Applications*, Springer Series on Chemical Sensors and Biosensors (2018) 16: 133–178
DOI 10.1007/5346_2017_18, © Springer International Publishing AG 2017,
Published online: 1 November 2017

nucleic acids, metabolites, whole cells, microorganisms, antibodies and antigens. The focus of the chapter is directed to general concepts and applications for the sensorial analysis of DNA and DNA-binding molecules.

The various efforts for specific and sensitive detection can either be classified according to the electrode material (e.g. metals, metal oxides, glassy carbon, semiconductors), the electrode geometry (e.g. conventional electrode arrangement or "in-plane" measurement), the electrode modification (e.g. polyelectrolytes, conductive polymer films, carbon nanotubes, nanoparticles), the analyte (e.g. proteins, antibodies, nucleic acids) or the amplification protocol used (e.g. enzyme labels, dendrimers, nanoparticles). Numerous approaches in literature apply these main elements in various combinations. In the first section of this chapter, general concepts for analyte detection by the use of impedance spectroscopy as well as strategies enhancing the sensitivity will be discussed. In the second section of this chapter, impedimetric DNA analysis and the detection of binding events to DNA will be explained on the basis of a developed sensorial concept more in detail.

1.1 General Principles Used in Impedimetric Analyte Detection

Impedimetric biosensors follow the idea that the impedance of a working electrode should determine the overall impedance of an electrochemical cell. Thus, after modification with the recognition element, this electrode is turned into the sensing electrode. In Fig. 1a a schematic structure of such an impedimetric sensor concept is depicted. Different options exist to evaluate the recognition event at the sensor surface; the overall impedance can be detected classically by measuring the whole frequency range or selected frequencies; it can also be analysed in potential jump experiments by following the time course of the current behaviour as well as by changes in electrode capacitance or resistance directly.

1.1.1 Capacitance and Resistance Measurements

When a sensor electrode is immersed in an aqueous solution, an electrochemical double layer is formed (Fig. 1b). The capacitance, C_{dl}, depends on all compounds present at the interface, which are predominantly solvent molecules, ions, immobilized linker or biomolecules. If an additional film is deposited for immobilization or to promote the detection process, then a parallel circuit of the capacitance of this membrane (C_M) and the membrane resistance (R_M) can appear in series to the impedance of the working electrode. A change in capacitance of the WE is induced when the dielectric constant or the thickness of the "condensator" on the transducer surface changes. Both aspects have been a matter of investigation [1, 2]. For the construction of a capacitive biosensor, the electrode surface is usually

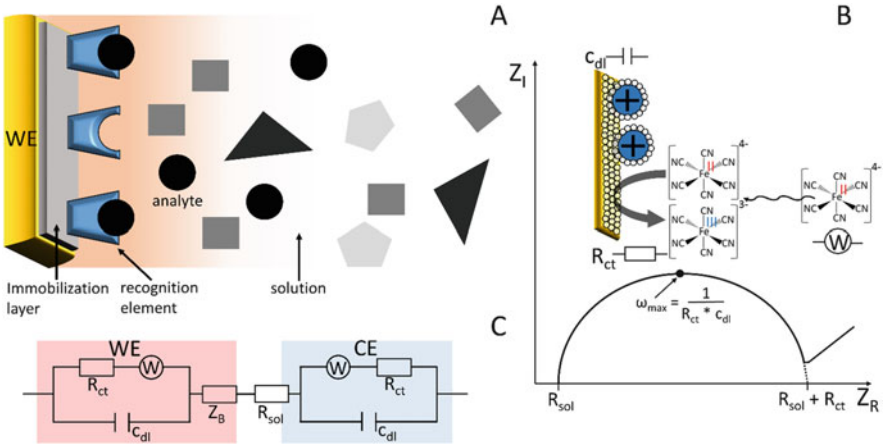

Fig. 1 (**a**) Schematic structure of an impedimetric biosensor. It consists of the transducing electrode (WE), an immobilization layer and the recognition element. (**b**) Nyquist plot of an electrode in electrolyte contact (Z_I imaginary impedance, Z_R real impedance, ω angular frequency). The solution resistance (R_{sol}) is determined by the ion concentration and the cell geometry. The double-layer capacitance (C_{dl}) is given by the charge stored in the double layer at the interface. The charge transfer resistance (R_{ct}) originates from redox reactions at the electrode, and the Warburg impedance (W) results from the current limitation by diffusion of the redox species to the interface. (**c**) Equivalent circuit of a whole electrochemical cell with Z_B as the impedance of the biological material. In a sensor arrangement, it is immobilized on top of the working electrode. Z_B can appear as separate impedance element, but mostly the biological component changes R_{ct} and C_{dl} of the basic electrode. The working electrode (WE) is intended to be the overall impedance-determining element. This is often accomplished by using a much larger counter electrode (CE), and sufficiently high ion concentrations in solution

covered by an additional insulating layer to reduce faradaic currents (i.e. to increase the charge transfer resistance R_{ct} in parallel to the capacitance). The bio-recognition element is usually immobilized on top of this layer.

Capacitance measurements in the absence of faradaic currents also allow to analyse the influence of the electrical field on the biological recognition event by applying different DC working potentials [3]. The interaction between the recognition element and the analyte as well as their orientation might be influenced by the applied DC potential, particularly if charged components interact with each other.

An alternative approach for the impedimetric detection of a recognition event is the determination of the charge transfer resistance, R_{ct}, at the sensing electrode. This approach has been followed intensively in the literature. Faradaic impedance measurements are usually performed in the presence of a redox couple in solution and rely on the changing barrier for the redox conversion by a (bio)catalytic process or the formation of a recognition complex or a subsequent complex. The impedance spectra are often recorded for DC potentials equal to the open circuit potential (OCP) of the employed redox couple. Although used quite often, the presence of a redox couple is not absolutely necessary. The measurement in an inert electrolyte solution results usually in a much higher impedance, but as long as the impedance

changes upon the bio-recognition process are reproducible, also this kind of measurement can result in reliable data. Particularly interesting is this approach when the conductivity of the recognition layer is changed by the specific binding event (reported, e.g. with proteins embedded in a lipid layer) [4, 5].

1.1.2 Sensor and Sensor Preparation

Typical transducer elements are carbon and metal electrodes. Preferentially, gold is chosen, because it allows the application of the thiol chemistry for immobilization [6, 7]. Besides this, thin oxide layers, like indium tin oxide (ITO), fluorine doped tin oxide (FTO) or platinum/platinum hydroxide electrodes, provide hydroxyl groups for silanization chemistry [8]. Metal oxides of platinum [9], tantalum [10] and titanium [11] have also been used for capacitance-based detection. More recently, graphene [12–14] and graphene oxide [15] or nanocrystalline diamond have found applications [16].

Various surface modification strategies have been employed for the immobilization of the biomolecule used as recognition element. Particularly, self-assembled monolayers (SAMs) are frequently applied. Such films are formed spontaneously by chemisorption and self-organization from solution [7, 17]. Long-chain thiols can effectively block the electrode surface from unwanted reactions and, thus, are often applied in capacitive sensors. Since the SAM film itself does not have specific recognition properties, the bio-compound is normally coupled to the surface with functionalized SAMs [18, 19]. Alternatively, the SAM layer has to be structured in order to create recognition sites. This can be termed as a kind of surface imprinting [20, 21]. Another method to obtain well-ordered recognition layers is the transfer of a lipid bilayer (from liposomes) or a Langmuir-Blodgett (LB) film onto the electrode surface [22, 23]. For larger proteins these lipid films have to be tethered in order to create space between the electrode and the lipid film [24, 25]. Other immobilization protocols rely on the preparation of thin polymer films, electropolymers or bioaffinity layers (e.g. avidin films capable for binding biotinylated biomolecules). Polyelectrolyte films have also been introduced for biomolecule immobilization. This technique is based on the layer-by-layer adsorption of oppositely charged polymers on the transducer surface and is particularly suited for the preparation of multilayers [26, 27].

Semiconductor-based structures are a special field in impedance-related sensors. These are mainly semiconductor/insulator/electrolyte structures, which detect chemical changes at the insulator surface in contact with the solution by analysing the space charge region in the semiconductor. The classical ion-sensitive field-effect transistor (ISFET), which can be combined with enzymes or antibodies yielding enzyme FETs (ENFETs) or immuno-FETs (IMFETs), will not be the focus of this chapter. Although this device has an inherent impedance conversion from the high impedance line between the semiconductor bulk and the gate to the low impedance line between source and drain, the output is a simple source-drain

current, and thus the device does not follow the general idea of impedance measurements discussed here.

In contrast to the transduction process itself, impedance measurements have found increasing application in optimizing biosensors, mainly by following the different steps of surface modification during sensor preparation. This includes the formation of SAMs and LB films, the adsorption of molecules or polymers and also the binding of the recognition element to the transducer surface [28, 29]. Impedance measurements can thus be seen as an efficient quality control method in the sensor fabrication process.

1.1.3 Impedimetric Enzyme- and Cell-Based Sensors

In the field of enzyme-based sensors, amperometric electrodes are by far the most attractive transducers. However, the change in redox conversion of a redox-active compound by the turnover of an enzyme (in the presence of substrate) can also be analysed by following the R_{ct}. For example, this has been demonstrated for glucose detection using glucose oxidase and parabenzoquinone [28] or Prussian blue [30] as mediator (in the latter case probably for the hydrogen peroxide which is liberated during glucose oxidation). Alternatively, a conductive polymer such as polyaniline can be used as immobilization platform for several dehydrogenases and at the same time as "molecular wire", establishing communication between the enzyme and the electrode. Consequently, substrate conversion at the enzyme will result in changes in R_{ct} of the polymer-covered sensing electrode [31]. From the concept very attractive, this type of sensor construction needs, however, more studies for reliable signal generation. The process of electron transfer between enzymes and conducting polymers is not completely understood, but several functional systems have already been reported [32, 33].

Another direction of research exploits sequential enzyme reactions, terminated by a peroxidase reaction as the signalling reaction. Here, the production of hydrogen peroxide by a first enzyme is indicated by the formation of a precipitate on the electrode due to the action of peroxidase in the presence of a suitable second substrate. This finally leads to an increase in electrode impedance [34].

Another approach of using impedance for sensing can be seen in the incorporation of a "signalling" protein in a lipid layer and evaluating the conformational change upon interaction with a specific analyte. Often, this is accompanied by alterations in ion mobility through the surface-confined film; consequently, conductivity changes can be analysed. One example of sensing substrates and inhibitors has been given in [35]. The authors used peptide-tethered lipid membranes on a gold support in combination with cytochrome c oxidase. In this case, electrochemical impedance spectroscopy (EIS) was used to study proton transport across the membrane. The resulting impedance spectra could be correlated to the inhibitor and substrate concentration of the enzyme. Other examples are the detection of paraoxon [36], quinacrine [37] or the bacterial toxin streptolysin [38].

In bioanalysis not only substrates and inhibitors are determined, but also the enzyme activity itself has to be analysed. In this direction, an interesting approach has been introduced by using degradable polymer films (see Fig. 2). These polymers can be coated onto an electrode; their degradation by a biocatalytic reaction can occur directly by the enzyme acting on the polymer chains or by products of the enzymatic conversion. The diminished film thickness is easily followed by impedance measurements. This has been demonstrated for enzymes such as chymotrypsin, lipase [39] and collagenase [40].

This sensing concept can also be used for the detection of several enzyme substrates such as urea [41–43], glucose [44] and creatinine [43]. Here, the electrode is covered with a hydrolyzable polymer, and the enzymatic analyte conversion changes the pH near the surface which facilitates the polymer degradation. The process can easily be analysed by detecting the capacitance of the electrode. Not only the pH can be applied as trigger but also hydrogen peroxide generated by several oxidases [44]. The approach can also be combined with immunoassays using enzymes as labels [45].

Another direction of developments is cell-based assays for the detection of specific analytes or for the screening of large substance libraries for their biological effect. This relies on the concept of effect monitoring. Here, parameters are needed that report the response of a whole biological system with respect to the stimulus under investigation. Impedance is one of the suitable parameters, because it can be used for the indirect detection of metabolic activity, cell adhesion on surfaces or response to potential drugs and for cytotoxicity tests [46, 47]. Examples have been reported analysing the status of a cell culture [48, 49]. Figure 3 illustrates a typical experimental setup for cell-based measurements and a simplified equivalent circuit, describing the impedance of a cell layer as a parallel circuit of intracellular and extracellular pathways. It has to be mentioned that cells can also be cultivated directly on top of the working electrode with an appropriate surface modification.

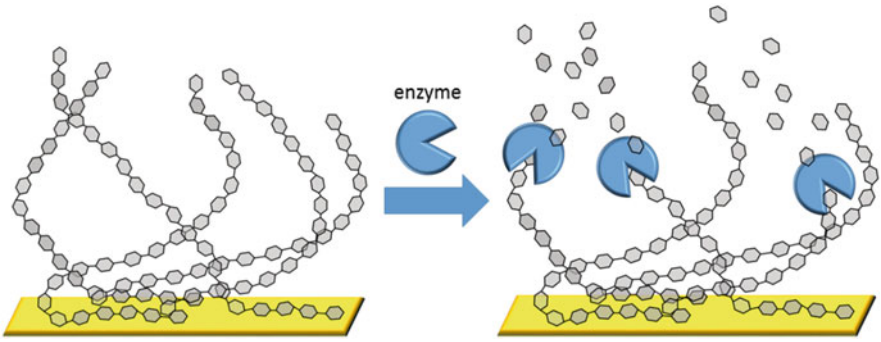

Fig. 2 Schematic illustration of the biocatalytic decomposition of immobilized polymer chains by enzymes such as chymotrypsin, lipase or collagenase. This principle enables the determination of the enzymatic activity, since the changing surface properties can be recorded via impedance

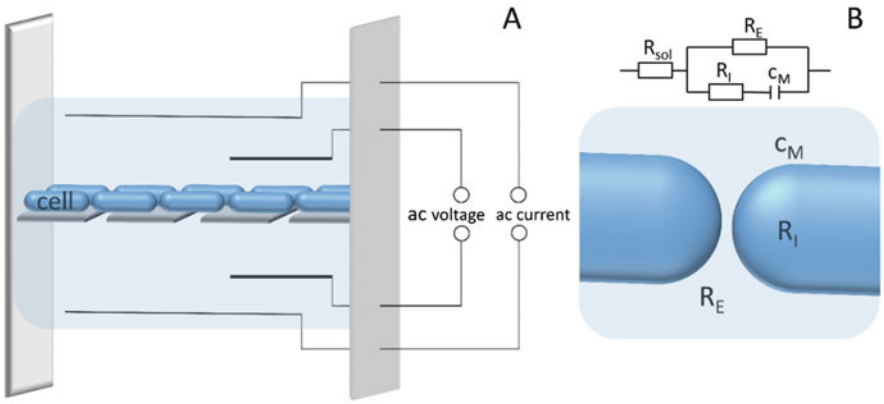

Fig. 3 (**a**) Schematic representation of the experimental setup of an impedimetric cell-based assay in a four-electrode arrangement. (**b**) Simplified equivalent circuit for the analysis of such cell layers, consisting of a solution resistance (R_{sol}), the resistance for the internal (R_I) and external charge carrier transport (R_E) and the cell membrane capacitance c_M

Impedance is not only suited to give information on the status of surface-fixed cells but can also be used to count the number of cells in a solution. This has been intensively investigated in microbiology and was further used for the detection, quantification and identification of bacteria [50]. Different capture molecules have been used such as antibodies [51–55], carbohydrate structures [56] or phages [57]. The sensitivity varies among the reports but is in the interesting range from 10^3 colony-forming units (CFU)/ml to 10^6 CFU/ml. Developments have resulted in micro-machined devices for cell counting or cell differentiation [51, 58]. The potential for virus detection has also been elucidated [59, 60].

1.1.4 Impedimetric Immunosensing

Impedimetric analyte detection is frequently applied for immunosensing. This originates from the fact that classical immunoassays are widespread and often used in clinical diagnostics, food quality control and environmental analysis and for the detection of pathogens, toxins and explosives or drugs. Although immunosensing is an established technique, driving forces for sensorial developments via an impedimetric detection scheme are coming from the demands of on-site detection (i.e. point-of-care diagnostics) with the need of rather simple equipment and the potential for label-free analysis.

In immune sensing the sensor chip can either be modified with an antibody or the antigen itself is immobilized, which in turn binds then the complementary antibody. In both cases the binding event results in a change of the electrical surface properties, although in the latter case, larger changes can be expected because of the high molecular weight and the low dielectric constant of the antibodies.

Initially, capacitive sensors have been preferably used for the detection of immune reactions [7, 61]. Charge transfer can be diminished, e.g. by long-chain SAM layers. In combination with a potential jump method, very sensitive measurements have been reported [62]. Here, the impedance is not detected by applying different frequencies during the measurement, but in the time domain by following the current response to a jump in potential. This simplifies the measurement and accelerates the speed, but needs a transfer into the frequency domain for reliable data interpretation [63, 64]. In order to reduce the influence of nonspecific binding events, which would influence the capacitance in a similar way compared to the specific interaction, a differential mode of measurement has been proposed [9]. Alternatively, antibodies can be incorporated into LB films while retaining their binding properties [22, 65].

Resistance-based sensors have also been developed [66–70]. For example, the human mammary tumour-associated glycoprotein has been detected with specific antibodies immobilized on gold by spontaneous adsorption. The binding of the complementary antigen resulted in a change of R_{ct} [66]. Sensitivity can be enhanced by secondary reactions as shown, for example, with enzyme labels, resulting in a precipitation on the electrode [71, 72] or second binding complexes [68, 71]. Alternatively, the specific electrode area can be enhanced by micro- or nanostructuring [70, 73]. Another system used ultrathin platinum layers and evaluated the conductivity changes based on an impedance model analysis [67]. But also the change in ion conductivity of a lipid bilayer with incorporated ion channels can be used for detecting the antibody-antigen binding event [74, 75].

A special approach for immobilization can be seen in the use of conducting polymers such as polypyrrole. This can help to amplify the response since the conductivity of the polymeric network is strongly influenced by conformational changes induced by binding events [76–78]. Biotinylated polypyrrole films were used for the immobilization of antibodies via avidin [79]. Antigen binding was connected to an increase in R_{ct}. The detection limit for human IgG was 10 pg mL^{-1}.

Molecular imprinted polymers (MIPs) are a rather new group within the recognition elements. They provide a surface which acts as a "negative" of the analyte and thus can recognize it within a mixture. Although the quality of "complementarity" of the binding cavities does not reach the level of antibodies, MIPs have some advantages. Because of their chemical nature, they can be reproducibly fabricated in different formats, and they provide a rather good long-term stability in different environments. Besides their usage in chromatographic separation concepts, further interesting examples have been reported for applications in sensors. For a sensorial transduction of the binding event, particularly thin surface films are suited. Here, significant progress has been made in surface-imprinting techniques during the last decade [80, 81]. In addition to voltammetric detection techniques, also impedance-based sensing concepts have been reported. Capacitive sensors have been developed for organic molecules [20, 82] but also for whole cells and viruses [83]. For the detection of low-molecular-weight compounds such as L-nicotine [84] or amino acids [85], the resistance has been evaluated. The creation of artificial binding pockets for the recognition of proteins is still not a routine

procedure, but significantly achievements can be seen presently. Thus, also first examples for protein sensing have been demonstrated [86, 87], and even for larger biological particles, the MIP techniques seem to be feasible [88].

1.1.5 Impedimetric Nucleic Acid Sensing

Besides immunosensing, the impedimetric detection of nucleic acids has been a matter of research for many years. Mainly two different basic approaches have been exploited to enable a reliable identification of a specific DNA sequence. On the one hand, much work has been dedicated to the realization and improvement of new sequencing techniques for a base-per-base read-out of DNA. On the other hand, various methods have been designed, which rely on the detection of specific hybridization events between two complementary strands and trigger the transduction to an analytical signal. Therefore, single-stranded DNA (ssDNA) is immobilized onto an electrode and acts as a recognition element (probe ssDNA) for the binding of complementary ssDNA (target DNA). If target DNA is available in the sample, the strong interaction between the probe and the target results in a hybridization event between both strands, forming a double strand. This elementary principle has been combined with various transduction techniques, which exploit, e.g. the mass accumulation (piezoelectric) [89, 90], changes in the optical density [91, 92], the detection of an optically active label [93, 94] or electrochemical changes [95–97]. The latter transduction principle represents a promising approach, since it enables a simple, cheap and portable operation for the utilization in future point-of-care (POC) diagnostics. Furthermore, this field of research benefits from the continuous progress in the miniaturization of electronic components, which offer the possibility for a parallel detection of different analytes in a small device format.

Most electrochemical approaches rely on the utilization of redox molecules for the read-out of hybridization events. Therefore, one approach is to couple a redox label covalently to the target strand, followed by its detection via voltammetric measurements [95, 98, 99]. This provides a high sensitivity but has the drawbacks of time-consuming and expensive overall procedure and sensor preparation as well as a possible negative influence of the label on the hybridization efficiency. A further improvement of applicability has been achieved by using indirect labelling assays. In this case, a labelled reporter probe can bind to the target overhang of the hybridized probe-target complex. While this principle avoids a pretreatment of the target and results in a higher selectivity, an extension of the analysis time due to the second hybridization step is less beneficial for POC applications.

Currently, the electrochemical detection of hybridization events in the absence of any label is often based on the direct oxidation of the bases [100, 101], which requires high working potentials, or by recording the changes of the electrochemical properties of the electrode surface [96]. For the latter, ssDNA and double-stranded DNA (dsDNA) have been discriminated using a hanging mercury drop electrode [102, 103]. Desorption of denaturated ssDNA was accompanied by a

larger dielectric loss than desorption of native dsDNA. This was explained with the higher flexibility of the ssDNA compared to the rigid dsDNA double strand.

For a sensorial application, more interesting are investigations on gold electrodes. Here, immobilization is often accomplished via thiol chemistry by additionally applying a short thiol as blocking agent reducing nonspecific adsorption of DNA to the surface. The protocols seem to work reproducibly in the different groups; however, the procedure is rather time-consuming. Reduction of the preparation time can be achieved by applying electric fields during the deposition process of the charged DNA molecules [104, 105]. Although gold is very often used, there are also reports on other types of electrodes. Several carbon surfaces have been used such as carbon nanotubes [106, 107], nanoporous carbon [108], boron-doped diamond [109] or graphene [13, 14]. From the application point of view, it is interesting that first studies on screen-printed electrodes demonstrate the applicability of impedance measurements also for such electrode surfaces which are less defined compared to pure electrode materials [110, 111].

The hybridization event is well suited for an impedimetric detection particularly since the molecular structure is changing from a rather flexible single strand to a rather rigid double strand of defined geometry. Furthermore, the charge situation is drastically changed since every DNA molecule binding to the surface increases the negative charge according to the number of nucleotides it consists of. This provides the basis for an impedimetric detection of such surface alterations by analysing the capacitance or – more commonly – resistance changes of the sensing electrode. In the latter case, often a strongly charged redox species such as ferri-/ferrocyanide has been applied. Consequently, EIS can be used for the detection of the presence of a particular DNA sequence, different oligonucleotide concentrations, and also single base pair mismatches in a defined sequence [112, 113]. During these studies it has been found, that the position of the mismatch has an influence on the impedimetric signal strength. In conclusion, it is not only the lowered affinity which contributes, but also secondary structural effects [112, 113] (see Sect. 2 of this chapter).

Besides the surface concentration of the capture probe, the length of the capture probe and also the influence of the buffer concentration have been investigated [114–116]. These studies clearly demonstrate the importance to control all preparation steps in order to get reliable sensing electrodes. As long as the hybridization efficiency is not influenced, the impedimetric signal change will increase with a higher surface density of the capture probe. Another aspect is the verification of stable impedance signals, which are not influenced by the measuring conditions (linearity of response) [117]. Only by analysing the reproducibility of impedance data, reliable conclusions on analyte-induced impedance changes can be drawn. Since impedance spectroscopy is a label-free method, nonspecific binding is a severe problem and needs to be investigated in the medium intended for the determination of a specific analyte. Often, it is beneficial to prepare a reference surface and take only the difference of measuring signals at the sensing and reference surface as analytical parameter.

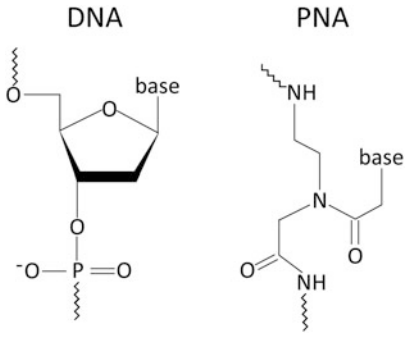

Fig. 4 Chemical structure of DNA and PNA, illustrating the different backbones for the linkage of the bases

As a modification of this approach, the use of peptide nucleic acid (PNA) can be seen (Fig. 4). When this uncharged molecule is applied as capture probe, the relative change in charge density becomes larger when DNA binds to the surface. Consequently, in most cases a charged redox couple has been applied, and R_{ct} is used as sensing parameter. Furthermore, there is also potential for higher hybridization efficiencies since no electrostatic repulsion has to be overcome during the hybridization of DNA to the PNA-modified surface. Impedance spectroscopy is not only helpful to discriminate between full- and mismatch DNA [118] but also for studying the influence of the ionic strength [119, 120] or analysing the binding kinetics [121]. However, also a capacitive approach can be used based on PNA [122].

In most studies the length of capture probe is equal to the target DNA. However, for practical applications often an amplification of DNA or a transcription from an RNA pool is necessary. Here, much longer strands appear, which have to be denatured prior to analysis. Some studies have been dealing with the influence of the target length on the impedimetric signal. Here, different effects have to be considered: (a) the decreasing hybridization efficiency with increasing length, (b) the increasing charge with increasing length and (c) the raising distance between the electrode surface and a part of the DNA charges with increasing DNA length. Although some first studies on this subject have been reported (see also Sect. 2 of this chapter), more research is necessary to evaluate the interplay between the conditions (capture probe density, buffer concentration, position of the complementary sequence within the target) and the target length comprehensively [123–125].

Examples showing the potential for detecting full PCR products have been demonstrated [126]. As a further advancement the real-time detection of a PCR amplification process is feasible [127]. Finally, it is possible to develop first analytical systems, which can avoid a PCR before the impedimetric detection by extracting RNA or DNA directly from bacterial samples [128, 129].

Another variation can be seen in the design of the capture probe. Usually, ssDNA is fixed with one end to the sensor surface; however, also a hairpin structure can be successfully applied. This has been extensively used in voltammetric DNA analysis since by the conformational change of the hairpin probe after

hybridization, the localization of a redox label can be changed significantly allowing a clear signal discrimination [116, 130]. Subsequently, this has also been applied to the impedimetric detection but without the necessity of a label attachment [13, 108].

In analogy to the immune detection using conducting polymers, also probe DNA can be linked to conducting polymer films to evaluate the change in interfacial properties after target DNA binding. Here, an increase in resistance was observed which could be used for sensorial detection of suitable sensitivity [77, 131–133]. As an alternative to polypyrrole [131], polyaniline [109], polythiophene [134] or a quinone-containing polymer can be used [135].

The impedance technique cannot solely be applied for the detection of nucleic acids, but also for the analysis of DNA-analyte interactions. Several small organic molecules, but also large proteins show a specific interaction with DNA duplexes. For small molecules different binding modes such as groove binding [114, 136] or intercalation [112, 114, 137, 138] can be exploited. Examples for the latter are Bengal rose, methylene blue, proflavine, nogalamycin, etc. The lower binding affinity of intercalators to ssDNA compared to dsDNA can also help in the detection process of hybridization events [139]. However, often the binding properties of these small molecules are used for the analytical determination of these substances. Examples are cisplatin [140], mithramycin [136] and bleomycin [110] – compounds which are applied as anticancer drugs.

A special group of analytes are metal ions. Here, it has been found that metal ions exhibit different interactions with DNA duplexes but also PNA-DNA hybrids. Particularly, Ni^{2+} ions seem to have rather strong interaction with dsDNA, which can be used even for mismatch discrimination [141, 142]. Furthermore, it has been found that Pb^{2+} can interact with G-quadruplex-forming sequences [143], Ag^{+} interacts with C-C mismatches [143, 144] and Hg^{2+} with T-T mismatches [143]. Metalation of DNA results in different conformational changes compared to normal B-DNA (predominant dsDNA conformation under physiological conditions). This has also been exploited for the discrimination of different mismatches [145]. DNAzymes as nucleic acid-based biocatalysts can show a rather strong specificity for a particular metal ion. This is used for metal ion detection (e.g. Pb^{2+} or Cu^{2+} [146, 147]) exploiting the impedance change by the action of the DNAzyme towards a target strand.

Furthermore, the interaction of proteins with DNA strands can be detected in a label-free format. Here, the focus is, on the one side, on enzymes such as telomerase [148], kinases [149] or restriction enzymes [115, 150, 151] and, on the other side, on specific binding proteins such as antibodies [114], receptors [151] or transcription factors [115].

Another field of research uses specific, three-dimensional DNA structures – so-called aptamers – which can exhibit a selective interaction with a binding partner, thus following the example of antibody-antigen interaction [152, 153]. Aptamers have seen a tremendous development in the last decade because of the less sophisticated generation by a selection process compared to antibodies [154] and the rather small size. Although the binding behaviour is strongly related to the

selection conditions, several examples with sufficient analytical performance have been demonstrated – although often an amplification strategy is necessary (see Sect. 1.2). Also in this area, the systems relying on the detection of R_{ct} are the dominating ones. Bogomolova et al. have studied the influence of several experimental parameters on the detection possibilities clearly demonstrating pitfalls in the measurements when not sufficient stability can be provided on the surface [117]. Particularly, the increase in R_{ct} with only buffer incubations or high ferri-/ferrocyanide concentrations is rather often ignored during sensor developments. White et al. showed the importance of optimizing the surface chemistry for aptamer fixation in order to ensure a high sensing performance [155]. Applications of impedimetric aptasensing have been shown for small molecules such as cocaine [156], ochratoxin A [157], progesterone [158], tobramycin [159], neomycin B [160] and proteins such as thrombin [12, 161, 162], lysozyme [15], cytochrome c [163] and others [106, 164, 165] but also for more complex biological particles such as viruses [166] and bacteria [167]. In addition, a capacitance-based approach has also been reported for IgE detection [16].

1.2 Amplification Strategies to Enhance the Signal of Impedimetric Analysis

Despite the potential for a direct binding detection, many interfacial impedimetric assays suffer from the fact that the generated signals (changes in resistance, capacitance or overall impedance) are relatively small. This problem is intensified if small amounts of the analyte need to be detected. This has led to the development of several amplification strategies. They can be classified according to the basic principle used:

1. Embedment of the recognition element in a polymeric or lipid layer
2. Sandwich type of analysis with a labelled second binding partner:
   (a) Label such as liposomes, nanoparticles and dendrimers can be used, which can change the impedance at the surface significantly.
   (b) Label such as enzymes or nucleic acid structures with intercalated metal complexes possessing catalytic functions are applied, both leading to precipitations on the sensor surface during the conversion of substrate molecules.
3. Hybridization chain reaction on the sensing surface
4. Enlargement of the electrode surface by micro- and nanostructuring (and thus enhancement of the amount of recognition elements per geometrical area)
5. Application of interdigitated electrodes with small distances between the electrodes
6. Application of nanoelectrodes

In order to increase the capacitance change due to an altered dielectric constant, polymeric membranes were used for fixation of the recognition element. Indeed, the incorporation of antibodies into a membrane induces a change of C_{dl}. As an example Maupas et al. have modified platinum electrodes with different polymeric layers and used them in a flow-injection system for real-time immune detection [9]. Receptor-ligand binding is often accompanied by structural changes of the complex. This can be used for a sensitive ligand detection, particularly when a receptor is chosen, which is a chemically gated transport protein, e.g. the nicotinic acetylcholine receptor. Incorporated in a lipid membrane, acetylcholine, but also the receptor antagonists, can be measured by capacitance changes [168].

As mentioned above a conducting polymer layer can be nicely applied for an enhanced signal generation. Here, the changes in polymer conformations are exploited, and analysis is mostly focused on resistance changes [76] (see Fig. 5b).

A very simple amplification route has been introduced by the Willner group [169, 170]. In this case the binding of negatively charged liposomes to the recognition surface can drastically alter the charge transfer of a redox couple, particularly when it possesses the same charge, e.g. ferri-/ferrocyanide. Figure 5a illustrates the general assay procedure. In the scheme, the DNA hybridization is followed by one or several secondary binding steps resulting in an accumulation of highly charged nanostructures on the electrode. As an alternative to liposomes, also dendrimers can be used [171]. Furthermore, gold nanoparticles can be easily prepared and surface – modified in a well-defined way. Applied in a sandwich assay for nucleic acid detection, they can increase R_{ct} significantly. Binding can be realized via biotin-streptavidin [172] or via hybridization [173, 174]. The nanoparticles can further be used as template for additional gold or silver deposition, which can maximize the changes on the sensing surface but also prevent a reusable application [175, 176]. As a variation of this approach, also quantum dots and composites can be applied as label in the second binding reaction [177]. Composites can consist, for example, of gold nanoparticles (Au-NP) with carbon nanotubes (CNTs) or Au-NP with reduced graphene oxide flakes [178, 179].

Another principle could be demonstrated, which is mainly based on the binding of gold nanoparticles (positively charged) to DNA and enables the discrimination between ssDNA and dsDNA [180, 181]. The preferred binding of the Au-NPs to ssDNA is diminished after hybridization and dsDNA formation and can thus be used for the label-free DNA detection.

A smart amplification approach has been taken over from classical immunoassays and is based on the application of an enzyme label bound to a component of the sensing system. The enzyme label may catalyse the formation of a gas in front of the electrode (e.g. catalase decomposes hydrogen peroxide to oxygen) [182], but mainly it catalyses the formation of an insoluble product, which precipitates onto the electrode surface and amplifies consequently the changes of R_{ct} and C_{dl} [183–186]. This concept is schematically illustrated in Fig. 5c. The principle was introduced for the detection of DNA [183] and antibodies against dinitrophenyl at an electrode functionalized with the SAM technique [184] and has found considerable attention in the scientific community. As enzymes, mainly horseradish

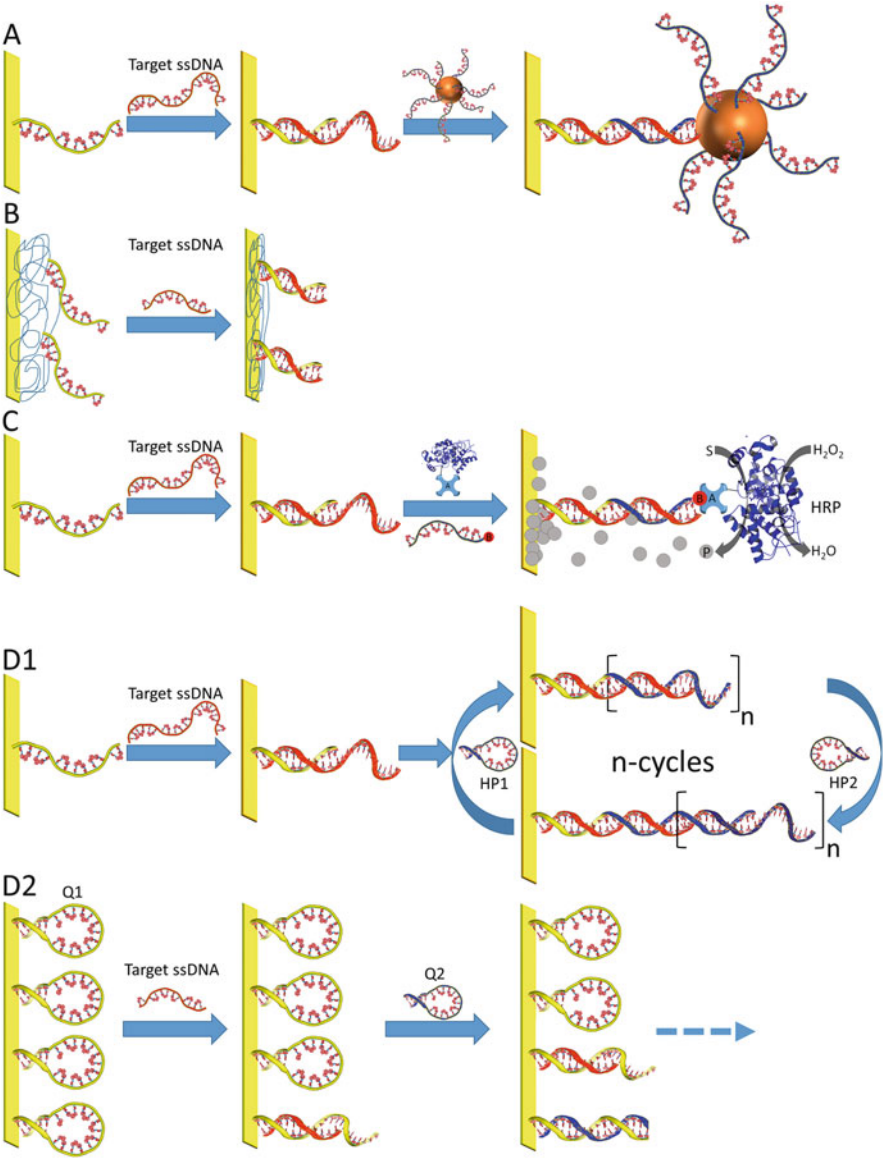

Fig. 5 Amplification strategies for the impedimetric DNA detection – part I. Probe DNA, target DNA and secondary probes are illustrated in yellow, orange and blue, respectively. (**a**) Probe DNA-modified electrode before and after hybridization with target DNA and subsequent binding of DNA-modified gold nanoparticle at the overhang of the probe-target complex. The target DNA possesses one recognition sequence for the immobilized probe and another for the probe attached to the nanoparticle. The impedimetric signal is enhanced due to the increased mass and negative charge upon nanoparticle binding. Alternatively to nanoparticles also liposomes or dendrimers can be applied. (**b**) Immobilization of probe DNA on a layer of a conducting polymer. Target binding results in structural changes, which lead to alterations in the electrochemical polymer properties

peroxidase (HRP) and alkaline phosphatase have been used. As an alternative, the catalytic activity of metal complexes intercalated into dsDNA or G-quadruplexes can be exploited [187]. Application has been shown for the detection of single nucleotide polymorphism [188], PCR products [189], autoantibodies [72], bacteria [51] and others. The liposome-based sandwich assay can also be combined with the enzymatic precipitation strategy. For example, amplified DNA detection was achieved using liposomes with multiple HRP tags, which resulted in an amplification factor of approximately 10^5 [185].

The precipitation-based amplification technique enables the detection of very low surface concentrations of the formed binding complexes and thus, low concentrations of binding partners in solution. However, a regeneration of the sensor surface is difficult, if not almost impossible, and impedes a repeated usage of the sensor clearly limiting the applicability of this sensing concept. As an alternative one can see the application of an enzyme such as exonuclease III, which can act from the 3′end of dsDNA. By using a hairpin-type capture probe, the target DNA can consequently be recycled after a first binding event leading to a binding to another hairpin capture probe and subsequent enzymatic digestion [190]. This results in a much larger impedance change on the surface.

The participation of one analyte molecule in several binding events with capture probes on the sensing electrode can also be realized without the use of an enzyme. Here, the so-called hybridization chain reaction has been exploited [144, 191]. The presence of a target strand results in the repeated opening and hybridization of two hairpin structures. This can lead to the generation of long dsDNA or the opening of several hairpin capture strands on the sensing surface (Fig. 5d1, d2).

The amount of fixed recognition elements on the sensing surface is limited by the available area. In order to accommodate more recognition events and, thus, enhancing the signal at a given concentration, several ideas have been followed. One direction uses dendrimers onto which a large number of capture molecules can be

Fig. 5 (continued) and can be detected impedimetrically. (**c**) Probe DNA-modified electrode before and after hybridization with target DNA and subsequent binding of a biotin-modified ssDNA at the overhang of the probe-target complex. Biospecific binding of avidin-modified horseradish peroxidase (HRP) to the biotin-labelled DNA leads to a fixation of the enzyme. The enzymatic production of an insoluble product, which precipitates on the DNA electrode, disturbs the access of ferri-/ferrocyanide to the surface and thus increases the impedance. (**d1**) Hybridization chain reaction to prolong DNA on the sensing surface: probe DNA-modified electrode before and after hybridization with target DNA and subsequent binding of hairpin DNA (HP1) at the overhang of the probe-target complex. Due to the hybridization, the hairpin opens and allows the binding of hairpin DNA 2 (HP2), which in turn also provides a binding sequence for hairpin 1. Thus, the bound DNA strand can be extended by repetitive hybridization cycles between hairpins 1 and 2 and results in an enhanced accumulation of DNA in front of the electrode. (**d2**) Hybridization chain reaction to induce several hybridization events on the sensing surface: Hairpin probe DNA-modified electrode before and after hybridization with target DNA. Target binding results in an opening of the hairpin probe. This enables the binding of the second hairpin to the probe via a displacement of the target DNA. The free target can now bind to another hairpin probe, which results in the formation of several hybridized strands and amplifies the signal

bound [192, 193]. The modification of electrodes with gold nanoparticles is another way to enlarge the active area and to enhance the sensitivity in impedimetric analysis (Fig. 6a) [136, 194, 195]. The increase in electrode roughness can also be achieved by applying other techniques such as the preparation of anodic alumina films covered with a thin gold layer [196].

Instead of using the surface of a single working electrode, an in-plane geometry can be applied, which makes use of two closely spaced electrodes. Two electrodes are prepared on an insulating substrate in a fingerlike structure leaving a small non-conductive gap between them. These electrodes are termed as interdigitated electrodes (IDEs) and can be formed from different metals [197–199], but for impedimetric analysis, mainly gold is used [200]. The geometry takes advantage of the changed conditions for the current flow, which occurs mainly very near to the surface and thus, shows a much higher sensitivity towards surface changes compared to the conventional design. The bio-recognition element can be immobilized on both electrodes, in the gap between the electrodes or on top of both. This electrode design has an additional advantage since by preparing the electrodes on a chip, the whole electrochemical setup is already integrated and no external electrodes are needed. The basic scheme is exemplified in Fig. 6b. A highly sensitive response of the sensor requires strong electrical fields due to short distances between the electrodes [201]. Typical distances between the electrode fingers are in the range of 1–10 μm and are limited by the fabrication procedure. However, electrode widths from 500 nm to less than 200 nm have been achieved meanwhile [197]. A theoretical analysis demonstrates that 80% of the current between the electrodes with a spacing of about 250 nm will flow in a layer not higher than 250 nm above the surface. This may illustrate that a reproducible

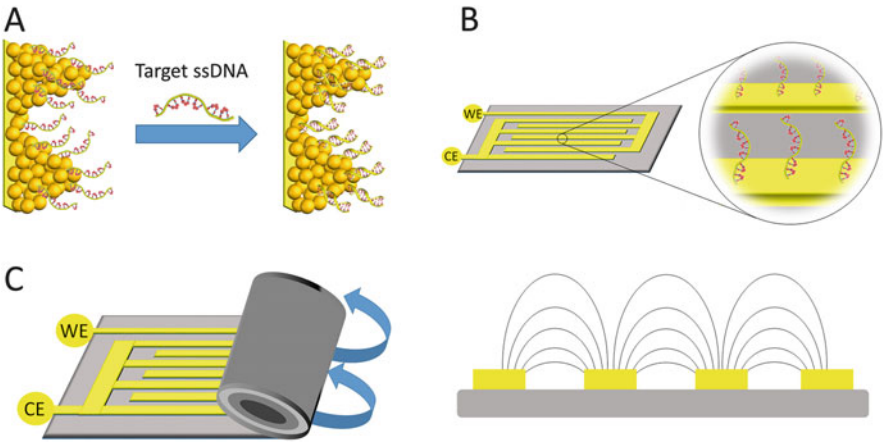

Fig. 6 Amplification strategies for the impedimetric DNA detection – part II. (**a**) Enlargement of the electrode surface by micro- and nanostructuring, for example, with Au-NP. (**b**) Application of IDEs with small distances between the electrodes (field lines are illustrated by black lines). (**c**) Rolled IDE geometry leading to an enhanced electric field inside the rolled electrode

production of IDEs with dimensions in the nm range will significantly increase the sensitivity for a direct binding analysis. This kind of measurement has been applied for the detection of DNA hybridization without the need of a label, relying mainly on the altered charge accumulation after double strand formation [197, 199, 200].

An interesting approach has been reported by preparing three-dimensional IDEs by introducing insulating barriers between the fingers of the IDEs. This design forces the current to flow very close to the surface of these barriers. If, for instance, biomolecular recognition events occur, a pronounced influence on the current can be envisaged. An enhanced sensitivity has been found in consequence [202].

The use of IDEs can also be advantageously combined with other amplification strategies described so far. For example, the DNA hybridization can be extremely sensitively detected by the use of Au-NPs coupled to an oligonucleotide. The catalytic properties of the nanoparticle surface can be used for a silver deposition and thus an enlargement of the particles. When this enlargement proceeds to an extent that the surface-bound particles face each other, then a conductive pathway is formed between the two electrodes [203, 204].

An alternative approach for sensitivity enhancement in immunosensing uses conducting polymer chains coupled to the antigen [205]. After binding of the modified antigen to the recognition surface, the conductance of the gap increases, and detection becomes possible. The same effect can be induced, if an enzyme label is coupled to the antigen. In this case, the sensor surface can be additionally covered with a membrane permeable for iodine, which is produced by the enzyme label HRP. After binding of the antigen-HRP conjugate, iodine is generated from iodide and hydrogen peroxide, which leads to an increased conductance of the promoting film consisting of tetra-tert-butyl copper phthalocyanine within the gap [206].

Recently, ultrasensitive impedimetric detection has been reported based on three-dimensional nanomembranes. The drastic enhancement in sensitivity compared to planar electrodes has been described as a result of the rolled electrode geometry leading to an enhanced electric field inside the rolled electrodes (Fig. 6c). This has been exemplified with the analysis of DNA down to femtomolar concentrations [207].

The various examples in literature may illustrate the potential of the impedance technique for analytical purposes. However, reproducibility and reliability of the sensors are often a problem, particularly when they are repeatedly used or applied in real samples. Other issues are related to signal stability and nonspecific impedance changes. These issues need to be carefully evaluated under the conditions of analytical application. Advantageously, a reference sensor can be applied which is similarly prepared as the sensing electrode, but without the selected recognition element. This approach is also used in other label-free methods such as SPR.

In the following section, the developments of an impedimetric DNA sensor and the application for the detection of nucleic acids and binding partners of nucleic acids will be discussed in more detail.

2 Impedimetric DNA Detection

As mentioned before, the continuous progress in genomics has led to increasing interests in the detection of DNA sequences. Therefore, the design of easy and fast DNA detection devices with low costs and high accuracy remains an important task. Particularly, the transfer of the location of analysis from the laboratory directly to the point of care has increased the requirements for the development of new diagnostic tools [208]. Here, in particular impedance spectroscopy represents an efficient measuring tool, which allows careful control of all sensor preparation steps but can also be used as a transduction method for sequence-specific detection.

2.1 Sensor Concept

For the construction of an impedimetric DNA sensor, a ssDNA layer has to be attached to an electrode surface, which converts the biochemical signal into an electrical signal. As exemplified in Fig. 7, a thiol-modified probe DNA is used for the immobilization to a gold electrode via chemisorption. Here, mainly short probes with a length of around 15–30 nucleotides are used due to a higher hybridization efficiency and specificity compared to longer DNA strands [89]. In order to avoid nonspecific interactions between the electrode and DNA or other compounds, the passivation of the surface with short hydrophilic thiols, e.g. mercaptobutanol (MCB) or mercaptohexanol (MCH), has been shown to be beneficial [112, 114, 115, 124]. This is of particular interest since it has been found that DNA bases and gold form strong interactions, which can decrease the hybridization efficiency [209]. A passivation with a hydrophilic thiol counteracts this interaction, since the formation of gold-thiol bonds is energetically favoured and promotes the orientation of the probe DNA towards the solution.

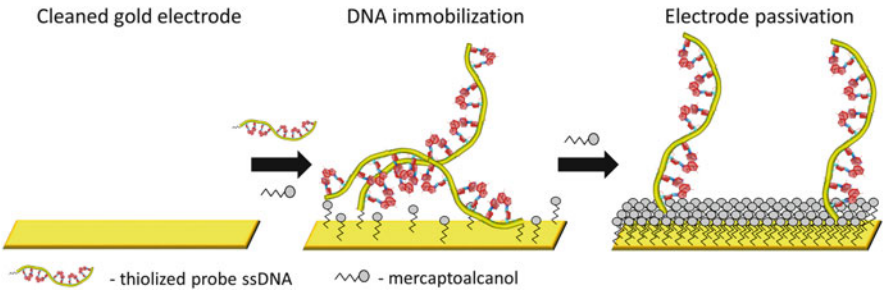

Fig. 7 Illustration of the step-wise construction of a DNA-modified electrode. A cleaned gold electrode is incubated in a mixture containing thiolized probe DNA and a mercaptoalcanol compound. For the passivation the DNA-modified electrode is again immersed in a mercaptoalcanol-containing solution. Afterwards, the sensor is ready for hybridization experiments

In order to achieve a reliable system for DNA analysis, the surface concentration of the probe DNA has to be controlled and characterized. Among others, the use of labelled target DNA with redox molecules like methylene blue [99] or ferrocene [210] in combination with a voltammetric read-out is valuable to determine the capturing properties of DNA-modified electrodes. On the basis of the transferred charge of the label, conclusions can be drawn on the amount of hybridized DNA and accordingly about the concentration of hybridizable probe DNA on the electrode surface. For the impedimetric DNA detection, a surface coverage between 5 and 15 pmol/cm^2 has been shown to be sufficient to allow the binding of target DNA and achieve signal changes upon hybridization [114].

Impedimetric experiments are performed in the presence of the redox system ferri-/ferrocyanide. As illustrated in Fig. 8, the detection principle is based on the electrostatic repulsion between the negatively charged redox species and the negatively charged sugar-phosphate backbone of the DNA. Consequently, the immobilization of probe DNA already disturbs the access of the redox system to the electrode and changes the interfacial impedance. After hybridization a further accumulation of negative charges in front of the electrode is induced, depending on the amount of bound DNA. Therefore, the charge transfer is reduced, and an increase in impedance can be observed. The impedance spectra of a DNA-modified electrode in the single-stranded and double-stranded situation are shown in Fig. 8, too. For the analysis of these spectra, a simplified Randles equivalent circuit can be used, consisting of R_{sol}, R_{ct} and a constant phase element (CPE), which represents the double-layer capacitance. For a better evaluation of the results, the frequency range is restricted, and thus the Warburg impedance can be excluded. While for the

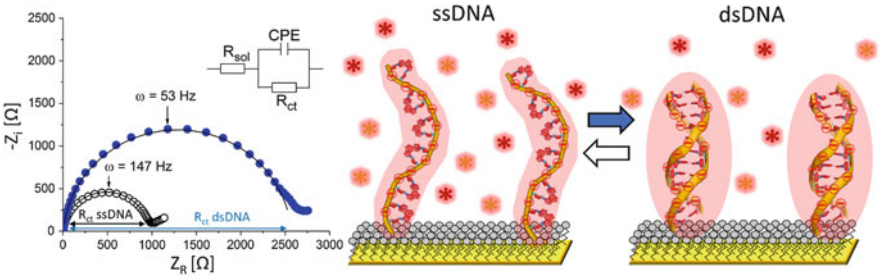

Fig. 8 Principle of impedimetric DNA detection. Left: impedance spectra of a DNA-modified electrode before (open circles) and after hybridization with complementary 25mer target DNA (blue circles). The measurements are performed in 0.1 M sodium phosphate buffer in the presence of 2 mM ferri-/ferrocyanide. Inset: equivalent circuit used for the analysis of the impedance data, R_{sol}, solution resistance; R_{ct}, charge transfer resistance; and CPE, constant phase element, which represents the capacitive properties of the electrode surface. For an ideally planar surface, this is a capacitance only; for real electrodes often a constant phase element has to be used with $Z_{CPE} = 1/A(j\omega)^{\alpha}$. For polycrystalline gold α values are however close to 1. Right: schematic illustration of the changing barrier for ferri-/ferrocyanide (illustrated as red and orange stars) at a DNA-modified electrode before (ssDNA) and after hybridization (dsDNA). Upon hybridization an increase of the negative charge in front of the electrode disturbs the permeation of the negatively charged redox system to the electrode; consequently, R_{ct} increases

capacitance only minor changes can be obtained upon hybridization, R_{ct}, which corresponds to the diameter of the semicircle in the Nyquist plot, is clearly increased. Thus, the R_{ct} value gives access to the read-out of hybridization events via impedance spectroscopy. The evaluation of the results can be stated as absolute R_{ct} change before and after hybridization or as a ratio between both situations. The latter represents the relative increase of the impedance and is used as the sensing parameter for the description in this chapter.

It has to be mentioned here that this analysis is based on conditions when the impedance is dominated by the sensing electrode, which can be achieved by a much larger area of the counter electrode.

2.2 Sensor Properties

2.2.1 Reusability

The reusability is a key parameter for the design of advanced sensor systems for a sustainable and economical application. For DNA sensors the electrode needs to be regenerated after hybridization via denaturation of the dsDNA into two single strands. Therefore, the strong interactions between the complementary bases have to be reduced. However, due to the potential impact on the impedimetric read-out, the denaturation procedure has to fulfil some requirements: Besides a high hybridization efficiency even after several denaturation cycles, the process should not alter the surface properties of the electrode and falsify the signals. Since impedance spectroscopy responds sensitively to a change in surface properties, this is a critical step for the construction of a reusable impedimetric DNA sensor.

The application of thermal treatments or chemicals, which destabilize the double strand, has been shown to achieve high denaturation efficiencies in solution. However, since electrochemical approaches are temperature sensitive and this step takes time, the usage of a thermal treatment for the denaturation is not very advantageous. Kafka et al. have tested various chemical compounds such as isopropanol, guanidine hydrochloride, sodium carbonate and urea, which are well known to impair the structure of dsDNA, for the denaturation of 18mer dsDNA on gold electrodes [112]. For isopropanol and guanidine hydrochloride, a significant increase in impedance has been found, which also results in diminished impedance changes after a few hybridization/denaturation cycles. In contrast, the denaturation with sodium carbonate can conserve the electrode functionality but increases the initial impedance signal during four detection cycles tenfold. Better results have been obtained with urea as denaturation reagent, which causes only minor effects on the sensor operation. The denaturation is completed within 30 s and enabled the repeated usage of the sensor for up to 12 detection cycles [112].

For longer DNA strands (25mer), only insufficient denaturation efficiency has been found. As an alternative the electrostatic repulsion between individual DNA strands has been exploited for the development of a denaturation procedure based

on deionized water [124]. The denaturation with deionized water leads to a destabilization of the dsDNA due to the absence of stabilizing cations. For an effective regeneration of the sensor with water, strong convective conditions have to be adjusted to achieve a sufficient denaturation efficiency. This procedure enables not only a nearly complete denaturation over several measuring cycles (98.5 ± 2%) but also ensures a constant hybridization efficiency (97 ± 1%), without changing the surface properties of the electrode. This demonstrates that a gentle denaturation of dsDNA with deionized water is feasible.

2.2.2 Signal Stability

For reliable DNA detection, a stable initial sensor signal needs to be provided. However, especially for electrochemical sensors that rely on a label-free application, signal stability has been shown to be an important but also a challenging issue.

For the sensor system described here, applying 18mers as capture probe and mercaptobutanol as blocking agent, only small signal changes have been observed [112]. This results in a stable detection of the hybridized and denatured situation. However, when a 25mer and mercaptobutanol are used, a clear increase of the impedance during the measuring cycles is observed (Fig. 9a). This indicates a change of the electrode surface properties during the measuring procedure. A signal increase is also determined in the absence of target DNA, which suggests a time-dependent electrode altering [124]. Interestingly, the relative signal increase after hybridization seems to be less affected by these impedance alterations (R_{ct} ratio, first cycle 2.48, second cycle 2.31, third cycle 2.27). However, such instability limits the reliability for sensing applications.

Two factors have been found to be crucial to control the signal stability for the impedimetric DNA detection. On the one hand, it is observed that the solution properties have a strong influence on the interfacial impedance [112, 120, 124, 208]. Usually, a high ionic strength above 1 M is used during immobilization and

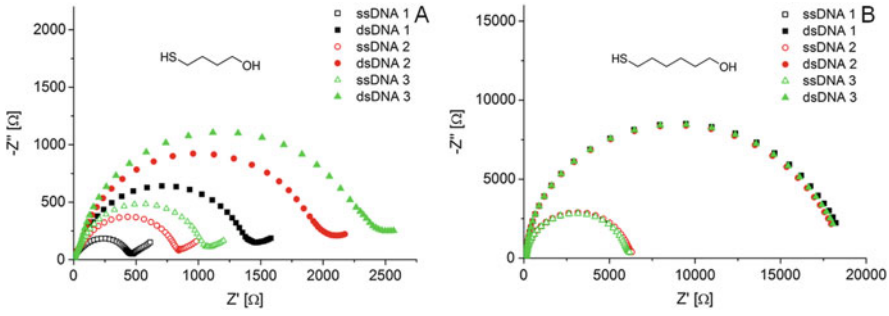

Fig. 9 Impedance spectra of ssDNA-modified electrodes prepared with mercaptobutanol (**a**) and mercaptohexanol (**b**) for three successive hybridization/denaturation cycles according to [124] (2 mM ferri-/ferrocyanide, 10 kHz–1 Hz frequency range, 5 mV AC amplitude, OCP)

hybridization to ensure a high probe DNA coverage and high binding efficiencies [211–213]. Measurements in turn are performed at lower ion concentrations. Such changes of the ionic composition during the preparation and measurement are influencing the time-dependent signal behaviour [124]. This might be attributed to a rearrangement of probe DNA after buffer changes. By limiting the number of buffer changes, the time-dependent impedance increase between the first and the third hybridization/denaturation cycle can be reduced from 142 to 50%.

Another factor which has been shown to significantly influence the signal stability is the mercaptoalcanol compound used during electrode preparation. As illustrated in Fig. 9b, by exchanging mercaptobutanol (MCB) for mercaptohexanol (MCH), the impedance is completely stabilized over several hybridization/denaturation cycles (R_{ct} ratio 2.73 $\pm$ 0.25, [124]). Furthermore, the absolute impedance is increased by about one order of magnitude compared to MCB as blocking agent, which suggests a better isolation of the MCH-passivated DNA electrode. This effect is predominantly attributed to the longer chain length of MCH compared to MCB, resulting in a more ordered monolayer due to the stronger hydrophobic interactions between the aliphatic chains. Thus, nonspecific DNA-gold binding is diminished, and the susceptibility for nonspecific interactions is reduced, resulting in an improved sensorial operation.

2.2.3 Sensitivity and Selectivity

For sensor application the dynamic range of measurements needs to be characterized. In Fig. 10b the concentration dependency for a 18mer DNA is illustrated. A sigmoidal binding curve is found, which shows an increasing impedance signal after hybridization with concentrations between 0.01 and 10 μM target DNA [112]. The half-maximum concentration corresponds to 350 $\pm$ 40 nM, and the linear concentration range is between 0.1 and 1 μM. The range is similar to an impedimetric sensor, which uses longer 25mer target DNA [124].

The selectivity of a DNA sensor, which relies on hybridization, depends on the hydrogen bonds between the base pairs A-T and G-C, the sequence-specific arrangement of bases in a DNA strand and the diminished stability of dsDNA with non-complementary strand areas. However, even if high selectivity is provided by the recognition element, particularly for a label-free application, also non-specific interactions, e.g. target binding to the gold electrode, can influence the sensorial output. Kafka et al. have tested the specificity of the recognition interface of an 18mer-modified gold electrode by performing alternating incubations with complementary and non-complementary ssDNA [112]. For complementary target DNA, the R_{ct} increases about three times after hybridization in relation to the denatured situation. In contrast, only negligible effects on the signal can be found after incubation with non-complementary ssDNA (<5%). This demonstrates that also in the presence of non-complementary DNA, the impedimetric signal is not influenced, which is important if complex samples need to be analysed. Here, the

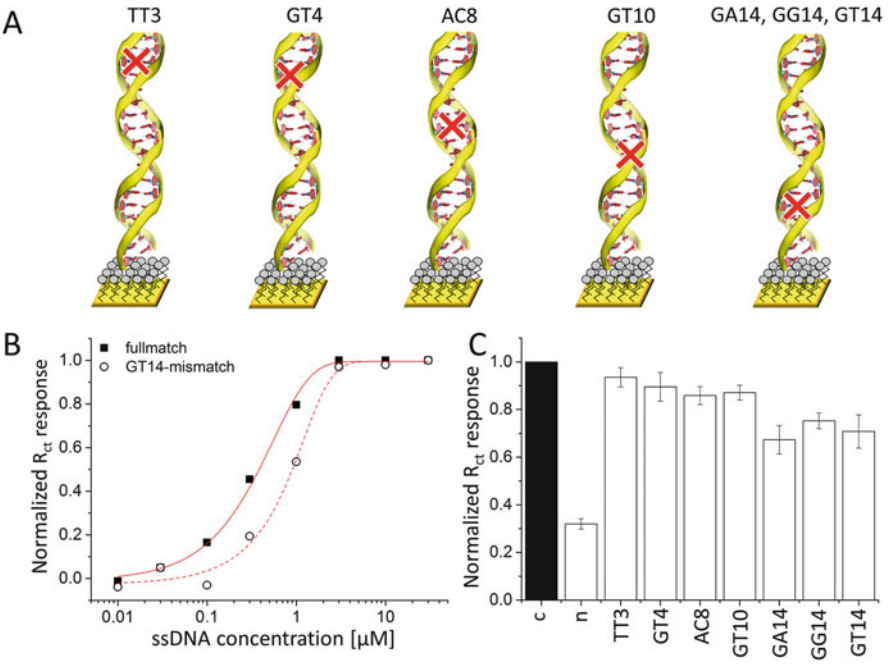

Fig. 10 (**a**) Schematic illustration of the mismatch position within a hybridized 18mer dsDNA. (**b**) Relative ratio of R_{ct} of 18mer ssDNA-modified electrodes in dependence on the target DNA concentration. The hybridization studies are performed with complementary (closed squares) or GT14-mismatch targets (open circles). (**c**) Normalized R_{ct} ratio of 18mer-modified gold electrode after hybridization with different target DNAs (*c* complementary, *n* non-complementary, mismatch DNA TT3, GT4, AC8, GT10, GA14, GG14 and GT14). The normalized R_{ct} response is calculated as follows: $\left(\frac{R_{ct,\ \text{hybridized}}}{R_{ct,\ \text{denatured}}} - 1\right) / \left(\frac{R_{ct,\ \text{hybridized}}}{R_{ct,\ \text{denatured}\ 30\ \mu M}} - 1\right)$

repulsion between the immobilized probe and the non-complementary DNA and the passivation reagent helps to avoid nonspecific binding to the electrode.

2.2.4 Mismatch Detection

DNA sensors capable of detecting single base pair mismatches within DNA duplexes are of high importance in medical diagnostics for the screening of genetic mutations and diseases. The great interest can be attributed to the significant appearance of single nucleotide polymorphism (SNPs) in the human DNA.

Consequently, the suitability of impedance spectroscopy for the discrimination of single base pair mismatches has been evaluated for the developed sensor platform at different concentrations [112]. Also for mismatch DNA, an increase of R_{ct} can be observed after hybridization. However, in comparison to the complementary target DNA, the binding curve of the mismatch DNA is shifted to slightly

higher concentrations (Fig. 10b). This can be attributed to the decreased affinity between the mismatch target and the probe. When the target concentration is fixed, the influence of the mismatch position is found to affect the sensorial output (Fig. 10c). For target DNA with a GT mismatch at position 4, 10 or 14 counted from 5′-end of the target, a decreasing impedance response has been obtained after hybridization. This means that the impact of the GT mismatch on the impedance increases when the location of the mismatch is shifted within the hybridized duplex to the electrode surface. An exchange of the type of mismatch at position 14 by a GG or a GA results in similar signal changes upon hybridization. This indicates that especially the position of the mismatch within the duplex determines impedance response and to a less extent the type of mismatch. Additional experiments with a mismatch at position 3 (TT) or 8 (AC) confirm this signal dependency and demonstrate that such small structural differences between the targets can be resolved with impedance spectroscopy for an analytical detection of SNPs.

2.3 Factors Influencing the Sensing Performance

2.3.1 Buffer Concentration

The negative charge of both DNA and the redox system ferri-/ferrocyanide results in a repulsion between both molecules and therefore modulates the interfacial impedance. This provides the basis for the detection of DNA binding via impedance spectroscopy. However, the impact of the negative charge is among others strongly dependent on the presence of cations, which electrostatically shield opposite charges. Therefore, the ionic strength of the buffer has not only an influence on the impedance signal itself, but also on the hybridization efficiency. For the impedimetric system introduced here, the influence of the buffer concentration used during the impedimetric measurement has been analysed [112]. Thus, the phosphate buffer concentration is varied between 1 mM and 1 M, while hybridization has been performed under constant high ionic strength in order to exclude an influence of the hybridization efficiency on the impedimetric study. As expected, a high phosphate buffer concentration (1 M) results in a low R_{ct} ratio between ssDNA and dsDNA on the surface. Medium phosphate buffer concentrations of 0.05 and 0.1 M give the highest R_{ct} ratio upon hybridization, since very low ion concentrations are not beneficial for ferri-/ferrocyanide conversion at the electrode.

2.3.2 DNA Probe Concentration and Length

The probe immobilization is one key point to influence the sensing performance of an impedimetric DNA sensor. Particularly, the probe density is found to be critical, since high probe amounts can significantly slow down the hybridization kinetics due to steric and electrostatic hindrance [213]. On the other hand, small probe

densities can affect the sensitivity. In a systematic study, Witte et al. have characterized the influence of the surface coverage of an 18mer probe on the impedance signal after hybridization with complementary DNA [114]. Therefore, DNA-modified electrodes with surface coverages between 3 and 15 pmol/cm^2 have been fabricated. As shown in Fig. 11, for all probe surface concentrations, an enhanced impedance signal is obtained after hybridization, which rises with an increasing amount of probes on the electrode. As a result the discrimination between the hybridized and the denatured situation is improved at higher probe densities. This rises the sensitivity for the detection of hybridization events. A similar impedance behaviour has been found for hybridization studies with various surface densities of PNA probes [214]. Compared to lower probe densities, the distance between the immobilized DNA becomes smaller for higher DNA amounts. This reduces the areas of unhindered access of the redox species to the surface and thus, enhances the electrostatic repulsion for ferri-/ferrocyanide. The restricted access of the redox system in turn enhances the signal response of the impedimetric sensor.

Another factor, which may influence the sensorial performance, is the length of the used capturing DNA. By comparing 18mer and 25mer probes under the same assembly conditions, a different amount of bound DNA has been detected [115]. The surface coverage of the 25mer (~9 pmol/cm^2) was only approximately the half of the concentration obtained for the 18mer (~15 pmol/cm^2).

Also for the impedimetric signal response, differences have been found for the probes with varying length (18mer and 25mer) [115]. If the same surface concentration is used for both, the 18mer and 25mer, R_{ct} is enhanced for the longer probe in the denatured situation and in the hybridized situation. The overall increase of the

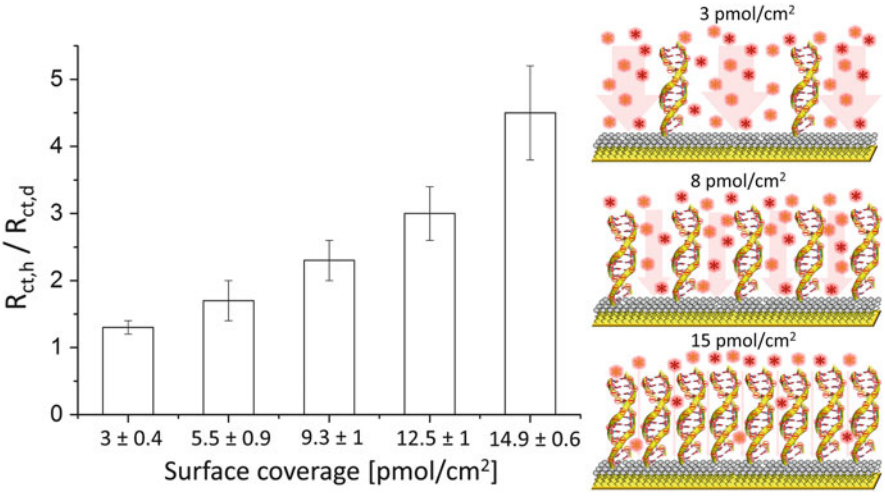

Fig. 11 Left: R_{ct} ratio of a 18mer-modified gold electrode with different surface concentrations before and after hybridization. Right: schematic illustration of DNA-modified gold electrodes with different surface concentrations. Ferri-/ferrocyanide is illustrated as red and orange stars

impedance due to the extension of the probe length can be attributed to the increased negative net charge of a 25mer ssDNA and dsDNA compared to a 18mer. Thus, the electrostatic repulsion between DNA and ferri-/ferrocyanide is enforced. The relative R_{ct} change due to hybridization is, however, rather similar for the 18mer and 25mer and enables a good discrimination between ssDNA and dsDNA.

This demonstrates that the control of the surface properties by adjustment of the probe density and the probe length is of significant importance for the design of impedimetric DNA sensors. This is not only interesting in order to increase the sensitivity but also to provide a reliable sensing system.

2.3.3 Size of the Target DNA

Even if in the literature a lot of reports on impedance spectroscopy for DNA sensing can be found, often only short target strands in the range of around 20 nucleotides are used for the sensorial characterization. This is sufficient to classify the system but misses the requirements for an analytical application. Analytically interesting DNA targets are significantly longer and behave differently compared to shorter ones in terms of hybridization kinetics and efficiency [215]. Also the probability for the formation of secondary structures, e.g. self-hybridization or hetero-hybridization, between two targets is increased for long sequences. This will significantly affect the sensorial properties for hybridization-based approaches.

The developed DNA electrodes have been used to analyse the influence of the target length and the position of the recognition sequence on the impedimetric signal response by using 25mer probe-modified gold electrodes (Fig. 12) [124]. Therefore, hybridization studies with differently sized complementary targets (35mer, 45mer and 80mer) with an overhang exposed to the solution after target-probe complex formation have been performed and compared to the signal obtained for the binding of a 25mer (without an overhang). An increasing impedance signal upon hybridization can be obtained for all target sequences, which demonstrates that impedance spectroscopy can also be used for the detection of longer strands. However, the signal response is found to decrease with increasing target length. This finding is rather surprising, since the binding of longer strands is associated with a much higher raise of mass accumulation and negative charges in comparison to shorter targets. Comparative studies with SPR have shown different hybridization efficiencies of the target sequences. While for the hybridization of the 25mer the SPR signal is already in the steady state at the end of the hybridization time period of 10 min, for longer targets the SPR signal is still increasing. This shows that the hybridization kinetics is slower for longer strands, which is in good agreement with other reports [215]. From the SPR data, the precise mass and concentration of bound DNA can be determined and correlated to the impedance data. An elongation of the target length results in an increase of bound mass, but in a decrease of surface concentration of the target-probe complexes. In consequence, it is found that the impedance signal is more affected by the surface concentration of

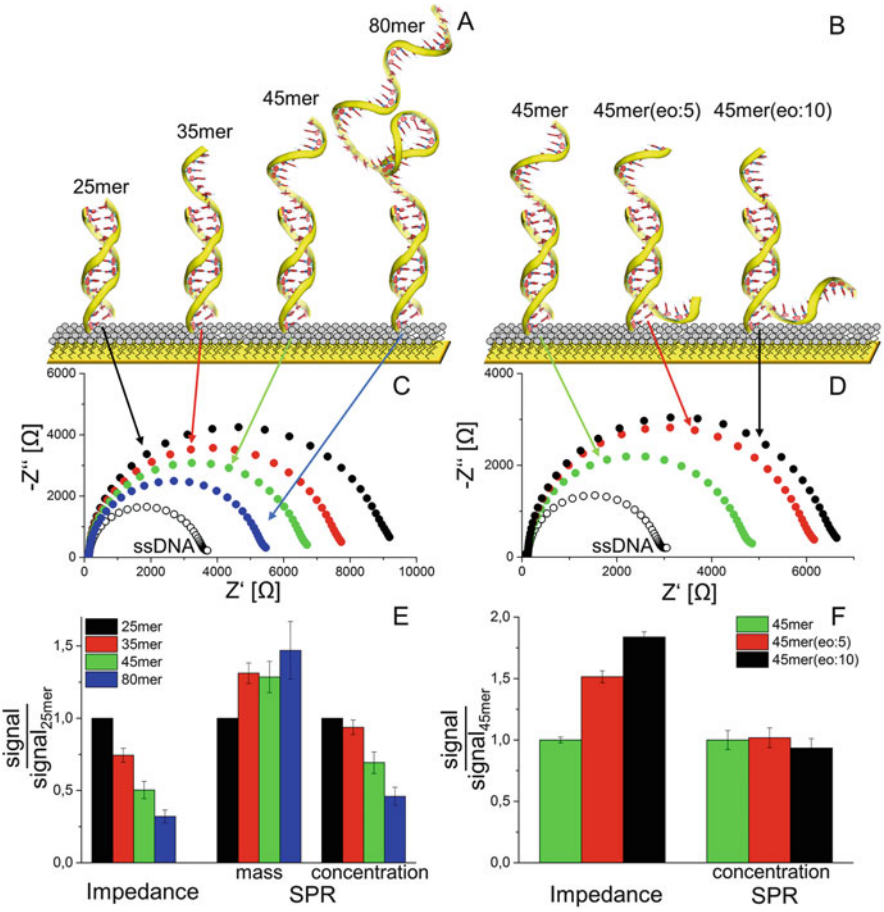

Fig. 12 Influence of target length and recognition sequence position on the impedimetric DNA detection. (**a**, **b**) Schematic illustration of different probe-target complexes with an overhang exposed to solution or to the electrode (in the latter case, 5 or 10 nucleotide overhangs (eo) have been used). (**c**, **d**) Impedance spectra of a 25mer-modified gold electrode before and after hybridization with different targets (2 mM ferri-/ferrocyanide, 10 kHz–1 Hz frequency range, 5 mV AC amplitude, OCP). (**e**, **f**) Normalized hybridization signal of impedance and SPR experiments for the hybridization with the different targets according to [124]. While the impedimetric signal corresponds to the R_{ct} ratio between the hybridized and denatured situation, mass and concentration of bound targets are calculated from the SPR signal

the hybridized strands than by the absolute attached mass when a large part of the DNA is located away from the surface. Probably, the overhang does not significantly disturb the reaction of ferri-/ferrocyanide at the electrode.

A further hint that DNA far away from the electrodes does not significantly participate in the impedimetric signal generation is found by performing a second hybridization step with a 20mer at the overhang of the pre-hybridized 45mer-25mer

or 80mer-25mer target-probe complex [124]. While successful binding of the 20mer to the overhang with a hybridization efficiency of around 70% can be determined via SPR, only negligible signal changes can be obtained with the impedimetric sensor in 0.1 M buffer.

Besides the target length, also the recognition sequence position is of importance, particularly for the analysis of hybridization events at electrode surfaces. Here, an overhang orientation to the solution or to the electrode will influence the hybridization kinetics and also the signal behaviour. The sensing system introduced here has been used to analyse the influence of three different 45mer targets which possess a 0-, 5- and 10-nucleotide-long overhang exposed to the electrode [124]. As illustrated in Fig. 12, the impedance signal upon hybridization rises with increasing length of the overhang exposed to the electrode. Evaluating SPR measurements show that this effect is not attributed to different hybridization efficiencies of the respective 45mer. Consequently, the orientation of an overhang near to the electrode significantly improves the impedimetric signal response. Probably, a further accumulation of negative charges directly in front of the surface impedes the access of ferri-/ferrocyanide stronger compared to the counterpart with an overhang exposed to the solution. However, it needs to be mentioned that the influence of the overhang orientation on the hybridization efficiency and the sensor signal is controversial [90, 123, 124, 215, 216]. This is probably due to the fact that different experimental conditions, such as the immobilization chemistry, the surface concentration, the length of the probe and in addition, different measuring techniques, have been applied for quantification.

2.4 Detection of DNA-Binding Molecules

Besides the use of impedance spectroscopy for the analysis of hybridization events, also the investigation of DNA-binding molecules such as groove binders, intercalators, proteins, antibodies and enzymes has been followed with growing interest. Upon interaction with the DNA-binding molecule, the impedance signal can be influenced by a change in the charge situation, a modification in the access of the redox species or a change of the DNA structure (Fig. 13). This opens the way to construct new sensing schemes for several applications: analysis of genotoxic compounds, identification of DNA-binding proteins or low-molecular-weight binders and the influence of pharmaceuticals on the DNA metabolism.

2.4.1 Low-Molecular-Weight Compounds

Groove Binder Groove binders are a group of molecules, which are able to bind to the minor or major groove of DNA. For example, spermine is found to bind to the DNA grooves and thereby has a significant role in the regulation of cell proliferation and for the stabilization of DNA. Spermine is an aliphatic polycationic

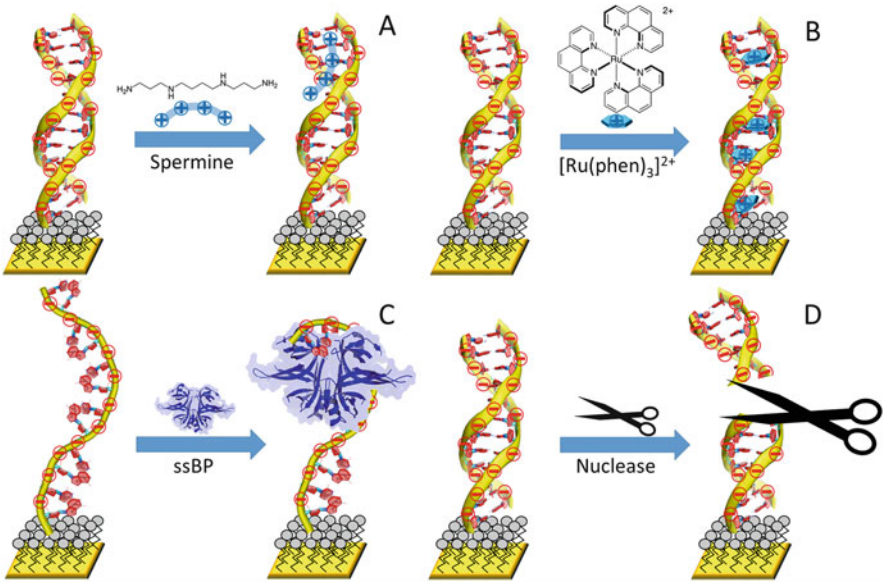

Fig. 13 Different impedimetric detection schemes based on DNA as recognition element. (**a**) dsDNA before and after incubation with the groove binder spermine or (**b**) with the intercalator phenanthroline with a ruthenium (II) complex ($[Ru(phen)_3]^{2+}$). For both spermine and $[Ru(phen)_3]^{2+}$, the interaction with dsDNA results in a decrease of the impedance. This can be explained by the compensation of the negative charge of DNA by the positively charged binding molecules, which favour permeability of the negatively charged ferri-/ferrocyanide ions to the electrode. (**c**) ssDNA before and after incubation with single-stranded binding protein (SSBP). The binding results in an enhanced impedance due to steric and electrostatic hindrance. (**d**) dsDNA before and after incubation with endonuclease BamHI. The DNA is cleaved by the enzyme, which results in a decrease of DNA mass and charge in front of the electrode and reduces the impedance

compound and forms strong interactions with the negatively charged DNA backbone.

The DNA-spermine interaction has been studied by using dsDNA-modified electrodes [114]. Upon incubation of the electrode with spermine, a decrease of R_{ct} has been found, which can be explained by the changed charge situation at the electrode surface. The positively charged amino groups of spermine compensate the intrinsic negative charge of the DNA and thus, allow a better access of the negatively charged ferri-/ferrocyanide ions to the electrode (Fig. 13a). Based on these principles, spermine concentrations between 0.1 and 10 mM can be detected, resulting in a sigmoidal binding curve. The maximum suppression of R_{ct} is found at high spermine concentrations of 10 mM and corresponds to around 40% of the initial signal. Control experiments with ssDNA show only minor impedance changes after exposure to 10 mM spermine. This demonstrates that the impedimetric signal transduction can be used for the analysis of spermine-DNA interaction in a concentration-dependent manner.

Intercalator DNA intercalators are small, planar, aromatic compounds, which are able to insert between the bases of dsDNA (Fig. 13b). The binding of the intercalator is mainly promoted by π-stacking, but may also have contributions from electrostatic, van der Waals and hydrophobic interactions.

The DNA sensor system has been used to analyse the intercalation by a phenanthroline, which is part of a ruthenium (II) complex ($[Ru(phen)_3]^{2+}$) in dsDNA [114]. Besides the interaction between the aromatic system of the phenanthroline and the heterocyclic bases of the neighbouring base pairs, also the positive charge of the ruthenium complex facilitates the binding. A maximum decrease of R_{ct} is found after incubation of the dsDNA-modified electrode in 1 μM $[Ru(phen)_3]^{2+}$, which corresponds to about 17% of the initial state. Similar to the experiments with the groove binder spermine, the detection principle is based on the compensation of the negative charge of the DNA by the positively charged intercalator. In comparison, the usage of ssDNA-modified electrodes results only in minor impedance changes due to the lack of binding sites for the intercalator.

2.4.2 Protein Binding

Single-Stranded Binding Protein In addition to the detection of small molecules, also the analysis of protein-DNA interactions is of interest. In one approach the binding of the single-stranded binding protein (SSBP) to ssDNA-modified electrodes has been investigated [114]. SSBP prevents the binding of complementary ssDNA, stabilizes the secondary structure and protects ssDNA from decomposition by nucleases. The protein consists of four identical subunits, which are able to bind to ssDNA. After incubation with SSBP, an R_{ct} increase of around 60% has been found for ssDNA-modified electrodes. In contrast, for a dsDNA-modified electrode, no changes of the impedance are obtained. These results display that the selective binding of SSBP to ssDNA can be followed via impedance measurements, without observing nonspecific binding of the protein to the electrode surface. The increase of the impedance can be correlated to different reasons. On the one hand, due to the large size of the protein, the docking of the protein to ssDNA can sterically block the surface and impede the diffusion of ferri-/ferrocyanide to the electrode (Fig. 13c). On the other hand, also the electrostatic repulsion between the protein and the redox species can influence the signal behaviour, since the measurements have been performed at pH 7 and the isoelectric point of SSBP is 6. This means that the protein is negatively charged, which facilitates the repulsion.

Antibody Against dsDNA In a further approach, the usage of EIS for the detection of antibody binding to dsDNA has been demonstrated [114]. While for dsDNA a decrease of the impedance signal of around 12% is obtained, nearly no impedance change is found for ssDNA-modified electrodes. Apparently, the antibody binding changes the permeability of the electrode surface for the redox system in such a way that the accessibility is improved. This is in contrast to the results obtained for the binding studies with the single-stranded binding protein. This discrepancy can have

different reasons such as size and charge distribution of the protein as well as changes of the secondary structure and charge density of the DNA strands. Obviously, the charge compensation by antibody binding plays a major role.

Sequence-Specific Binding Another group of proteins, showing strong interactions with DNA, are transcription factors. They are of interest in molecular biology due to the role in regulation of protein synthesis. In one study, the binding of the transcription factor NF-κB to dsDNA-modified electrodes, containing a specific recognition sequence, has been analysed by using impedimetric read-out [115]. NF-κB is of importance since it is involved in the regulation of the immune and inflammatory response as well as cell proliferation. The binding to DNA is facilitated by the N-terminus (Rel homology domain) of the protein. After incubation of DNA-modified electrodes containing a specific recognition sequence with NF-κB, a decreased R_{ct} of about 13% is found. In contrast, the sensor incubation in binding buffer without transcription factor results in no impedance changes. Also for dsDNA-modified electrodes with a missing NF-κB recognition sequence, no decrease of the signal is obtained after contact with NF-κB. This suggests that the impedance changes are induced by the binding of the transcription factor to the specific dsDNA sequence. Here, NF-κB is found to be detectable in the range between 1 and 33 μg/ml. The decreasing impedance is attributed to the electrostatic neutralization of the DNA backbone upon NF-κB binding. This explanation is in good agreement with another study, showing that NF-κB binding results in a compensation of the negative charges of the DNA due to positively charged residues at the binding site of the protein [217].

2.4.3 Sequence-Specific DNA Cleavage

In some cases, the protein-DNA interaction results in a non-persistent fixation to the DNA and leads to a change of the DNA structure. This is valid, for example, for nucleases with their natural function of catalysing strand breaks into dsDNA (Fig. 13d). The DNA sensor system has been tested for analysing the sequence-specific cleavage of immobilized dsDNA by the restriction endonuclease BamHI [115]. BamHI is sequence specific and catalyses the cleavage of dsDNA between guanine bases. Compared to the solution conditions, the access of the enzyme to the substrate strands on the surface is hindered. It is found, however, that after 2 h, the whole dsDNA is cleaved by the enzyme, which results in a decrease of DNA mass and charge in front of the electrode. Therefore, the impedance signal is diminished by around 66% after restriction. No comparable signal change is found for dsDNA-modified electrodes without the specific cleavage sites for BamHI. This demonstrates that impedance spectroscopy can be used for the label-free determination of activity of the DNA cleaving enzyme.

3 Conclusions

The design and construction of impedimetric sensors provide a promising area of research, which has gained great interest during the last two decades. This can be attributed to the cost-effective operation, the feasibility to detect the analyte binding in a label-free fashion but also to follow and therefore control the different fabrication steps during the sensor preparation. Furthermore, an improved understanding of the physicochemical properties of biomolecules at electrode interfaces as well as the combination with novel nanostructures has led to advanced impedimetric detection schemes with high sensitivity. Various concepts have been introduced for different analytes such as proteins, nucleic acids, metabolites, whole cells, microorganisms, antibodies and antigens. Current issues concentrate on problems such as selectivity in the presence of interfering molecules as well as the prevention of nonspecific binding to the electrode. Other problems are related to instabilities in impedance signals, pitfalls in reproducible electrode preparations and also to the influence of the electric field on the biomolecule behaviour at the interface. For more complex electrode structures, the data evaluation can cause problems since the validity of the equivalent circuit used for analysis needs to be verified. Even if some examples have demonstrated that impedance spectroscopy could fulfil the requirements for the practical application, more work is needed to explore the perspectives of impedimetric sensors in medicine, gene analysis, food industry or environmental analysis.

References

1. Saby C, Jaffrezic-Renault N, Martelet C, Colin B, Charles M-H, Delair T, Mandrand B (1993) Immobilization of antibodies onto a capacitance silicon-based transducer. Sensors Actuators B 16:458–462. https://doi.org/10.1016/0925-4005(93)85228-3
2. Berggren C, Bjarnason B, Johansson G (2001) Capacitive biosensors. Electroanalysis 13:173–180. https://doi.org/10.1002/1521-4109(200103)13:3<173::AID-ELAN173>3.0.CO;2-B
3. Bart M, Stigter ECA, Stapert HR, de Jong GJ, van Bennekom WP (2005) On the response of a label-free interferon-γ immunosensor utilizing electrochemical impedance spectroscopy. Biosens Bioelectron 21:49–59. https://doi.org/10.1016/j.bios.2004.10.009
4. Stelzle M, Weissmueller G, Sackmann E (1993) On the application of supported bilayers as receptive layers for biosensors with electrical detection. J Phys Chem 97:2974–2981. https://doi.org/10.1021/j100114a025
5. Knoll W, Köper I, Naumann R, Sinner E-K (2008) Tethered bimolecular lipid membranes – a novel model membrane platform. Electrochim Acta 53:6680–6689. https://doi.org/10.1016/j.electacta.2008.02.121
6. Knichel M, Heiduschka P, Beck W, Jung G, Göpel W (1995) Utilization of a self-assembled peptide monolayer for an impedimetric immunosensor. Sensors Actuators B 28:85–94. https://doi.org/10.1016/0925-4005(94)01543-Q
7. Rickert J, Göpel W, Beck W, Jung G, Heiduschka P (1996) A 'mixed' self-assembled monolayer for an impedimetric immunosensor. Biosens Bioelectron 11:757–768. https://doi.org/10.1016/0956-5663(96)85927-6

8. Sadik OA, Xu H, Gheorghiu E, Andreescu D, Balut C, Gheorghiu M, Bratu D (2002) Differential impedance spectroscopy for monitoring protein immobilization and antibody−antigen reactions. Anal Chem 74:3142–3150. https://doi.org/10.1021/ac0156722
9. Maupas H, Soldatkin AP, Martelet C, Jaffrezic-Renault N, Mandrand B (1997) Direct immunosensing using differential electrochemical measurements of impedimetric variations. J Electroanal Chem 421:165–171. https://doi.org/10.1016/S0022-0728(96)04837-1
10. Gebbert A, Alvarez-Icaza M, Stoecklein W, Schmid RD (1992) Real-time monitoring of immunochemical interactions with a tantalum capacitance flow-through cell. Anal Chem 64: 997–1003. https://doi.org/10.1021/ac00033a007
11. Roxana Varlan A, Suls J, Sansen W, Veelaert D, De Loof A (1997) Capacitive sensor for the allatostatin direct immunoassay. Sensors Actuators B 44:334–340. https://doi.org/10.1016/S0925-4005(97)00225-6
12. Loo AH, Bonanni A, Pumera M (2011) Impedimetric thrombin aptasensor based on chemically modified graphenes. Nanoscale 4:143–147. https://doi.org/10.1039/C1NR10966A
13. Bonanni A, Pumera M (2011) Graphene platform for hairpin-DNA-based impedimetric genosensing. ACS Nano 5:2356–2361. https://doi.org/10.1021/nn200091p
14. Hu Y, Wang K, Zhang Q, Li F, Wu T, Niu L (2012) Decorated graphene sheets for label-free DNA impedance biosensing. Biomaterials 33:1097–1106. https://doi.org/10.1016/j.biomaterials.2011.10.045
15. Erdem A, Eksin E, Muti M (2014) Chitosan–graphene oxide based aptasensor for the impedimetric detection of lysozyme. Colloids Surf B Biointerfaces 115:205–211. https://doi.org/10.1016/j.colsurfb.2013.11.037
16. Tran DT, Vermeeren V, Grieten L, Wenmackers S, Wagner P, Pollet J, Janssen KPF, Michiels L, Lammertyn J (2011) Nanocrystalline diamond impedimetric aptasensor for the label-free detection of human IgE. Biosens Bioelectron 26:2987–2993. https://doi.org/10.1016/j.bios.2010.11.053
17. Bain CD, Troughton EB, Tao YT, Evall J, Whitesides GM, Nuzzo RG (1989) Formation of monolayer films by the spontaneous assembly of organic thiols from solution onto gold. J Am Chem Soc 111:321–335. https://doi.org/10.1021/ja00183a049
18. Wink T, van Zuilen SJ, Bult A, van Bennekom WP (1997) Self-assembled monolayers for biosensors. Analyst 122:43R–50R. https://doi.org/10.1039/A606964I
19. Ariga K, Nakanishi T, Michinobu T (2006) Immobilization of biomaterials to nano-assembled films (self-assembled monolayers, langmuir-blodgett films, and layer-by-layer assemblies) and their related functions. J Nanosci Nanotechnol 6:2278–2301. https://doi.org/10.1166/jnn.2006.503
20. Prodromidis MI, Hirsch T, Mirsky VM, Wolfbeis OS (2003) Enantioselective artificial receptors formed by the spreader-bar technique. Electroanalysis 15:1795–1798. https://doi.org/10.1002/elan.200302756
21. Mirsky VM (2002) New electroanalytical applications of self-assembled monolayers. TrAC Trends Anal Chem 21:439–450. https://doi.org/10.1016/S0165-9936(02)00601-5
22. Barraud A, Perrot H, Billard V, Martelet C, Therasse J (1993) Study of immunoglobulin G thin layers obtained by the Langmuir-Blodgett method: application to immunosensors. Biosens Bioelectron 8:39–48. https://doi.org/10.1016/0956-5663(93)80042-N
23. Lei-Guang W, Yu-Hua L, Ti Tien H (1995) Electrochemical transduction of an immunological reaction via s-BLMs. Bioelectrochem Bioenerg 36:145–147. https://doi.org/10.1016/0302-4598(94)05014-L
24. Terrettaz S, Mayer M, Vogel H (2003) Highly electrically insulating tethered lipid bilayers for probing the function of ion channel proteins. Langmuir 19:5567–5569. https://doi.org/10.1021/la034197v
25. Jeuken LJC, Connell SD, Henderson PJF, Gennis RB, Evans SD, Bushby RJ (2006) Redox enzymes in tethered membranes. J Am Chem Soc 128:1711–1716. https://doi.org/10.1021/ja056972u

26. Cassier T, Lowack K, Decher G (1998) Layer-by-layer assembled protein/polymer hybrid films: nanoconstruction via specific recognition. Supramol Sci 5:309–315. https://doi.org/10.1016/S0968-5677(98)00024-8
27. Calvo EJ, Battaglini F, Danilowicz C, Wolosiuk A, Otero M (2000) Layer-by-layer electrostatic deposition of biomolecules on surfaces for molecular recognition, redox mediation and signal generation. Faraday Discuss 116:47–65. https://doi.org/10.1039/B001665I
28. Shervedani RK, Mehrjardi AH, Zamiri N (2006) A novel method for glucose determination based on electrochemical impedance spectroscopy using glucose oxidase self-assembled biosensor. Bioelectrochemistry 69:201–208. https://doi.org/10.1016/j.bioelechem.2006.01.003
29. Ye J-S, Ottova A, Tien HT, Sheu F-S (2003) Nanostructured platinum-lipid bilayer composite as biosensor. Bioelectrochemistry 59:65–72. https://doi.org/10.1016/S1567-5394(03)00003-3
30. Wang H, Ohnuki H, Endo H, Izumi M (2015) Impedimetric and amperometric bifunctional glucose biosensor based on hybrid organic–inorganic thin films. Bioelectrochemistry 101:1–7. https://doi.org/10.1016/j.bioelechem.2014.06.007
31. Voitechovič E, Bratov A, Abramova N, Razumienė J, Kirsanov D, Legin A, Lakshmi D, Piletsky S, Whitcombe M, Ivanova-Mitseva PK (2015) Development of label-free impedimetric platform based on new conductive polyaniline polymer and three-dimensional interdigitated electrode array for biosensor applications. Electrochim Acta 173:59–66. https://doi.org/10.1016/j.electacta.2015.05.011
32. Sarauli D, Xu C, Dietzel B, Schulz B, Lisdat F (2014) A multilayered sulfonated polyaniline network with entrapped pyrroloquinoline quinone-dependent glucose dehydrogenase: tunable direct bioelectrocatalysis. J Mater Chem B 2:3196–3203. https://doi.org/10.1039/C4TB00336E
33. Sarauli D, Borowski A, Peters K, Schulz B, Fattakhova-Rohlfing D, Leimkühler S, Lisdat F (2016) Investigation of the pH-dependent impact of sulfonated polyaniline on bioelectrocatalytic activity of xanthine dehydrogenase. ACS Catal 6:7152–7159. https://doi.org/10.1021/acscatal.6b02011
34. Alfonta L, Katz E, Willner I (2000) Sensing of acetylcholine by a tricomponent-enzyme layered electrode using faradaic impedance spectroscopy, cyclic voltammetry, and microgravimetric quartz crystal microbalance transduction methods. Anal Chem 72:927–935. https://doi.org/10.1021/ac990439d
35. Naumann R, Schmidt EK, Jonczyk A, Fendler K, Kadenbach B, Liebermann T, Offenhäusser A, Knoll W (1999) The peptide-tethered lipid membrane as a biomimetic system to incorporate cytochrome c oxidase in a functionally active form. Biosens Bioelectron 14:651–662. https://doi.org/10.1016/S0956-5663(99)00036-6
36. Schasfoort RBM, Niedziela T (1994) Detection of inhibitory compounds of acetylcholine esterase with a novel ion responding impedance sensor (IRIS). Sensors Actuators B 18:175–177. https://doi.org/10.1016/0925-4005(94)87079-9
37. Tong Y, Han X, Song Y, Jiang J, Wang E (2003) Characterization and property of DNA incorporated bilayer lipid membranes. Biophys Chem 105:1–9. https://doi.org/10.1016/S0301-4622(02)00336-8
38. Wilkop T, Xu D, Cheng Q (2007) Characterization of pore formation by streptolysin O on supported lipid membranes by impedance spectroscopy and surface plasmon resonance spectroscopy. Langmuir 23:1403–1409. https://doi.org/10.1021/la0625502
39. Sumner C, Sabot A, Turner K, Krause S (2000) A transducer based on enzyme-induced degradation of thin polymer films monitored by surface plasmon resonance. Anal Chem 72:5225–5232. https://doi.org/10.1021/ac000411y
40. Saum AGE, Cumming RH, Rowell FJ (1998) Use of substrate coated electrodes and AC impedance spectroscopy for the detection of enzyme activity. Biosens Bioelectron 13:511–518. https://doi.org/10.1016/S0956-5663(97)00129-2
41. McNeil CJ, Athey D, Ball M, Ho WO, Krause S, Armstrong RD, Des Wright J, Rawson K (1995) Electrochemical sensors based on impedance measurement of enzyme-catalyzed

polymer dissolution: theory and applications. Anal Chem 67:3928–3935. https://doi.org/10.1021/ac00117a018
42. Sheppard NF, Mears DJ, Guiseppi-Elie A (1996) Model of an immobilized enzyme conductimetric urea biosensor. Biosens Bioelectron 11:967–979. https://doi.org/10.1016/0956-5663(96)87656-1
43. Ho WO, Krause S, McNeil CJ, Pritchard JA, Armstrong RD, Athey D, Rawson K (1999) Electrochemical sensor for measurement of urea and creatinine in serum based on ac impedance measurement of enzyme-catalyzed polymer transformation. Anal Chem 71:1940–1946. https://doi.org/10.1021/ac981367d
44. Gooding JJ, Hall EAH (1996) Membrane properties of acrylate bulk polymers for biosensor applications. Biosens Bioelectron 11:1031–1040. https://doi.org/10.1016/0956-5663(96)87662-7
45. Fernández-Sánchez C, McNeil CJ, Rawson K, Nilsson O (2004) Disposable noncompetitive immunosensor for free and total prostate-specific antigen based on capacitance measurement. Anal Chem 76:5649–5656. https://doi.org/10.1021/ac0494937
46. Hug TS (2003) Biophysical methods for monitoring cell-substrate interactions in drug discovery. Assay Drug Dev Technol 1:479–488. https://doi.org/10.1089/154065803322163795
47. Yotter RA, Wilson DM (2004) Sensor technologies for monitoring metabolic activity in single cells-part II: nonoptical methods and applications. IEEE Sensors J 4:412–429. https://doi.org/10.1109/JSEN.2004.830954
48. K'Owino IO, Sadik OA (2005) Impedance spectroscopy: a powerful tool for rapid biomolecular screening and cell culture monitoring. Electroanalysis 17:2101–2113. https://doi.org/10.1002/elan.200503371
49. Kyle AH, Chan CTO, Minchinton AI (1999) Characterization of three-dimensional tissue cultures using electrical impedance spectroscopy. Biophys J 76:2640–2648. https://doi.org/10.1016/S0006-3495(99)77416-3
50. Vistejnova L, Dvorakova J, Hasova M, Muthny T, Velebny V, Soucek K, Kubala L (2009) The comparison of impedance-based method of cell proliferation monitoring with commonly used metabolic-based techniques. Neuro Endocrinol Lett 30(Suppl 1):121–127
51. Ruan C, Yang L, Li Y (2002) Immunobiosensor chips for detection of *Escherichia coli* O157:H7 using electrochemical impedance spectroscopy. Anal Chem 74:4814–4820. https://doi.org/10.1021/ac025647b
52. Laczka O, Baldrich E, Muñoz FX, del Campo FJ (2008) Detection of *Escherichia coli* and *Salmonella typhimurium* using interdigitated microelectrode capacitive immunosensors: the importance of transducer geometry. Anal Chem 80:7239–7247. https://doi.org/10.1021/ac800643k
53. Susmel S, Guilbault GG, O'Sullivan CK (2003) Demonstration of labeless detection of food pathogens using electrochemical redox probe and screen printed gold electrodes. Biosens Bioelectron 18:881–889. https://doi.org/10.1016/S0956-5663(02)00214-2
54. Radke SM, Alocilja EC (2005) A high density microelectrode array biosensor for detection of *E. coli* O157:H7. Biosens Bioelectron 20:1662–1667. https://doi.org/10.1016/j.bios.2004.07.021
55. Chan KY, Ye WW, Zhang Y, Xiao LD, Leung PHM, Li Y, Yang M (2013) Ultrasensitive detection of *E. coli* O157:H7 with biofunctional magnetic bead concentration via nanoporous membrane based electrochemical immunosensor. Biosens Bioelectron 41:532–537. https://doi.org/10.1016/j.bios.2012.09.016
56. Guo X, Kulkarni A, Doepke A, Halsall HB, Iyer S, Heineman WR (2012) Carbohydrate-based label-free detection of *Escherichia coli* ORN 178 using electrochemical impedance spectroscopy. Anal Chem 84:241–246. https://doi.org/10.1021/ac202419u
57. Shabani A, Zourob M, Allain B, Marquette CA, Lawrence MF, Mandeville R (2008) Bacteriophage-modified microarrays for the direct impedimetric detection of bacteria. Anal Chem 80:9475–9482. https://doi.org/10.1021/ac801607w

58. Jönsson M, Welch K, Hamp S, Strømme M (2006) Bacteria counting with impedance spectroscopy in a micro probe station. J Phys Chem B 110:10165–10169. https://doi.org/10.1021/jp060148q
59. Wang R, Wang Y, Lassiter K, Li Y, Hargis B, Tung S, Berghman L, Bottje W (2009) Interdigitated array microelectrode based impedance immunosensor for detection of avian influenza virus H5N1. Talanta 79:159–164. https://doi.org/10.1016/j.talanta.2009.03.017
60. Fumagalli L, Esteban-Ferrer D, Cuervo A, Carrascosa JL, Gomila G (2012) Label-free identification of single dielectric nanoparticles and viruses with ultraweak polarization forces. Nat Mater 11:808–816. https://doi.org/10.1038/nmat3369
61. Bataillard P, Gardies F, Jaffrezic-Renault N, Martelet C, Colin B, Mandrand B (1988) Direct detection of immunospecies by capacitance measurements. Anal Chem 60: 2374–2379. https://doi.org/10.1021/ac00172a011
62. Berggren C, Johansson G (1997) Capacitance measurements of antibody−antigen interactions in a flow system. Anal Chem 69:3651–3657. https://doi.org/10.1021/ac970203e
63. Yoo J-S, Park S-M (2000) An electrochemical impedance measurement technique employing fourier transform. Anal Chem 72:2035–2041. https://doi.org/10.1021/ac9907540
64. Haber E, Ascher U, Oldenburg D (2004) Inversion of 3D electromagnetic data in frequency and time domain using an inexact all-at-once approach. Geophysics 69:1216–1228. https://doi.org/10.1190/1.1801938
65. Hou Y, Tlili C, Jaffrezic-Renault N, Zhang A, Martelet C, Ponsonnet L, Errachid A, Samitier J, Bausells J (2004) Study of mixed Langmuir–Blodgett films of immunoglobulin G/amphiphile and their application for immunosensor engineering. Biosens Bioelectron 20: 1126–1133. https://doi.org/10.1016/j.bios.2004.05.017
66. Jie M, Ming CY, Jing D, Cheng LS, Na LH, Jun F, Xiang CY (1999) An electrochemical impedance immunoanalytical method for detecting immunological interaction of human mammary tumor associated glycoprotein and its monoclonal antibody. Electrochem Commun 1:425–428. https://doi.org/10.1016/S1388-2481(99)00071-5
67. Pak SC, Penrose W, Hesketh PJ (2001) An ultrathin platinum film sensor to measure biomolecular binding. Biosens Bioelectron 16:371–379. https://doi.org/10.1016/S0956-5663(01)00152-X
68. Pei R, Cheng Z, Wang E, Yang X (2001) Amplification of antigen–antibody interactions based on biotin labeled protein–streptavidin network complex using impedance spectroscopy. Biosens Bioelectron 16:355–361. https://doi.org/10.1016/S0956-5663(01)00150-6
69. Hleli S, Martelet C, Abdelghani A, Burais N, Jaffrezic-Renault N (2006) Atrazine analysis using an impedimetric immunosensor based on mixed biotinylated self-assembled monolayer. Sensors Actuators B 113:711–717. https://doi.org/10.1016/j.snb.2005.07.023
70. Chen X, Wang Y, Zhou J, Yan W, Li X, Zhu J-J (2008) Electrochemical impedance immunosensor based on three-dimensionally ordered macroporous gold film. Anal Chem 80: 2133–2140. https://doi.org/10.1021/ac7021376
71. Katz E, Willner I (2003) Probing biomolecular interactions at conductive and semiconductive surfaces by impedance spectroscopy: routes to impedimetric immunosensors, DNA-sensors, and enzyme biosensors. Electroanalysis 15:913–947. https://doi.org/10.1002/elan.200390114
72. Balkenhohl T, Lisdat F (2007) An impedimetric immunosensor for the detection of autoantibodies directed against gliadins. Analyst 132:314–322. https://doi.org/10.1039/B609832K
73. Yun Y, Bange A, Heineman WR, Halsall HB, Shanov VN, Dong Z, Pixley S, Behbehani M, Jazieh A, Tu Y, Wong DKY, Bhattacharya A, Schulz MJ (2007) A nanotube array immunosensor for direct electrochemical detection of antigen–antibody binding. Sensors Actuators B 123:177–182. https://doi.org/10.1016/j.snb.2006.08.014
74. Woodhouse GE, King LG, Wieczorek L, Cornell BA (1999) Kinetics of the competitive response of receptors immobilised to ion-channels which have been incorporated into a tethered bilayer. Faraday Discuss 111:247–258. https://doi.org/10.1039/A809608B

75. Cornell BA, Braach-Maksvytis VLB, King LG, Osman PDJ, Raguse B, Wieczorek L, Pace RJ (1997) A biosensor that uses ion-channel switches. Nature 387:580–583. https://doi.org/10.1038/42432
76. Sargent A, Loi T, Gal S, Sadik OA (1999) The electrochemistry of antibody-modified conducting polymer electrodes. J Electroanal Chem 470:144–156. https://doi.org/10.1016/S0022-0728(99)00231-4
77. Li CM, Sun CQ, Song S, Choong VE, Maracas G, Zhang XJ (2005) Impedance labelless detection-based polypyrrole DNA biosensor. Front Biosci 10:180–186. https://doi.org/10.2741/1519
78. Ramanavicius A, Finkelsteinas A, Cesiulis H, Ramanaviciene A (2010) Electrochemical impedance spectroscopy of polypyrrole based electrochemical immunosensor. Bioelectrochemistry 79:11–16. https://doi.org/10.1016/j.bioelechem.2009.09.013
79. Ouerghi O, Touhami A, Jaffrezic-Renault N, Martelet C, Ouada HB, Cosnier S (2002) Impedimetric immunosensor using avidin–biotin for antibody immobilization. Bioelectrochemistry 56:131–133. https://doi.org/10.1016/S1567-5394(02)00029-4
80. Cheong WJ, Yang SH, Ali F (2013) Molecular imprinted polymers for separation science: a review of reviews. J Sep Sci 36:609–628. https://doi.org/10.1002/jssc.201200784
81. Scheller FW, Yarmana A, Gyurcsányic RE (2015) Electrochemical approaches for molecular surface imprinting of polymers toward fully synthetic receptors for selective recognition of proteins. In: Rodríguez-Hernández J, Cortajarena AL (eds) Design of polymeric platforms for selective biorecognition. Springer, Berlin, pp 347–356
82. Liu X, Li C, Wang C, Li T, Hu S (2006) The preparation of molecularly imprinted poly(o-phenylenediamine) membranes for the specific O,O-dimethyl-α-hydroxylphenyl phosphonate sensor and its characterization by AC impedance and cyclic voltammetry. J Appl Polym Sci 101:2222–2227. https://doi.org/10.1002/app.23514
83. Idil N, Hedström M, Denizli A, Mattiasson B (2017) Whole cell based microcontact imprinted capacitive biosensor for the detection of Escherichia coli. Biosen Bioelectron 87:807–815. https://doi.org/10.1016/j.bios.2016.08.096
84. Thoelen R, Vansweevelt R, Duchateau J, Horemans F, D'Haen J, Lutsen L, Vanderzande D, Ameloot M, van de Ven M, Cleij TJ, Wagner P (2008) A MIP-based impedimetric sensor for the detection of low-MW molecules. Biosens Bioelectron 23:913–918. https://doi.org/10.1016/j.bios.2007.08.020
85. Huang J, Wei Z, Chen J (2008) Molecular imprinted polypyrrole nanowires for chiral amino acid recognition. Sensors Actuators B 134:573–578. https://doi.org/10.1016/j.snb.2008.05.038
86. Cai D, Ren L, Zhao H, Xu C, Zhang L, Yu Y, Wang H, Lan Y, Roberts MF, Chuang JH, Naughton MJ, Ren Z, Chiles TC (2010) A molecular-imprint nanosensor for ultrasensitive detection of proteins. Nat Nanotechnol 5:597–601. https://doi.org/10.1038/nnano.2010.114
87. Jetzschmann KJ, Jágerszki G, Dechtrirat D, Yarman A, Gajovic-Eichelmann N, Gilsing H-D, Schulz B, Gyurcsányi RE, Scheller FW (2015) Vectorially imprinted hybrid nanofilm for acetylcholinesterase recognition. Adv Funct Mater 25:5178–5183. https://doi.org/10.1002/adfm.201501900
88. Lieberzeit PA, Dickert FL (2008) Rapid bioanalysis with chemical sensors: novel strategies for devices and artificial recognition membranes. Anal Bioanal Chem 391:1629–1639. https://doi.org/10.1007/s00216-008-1909-z
89. Lucarelli F, Tombelli S, Minunni M, Marrazza G, Mascini M (2008) Electrochemical and piezoelectric DNA biosensors for hybridisation detection. Anal Chim Acta 609:139–159. https://doi.org/10.1016/j.aca.2007.12.035
90. Kleo K, Kapp A, Ascher L, Lisdat F (2011) Detection of vaccinia virus DNA by quartz crystal microbalance. Anal Biochem 418:260–266. https://doi.org/10.1016/j.ab.2011.07.016
91. Willets KA, Van Duyne RP (2007) Localized surface plasmon resonance spectroscopy and sensing. Annu Rev Phys Chem 58:267–297. https://doi.org/10.1146/annurev.physchem.58.032806.104607

92. Homola J (2008) Surface plasmon resonance sensors for detection of chemical and biological species. Chem Rev 108:462–493. https://doi.org/10.1021/cr068107d
93. Piunno PAE, Krull UJ, Hudson RHE, Damha MJ, Cohen H (1995) Fiber-optic DNA sensor for fluorometric nucleic acid determination. Anal Chem 67:2635–2643. https://doi.org/10.1021/ac00111a022
94. Ho H-A, Leclerc M (2004) Optical sensors based on hybrid aptamer/conjugated polymer complexes. J Am Chem Soc 126:1384–1387. https://doi.org/10.1021/ja037289f
95. Drummond TG, Hill MG, Barton JK (2003) Electrochemical DNA sensors. Nat Biotechnol 21:1192–1199. https://doi.org/10.1038/nbt873
96. Lisdat F, Schäfer D (2008) The use of electrochemical impedance spectroscopy for biosensing. Anal Bioanal Chem 391:1555. https://doi.org/10.1007/s00216-008-1970-7
97. Paleček E, Bartošík M (2012) Electrochemistry of nucleic acids. Chem Rev 112:3427–3481. https://doi.org/10.1021/cr200303p
98. Kelley SO, Boon EM, Barton JK, Jackson NM, Hill MG (1999) Single-base mismatch detection based on charge transduction through DNA. Nucleic Acids Res 27:4830–4837. https://doi.org/10.1093/nar/27.24.4830
99. Pänke O, Kirbs A, Lisdat F (2007) Voltammetric detection of single base-pair mismatches and quantification of label-free target ssDNA using a competitive binding assay. Biosens Bioelectron 22:2656–2662. https://doi.org/10.1016/j.bios.2006.10.033
100. Paleček E, Fojta M, Tomschik M, Wang J (1998) Electrochemical biosensors for DNA hybridization and DNA damage. Biosens Bioelectron 13:621–628. https://doi.org/10.1016/S0956-5663(98)00017-7
101. Wang J, Rivas G, Fernandes JR, Lopez Paz JL, Jiang M, Waymire R (1998) Indicator-free electrochemical DNA hybridization biosensor. Anal Chim Acta 375:197–203. https://doi.org/10.1016/S0003-2670(98)00503-0
102. Hasoň S, Dvořák J, Jelen F, Vetterl V (2002) Interaction of DNA with echinomycin at the mercury electrode surface as detected by impedance and chronopotentiometric measurements. Talanta 56:905–913. https://doi.org/10.1016/S0039-9140(01)00664-6
103. Strašák L, Dvořák J, Hasoň S, Vetterl V (2002) Electrochemical impedance spectroscopy of polynucleotide adsorption. Bioelectrochemistry 56:37–41. https://doi.org/10.1016/S1567-5394(02)00019-1
104. Fixe F, Branz HM, Louro N, Chu V, Prazeres DMF, Conde JP (2004) Immobilization and hybridization by single sub-millisecond electric field pulses, for pixel-addressed DNA microarrays. Biosens Bioelectron 19:1591–1597. https://doi.org/10.1016/j.bios.2003.12.012
105. Jambrec D, Gebala M, La Mantia F, Schuhmann W (2015) Potential-assisted DNA immobilization as a prerequisite for fast and controlled formation of DNA monolayers. Angew Chem Int Ed 54:15064–15068. https://doi.org/10.1002/anie.201506672
106. Kara P, de la Escosura-Muñiz A, Maltez-da Costa M, Guix M, Ozsoz M, Merkoçi A (2010) Aptamers based electrochemical biosensor for protein detection using carbon nanotubes platforms. Biosens Bioelectron 26:1715–1718. https://doi.org/10.1016/j.bios.2010.07.090
107. Benvidi A, Rajabzadeh N, Mazloum-Ardakani M, Heidari MM (2015) Comparison of impedimetric detection of DNA hybridization on chemically and electrochemically functionalized multi-wall carbon nanotubes modified electrode. Sensors Actuators B 207(Part A): 673–682. https://doi.org/10.1016/j.snb.2014.10.043
108. Poh HL, Bonanni A, Pumera M (2012) Nanoporous carbon as a sensing platform for DNA detection: the use of impedance spectroscopy for hairpin-DNA based assay. RSC Adv 2: 1021–1024. https://doi.org/10.1039/C1RA00812A
109. Gu H, di Su X, Loh KP (2005) Electrochemical impedance sensing of DNA hybridization on conducting polymer film-modified diamond. J Phys Chem B 109:13611–13618. https://doi.org/10.1021/jp050625p
110. Erdem A, Congur G (2013) Impedimetric detection of in situ interaction between anti-cancer drug bleomycin and DNA. Int J Biol Macromol 61:295–301. https://doi.org/10.1016/j.ijbiomac.2013.07.012

111. Hayat A, Sassolas A, Marty J-L, Radi A-E (2013) Highly sensitive ochratoxin A impedimetric aptasensor based on the immobilization of azido-aptamer onto electrografted binary film via click chemistry. Talanta 103:14–19. https://doi.org/10.1016/j.talanta.2012.09.048
112. Kafka J, Pänke O, Abendroth B, Lisdat F (2008) A label-free DNA sensor based on impedance spectroscopy. Electrochim Acta 53:7467–7474. https://doi.org/10.1016/j.electacta.2008.01.031
113. Bonanni A, Pumera M, Miyahara Y (2010) Rapid, sensitive, and label-free impedimetric detection of a single-nucleotide polymorphism correlated to kidney disease. Anal Chem 82:3772–3779. https://doi.org/10.1021/ac100165q
114. Witte C, Lisdat F (2011) Direct detection of DNA and DNA-ligand interaction by impedance spectroscopy. Electroanalysis 23:339–346. https://doi.org/10.1002/elan.201000410
115. Tersch C, Lisdat F (2011) Label-free detection of protein–DNA interactions using electrochemical impedance spectroscopy. Electrochim Acta 56:7673–7679. https://doi.org/10.1016/j.electacta.2011.06.063
116. Gębala M, Schuhmann W (2010) Controlled orientation of DNA in a binary SAM as a key for the successful determination of DNA hybridization by means of electrochemical impedance spectroscopy. ChemPhysChem 11:2887–2895. https://doi.org/10.1002/cphc.201000210
117. Bogomolova A, Komarova E, Reber K, Gerasimov T, Yavuz O, Bhatt S, Aldissi M (2009) Challenges of electrochemical impedance spectroscopy in protein biosensing. Anal Chem 81:3944–3949. https://doi.org/10.1021/ac9002358
118. Degefa TH, Kwak J (2008) Electrochemical impedance sensing of DNA at PNA self assembled monolayer. J Electroanal Chem 612:37–41. https://doi.org/10.1016/j.jelechem.2007.09.004
119. Keighley SD, Estrela P, Li P, Migliorato P (2008) Optimization of label-free DNA detection with electrochemical impedance spectroscopy using PNA probes. Biosens Bioelectron 24:906–911. https://doi.org/10.1016/j.bios.2008.07.041
120. Revenga-Parra M, García T, Pariente F, Lorenzo E, Alonso C (2011) Effects of ionic strength and probe DNA length on the electrochemical impedance spectroscopic response of biosensors. Electroanalysis 23:100–107. https://doi.org/10.1002/elan.201000365
121. Liu J, Tian S, Nielsen PE, Knoll W (2005) In situ hybridization of PNA/DNA studied label-free by electrochemical impedance spectroscopy. Chem Commun 23:2969–2971. https://doi.org/10.1039/B419425J
122. Thipmanee O, Numnuam A, Limbut W, Buranachai C, Kanatharana P, Vilaivan T, Hirankarn N, Thavarungkul P (2016) Enhancing capacitive DNA biosensor performance by target overhang with application on screening test of HLA-B*58:01 and HLA-B*57:01 genes. Biosens Bioelectron 82:99–104. https://doi.org/10.1016/j.bios.2016.03.065
123. Shamsi MH, Kraatz H-B (2011) The effects of oligonucleotide overhangs on the surface hybridization in DNA films: an impedance study. Analyst 136:3107–3112. https://doi.org/10.1039/C1AN15253J
124. Riedel M, Kartchemnik J, Schöning MJ, Lisdat F (2014) Impedimetric DNA detection – steps forward to sensorial application. Anal Chem 86:7867–7874. https://doi.org/10.1021/ac501800q
125. Corrigan DK, Schulze H, McDermott RA, Schmüser I, Henihan G, Henry JB, Bachmann TT, Mount AR (2014) Improving electrochemical biosensor performance by understanding the influence of target DNA length on assay sensitivity. J Electroanal Chem 732:25–29. https://doi.org/10.1016/j.jelechem.2014.08.026
126. Corrigan DK, Schulze H, Henihan G, Ciani I, Giraud G, Terry JG, Walton AJ, Pethig R, Ghazal P, Crain J, Campbell CJ, Mount AR, Bachmann TT (2012) Impedimetric detection of single-stranded PCR products derived from methicillin resistant *Staphylococcus aureus* (MRSA) isolates. Biosens Bioelectron 34:178–184. https://doi.org/10.1016/j.bios.2012.01.040
127. Aydemir N, McArdle H, Patel S, Whitford W, Evans CW, Travas-Sejdic J, Williams DE (2015) A label-free, sensitive, real-time, semiquantitative electrochemical measurement method for DNA polymerase amplification (ePCR). Anal Chem 87:5189–5197. https://doi.org/10.1021/acs.analchem.5b00079

128. Henihan G, Schulze H, Corrigan DK, Giraud G, Terry JG, Hardie A, Campbell CJ, Walton AJ, Crain J, Pethig R, Templeton KE, Mount AR, Bachmann TT (2016) Label- and amplification-free electrochemical detection of bacterial ribosomal RNA. Biosens Bioelectron 81:487–494. https://doi.org/10.1016/j.bios.2016.03.037
129. Corrigan DK, Schulze H, Henihan G, Hardie A, Ciani I, Giraud G, Terry JG, Walton AJ, Pethig R, Ghazal P, Crain J, Campbell CJ, Templeton KE, Mount AR, Bachmann TT (2013) Development of a PCR-free electrochemical point of care test for clinical detection of methicillin resistant *Staphylococcus aureus* (MRSA). Analyst 138:6997–7005. https://doi.org/10.1039/C3AN01319G
130. Fan C, Plaxco KW, Heeger AJ (2003) Electrochemical interrogation of conformational changes as a reagentless method for the sequence-specific detection of DNA. Proc Natl Acad Sci 100:9134–9137. https://doi.org/10.1073/pnas.1633515100
131. Korri-Youssoufi H, Garnier F, Srivastava P, Godillot P, Yassar A (1997) Toward bioelectronics: specific DNA recognition based on an oligonucleotide-functionalized polypyrrole. J Am Chem Soc 119:7388–7389. https://doi.org/10.1021/ja964261d
132. Wang J, Jiang M, Fortes A, Mukherjee B (1999) New label-free DNA recognition based on doping nucleic-acid probes within conducting polymer films. Anal Chim Acta 402:7–12. https://doi.org/10.1016/S0003-2670(99)00531-0
133. Baur J, Gondran C, Holzinger M, Defrancq E, Perrot H, Cosnier S (2010) Label-free femtomolar detection of target DNA by impedimetric DNA sensor based on Poly(pyrrole-nitrilotriacetic acid) film. Anal Chem 82:1066–1072. https://doi.org/10.1021/ac9024329
134. Gautier C, Cougnon C, Pilard J-F, Casse N (2006) Label-free detection of DNA hybridization based on EIS investigation of conducting properties of functionalized polythiophene matrix. J Electroanal Chem 587:276–283. https://doi.org/10.1016/j.jelechem.2005.11.021
135. Piro B, Haccoun J, Pham MC, Tran LD, Rubin A, Perrot H, Gabrielli C (2005) Study of the DNA hybridization transduction behavior of a quinone-containing electroactive polymer by cyclic voltammetry and electrochemical impedance spectroscopy. J Electroanal Chem 577:155–165. https://doi.org/10.1016/j.jelechem.2004.12.002
136. Li C-Z, Liu Y, Luong JHT (2005) Impedance sensing of DNA binding drugs using gold substrates modified with gold nanoparticles. Anal Chem 77:478–485. https://doi.org/10.1021/ac048672l
137. Regan EM, Hallett AJ, Wong LCC, Saeed IQ, Langdon-Jones EE, Buurma NJ, Pope SJA, Estrela P (2014) A novel cobalt complex for enhancing amperometric and impedimetric DNA detection. Electrochim Acta 128:10–15. https://doi.org/10.1016/j.electacta.2013.10.028
138. Jambrec D, Haddad R, Lauks A, Gebala M, Schuhmann W, Kokoschka M (2016) DNA intercalators for detection of DNA hybridisation: SCS(MI)–MP2 calculations and electrochemical impedance spectroscopy. ChemPlusChem 81:604–612. https://doi.org/10.1002/cplu.201600173
139. Gebala M, Stoica L, Neugebauer S, Schuhmann W (2009) Label-free detection of DNA hybridization in presence of intercalators using electrochemical impedance spectroscopy. Electroanalysis 21:325–331. https://doi.org/10.1002/elan.200804388
140. Yan F, Sadik OA (2001) Enzyme-modulated cleavage of dsDNA for supramolecular design of biosensors. Anal Chem 73:5272–5280. https://doi.org/10.1021/ac015516v
141. Bin X, Kraatz H-B (2009) Interaction of metal ions and DNA films on gold surfaces: an electrochemical impedance study. Analyst 134:1309–1313. https://doi.org/10.1039/B821670C
142. Li C, Li X, Liu X, Kraatz H-B (2010) Exploiting the interaction of metal ions and peptide nucleic acids−DNA duplexes for the detection of a single nucleotide mismatch by electrochemical impedance spectroscopy. Anal Chem 82:1166–1169. https://doi.org/10.1021/ac902813y
143. Lin Z, Li X, Kraatz H-B (2011) Impedimetric immobilized DNA-based sensor for simultaneous detection of Pb^{2+}, Ag^{+}, and Hg^{2+}. Anal Chem 83:6896–6901. https://doi.org/10.1021/ac2014096

144. Liu G, Yuan Y, Wei S, Zhang D (2014) Impedimetric DNA-based biosensor for silver ions detection with Hemin/G-Quadruplex nanowire as enhancer. Electroanalysis 26:2732–2738. https://doi.org/10.1002/elan.201400439
145. Long Y-T, Li C-Z, Sutherland TC, Kraatz H-B, Lee JS (2004) Electrochemical detection of single-nucleotide mismatches: application of M-DNA. Anal Chem 76:4059–4065. https://doi.org/10.1021/ac049482d
146. Shi L, Liang G, Li X, Liu X (2012) Impedimetric DNA sensor for detection of Hg^{2+} and Pb^{2+}. Anal Methods 4:1036–1040. https://doi.org/10.1039/C2AY05758A
147. Xu M, Gao Z, Wei Q, Chen G, Tang D (2015) Hemin/G-quadruplex-based DNAzyme concatamers for in situ amplified impedimetric sensing of copper(II) ion coupling with DNAzyme-catalyzed precipitation strategy. Biosens Bioelectron 74:1–7. https://doi.org/10.1016/j.bios.2015.05.056
148. Pavlov V, Willner I, Dishon A, Kotler M (2004) Amplified detection of telomerase activity using electrochemical and quartz crystal microbalance measurements. Biosens Bioelectron 20:1011–1021. https://doi.org/10.1016/j.bios.2004.06.020
149. Wilner OI, Guidotti C, Wieckowska A, Gill R, Willner I (2008) Probing kinase activities by electrochemistry, contact-angle measurements, and molecular-force interactions. Chem Eur J 14:7774–7781. https://doi.org/10.1002/chem.200800765
150. Jin Y (2009) Label-free monitoring of site-specific DNA cleavage by EcoRI endonuclease using cyclic voltammetry and electrochemical impedance. Anal Chim Acta 634:44–48. https://doi.org/10.1016/j.aca.2008.12.005
151. Wang H-B, Zhang H-D, Xu S-P, Gan T, Huang K-J, Liu Y-M (2014) A sensitive and label-free electrochemical impedance biosensor for protein detection based on terminal protection of small molecule-linked DNA. Sensors Actuators B 194:478–483. https://doi.org/10.1016/j.snb.2014.01.002
152. Ni X, Castanares M, Mukherjee A, Lupold SE (2011) Nucleic acid aptamers: clinical applications and promising new horizons. Curr Med Chem 18:4206–4214. https://doi.org/10.2174/092986711797189600
153. Zhou W, Huang P-JJ, Ding J, Liu J (2014) Aptamer-based biosensors for biomedical diagnostics. Analyst 139:2627–2640. https://doi.org/10.1039/C4AN00132J
154. Stoltenburg R, Reinemann C, Strehlitz B (2007) SELEX – a (r)evolutionary method to generate high-affinity nucleic acid ligands. Biomol Eng 24:381–403. https://doi.org/10.1016/j.bioeng.2007.06.001
155. White RJ, Phares N, Lubin AA, Xiao Y, Plaxco KW (2008) Optimization of electrochemical aptamer-based sensors via optimization of probe packing density and surface chemistry. Langmuir 24:10513–10518. https://doi.org/10.1021/la800801v
156. Zhang D-W, Zhang F-T, Cui Y-R, Deng Q-P, Krause S, Zhou Y-L, Zhang X-X (2012) A label-free aptasensor for the sensitive and specific detection of cocaine using supramolecular aptamer fragments/target complex by electrochemical impedance spectroscopy. Talanta 92:65–71. https://doi.org/10.1016/j.talanta.2012.01.049
157. Castillo G, Lamberti I, Mosiello L, Hianik T (2012) Impedimetric DNA aptasensor for sensitive detection of ochratoxin A in food. Electroanalysis 24:512–520. https://doi.org/10.1002/elan.201100485
158. Contreras Jiménez G, Eissa S, Ng A, Alhadrami H, Zourob M, Siaj M (2015) Aptamer-based label-free impedimetric biosensor for detection of progesterone. Anal Chem 87:1075–1082. https://doi.org/10.1021/ac503639s
159. González-Fernández E, de-los Santos-Álvarez N, Lobo-Castañón MJ, Miranda-Ordieres AJ, Tuñón-Blanco P (2011) Impedimetric aptasensor for tobramycin detection in human serum. Biosens Bioelectron 26:2354–2360. https://doi.org/10.1016/j.bios.2010.10.011
160. de-los Santos-Álvarez N, Lobo-Castañón MJ, Miranda-Ordieres AJ, Tuñón-Blanco P (2007) Modified-RNA aptamer-based sensor for competitive impedimetric assay of neomycin B. J Am Chem Soc 129:3808–3809. https://doi.org/10.1021/ja0689482

161. Xu H, Gorgy K, Gondran C, Le Goff A, Spinelli N, Lopez C, Defrancq E, Cosnier S (2013) Label-free impedimetric thrombin sensor based on poly(pyrrole-nitrilotriacetic acid)-aptamer film. Biosens Bioelectron 41:90–95. https://doi.org/10.1016/j.bios.2012.07.044
162. Radi A-E, Acero Sánchez JL, Baldrich E, O'Sullivan CK (2005) Reusable impedimetric aptasensor. Anal Chem 77:6320–6323. https://doi.org/10.1021/ac0505775
163. Ocaña C, Arcay E, del Valle M (2014) Label-free impedimetric aptasensor based on epoxy-graphite electrode for the recognition of cytochrome c. Sensors Actuators B 191:860–865. https://doi.org/10.1016/j.snb.2013.10.040
164. Queirós RB, de-los Santos-Álvarez N, Noronha JP, Sales MGF (2013) A label-free DNA aptamer-based impedance biosensor for the detection of *E. coli* outer membrane proteins. Sensors Actuators B 181:766–772. https://doi.org/10.1016/j.snb.2013.01.062
165. Erdem A, Congur G (2014) Dendrimer modified 8-channel screen-printed electrochemical array system for impedimetric detection of activated protein C. Sensors Actuators B 196: 168–174. https://doi.org/10.1016/j.snb.2014.01.103
166. Labib M, Zamay AS, Muharemagic D, Chechik AV, Bell JC, Berezovski MV (2012) Aptamer-based viability impedimetric sensor for viruses. Anal Chem 84:1813–1816. https://doi.org/10.1021/ac203412m
167. Labib M, Zamay AS, Kolovskaya OS, Reshetneva IT, Zamay GS, Kibbee RJ, Sattar SA, Zamay TN, Berezovski MV (2012) Aptamer-based impedimetric sensor for bacterial typing. Anal Chem 84:8114–8117. https://doi.org/10.1021/ac302217u
168. Eldefrawi ME, Sherby SM, Andreou AG, Mansour NA, Annau Z, Blum NA, Valdes JJ (1988) Acetylcholine receptor-based biosensor. Anal Lett 21:1665–1680. https://doi.org/10.1080/00032718808066519
169. Patolsky F, Lichtenstein A, Willner I (2000) Electrochemical transduction of liposome-amplified DNA sensing. Angew Chem Int Ed 39:940–943. https://doi.org/10.1002/(SICI)1521-3773(20000303)39:5<940::AID-ANIE940>3.0.CO;2-Y
170. Patolsky F, Lichtenstein A, Willner I (2001) Electronic transduction of DNA sensing processes on surfaces: amplification of DNA detection and analysis of single-base mismatches by tagged liposomes. J Am Chem Soc 123:5194–5205. https://doi.org/10.1021/ja0036256
171. Zhu N, Gao H, Gu Y, Xu Q, He P, Fang Y (2009) PAMAM dendrimer-enhanced DNA biosensors based on electrochemical impedance spectroscopy. Analyst 134:860–866. https://doi.org/10.1039/B815488K
172. Bonanni A, Esplandiu MJ, del Valle M (2008) Signal amplification for impedimetric genosensing using gold-streptavidin nanoparticles. Electrochim Acta 53:4022–4029. https://doi.org/10.1016/j.electacta.2007.11.030
173. Patolsky F, Ranjit KT, Lichtenstein A, Willner I (2000) Dendritic amplification of DNA analysis by oligonucleotide-functionalized Au-nanoparticles. Chem Commun 12: 1025–1026. https://doi.org/10.1039/B002221G
174. Liu X, Qin Y, Deng C, Xiang J, Li Y (2015) A simple and sensitive impedimetric aptasensor for the detection of tumor markers based on gold nanoparticles signal amplification. Talanta 132:150–154. https://doi.org/10.1016/j.talanta.2014.08.072
175. Deng C, Chen J, Nie Z, Wang M, Chu X, Chen X, Xiao X, Lei C, Yao S (2009) Impedimetric aptasensor with femtomolar sensitivity based on the enlargement of surface-charged gold nanoparticles. Anal Chem 81:739–745. https://doi.org/10.1021/ac800958a
176. Wang W, Yuan X, Zhang W, Gao Q, Qi H, Zhang C (2012) Cascade signal amplification for ultra-sensitive impedimetric detection of DNA hybridization using a hairpin DNA as probe. Electrochim Acta 78:377–383. https://doi.org/10.1016/j.electacta.2012.06.007
177. Peng H, Soeller C, Cannell MB, Bowmaker GA, Cooney RP, Travas-Sejdic J (2006) Electrochemical detection of DNA hybridization amplified by nanoparticles. Biosens Bioelectron 21:1727–1736. https://doi.org/10.1016/j.bios.2005.08.011
178. Zhou N, Yang T, Jiang C, Du M, Jiao K (2009) Highly sensitive electrochemical impedance spectroscopic detection of DNA hybridization based on Aunano–CNT/PANnano films. Talanta 77:1021–1026. https://doi.org/10.1016/j.talanta.2008.07.058

179. Jiang L, Qian J, Yang X, Yan Y, Liu Q, Wang K, Wang K (2014) Amplified impedimetric aptasensor based on gold nanoparticles covalently bound graphene sheet for the picomolar detection of ochratoxin A. Anal Chim Acta 806:128–135. https://doi.org/10.1016/j.aca.2013.11.003
180. Gao Q, Zhang W, Guo Y, Qi H, Zhang C (2011) Highly sensitive impedimetric sensing of DNA hybridization based on the target DNA-induced displacement of gold nanoparticles attached to ssDNA probe. Electrochem Commun 13:335–337. https://doi.org/10.1016/j.elecom.2011.01.018
181. Yang Y, Li C, Yin L, Liu M, Wang Z, Shu Y, Li G (2014) Enhanced charge transfer by gold nanoparticle at DNA modified electrode and its application to label-free DNA detection. ACS Appl Mater Interfaces 6:7579–7584. https://doi.org/10.1021/am500912m
182. Bresler HS, Lenkevich MJ, Murdock JF, Newman AL, Roblin RO (1992) Application of capacitive affinity biosensors. Biosensor design and application. American Chemical Society, Washington, pp 89–104
183. Patolsky F, Katz E, Bardea A, Willner I (1999) Enzyme-linked amplified electrochemical sensing of oligonucleotide−DNA interactions by means of the precipitation of an insoluble product and using impedance spectroscopy. Langmuir 15:3703–3706. https://doi.org/10.1021/la981682v
184. Bardea A, Katz E, Willner I (2000) Probing antigen–antibody interactions on electrode supports by the biocatalyzed precipitation of an insoluble product. Electroanalysis 12:1097–1106. https://doi.org/10.1002/1521-4109(200010)12:14<1097::AID-ELAN1097>3.0.CO;2-X
185. Alfonta L, Singh AK, Willner I (2001) Liposomes labeled with biotin and horseradish peroxidase: a probe for the enhanced amplification of antigen−antibody or oligonucleotide−DNA sensing processes by the precipitation of an insoluble product on electrodes. Anal Chem 73:91–102. https://doi.org/10.1021/ac000819v
186. Yoon HC, Yang H, Kim YT (2002) Biocatalytic precipitation induced by an affinity reaction on dendrimer-activated surfaces for the electrochemical signaling from immunosensors. Analyst 127:1082–1087. https://doi.org/10.1039/B203299F
187. Zhou X, Xue S, Jing P, Xu W (2016) A sensitive impedimetric platform biosensing protein: insoluble precipitates based on the biocatalysis of manganese(III) meso-tetrakis (4-N-methylpyridiniumyl)-porphyrinin in HCR-assisted dsDNA. Biosens Bioelectron 86:656–663. https://doi.org/10.1016/j.bios.2016.07.065
188. Patolsky F, Lichtenstein A, Willner I (2001) Detection of single-base DNA mutations by enzyme-amplified electronic transduction. Nat Biotechnol 19:253–257. https://doi.org/10.1038/85704
189. Lucarelli F, Marrazza G, Mascini M (2005) Enzyme-based impedimetric detection of PCR products using oligonucleotide-modified screen-printed gold electrodes. Biosens Bioelectron 20:2001–2009. https://doi.org/10.1016/j.bios.2004.08.025
190. Chen Y, Jiang B, Xiang Y, Chai Y, Yuan R (2011) Target recycling amplification for sensitive and label-free impedimetric genosensing based on hairpin DNA and graphene/Au nanocomposites. Chem Commun 47:12798–12800. https://doi.org/10.1039/C1CC14902D
191. Evanko D (2004) Hybridization chain reaction. Nat Methods 1:186–187. https://doi.org/10.1038/nmeth1204-186a
192. Li A, Yang F, Ma Y, Yang X (2007) Electrochemical impedance detection of DNA hybridization based on dendrimer modified electrode. Biosens Bioelectron 22:1716–1722. https://doi.org/10.1016/j.bios.2006.07.033
193. Erdem A, Congur G (2014) Dendrimer enriched single-use aptasensor for impedimetric detection of activated protein C. Colloids Surf B Biointerfaces 117:338–345. https://doi.org/10.1016/j.colsurfb.2014.03.003
194. Fu Y, Yuan R, Xu L, Chai Y, Zhong X, Tang D (2005) Indicator free DNA hybridization detection via EIS based on self-assembled gold nanoparticles and bilayer two-dimensional 3-mercaptopropyltrimethoxysilane onto a gold substrate. Biochem Eng J 23:37–44. https://doi.org/10.1016/j.bej.2004.10.008

195. Ensafi AA, Taei M, Rahmani HR, Khayamian T (2011) Sensitive DNA impedance biosensor for detection of cancer, chronic lymphocytic leukemia, based on gold nanoparticles/gold modified electrode. Electrochim Acta 56:8176–8183. https://doi.org/10.1016/j.electacta.2011.05.124
196. Chen C-C, Lai Z-L, Wang G-J, Wu C-Y (2016) Polymerase chain reaction-free detection of hepatitis B virus DNA using a nanostructured impedance biosensor. Biosens Bioelectron 77:603–608. https://doi.org/10.1016/j.bios.2015.10.028
197. Van Gerwen P, Laureyn W, Laureys W, Huyberechts G, Op De Beeck M, Baert K, Suls J, Sansen W, Jacobs P, Hermans L, Mertens R (1998) Nanoscaled interdigitated electrode arrays for biochemical sensors. Sensors Actuators B 49:73–80. https://doi.org/10.1016/S0925-4005(98)00128-2
198. Laureyn W, Nelis D, Van Gerwen P, Baert K, Hermans L, Magnée R, Pireaux J-J, Maes G (2000) Nanoscaled interdigitated titanium electrodes for impedimetric biosensing. Sensors Actuators B 68:360–370. https://doi.org/10.1016/S0925-4005(00)00489-5
199. Gheorghe M, Guiseppi-Elie A (2003) Electrical frequency dependent characterization of DNA hybridization. Biosens Bioelectron 19:95–102. https://doi.org/10.1016/S0956-5663(03)00179-9
200. Dharuman V, Grunwald T, Nebling E, Albers J, Blohm L, Hintsche R (2005) Label-free impedance detection of oligonucleotide hybridisation on interdigitated ultramicroelectrodes using electrochemical redox probes. Biosens Bioelectron 21:645–654. https://doi.org/10.1016/j.bios.2004.12.020
201. Montelius L, Tegenfeldt JO, Ling TGI (1995) Fabrication and characterization of a nanosensor for admittance spectroscopy of biomolecules. J Vac Sci Technol A 13:1755–1760. https://doi.org/10.1116/1.579765
202. Bratov A, Abramova N, Ramón-Azcón J, Merlos A, Sánchez-Baeza F, Marco M-P, Domínguez C (2008) Characterisation of the interdigitated electrode array with tantalum silicide electrodes separated by insulating barriers. Electrochem Commun 10:1621–1624. https://doi.org/10.1016/j.elecom.2008.07.037
203. Möller R, Csáki A, Köhler JM, Fritzsche W (2001) Electrical classification of the concentration of bioconjugated metal colloids after surface adsorption and silver enhancement. Langmuir 17:5426–5430. https://doi.org/10.1021/la0102408
204. Park S-J, Taton TA, Mirkin CA (2002) Array-based electrical detection of DNA with nanoparticle probes. Science 295:1503–1506. https://doi.org/10.1126/science.1067003
205. Sergeyeva TA, Lavrik NV, Piletsky SA, Rachkov AE, El'skaya AV (1996) Polyaniline label-based conductometric sensor for IgG detection. Sensors Actuators B 34:283–288. https://doi.org/10.1016/S0925-4005(97)80006-8
206. Sergeyeva TA, Lavrik NV, Rachkov AE, Kazantseva ZI, El'skaya AV (1998) An approach to conductometric immunosensor based on phthalocyanine thin film. Biosens Bioelectron 13:359–369. https://doi.org/10.1016/S0956-5663(97)00117-6
207. Medina-Sánchez M, Ibarlucea B, Pérez N, Karnaushenko DD, Weiz SM, Baraban L, Cuniberti G, Schmidt OG (2016) High-performance three-dimensional tubular nanomembrane sensor for DNA detection. Nano Lett 16:4288–4296. https://doi.org/10.1021/acs.nanolett.6b01337
208. Daniels JS, Pourmand N (2007) Label-free impedance biosensors: opportunities and challenges. Electroanalysis 19:1239–1257. https://doi.org/10.1002/elan.200603855
209. Kimura-Suda H, Petrovykh DY, Tarlov MJ, Whitman LJ (2003) Base-dependent competitive adsorption of single-stranded DNA on gold. J Am Chem Soc 125:9014–9015. https://doi.org/10.1021/ja035756n
210. Gong P, Levicky R (2008) DNA surface hybridization regimes. Proc Natl Acad Sci 105:5301–5306. https://doi.org/10.1073/pnas.0709416105
211. Herne TM, Tarlov MJ (1997) Characterization of DNA probes immobilized on gold surfaces. J Am Chem Soc 119:8916–8920. https://doi.org/10.1021/ja9719586

212. Steel AB, Herne TM, Tarlov MJ (1998) Electrochemical quantitation of DNA immobilized on gold. Anal Chem 70:4670–4677. https://doi.org/10.1021/ac980037q
213. Peterson AW, Heaton RJ, Georgiadis RM (2001) The effect of surface probe density on DNA hybridization. Nucleic Acids Res 29:5163–5168. https://doi.org/10.1093/nar/29.24.5163
214. Keighley SD, Li P, Estrela P, Migliorato P (2008) Optimization of DNA immobilization on gold electrodes for label-free detection by electrochemical impedance spectroscopy. Biosens Bioelectron 23:1291–1297. https://doi.org/10.1016/j.bios.2007.11.012
215. Baker BA, Milam VT (2011) Hybridization kinetics between immobilized double-stranded DNA probes and targets containing embedded recognition segments. Nucleic Acids Res 39:e99–e99. https://doi.org/10.1093/nar/gkr293
216. McKendry R, Zhang J, Arntz Y, Strunz T, Hegner M, Lang HP, Baller MK, Certa U, Meyer E, Güntherodt H-J, Gerber C (2002) Multiple label-free biodetection and quantitative DNA-binding assays on a nanomechanical cantilever array. Proc Natl Acad Sci 99:9783–9788. https://doi.org/10.1073/pnas.152330199
217. Tisné C, Delepierre M, Hartmann B (1999) How NF-κB can be attracted by its cognate DNA1. J Mol Biol 293:139–150. https://doi.org/10.1006/jmbi.1999.3157

Label-Free Impedimetric Biosensing Using 3D Interdigitated Electrodes

Andrey Bratov, Sergi Brosel-Oliu, and Natalia Abramova

Abstract The use of impedimetric biosensors based on interdigitated electrode arrays (IDEAs) for biochemical applications has gained increased interest during the last two decades. Recently, a concept of a three-dimensional interdigitated electrode array (3D-IDEA) with insulating barriers separating electrodes digits was introduced. The functional mechanism of the device is based on registration of changes in conductivity at the surface of the barrier provoked by electrical charge redistribution caused by surface chemical reactions. The specific design of this sensor structure permits to enhance its sensitivity for biochemical reactions taking place at the sensor surface in comparison with planar sensors. Discussion of the sensor properties and parameters is presented stressing the important effect of surface conductivity on IDEA sensors response. Examples of application of 3D-IDEA transducers modified with antibodies, proteins, DNA molecules, peptides and aptamers for label-free biosensing are encountered throughout this paper. Another advantage that presents 3D-IDEA is the possibility to use it as a valuable tool to study surface chemical reactions at the insulator–solution interface which are rather difficult to achieve with conventional experimental methods.

A. Bratov (✉) and S. Brosel-Oliu
BioMEMS Group, Instituto de Microelectrónica de Barcelona, Centro Nacional de Microelectrónica (IMB-CNM, CSIC), Esfera UAB-CEI, Campus UAB, Bellaterra, 08193 Barcelona, Spain
e-mail: andrei.bratov@imb-cnm.csic.es

N. Abramova
BioMEMS Group, Instituto de Microelectrónica de Barcelona, Centro Nacional de Microelectrónica (IMB-CNM, CSIC), Esfera UAB-CEI, Campus UAB, Bellaterra, 08193 Barcelona, Spain

Lab. Artificial Sensors Syst., ITMO University, Kronverskiy pr. 49, 197101 St. Petersburg, Russia

M. J. Schöning, A. Poghossian (eds.), *Label-Free Biosensing: Advanced Materials, Devices and Applications*, Springer Series on Chemical Sensors and Biosensors (2018) 16: 179–198
DOI 10.1007/5346_2017_7, © Springer International Publishing AG 2017,
Published online: 11 June 2017

Keywords Biosensor, Impedance, Interdigitated electrodes, Surface charge, Surface conductivity

Contents

1 Introduction

For a wide variety of applications, detection and study of molecular interactions at the solid/liquid interface are of great interest. Large biomolecules due to the presence of ionizable groups are electrically charged and their interaction with a solid surface may affect the density and distribution of the surface charge which gives a possibility for the development of direct label-free biosensors based on this effect. Examples are semiconductor field-effect devices for detection of surface binding of charged macromolecules [1–3] and interdigitated electrode arrays (IDEAs) [4]. Among different electrochemical biosensors, impedimetric transducers gained much interest due to their ability to perform label-free detection [5–7]. These devices provide viable solutions for the monitoring of a wide range of analytes with several advantages over other techniques, such as small size, low cost, direct and fast response. Moreover, in contrast with other electrochemical transducers, like amperometric or potentiometric, no reference electrode is required which simplifies the measurement and permits sensor miniaturization. In recent years, a great effort has been made in this research area to understand the fundamentals of these biosensors and achieve really usable analytical devices with a higher sensitivity and accuracy, better reproducibility and lower detection limit [8]. A wide range of different impedimetric biosensors was reported and the number of publications grows from year to year. Impedimetric biosensors are used to register changes in the electrical properties at the electrode surface modified with bio-receptor molecules. In the presence of redox active species in test solution, Faradaic charge transfer resistance [9] is measured, which may be affected by interactions of a target biomolecule with a probe-functionalized sensor surface. Biochemical reactions at the sensor surface may be also registered in non-Faradaic measurements as capacitance changes [10].

Application of modern technologies for impedimetric sensor development [11] permitted to reduce significantly the sensors dimensions by forming two in-plane microband electrodes forming an IDEA. The use of IDEAs for biochemical sensing applications has gained increased interest during the last two decades making IDEA one of the most commonly used electrochemical sensor structures [8]. Among advantages of this type of sensors is a possibility of label-free biosensing. When a

target biomolecule interacts with a probe-functionalized sensor surface, changes in the electrical properties of the surface (e.g. dielectric constant, and resistance) can result solely from the presence of the target molecule. Thus, no label is required for impedance sensing.

Recently, Bratov et al. introduced the concept of a three-dimensional (3D-) IDEA with electrode fingers separated by an insulating barrier made of silicon dioxide (SiO_2) [12, 13]. The specific design of this sensor structure permits to enhance its sensitivity for biochemical reactions taking place at the sensor surface in comparison with planar sensors. Discussion of the 3D-IDEA sensor properties and parameters along with examples of their application for label-free biosensing is encountered throughout this paper.

2 Impedance of Interdigitated Electrode Arrays

Electrochemical impedance spectroscopy (EIS) permits to study changes occurring on the solid/liquid interface on the surface of electrodes produced by physical, chemical or biological interactions [6]. The impedance measurements may be carried out in faradaic or non-faradaic modes. In the first case, the presence of a redox couple that discharges on the electrode surface is required. The charge transfer resistance of this electrochemical reaction is the main parameter that is affected by the surface biochemical reactions [9]. In the non-faradaic mode, in the absence of charge transfer at the electrode surface, a transient current flows across the interface that mainly depends on the capacitance of the interface. This mode of impedance measurements is considered as a more amenable method for direct biosensing applications [5].

Different kinds of electrodes may be used as impedimetric transducers, but IDEAs present certain advantages, like small size, increased signal–noise ratio and fast establishment of a steady state compared to other electrodes systems [14]. Planar IDEA devices are formed by a pair of comb-like metal electrodes on a planar insulating substrate by conventional micro-fabrication techniques. In this case, impedance is measured between the two electrodes and depends on the solution conductivity and the interfacial properties of the electrodes: interfacial capacitance [10] and surface conductivity [15]. While traditional macro-electrodes with large surface area can be used to carry out measurements of interfacial capacitance, in micro-scale transducers the surface charge also plays an important role [4].

A planar IDEA sensor presented schematically in Fig. 1 is formed by a pair of comb-like electrodes (2, 3) on an insulating substrate (1). Contact pads (4) are used for wiring. The sensor geometry is characterized by the number and length of the electrode digits, their width (w) and interdigital spacing (s). Penetration of the electric field under applied potential is approximately equal to the distance between the centres of the electrode digits ($w + s$).

An impedance spectrum, obtained by measuring the impedance between the two electrodes in a wide frequency range, may be fitted to an electrical equivalent circuit (EC) composed of elements reflecting physical–chemical parameters of the sensor

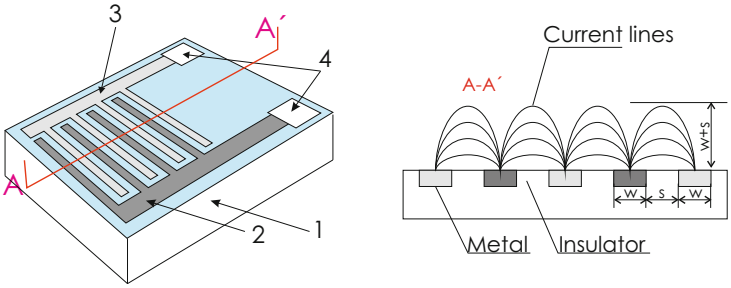

Fig. 1 Planar interdigitated electrode array (IDEA) device and its cross-section. 1 – insulating substrate; 2, 3 – electrodes collector bars; 4 – contact pads, w – electrode digit width, s – separation between the digits and $w + s$ – depth of the electric current penetration. *Reprinted from* [12] *with permission*

system. The equivalent circuit presented in Fig. 2a is most commonly used for interpretation of the impedance spectra of an IDEA sensor in non-faradaic measurement mode in the absence of an active redox pair in the test solution. Elements of the equivalent circuit have the following physical significance: R_C – contact resistance of wires, contacts and collector bars; C_G – geometrical (stray) capacitance between two electrodes through the medium in contact (typically water solution); C_P – the parasitic capacitance introduced by the sensor substrate and electrical cables; R_S – electrical resistance of water solution between two electrodes and C_{DL} – double-layer capacitance at the electrode/solution interface. Another parameter that is often used for registering affinity reactions on a sensor surface is a capacitance of a biomolecules layer, C_F, that goes in series with the double-layer capacitance, C_{DL} [10]. In some cases, it is also necessary to account for a Warburg impedance, not shown here, that may appear due to concentration polarization [16].

As both electrodes are symmetrical, of the same size and are made of the same material, the equivalent circuit may be simplified as presented in Fig. 2b.

In this case, C_P, which depends only on the sensor geometry and dielectric properties of the substrate material, is included in the capacitance C_G. The series combination of C_{DL} and C_F will manifest itself in spectra as just one element, $C_{DL}^{(CPE)}$, of the electrode/solution interface. Taking into consideration that the electrical double-layer (EDL) capacitance mainly depends on the electrolyte solution concentration, changes in $C_{DL}^{(CPE)}$ may be attributed to the formation of an additional layer on the electrode surface.

The impedance of solid electrodes usually deviates from purely capacitive behaviour due to surface effects, like roughness, and inhomogeneous current distribution due to microscopic chemical inhomogeneities [5], thus modelling the electrode–solution interface as purely capacitive is often simplistic and can reduce the quality of data fitting. Capacitive behaviour of the interface is usually empirically modelled as a constant phase element (CPE) expressed as [16]:

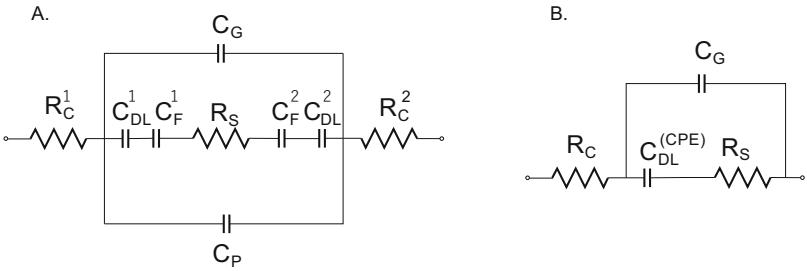

Fig. 2 Equivalent electrical circuit of an IDEA (**a**) and its simplified form (**b**). The circuit elements are explained within the text

$$Z_{\mathrm{CPE}} = \frac{1}{(j\omega)^{\alpha} T}, \tag{1}$$

where $j = \sqrt{(-1)}$ (imaginary unit); ω is angular frequency (rad s^{-1}); T is a constant in F $cm^{-2} \cdot s^{\alpha - 1}$ [16] and α is an empirical constant representing the behaviour of the CPE. When the exponent α is equal to 1, the CPE behaves similarly to a capacitor; however, due to dispersion in local capacitance values at metal/solution interface, the interfacial capacitance is expressed as CPE with typical α values for metal electrodes falling between 0.98 and 0.7. For these α values close to unity, the "average" double-layer capacitance may be estimated from the value of T [16]. Impedance data treatment and equivalent circuit fitting using EIS software package, like the Z-Plot/Z-View (Scribner Associates, Southern Pines, NC, USA), permit to calculate the average interfacial capacitance from the CPE impedance values.

Figure 3 shows the impedance spectra simulation based on the EC presented in Fig. 2b measured at different conductivity values of a sample solution. On the Nyquist plot at high frequencies (10^4–10^6 Hz), we see a semicircle associated with a parallel combination of C_G and R_S, the diameter of which is dependent on the solution resistance. At low frequencies ($<10^4$ Hz), the impedance is dominated by the CPE representing the EDL capacitance. On the right side of Fig. 3, a Bode diagram of impedance spectra is presented. At low frequencies, the impedance is determined by the double-layer capacitance. At higher frequencies, the impedance of this capacitance becomes lower than the resistance of the electrolyte solution and the sensor impedance becomes frequency independent. At high frequencies, the impedance of the geometrical capacitance C_G becomes lower than R_S and sensor impedance starts to decrease with increasing frequency.

The resistance R_S of the equivalent circuit is linked to the bulk resistivity ρ_S of an electrolyte solution by a geometric factor, the cell constant K_{Cell}, according to Eq. (2):

$$R_S = \rho_S \cdot K_{\mathrm{Cell}} \tag{2}$$

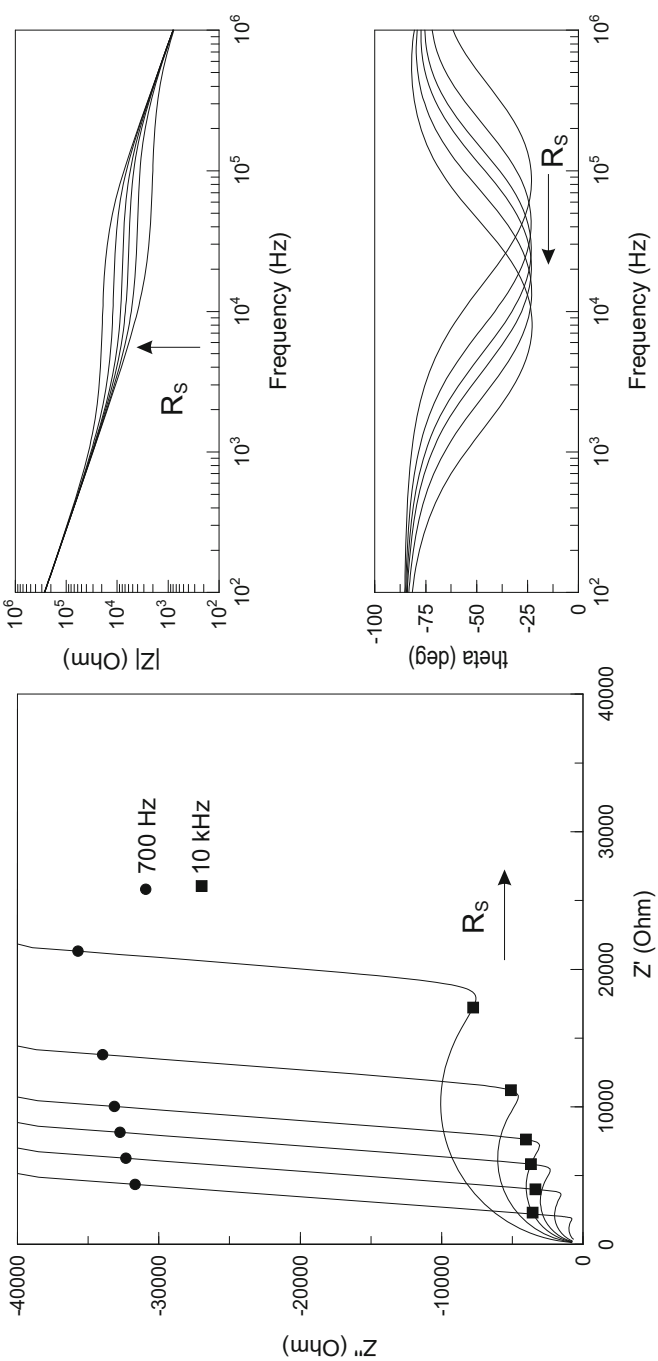

Fig. 3 Simulation of the impedance spectra of an IDEA sensor measured in water solutions with different conductivity using equivalent circuit presented in Fig. 2b presented as Nyquist (*left*) and Bode (*right*) plots. Parameters used: R_C – 100 Ω, C_G – 200 pF, $C_{DL}{}^{(CPE)}$ – 8 nF, α – 0.95 and R_S – 2–20 kΩ

This geometric factor takes into account the shape of the conductivity cell and the distribution of the electric field. Various models were proposed [17–19] to calculate the cell constant of interdigitated electrodes, though for IDEA-based conductivity sensors the most used is of Olthuis et al. [19].

Equation (2) implies that R_S is linearly dependent on ρ_S at all the solution electrolyte concentrations till deionized water (18 MΩ·cm). However, even in early papers of the Twente University group [19, 20] we may note that at solution resistivities higher than 7–8 kΩ·cm the sensor response declines from linearity. In their later paper [21], it is shown that experimental R_S values measured in demineralized pure water are much lower than expected from the model calculations. This was explained by contamination of water from glassware and tubing and by CO_2 contamination.

Decline of R_S determined for IDEA sensors from impedance measurements in poorly conducting solutions was experimentally confirmed for conventional flat IDEA sensors [15], attributing this effect to the surface conductivity within the interdigital spacing. At neutral pH, the surface of SiO_2 (or glass) forming the IDEA substrate is negatively charged due to the presence of ionized surface OH groups. From the requirement of electroneutrality, this negative surface charge has to be compensated by cations from the bulk of the solution. As a result, positively charged counterions accumulate within the EDL. When a tangential electric field is applied at the solid/solution interface, due to a higher concentration within the diffuse part of the EDL of counterions compensating the surface charge, the local electric current can be higher than that typical of the bulk electrolyte solution. Moreover, modern EDL models of the solid/liquid interface [22, 23] assume that under electric potential gradient part of ions which can migrate under the electric field is located in a stagnant layer of EDL and ion mobilities within the immobile compact part of the EDL may be quite high.

Thus, the resistance R_S of an IDEA device determined from impedance spectra should be presented as a parallel combination of the bulk resistance, R_{Bulk}, of the electrolyte solution and the surface resistance of the space between electrode digits, R_{Surf}:

$$R_S = \frac{R_{Bulk} \cdot R_{Surf}}{R_{Bulk} + R_{Surf}} \tag{3}$$

This means that the sensor response measured in solutions with low electrolyte conductivity permits to control changes in the surface charge due to surface reaction with charged species, e.g. biomolecules. This approach was used for IDEA sensors with interdigital space modified with DNA molecules for hybridization monitoring [24–27]. However, obtained results are contradictory, as in [24, 25] the determined R_S values decrease upon hybridization, while in [26, 27] the increase is presented.

As it was mentioned earlier, 90% of the current flowing between the electrodes is located in a layer with a thickness equal to the separation between electrode centres (see Fig. 1). Reduction of electrode digits width and spacing will reduce the effect of the bulk solution resistance enhancing the sensor sensitivity to surface charge

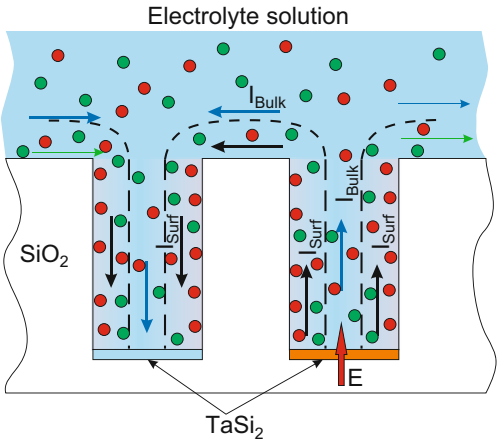

Fig. 4 Three-dimensional interdigitated electrode array (3D-IDEA) with insulating (SiO_2) barriers separating electrode digits of $TaSi_2$. I_{Bulk} – electric current through the bulk solution phase, and I_{Surf} – current close to the surface of the barrier. *Reprinted from* [30] *with permission*

variation. This approach, though without taking into consideration the surface conductivity, was proposed by Van Germen and Laureyn [28, 29] who presented nanoscale IDEA devices. Their work received much scientific attention, however, very little practical implementation. We may attribute it to the fact that once out of the clean room the sensors are exposed to outdoor ambient. Adsorption of carbon micro-/nanoparticles present in the air on the surface will alter the sensor electrical parameters affecting their reproducibility and stability. We have noticed this effect even on micron-scale IDEA planar devices with gold or platinum electrodes.

To enhance the effect of the surface conductivity on the impedance of an IDEA sensor, it was proposed [12, 13] to separate adjacent electrode digits by insulating SiO_2 barriers, as presented in Fig. 4. In this case, penetration of the electric current into the solution bulk remains the same as for a flat device with the same electrodes geometry, but the path of the current along the surface of the barrier becomes much longer permitting to enhance the sensitivity to surface charge variations. Analysis of the 3D-IDEA sensor geometry on its response was presented in [15, 31].

3 Three-Dimensional Sensor Design, Fabrication and Characterization

IDEA sensors are formed by a pair of comb-like metal electrodes deposited on an insulating substrate, which may be a polymer, glass or silicon covered with a thick oxide layer. In this particular case, we used a silicon wafer oxidized thermally by "wet" oxidation at 950°C to give a good quality silicon dioxide layer of 2,500 nm. In the next step, a 230 nm thick layer of tantalum silicide, which is a highly conductive material, is deposited by magnetron sputtering. The reason of using $TaSi_2$ instead of traditional noble metals, like gold or platinum, is that these metals are

regarded as contaminating and are not allowed to be used in standard microelectronics processes within the clean room facilities.

The first photolithographic step defines collector bars and digits of two electrodes. The patterning is done by a reactive ion etching technique. The electrodes width and separation depend on the design requirements, but most of our work was performed using a symmetrical IDEA with 216 digits of 3 μm width separated by a 3 μm gap between the adjacent electrodes. The electrode digits are 1.5 mm long and the aperture (overlapping) between the electrodes digits is 1.4 mm. To form the contact pads, 1 μm of aluminium is deposited and patterned using standard photolithographic and etching steps leaving metal only at extremes of the two collector bars.

The final step is the formation of insulating barriers between the electrode digits. To do this, the wafer with formed IDEA devices is covered with a 4 μm thick silicon oxide deposited by the low-pressure chemical vapour deposition (LPCVD). This layer defines the barrier height. Photolithography is used to define the openings in the oxide layer over the electrodes digits and contact pads. These zones are opened by deep reactive ion etching (DRIE), which permits to obtain barriers with nearly vertical walls. The sensor design is presented schematically in Fig. 5 along with

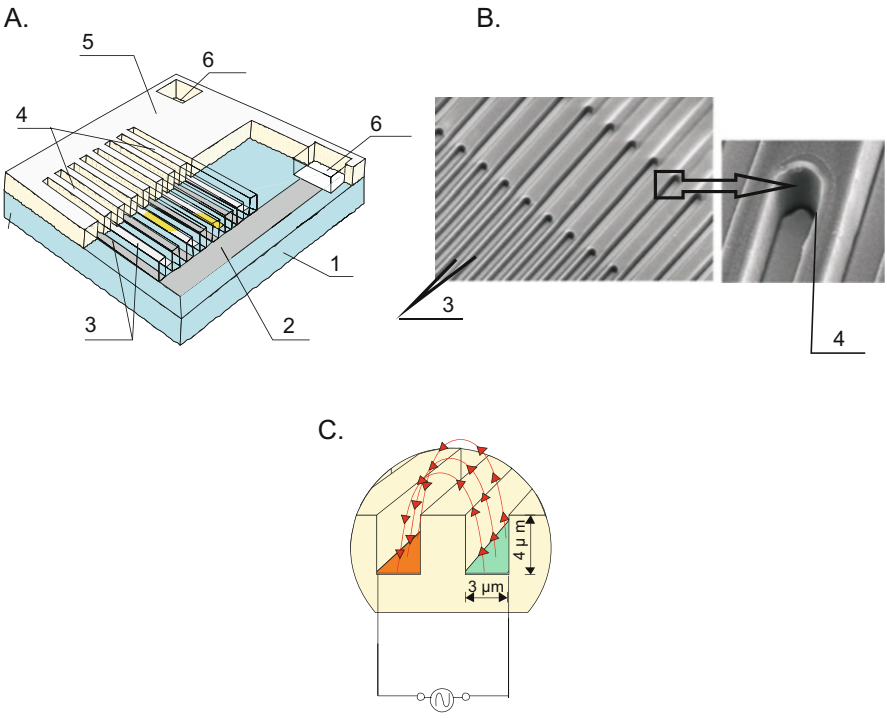

Fig. 5 (**a**) Design of the studied device with microcapillaries on its surface (1 – insulating substrate, 2 – electrode collector bar, 3 – electrodes digits, 4 – microcapillaries opened over electrode digits, 5 – silicon dioxide cover layer and 6 – contact pads). (**b**) Electronic microscopy image of the sensor surface. (**c**) Sensor electrical connection scheme (electrical field lines passing over the barrier separating two electrode digits are shown). *Reprinted from* [30] *with permission*

optical and electronic microscopy images of the sensor surface and obtained barrier profile. After being cut from the wafer, the sensors are glued to a printed circuit board substrate and are wire bonded for electrical connections. Contact pads and wires were encapsulated using epoxy resin.

Characterization of sensors was performed by impedance measurements in a 100 Hz–1 MHz frequency range with a 25–100 mV (amplitude) voltage excitation using a PARSTAT 2263 Advanced Electrochemical System or Quadtech precision LCR analyzer. Z-Plot/Z-View software package (Scribner Associates, Southern Pines, NC, USA) was used for impedance data treatment and an equivalent circuit fitting.

The equivalent circuit presented in Fig. 2b was used for spectra fitting. The goodness of the fit may be assessed using the chi-squared and the weighted sum of squares parameters. The first parameter is the square of the standard deviation between the original data and the calculated spectrum and the second is proportional to the average percentage error between the original data points and the calculated values. For all spectra measured in this work, the chi-square parameter was typically smaller than 0.0025 and the weighted sum of squares was in the 0.18–0.30 range. The relative error of the R_S values obtained by fitting is typically below 0.8%.

4 Direct Label-Free Analyte Detection

Large biomolecules are electrically charged and their interaction with a solid surface affects the density and distribution of the surface charge which gives a possibility of direct label-free detection. Taking an advantage that most of bioaffinity reactions are irreversible, it is possible to perform the reaction under required optimal conditions and then make impedance measurements in a low conducting electrolyte solution, usually 10^{-5} M KCl with controlled conductivity of ≈2.50 μS/cm. Differences in R_S values determined before and after biorecognition reaction are the measure of the sensor sensitivity.

For better understanding of how surface charge changes affect 3D-IDEA sensor parameters, a model system based on charged polyelectrolyte molecules may be used. Experiments with deposition of polyethyleneimine (PEI) [15] followed by poly(sodium 4-styrenesulfonate) (PSS) layer formation on the sensor surface [30, 32] showed the effectiveness of the barrier structure of 3D-IDEA devices resulting in their high sensitivity to surface charge changes.

The layer-by-layer (LbL) self-assembly of oppositely charged polyelectrolytes is one of the simplest ways to construct multilayer structures [33] and, as many of biomolecules are charged, may be used for their immobilization on the sensor surface as biorecognition elements. Protamine is a low molecular weight protein, rich in basic arginine residues, and has 20 positive charges at physiological pH. The polycationic structure of protamine allows the tight electrostatic binding of polyanionic heparin to form a stable complex. Modification of the negatively charged silicon dioxide sensor surface with protamine permits to register protamine–heparin complex formation

[34] as changes in the surface conductivity determined from the sensor impedance measured in an electrolyte solution. Figure 6 shows the effect of the successive deposition of protamine and heparin layers on R_S values of the sensors.

As follows, adsorption of protamine on a silicon dioxide sensor surface causes increase of R_S values. The SiO_2 surface at neutral pH is negatively charged. Mobile cations from solution arrive to compensate this charge increasing the surface conductivity. The protamine layer is positively charged and anions at the surface are less mobile than cations which provokes the increase in resistance. Heparin behaves as a polyanion and its deposition over the protamine layer compensates its electrical charges and results in considerable decrease of the resistance as the negatively charged surface attracts more mobile cations.

Obtained results [34] show that the limit of detection of a protamine modified 3D-IDEA sensor is really low and changes in measured spectra and consecutive R_S values were registered at 0.01 U/ml.

A bacterial endotoxin biosensor [35] based on Concanavalin A (Con A) biorecognition element immobilized on the sensor surface via its interactions with PEI and glycogen (Gly) (Fig. 7) is another example of the LbL method application. Endotoxins, also known as lipopolysaccharides (LPS), being the major structural component of external membrane of gram-negative bacteria are their ubiquitous markers.

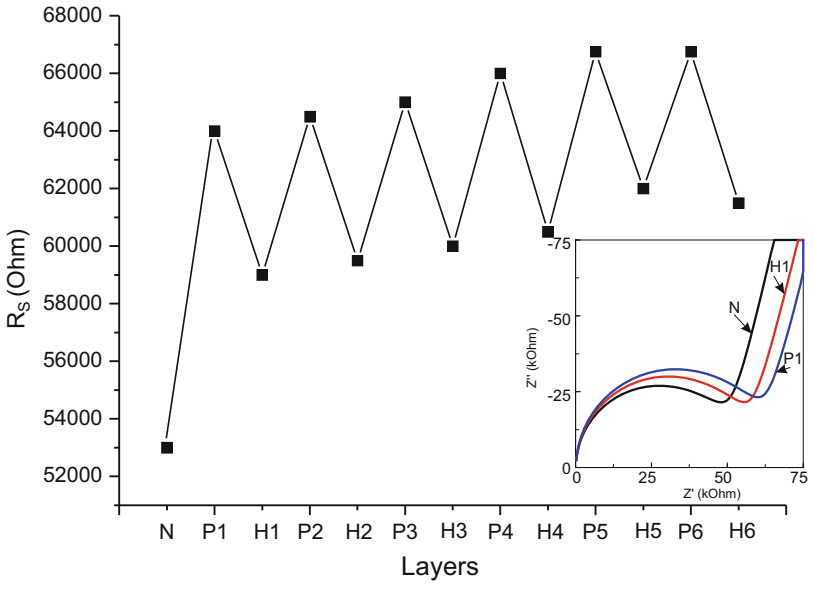

Fig. 6 R_S values obtained by fitting impedance spectra of the IDEA devices measured in 10^{-5} M KCl solution after the successive deposition of protamine (P#) and heparin (H#). N refers to a native clean SiO_2 surface and # denotes the successive layer number. In the *inset*, impedance spectra corresponding to the first three points on the graph are presented. *Reprinted from* [34] *with permission*

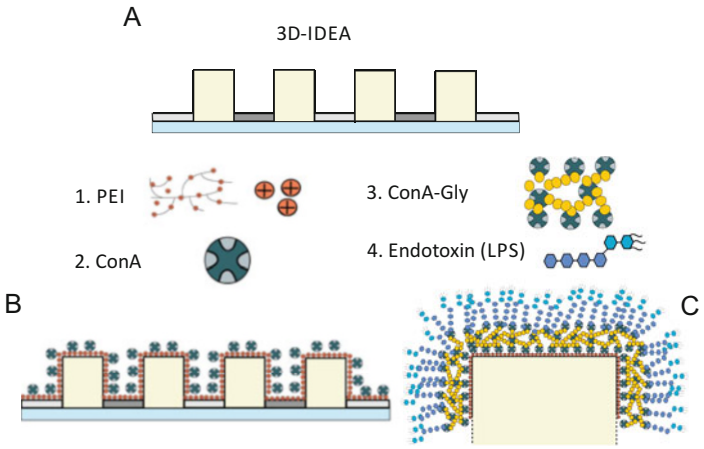

Fig. 7 Scheme of the layer-by-layer (LbL) assembling of PEI-(ConA-Gly)$_2$-ConA multilayer on the sensor surface and its interaction with lipopolysaccharides (LPS). (**a**) IDE sensor with barriers, (**b**) sensor modified with PEI and concanavalin A (Con A) and (**c**) sensor modified with PEI-(ConA-Gly)$_2$-ConA after interaction with LPS

Con A is a lectin-type carbohydrate-binding protein with well-characterized structure that recognizes specifically α-D-glucose and α-D-mannose groups and possesses certain affinity for some bacteria and for their endotoxins [36].

The sensor response presented in Fig. 8 follows the Langmuir isotherm for irreversible adsorption which, being presented in a semi-logarithmic scale, shows a linear response in the 1–50 μg/mL LPS concentration range. The detection limit is around 1 μg/mL.

The LbL method of biomolecule immobilization [33] may be regarded as a universal one, though certain precautions should be taken to prevent non-specific interactions with the underlying charged polyelectrolyte layer. For this, various blocking reagents (e.g. bovine serum albumin, BSA) may be used [1, 35] to enhance the selectivity in the sensor response.

Traditional methods employ covalent attachment of biorecognition molecules for their immobilization onto a sensor surface. For silicon oxide surfaces, a large variety of organo-functional silanes may be used [37]. Epoxysilane (3-(glycidoxypropyl) trimethoxysilane, GPTS) readily reacts with the amine group of biomolecules and is often used for their immobilization. In this way, immobilization of the sulfonamide antigen SA2-OVA on the 3D-IDEA sensor surface modified with GPTS was performed [13]. Specific antibody binding was assessed by placing the sensor in solutions containing a mixture of the specific antiserum and different concentrations of sulfapyridine. After washing the sensor, the impedimetric spectra were recorded for 1 min. In parallel, the standard Enzyme-Linked Immuno-Sorbent Assay (ELISA) method was employed using the same immunoreagents.

Figure 9 shows the response of the immunosensors to the changes in the sulfapyridine concentration in standard solutions. For comparison, results of a standard

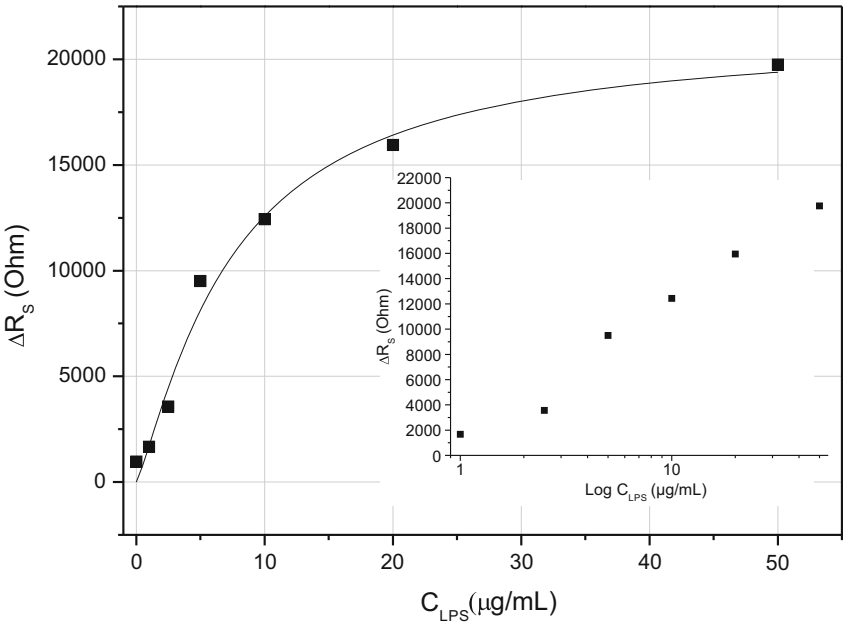

Fig. 8 PEI-(ConA-Gly)$_2$-ConA sensor response to *Escherichia coli* LPS. In the *inset*, the response is presented in a semi-logarithmic scale

ELISA performed with the same immunoreagents are presented. In both methods, detectability, estimated with the help of the IC_{50} (the concentration of a drug that is required for 50% inhibition) parameter, the sensitivity and the accuracy are the same. However, the analysis with sensors is much faster and the procedure is easier to perform than a traditional ELISA.

As follows from Fig. 9b, immunochemical reaction on a sensor surface in case of the standard planar IDEA immunosensor produces only minor changes in the impedance spectra. In comparison to this, response of the three-dimensional sensor shows considerable improvement in sensitivity.

The same immobilization strategy was used to attach DNA molecule to the sensor surface [13]. An oligonucleotide sequence 5′-aminohexyl-CGA GTC ATT GAG TCA TCG AG-3′ with amino group in 5′ position was covalently attached to sensors surface that was previously modified with GPTS by immersing sensors into a solution of oligonucleotide in carbonate buffer for 24 h.

Immobilization of the oligonucleotide on the sensor surface using the procedure mentioned above resulted in a decrease of the measured resistance, R_S, as it is shown in Fig. 10. Hybridization with the complementary oligonucleotide produced a further decrease of 8.8 kΩ in the resistance [13]. It should be noted that experiments were performed on three sensors and the relative error of the determined R_S values was less than 0.8%. Hybridization of the oligonucleotides was also confirmed by fluorescence

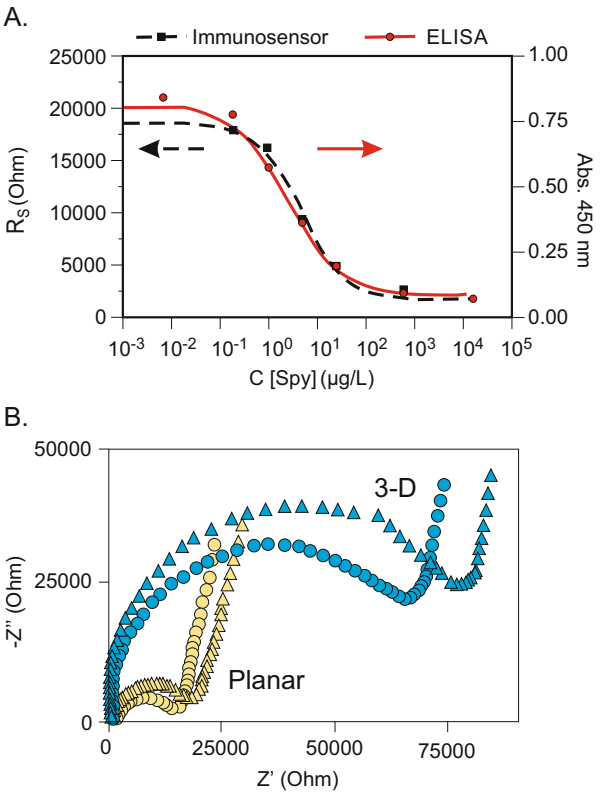

Fig. 9 (**a**) Response of the 3D-IDEA sensor with 4 µm barriers modified with antigen SA2-OVA to sulfapyridine (*dashed line*). For comparison, results obtained with the standard competitive ELISA (*solid line*) are shown. (**b**) Nyquist plots of impedance spectra corresponding to 3D-IDEA sensor with 4 µm insulating SiO_2 barriers and planar IDEA sensors with gold electrodes of the same geometry modified with 1 µg/mL antigen (*circles*) and after the immunoreaction with 1/1,000 antiserum (*triangles*). *Reprinted from* [13] *with permission*

microscopy visualizing the presence of fluorescein on the surface of sensors subjected to the reaction.

Another important field of biosensors application is bacteria detection. As many bacteria bear negative charge, it is possible to register their interaction with specifically modified impedimetric sensor surfaces [38].

An interesting class of the effective biological recognition elements for bacteria selective detection is presented by antimicrobial peptides (AMPs). A synthesized potent AMP derived from human lactoferrin was covalently immobilized on a 3D-IDEA sensor and showed very high sensitivity to the presence of *Streptococcus sanguinis* [39], an important early colonizer of peri-implantitis, an inflammation gum disease involving the destruction of tissues caused by biofilm formation which constitutes a major cause of implant failure in dentistry.

The peptide hlf1-11 through the amino group present at its N-terminus was covalently attached to the IDEA surface modified as previously with epoxysilane.

As follows from the Nyquist plots (Fig. 11), interaction of the sensor modified with AMP with bacteria adhesion provokes changes in R_S. It should be noted that due to the formation of an additional layer over the electrodes an increase in C_{DL} and

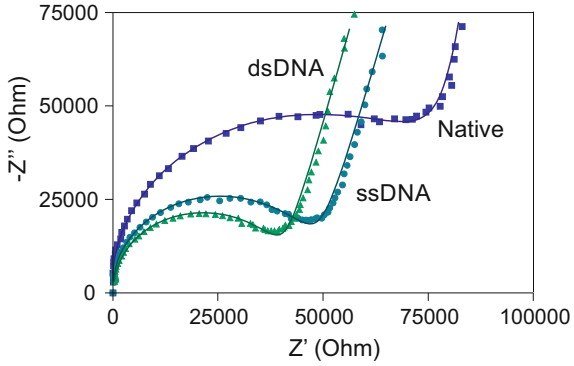

Fig. 10 Impedance spectra of the sensor after its modification with ssDNA and further hybridization (dsDNA). With the *lines*, fitting results are presented

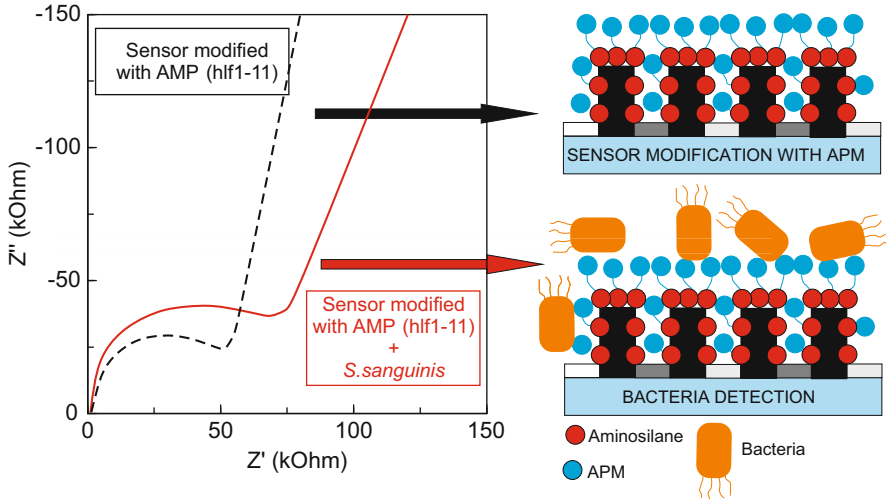

Fig. 11 Changes in the impedance spectrum of the sensor modified with aminosilane and antimicrobial peptide (AMP) after its interaction with *Streptococcus sanguinis* bacteria. *Reprinted from* [39] *with permission*

decrease in the CPE α parameter occur. However, ΔRs was chosen as a principle sensor parameter due to its large-scale variation and higher reproducibility.

To evaluate the sensitivity of the developed biosensor in bacterial detection, EIS analysis was performed after incubation of sensors in KCl solutions of *S. sanguinis* at different concentrations. KCl solutions with low conductivity were used to reduce the effect of the bulk solution electrolyte on the impedance response during bacterial incubation. As illustrated in Fig. 12a, a linear correlation between ΔRs and the logarithm of the cell concentration was observed in the range of 10^1–10^5 cfu/mL (cfu – colony forming units) with sensitivity of the system 3.5 ± 0.5 kΩ per bacteria

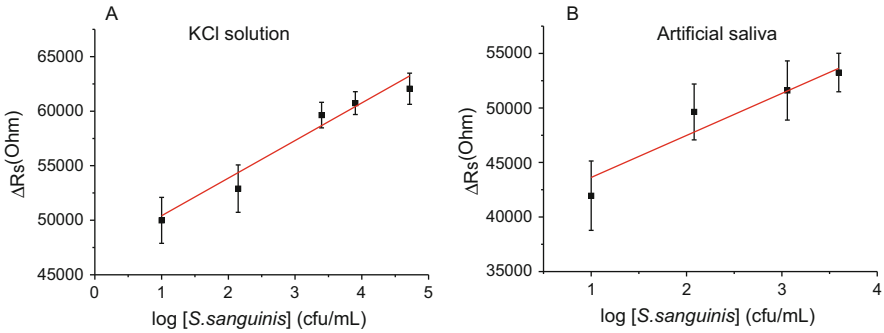

Fig. 12 Linear regression fit of the AMP sensor response to the *S. sanguinis* concentration after 1 h incubation in KCl solution (**a**) and artificial saliva (**b**). *Reprinted from* [39] *with permission*

concentration decade. The determined limit of detection was found to be as low as 35 cfu/mL [37].

As the bacterial detection should be performed in saliva, the assay was also done using artificial saliva for sensor incubation. The saliva medium matrix effect resulted in slightly higher detection limit (8.6 10^2 cfu/mL) without affecting the sensitivity (see Fig. 12b).

Aptamers form another interesting class of biorecognition elements that may be successfully used for selective bacteria detection [40, 41]. Aptamers are short oligonucleotides that bind targets with high specificity and affinity, including whole bacterial cells. Their small size, the lack of immunogenicity, the lower cost and higher reproducibility of production compared to antibodies make them very attractive for impedance-based biosensors.

To immobilize the aptamer on the 3D-IDEA, the surface was initially modified with mercaptosilane. After that, a 5′ disulphide-modified DNA aptamer was attached to the surface using a thiol/disulphide exchange reaction. Thus prepared aptasensors were incubated in solutions containing *Escherichia coli* in a concentration range from 10^1 to 10^6 cfu/mL for 30 min, and gently rinsed with water and their impedance spectra were measured. The impedance response, expressed as ΔRs, increased proportionally with the logarithmic value of bacterial concentration (see Fig. 13a), allowing to achieve a linear calibration regression with $R^2 = 0.98$ and a limit of detection of 2.9 10^2 cfu/mL. Much smaller response was obtained when the aptasensor was incubated with other bacterial strains, confirming the selectivity of suggested method (Fig. 13b).

This work shows that the proposed approach allows to obtain an aptasensor for detection and identification of pathogenic *E. coli* O157:H7 with a low limit of detection, logarithmic linear response, selectivity and short detection time.

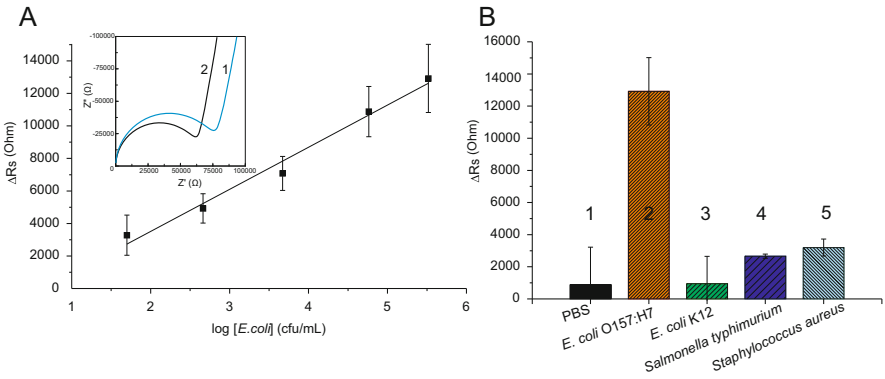

Fig. 13 (**a**) Calibration curve of the sensor. In the *inset*: impedance spectra of the sensor modified with aptamer (1) and after interaction with *E. coli* (2); (**b**) Selectivity of the sensor showing the response in the presence of other bacteria, 1 – PBS without bacteria, 2 – *E. coli* O157:H7, 3 – *E. coli* K12, 4 – *Salmonella typhimurium* and 5 – *Staphylococus aureus*

5 Conclusions

A three-dimensional impedimetric transducer based on an IDEA is presented. Due to the presence of insulating barriers that separate the adjacent digits of the electrodes, the main portion of the probing electrical current goes close to the surface of the barrier. Chemical modification of the barrier surface with biomolecules (antigens, DNA, enzymes, etc.) permits to realize direct label-free detection of subsequent analytes in solution. The functional mechanism of the device is based on registration of changes in conductivity at the surface of the barrier provoked by biochemical reactions of immobilized biomolecules. To obtain higher sensitivity in control of electrical charge changes at the surface produced by irreversible surface reactions, measurements of the device impedance should be performed in poorly conducting electrolyte solutions. Presented examples show that the 3D-IDEA is a highly sensitive transducer that can be used to develop biosensors of various types for direct label-free measurements.

It may be mentioned that the 3D-IDEA can also be used for reversible surface chemical reactions monitoring [4]. In this case, experiments may be performed in electrolyte solutions with rather high conductivity [4, 30, 34, 42] by registering impedance changes at a fixed frequency. This gives in real time the information about surface charging permitting to perform kinetic studies [30, 34]. Experimentally, the use of the device is quite simple and this method may be used as complementary to laborious traditional electrokinetic techniques used in colloid chemistry. This means that the transducer application is not limited to (bio)chemical sensors development but may be used as a sensitive tool in different fields where monitoring of surface charging is required.

Acknowledgments The authors acknowledge financial support from the Spanish Ministry of Economy and Competitiveness (project CTQ2014-54553-C3-1-R and S.B.O. fellowship of FPI-MICINN program BES-2015-071250), co-funded by the European Regional Development Fund (Feder) and from the Government of Russian Federation (Grant 074-U01). S.B.O. also acknowledges the PhD program in Biotechnology of Universitat Autònoma de Barcelona.

References

1. Bronder TS, Poghossian A, Scheja S, Wu C, Keusgen M, Mewes D, Schoening MJ (2015) DNA immobilization and hybridization detection by the intrinsic molecular charge using capacitive field-effect sensors modified with a charged weak polyelectrolyte layer ACS Appl Mater Interfaces 7(36):20068–20075. doi:10.1021/acsami.5b05146
2. Poghossian A, Schöning MJ (2014) Label-free sensing of biomolecules with field-effect devices for clinical applications Electroanalysis 26(6):1197–1213. doi:10.1002/elan.201400073
3. Poghossian A, Weil M, Cherstvy AG, Schoening MJ (2013) Electrical monitoring of polyelectrolyte multilayer formation by means of capacitive field-effect devices Anal Bioanal Chem 405(20):6425–6436. doi:10.1007/s00216-013-6951-9
4. Bratov A, Abramova N, Pilar Marco M, Sanchez-Baeza F (2012) Three-dimensional interdigitated electrode array as a tool for surface reactions registration Electroanalysis 24(1):69–75. doi:10.1002/elan.201100392
5. Daniels JS, Pourmand N (2007) Label-free impedance biosensors: opportunities and challenges Electroanalysis 19(12):1239–1257. doi:10.1002/elan.200603855
6. Katz E, Willner I (2003) Probing biomolecular interactions at conductive and semiconductive surfaces by impedance spectroscopy: routes to impedimetric immunosensors, DNA-sensors, and enzyme biosensors Electroanalysis 15(11):913–947. doi:10.1002/elan.200390114
7. Lillie G, Payne P, Vadgama P (2001) Electrochemical impedance spectroscopy as a platform for reagentless bioaffinity sensing Sens Actuator B Chem 78(1–3):249–256. doi:10.1016/S0925-4005(01)00821-8
8. Bratov A, Abramova N (2010) Chemical sensors and biosensors based on impedimetric interdigitated electrode array transducers. In: Harrison RV (ed) Chemical sensors: properties, performance and applications. Nova Science Publishers, New York, NY, pp 93–115. ISBN: 978-160741897-9
9. Lisdat F, Schafer D (2008) The use of electrochemical impedance spectroscopy for biosensing Anal Bioanal Chem 391(5):1555–1567. doi:10.1007/s00216-008-1970-7
10. Berggren C, Bjarnason B, Johansson G (2001) Capacitive biosensors Electroanalysis 13 (3):173–180
11. Suzuki H (2000) Advances in the microfabrication of electrochemical sensors and systems Electroanalysis 12(9):703–715. doi:10.1002/1521-4109(200005)12:9<703::aid-elan703>3.0.co;2-7
12. Bratov A, Abramova N, Ramon-Azcon J, Merlos A, Sanchez-Baeza F, Marco MP, Dominguez C (2008) Characterisation of the interdigitated electrode array with tantalum silicide electrodes separated by insulating barriers Electrochem Commun 10(10):1621–1624. doi:10.1016/j.elecom.2008.07.037
13. Bratov A, Ramon-Azcon J, Abramova N, Merlos A, Adrian J, Sanchez-Baeza F, Marco MP, Dominguez C (2008) Three-dimensional interdigitated electrode array as a transducer for label-free biosensors Biosens Bioelectron 24(4):729–735. doi:10.1016/j.bios.2008.06.057
14. Varshney M, Li Y, Srinivasan B, Tung S (2007) A label-free, microfluidics and interdigitated array microelectrode-based impedance biosensor in combination with nanoparticles immunoseparation for detection of *Escherichia coli* O157 : H7 in food samples Sens Actuator B Chem 128(1):99–107. doi:10.1016/j.snb.2007.03.045

15. Baecker M, Kramer F, Huck C, Poghossian A, Bratov A, Abramova N, Schöning MJ (2014) Planar and 3D interdigitated electrodes for biosensing applications: the impact of a dielectric barrier on the sensor properties Phys Status Solidi A 211(6):1357–1363. doi:10.1002/pssa.201330416
16. Lasia A (1999) Electrochemical impedance spectroscopy and its applications Mod Aspect Electroc 32(32):143–248
17. Aoki A, Matsue T, Uchida I (1990) Electrochemical response at microarray electrodes in flowing streams and determination of catecholamines Anal Chem 62:2206–2210
18. Belmont C, Girault HH (1994) Coplanar interdigitated band electrodes for electrosynthesis. 2. Methoxylation of furan J Appl Electrochem 24:719–724
19. Olthuis W, Streekstra W, Bergveld P (1995) Theoretical and experimental-determination of cell constants of planar-interdigitated electrolyte conductivity sensors Sens Actuator B Chem 24:252–256
20. Olthuis W, Volancschi A, Bomer JG, Bergveld P (1993) A new probe for measuring electrolytic conductance Sens Actuator B Chem 13–14:230–233
21. Timmer B, Sparreboom W, Olthuis W, Bergveld P, van den Berg A (2002) Optimization of an electrolyte conductivity detector for measuring low ion concentrations Lab Chip 2 (2):121–124. doi:10.1039/b201225a
22. Dukhin S, Shilov VN (1974) Dielectric phenomena and the double layer in disperse systems and polyelectrolytes. Wiley, New York, NY
23. Shilov VN, Delgado AV, Gonzalez-Caballero F, Grosse C (2001) Thin double layer theory of the wide-frequency range dielectric dispersion of suspensions of non-conducting spherical particles including surface conductivity of the stagnant layer Colloids Surf A Physicochem Eng Asp 192(1–3):253–265
24. Berdat D, Marin A, Herrera F, Gijs MAM (2006) DNA biosensor using fluorescence microscopy and impedance spectroscopy Sens Actuator B Chem 118(1–2):53–59. doi:10.1016/j.snb.2006.04.064
25. Berdat D, Rodriguez ACM, Herrera F, Gijs MAM (2008) Label-free detection of DNA with interdigitated micro-electrodes in a fluidic cell Lab Chip 8(2):302–308. doi:10.1039/b712609c
26. Gheorghe M, Guiseppi-Elie A (2003) Electrical frequency dependent characterization of DNA hybridization Biosens Bioelectron 19(2):95–102. doi:10.1016/s0956-5663(03)00179-9
27. Guiseppi-Elie A, Lingerfelt L (2005) Impedimetric detection of DNA hybridization: towards near-patient DNA diagnostics. In: Immobilisation of DNA on chips I. Topics in current chemistry, vol 260. pp 161–186. doi:10.1007/128_006
28. Laureyn W, Nelis D, Van Gerwen P, Baert K, Hermans L, Magnee R, Pireaux JJ, Maes G (2000) Nanoscaled interdigitated titanium electrodes for impedimetric biosensing Sens Actuator B Chem 68(1–3):360–370. doi:10.1016/s0925-4005(00)00489-5
29. Van Gerwen P, Laureyn W, Laureys W, Huyberechts G, De Beeck MO, Baert K, Suls J, Sansen W, Jacobs P, Hermans L, Mertens R (1998) Nanoscaled interdigitated electrode arrays for biochemical sensors Sens Actuator B Chem 49(1–2):73–80. doi:10.1016/s0925-4005(98)00128-2
30. Bratov A, Abramova N (2013) Response of a microcapillary impedimetric transducer to changes in surface conductance at liquid/solid interface J Colloid Interface Sci 403:151–156. doi:10.1016/j.jcis.2013.04.030
31. Guimera A, Gabriel G, Prats-Alfonso E, Abramova N, Bratov A, Villa R (2015) Effect of surface conductivity on the sensitivity of interdigitated impedimetric sensors and their design considerations Sens Actuator B Chem 207:1010–1018. doi:10.1016/j.snb.2014.10.134
32. Bratov A, Abramova N (2012) A new microcapillary device for controlling surface conductivity changes at solid-liquid interface Chem Lett 41(10):1244–1246. doi:10.1246/cl.2012.1244
33. Ai H, Jones SA, Lvov YM (2003) Biomedical applications of electrostatic layer-by-layer nano-assembly of polymers, enzymes, and nanoparticles Cell Biochem Biophys 39(1):23–43. doi:10.1385/cbb:39:1:23

34. Abramova N, Bratov A (2015) Monitoring protamine-heparin interactions using microcapillary impedimetric sensor Electroanalysis 27(3):663–669. doi:10.1002/elan.201400581
35. Brosel-Oliu S, Galyamin D, Abramova N, Muñoz-Pascual F, Bratov A (2017) Impedimetric label-free sensor for specific bacteria endotoxin detection by surface charge registration Electrochim Acta 243:142–151. doi:10.1016/j.electacta.2017.05.060
36. Miao P (2013) Electrochemical sensing strategies for the detection of endotoxin: a review RSC Adv 3(25):9606–9617. doi:10.1039/c3ra00047h
37. Cass T, Ligler FS (1998) Immobilized biomolecules in analysis: a practical approach. In: A practical approach series, vol 198. Oxford University Press, Oxford
38. Brosel-Oliu S, Uria N, Abramova N, Bratov A (2015) Impedimetric sensors for bacteria detection. In: Rinken T (ed) Biosensors – micro and nanoscale applications. InTech, Rijeka. doi:10.5772/60741. ISBN: 978-953-51-4250-8
39. Hoyos-Nogues M, Brosel-Oliu S, Abramova N, Munoz F-X, Bratov A, Mas-Moruno C, Gil F-J (2016) Impedimetric antimicrobial peptide-based sensor for the early detection of periodontopathogenic bacteria Biosens Bioelectron 86:377–385. doi:10.1016/j.bios.2016.06.066
40. Luo C, Lei Y, Yan L, Yu T, Li Q, Zhang D, Ding S, Ju H (2012) A rapid and sensitive aptamer-based electrochemical biosensor for direct detection of *Escherichia Coli* O111 Electroanalysis 24(5):1186–1191. doi:10.1002/elan.201100700
41. Queiros RB, de-los-santos-Alvarez N, Noronha JP, Sales MGF (2013) A label-free DNA aptamer-based impedance biosensor for the detection of *E. coli* outer membrane proteins Sens Actuator B Chem 181:766–772. doi:10.1016/j.snb.2013.01.062
42. Bratov A, Abramova N, Ipatov A, Merlos A (2013) An impedimetric chemical sensor for determination of detergents residues Talanta 106:286–292. doi:10.1016/j.talanta.2012.10.083

Electrochemical Nanocavity Devices

Philipp Rinklin, Dirk Mayer, and Bernhard Wolfrum

Abstract Nanocavity sensors comprise one or several sensing elements within a highly confined channel or gap, typically produced by microfabrication technology. Depending on the specific design and implementation, such devices can offer several benefits for the detection of molecules or cellular signals. This chapter describes fundamental aspects of nanocavity sensors as well as state-of-the-art fabrication and research applications. In the first part of the chapter, we introduce single-electrode nanocavity devices and highlight their application for the capacitive sensing of extracellular voltage signals. Next, we discuss several implementations of multi-electrode nanocavity devices, which are used for electrochemical detection of molecules. These devices exhibit very high sensitivities due to the amplification of signals by redox cycling within the confined space of the nanocavity. We highlight recent approaches for using multi-electrode cavity sensors and sensor arrays for biosensing applications. Finally, we present novel fabrication approaches that allow cost-effective rapid prototyping of nanocavity devices.

P. Rinklin
Neuroelectronics, Munich School of Bioengineering, Department of Electrical and Computer Engineering, Technical University of Munich, Boltzmannstraße 11, 85748 Garching, Germany

D. Mayer
Institute of Bioelectronics (ICS-8/PGI-8), Forschungszentrum Jülich, Wilhelm-Johnen-Straße, 52425 Jülich, Germany

B. Wolfrum (✉)
Neuroelectronics, Munich School of Bioengineering, Department of Electrical and Computer Engineering, Technical University of Munich, Boltzmannstraße 11, 85748 Garching, Germany

Institute of Bioelectronics (ICS-8/PGI-8), Forschungszentrum Jülich, Wilhelm-Johnen-Straße, 52425 Jülich, Germany
e-mail: bernhard.wolfrum@tum.de

M. J. Schöning, A. Poghossian (eds.), *Label-Free Biosensing: Advanced Materials, Devices and Applications*, Springer Series on Chemical Sensors and Biosensors (2018) 16: 199–214
DOI 10.1007/5346_2017_8, © Springer International Publishing AG 2017,
Published online: 23 June 2017

Keywords Electrochemical biosensors, Extracellular recording, Microelectrode arrays, Microfabrication, Nanocavity, Redox cycling

Contents

1 Introduction

The detection of signals from biological systems is of major interest for analytical applications and understanding fundamental biological processes. While analytical applications usually target the detection of specific biomolecules including peptides, proteins, or nucleic acid sequences, fundamental investigations on cell–cell communication also require the spatiotemporal detection of electrophysiological signals such as action potentials.

Over the last decades a variety of physical and chemical sensor techniques have been developed to gather information from biological systems. In particular, efforts have been made to employ already existing silicon microfabrication technologies for the development of chip-based biosensor concepts. A particularly interesting feature of electrical chip-based devices is the transduction of specific biological and chemical molecular cues into quantitative electrical signals. This can be realized, for example, via electrochemical, capacitive, or impedimetric sensing concepts. Electrical readout systems for biosensor applications have therefore emerged as a powerful quantitative method for assessing molecular and cellular signals.

Here, we will describe in detail a particular class of electrical and electrochemical sensors termed nanocavity or nanogap sensors. As the name already suggests, this type of sensor relies on a nanometer-sized cavity with integrated electrodes that can be addressed via external circuitry. We will discuss different implementations as well as applications of these sensor types and describe the corresponding fabrication processes and operation principles, which can be divided into capacitive and electrochemical approaches. Capacitive methods of nanocavity operation find applications in the sensing (or stimulation) of electrical signals from cells such as extracellular action potentials. In contrast, electrochemical implementations of nanocavity sensors are employed for molecular sensing and typically require a more complex architecture due to the integration of several independently addressable electrodes within the nanocavity.

The beauty of electrochemical techniques for molecular sensing lies in the simple concept of generating an electrical signal that is associated with a redox

reaction of a specific molecule. This concept makes it easy to read out and process signals by purely electrical circuitry. Furthermore, electrochemical detectors can be readily integrated into chip-based systems with many sensors operating in parallel. For the detection of small amounts of molecules, an amplification strategy is required that can deliver adequate signals for further processing. To achieve this goal, nanocavity devices make use of a signal amplification strategy called redox cycling, where a redox active molecule is repetitively oxidized and reduced at two independently biased electrodes (see Fig. 1). This well-known electrochemical concept has been implemented in a variety of applications for several decades.

Already during the mid-1960s, Anderson and Reilly conducted first redox cycling experiments using the quinone/hydroquinone redox couple in a thin-layer electrochemical cell [1]. In their experiment, the distance between the electrodes was set via a micrometer screw gauge [2] and electrode separations down to approximately 10 μm were achieved to amplify electrochemical currents [3]. Later, redox cycling amplification provided the basis for electrochemical scanning microscopy, which was developed in the 1980s [4, 5] and is used for the topographical and material-specific investigation of surfaces.

The first chip-based devices relying on redox cycling for signal amplification were developed by Sanderson and Anderson [6]. They made use of microfabricated interdigitated gold electrodes, which had a spacing of 100 μm. A more thorough description of these devices is given by Niwa et al. [7]. With the rise of nanofabrication technology, much smaller redox cycling devices have emerged as a powerful class of sensors for amplifying the signals of low quantities of molecules. Ultimately, even single molecules can be resolved by this technology using appropriate electrical readout circuitry [8–12]. A variety of investigations discussing both, the implementation strategies and applications of nanoscaled redox cycling devices with planar (i.e., interdigitated arrays) and vertical (nanocavity) arrangements are currently published in literature.

The aim of this chapter is to provide an overview of the implementation and use of nanocavity devices for sensing applications. In the first part, we will introduce single-electrode nanocavity devices for capacitive sensing of extracellular

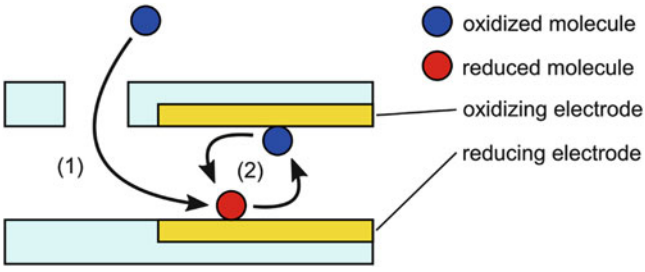

Fig. 1 Schematic of the redox cycling process for electrochemical signal amplification. A molecule entering the nanocavity (1) is reduced at an appropriately biased electrode. A second electrode biased at a different potential oxidizes the molecule. If both electrodes are in close proximity, efficient diffusive transport between the electrodes (2) can lead to a manifold increase in the signal obtained from the molecule

electrical signals originating from cells. In the second part, we will address multi-electrode nanocavity devices for electrochemical sensing approaches and discuss the major implementation strategies and applications for sensing of biomolecules. We will then briefly take a look at the possibility of using alternative low-cost fabrication methods based on inkjet printing that might have the potential of implementing disposable nanocavity devices for a broad range of applications.

2 Single-Electrode Nanocavity Devices

The most basic types of nanocavity sensors rely on a single electrode that is integrated within a nanocavity. These devices are typically integrated in sensor arrays and find applications for the extracellular detection of action potentials in cell networks *in vitro*. In general, such investigations are carried out on cardiac or neuronal cell types. These cells are able to produce action potentials and can readily be grown on planar substrates that include functionality for either recording from or stimulating cells within a network. Figure 2 shows the implementation of such a nanocavity array that was developed for the detection of action potentials in a cardiac cell culture [13].

A prominent application for single-electrode nanocavity devices is the investigation of on-chip cellular communication, which is of interest in a variety of research fields. Examples include pharmacological applications, where the sensors can be used to test the response of cell networks to specific drugs or the

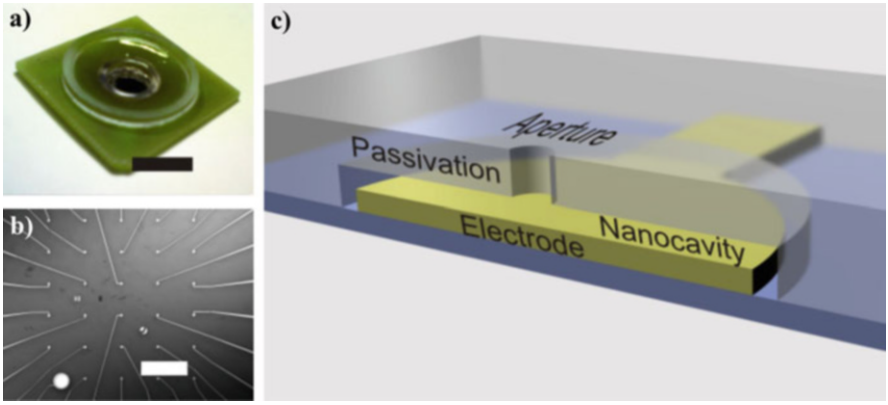

Fig. 2 Nanocavity sensor array for cell recordings and schematic of a nanocavity electrode. (**a**) Nanocavity chip bonded to a printed circuit board and encapsulated for use in cell culture (scale bar corresponds to 1 cm). (**b**) Microscopic image of the chip showing the layout of the nanocavity electrodes. 5 × 6 sensors are arranged with a pitch of 350 μm in the vertical and 400 μm in the horizontal direction (scale bar corresponds to 500 μm). (**c**) Schematic drawing of a cross section through a single nanocavity sensor ([13], adapted by permission of The Royal Society of Chemistry)

development of cell-based biosensors for detecting the presence of molecules, which modulate the electrical activity of the cells. In the latter case, the cell acts as a biological transducer, which reacts to the presence of the target molecules with a change in activity that can be monitored using external electrodes. Since the early work of Thomas et al. [14], these types of applications are usually carried out by so-called microelectrode arrays or MEAs, which locally pick up a voltage signal at the cell–sensor interface [15].

In the last decades a lot of effort has been directed at improving devices for extracellular recording in terms of signal quality, price, sensor density, long-term recordings, and high-throughput capabilities [15–21]. Typically, the recording of action potentials from confluent cell cultures, slices, and even 3D tissue can be readily performed using simple planer microelectrode arrays. However, interfacing individual cells or subcellular compartments in low-density networks remains challenging. The reason for this lies in the poor signal-to-noise ratio, which is usually obtained when recording signals with conventional planar metal microelectrodes of very small (<10 μm) dimensions. In general, the signal quality in such a recording is largely determined by the so-called junction resistance, which describes the coupling of the cell to the electrode. Furthermore, the interfacial impedance of the sensor itself plays an important role for electrodes with subcellular resolution. As the impedance scales inversely with the electrode–electrolyte interface area, small electrodes exhibit a high impedance causing an increase in the noise level of the recording.

There are several approaches to overcome this problem. Historically, electrode surfaces have been modified to increase the electrode–electrolyte interface and thereby reduce the impedance. For example, this can be done by depositing platinum black [14], nanoflakes [22], nanopillars [23, 24], or nanotubes [25–29] as well as introducing porous structures [30, 31]. However, these methods often generate irreproducible or unstable results and sometimes have unfavorable effects on the junction resistance of the cell–electrode interface. CMOS technology enables on-chip amplification of signals using a high sensor density [32–37] but requires more sophisticated and expensive fabrication procedures.

Nanocavity sensors provide a relatively simple alternative for improving the cell–electrode interface without modifying the bulk properties of the interfacing electrode material. The concept is similar to the planar patch clamp method, where a small aperture connects the cell to a channel structure within the substrate [38–40]. However, unlike planar patch clamp implementations, nanocavity sensors do not provide externally addressable channel structures. The apertures, which define the lateral resolution of the cell–sensor contact, are located within the passivation layer of a microelectrode array and therefore allow the integration of a high sensor density. The additional area of the electrode–electrolyte interface within the nanocavity reduces the impedance of the sensor without compromising the lateral resolution of an individual sensor [13, 41]. An example of the cross-section of a cell–electrode contact used for stimulation of an individual cell in a cell network is

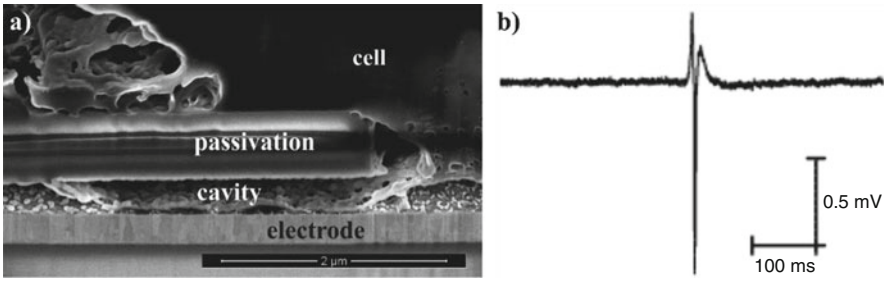

Fig. 3 Properties of the cell–nanocavity interface. (**a**) Scanning electron micrograph of a focused ion beam (FIB) cross-section of an HL-1 cell on a nanocavity sensor. In-between passivation and electrode, cellular protrusion into the cavity can be observed. The cleft between cell and electrode is small, allowing for a tight sensor–cell sealing and therefore a good signal transduction (adapted from [42], published by The Royal Society of Chemistry). (**b**) Extracellular recording of an HL-1 action potential demonstrating the high signal-to-noise ratio achievable with nanocavity devices ([13], reproduced by permission of The Royal Society of Chemistry)

shown in Fig. 3a [42]. Typically, these interfaces yield relatively stable extracellular recordings with high signal-to-noise ratio. An example of such a signal is shown in Fig. 3b.

2.1 Fabrication

The production of nanocavity sensor arrays only requires minor adaptations to the standard lithographical fabrication process of microelectrode arrays. A schematic of such a fabrication process is shown in Fig. 4. Typically, nanocavity sensors are fabricated on insulated silicon or glass wafers. In a first step, feedlines, bond pads, and electrode structures are generated using metal deposition in combination with either lift-off or reactive ion etching for patterning. A second lithography is used to structure a sacrificial chromium layer on top of each electrode, which determines the lateral and vertical extension of the later nanocavity. The whole surface is subsequently insulated using a passivation layer of silicon dioxide, silicon nitride, or polyimide. Microapertures are subsequently patterned on top of each sensor within the passivation layer using a third lithography step in combination with either reactive ion etching or development of a photocurable passivation layer. Finally, the chromium sacrificial layer is removed using a wet-etching process, which releases the nanocavities above the microelectrodes. Overall, compared to the standard fabrication process for microelectrode arrays, one additional lithography, as well as an additional wet-etching step, is required to define the nanocavity. In principle, the additional lithography step can even be avoided if a chromium layer is deposited on top of the noble metal (typically gold or platinum). In many processes this is usually done to facilitate adhesion between the metal feedlines and

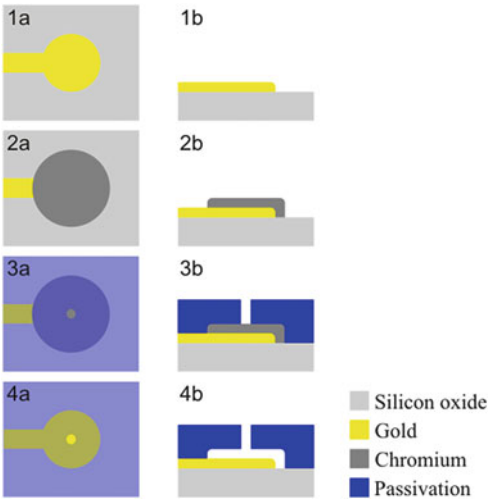

Fig. 4 Fabrication scheme of the nanocavity sensors. Left and right columns show the top and side view of the sensor, respectively. In a first step, the electrodes and feedlines are patterned (1) followed by the deposition of a sacrificial chromium layer (2). The device is then insulated with a silicon nitride/silicon oxide layer deposited via plasma-enhanced chemical vapor deposition (PECVD). Finally, an aperture is etched by reactive ion etching (3) and the chromium layer is removed using wet chemical etching ([13], reproduced by permission of The Royal Society of Chemistry)

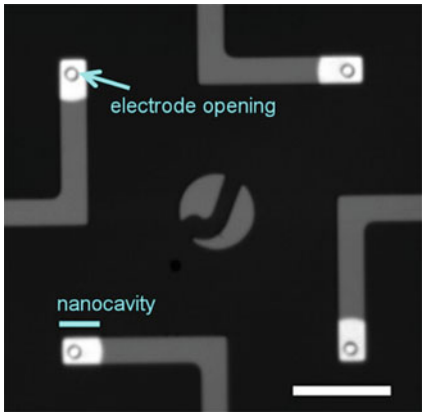

Fig. 5 Microscopic image of four nanocavity sensors created by back-etching of a sacrificial chromium adhesion layer. The back-etched nanocavities (marked in *light blue*) are visible as *rectangular bright areas* at the end of the feedlines; the *circular structures* show the microelectrode apertures (scale bar (*white*): 100 µm; [42], reproduced by permission of The Royal Society of Chemistry)

microelectrodes with a ceramic passivation layer. In this case, the cavity is generated by simply back-etching the adhesion layer [43]. While this process avoids additional patterning by lithography, care has to be taken to stop the wet-etching process at the desired length of the cavity (see Fig. 5). Furthermore, after etching

the cavity is bounded at the end by a thin layer of chromium, which might be detrimental to cells during long-term cultivation. Apart from that, back-etching of a sacrificial adhesion layer provides a straightforward approach for fabricating single-electrode nanocavity sensors that can be easily implemented in standard fabrication procedures.

3 Multi-Electrode Devices (Electrochemical Sensors)

3.1 Nanocavity Redox Cycling Sensors

In the previous section, we have introduced the fabrication process and application of nanocavity sensors exhibiting a single aperture and a single electrode. Now, we will highlight the fabrication and applications of nanocavity sensors with multiple electrodes. While the fabrication approaches for multi- and single-electrode nanocavity sensors are similar, they are typically employed for very different applications. As opposed to applications of single-electrode nanocavity devices for the recording or stimulation of voltage signals, multi-electrode devices typically find application in the electrochemical sensing of redox-active molecules via redox cycling amplification as outlined above. The group of Lemay has implemented sacrificial-layer etching techniques to fabricate fluidic channels with integrated electrodes for this purpose [44]. The first devices that were produced in this way relied on reactive ion etching of a sacrificial layer of amorphous silicon, which had been previously deposited between two platinum electrodes during the fabrication process [44, 45]. Although, using this approach, it was difficult to generate devices with defined geometrical spacing and the electrode spacing was still relatively large (approximately 300 nm), they could demonstrate a strong redox cycling amplification effect and analyze the fluctuations of less than 100 molecules within the fluidic channel. A goal of this work was to boost the sensitivity of microfabricated devices to ultimately reach single-molecule resolution via electrochemical detection, a concept that had so far only been demonstrated using probe-based techniques by the group of Bard [8, 46, 47] and later by Sun and Mirkin [9]. In their next generation of multi-electrode devices, the silicon sacrificial layer was replaced by a chromium sacrificial layer, which could be removed via a simple wet etching process as described above in the case of single-electrode devices. This process facilitated the fabrication of multi-electrode systems with an electrode spacing below 60 nm [45]. The fabrication of such devices is shown in Fig. 6a–h. It follows a similar procedure as the production of single-electrode cavity devices, described previously. However, the integration of electrodes within the top of the fluidic channel requires additional lithography steps after the deposition of the sacrificial layer. A typical fabricated sensor with top and bottom electrodes is shown in Fig. 6i. Due to the elongated channel structure and small electrode spacing these devices exhibited a very strong amplification (approximately 3 orders of magnitude) of the

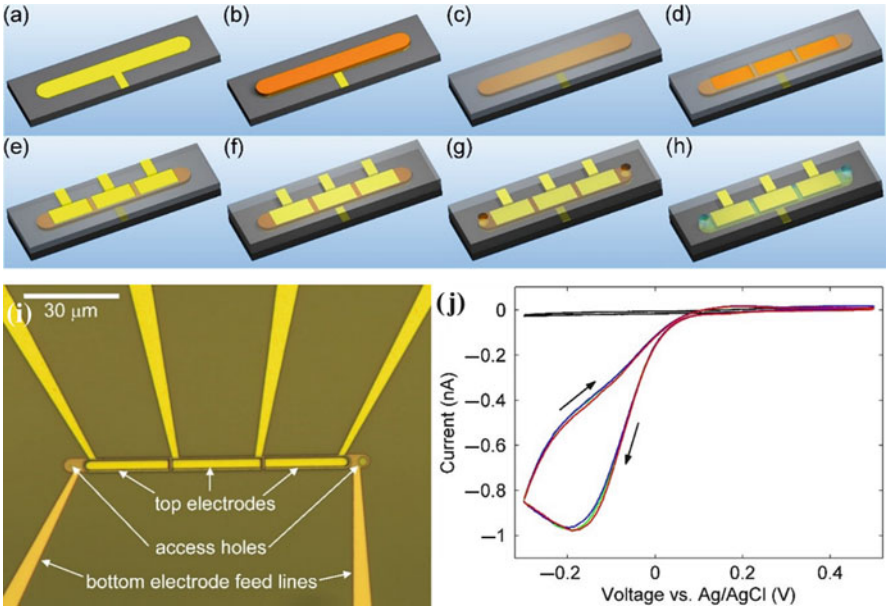

Fig. 6 Multi-electrode nanocavity devices for electrochemical measurements. (**a**–**h**) Sketch of the fabrication process of a nanofluidic redox cycling device. First the bottom electrode is patterned (**a**) followed by deposition of a sacrificial chromium layer (**b**). SiO_2 is sputtered to passivate the bottom layer (**c**). Access patterns are then etched (**d**) allowing the deposition of the top electrodes (**e**). The whole structure is insulated by sputtered SiO_2 (**f**) before access holes are etched (**g**) and the sacrificial chromium layer is removed (**h**). (**i**) Microscopic top-view image of a typical device just before the removal of the sacrificial chromium layer. Feedlines connect to the bottom electrode and three top electrodes. Access holes are visible at the end of the channels. (**j**) Redox-cycling currents obtained from a 45 µM catechol solution in the presence of 0, 100, and 500 µM interfering ascorbic acid concentration (*red*, *green*, and *blue curves*, respectively; scan rate 50 mV s^{-1}). The *black curve* was recorded in background electrolyte (100 mM phosphate buffer, pH 7.2). Adapted with permission from [45]. Copyright 2008 American Chemical Society

electrochemical current, when operated in redox cycling mode as opposed to using only a single electrode within the channel. As this amplification is selective towards species that can participate in redox cycling, this opens the possibility for rejecting the interference of unwanted molecules.

A prominent target for electrochemical detection are catechols or catecholamines, which play an important role in neurochemistry [48–50]. The nanofluidic redox cycling devices delivered an area-specific sensitivity of approximately 106 A M^{-1} m^{-2} for the detection of catechol in buffer solution corresponding to a current of about 33 fA per molecule. It could be demonstrated that the interference of ascorbic acid could be virtually eliminated during the detection of catechol due to its inability to participate in prolonged redox cycling (see Fig. 6j). Selectivity in such devices can further be enhanced by tuning the electrode potentials for specific targets. This method has recently been demonstrated by the group of Rassaei who

used potential step and sweeping protocols to distinguish between three different redox-active tracers in a nanofluidic redox cycling device [51].

Using careful refinement in the fabrication process of nanofluidic redox cycling devices, the group of Lemay was able to push the limit for electrochemical detection and discern the fluctuation of individual molecules diffusing into or out of the nanocavity [10, 52]. Resolving single molecules by electrochemical means is highly interesting as it describes a transition in the detection scheme from amplitude-based ensemble average measurements, where the signal amplitude is proportional to the concentration of molecules, to a stochastic detection where the frequency of events is proportional to the concentration [11, 12]. In principle, this allows the exchange of time versus sensitivity as the experimentalist simply has to wait longer for a sufficient number of detection events to occur [53]. It should be mentioned, however, that in realistic scenarios at very low concentrations, this time can be very long and beyond reasonable applicability. Furthermore, dynamic adsorption effects of molecules at the walls of the nanocavity or the electrodes further complicate highly sensitive measurements [11, 54–57]. An elegant way to speed up the response time of cavity-based redox cycling sensors is the introduction of a flow within the nanofluidic channel [58].

3.2 Applications in Electrochemical Biosensing

So how can these sensitive devices be used as a biosensor? An impressive application of nanofluidic redox cycling sensors was demonstrated by Rassei et al. [59]. In their work, they immobilized the enzyme tyrosinase, which is commonly used for the detection of phenolic compounds, within the femtoliter-scale volume of their nanocavity (see Fig. 7).

The use of tyrosinase in combination with the nanofluidic redox cycling sensor allowed the detection of phenol, which was catalyzed to catechol/quinone via the monophenolase activity of tyrosinase. The phenol substrate itself without conversion could not be detected by electrochemical means due to the inapplicable redox potential. The authors demonstrated the detection of only approximately 70,000 product molecules of the quinone/catechol redox couple within the nanochannel. In particular, due to the confined scale and large amplification factor, this method did not rely on long incubation times that are typically necessary for low enzymatic turnover rates. Thus, the presented sensor concept allowed the detection of very few enzymatically generated product molecules in real time, which could be used in the future to study small-volume systems given by individual cells.

The implementation of nanocavity devices ranges from the previously presented channel structures to arrays with multiple detection sites for spatiotemporal studies of concentration fluctuations [60–62]. In particular, Matsue, Ino, and coworkers designed an elegant strategy for the spatiotemporal investigation of embryoid bodies using a nanocavity redox cycling chip [62]. In their work, they exploited

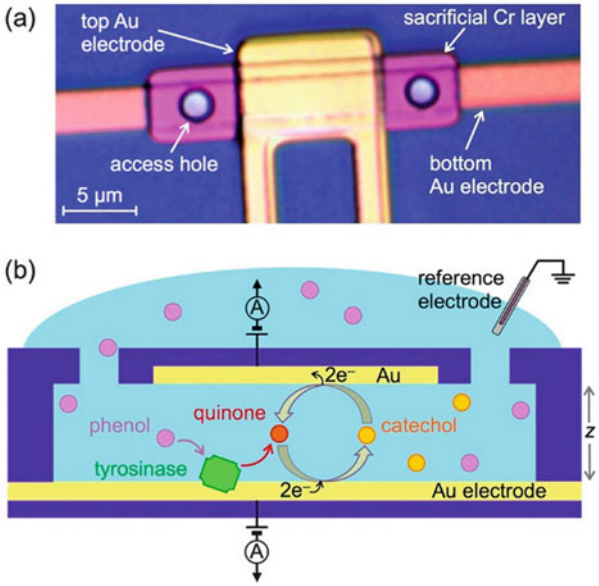

Fig. 7 Nanofluidic bioelectrochemical detection. (**a**) Optical micrograph (top view) of a nanogap device. The active detection region is defined by the $10 \times 3\ \mu m^2$ area in which the two electrodes overlap. (**b**) Schematic principle of operation of the electrochemical bionanofluidic device: Immobilized tyrosinase enzymatically transforms inactive monophenolic substrate molecules into electrochemically active *o*-quinones. These molecules subsequently undergo redox cycling, yielding a highly amplified electrical current, thus enabling sensitive detection and direct signal transduction (channel height $z = 200$ nm; reprinted with permission from [59])

the possibility of a redox cycling crossbar architecture (see Fig. 8). This way, they were able to integrate a number of sensors on a single chip that scaled according to

$$N_{\text{sensor}} = {N_{\text{feedlines}}}^2/2, \tag{1}$$

where N_{sensor} and $N_{\text{feedlines}}$ are the number of sensor sites and feedlines, respectively. They demonstrated the applicability of their system for bioassays by electrochemically imaging the alkaline phosphatase activity of embryoid bodies from embryonic stem cells in a high-throughput approach.

Very recently, the group of Estrella introduced two alternative methods for fabricating large-area horizontal and vertical nanogap sensors and demonstrated the possibility of detecting PNA-DNA binding events based on dielectric spectroscopy [63]. Apart from pure sensing applications, nanocavity devices have also been used for fundamental studies on e.g., charge transfer and transport effects [64–66]. These detailed mechanistic studies are made possible due to the fast diffusive mass transport that is encountered in highly confined cavity devices.

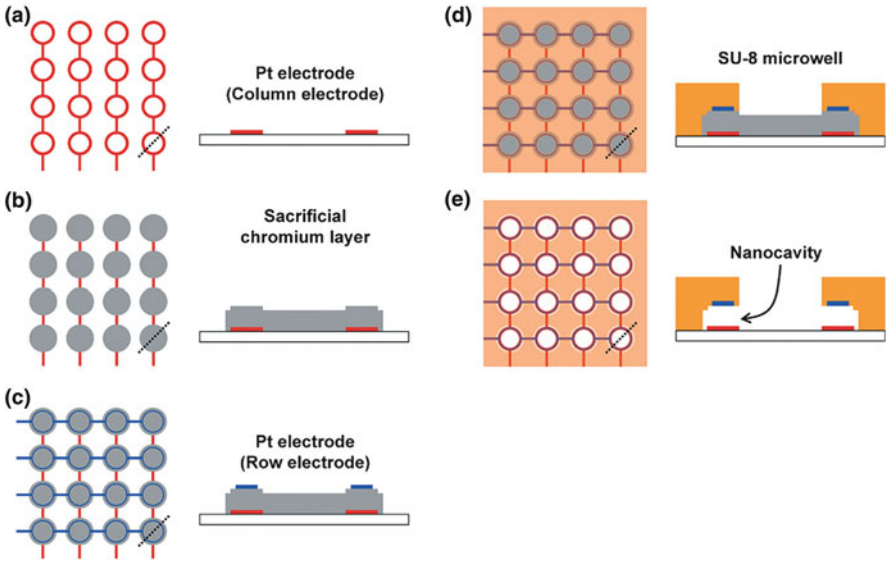

Fig. 8 Schematic illustration of the device fabrication process. (**a**) Ti/Pt is sputtered onto a glass substrate to fabricate the column electrodes that contain the bottom ring electrodes. (**b**) A sacrificial Cr layer is sputtered on the bottom ring electrodes. (**c**) Cr/Pt is then sputtered to fabricate the row electrodes that contain the top ring electrodes. (**d**) A SU-8 layer is fabricated on the device to form 4 × 4 microwells (diameter: 150 µm, depth: 50 µm, gap: 300 µm). (**e**) The Cr sacrificial layer is etched to prepare nanocavities between the top and bottom ring electrodes ([62] – published by The Royal Society of Chemistry)

3.3 Next-Generation Fabrication Approaches

In general, sacrificial-layer etching in combination with either electron-beam or optical lithography presents opportunities for producing defined nanocavity devices with excellent control of the geometric features [67–70]. Additionally, integration schemes of such devices with CMOS technology have been proposed, which promise scalability for future biosensor systems [71]. However, applications aiming at disposable low-cost systems call for other preparation methods that do not require advanced clean-room technology. The group of Marken, for instance, has developed an innovative method for the low-cost fabrication of microgap systems based on chemical etching of a thin epoxy layer between two electrodes [72–76]. With this approach they were able to demonstrate the detection of various redox couples as well as suppression of oxygen and ascorbate interference. Nevertheless, the production process is not suited for high-throughput fabrication.

An interesting alternative to conventional clean-room technology are additive fabrication approaches. While typically being limited in the lateral resolution to feature sizes on the order of a few micrometers, they can take full advantage of the nanocavity design in a vertical layout. A corresponding inkjet-printed system is depicted in Fig. 9 [53, 77].

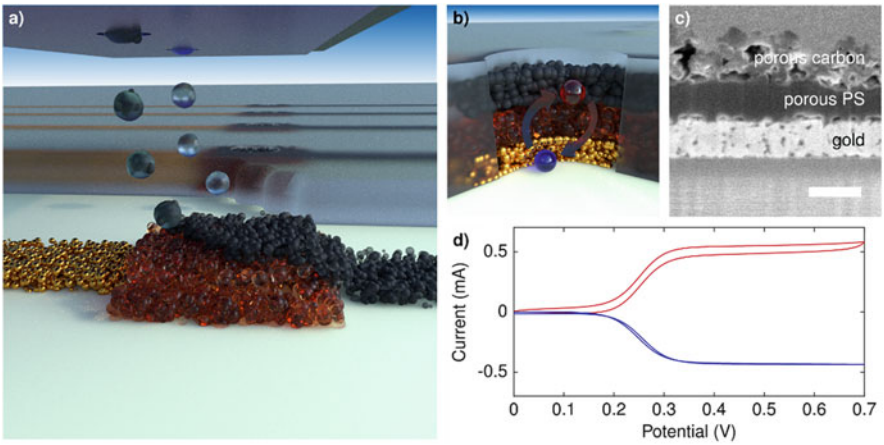

Fig. 9 Printed redox cycling sensor array. Schematic overview of the printing process (**a**) and a sensor cross-section (**b**). (**c**) SEM image of a FIB cut of the printed sensor layers (scale bar: 200 nm) (**d**) Exemplary cyclic voltammetry traces recorded with a printed redox cycling sensor (500 µM $Fc(MeOH)_2$ at 20 mV s^{-1}). Reprinted with permission from [53]. Copyright 2016 American Chemical Society

In this example, the bottom electrode of the sensor system is printed first. Then, a porous dielectric layer and a conductive but porous layer are printed on top of the stack. Finally, a non-porous dielectric layer is printed to insulate the sensor versus the electrolyte (compare Fig. 9a). Molecules can now enter the "cavity" via the porous top electrode and redox cycling between the top and bottom electrode can be observed (see Fig. 9b–d). Although this structure rather resembles the layout of a nanoporous redox cycling device [78–83], principles for nanocavity layouts can be readily adopted. Overall, advances in state-of-the-art printing technologies provide the potential means for developing low-cost disposable nanocavity devices for biosensing applications.

4 Summary and Outlook

Nanocavity devices offer various benefits compared to standard planar single- and multi-electrode configurations for sensing applications. In the context of single-electrode devices for the capacitive sensing of extracellular voltage signals, they can increase the resolution of the sensing spot while at the same time offering an improved signal-to-noise ratio by increasing the junction resistance and lowering the interfacial impedance of the electrode. Multi-electrode nanocavity devices, on the other hand, find various applications in the field of redox cycling-based amplification and discrimination of electrochemical signals of different sources (see Table 1 for a comparison of different sensor architectures and their respective

Table 1 Comparison of different redox-cycling sensor array architectures giving the type of sensor, target, fabrication method, area-specific sensitivity, and the ratio of the redox-cycling current to the diffusion-limited current of a microelectrode of equal area (Γ_{sen}) as well as the ratio of the redox cycling current to the current obtained in regular amperometric operation (Γ_{sel})

Type	Target	Fabrication method	Area-specific sensitivity (A M^{-1} m^{-2})	Γ_{sen}	Γ_{sel}
Nanofluidic	Catechol	E-beam	~1.1 × 10^6	~34	~10^3
Nanocavity	Dopamine	Optical	~0.9 × 10^5	~8	
Nanocavity (crossbar)	$Fc(MeOH)_2$	Optical	~(2–17) × 10^4	~0.2–1.5	
Nanoporous (e-beam)	$Fc(MeOH)_2$	E-beam	~(2–81) × 10^4	~16–46	~500
Nanoporous (alumina)	$[Fe(CN)_6]^{3-/4-}$	Porous alumina	~3.6 × 10^4	~730	
Nanoporous (printed)	$Fc(MeOH)_2$	Inkjet printing	~5.9 × 10^3	~1.2	~30

Adapted with permission from [53]. Copyright 2016 American Chemical Society

performances). The enhanced sensitivity offered by these devices allows the detection of electrochemical currents originating from minute quantities of molecules, ultimately down to the single-molecule level. In addition, the detection scheme facilitates selectivity towards target analytes by discriminating molecules that cannot participate in repeated redox reactions. Finely tuned electrode potentials can be used to differentiate signals from different redox-active compounds.

Biosensing detection strategies of analytes in these devices can include impedance-based methods, the blocking of a redox-active tracer, enzymatic conversion between non redox-active and redox-active compounds and interactions of the analyte with a flexible linker molecule containing a redox-active moiety [84]. Finally, low-cost fabrication techniques, such as inkjet printing, are compatible with vertical nanocavity architectures. We believe that in the future this could open up the possibility of producing highly sensitive disposable biosensing platforms for point-of-care applications.

References

1. Anderson LB, Reilley CN (1965) J Electroanal Chem 10(1959):295
2. Oglesby DM, Omang SH, Reilley CN (1965) Anal Chem 37:1312
3. Anderson LB, Reilley CN (1959) J Electroanal Chem 10:538
4. Liu HY, Fan FRF, Lin CW, Bard AJ (1986) J Am Chem Soc 108:3838
5. Bard AJ, Fan FR, Kwak J, Lev O (1989) Anal Chem 61:132
6. Sanderson DG, Anderson LB (1985) Anal Chem 57:2388
7. Niwa O, Morita M, Tabei H (1990) Anal Chem 62:447
8. Fan F-RF, Bard AJ (1995) Science 267:871
9. Sun P, Mirkin MV (2008) J Am Chem Soc 130:8241

10. Zevenbergen MAG, Singh PS, Goluch ED, Wolfrum BL, Lemay SG (2011) Nano Lett 11:2881
11. Singh PS, Kätelhön E, Mathwig K, Wolfrum B, Lemay SG (2012) ACS Nano 6:9662
12. Lemay SG, Kang S, Mathwig K, Singh PS (2013) Acc Chem Res 46:369
13. Hofmann B, Kätelhön E, Schottdorf M, Offenhäusser A, Wolfrum B (2011) Lab Chip 11:1054
14. Thomas CA, Springer PA, Loeb GE, Berwald-Netter Y, Okun LM (1972) Exp Cell Res 74:61
15. Rutten WLC (2002) Annu Rev Biomed Eng 4:407
16. Pine J (1980) J Neurosci Methods 2:19
17. Cogan SF (2008) Annu Rev Biomed Eng 10:275
18. Xie C, Lin Z, Hanson L, Cui Y, Cui B (2012) Nat Nanotechnol 7:185
19. Spira ME, Hai A (2013) Nat Nanotechnol 8:83
20. Santoro F, Dasgupta S, Schnitker J, Auth T, Neumann E, Panaitov G, Gompper G, Offenhäusser A (2014) ACS Nano 8:6713
21. VanDersarl JJ, Renaud P (2016) Sci Rep 6:32485
22. Kim J-H, Kang G, Nam Y, Choi Y-K (2010) Nanotechnology 21:085303
23. Brüggemann D, Wolfrum B, Maybeck V, Mourzina Y, Jansen M, Offenhäusser A (2011) Nanotechnology 22:265104
24. Nick C, Quednau S, Sarwar R, Schlaak HF, Thielemann C (2014) Microsyst Technol 20:1849
25. Gabay T, Ben-David M, Kalifa I, Sorkin R, Abrams ZR, Ben-Jacob E, Hanein Y (2007) Nanotechnology 18:035201
26. Shoval A, Adams C, David-Pur M, Shein M, Hanein Y, Sernagor E (2009) Front Neuroeng 2:4
27. Greenbaum A, Anava S, Ayali A, Shein M, David-Pur M, Ben-Jacob E, Hanein Y (2009) J Neurosci Methods 182:219
28. Heim M, Yvert B, Kuhn A (2012) J Physiol Paris 106:137
29. David-Pur M, Bareket-Keren L, Beit-Yaakov G, Raz-Prag D, Hanein Y (2014) Biomed Microdevices 16:43
30. Seker E, Berdichevsky Y, Begley MR, Reed ML, Staley KJ, Yarmush ML (2010) Nanotechnology 21:125504
31. Urbanová V, Li Y, Vytřas K, Yvert B, Kuhn A (2011) J Electroanal Chem 656:91
32. Berdondini L, Imfeld K, Maccione A, Tedesco M, Neukom S, Koudelka-Hep M, Martinoia S (2009) Lab Chip 9:2644
33. Bakkum DJ, Frey U, Radivojevic M, Russell TL, Müller J, Fiscella M, Takahashi H, Hierlemann A (2013) Nat Commun 4:2181
34. Bertotti G, Velychko D, Dodel N, Keil S, Wolansky D, Tillak B, Schreiter M, Grall A, Jesinger P, Röhler S, Eickenscheidt M, Stett A, Möller A, Boven KH, Zeck G, Thewes R (2014) In: 2014 I.E. biomedical circuits and systems conference (BioCAS) proceedings, pp 304–307
35. Ballini M, Müller J, Livi P, Chen Y, Frey U, Stettler A, Shadmani A, Viswam V, Jones IL, Jäckel D, Radivojevic M, Lewandowska MK, Gong W, Fiscella M, Bakkum DJ, Heer F, Hierlemann A (2014) IEEE J Solid State Circuits 49:2705
36. Müller J, Ballini M, Livi P, Chen Y, Radivojevic M, Shadmani A, Viswam V, Jones IL, Fiscella M, Diggelmann R, Stettler A, Frey U, Bakkum DJ, Hierlemann A (2015) Lab Chip 15:2767
37. Amin H, Maccione A, Marinaro F, Zordan S, Nieus T, Berdondini L (2016) Front Neurosci 10:121
38. Fertig N, Blick RH, Behrends JC (2002) Biophys J 82:3056
39. Li X, Klemic KG, Reed MA, Sigworth FJ (2006) Nano Lett 6:815
40. Behrends J, Fertig N (2007) Planar patch clamping. In: Walz W (ed) Neuromethods. Humana Press, Totowa, pp 411–433
41. Schottdorf M, Hofmann B, Kätelhön E, Offenhäusser A, Wolfrum B (2012) Phys Rev E 85:031917
42. Czeschik A, Rinklin P, Derra U, Ullmann S, Holik P, Steltenkamp S, Offenhäusser A, Wolfrum B (2015) Nanoscale 7:9275

43. Czeschik A, Offenhäusser A, Wolfrum B (2014) Phys Status Solidi A 211:1462
44. Zevenbergen MAG, Krapf D, Zuiddam MR, Lemay SG (2007) Nano Lett 7:384
45. Wolfrum B, Zevenbergen M, Lemay S (2008) Anal Chem 80:972
46. Bard AJ, Fan F-RF (1996) Acc Chem Res 29:572
47. Fan F-RF, Kwak J, Bard AJ (1996) J Am Chem Soc 118:9669
48. Wightman RM, Jankowski JA, Kennedy RT, Kawagoe KT, Schroeder TJ, Leszczyszyn DJ, Near JA, Diliberto EJ, Viveros OH (1991) Proc Natl Acad Sci 88:10754
49. Amatore C, Arbault S, Guille M, Lemaître F (2008) Chem Rev 108:2585
50. Cans A-S, Ewing AG (2011) J Solid State Electrochem 15:1437
51. Zafarani HR, Mathwig K, Lemay SG, Sudhölter EJR, Rassaei L (2016) ACS Sens 1:1439
52. Kang S, Nieuwenhuis AF, Mathwig K, Mampallil D, Lemay SG (2013) ACS Nano 7:10931
53. Wolfrum B, Kätelhön E, Yakushenko A, Krause KJ, Adly N, Hüske M, Rinklin P (2016) Acc Chem Res 49:2031
54. Kang S, Mathwig K, Lemay SG (2012) Lab Chip 12:1262
55. Kätelhön E, Krause KJ, Mathwig K, Lemay SG, Wolfrum B (2014) ACS Nano 8:4924
56. Mampallil D, Mathwig K, Kang S, Lemay SG (2014) J Phys Chem Lett 5:636
57. Krause KJ, Mathwig K, Wolfrum B, Lemay SG (2014) Eur Phys J Spec Top 223:3165
58. Mathwig K, Lemay SG (2013) Electrochim Acta 112:943
59. Rassaei L, Mathwig K, Kang S, Heering HA, Lemay SG (2014) ACS Nano 8:8278
60. Kätelhön E, Hofmann B, Lemay SG, Zevenbergen MAG, Offenhäusser A, Wolfrum B (2010) Anal Chem 82:8502
61. Kätelhön E, Mayer D, Banzet M, Offenhäusser A, Wolfrum B, Beilstein J (2014) Nanotechnology 5:1137
62. Kanno Y, Ino K, Shiku H, Matsue T (2015) Lab Chip 15:4404
63. Hammond JL, Rosamond MC, Sivaraya S, Marken F, Estrela P (2016) Sensors 16:2128
64. Zevenbergen MAG, Wolfrum BL, Goluch ED, Singh PS, Lemay SG (2009) J Am Chem Soc 131:11471
65. Xiong J, Chen Q, Edwards MA, White HS (2015) ACS Nano 9:8520
66. Chen Q, McKelvey K, Edwards MA, White HS (2016) J Phys Chem C 120:17251
67. Rassaei L, Singh PS, Lemay SG (2011) Anal Chem 83:3974
68. Dawson K, O'Riordan A (2014) Annu Rev Anal Chem 7:163
69. Lim Y, Heo J-I, Shin H (2014) Sens Actuators B 192:796
70. Zafarani HR, Mathwig K, Sudhölter EJR, Rassaei L (2016) J Electroanal Chem 760:42
71. Singh PS (2015) IEEE Access 3:249
72. Dale SEC, Marken F (2013) Faraday Discuss 164:349
73. Hasnat MA, Gross AJ, Dale SEC, Barnes EO, Compton RG, Marken F (2014) Analyst 139:569
74. Lewis GEM, Dale SEC, Kasprzyk-Hordern B, Lubben AT, Barnes EO, Compton RG, Marken F (2014) Phys Chem Chem Phys 16:18966
75. Gross AJ, Marken F (2014) Electrochem Commun 46:120
76. Montiel MA, Iniesta J, Gross AJ, Marken F (2017) Electrochim Acta 224:487
77. Adly NY, Bachmann B, Krause KJ, Offenhäusser A, Wolfrum B, Yakushenko A (2017) RSC Adv 7:5473
78. Ma C, Contento NM, Gibson LR, Bohn PW (2013) Anal Chem 85:9882
79. Hüske M, Stockmann R, Offenhäusser A, Wolfrum B (2013) Nanoscale 6:589
80. Zhu F, Yan J, Pang S, Zhou Y, Mao B, Oleinick A, Svir I, Amatore C (2014) Anal Chem 86:3138
81. Fu K, Han D, Ma C, Bohn PW (2016) Faraday Discuss 193:51
82. He D, Yan J, Zhu F, Zhou Y, Mao B, Oleinick A, Svir I, Amatore C (2016) Anal Chem 88:8535
83. Wang Y, Lin X, Su B (2016) Electrochem Commun 72:1
84. Steentjes T, Sarkar S, Jonkheijm P, Lemay SG, Huskens J (2017) Small 13:1603268

Computational Modeling of Biomolecule Sensing with a Solid-State Membrane

Craig C. Wells, Dmitriy V. Melnikov, and Maria E. Gracheva

Abstract In this work, we theoretically study the interaction between a solid-state membrane equipped with a nanopore and a tethered, negatively charged polymer chain subjected to a time-dependent applied electrolyte bias. In order to describe the movement of the chain in the biomolecule-membrane system immersed in an electrolyte solution, Brownian dynamics is used. We show that we can control the polymer's equilibrium position with various applied electrolyte biases: for a sufficiently positive bias, the chain extends inside the pore, and the removal of the bias causes the polymer to leave the pore. Corresponding to a driven process, we find that the time it takes for a biomolecular chain to enter and extend into a nanopore in a positive bias almost increases linearly with chain length while the time it takes for a polymer chain to escape the nanopore is mainly governed by diffusion. In addition to attaching the polymer chain to the mouth of the nanopore, the chain is attached to a molecule with a radius larger than that of the nanopore's, acting as a molecular stop. This allows the polymer to thread the nanopore but not translocate it. In this new system, the chain's variation of movement was compared to that of the freely translocating polymer chain. The results show the free polymer having greater variation in the radial direction, indicating the restrictions imposed by the molecular stop and bias aid in controlling the position and movement of the polymer chain in the nanopore.

Keywords Brownian dynamics, Nanopore, Polymer, Protein, Solid-state membrane

C. C. Wells, D. V. Melnikov, and M. E. Gracheva (✉)
Department of Physics, Clarkson University, Potsdam, NY 13699, USA
e-mail: gracheva@clarkson.edu

M. J. Schöning, A. Poghossian (eds.), *Label-Free Biosensing: Advanced Materials, Devices and Applications*, Springer Series on Chemical Sensors and Biosensors (2018) 16: 215–238
DOI 10.1007/5346_2017_5, © Springer International Publishing AG 2017,
Published online: 7 June 2017

Contents

1 Introduction

Nanopores in membranes have the possibility of being used as sensors for biomolecular identification and characterization [1]. For this purpose, a molecule can be forced through a nanopore by fluid flow, electric bias applied across the membrane, or both. By measuring the ionic current blockage created by the translocating biomolecule using the resistive pulse technique, the size and composition can be correlated to a specific molecule [2–4].

A nanopore with tethered polymer chain surface modifications has an advantage in that the molecules along the inner surface create a means for selective transport. Tailored nanopores with these functionalizations can allow only specific biomolecules to enter and translocate them, making the biomolecule the only species to be detected by the pore [5]. A nanopore's surface functionalized in such a way provides a simplified alternative to analyzing complex resistive pulse patterns.

Surface functionalizations have been a growing field of study since the early 2000s, when they were being applied to biological nanopores. These modifications included tethering polymer chains and oligonucleotides to the surface of staphylococcal α-hemolysin (αHL) pores to characterize the pore [6, 7].

Nanopores in solid-state membranes have recently emerged to provide a more practical means of studying traits of various biomolecules since the size and functionality of these nanopores can be tuned to a specific task. For an artificial nanopore, the ability to control the geometry, as well as an electrical environment of the structure is a tradeoff from losing the compatibility biological nanopores have with certain biomolecules. Thus, applications of functionalized solid-state nanopores, fabricated by either ion or electron beam sculpting [8–10], are potentially more versatile. For example, molecular dynamics (MD) simulations have shown the effect of alternating electric field on a DNA trapped in a nanopore [11].

Solid-state nanopores have been functionalized with polymers in the attempt to create more selective nanopores. By attaching polymer chains to a pore, a gating effect can be created, rendering the pore open or closed to specific ions or molecules (an "on state," or open state, corresponds to a high ionic current within the pore

while the "off state," or closed state, results in a zero or low ionic current). The state of the pore can depend on how the tethered polymer chain interacts with it and on the environment it is in. Nanopores modified with polymer brushes in polyethylene terephthalate (PET) films have been shown to display gating effects dependent on temperature and pH [12, 13].

Single-stranded DNA (ssDNA) and hairpin loop DNA [14–16] molecules have been used for surface functionalizations. Since DNA carries a negative charge, a chain subject to an electric field will align with it. Molecular dynamics simulations have shown how surface tethered ssDNA changes the effective pore diameter when a voltage applied along the pore [17]. Coarse grained molecular dynamics (CGMD) and experiments have studied ssDNA translocating through such a surface modified nanopore [15, 18]. A blockage of ionic current has also been found when a complementary DNA translocates a pore with its tethered counterpart due to the hybridization interactions taking place [18].

Other polymers have been used in surface functionalization of nanopores as well. Peptide nucleic acid (PNA) has been used to mimic the structure and bases of DNA and have been bonded with polymide membranes via a track etching technique [5, 19]. Biological and synthetic molecules have also been tethered to nanopores, achieving similar results in nanopore characterization [15, 20, 21].

A negatively charged polymer chain of various lengths tethered to the surface of a SiO_2 membrane at the nanopore opening when a time-dependent electrolyte bias is applied across it is studied. Here, the Brownian dynamics is used to study how the tethered polymer enters and exits the nanopore under the time-dependent switching bias [22].

Modifications can also be made to a polymer chain. For example, attaching a chain to a much larger biomolecule, such that the chain can be threaded through a nanopore but the molecule it is attached to cannot, is a modification that might provide spatial control of the chain could result in a better resolution of ionic current. Experiments where a polymer chain's free end is attached to a molecular stop, a molecule too large to enter a given nanopore, have been conducted using biological nanopores and the protein streptavidin or NeutrAvidin with a strand of ssDNA attached [23–25].

In this chapter, Sect. 2 describes the system schematic and computational model for the surface modified nanopore and modified polymer chain. Section 3 describes the results of the polymer-nanopore simulations. In Sect. 4, the findings are briefly summarized.

2 Model and Methods

2.1 Nanopore-Membrane System

Our modeled SiO_2 membrane equipped with a cylindrical nanopore is shown in Fig. 1. The membrane has a thickness of $L = 260$ Å and the pore radius is

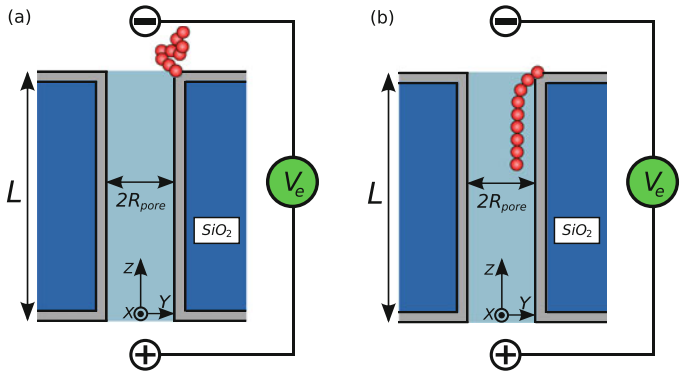

Fig. 1 Schematics of simulated system at different applied electrolyte biases V_e. Attached to the nanopore is a strand of beads representing a polymer chain in (**a**) $V_e = 0$ and (**b**) $V_e > 0$ electrolyte bias environment. The membrane consists of an uncharged bulk and a negatively charged surface layer. The x, y, and z axes originate at the bottom center of the cylindrical pore

$R_{\text{pore}} = 10$ Å. There is a 4 Å thick negatively charged surface layer on the membrane with a volume charge density of $\rho_{SiO_2} = 4 \times 10^{20}\ e/\text{cm}^3$ (which corresponds to a surface charge density of $1.6 \times 10^{13}\ e/\text{cm}^2$), where e is the positive elementary charge. The 252 Å thick layer of SiO_2 underneath the charged surface layer is uncharged. A polymer chain is attached to the opening of the nanopore and is represented with beads. The membrane is submerged in an aqueous KCl electrolyte solution of bulk concentration $C_{\text{KCl}} = 0.2\text{M}$ and an electrolyte bias, V_e, is applied across the pore.

2.2 Computational Model of Surface Modified Nanopore

Using Brownian dynamics (BD) approach, the movement of the tethered polymer is calculated utilizing the parameters to describe an anchored ssDNA. Every bead in the polymer chain carries a charge of $q_i = -1e$ which models the phosphate backbone of the ssDNA. The first bead of the chain, $i = 0$, is fixed at the top of the nanopore at position $z = 260$ Å, $x = 0$ Å, $y = R_{\text{pore}}$, while the remaining i-th beads are free to move. The remaining bead's position at time t is determined by the Langevin equation [26]:

$$\mathbf{r}_i(t) = \mathbf{r}_i(t - \delta t) - \nabla_i U[\mathbf{r}_i(t - \delta t)]\frac{\delta t}{\xi} + \sqrt{\frac{6\delta t k_b T}{\xi}}\mathbf{n}_i, i = 2, \ldots, N_b \qquad (1)$$

where N_b is the number of beads in the chain, the time step $\delta t = 5$ ps, and $\mathbf{r}_i = (t - \delta t)$ is the i-th's bead position at the previous time step. The second term in Eq. (1) accounts for all the forces each freely moving bead experiences, and the

last term accounts for a stochastic force. The three-dimensional unit vector $\mathbf{n}_i$ has randomly chosen values for its x, y, and z-components in the range $[-1, 1]$ and is responsible for the direction of the force that causes random bead movement. The net potential energy has the following form:

$$U(\mathbf{r}_i) = U_{\text{el}} + U_b + U_m + U_C + q_i\phi(\mathbf{r}_i), \tag{2}$$

where the elastic bond energy is

$$U_{\text{el}} = k_{\text{el}} \sum_{j=i\pm1} \left(r_{ij} - r_0\right)^2, \tag{3}$$

with $k_{\text{el}} = 171$ kcal/(mol Å) being the elastic constant, $r_0 = 3.4$ Å being the equilibrium bond length, and $r_{ij} = |\mathbf{r}_i - \mathbf{r}_j|$, $j = i \pm 1$, being the bond length between neighboring i-th and j-th beads [22, 26].

The short-range Lennard–Jones (LJ) interaction energy among all beads defines the excluded volume effects and is expressed by

$$U_b = \epsilon_b \sum_{j, j\neq i} \left[\left(\frac{\sigma_b}{r_{ij}}\right)^{12} - 2\left(\frac{\sigma_b}{r_{ij}}\right)^{6} \right] \tag{4}$$

Here, $\sigma_b = 6.5$ Å is the LJ bead-bead radius and $\epsilon_b = 0.1$ kcal/mol is the interaction strength. The LJ interaction between the beads that make up the polymer and the membrane is also considered. This potential energy, U_m, is similar to Eq. (4) where σ_b is replaced with $\sigma_b = 2.5$ Å, $\epsilon_b = \epsilon_m$, and r_{ij} is replaced with the distance between the i-th bead and the membrane surface. Note that $\sigma_m < \sigma_b$ because beads have the ability to be closer to the membrane than they do each other.

As was already mentioned, each bead has a negative q_i charge. The charge is screened by the ionic solution and the resulting interaction potential energy is represented by

$$U_c = \frac{1}{4\pi\varepsilon_0\varepsilon_r^{\text{KCl}}} \sum_{j, j\neq i} \frac{q_i q_j}{r_{ij}} \exp\left[\frac{-r_{ij}}{L_D}\right] \tag{5}$$

where $\varepsilon_r^{\text{KCl}} = 78$ is the relative permittivity of the KCl electrolyte solution, and L_D is the Debye screening length,

$$L_D = \left[\varepsilon_0\varepsilon_r^{\text{KCl}} k_B T / \left(2e^2 C_{\text{KCl}}\right)\right]^{1/2}, \tag{6}$$

which is ≈0.68 nm for our bulk KCl concentration at temperature $T = 100$ K. Since this L_D is smaller than the radius of the nanopore, the continuum Poisson–Nernst–Planck (PNP) approach to find the electric potential energy $q_i\phi$ is used.

In order to define the electric potential, in this approach the Poisson equation

$$\nabla \cdot [\varepsilon(\mathbf{r}) \nabla \phi(\mathbf{r})] = -\rho(\mathbf{r}), \tag{7}$$

is solved self-consistently with the steady-state Nernst–Planck equations

$$\nabla \cdot [\mu_i C_i \nabla \phi + z_i D_i \nabla C_i] = 0, i = \mathrm{K}^+, \mathrm{Cl}^-, \tag{8}$$

to determine local ionic concentrations of $C_{\mathrm{K}^+}(\mathbf{r})$ and $C_{\mathrm{Cl}^-}(\mathbf{r})$. In Eq. (8), μ_i is the mobility, $z_i = \pm 1$ based on the charge of the ion, and $D_i = \mu_i k_B T/e$, the diffusion coefficient, is $D_{\mathrm{K}^+} = 1.95 \times 10^{-5}$ cm^2/s and $D_{\mathrm{Cl}^-} = 2.03 \times 10^{-5}$ cm^2/s.

The total charge density, $\rho(\mathbf{r})$, in Eq. (7) is composed of the charge in the electrolyte, $\rho_e(r)$, and on the membrane, $\rho_m(r)$. These charge densities are described by

$$\rho_e(\mathbf{r}) = e\{C_{\mathrm{K}^+}(\mathbf{r}) - C_{\mathrm{Cl}^-}(\mathbf{r})\}, \tag{9}$$

and

$$\rho_m(\mathbf{r}) = -eN_{\mathrm{SiO_2}}(\mathbf{r}), \tag{10}$$

respectively.

When solving for $\phi(\mathbf{r})$, the electrostatic potential difference is set to the applied V_e on the top and bottom boundaries (in z-direction) of the simulation domain, while normal derivatives of the potentials are set to zero on other boundaries, similar to our previous publications [26–28]. The resultant $\phi(\mathbf{r})$ is shown in Figs. 2 and 3.

Note that using the Einstein–Smoluchowski equation [29], we estimate the ionic relaxation time, the time it takes for the flow of ions to reach a steady state, to be $\tau_i \sim L_D^2/(D_i) \sim 0.1$ ns. Additionally, we find the dielectric relaxation time, τ_d, given by $\tau_d \sim \varepsilon_0 \varepsilon_r^{\mathrm{KCl}}/\sigma$, is ~0.3 ns where $\sigma = 0.025$ $(\Omega$ cm$)^{-1}$ is the conductivity of our solution. Although the applied electrolyte bias changes over the course of the simulation, the steady-state Nernst–Planck equations are still viable because the relaxation times are smaller compared to other times characterizing the motion of the polymer.

2.3 *Computational Model of a Polymer Chain Attached to a Molecular Stop*

We will continue using the Brownian dynamics approach to our model, as described in Eqs. (1) and (2), for a polymer chain attached to the surface of a molecular stop instead of the mouth of the nanopore, shown in Fig. 4. The molecular stop is modeled as a sphere with the parameters of NeutrAvidin, which

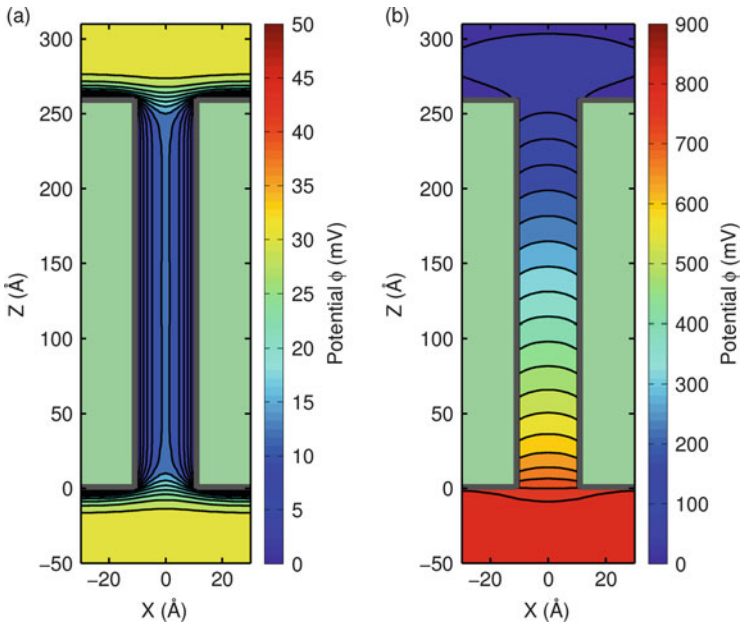

Fig. 2 Contour plots of the electrostatic potential distribution at electrolyte bias (**a**) $V_e = 0$ and (**b**) $V_e = 0.8$ V

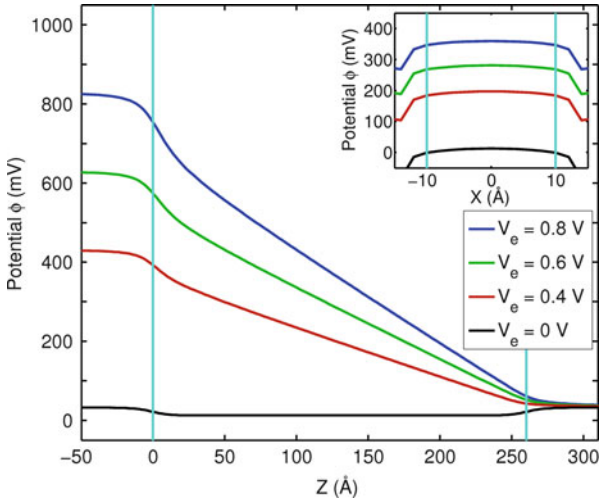

Fig. 3 Electrostatic potential $\phi(\mathbf{r})$ for electrolyte bias $V_e = 0$, 0.4, 0.6, and 0.8 V along the z axis through the center of the nanopore (at $x = y = 0$ Å). The nanopore entrance and exit are indicated by the vertical lines at 260 and 0 Å respectively. (*Inset*) Electrostatic potential along the x axis through the center of the nanopore (at $z = 130$ Å). The nanopore boundaries are indicated by the vertical lines at -10 and 10 Å

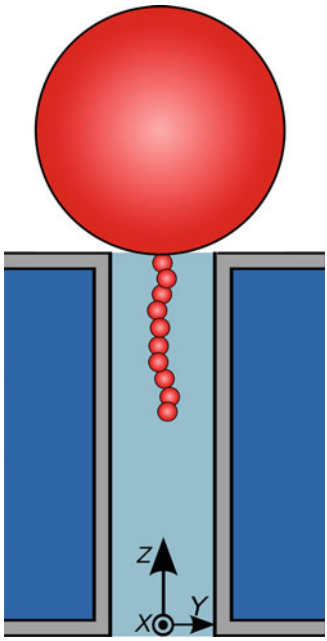

Fig. 4 A schematic of a polymer chain extended inside a nanopore attached to a molecular stop

has approximate mass of $M = 52.8$ kDa and radius of $r = 0.066M^{1/3} \approx 25$ Å [30]. The stop, with index $i = 0$, is represented as an uncharged hard sphere of radius $R_{\text{stop}} = 25$ Å, where $R_{\text{stop}} > R_{\text{pore}}$. Each bead of the polymer chain attached to the stop continues to have the same properties previously described.

Equation (1) is modified to include the larger molecule as well as the bead attached to it, making the translational BD model

$$\mathbf{r}_i(t) = \mathbf{r}_i(t - \delta t) - \nabla_i U[\mathbf{r}_i(t - \delta t)]\frac{\delta t}{\xi_i} + \sqrt{\frac{6\delta t k_b T}{\xi_i}}\mathbf{n}_i, i = 0, 1, 2, \ldots, N_b, \qquad (11)$$

where N_b is the number of beads in the polymer chain, which excludes the molecular stop. The potential energy in Eq. (11) is Eq. (2) and to maintain computational scheme stability with the introduction of a new drag coefficient, the time step is changed to $\delta t = 0.1$ ps.

In the nanopore, the beads will experience a drag coefficient of $\xi_i = 7.5 \times 10^{-9}$ Ns/m for $i = 1, 2, \ldots, N_b$. For the molecular stop, $i = 0$, the drag coefficient is approximated by using the bulk diffusion coefficients given by the generalized diffusion tensor [31],

$$\mathbf{D} = \begin{pmatrix} \mathbf{D}_{TT} & \mathbf{D}_{TR} \\ \mathbf{D}_{RT} & \mathbf{D}_{RR} \end{pmatrix}. \qquad (12)$$

In Eq. (12), R and T stand for the rotational and translational motion, respectively. Since the molecular stop is modeled as a sphere, the elements in the diffusion tensor are $\mathbf{D}_{TR} = \mathbf{D}_{RT} = 0$, $\mathbf{D}_{TT} = \frac{k_b T}{\xi^S_{(T)}}\mathbf{I}$, and $\mathbf{D}_{RR} = \frac{k_b T}{\xi^S_{(R)}}\mathbf{I}$, where k_b is the Boltzmann constant, $T = 300$ K, $\mathbf{I}$ is the identity matrix, and $\xi^S_{(T),(R)}$ is the drag coefficient for translational and rotational motion, respectively [32]. The translational drag coefficient is calculated using $\xi_0 = \xi^S_{(T)} = 6\pi\eta R_{\text{stop}}$ and the rotational drag coefficient is $\xi^S_{(R)} = 8\pi\eta {R_{\text{stop}}}^3$ [32, 33].

For beads $i = 1, \ldots, N_b$, Eqs. (3)–(8) are used to describe each bead's potential energy. Since the first bead in the polymer chain is attached to the molecular stop at the surface, U_{el} is calculated using Eq. (3) between the center of the smaller bead and the surface point of the molecular stop it is attached to. For the bead-bead and bead-membrane LJ interaction energy for $i = 0$, the hard sphere of radius R_{stop} is accounted for by replacing r_{0j} with $r_{0j} - R_{\text{stop}}$ in Eq. (4), giving

$$U_b = \epsilon_b \sum_{j=1}^{N_b} \left[\left(\frac{\sigma_b}{r_{0j} - R_{\text{stop}}} \right)^{12} - 2 \left(\frac{\sigma_b}{r_{0j} - R_{\text{stop}}} \right)^{6} \right]. \tag{13}$$

The Coulomb interaction energy described in Eq. (5) now includes bead $i = 0$, and will be zero for the molecular stop since the stop has a zero net charge.

The rotational motion of the large bead must also be considered, so a body fixed axes (BFA) reference frame is introduced with an origin at the center of the molecular stop. Since the stop is a sphere, only the rotation about an instantaneous axis directed along the vector of the net torque acting on it is considered [32]. Additionally, only one component of the angular velocity needs to be used along the previously described axis such that $\omega = \Delta\Omega/\delta t$, with $\Delta\Omega$ as the rotated angle during timespan δt. The rotational Langevin equation for the molecule is therefore

$$\xi^S_{(R)}\boldsymbol{\omega} = -\boldsymbol{\rho} \times \nabla U \left[\mathbf{r}^{\text{surface}}_{\text{stop}}(t - \delta t) \right] + \sqrt{\frac{6 k_b T \xi^S_{(R)}}{\delta t}}\mathbf{n}, \tag{14}$$

where $\mathbf{r}^{\text{surface}}_{\text{stop}}$ is the position vector of the location where the molecular stop and the polymer chain are bound on the surface of the molecule, and $\boldsymbol{\rho} = \mathbf{r}^{\text{surface}}_{\text{stop}} - \mathbf{r}_0$ is the position vector of the bonding site in the BFA. Equation (14) uses the torque due to the external forces and due to the random forces as expressed by the first term and second term, respectively. In order to calculate the resultant position of the binding site, for every time step the z-axis of the BFA is aligned with the instantaneous axis

of rotation where the position vectors in this new frame is $\boldsymbol{\rho}'$ and is calculated by $\boldsymbol{\rho}'(t-\delta t) = \mathbf{Z}_{\theta\phi}\boldsymbol{\rho}(t-\delta t)$ with

$$\boldsymbol{Z}_{\theta\phi} = \begin{pmatrix} \cos\theta\cos\phi & \cos\theta\sin\phi & -\sin\theta \\ -\sin\phi & \cos\phi & 0 \\ \sin\theta\cos\phi & -\sin\theta\sin\phi & \cos\theta \end{pmatrix}. \tag{15}$$

Here θ is the angle made between the z-axis of the BFA and the instantaneous axis of rotation and ϕ is the angle made between the x-axis of the BFA and the xy-projection of the instantaneous axis of rotation. Afterwards, the molecule is rotated about the instantaneous axis by angle $\Delta\Omega$ so that the surface binding position is updated as $\boldsymbol{\rho}'(t) = \mathbf{Z}_{\Delta\Omega}\boldsymbol{\rho}(t-\delta t)$ with

$$\boldsymbol{Z}_{\Delta\Omega} = \begin{pmatrix} \cos\Delta\Omega & \sin\Delta\Omega & 0 \\ -\sin\Delta\Omega & \cos\Delta\Omega & 0 \\ 0 & 0 & 1 \end{pmatrix}. \tag{16}$$

The position vector $\boldsymbol{\rho}'(t)$ is then transformed back to the BFA system by $\boldsymbol{\rho}(t) = (\boldsymbol{Z}_{\theta\phi})^T\boldsymbol{\rho}'(t)$ [32].

3 Results

3.1 Surface Modified Nanopore

For the surface modified nanopore, we study how the varying applied electrolyte bias, V_e, and length of polymer chain, N_b, affect the interaction between a tethered polymer and a nanopore in a SiO_2 membrane. Approximately 10^3 simulations were executed for each combination of V_e and N_b, each beginning by calculating the electric potential of the system via the PNP model described in Eqs. (7)–(10). The attached polymer chain is initially relaxed for 10^7 time steps (50 μs) without an electrolyte bias being applied. The R_g of the freely floating tethered polymer saturates over the course of the relaxation period, indicating it has reached an equilibrium configuration.

The data collection BD simulations last between 120 and 700 million time steps (0.6–3.5 ms) for $N_b = 10, 15, 20, 30, 40, 50, 60$. During these simulations, $V_e = 0.4$, 0.6, or 0.8 V is applied initially, just after the relaxation period. After a time interval, long enough for a polymer chain of length N_b to find, enter, and extend into the pore when subject to V_e, the applied electrolyte bias is switched to $V_e = 0$. After the electrolyte bias is switched off, the polymer chain escapes the nanopore confinement due to its random motion and is found floating outside the pore again.

Several characteristic times described later are recorded during the course of the simulation. The radius of gyration, $R_g = \left[\left(2N_b^2\right)^{-1}\sum_{ij} r_{ij}^2\right]^{1/2}$, and Z_{cm}, the z-coordinate of the center of mass position, of the entire chain are also calculated.

We first define the characteristic times associated with the polymer chain-nanopore interactions and describe how they depend on V_e and N_b. Over the course of a simulation, given a sufficient amount of time steps allocated to $V_e > 0$ for a strong enough V_e, there will be two equilibrium configurations the tethered molecule can exhibit: one inside the nanopore and one outside. After being relaxed, a polymer chain remains above the membrane until enough beads find the pore entrance (through random motion) and become captured by the electric field produced by the applied bias, pulling the polymer inside. The chain then enters the pore and extends inside where it remains due to the positive electrolyte bias. While the electric field pulls on the polymer inside the pore, the movement of the tethered biomolecule in the z-direction is restricted. When the applied bias is switched off in the simulation, the polymer always exits the pore and floats freely above it, allowing for a larger variation in the probability of the center of mass z-coordinate's $P(Z_{\mathrm{cm}})$.The maximum $P(Z_{\mathrm{cm}})$ values, achieved at $Z_{\mathrm{cm}}^{\mathrm{in}}$ and $Z_{\mathrm{cm}}^{\mathrm{out}}$ positions inside and outside the pore, respectively, are calculated and used in determining the duration of time it takes for a tethered molecule to enter and exit the pore. As seen in Fig. 5, two maxima in $P(Z_{\mathrm{cm}})$ exist for each V_e, one inside the pore and one outside. The probability distribution when the polymer is above the membrane, $P(Z_{\mathrm{cm}} > 260)$ Å, is wider but with a smaller maximum probability than the distribution found inside the pore, showing that variation in the tethered chain's

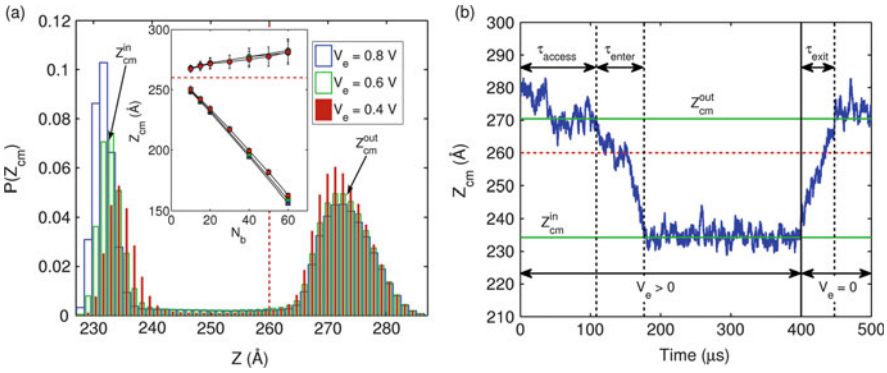

Fig. 5 (**a**) The probability of the chain's center of mass in the z-coordinate, $P(Z_{\mathrm{cm}})$, for all V_e and $N_b = 20$. The two peaks correspond to the most likely z-coordinate position inside and outside the nanopore, when the applied bias is on and off respectively. (*Inset*) The peak positions, when $P(Z_{\mathrm{cm}})$ is maximum, inside the pore ($Z_{\mathrm{cm}}^{\mathrm{in}}$), $Z_{\mathrm{cm}} < 260$ Å, and outside the pore ($Z_{\mathrm{cm}}^{\mathrm{out}}$), $Z_{\mathrm{cm}} > 260$ Å, for various N_b. The *dashed line* shows the location of the nanopore entrance. (**b**) The center of mass z-coordinate, Z_{cm}, over a course of a single simulation for $N_b = 20$ and $V_e = 0.4$ V. At 400 μs (*vertical*, *solid line*), the applied bias is switched off and $V_e = 0$. The pore entrance is located at 260 Å (*horizontal*, *dashed line*) and the most likely positions inside and outside the pore for Z_{cm}: $Z_{\mathrm{cm}}^{\mathrm{in}}$ and $Z_{\mathrm{cm}}^{\mathrm{out}}$, respectively, are calculated from the data collected from each simulation

motion in the z-coordinate is reduced due to the applied bias and nanopore constriction. As a result, $Z_{\rm cm}^{\rm in} \sim N_b^1$ for $P(Z_{\rm cm} < 260)$ Å, as shown in the inset of Fig. 5. The inset also shows how $Z_{\rm cm}^{\rm out}$ of the polymer chain outside the nanopore increases as N_b does. Once the applied bias is switched off ($V_e = 0$), the polymer eventually is found freely floating outside of the pore in which case $R_g \sim N_b^\nu$ where $\nu = 0.57$ is comparable to the Flory exponent in three dimensions. [34]

The positions $Z_{\rm cm}^{\rm in}$ and $Z_{\rm cm}^{\rm out}$ are recorded to define access, enter, and exit time periods, as shown in Fig. 5. At the beginning of the simulation, after the polymer has been relaxed and the electrolyte bias is applied across the membrane, the polymer starts accessing the pore. The duration of time a polymer takes to access a pore is denoted as $\tau_{\rm access}$. We define the end of this process once the chain's $Z_{\rm cm}$ departs from its most likely position outside the nanopore without returning to it before fully entering and reaching its most likely position inside. The time it takes the biomolecule to enter the pore, $\tau_{\rm enter}$, is the time the chain takes to travel from its most probable $Z_{\rm cm}$ position outside to its most probable position inside the pore without returning outside. Similarly, a polymer chain exiting the nanopore is defined by its $Z_{\rm cm}$ reaching its most probable location outside the pore after the applied bias is removed from the system. For short chains, with the lengths comparable to the pore opening, it is possible, however unlikely, for the polymer to leave the pore prior to the bias switching off. In these cases, the period of time when the chain exits, τ_0, is only computed for simulations where the polymer is located inside the nanopore when the applied bias is turned off.

The results for average enter times, $\langle \tau_{\rm enter} \rangle$, calculated in this way can be seen in Fig. 6. Histograms of $\langle \tau_{\rm enter} \rangle$ for each V_e and N_b are similar to the one shown in the inset of Fig. 6, where the probability distribution of $\tau_{\rm enter}$ reaches a maximum that is close to the average enter time. We found the average enter time is dependent on the chain length and applied voltage as $\langle \tau_{\rm enter} \rangle \sim N_b^\alpha$ where $\alpha \sim 1$ but different for each bias: $\alpha = 1.08$, 1.16, and 1.47 for $V_e = 0.8$, 0.6, and 0.4 V, respectively.

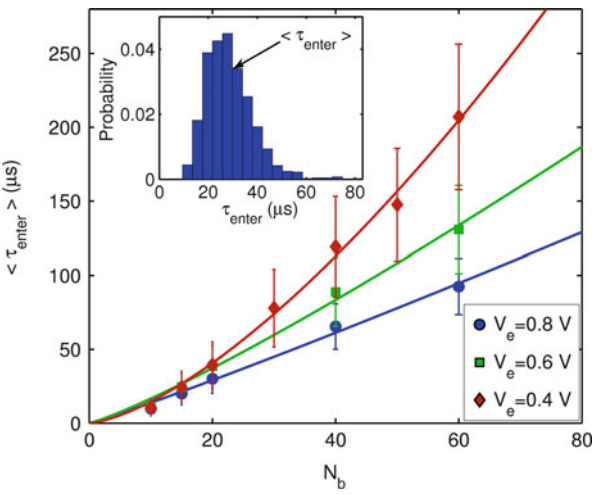

Fig. 6 The average time it takes for a chain to enter the nanopore, $\langle \tau_{\rm enter} \rangle$, for all studied biases and chain lengths. Longer polymer chains exposed to smaller biases take longer to extend into the nanopore. The curves are best fits to data. (*Inset*) The probability histogram of $\tau_{\rm enter}$ for $V_e = 0.8$ V, $N_b = 20$

According to a standard equilibrium analysis [34–37], a driven translocation through an entropic barrier, such as a polymer chain entering a pore, results in $\tau_{\text{ener}} \sim N_b$ while an unbiased translocation, such as a biomolecule exiting the nanopore, follows the scaling law of $\tau_{\text{exit}} \sim N_b^2$. Our results agree with this, as the largest applied bias yields $\langle \tau_{\text{enter}} \rangle \sim N_b^{1.08}$.

The average exit times $\langle \tau_{\text{exit}} \rangle$ were also studied for each electrolyte bias V_e and number of beads N_b. The calculated values for $\langle \tau_{\text{exit}} \rangle$ are displayed in Fig. 7. Similar to $\langle \tau_{\text{enter}} \rangle$, for all simulations of a given bias and chain length, histograms were made to compare the value of τ_{exit} where its probability is maximum to $\langle \tau_{\text{exit}} \rangle$ to ensure they correspond. Despite the previously applied V_e, all of the exit times are approximately the same for a set polymer chain length, that is, once the applied bias is switched off ($V_e = 0$), the escape duration scales the same way with respect to chain length regardless of the bias that was originally used to force the chain inside. We find that $\langle \tau_{\text{exit}} \rangle$ scales with number of beads as $N_b^{1.88}$. This value closely resembles the results seen from free diffusion ($\sim N_b^2$), but since the pore restricts the movement of the polymer, $\langle \tau_{\text{exit}} \rangle \sim N_b^{\alpha}$ where $\alpha < 2$.

As one can see from comparison of Figs. 6 and 7, $\tau_{\text{enter}} < \tau_{\text{exit}}$ for the same N_b and V_e, that is, a polymer subject to a bias will enter a nanopore faster than a polymer leaving once the bias has been removed. This behavior appears in situations where the polymer length is sufficiently larger as compared to the diameter of the pore ($N_b > 20$). Since τ_{enter} is mostly driven by the potential created by the electrolyte bias, the duration of the polymer chain entering is shorter than of it exiting, which is primarily a thermally driven process.

For all chain lengths, a larger applied bias yields a shorter $\langle \tau_{\text{access}} \rangle$ due to the ease of polymer capture for a stronger bias. As random movement dominates the polymer chain's motion outside the pore, beads will come near and breach the entrance of the nanopore. Once enough of the chain is subjected to the applied bias, the biomolecule is captured, overcoming the entropic barrier that had been keeping

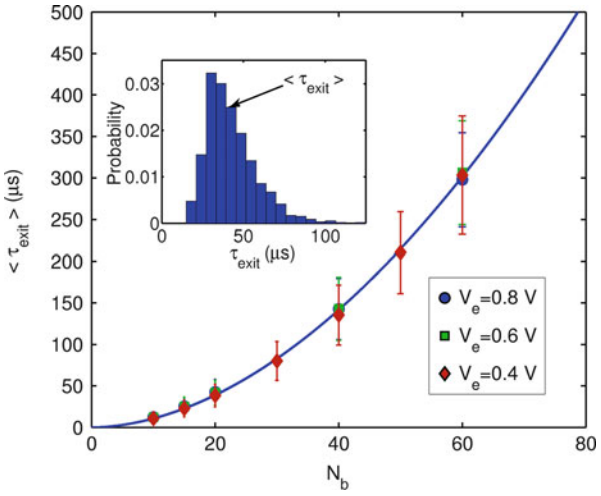

Fig. 7 The average time it takes for a chain to exit the nanopore, $\langle \tau_{\text{exit}} \rangle$, for all biases and chain lengths. (*Inset*) The probability histogram of τ_{exit} for $V_e = 0.8$ V, $N_b = 20$

the polymer from extending into the pore. In our simulations, $V_e = 0.8$ and 0.6 V behave similarly in respect to being captured by the pore, however, both biases will yield small τ_{access} compared to $V_e = 0.4$ V. Figure 8 shows that the access time histograms exhibit an exponential probability distribution. A small bias such as $V_e = 0.4$ V yields τ_{access} histogram that decays more slowly than larger biases, resulting in larger $\langle \tau_{\text{access}} \rangle$. This is because a polymer chain in a weak bias needs to be oriented in a specific way to begin entering the pore, otherwise the bias will not be strong enough to perturb the chain and capture the polymer. For any strong bias, such as $V_e = 0.8$ and 0.6 V, it does not matter how the chain is oriented, as long as enough beads start entering the pore, all of it will be pulled in. This is not the case for weaker biases, like $V_e = 0.4$ V, since the random motion of the biomolecule can overcome the attractive potential created by the electrolyte bias.

By looking at how the polymer chain successfully enters the nanopore through comparing Z_{cm} positions against corresponding R_g values during this period, the proper capture conditions can be determined. Figure 9 shows this relation for a polymer chain length of $N_b = 40$ exposed to an electrolyte bias of $V_e = 0.8$ (data

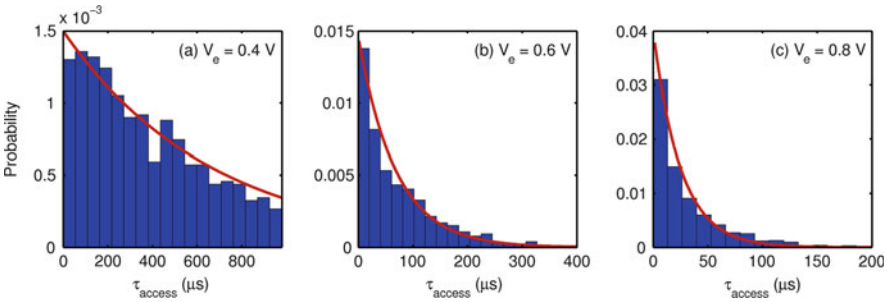

Fig. 8 Access time histograms for $N_b = 20$ at different applied electrolyte bias V_e: (**a**) $V_e = 0.4$ V; (**b**) $V_e = 0.6$ V; (**c**) $V_e = 0.8$ V. An exponential distribution function $Ae^{-A\tau_{\text{access}}}$ (*solid line*) was fitted for each N_b and V_e in order to determine $\langle \tau_{\text{access}} \rangle$ where $\langle \tau_{\text{access}} \rangle = 1/A$

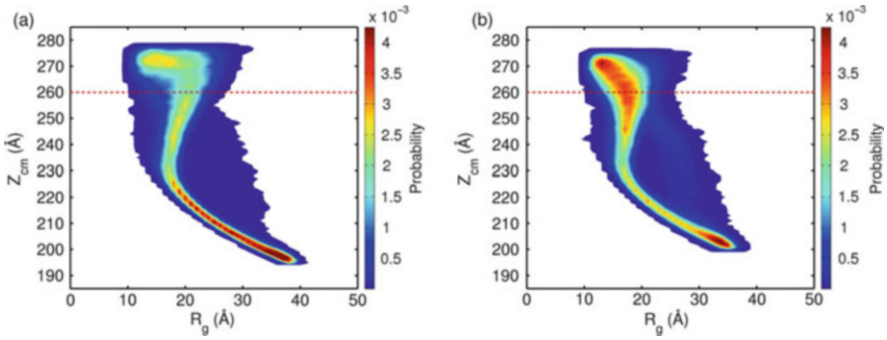

Fig. 9 Contour plots of Z_{cm} positions of a tethered polymer chain $N_b = 40$ long and its corresponding R_g for all simulations with electrolyte bias (**a**) $V_e = 0.8$ V and (**b**) $V_e = 0.4$ V while the polymer is entering the pore

from ~1,000 data collection runs) and 0.4 V (data from ~800 data collection runs). Since the time it takes for a chain of $N_b = 40$ to enter the nanopore for $V_e = 0.8$ V is short compared to $V_e = 0.4$ V (~37 and ~119 μs, respectively), and there being a lower probability of finding the chain above the nanopore for $V_e = 0.8$ V while it is entering, we observe that once the chain is captured, it will quickly enter. This is not the case for the weaker bias of $V_e = 0.4$ V as Fig. 9 shows the probability of finding the polymer above the pore during the entering process to be higher than for larger biases. This, in addition to τ_{enter} being over three times larger when $V_e = 0.4$ V compared to $V_e = 0.8$ V, indicates an increased time devoted to the chain orienting itself in a favorable way to begin extending into the pore.

The differences in how a polymer chain enters the nanopore when exposed to a weak bias ($V_e = 0.4$ V) and a strong bias ($V_e = 0.8$ V) are further seen by looking at how R_g changes as the polymer extends inside the pore. For a large bias, there is little preference on R_g of the chain prior to the Z_{cm} passing through the pore opening. As the polymer's Z_{cm} decreases towards the location of the pore's mouth, $R_g \sim 20$ Å and starts to decrease as Z_{cm} decreases. This is due to how the chain will extend into the pore by the beads that are initially captured, resulting in a brief period of R_g increase followed by a decrease as more of the chain is forced into the compact space of the nanopore. Eventually, the entire polymer will be pulled into the nanopore and extend, effectively increasing it's R_g, as seen in Fig. 9.

For the weaker bias, most of the time the chain spends above and at the pore entrance while $R_g < 20$ Å, showing the chain typically having a smaller radius of gyration prior to successfully being captured by the nanopore. Chains that are more unraveled will not be able to enter the pore when exposed to a weaker bias since random motion upon entering/neighboring beads can easily pull it back outside. By reducing R_g of the chain, the effect of the chain's random motion is diminished and the polymer has a greater chance at entering. This can be seen in Figs. 10 and 11 (data from ~32 data collection runs used to create scatter plots). Both figures show a single simulation of a chain of length $N_b = 40$ in a $V_e = 0.4$ V applied electrolyte bias. The Z_{cm} and R_g of the entering chains are traced on top of a scatter plot showing the results of all corresponding simulations during the enter period.

Figure 10 shows an example of the chain's most probable path of successfully entering the nanopore which is in a hairpin formation. As described previously, the chain is initially hovering above the nanopore with a small R_g. The chain breaches the mouth of the pore by the middle of the chain, reducing its R_g further. Once the rest of the chain is pulled inside of the pore, its R_g begins increasing as the chain is less self-obstructing.

Figure 11 accounts for another way the polymer chain can enter the pore, free end first. The entering process starts similarly, with a small R_g; however, the traced path is different once Z_{cm} is lower than the pore entrance. When the polymer enters free end first, its R_g does not decrease as Z_{cm} is just below the pore entrance. Instead, chain's R_g steadily increases as Z_{cm} decreases for the duration of the entering period, a result of the chain not self-obstructing. We observe that this possible way of entering the pore is less successful for both weak and strong biases, as seen in Fig. 9.

In Fig. 12, the capture probability during the first 300 μs summarizes the results of the above discussion. For a strong bias, such as $V_e = 0.8$ V, the probability of having a short τ_{access} is close to 1. For the weaker bias of $V_e = 0.6$ V, the probability

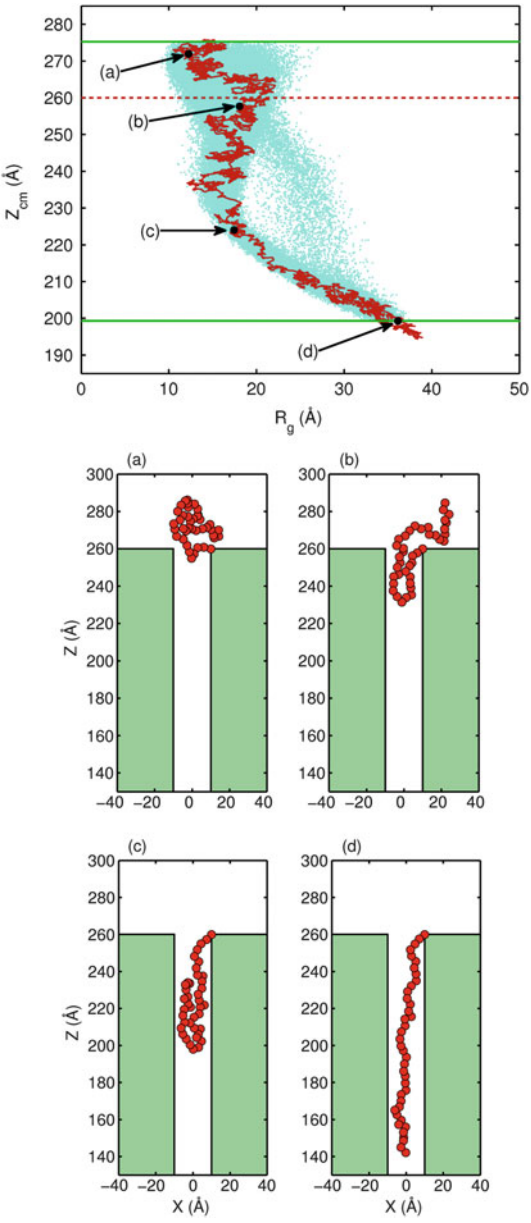

Fig. 10 A single simulation trace on top of a scatter of Z_{cm} positions and R_g lengths of a $N_b = 40$ chain entering the nanopore subject to $V_e = 0.4$ V (*top*). The points (*a*)–(*d*) indicated on the trace have their configurations displayed, showing the process of how the chain enters the nanopore. In this particular case, the chain is captured by the pore in a hairpin formation

of the polymer being captured by the pore also remains ∼1, even for longer chain lengths. Once the gyration radius of the freely floating polymer chain exceeds the radius of the nanopore (between $N_b = 20$ and 40), the capture rate has a noticeable decline for strong biases, as seen in Fig. 12.

For a weak bias, the capture probability quickly declines for short allowances of τ_{access} as N_b increases. This decline in capture probability between $V_e = 0.6$ V and

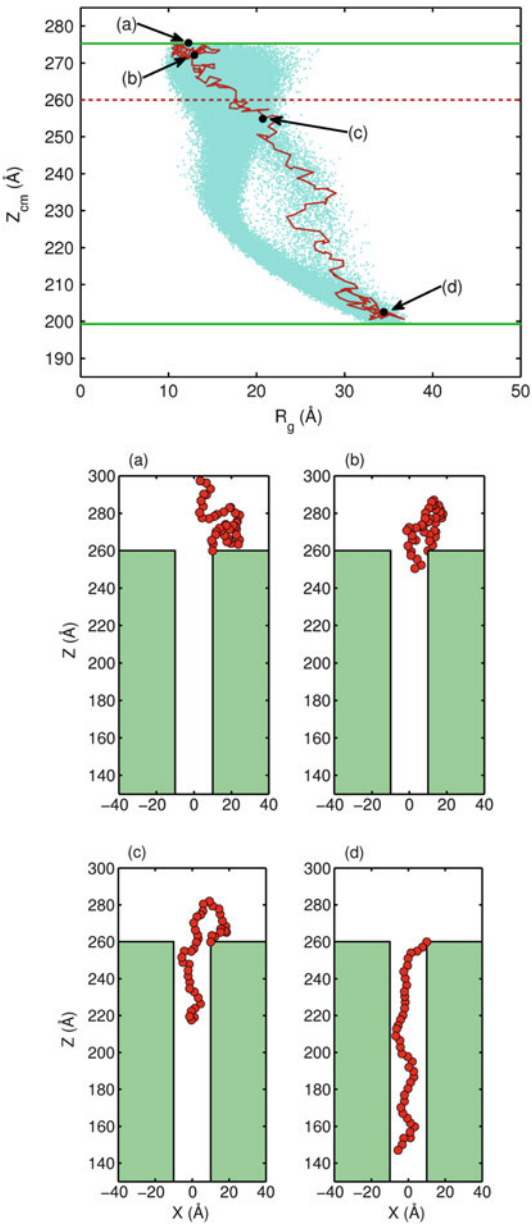

Fig. 11 A single simulation trace on top of a scatter of Z_{cm} positions and R_g lengths of a $N_b = 40$ chain entering the nanopore subject to $V_e = 0.4$ V (*top*). The points (*a*)–(*d*) indicated on the trace have their configurations displayed, showing the process of how the chain enters the nanopore. In this situation, the chain is captured by the pore by threading through via the free end

$V_e = 0.4$ V shown in Fig. 12 indicates the existence of a free energy barrier that a polymer chain in weaker biases are not able to overcome [38]. For small N_b, a chain in a bias that is not strong enough to overcome the free energy barrier created by the pore easily will need to be configured in such a way that perturbation is possible, leading to the polymer being captured and extending into the pore.

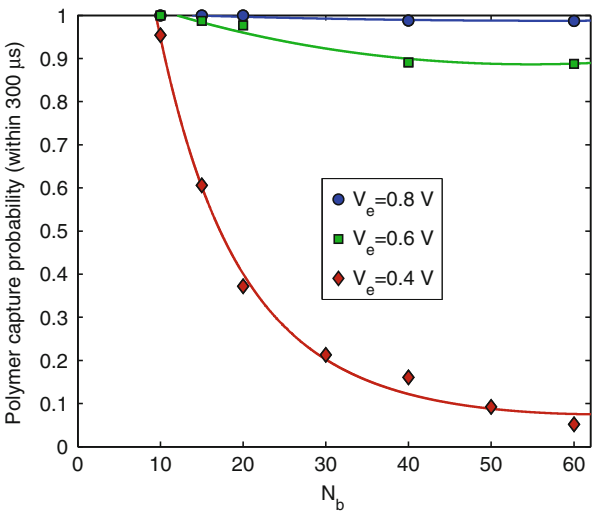

Fig. 12 Capture probability of a polymer within 300 μs as a function of N_b for different V_e. The capture probability within 300 μs is equivalent to $P(\tau_{\text{access}} < 300\ \mu\text{s})$ as the polymer chain is captured by the nanopore after τ_{access} is over. The curves are fitted by $P(\tau_{\text{access}} < 300\ \mu\text{s}) = B\exp(-CN_b(1 - DN_b))$, where B, C, and D are positive fitting parameters [38]

3.2 *Molecular Stop*

For the modified polymer chain, the BD simulation for the molecular stop-nanopore system uses applied electrolyte biases of $V_e = 0.4$, 0.6, or 0.8 V over the length of the pore, and the attached polymer chain is of length $N_b = 20$. Initially, the polymer chain is relaxed for 10^8 time steps (10 μs) inside the nanopore at the V_e that will be applied during the proceeding simulation. Afterwards, the data collection BD simulation lasts 10^9 time steps, during which time the polymer chain spends the entirety of the simulation extended inside the nanopore, hanging from the molecular stop. The variation of each bead in the x, y, r, and z-directions over the course of the simulation are calculated as the polymer chain exhibits various conformations in its equilibrium state. These variations are also compared to the variation of position for the freely translocating polymer chain.

The results for the position and variation in movement for each bead of the polymer chain in the z-direction are seen in Fig. 13a. As shown in the mean position, a larger bias will pull the polymer chain more, forcing each bead to extend deeper into the nanopore. This stronger bias also holds the polymer chain taut, restricting its movement in the z-direction. As a result, the standard deviation from the mean, σ_z, for chains in a larger applied bias is smaller for each bead. Figure 13b also shows how the polymer chain's variation in movement increases as it approaches the free end, ending in a much greater σ_z for the final bead in the chain compared to the first bead, which is attached to the molecular stop. To ensure a sufficient amount of data points have been taken, histograms are made, as seen in Fig. 15. The position of each bead in the polymer chain should be approximately a Gaussian distribution, where the mean and standard deviation for each bead correspond to those shown in Fig. 13. This distribution was calculated for the middle bead and superimposed onto the histogram. Discrepancies in the data and the

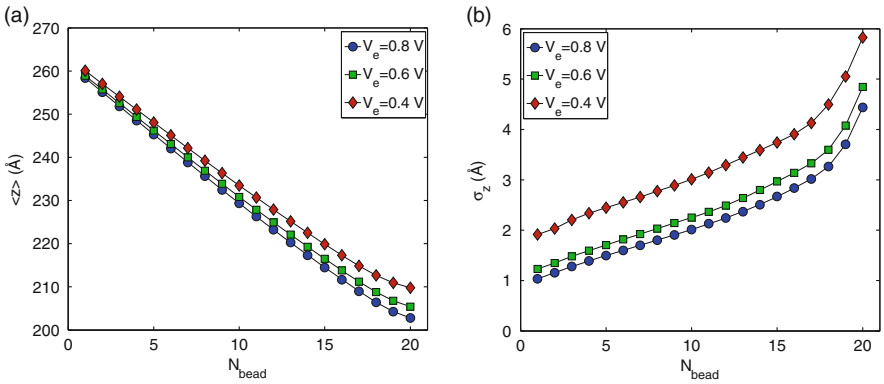

Fig. 13 (**a**) Average z-coordinate position, $\langle z \rangle$, for each bead in a $N_b = 20$ chain attached to a molecular stop exposed to an applied electrolyte bias $V_e = 0.4$, 0.6, and 0.8 V. The entrance to the nanopore is located at $z = 260$ Å and the first small bead attached to the molecular stop. Stronger applied biases pull the polymer chain deeper into the nanopore and reduce the movement of the molecular stop outside the pore. (**b**) Average z-coordinate standard deviation, σ_z, for each bead in the molecular stop-polymer chain system for each applied bias. Stronger biases reduce the variation of movement for every bead. Regardless of applied bias, the end of the polymer chain attached to the molecular stop varies little in the z-direction due to the rest of the chain pulling on it from below and the molecular stop keeping it in place, while the other end varies much more because it is only anchored by the preceding bead

distribution are expected, as the movement of the bead in the z-direction should be more restrictive in the direction it is being pulled in. As a result, the histogram should deviate more on the side facing the molecular stop than on the side facing the free end, which it does in Fig. 15.

The standard deviation for each bead in the polymer chain is also calculated in the x- and r-direction for the molecular stop-polymer chain system, which is then compared to the variation in position for the freely translocating polymer chain. The standard deviation of these positions, $\sigma_{x,r}$, shown in Fig. 14, is overall lower for the molecular stop-polymer chain system than it is for the freely translocating system, which is to be expected since the chain attached to the molecular stop is held taut, reducing movement in each direction. For the freely translocating polymer chain, the standard deviation is symmetric about the center of the chain where the ends have the most variation in the x- and r-direction since they are only bound to a single bead and the beads in the center have approximately the same $\sigma_{x,r}$. A freely translocating chain experiences nearly the same standard deviation regardless of applied bias, whereas the chain attached to the molecular stop will have smaller variations for larger applied biases. The free end of the molecular stop-polymer chain system will still have the largest $\sigma_{x,r}$ in the chain since its movement is not as restricted as other beads in the chain, but the bead attached to the molecular stop also has a larger $\sigma_{x,r}$ compared to the minimum $\sigma_{x,r}$ of the chain. This is due to this bead being bound to the molecular stop, which is still diffusing randomly at the entrance of the nanopore, dragging the smaller bead with it in the xy-plane. As a

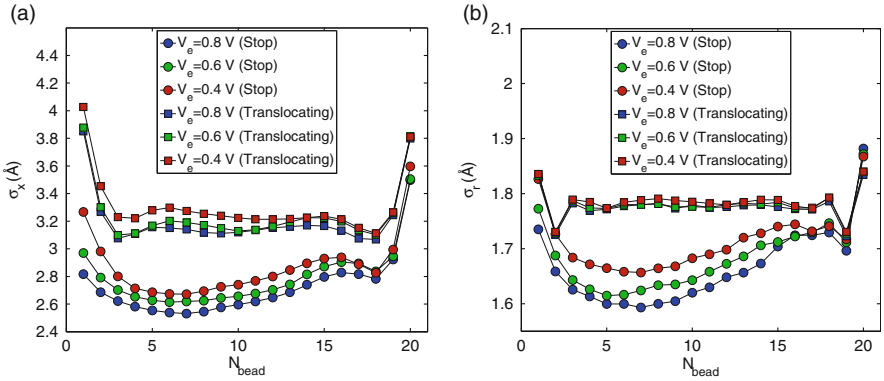

Fig. 14 Average (**a**) x-coordinate standard deviation, σ_x, and (**b**) r-coordinate standard deviation, σ_r, for each bead in the molecular stop-polymer chain system and the freely translocating polymer chain for each applied bias. The variation in the x and r-directions for the molecular stop-polymer chain system is slightly effected by the strength of the applied bias, with stronger biases having smaller standard deviations. Compared to the freely translocating polymer chain, the molecular stop-polymer chain system has less variation in its movement in the x and r-directions. While the molecular stop-polymer chain system's standard deviation is effected by differences in the applied bias, the freely translocating polymer chain only changes negligibly when V_e does. The results in the y-direction are similar to those in the x-direction

result, the $\sigma_{x,r}$ in the polymer chain will decrease for beads further away from the molecular stop before increasing again for beads close to the free end, as seen in Fig. 14. Histograms of the data are also made and compared to their expected distributions, where each bead's position should exhibit a Gaussian distribution in the x- and y-direction and a Rayleigh distribution in the r-direction. Figure 15 shows that the histograms are a good fit for these distributions with only slight discrepancies due to the physical restrictions of our system, such as the walls of the nanopore.

4 Conclusion

In this work, we examined the interaction between a solid-state nanopore and a negatively charged polymer chain attached to the mouth of the pore. The movement of the polymer is characterized using a Brownian dynamics model along with the self-consistent PNP model to describe the electric potential produced by the membrane-nanopore system and electrolyte bias [26]. We apply a time-dependent electrolyte bias for tethered chains of various length in order to see how and under what conditions the biomolecule will be captured by the nanopore, enter it, and leave it.

We find that the time it takes to accomplish each of these tasks depends on the strength of the applied bias and the length of the biomolecule. While the polymer is entering the pore, the relation between the time it takes to enter and extend

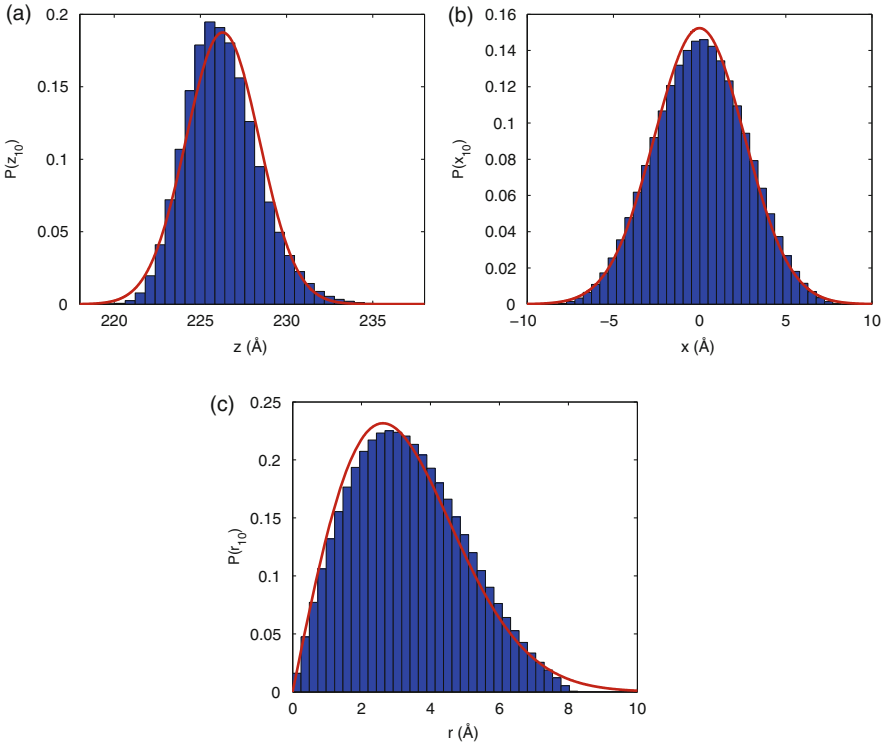

Fig. 15 The probability of the center of mass of 10th bead in the chain in (**a**) the z-coordinate, $P(z_{10})$, (**b**) the x-coordinate, $P(x_{10})$, and (**c**) the r-coordinate, $P(r_{10})$, for $V_e = 0.8$ V. (**a**) The probability for this histogram corresponds to a Gaussian distribution, which is graphed with the histogram. The mean and standard deviation of the Gaussian displayed were taken from Fig. 13. (**b**) The probability for this histogram also corresponds to a Gaussian distribution, which is graphed with the histogram. The standard deviation of the Gaussian displayed was taken from Fig. 14. (**c**) The probability for this histogram corresponds to a Rayleigh distribution, $\frac{r}{\sigma_x \sigma_y} e^{-r^2/\left(2\sigma_x \sigma_y\right)}$, which is graphed with the histogram. The standard deviations used in the Rayleigh distribution displayed are taken from Fig. 14 and the y-direction counterpart

inside is $\sim N_b^{\alpha}$ where $\alpha \sim 1.0$. This indicates the polymer approaching the behavior of a driven motion as stronger biases are applied.

Once the polymer is located inside the pore exhibiting an extended configuration for $V_e > 0$, switching the bias to $V_e = 0$ makes the biomolecule diffuse out of the pore in the same way regardless the strength of the previously applied bias. The relation between the time it takes for the chain to exit the pore and the length of the chain is $\sim N_b^{1.88}$, corresponding to the result given by diffusion altered by the presence of the pore restricting the chain's movement.

In order for the polymer to enter the pore, it must overcome a free energy barrier while accessing it. This is easily done for chains that are subject to a strong electrolyte bias such as $V_e = 0.8$ and 0.6 V in our model. In these cases, when the

chain length is small and its radius of gyration is less than the radius of the pore, the biomolecule will successfully access the pore nearly always within 300 μs. Even for longer chains, the bias is strong enough to perturb it easily, resulting in predictably small access times. For weaker biases, the polymer chain is much harder to unravel and must be configured favorably before extending into the nanopore.

Giving consideration to the possible influences of the electro-osmotic flow, we would expect an increase in the time it takes for the polymer chain to be captured by the nanopore. This is due to how the negatively charged nanopore surface in a positive applied electrolyte bias will cause an outwardly directed electro-osmotic flow resulting in a tethered polymer to be pushed out and away from the nanopore [28, 39].

A charged polymer chain attached to a molecular stop exposed to an applied electrolyte bias encouraging the strand to extend into a cylindrical nanopore will cause the polymer to be pulled taut, reducing σ_z with increasing V_e. A bead's standard deviation in the z-direction is larger the further that bead is from the molecular stop, with the last bead having the largest σ_z since it is only bound by a single bead making it less restricted in its movement. The variation in movement for beads in the x, y-plane are also reduced for increasing V_e. Largest $\sigma_{x,y,r}$ values are exhibited in the free end, similar to the z-direction; however the part of the chain attached to the molecular stop also experiences an increase in $\sigma_{x,y,r}$. This is due to how the molecular stop randomly diffuses outside the nanopore, pulling the chain along with it. Compared to the freely translocating chain, the molecular stop-polymer chain system has a smaller standard deviation due to the restrictions imposed by the bias, neighboring chain segments, and the molecular stop.

In this chapter, we studied the behavior of a polymer chain attached to a nanopore's surface or a molecular stop while it is pulled into the pore. We find that a chain attached to a molecular stop offers greater control over the chain dynamics while it samples the nanopore electrostatic landscape.

Acknowledgments This work was supported by the NSF (DMR and CBET divisions) through a CAREER award No. 1352218 (M.G.) and by the XSEDE award for computational resource TG-PHY110023.

References

1. Kasianowicz JJ, Robertson JW, Chan ER, Reiner JE, Stanford VM (2008) Nanoscopic porous sensors. Annu Rev Anal Chem 1:737–766
2. Howorka S, Siwy Z (2009) Nanopore analytics: sensing of single molecules. Chem Soc Rev 38 (8):2360–2384
3. Wanunu M, Sutin J, McNally B, Chow A, Meller A (2008) DNA translocation governed by interactions with solid-state nanopores. Biophys J 95(10):4716–4725
4. Kasianowicz JJ, Brandin E, Branton D, Deamer DW (1996) Characterization of individual polynucleotide 14 molecules using a membrane channel. Proc Natl Acad Sci 93 (24):13770–13773
5. Gyurcsányi RE (2008) Chemically-modified nanopores for sensing. TrAC Trends Anal Chem 27(7):627–639

6. Howorka S, Movileanu L, Lu X, Magnon M, Cheley S, Braha O, Bayley H (2000) A protein pore with a single polymer chain tethered within the lumen. J Am Chem Soc 122 (11):2411–2416
7. Howorka S, Bayley H (2002) Probing distance and electrical potential within a protein pore with tethered DNA. Biophys J 83(6):3202–3210
8. Li J, Stein D, McMullan C, Branton D, Aziz MJ, Golovchenko JA (2001) Ion-beam sculpting at nanometre length scales. Nature 412(6843):166–169
9. Lo CJ, Aref T, Bezryadin A (2006) Fabrication of symmetric sub-5 nm nanopores using focused ion and electron beams. Nanotechnology 17(13):3264
10. Storm A, Chen J, Ling X, Zandbergen H, Dekker C (2003) Fabrication of solid-state nanopores with single-nanometre precision. Nat Mater 2(8):537–540
11. Sigalov G, Comer J, Timp G, Aksimentiev A (2008) Detection of DNA sequences using an alternating electric field in a nanopore capacitor. Nano Lett 8(1):56–63
12. Yameen B, Ali M, Neumann R, Ensinger W, Knoll W, Azzaroni O (2009) Synthetic proton-gated ion channels via single solid-state nanochannels modified with responsive polymer brushes. Nano Lett 9(7):2788–2793
13. Yameen B, Ali M, Neumann R, Ensinger W, Knoll W, Azzaroni O (2009) Ionic transport through single solid-state nanopores controlled with thermally nanoactuated macromolecular gates. Small 5(11):1287–1291
14. Iqbal SM, Akin D, Bashir R (2007) Solid-state nanopore channels with DNA selectivity. Nat Nanotechnol 2(4):243–248
15. Ramachandran A, Guo Q, Iqbal SM, Liu Y (2011) Coarse-grained molecular dynamics simulation of DNA translocation in chemically modified nanopores. J Phys Chem B 115 (19):6138–6148
16. Kohli P, Harrell CC, Cao Z, Gasparac R, Tan W, Martin CR (2004) DNA-functionalized nanotube membranes with single-base mismatch selectivity. Science 305(5686):984–986
17. Höfler L, Gyurcsányi RE (2008) Coarse grained molecular dynamics simulation of electromechanically-gated DNA modified conical nanopores. Electroanalysis 20(3):301–307
18. Vlassiouk I, Takmakov P, Smirnov S (2005) Sensing DNA hybridization via ionic conductance through a nanoporous electrode. Langmuir 21(11):4776–4778
19. Ali M, Neumann R, Ensinger W (2010) Sequence-specific recognition of DNA oligomer using peptide nucleic acid (PNA)-modified synthetic ion channels: PNA/DNA hybridization in nanoconfined environment. ACS Nano 4(12):7267–7274
20. Wanunu M, Meller A (2007) Chemically modified solid-state nanopores. Nano Lett 7 (6):1580–1585
21. Jovanovic-Talisman T, Tetenbaum-Novatt J, McKenney AS, Zilman A, Peters R, Rout MP, Chait BT (2009) Artificial nanopores that mimic the transport selectivity of the nuclear pore complex. Nature 457(7232):1023–1027
22. Wells CC, Jou IA, Melnikov DV, Gracheva ME (2016) Nanopore gating with an anchored polymer in a switching electrolyte bias. J Chem Phys 144(10):104901
23. Stoddart D, Heron AJ, Mikhailova E, Maglia G, Bayley H (2009) Single-nucleotide discrimination in immobilized DNA oligonucleotides with a biological nanopore. Proc Natl Acad Sci 106(19):7702–7707
24. Purnell RF, Schmidt JJ (2009) Discrimination of single base substitutions in a DNA strand immobilized in a biological nanopore. ACS Nano 3(9):2533–2538
25. Lu B, Fleming S, Szalay T, Golovchenko J (2015) Thermal motion of DNA in an MspA pore. Biophys J 109(7):1439–1445
26. Jou IA, Melnikov DV, McKinney CR, Gracheva ME (2012) DNA translocation through a nanopore in a single-layered doped semiconductor membrane. Phys Rev E 86(6):061906
27. Nikolaev A, Gracheva ME (2011) Simulation of ionic current through the nanopore in a double-layered semiconductor membrane. Nanotechnology 22(16):165202
28. Jou IA, Melnikov DV, Nadtochiy A, Gracheva ME (2014) Charged particle separation by an electrically tunable nanoporous membrane. Nanotechnology 25(14):145201

29. Einstein A (1956) Investigations on the theory of the Brownian movement. Courier Corporation, North Chelmsford
30. Erickson HP (2009) Size and shape of protein molecules at the nanometer level determined by sedimentation, gel filtration, and electron microscopy. Biol Proced Online 11(1):32
31. Fernandes MX, de la Torre JG (2002) Brownian dynamics simulation of rigid particles of arbitrary shape in external fields. Biophys J 83(6):3039–3048
32. Jou IA, Melnikov DV, Gracheva ME (2016) Protein permeation through an electrically tunable membrane. Nanotechnology 27(20):205201
33. Landau LD, Lifshitz EM (1959) Fluid mechanics. Pergamon Press, London
34. De Gennes PG (1979) Scaling concepts in polymer physics. Cornell University Press, Ithaca
35. Kramers HA (1940) Brownian motion in a field of force and the diffusion model of chemical reactions. Physica 7(4):284–304
36. Sung W, Park P (1996) Polymer translocation through a pore in a membrane. Phys Rev Lett 77 (4):783
37. Muthukumar M (1999) Polymer translocation through a hole. J Chem Phys 111(22):10371–10374
38. Ledesma-Aguilar R, Sakaue T, Yeomans JM (2012) Length-dependent translocation of polymers through nanochannels. Soft Matter 8(6):1884–1892
39. Luan B, Aksimentiev A (2010) Control and reversal of the electrophoretic force on DNA in a charged nanopore. J Phys Condens Matter 22(45):454123

Amperometric Sensors Based on Carbon Nanotubes in Layer-by-Layer Films

Danilo A. Oliveira, Osvaldo N. Oliveira, Jr., and José R. Siqueira, Jr.

Abstract Electrochemical sensors have been among the main applications of carbon nanotubes (CNTs) over the last decade, as biocompatibility and possible conjugation with biomolecules afforded by nanotubes were exploited. Amperometric sensors are among the several electrochemical (bio)sensing systems with CNTs incorporated onto electrodes to detect substances of biological and clinical interest. The layer-by-layer (LbL) technique, in particular, has been used to arrange CNTs with many materials in nanostructured films, leading to sensors and biosensors with enhanced properties to be employed in the biomedical field. This chapter brings an overview of the use of CNTs-based LbL films as amperometric sensors and their advantages as sensing platform.

Keywords Biological detection, Carbon nanotubes, Clinical diagnosis, Electrochemical sensors, Layer-by-layer technique

Contents

D. A. Oliveira and J. R. Siqueira, Jr. (✉)
Institute of Exact Science, Natural and Education, Federal University of Triângulo Mineiro, 38064-200 Uberaba, MG, Brazil
e-mail: jose.siqueira@uftm.edu.br

O. N. Oliveira, Jr. (✉)
São Carlos Institute of Physics, University of São Paulo, 13566-590 São Carlos, SP, Brazil
e-mail: chu@ifsc.usp.br

M. J. Schöning, A. Poghossian (eds.), *Label-Free Biosensing: Advanced Materials, Devices and Applications*, Springer Series on Chemical Sensors and Biosensors (2018) 16: 239–260
DOI 10.1007/5346_2017_14, © Springer International Publishing AG 2017,
Published online: 24 October 2017

1 Introduction

Carbon nanotubes were first reported in the early 1990s [1, 2] and have since that time brought new perspectives to nanotechnology, with novel devices for various areas, including in biomedical fields [3–7]. The use of CNTs in sensors and biosensors, in particular, has been widespread for substances of biological and clinical interest. The physical and chemical properties, in addition to their biocompatibility, allowed CNTs to be employed with different biological materials in electrochemical sensors to detect many substances [3–7]. Optimization in performance for specific detection systems can be achieved with novel functional structures where nanometric control is based on CNTs [8, 9], which requires infrastructure and knowledge for manipulating nanomaterials in the form of nanostructured films [8, 9]. Of special importance is the ability to control materials incorporated in the sensor device at the molecular level, and this can be done with the layer-by-layer (LbL) technique that allows for producing nanostructured, organized films with a variety of materials [8–12]. Indeed, the LbL method affords control of the film architecture and thickness, and may provide synergy between properties of distinct materials at the nanoscale. The film formation methodology is based on electrostatic interactions of layers with opposite charges of both organic and inorganic substances, such as carbon nanotubes, nanoparticles, and biomolecules [8–12].

This chapter gives an overview of the use of CNTs in LbL films applied in electrochemical biosensors of biomedical interest and clinical diagnosis. The advantages of using carbon nanotubes in electrochemical sensors are discussed alongside a review of the layer-by-layer technique and the reasons why it is attractive to apply nanostructures in biosensors. Emphasis will be placed on electrochemical sensors reported in the last 10 years with CNTs in LbL films. Perspectives and trends of this well-known nanomaterial in the field of sensing research will also be highlighted.

2 Carbon Nanotubes as Materials for Electrochemical Sensors

Electrochemical sensors are analytical devices based on charge transfer reactions, i.e. Faradaic or non-Faradaic processes, whose principle of detection may be potentiometric, conductometric, amperometric, or voltammetric [13]. Biosensors are chemical sensors containing a biologically active material (e.g., enzymes, antigens, antibodies, DNA, organelles, among others) incorporated to a transducer, which must be able to convert the generated biochemical signal into a measurable

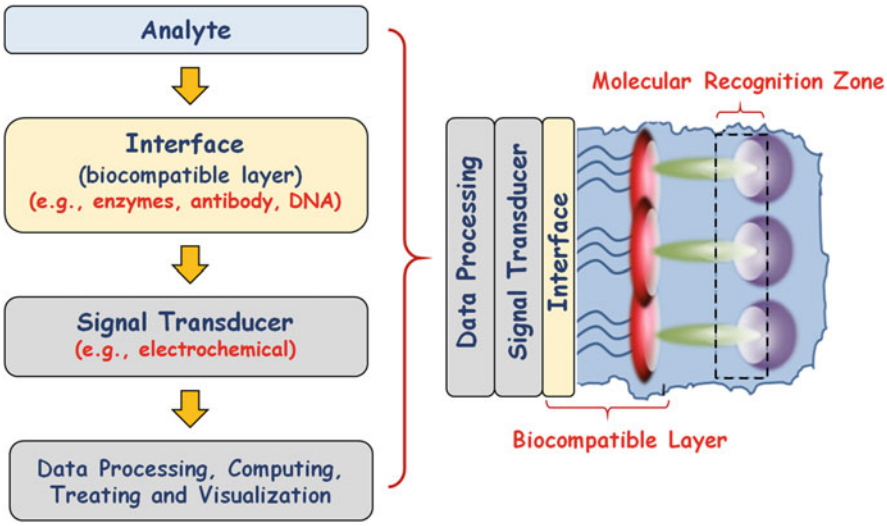

Fig. 1 Schematic representation of a biosensor block diagram. Modified with permission from Oliveira et al. [8]. Copyright 2014 American Chemical Society

signal (electric current, temperature variation, light absorption, etc.) [13]. Figure 1 presents a schematic block diagram of a biosensor.

CNTs are promising materials for sensor applications due to their physico-chemistry properties. The main interest in using carbon nanotubes in chemical and biochemical detection arises from their remarkable electronic properties, which distinguish them from other nanometric structures [3–6, 14]. In particular, CNTs exhibit an sp^2 hybridization, the 2s and two 2p orbitals hybridize to form three sp^2 orbitals, permitting three σ bonds, separated by an angle of 120°, and a fourth electron being in the pz orbital in a perpendicular plane, that does not participate in the sp^2 hybridization. This fourth electron is used to form a π-delocated bond. The ability of the π electron to move freely between carbon atoms gives rise to a high electrical conductivity [15]. In addition, CNTs present a high one-dimensional surface area, which may permit excellent ability to mediate rapid electron transfer kinetics for a wide range of electroactive species. Also, CNTs have catalytic activities for many electrochemical reactions in that electron transport excludes the need for redox mediators. Moreover, CNTs can be functionalized with many different radicals, increasing the range of chemical species that can be immobilized over their surface, as well as facilitating their incorporation onto diverse electrodes surface [3–6, 14].

There are two main types of CNTs, the single-walled carbon nanotubes (SWCNTs) and the multiwalled carbon nanotubes (MWCNTs) [5, 6, 14]. In addition, CNTs behave as a metal or semiconductor according to the arrangement of the carbon atoms that make up the cylindrical shape of the nanotube [5, 6, 14]. Electrodes modified with CNTs have higher conductivity than graphite and show superior performance compared to electrodes such as Au, Pt, and other carbon

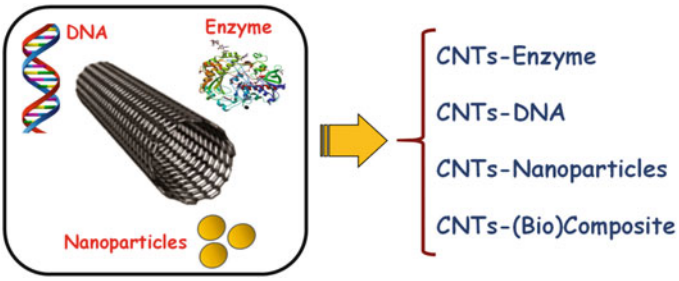

Fig. 2 Schematics of various types of materials combined with CNTs in electrochemical biosensors

electrodes. CNTs have a hollow core, which is suitable for incorporating host molecules. For instance, proteins and enzymes can be immobilized onto the nanotube surface without losing biological activity [3–7]. Figure 2 shows different types of sensors based on CNTs combined with various materials, such as DNA, enzymes, and nanoparticles [16]. Significantly, in addition to the intrinsic advantages of CNTs, synergy can be obtained by combining them with other substances. CNT-based electrochemical biosensors, for example, may be small with large surface area, and exhibit high sensitivity, fast response time, improved charge transfer, and high biocompatibility with different types of biomolecules [3–7]. Furthermore, CNTs possess electrochemical properties similar to other carbon electrodes widely used in electrochemical applications. Unlike other carbon-based nanomaterials, such as fullerenes, CNTs have varied electrochemical properties which yield electrochemical sensors with improved sensor characteristics. Moreover, CNTs display high chemical stability, mechanical strength and may mediate electron transfer reactions with electroactive species in solution [3–7, 16–18].

3 Layer-by-Layer Technique for Incorporation of CNTs in Sensors

CNTs can be immobilized with good control of their properties using various techniques of film preparation [8, 9]. For sensors and biosensors, one of the most effective ways of manipulating nanotubes is in the form of ultrathin films [8, 9], which require the CNTs to be functionalized. Attachment of carboxyl and other functional groups is one of the most popular ways for functionalization, and such CNTs can be purchased commercially [19, 20]. Chemical modification and solubilization of CNTs promotes new features from functionalization, which can be exploited in the formation of polymer nanocomposites and conjugation with biological species [17–20].

CNTs-modified electrodes have been prepared with various methods, including the LbL technique that allows for films with controlled architecture to be produced

[8, 9]. The LbL technique is advantageous owing to the simplicity of the experimental apparatus to fabricate the films, which can coat surfaces of any shape or size. It may be considered as an extension of the self-assembly methods based on chemical interactions (usually covalent bonds) between deposited layers [21]. Instead of chemical adsorption between layers, the technique described by Decher [22–24] is based on physical (electrostatic) interactions of oppositely charged layers. A typical procedure to produce LbL films from polyelectrolytes is described in Fig. 3. A solid substrate charged, for example, negatively, is immersed into a cationic solution, so that a polycation layer adsorbs on the substrate. Then, the substrate is immersed into an anionic solution, promoting the adsorption of the polyanion in the previously adsorbed layer of polycation. A bilayer is obtained, and the repetition of the process leads to a multilayer LbL film.

The potential of the LbL method can be inferred from the variety of types of materials used, ranging from polyelectrolytes and polymers with dyes to ceramic, metallic, and semiconducting materials, in addition to biological materials [8–12]. With the richness in properties that can be achieved, LbL films have been used in many areas, including in fuel cells, solar cells, supercapacitors, and sensors [8–12]. For electrochemical sensing [8, 9, 12], nanomaterials and biological materials have been integrated to exploit the compatibility in size when components of electronic circuits having dimensions comparable to biomolecules. The electrostatic interactions and charge transfer can be detected by amperometrical methods, being advantageous for detection of biological species. In addition, the high reactivity and effective area of these nanomaterials provide a natural combination for biological molecules [8, 9, 12].

In amperometric sensors based on LbL films, CNTs can be incorporated with various biomolecules to produce modified electrodes or probes. For example, an enzyme may be immobilized as a recognition element on the device's surface [3–7, 16–18].

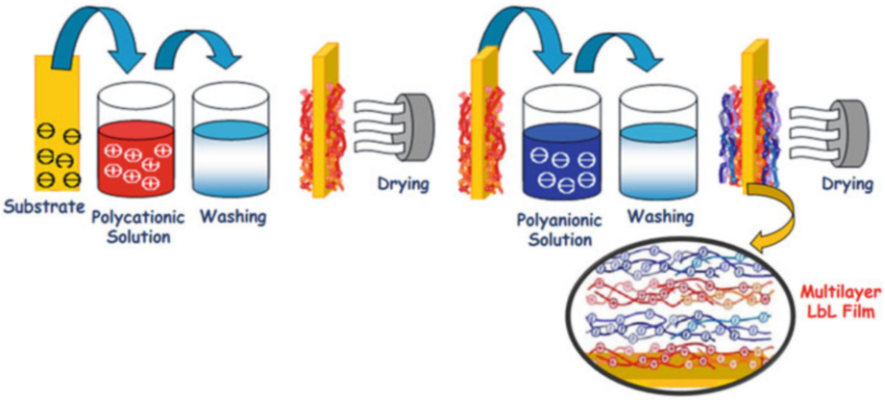

Fig. 3 Schematic representation of the fabrication process of LbL films. Modified with permission from Siqueira et al. [9]. Copyright 2010 Elsevier

4 Carbon Nanotubes in Layer-by-Layer Films for Sensing Applications

4.1 Sensors for Clinical Diagnostics

Two important compounds in clinical analysis and diagnosis are nitrite (NO_2) and hydrogen peroxide (H_2O_2). When in excess in the body, nitrite can lead to esophagus cancer, malformation of fetuses and other diseases, while hydrogen peroxide is cytotoxic and may be a signaling molecule for several biological processes [25]. Zhang and coworkers described an electrode based on cationic 2,9,16,23-tetra[4-(*N*-methyl)pyridinyloxy-phthalocyaninecobalt (II) ($[TMPyPcCo]^{4+}$) and acid-treated multiwalled carbon nanotubes (aCNTs) that were alternately self-assembled on a glassy carbon electrode (GCE), as shown in Fig. 4. In the $[TMPyPcCo/aCNTs]_n$ films, $[TMPyPcCo]^{4+}$ is anchored on the surface of a CNT without any inert polymeric binders, which helps to expose the most active sites for electrocatalysis. The amperometric responses to NO_2 and H_2O_2 varied linearly with concentration between 5 μM and 30 mM and from 10 μM to 9 mM, respectively. In addition, the stability, reproducibility, and selectivity of the measurements make

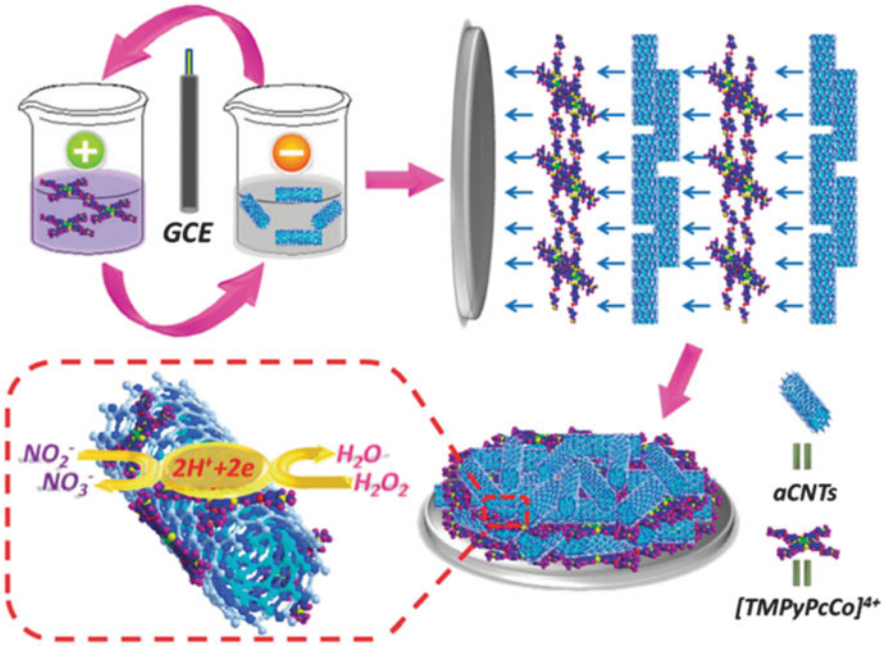

Fig. 4 Schematic representation of the LbL $[TMPyPcCo/aCNTs]_n$ film developed by Zhang and coworkers, yielding an electrochemical bifunctional sensor for detection of nitrite and hydrogen peroxide. Modified with permission from Zhang et al. [25]. Copyright 2016 Royal Chemistry Society

the [TMPyPcCo/aCNTs] films suitable for detecting nitrite oxidation and peroxide reduction in real blood samples [25].

Other (bio)sensors to detect H_2O_2 with LbL films containing CNTs included the use of polyoxometalate clusters $K_6P_2W_{18}O_{62}$ (P_2W_{18}) [26], Prussian blue and poly(diallyldimethylammonium chloride) [27], horseradish peroxidase [28], iron oxide magnetic nanocrystals to mimic peroxidase [29], and redox-active iron (II) phthalocyanine nanoparticles [30]. As for detection of nitrite, an equally wide variety of materials have been conjugated with CNTs in electrochemical sensors made with the LbL technique. By way of illustration, a note can be made of $H_7P_2Mo_{17}V_1O_{62}$ and Pt-chitosan nanoparticles [31], positively charged gold nanoparticles and hemoglobin [32], vanodotungstophosphate α_2-$K_7P_2VW_{17}O_{62}{\cdot}18H_2O$ [33], and multihemic nitrite reductase [34].

Detection of another important compound, the reduced form of nicotinamide adenine dinucleotide, has been made with LbL films containing MWCNTs, gold nanoparticles (AuNPs) and red polyneutral red film [35], MWCNTs LbL films [36] and with polymerized phenothiazine [37].

Important biomarkers in biological fluids, such as ascorbic acid (AA), uric acid (UA), and dopamine (DA), have been extensively investigated using amperometric sensors made with LbL films containing CNTs. These modified electrodes can improve the electrocatalytic activity by oxidation of such substances. Examples include detection of AA with films comprising p-aminobenzene sulfonic acid [38], simultaneous detection of DA, AA, and UA with a multilayer film of chitosan, tin disulfide nanoparticles, and SWCNTs [39], detection of AA, UA, and epinephrine using poly(malachite green) [40], and use of electropolymerized β-cyclodextrin to detect UA [41]. With multiple-component film architecture, made with chitosan, AuNPs, Nano-SnO_2 and MWCNTs, Pan and coworkers studied the electrocatalytic activity of UA. The most significant feature was the separation of the oxidation peaks for AA and UA, which allowed for the simultaneous detection of these two analytes [42].

Enzymatic biosensors should be highlighted in this context since the LbL technique has been shown to be excellent in the preservation of protein activity. For instance, Zhang and coworkers reported a carbon nanotube-acetylcholinesterase/biopolymer LbL film, with renewable properties, as shown in Fig. 5 [43]. This study involved two LbL films in the same electrode, an internal consisting of layers with positively charged CNT-polyethylenimine (PEI) and negatively charged CNT-deoxyribonucleic acid, and an external made of alternating layers of positively CNT-PEI and negatively charged CNT-acetylcholinesterase (AChE) as outermost bilayer. The signal current associating to the CNT-AChE layer was inhibited after exposure to pesticides, causing desorption of this layer from the electrode, but allowing the internal layers to be kept intact. The same electrode was regenerated by self-assembling of new CNT-PEI/CNT-AChE bilayers atop the internal film, and was reused again for detection tests. The modified electrode was regenerated multiples times, observing the current recovered completely to the initial levels as indicated by the chronoamperometric curves in Fig. 5.

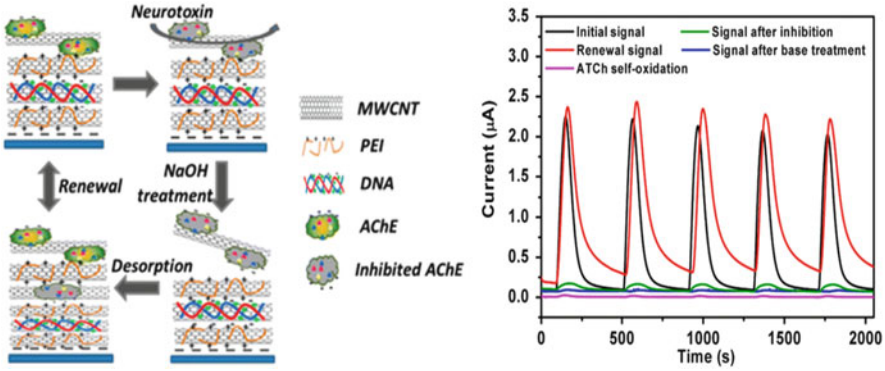

Fig. 5 Schematic representation of an acetylcholinesterase biosensor by amperometric measurements. Modified with permission from Zhang et al. [43]. Copyright 2015 American Chemical Society

In another study, SWCNTs were used as matrix for acetylcholinesterase to determine the concentration of acetylcholine with a resolution of 10 μM [44]. For detection of cholesterol carbon nanotubes were used in the matrix for immobilization of enzymes such as HRP and cholesterol oxidase [45, 46]. Chitosan derivatives served for immobilization of glucose oxidase, l-amino acid oxidase or polyphenol oxidase as biorecognition elements. This system combined with the CNTs presented an efficient self-assembly and enhanced sensitivity [47].

Various LbL-based electrochemical sensors have been fabricated to detect drugs in pharmaceutical formulations or in biological samples. For instance, LbL films adsorbed on a carbon glass electrode and containing functionalized MWCNTs and a molecularly imprinted polymer were used to detect tramadol. This is an important synthetic analgesic that can accumulate in the body to cause side effects such as nausea, vomiting, tachycardia, seizure, cardiopulmonary arrest, and even death. The printing process basically involved copolymerization of a multi-functional monomer with a reactant in the presence of a template molecule, also called a print molecule. When this model molecule was removed, a site was formed in the polymer matrix to bind to the tramadol. The principle of sensor operation was square wave voltammetry in the presence of $[Fe(CN)_6]^{3-/4-}$ as probe. The corresponding peak current decreased as the tramadol concentration in solution increased. This may occur due to some cavities of the sensor be filled with tramadol molecules, hampering electron transfer of the redox probe onto the sensor surface. The calibration curve exhibited two linear concentration ranges from 0.2 to 2.0 nM and 2.0 to 20.0 nM, with a limit of detection of 0.03 nM [48].

MWCNTs were combined with polyaniline (PANI) in LbL films to detect various substances, as in the case of nifedipine that is used for treating angina pectoris, high blood pressure, and cardiovascular diseases. Detection of nifedipine is relevant because it can be toxic to the body when found in excess, causing dizziness, changes in heartbeat, nausea, and vomiting. The sensor produced by

Wang et al. showed a synergistic effect for electrochemical oxidation of nifedipine, with a more intense anodic peak and a detection limit of 1 μM [49]. Another PANI-MWCNTs-based sensor was investigated to detect 2-chlorophenol, a highly toxic substance. Its maximum concentration permitted amounts 100 mg L^{-1}, which indicates the importance of a sensor capable of fast and reliable monitoring. With this sensor, the current peaks of PANI decreased with increasing chlorophenol concentration because the analyte adsorbed on the film, thus blocking the active sites of PANI. The lowest concentration detected was 1 ppm (1 mg L^{-1}) [50]. Choline, an essential nutrient for the human body, was also detected with an amperometric biosensor, which exhibited a linear response from 1 μM to 2 mM and a detection limit of 3 μM [51].

Paracetamol is an antipyretic and analgesic drug used worldwide. In general, it is safe and has no toxic effects in normal doses. However, in excess it can cause skin rashes, liver disorders, nephrotoxicity, and inflammation of the pancreas. Sensors for detecting paracetamol were made by combining MWCNTs with poly (amidoamine) dendrimers and ethylenediamine. When dendrimers were used, the anodic peak current increased linearly between 3.0×10^{-7} and 2.0×10^{-4} M, with detection limit of 1.0×10^{-7} M [52], while for ethylenediamine the linear range was 1–200 μM and detection limit 0.092 μM [53].

Chitosan was used with MWCNTs for detecting 17α-ethinylestradiol, a synthetic estrogen female hormone used in contraceptives, which is able to affect the endocrine system even at such low concentrations as ng L^{-1}. Detection with square wave voltammetry was possible with detection limit of 0.09 μM and linear range from 0.05 to 20 μM [54]. Graphene/MWCNTs films were employed to determine the concentration of the fat-loss drug clenbuterol using differential pulse voltammetry, where the linear range was between 0.01 and 0.5 μM with detection limit of 4.6 nM [55]. Copper tetrasulfonated phthalocyanine onto MWCNTs was tested as amperometric sensor to detect the antioxidant 2-mercaptoethanol in a linear range of 30 μM–6 mM and detection limit of 25 μM [56]. A sensor to detect sumatriptan, a substance used for treating migraine and headache, was developed with an LbL film comprising electropolymerized polypyrrole and MWCNTs. Oxidation of sumatriptan was detected using linear sweep voltammetry in the linear range 0.02–10.0 μM with detection limit of 6 nM [57]. A thin imprinted sol-gel combined with MWCNTs was used to detect clindamycin in human urine samples. This substance is an antibiotic whose side effects may include diarrhea and even infections when in excess. The anodic peak current in cyclic voltammograms varied with clindamycin concentration within a linear range from 0.5 to 80 μM and detection limit of ca. 24 nM [58].

Compounds used in the food industry have also been detected with LbL films containing MWCNTs. An example is quinolone yellow, a colorant used in beverage industry, which can cause asthma, rashes, and hyperactivity. Detection with cyclic voltammetry and amperometry was possible owing to oxidation of quinolone yellow, whose results could be analyzed with concentration dependence in a linear range between 0.02 and 10 μM, with a detection limit of 0.004 μM [59]. Glutamate is used to add flavor in food, and is a typical neurotransmitter in the mammalian

central nervous system and in the brain, related to neurological disorders such as schizophrenia, Parkinson's disease, epilepsy, and stroke. An amperometric sensor based on the oxidation of glutamate was developed by Tang and coworkers, which exhibited a wide determination range (0.2–250 μM) and high sensitivity of 433 $\mu A\ mM^{-1}\ cm^2$ [60].

Much has been discussed about the possible advantages of using aptamers in biosensors, and this has been exploited to detect the proteins thrombin and lysozyme. LbL films of ferrocene-appended poly(ethyleneimine) (Fc-PEI) and CNTs, with aptamers on the outermost layer could catch the target on the electrode interface. A barrier was thus created for electrons, with inhibition of electron transfer and decrease in the differential pulse voltammetry signal of Fc-PEI. This strategy proved to be highly successful, with a wide detection range (0.3–165 ng mL^{-1}) for the model targets thrombin and lysozyme (0.2 ng mL^{-1}–1.66 μg mL^{-1}) [61].

With regard to straightforward diagnosis of diseases, mention can be made of a biosensor to detect the swine influenza virus (SIV) H1N1, where the conductance of underlying SWCNTs in LbL films was altered by antibody–virus complexes. The resistance of the immunochips tended to increase upon adsorption of macromolecules such as poly-l-lysine, anti-SIV antibodies, and SIVs. Therefore, these devices are promising for point-of-care diagnosis and lab-on-a-chip systems [62].

In another work depicted in Fig. 6, detection of cancer cells was made with surface-confined ferrocene in LbL films with SWCNTs and a 3-mercaptopropionic acid (MPA)-modified gold substrate. Positively charged poly(ethyleneimine) functionalized with ferrocene (Fc-PEI) was used as current signal indicator and negatively charged SWCNTs were alternately assembled. Folic acid (FA) was covalently bonded onto the SWCNTs surface to recognize cancer cells according to the high affinity of FA for folate receptor (FR) on the cell surface, while bovine serum albumin (BSA) was employed as a blocker to minimize the non-specific adsorption of cells on the sensor interface. The sensor signal was based on the charge exchange between cancer cells and the electrolyte solution, where a decrease of the current signal was observed, as illustrated in Fig. 6. Once cells were captured onto the sensor interface, they isolated the interface from the electrolyte solution (resistance of 10^2–10^5 Ω), which inhibited the solvated anion transfer between the electrolyte solution and the ferrocene used as a probe, resulting in a decreased current response. The sensor was highly sensitive and selective, exhibiting a range from 10^1 to 10^6 cells/mL with detection limit of 10 cells/mL for human cervical carcinoma (HeLa) [63].

The incorporation of CNTs in LbL films was exploited in two types of sensors, one to amperometrically detect the neurotransmitter dopamine (DA) and a capacitive sensor to detect pH changes and penicillin G. In the first, LbL films of alternating layers of MWCNTs dispersed in polyaminoamide (PAMAM) dendrimers and nickel phthalocyanine (NiTsPc) were used in amperometric detection of DA. The electrochemical properties evaluated with cyclic voltammetry indicated that incorporation of MWCNTs in the film led to a threefold increase in peak current, in addition to a decrease of 50 mV in the oxidation potential of DA (0.75 V). The use of MWCNTs also enhanced the activity of NiTsPc in the two-oxidation processes of DA to

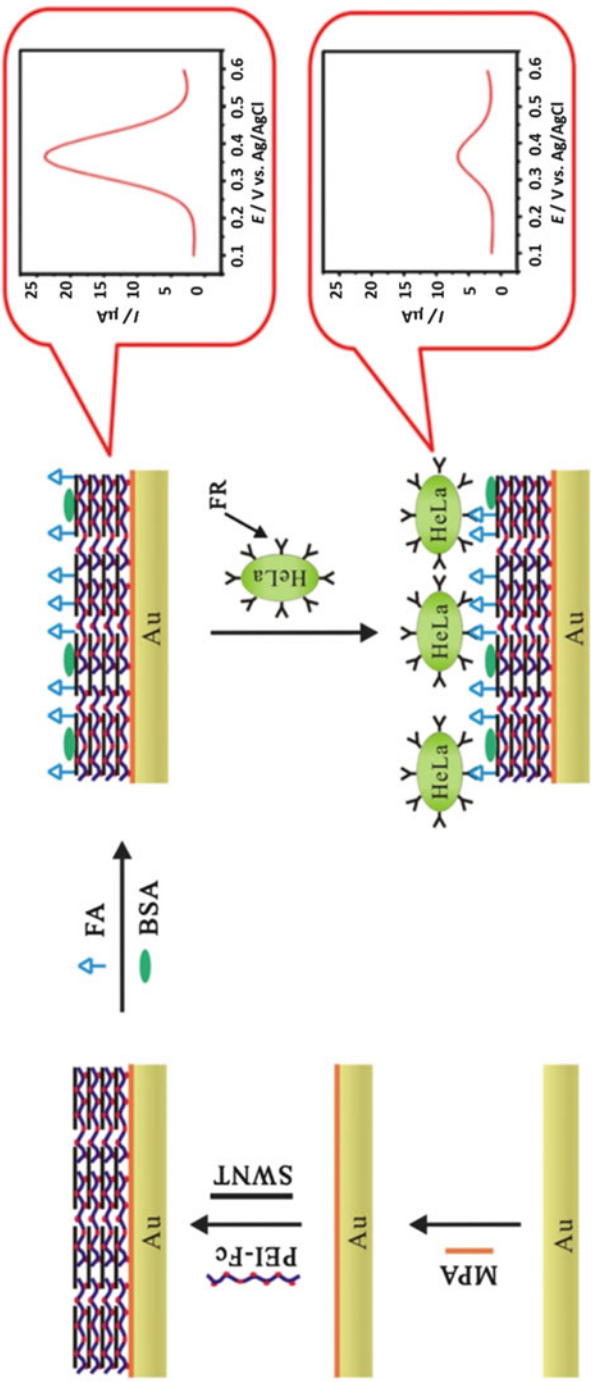

Fig. 6 Diagram of the electrochemical cytosensor with surface-confined probe for detection of HeLa cells. Modified with permission from Liu et al. [63]. Copyright 2013 Elsevier

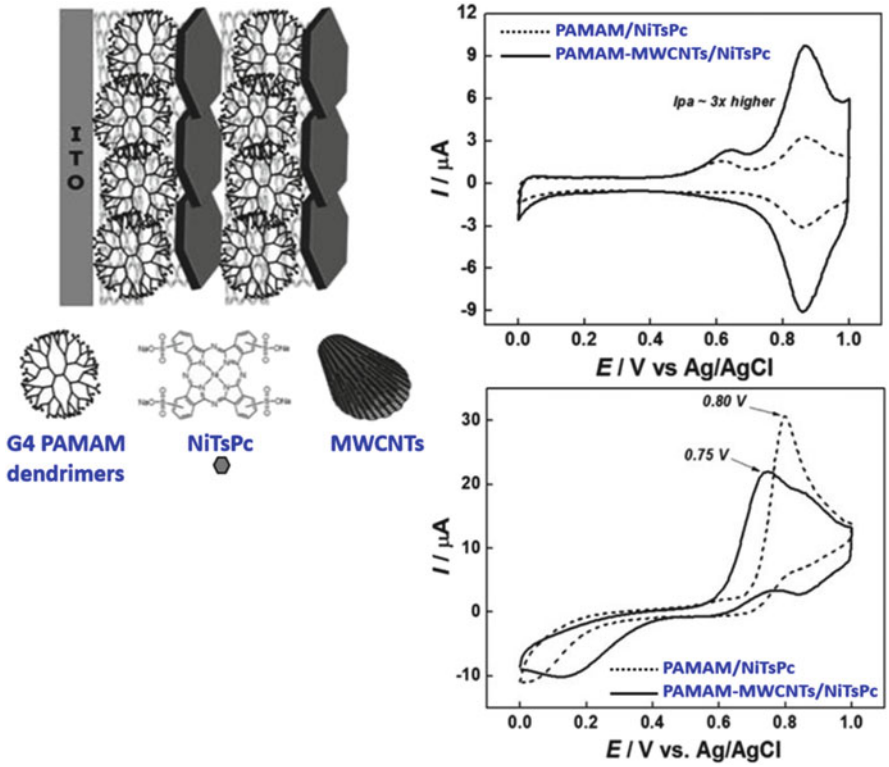

Fig. 7 Dopamine sensor based on PAMAM-MWCNTs/NiTsPc LbL films. Modified with permission from Siqueira et al. [64]. Copyright 2009 John Wiley & Sons, Inc.

dopaminequinone, where the anodic peak shifted from 0.80 to 0.75 V (see Fig. 7). The detection limit was of the order of 10^{-7} M. The latter allowed detection of DA even in the presence of AA, a typical interferent for DA. Another LbL film was obtained with layers of PAMAM and SWCNTs employed in field-effect-devices using a capacitive electrolyte-insulator-semiconductor structure. The adsorption of the film components was monitored by measuring the flat-band voltage shift in capacitance-voltage (C-V) curves, caused by the charges from the components. From constant capacitance measurements it was inferred that the EIS-PAMAM/SWCNT film displayed a high pH sensitivity (ca. 54.5 mV/pH), being capable of detecting penicillin G between 10^{-4} and 10^{-2} M, when a layer of enzyme penicillinase was adsorbed atop the PAMAM/SWNT film [64–66].

4.2 DNA Sensors

The ability of CNTs to help preserve activity of immobilized biomolecules for sensing and biosensing was also exploited in DNA-containing sensors, which are

normally advantageous owing to their high selectivity. For example, ultrasensitive detection of 3,3′,5,5′ tetramethylbenzidine (TMB) was achieved with LbL films made with a bioconjugate of DNAzyme-functionalized Pt nanoparticles/CNTs. Because TMB is oxidized by the DNAzyme, the electrochemical signal varied with TMB concentration to reach a detection limit of only 0.6 fM, with excellent selectivity against even a single mismatch [67].

In another example, an efficient sensor with poly-l-lysine (pLys) and Au-carbon nanotube (Au-CNTs) multilayers was developed to detect DNA, where the DNA probe was linked to an outer layer of positively charged pLys. The detection was via hybridization and accomplished by using methylene blue as the indicator, which possesses different affinities to double-stranded DNA (dsDNA) and single-stranded DNA (ssDNA) [68].

Detection of DNA damage is crucial for obvious biological implications and a suitable way for such detection is to use DNA-based sensors. Considerable DNA damage caused by reactive oxygen species formed in situ and the possible antioxidant effects of rutin and tea extracts were evaluated with an LbL film of MWCNTs, double-stranded calf thymus or herring sperm DNA deposited on a screen-printed carbon electrode. In this device, detection was made by measuring the changes in charge transfer resistance and voltammetric current of a negatively charged redox probe such as $[Fe(CN_6)]^{3-}$ [69]. Also relevant in this context was the assessment of oxidative DNA damage induced by cadmium ions (Cd^{2+}) with a sensor comprising carboxylic group-functionalized carbon nanotubes, pLys and dsDNA, in which differential pulse voltammetry was the principle of detection with methylene violet as the intercalating redox probe [70].

Sensors made with DNA-containing LbL films can also be used to detect chemical compounds of relevance, as it is the case of 2,4,6-trinitrotoluene (TNT), a well-known explosive material, sometimes used to generate charge transfer salts. A fast response, within 15 s, toward TNT was possible with a sensor fabricated on a glassy carbon modified with DNA-functionalized, SWCNTs hybrids, and poly (diallyldimethylammonium chloride) (PDDA). The limit of detection, obtained through the reduction peak of TNT, was 0.5 μg L^{-1} with a linear range at least up to 800 μg L^{-1} [71].

The combination of DNA and CNTs has been explored in immunosensors, which could serve as platform for determination of antigens and/or tumor markers. The concept was illustrated with the determination of alpha-fetoprotein with an amperometric immunosensor comprising LbL multilayers of thionine/DNA carbon nanotubes modified glass carbon electrodes. In this sensor, DNA served as cross-linker for thionine immobilization, which allowed for reaching a relatively low detection limit of 0.02 ng mL^{-1}. This performance was made possible because alpha-fetoprotein decreased the peak currents of thionine, a redox probe [72].

4.3 Glucose Sensors

Glucose sensors are perhaps the most investigated in history for at least two reasons: the immense market already in place and the availability of so much data, which serve as reference for the development of innovative approaches and devices. It is therefore not surprising that much has been done with LbL films containing CNTs for glucose sensing, and this will be illustrated here with a few examples.

Amperometric glucose sensors were obtained with LbL films of Cu/MnO_2/MWCNTs nanocomposites deposited on a glassy carbon electrode [73] and bamboo-like MWCNTs noncovalently functionalized with calf-thymus double-stranded DNA coated with glucose oxidase [74], to measure the concentration of glucose through its oxidation. In various examples, the matrix made with CNTs to immobilize glucose oxidase also contained polymers and/or metal nanoparticles to enhance sensitivity in electrochemical detection. For instance, a glucose sensor was obtained with LbL films of polyallylamine, poly(vinylsulfate), PDDA, and glucose oxidase adsorbed on perpendicularly aligned few-walled carbon nanotubes/thionine/Au [75]. In a similar work, graphene functionalized with capped AuNPs and MWCNTs comprised the matrix to adsorb the enzyme glucose oxidase, with which a relatively high sensitivity (29.72 mA M^{-1} cm^{-2}) and low detection limit (4.8 μM) were reached in detecting glucose [76]. Polymers with multifunctions can also be combined with CNTs, as in the glucose biosensor built with LbL films of MWCNTs dispersed in polyhistidine and glucose oxidase, which also contained one layer of Nafion as anti-interferent barrier. This biosensor was especially interesting because no previous treatment was required to generate functional groups or covalent attachment of bioactive groups. The linear range for detection was between 0.25 and 5.00 mM, with a detection limit of 2.2 μM [77].

The use of modified Pt electrodes with LbL films for amperometric glucose sensors has been reported by various authors, e.g., in Wang et al. [78], and Shirsat et al. [79]. SWCNTs dispersed in PDDA were deposited in LbL films alternated with glucose oxidase on Pt electrodes where the best performance was achieved with a 7-bilayer film, whose sensitivity toward glucose was 63.84 μA mM^{-1} cm^2 [78]. In another example, an amperometric glucose biosensor was made with LbL films of glucose oxidase on SWNTs and polypyrrole deposited on a platinum-coated polyvinylidene fluoride membrane. The biosensor exhibited a linear response range from 1 to 50 mM of glucose concentration with excellent sensitivity of 7.06 μA mM^{-1} [79].

A special film architecture designed to optimize the performance of electrochemical glucose sensors is depicted in Fig. 8 [80]. Pt nanoparticles were mixed with CNTs and cast on a GCE using chitosan (CS) as a binder (Pt nano-CNTs-CS) which served as matrix to adsorb an LbL film of concanavalin A (Con A) via electrostatic attraction with the positively charged chitosan. The biosensor was completed with adsorption of LbL alternating layers of Con A and glucose oxidase (GOD), whose optimized performance yielded a detection limit of 4.0×10^{-7} M and a linear range from 1.2 μM to 2.0 mM [78].

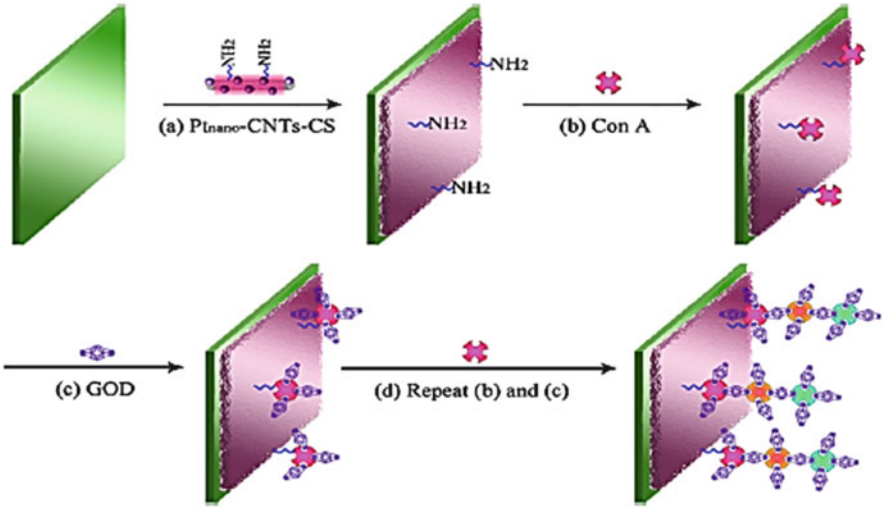

Fig. 8 Illustration of the biosensor prepared by Li et al. Adapted with permission from Wang et al. [78]. Copyright 2011 Elsevier

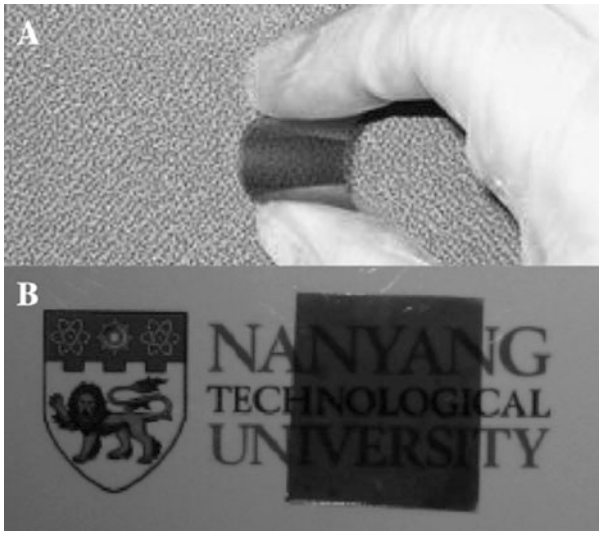

Fig. 9 Flexibility (**a**) and transparency (**b**) of the biosensor by Yan et al. Modified with permission from Yan et al. [81]. Copyright 2007 Elsevier

The trend toward flexible biosensors has also had an impact on glucose sensors built with LbL films. By way of illustration, transparent and flexible glucose biosensors were prepared using the LbL method where a polymer substrate was functionalized with MWNTs and glucose oxidase (see Fig. 9). Thin Ti and Au

layers were first deposited on the polymer substrate through plasma immersion ion implantation and sputtering, respectively. An organic monolayer was then formed on the gold surface using thiol chemistry. Subsequently, LbL films of negatively charged MWCNTs and glucose oxidase were assembled on the modified Au surface to yield a biosensor with a low detection limit of 10 μM [81].

Still with regard to the incorporation of metal nanoparticles in the LbL film to enhance sensitivity, gold nanoparticles, MWCNTs and glucose oxidase were combined with the positively charged poly(dimethyldiallylammonium chloride). The synergistic effect of the gold nanoparticles and MWCNTs led to a higher electrocatalytic activity in comparison to the films containing these components in separate. Indeed, amperometric glucose biosensing was possible at a relatively low potential (−0.2 V), with a detection limit of 128 μM [82]. Pt nanoparticles encapsulated in dendrimers were used with glucose oxidase layers deposited on the surface of carbon nanotubes to produce a biosensor capable of detecting glucose down to 2.5 μM [83].

5 Conclusions

In this chapter, we provided an overview highlighting the importance and advantages of the use of CNTs in LbL films with emphasis on their application in amperometric biosensors. Attention was mainly given to (bio)sensing systems for a variety of clinical diagnosis, as well as for glucose and DNA sensors. The advantages of CNTs manipulated by the LbL method were illustrated by describing a number of applications reported in the literature. In common in such applications one identifies the synergy in the arrangement of nanotubes with biomolecules and/or other compounds in nanostructured films deposited on electrodes.

The examples discussed in this chapter were chosen just by way of illustration, since we did not intend to provide a comprehensive survey of the literature in view of the thousands of papers published on electrochemical biosensors containing carbon nanotubes. We hope that such examples may serve to inspire the design of novel amperometric biosensors as different types of carbon nanotubes can be combined with a variety of nanomaterials and biomolecules.

Acknowledgments The authors thank the Brazilian funding agencies CAPES, CNPq (477668/2013-5), FAPEMIG (APQ-01358-13 and APQ-00756-16), and FAPESP (2013/14262-7) for their financial support.

References

1. Iijima S (1991) Helical microtubules of graphitic carbon. Nature 354:56–58
2. Iijima S, Ichihashi T (1993) Single-shell carbon nanotubes of 1-nm diameter. Nature 363:603–605

3. Katz E, Willner I (2004) Biomolecule-functionalized carbon nanotubes: applications in nanobioelectronics. ChemPhysChem 5:1084–1104
4. Balasubramanian K, Burghard M (2006) Biosensors based on carbon nanotubes. Anal Bioanal Chem 385:452–468
5. Allen BL, Kichambare PD, Star A (2007) Carbon nanotube field-effect-transistor-based biosensors. Adv Mater 19:1439–1451
6. Kim SN, Rusling JF, Papadimitrakopoulos F (2007) Carbon nanotubes for electronic and electrochemical detection of biomolecules. Adv Mater 19:3214–3228
7. Willner I, Willner B (2010) Biomolecule-based nanomaterials and nanostructures. Nano Lett 10:3805–3815
8. Oliveira Jr ON, Lost RM, Siqueira Jr JR, Crespilho FN, Caseli L (2014) Nanomaterials for diagnosis: challenges and applications in smart devices based on molecular recognition. ACS Appl Mater Interfaces 6:14745–14766
9. Siqueira Jr JR, Caseli L, Crespilho FN, Zucolotto V, Oliveira Jr ON (2010) Immobilization of biomolecules on nanostructured films for biosensing. Biosens Bioelectron 25:1254–1263
10. Ariga K, Hill JP, Ji Q (2007) Layer-by-layer assembly as a versatile bottom-up nanofabrication technique for exploratory research and realistic application. Phys Chem Chem Phys 9:2319–2340
11. Lutkenhaus JL, Hammond PT (2007) Electrochemically enabled polyelectrolyte multilayer devices: from fuel cells to sensors. Soft Matter 3:804–816
12. Zhao W, Xu JJ, Chen HY (2006) Electrochemical biosensors based on layer-by-layer assemblies. Electroanalysis 18:1737–1748
13. Hulanicki A, Glab S, Ingman F (1991) Chemical sensors: definitions and classification. Pure Appl Chem 63:1247–1250
14. Siqueira Jr JR, Oliveira Jr ON (2017) Carbon-based nanomaterials. Nanostructures. Elsevier, Amsterdam, pp 233–249
15. Littlejohn SD (2014) Background theory. Electrical properties of graphite nanoparticles in silicone. Springer, Berlin, pp 5–38
16. Merkoçi A (2007) Nanobiomaterials in electroanalysis. Electroanalysis 19:739–741
17. Gooding JJ (2005) Nanostructuring electrodes with carbon nanotubes: a review on electrochemistry and applications for sensing. Electrochim Acta 50:3049–3060
18. Wang J (2005) Carbon-nanotube based electrochemical biosensors: a review. Electroanalysis 17:7–14
19. Thostenson ET, Ren Z, Chou TW (2001) Advances in the science and technology of carbon nanotubes and their composites: a review. Compos Sci Technol 61:1899–1912
20. Charlier JC (2002) Defects in carbon nanotubes. Acc Chem Res 35:1063–1069
21. Maoz R, Sagiv J (1984) On the formation and structure of self-assembling monolayers. I. A comparative ATR-wettability study of Langmuir-Blodgett and adsorbed films on flat substrates and glass microbeads. J Coll Interface Sci 100:465–496
22. Decher GHJD, Hong JD, Schmitt J (1992) Buildup of ultrathin multilayer films by a self-assembly process: III. Consecutively alternating adsorption of anionic and cationic polyelectrolytes on charged surfaces. Thin Solid Films 210:831–835
23. Decher G, Lvov Y, Schmitt J (1994) Proof of multilayer structural organization in self-assembled polycation-polyanion molecular films. Thin Solid Films 244:772–777
24. Decher G (1997) Fuzzy nanoassemblies: toward layered polymeric multicomposites. Science 277:1232–1237
25. Zhang J, Chen Z, Wu H, Wu F, He C, Wang B, Wu Y, Ren Z (2016) An electrochemical bifunctional sensor for the detection of nitrite and hydrogen peroxide based on layer-by-layer multilayer films of cationic phthalocyanine cobalt (ii) and carbon nanotubes. J Mater Chem B 4:1310–1317
26. Guo SY, Xu L, Xu B, Sun Z, Wang L (2015) A ternary nanocomposite electrode of polyoxometalate/carbon nanotubes/gold nanoparticles for electrochemical detection of hydrogen peroxide. Analyst 140:820–826

27. Li J, Yao Y, Shiu KK (2010) Layer-by-layer assembly of Prussian blue and carbon nanotube composites with poly (diallyldimethylammonium chloride) for the sensitive detection of hydrogen peroxide. Anal Sci 26:431–435
28. Munge BS, Dowd RS, Krause CE, Millord LN (2009) Ultrasensitive hydrogen peroxide biosensor based on enzyme bound to layered nonoriented multiwall carbon nanotubes/poly-electrolyte electrodes. Electroanalysis 21:2241–2248
29. Miao Y, Wang H, Shao Y, Tang Z, Wang J, Ling Y (2009) Layer-by-layer assembled hybrid film of carbon nanotubes/iron oxide nanocrystals for reagentless electrochemical detection of H_2O_2. Sensors Actuators B Chem 138:182–188
30. Pillay J, Ozoemena KI (2009) Layer-by-layer self-assembled nanostructured phthalocyaninatoiron (II) /SWCNT-poly (m-aminobenzenesulfonic acid) hybrid system on gold surface: electron transfer dynamics and amplification of H_2O_2 response. Electrochim Acta 54:5053–5059
31. Bai Z, Zhou C, Gao N, Pang H, Ma H (2016) A chitosan–Pt nanoparticles/carbon nanotubes-doped phosphomolybdate nanocomposite as a platform for the sensitive detection of nitrite in tap water. RSC Adv 6:937–946
32. Zhang L, Yi M (2009) Electrochemical nitrite biosensor based on the immobilization of hemoglobin on an electrode modified by multiwall carbon nanotubes and positively charged gold nanoparticle. Bioprocess Biosyst Eng 32:485–492
33. Zhang D, Ma H, Chen Y, Pang H, Yu Y (2013) Amperometric detection of nitrite based on Dawson-type vanodotungstophosphate and carbon nanotubes. Anal Chim Acta 792:35–44
34. Silveira CM, Pimpão M, Pedroso HA, Rodrigues PRS, Moura JJG, Pereira MFR, Almeida MG (2013) Probing the surface chemistry of different oxidized MWCNT for the improved electrical wiring of cytochrome c nitrite reductase. Electrochem Commun 35:17–21
35. Sahin M, Ayrance E (2015) Electrooxidation of NADH on modified screen-printed electrodes: effects of conducting polymer and nanomaterials. Electrochim Acta 166:261–270
36. Sun Y, Ren Q, Liu X, Zhao S, Qin Y (2013) A simple route to fabricate controllable and stable multilayered all-MWNTs films and their applications for the detection of NADH at low potentials. Biosens Bioelectron 39:289–295
37. Gao Q, Sun M, Peng P, Qi H, Zhang C (2010) Electro-oxidative polymerization of phenothiazine dyes into a multilayer-containing carbon nanotube on a glassy carbon electrode for the sensitive and low-potential detection of NADH. Microchim Acta 168:299–307
38. Xi L, Zhang D, Wang F, Huang Z, Ni T (2016) Layer-by-layer assembly of poly (p-aminobenzene sulfonic acid)/quaternary amine functionalized carbon nanotube/p- aminobenzene sulfonic acid composite film on glassy carbon electrode for the determination of ascorbic acid. J Electroanal Chem 767:91–99
39. Pan Y, Zhang YZ, Li Y (2013) Layer-by-layer self-assembled multilayer films of single-walled carbon nanotubes and tin disulfide nanoparticles with chitosan for the fabrication of biosensors. J Appl Polym Sci 128:647–652
40. Raoof JB, Ojani R, Baghayeri M (2013) Fabrication of layer-by-layer deposited films containing carbon nanotubes and poly(malachite green) as a sensor for simultaneous determination of ascorbic acid, epinephrine, and uric acid. Turk J Chem 37:36–50
41. Wayu MB, DiPasquale LT, Schwarzmann MA, Gillespie SD, Leopold MC (2016) Electropolymerization of β-cyclodextrin onto multi-walled carbon nanotube composite films for enhanced selective detection of uric acid. J Electroanal Chem 783:192–200
42. Pan Y, Li Y, Jia J, Chen H (2015) Selective determination of uric acid in the presence of ascorbic acid using layer-by-layer gold nanoparticles, tin oxide nanoparticles and multi-walled carbon nanotubes assembled multilayer films. Electrochemistry 83:956–961
43. Zhang Y, Arugula MA, Kirsch JS, Yang X, Olsen E, Simonian AL (2015) Layer-by-layer assembled carbon nanotube-acetylcholinesterase/biopolymer renewable interfaces: SPR and electrochemical characterization. Langmuir 31:1462–1468
44. Lee D, Cui T (2012) Carbon nanotube thin film pH electrode for potentiometric enzymatic acetylcholine biosensing. Microelectron Eng 93:39–42

45. Cai X, Gao X, Wang L, Wu Q, Lin X (2013) A layer-by-layer assembled and carbon nanotubes/gold nanoparticles-based bienzyme biosensor for cholesterol detection. Sensors Actuators B Chem 181:575–583
46. Karimi S, Ghourchian H, Rahimi P, Rafiee-Pour HA (2012) A nanocomposite based biosensor for cholesterol determination. Anal Methods 4:3225–3231
47. Rivas GA, Miscoria SA, Desbrieres J, Barrera GD (2007) New biosensing platforms based on the layer-by-layer self-assembling of polyelectrolytes on Nafion/carbon nanotubes-coated glassy carbon electrodes. Talanta 71:270–275
48. Deiminiat B, Rounaghi GH, Arbab-Zavar MH (2017) Development of a new electrochemical imprinted sensor based on poly-pyrrole, sol–gel and multiwall carbon nanotubes for determination of tramadol. Sensors Actuators B Chem 238:651–659
49. Wang Q, Zhao R, Wang S, Guo H, Li J, Zhou H, Wang X, Wu X, Wang Y, Chen W, Zhang W (2016) A highly selective electrochemical sensor for nifedipine based on layer-by-layer assembly films from polyaniline and multiwalled carbon nanotube. J Appl Polym Sci 133:43452–43460
50. Silva JS, de Barros A, Constantino CJL, Simoes FR, Ferreira M (2014) Layer-by-layer films based on carbon nanotubes and polyaniline for detecting 2-chlorophenol. J Nanosci Nanotechnol 14:6586–6592
51. Qu F, Yang M, Jiang J, Shen G, Yu R (2005) Amperometric biosensor for choline based on layer-by-layer assembled functionalized carbon nanotube and polyaniline multilayer film. Anal Biochem 344:108–114
52. Zhang Y, Liu X, Li L, Guo Z, Xue Z, Lu X (2016) An electrochemical paracetamol sensor based on layer-by-layer covalent attachment of MWCNTs and a G4.0 PAMAM modified GCE. Anal Methods 8:2218–2225
53. Li Y, Feng S, Li S, Zhang Y, Zhong Y (2014) A high effect polymer-free covalent layer by layer self-assemble carboxylated MWCNTs films modified GCE for the detection of paracetamol. Sensors Actuators B Chem 190:999–1005
54. Pavinatto A, Mercante LA, Leandro CS, Mattoso LHC, Correa DS (2015) Layer-by-layer assembled films of chitosan and multi-walled carbon nanotubes for the electrochemical detection of 17α-ethinylestradiol. J Electroanal Chem 755:215–220
55. Zhai H, Liu Z, Chen Z, Liang Z, Su Z, Wang S (2015) A sensitive electrochemical sensor with sulfonated graphene sheets/oxygen-functionalized multi-walled carbon nanotubes modified electrode for the detection of clenbuterol. Sensors Actuators B Chem 210:483–490
56. Shaik M, Rao VK, Gupta M, Pandey P (2012) Layer-by-layer self-assembling copper tetrasulfonated phthalocyanine on carbon nanotube modified glassy carbon electrode for electro-oxidation of 2-mercaptoethanol. Thin Solid Films 526:256–260
57. Shahrokhian S, Kamalzadeh Z, Saberi RS (2011) Glassy carbon electrode modified with a bilayer of multi-walled carbon nanotube and polypyrrole doped with new coccine: application to the sensitive electrochemical determination of Sumatriptan. Electrochim Acta 56:10032–10038
58. Zhang Z, Hu Y, Zhang H, Yao S (2010) Novel layer-by-layer assembly molecularly imprinted sol–gel sensor for selective recognition of clindamycin based on Au electrode decorated by multi-wall carbon nanotube. J Coll Interface Sci 344:158–164
59. Zheng Y, Fu L, Wang A, Cai W (2015) Electrochemical detection of quinoline yellow in soft drinks based on layer-by-layer fabricated multi-walled carbon nanotube. Int J Electrochem Sci 10:3530–3538
60. Tang L, Zhu Y, Xu L, Yang X, Li C (2007) Amperometric glutamate biosensor based on self-assembling glutamate dehydrogenase and dendrimer-encapsulated platinum nanoparticles onto carbon nanotubes. Talanta 73:438–443
61. Du Y, Chend C, Li B, Zhou M, Wang E, Dong S (2010) Layer-by-layer electrochemical biosensor with aptamer-appended active polyelectrolyte multilayer for sensitive protein determination. Biosens Bioelectron 25:1902–1907
62. Lee D, Chander Y, Goyal SM, Cui T (2011) Carbon nanotube electric immunoassay for the detection of swine influenza virus H1N1. Biosens Bioelectron 26:3482–3487

63. Liu J, Qin Y, Li D, Wang T, Liu Y, Wang J, Wang E (2013) Highly sensitive and selective detection of cancer cell with a label-free electrochemical cytosensor. Biosens Bioelectron 41:436–441
64. Siqueira Jr JR, Abouzar MH, Bäcker M, Zucolotto V, Poghossian A, Oliveira ON, Schöning MJ (2009) Carbon nanotubes in nanostructured films: potential application as amperometric and potentiometric field-effect (bio-) chemical sensors. Phys Status Solidi A 206:462–467
65. Siqueira Jr JR, Gasparotto LHS, Oliveira Jr ON, Zucolotto V (2008) Processing of electroactive nanostructured films incorporating carbon nanotubes and phthalocyanines for sensing. J Phys Chem C 112:9050–9055
66. Siqueira Jr JR, Abouzar MH, Poghossian A, Zucolotto V, Oliveira Jr ON, Schöning MJ (2009) Penicillin biosensor based on a capacitive field-effect structure functionalized with a dendrimer/carbon nanotube multilayer. Biosens Bioelectron 25:497–501
67. Dong XY, Mi XN, Zhang L, Liang TM, Xu JJ, Chen HY (2012) DNAzyme-functionalized Pt nanoparticles/carbon nanotubes for amplified sandwich electrochemical DNA analysis. Biosens Bioelectron 38:337–341
68. Du M, Yang T, Zhang Y, Jiao K (2009) Sensitively electrochemical sensing for sequence-specific detection of phosphinothricin acetyltransferase gene: layer-by-layer films of poly-L-lysine and Au-carbon nanotube hybrid. Electroanalysis 21:2521–2526
69. Ziyatdinova G, Galandova J, Labuda J (2008) Impedimetric nanostructured disposable DNA-based biosensors for the detection of deep DNA damage and effect of antioxidants. Int J Electrochem Sci 3:223–235
70. Du M, Yang T, Jiao K (2010) Carbon nanotubes/(pLys/dsDNA) n layer-by-layer multilayer films for electrochemical studies of DNA damage. J Solid State Electrochem 14:2261–2266
71. Liu Y, Lan D, Wei W (2009) Layer-by-layer assembled DNA-functionalized single-walled carbon nanotube hybrids-modified electrodes for 2, 4, 6-trinitrotoluene detection. J Electroanal Chem 637:1–5
72. Jia LY, Gan N, Zheng L, Wang Q (2011) A novel amperometric immunosensor based on thionine/DNA self-assembled multilayers on carbon nanotubes modified glass carbon electrode. Mater Sci Eng Appl 160:1170–1175
73. Wang Y, Zhang S, Bai W, Zheng J (2016) Layer-by-layer assembly of copper nanoparticles and manganese dioxide-multiwalled carbon nanotubes film: a new nonenzymatic electrochemical sensor for glucose. Talanta 149:211–216
74. Primo EN, Gutierrez FA, Rubianes MD, Rivas GA (2015) Bamboo-like multiwalled carbon nanotubes dispersed in double stranded calf-thymus DNA as a new analytical platform for building layer-by-layer based biosensors. Electrochim Acta 182:391–397
75. Ma M, Miao Z, Zhang D, Du X, Zhang Y, Zhang C, Lin J, Chen Q (2015) Highly-ordered perpendicularly immobilized FWCNTs on the thionine monolayer-modified electrode for hydrogen peroxide and glucose sensors. Biosens Bioelectron 64:477–484
76. Yu Y, Chen Z, He S, Zhang B, Li X, Yaho M (2014) Direct electron transfer of glucose oxidase and biosensing for glucose based on PDDA-capped gold nanoparticle modified graphene/multi-walled carbon nanotubes electrode. Biosens Bioelectron 52:147–152
77. Dalmasso PR, Pedano ML, Rivas GA (2013) Supramolecular architecture based on the self-assembling of multiwall carbon nanotubes dispersed in polyhistidine and glucose oxidase: characterization and analytical applications for glucose biosensing. Biosens Bioelectron 39:76–81
78. Wang Y, Wang X, Wu B, Zhao Z, Yin F, Li S, Qin X, Chen Q (2008) Dispersion of single-walled carbon nanotubes in poly (diallyldimethylammonium chloride) for preparation of a glucose biosensor. Sensors Actuators B Chem 130:809–815
79. Shirsat MD, Too CO, Wallace GG (2008) Amperometric glucose biosensor on layer by layer assembled carbon nanotube and polypyrrole multilayer film. Electroanalysis 20:150–156
80. Li W, Yuan R, Chai Y, Zhong H, Wang Y (2011) Study of the biosensor based on platinum nanoparticles supported on carbon nanotubes and sugar–lectin biospecific interactions for the determination of glucose. Electrochim Acta 56:4203–4208

81. Yan XB, Chen XJ, Tay BK, Khor KA (2007) Transparent and flexible glucose biosensor via layer-by-layer assembly of multi-wall carbon nanotubes and glucose oxidase. Electrochem Commun 9:1269–1275
82. Liu Y, Wu S, Ju H, Xu L (2007) Amperometric glucose biosensing of gold nanoparticles and carbon nanotube multilayer membranes. Electroanalysis 19:986–992
83. Xu L, Zhu Y, Tang L, Yang X, Li C (2007) Biosensor based on self-assembling glucose oxidase and dendrimer-encapsulated Pt nanoparticles on carbon nanotubes for glucose detection. Electroanalysis 19:717–722

Graphene-Based Biosensors and Their Applications in Biomedical and Environmental Monitoring

Rinky Sha, Sushmee Badhulika, and Ashok Mulchandani

Abstract Graphene, one atom thick sheet of sp^2 bonded carbon atoms, is being envisioned as the next generation carbon material for highly diversified sensing applications and nanoelectronics. Graphene and its derivative, graphene oxide have opened up new era in the development of next generation biosensors due to their exceptional electrical, chemical, mechanical, optical properties and biocompatibility which include large surface to volume ration, excellent electrical conductivity, high thermal conductivity etc. This chapter covers the properties, functionalization of graphene and graphene oxide and their applications in biosensors. In specific, we discuss recent advancements of graphene/graphene oxide-based biosensors in significant applications of biomedical and environmental monitoring, emphasizing the sensing performances which include sensitivity, specificity, stability, reproducibility, limit of detection, and their applicability in real samples. Underlying sensing mechanisms have been systematically discussed in order to get better insight into how graphene and graphene oxide contribute to the performance of each biosensor. Wherever applicable, limitations of existing methodologies and future perspective have also been outlined and discussed.

R. Sha and S. Badhulika (✉)
Department of Electrical Engineering, Indian Institute of Technology Hyderabad, Kandi 502285, Telangana, India
e-mail: sbadh@iith.ac.in

A. Mulchandani (✉)
Department of Chemical and Environmental Engineering, University of California, Riverside, CA 92521, USA

Materials Science and Engineering Program, University of California, Riverside, CA 92521, USA
e-mail: adani@engr.ucr.edu

M. J. Schöning, A. Poghossian (eds.), *Label-Free Biosensing: Advanced Materials, Devices and Applications*, Springer Series on Chemical Sensors and Biosensors (2018) 16: 261–290
DOI 10.1007/5346_2017_9, © Springer International Publishing AG 2017,
Published online: 11 July 2017

Keywords Biomedical, Biosensors, Environmental monitoring, Graphene, Graphene oxide

Contents

1 Introduction

Biosensing has prime importance in improving the quality of human life in terms of disease diagnosis and therapy, environmental safety, and security [1–4]. This has led researchers to focus on developing simple, cost-effective biosensors with high sensitivity, selectivity, lower detection limit, and long-term stability. A biosensor is an analytical device that quantitatively or semi-quantitatively converts the information about the presence of a chemical species (analyte) to a measurable signal. It consists of two major components: (a) receptor and (b) transducer. The receptor is a biomolecule, which recognizes the analyte, and the transducer converts this biorecognition event into an analytically useful signal such as current, potential, and impedance. Most common biorecognition elements used in biosensing include enzyme, antibody, or oligonucleotide [4, 5]. In literature, various materials such as metal and metal oxide semiconductors [6, 7] have been reported as a transducer element to meet the increasing demand of biosensors in numerous fields such as biomedical, environmental, clinical, and military.

Recent advancements in nanotechnology have attracted significant attention in the development of point-of-care diagnostic devices for healthcare and environmental monitoring. Carbon nanomaterials such as graphene or graphene oxide (GO) have gained wide attention as next generation electrode materials for biosensing applications due to their excellent properties [8, 9]. Graphene was isolated from high-density graphite for the first time using simple scotch-tape method in 2004 by *Geim and Novoselov* at the University of Manchester [10]. So far, several methods have been developed for the synthesis of graphene. Synthesis methods can be classified into two approaches: (a) top-down approach (from graphite) and (b) bottom-up approach (from carbon precursors). Top-down approaches include synthesis of graphene using mechanical and chemical exfoliation techniques whilst bottom-up approaches comprise of chemical vapor deposition (CVD) and epitaxial growth techniques [11, 12]. Most common technique

used for the synthesis of GO is Hummers method wherein graphite is oxidized to graphite oxide in the presence of oxidizing reagents, potassium permanganate ($KMnO_4$), sodium nitrate ($NaNO_3$), and concentrated sulfuric acid (H_2SO_4) [13, 14]. This oxidation process introduces oxygen containing functional groups (hydroxyl, epoxy, carbonyl, and carboxyl groups) on the basal planes and at the edges of graphite layers, which make graphite oxide hydrophilic. Since inter layer distance is increased, GO would be easily chemically exfoliated from graphite oxide in polar solvents, mainly in water under mild sonication [15].

Graphene, a single-atom thick two-dimensional sheet of sp^2 bonded carbon atoms arranged in a perfect hexagonal lattice, is a basic building block of other carbon allotropes in different dimensions such as 0-D Fullerene (wrapped-up graphene), 1-D carbon nanotube (rolled up graphene), and 3-D Graphite (stack of graphene sheets) [16]. Graphene has a large specific surface area (theoretically, 2,630 $m^2\ g^{-1}$), excellent carrier mobility (200,000 $cm^2\ V^{-1}\ s^{-1}$), low intrinsic noise, high thermal conductivity (5,000 $Wm^{-1}\ K^{-1}$), high Young's modulus (~1.1 TPa), and transmittance of nearly 97% [17, 18]. In the unit cell of graphene, the bonding–antibonding gap closes at the corners of the Brillouin zone or K-points, which results in linear π-band dispersion around the K-points. Due to linear dispersion of π-bands, electrons in graphene behave like massless charge carriers with higher Fermi velocity (only 300 times smaller than speed of light), which results in excellent conductivity (~10^8 S/m > copper (59.6×10^6 S/m) in graphene [19]).

Graphene is an ideal sensing material for the detection of biomolecules (such as nucleic acid) which have higher redox potential as it has wide electrochemical potential window (2.5 V in 0.1 mM phosphate buffered saline) [20]. One of the basic requirements for a typical electrochemical biosensor is good electrocatalytic ability of the electrode. This property basically improves the redox reaction. In this regard, heterogeneous electron transfer and superior electrocatalytic properties of graphene make it a promising candidate for electrochemical biosensors. For the above-mentioned properties, graphene is considered to be most promising material for electrochemical sensors [21]. Moreover, graphene is a zero band gap semiconductor and its band structure can be changed in three ways, which include (a) constraining large-area graphene in one dimension to form graphene nanoribbons, (b) biasing bilayer graphene, and (c) applying strain to graphene [22]. Graphene shows ambipolar electric field-effect behavior, which makes it sensitive to both electron-donating and electron-withdrawing molecules [4]. All above-mentioned physicochemical and electronic properties make graphene a promising candidate for the fabrication of highly sensitive biosensors for detection of wide variety of analytes.

However, graphene is a zero band gap semiconductor and hydrophobic in nature which limits its scope in real-time biosensing applications. In order to improve its properties and expand the scope of applications, a graphene derivative, graphene oxide (GO), has been utilized widely. GO is a graphene sheet decorated with oxygen containing functional groups (e.g., hydroxyl, epoxy, carbonyl, and carboxyl groups) on the both sides of basal plane and edges and obtained by oxidation of graphite using well-known Hummers method. The presence of these hydroxyl and

epoxy groups offers facile surface functionalization with desired biomolecules and excellent aqueous dispersibility [23]. Unlike graphene, in GO, band gap can be introduced owing to quantum-confinement and chemically, thermally, or electrochemically tuned by controlling size, composition, and relative fraction of sp^3 hybridized domains of GO [20]. Moreover, various other properties such as high surface area, low production cost, good colloidal stability, and biocompatibility [24] provide GO a powerful platform for biosensing applications.

This chapter covers the properties, functionalization of graphene and GO, and their applications in biosensors for healthcare and environmental monitoring. Underlying sensing mechanisms are systematically discussed to provide better insight into how graphene and GO attributed in each biosensor. Additionally, summary on recent advancement of graphene and GO in the field of biosensors is made, emphasizing the sensing performances which include sensitivity, specificity, stability, reproducibility, limit of detection, and their applications in real samples. Finally, wherever applicable, limitations of existing methodologies and future perspective have also been outlined.

2 Functionalization of Graphene and GO

The hydrophobic nature of pristine graphene limits its scope and applications in the field of sensors. In order to enhance its solubility and expand its scope as a sensing material in developing highly sensitive biosensors with better specificity, it is essential to functionalize graphene. Band gap can also be engineered into graphene by tuning, doping, intercalation, etc., making it suitable for fabrication of nano field-effect transistor (FET)-based biosensors [25]. Different strategies have been reported for graphene functionalization that can be classified into two main categories: (1) covalent functionalization and (2) non-covalent functionalization [26].

2.1 Covalent Functionalization

Covalent functionalization is the most common technique used for functionalization of graphene which includes two methods: (a) formation of covalent bonds between free radicals or dienophiles and C=C bonds of pristine graphene and (b) the formation of covalent bonds between organic functional groups and the oxygen containing functional groups of GO. In the work done by Sinitskii et al., diazonium salt was used to produce free radicals, which react with sp^2 hybridized carbon atoms of graphene, therefore forming covalent bonds [27].

The ratio between carbon atoms with sp^2 and sp^3 hybridization in the graphitic lattice is an indication of the degree of oxidation or covalent functionalization reaction. This ratio is calculated by using the formula, I_D/I_G; where I_D = the intensity of defect peak appeared around ~1,350 cm^{-1} in Raman spectrum which

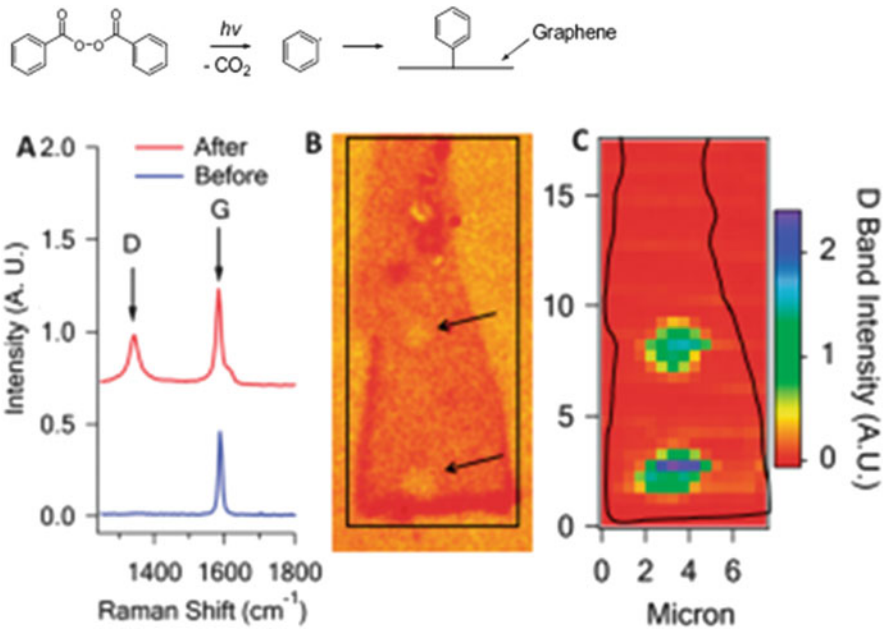

Fig. 1 Schematic illustration of free radicals addition to graphene; (**a**) Raman spectrum of graphene before and after covalent functionalization, (**b**) optical image of functionalized graphene, (**c**) intensity map of the D band for the boxed area shown in (**b**). The *black curve* shows the position of the graphene flake. Reprinted with permission from [28]

corresponds to carbon atoms with sp^3 hybridization and I_G = the intensity of graphitic peak occurred around ~1,580 cm^{-1} in Raman spectrum which corresponds to carbon atoms with sp^2 hybridization. Graphene is a two-dimensional sheet of sp^2 hybridized carbon atoms; as such, the coexistence of sp^3 carbon atoms is termed as lattice defects. As shown in Fig. 1, the I_D/I_G ratio increases with addition of free radicals to graphene sheet.

In addition to free radicals, dienophiles are also used to functionalize graphene by covalent method. In the work done by Georgakilas et al., graphene sheets were functionalized with dihydroxyl phenyl groups by pyrrolidine rings. The presence of hydroxyl group increases its dispersibility in organic solvents such as ethanol and *N*,*N* dimethylformamide (DMF). The increased value of the I_D/I_G ratio confirms the increase in the sp^3 carbon atoms [29]. He and Gao established a simple method for graphene functionalization with various functional groups and polymeric chains via nitrene cyclo-addition. The method is advantageous because the resultant functionalized graphene sheets are electrically conductive and show excellent dispersibility in solvents [30].

As discussed earlier, GO is a graphene sheet decorated with oxygen containing functional groups (e.g., hydroxyl, epoxy, carbonyl, and carboxyl groups) on both sides of basal plane and edges. GO can also be functionalized with functional groups by forming covalent bonds with oxygen atoms of GO. GO forms unstable

dispersion in water and organic solvents, like DMF/ethylene glycol, as exfoliated GO tend to aggregate and form larger particles of graphite oxide. For the stabilization of GO, various stabilizing groups such as large aromatic molecules [31], didodecyldimethyl-ammonium bromide [32], polystyrene [33], and elastomeric silicon foams [34] are added in the solution. However, the use of these stabilizing groups limits the use of graphene in technological applications [25]. Chromophores such as polythiophenes and oligothiophenes are also used to functionalize GO. In the work done by Liu et al., GO was functionalized with amine-terminated oligothiophenes through covalent amide bonds [35].

2.2 Non-covalent Functionalization

Although covalent functionalization methods have several advantages in terms of controllability over the degree of functionalization, better stability of the hybrid material, and reproducibility, they change the intrinsic electronic structure and physical properties of graphene by converting sp^2 carbon atoms to sp^3 carbon atoms, thus causing decrease in carrier mobility. In this regard, non-covalent functionalization by π interactions offers a simple and economic approach, which functionalizes graphene without disturbing its native electronic structure [20]. π-interactions are significant in context of nanomaterial synthesis and nanosensor fabrication as subtle changes in the electronic properties of π systems can lead to dramatic effects in structure and properties of the nano-system. Over the past two decades, extensive research has already been conducted to understand the nature of π-complexes, which include the nonpolar gas−π interaction, H–π interaction, π–π interaction, cation–π interaction, and anion–π interaction [36, 37]. Theoretical explanations based on "ab initio" calculations have been useful in proper understanding of the nature of π-interactions. The combined effect of attractive forces (e.g., electrostatic, van der Waals, dispersive, and inductive interactions) and repulsive forces (exchange repulsion) determines the strength of the π-interactions.

Non-covalent linkage between functional groups and graphene can be achieved through bi-functional linker molecules, e.g., in 1-pyrenebutanoic acid succinimidyl ester (PBASE). π-electron-rich pyrene group binds to graphene surface by strong π–π interaction whilst the succinimidyl ester group reacts with amine groups on biomolecule [26]. Since graphene is regarded as a larger aromatic molecule it can easily interact with any molecules with aromatic ring(s) on the surface. Therefore, various molecules can physically adsorb on the surface of graphene without the need of any coupling reagents. The negatively charged graphene derivative GO can easily be functionalized with positively charged molecules by electrostatic interaction. Metal nanoparticles (e.g., Au, Ag, Pt) are also used to functionalize graphene-based materials, like GO or reduced graphene oxide (rGO) by non-covalent method using various techniques such as in situ reduction and electrochemical deposition [20]. Figure 2 summarizes two important methods used for the functionalization of

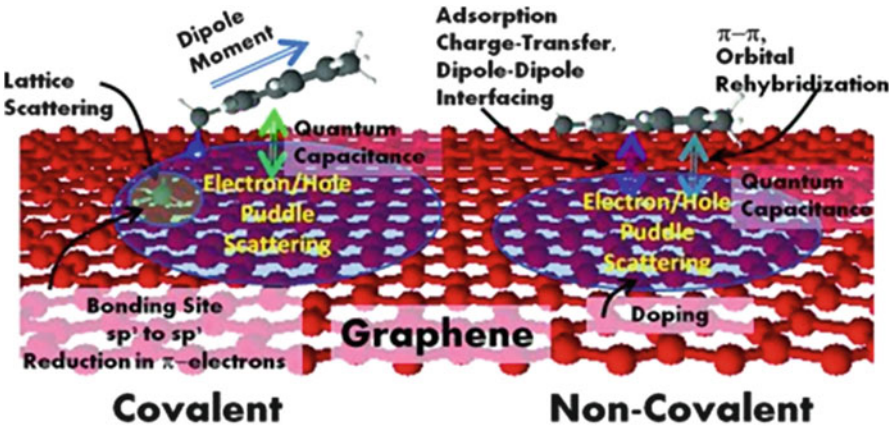

Fig. 2 Schematic diagram representing the effect of functionalization on the electrical properties such as charge density, doping, scattering, electron-hole puddle density, because of alteration in graphene's hybridization state (sp^2 to sp^3), graphene's quantum capacitance, dipole–dipole interaction, lattice defects, and charge transfer. Reprinted with permission from [38]

graphene and the effect of functionalization on the intrinsic electrical and physical properties of graphene.

3 Applications of Graphene and Graphene Oxide-Based Biosensors

3.1 Biomedical Applications

Biomolecules like proteins, DNA, cholesterol, etc. play a vital role in various disease developments; for example, high level of cholesterol in the bloodstream causes the risk of various diseases such as coronary heart disease, while DNA damage has been associated with Alzheimer's and cancer [39–41]. Therefore, early detection of biomolecules is of prime importance in disease diagnosis as well as therapy. Due to exceptional physicochemical properties such as larger specific surface area, faster electron transfer rate, and excellent carrier mobility, graphene-based materials have been used extensively as a sensing material in the fabrication of various biosensors [20].

3.1.1 Detection of Glucose

Continuous monitoring of glucose levels in blood is important for diagnosis and management of diabetes mellitus [42]. Detection of glucose can be realized by using glucose oxidase (GOx) enzyme as a recognition element. Unnikrishnan et al.

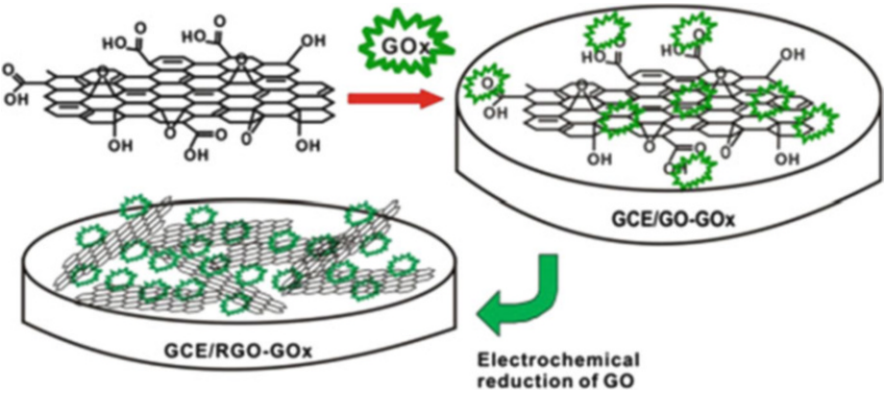

Fig. 3 Schematic illustration of immobilization of GOx to GO by single step followed by electrochemical reduction of GO to rGO. Reprinted with permission from [43]

demonstrated an rGO-based biosensor for electrochemical detection of glucose. The electrode was prepared by first immobilizing GOx to GO by a single step followed by electrochemical reduction of GO to rGO as shown in Fig. 3 [43]. The GO-GOx modified glassy carbon electrode (GCE) exhibited good stability, reproducibility, and selectivity with sensitivity of 1.85 μA mM^{-1} cm^{-2} in the concentration range of 0.1–27 mM. Liang et al. developed the electrochemically reduced carboxyl graphene (ERCGr) modified glucose biosensor where GOx was immobilized on the ERCGr modified electrode through self-assembly technique [44]. The sensor showed sensitivity of 7 μA mM^{-1} cm^{-2} in the concentration range of 2–18 mM and limit of detection of 0.02 mM with good selectivity and stability. In both cases, the electrochemical detection of glucose was achieved by observing the decrease of cathodic current of GOx flavin adenine dinucleotide (FAD) reduction to $FADH_2$ (hydroquinone form of FAD) resulting from oxidation of glucose at the surface of the biosensor. Although these biosensors showed higher sensitivity, sensors were not used to detect glucose in blood samples to confirm their applicability in practical applications.

Qian et al. reported a three-dimensional porous graphene–chitosan composite-based biosensor for glucose detection using ferrocenecarboxylic acid (FMCA) as a mediator [45]. Glucose was detected through its oxidation in the presence of FMCA at the biosensor surface. Figure 4 shows the calibration curve of the GOx–graphene–chitosan modified biosensor at 0.40 V in nitrogen-saturated 0.1M PBS (phosphate buffered solution; pH 7.0) containing 5 mM FMCA under stirred condition, where the inset exhibits the amperometric response of biosensor towards successive addition of glucose. This glucose biosensor exhibited linear relationship in the concentration range from 0.14 to 7.0 mM ($R^2 = 0.995$) with sensitivity of 11.2 μA mM^{-1} cm^{-2} and lower limit of detection of 17.5 μM.

Liu et al. fabricated biocompatible GO-based glucose biosensors [46]. GOx was immobilized on the surface of a GO modified electrode via covalent interaction. Glucose was detected by measuring the current resulting from the oxidation of

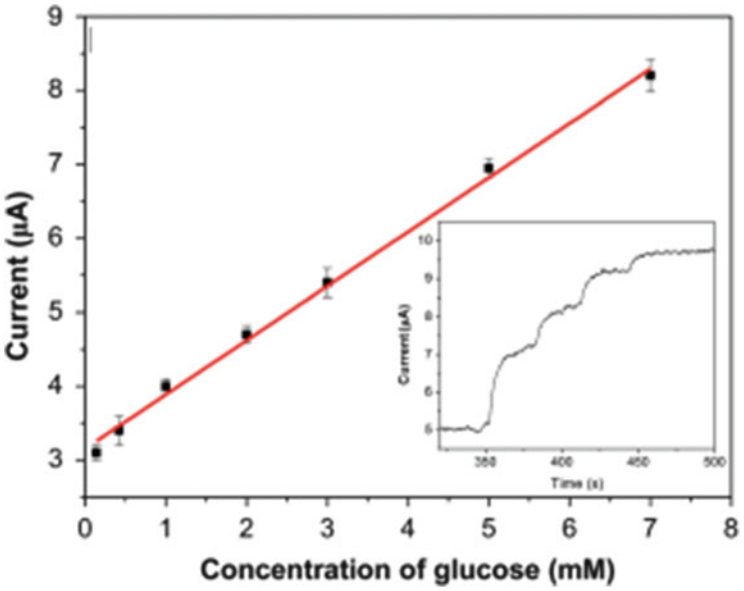

Fig. 4 Calibration curve of GOx–graphene–chitosan modified biosensor at 0.40 V in nitrogen-saturated 0.1M PBS (pH 7.0) containing 5 mM FMCA under stirred condition; *inset*: amperometric response of biosensor towards successive addition of glucose. Reprinted with permission from [45]

hydrogen peroxide (generated from the oxidation of glucose during the enzyme reaction). The glucose biosensor exhibited high sensitivity of 8 mA M^{-1} cm^{-2} with good stability and reproducibility. In order to use the developed biosensor for real-time applications, biocompatibility of the as-synthesized GO with human cells was also studied.

3.1.2 Detection of Hydrogen Peroxide (H_2O_2)

Detection of H_2O_2 is of great significance as it acts as an essential mediator in food, medicine, industry, and environmental control. It is the most valuable marker for oxidative stress. The overproduction of H_2O_2 causes the progression of diseases such as Alzheimer's, alcoholic liver disease, and cancer [47]. Detections of H_2O_2 have been well demonstrated using the enzyme horseradish peroxidase (HRP) as a recognition element. Lu et al. demonstrated a single-layer graphene nanoplatelet (SLGnP)-aromatic molecule, tetrasodium 1,3,6,8-pyrenetetrasulfonic acid (TPA)–HRP composite film for the detection of H_2O_2 wherein nafion was used as a binder [48]. The electrochemical detection of H_2O_2 was achieved by directly measuring current arising from the reduction of H_2O_2 at the surface of the SLGnP-TPA-HRP composite modified electrode. The composite not only enhanced the direct electron transfer between the enzyme and the electrode surface but also exhibited faster

response time (<1 s), good stability, and lower limit of detection of 0.1 μM. Zhou et al. fabricated an Au-graphene–HRP–chitosan biocomposite-based biosensor for the detection of H_2O_2, wherein graphene was functionalized with sulfonate groups ($–SO_3^-$) to eliminate the restacking of graphene sheets to graphite [49]. The biopolymer chitosan (CS) was used for HRP immobilization while Au nanoparticles were electrodeposited on the surface of HRP immobilized sulfonated graphene (GS)/CS composite-based electrode to enhance the electrocatalytic properties of the biosensor towards H_2O_2. The linear range for the fabricated H_2O_2 sensor was found to be 5–5.3 mM with limit of detection of 1.7 μM. Figure 5a depicts the amperometric response of Au/GS/HRP/CS/GCE at potential −0.3 V towards successive addition of H_2O_2 in 0.1M PBS and inset of Fig. 5a shows amplification of part A, whilst Fig. 5b shows corresponding calibration plot.

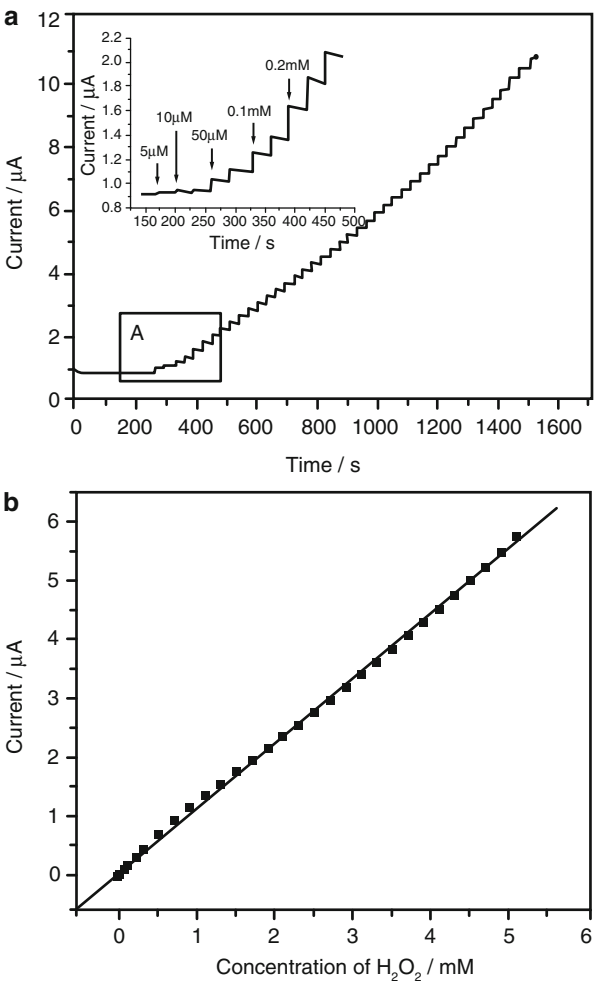

Fig. 5 (**a**) Amperometric response of Au/GS/HRP/CS/GCE at potential −0.3 V towards successive addition of H_2O_2 in 0.1M PBS; *inset*: amplification of part A; (**b**) corresponding calibration plot. Reprinted with permission from [49]

3.1.3 Detection of Cholesterol

Cholesterol is a type of lipid molecule and an important precursor of biological materials, such as bile acid, steroid hormones, and vitamin D. High levels of cholesterol in the bloodstream causes the risk of several diseases such as "coronary heart disease," diabetes mellitus, hypertension, and cerebral thrombosis. Thus, accurate and sensitive detection of cholesterol is of utmost importance in biomedical diagnostics [39, 40]. The detection of cholesterol can be achieved using the enzyme cholesterol oxidase (ChOx) immobilized onto graphene-based electrodes. Nandini et al. fabricated a one-dimensional gold nanostructure (AuNs)-thiol functionalized GO (GO-SH) composite-based biosensor for cholesterol sensing [50]. The enhanced electrochemical performance of GO-SH/AuNs composite-based cholesterol sensor in comparison to the pristine GO-SH-based sensor indicated the synergistic effect of both GO-SH and AuNs. Figure 6a shows a schematic presentation of the fabrication steps of the cholesterol biosensor. Figure 6b exhibits amperometric response of the Gr (graphite electrode)/GO-SH/AuNs/ChOx at potential −0.45 V towards successive addition of cholesterol in 0.1M PBS and inset of Fig. 6b displays the corresponding calibration plot. Detection of cholesterol was achieved by measuring current arising from the reduction of cholesterol to cholesteone at the surface of biosensor. The sensor exhibited lower limit of detection of 0.2 nM, sensitivity of 273 mA mM^{-1} cm^{-2} in the concentration range of 0.05–11.45 mM with superior repeatability, reproducibility, and stability. Cholesterol sensor was also used in serum sample to detect cholesterol and satisfactory results suggested its utility in practical applications. Dey et al. developed a graphene/platinum nanoparticles hybrid-based biosensor for cholesterol detection [51]. The biosensor showed limit of detection of 0.2 μM with sensitivity of 2.07 ± 0.1 μA μM^{-1} cm^{-2}.

3.1.4 Detection of Urea

Urea is a common organic compound and one of the final products of protein metabolism. Urea determination is important in biomedical field as its early detection helps to prevent various kidney and liver diseases [52]. Detection of urea can be realized by using urease enzyme as a biorecognition element. Srivastava et al. reported a multilayer graphene (MLG)-based biosensor for urea detection where MLG was synthesized by unzipping of multi-walled carbon nanotubes [53]. Urease and glutamate dehydrogenase (GLDH) were covalently attached with functionalized MLG. Detection of urea was achieved by measuring the peak current arising from the oxidation of ammonium ions (generated form hydrolysis of urea by urease in buffer solution) in the presence of nicotinamide adenine dinucleotide (NADH) by GLDH. Figure 7a exhibits cyclic voltammograms of the functionalized MLG-based biosensor towards successive addition of urea in the presence of 30 μL of NADH in PBS, whilst Fig. 7b presents the corresponding calibration

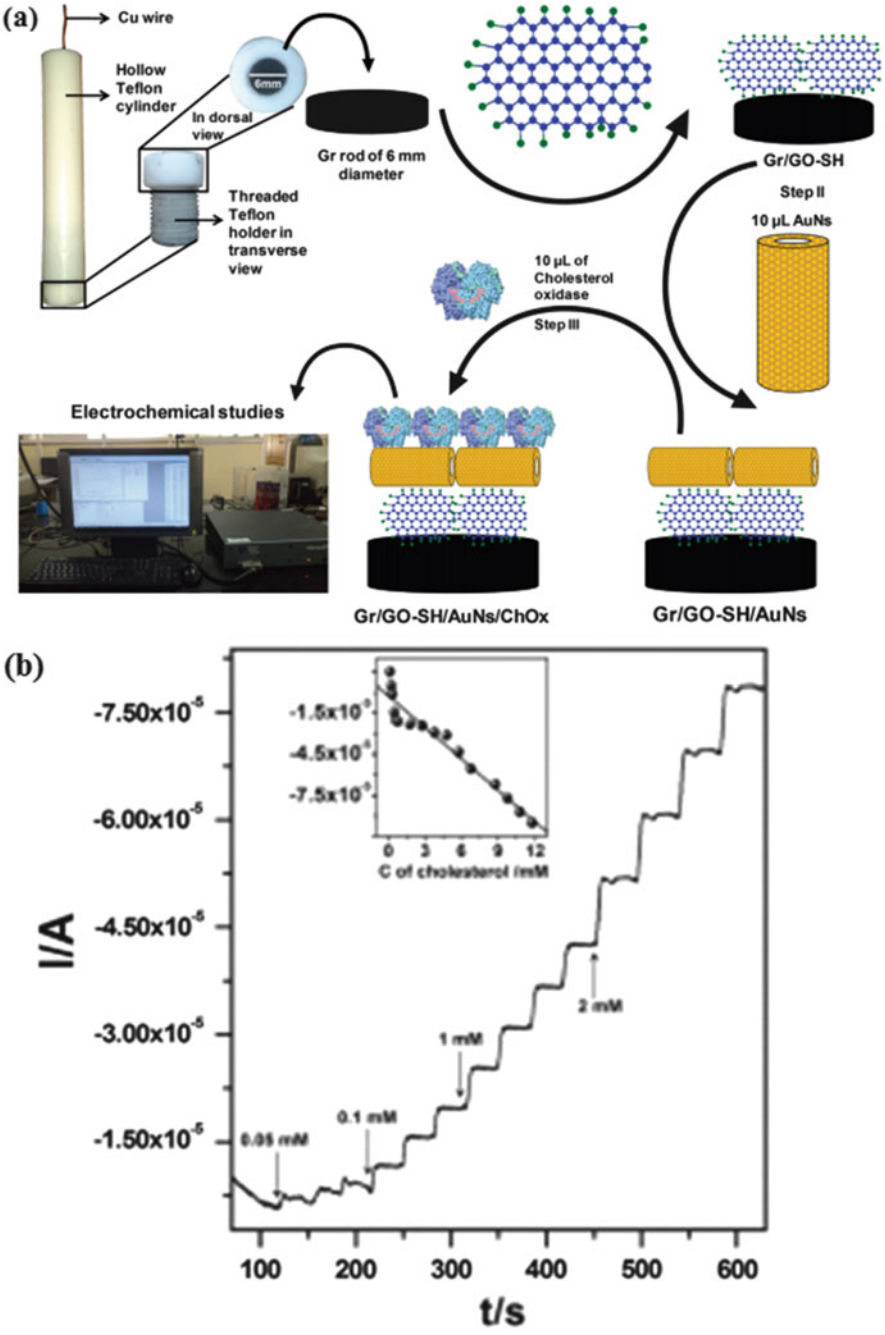

Fig. 6 (**a**) Schematic presentation of the fabrication steps of the cholesterol biosensor; (**b**) amperometric response of Gr/GO-SH/AuNs/ChOx at potential −0.45 V towards successive addition of cholesterol in 0.1M PBS; *inset*: corresponding calibration plot. Reprinted with permission from [50]

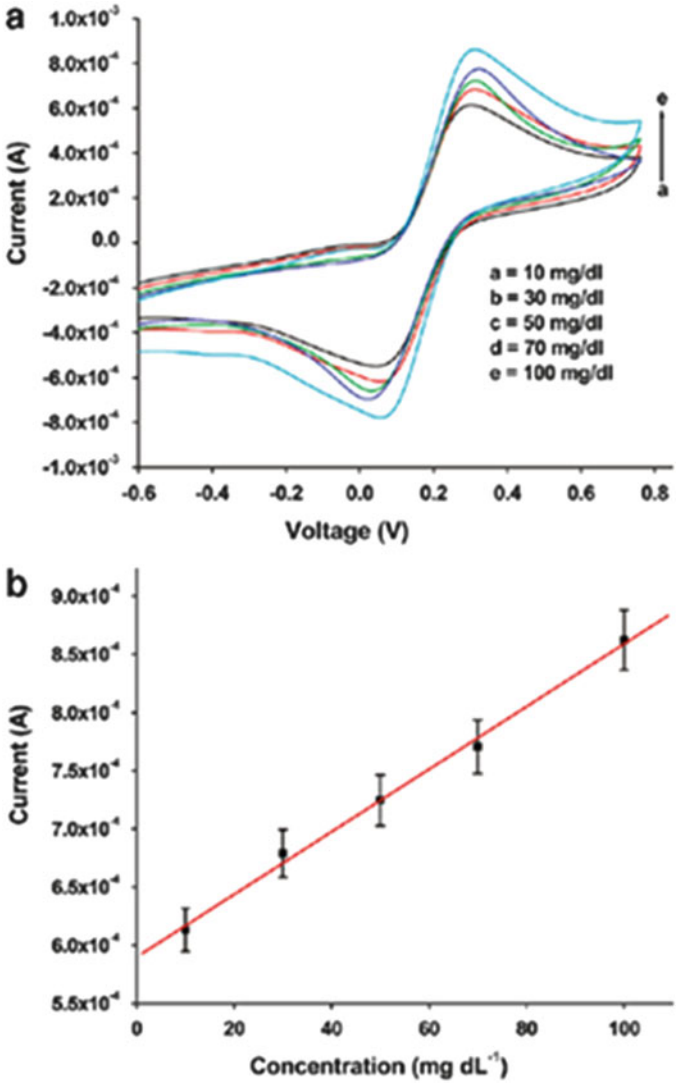

Fig. 7 (**a**) Cyclic voltammograms of functionalized MLG-based biosensor towards successive addition of urea in the presence of 30 μL of NADH in PBS; (**b**) corresponding calibration curve. Reprinted with permission from [53]

curve. The biosensor exhibited a sensitivity of 5.43 μA mg^{-1} dL cm^{-2}, lower detection limit of 3.9 mg/dL, and response time of 10 s in the concentration range of 10–100 mg/dL. Kumar et al. demonstrated a GnPs biosensor for the determination of urea wherein urease was covalently attached with edge functionalized GnP to enhance the overall sensitivity [54]. Urea was detected directly by measuring current at the potential 0 V resulting from ammonium ions adhered on the surface of

the GnPs s modified electrode. Linear range of detection was found to be in the range of 0.1–0.8 mg/mL with response time of 15 s and higher sensitivity of 33 μA $(mg/mL)^{-1}$.

3.1.5 Detection of DNA

Detection of DNA has attracted significant attention in the field of biomedicine and genetics. Determination of single stranded DNA (ss-DNA) is important for sequence-specific recognition and mutation [55], whilst detection of double stranded DNA (ds-DNA) is significant for visualization of the genomic information in living cells [56]. Zhou et al. demonstrated a chemically rGO (c-rGO)-based biosensor for the detection of four bases of DNA (guanine (G), adenine (A), thymine (T), and cytosine (C)), ss-DNA, and ds-DNA using differential-pulse-voltammetry (DVP) at physiological pH without a pre-hydrolysis step [57]. The enhanced electrocatalytic activity of the c-rGO-based biosensor towards the oxidation of A,T,C,G compared to the graphite-based biosensor (Fig. 8) could be ascribed to high density of edge-plane-like defective sites on c-rGO. These defective sites provide many active sites and thus, facilitating rapid electron transfer between the biosensor and target analytes.

Determination of sex in forensic science or genotyping is performed by monitoring the amelogenin gene (AMEL), one of the major matrix protein secreted by tooth enamel. AMEL genes are located in the X- and Y-chromosomes in humans and thus females have two identical AMEL genes (XX) while males having two non-identical (XY) genes. Benvidi et al. reported a label-free biosensor for the sensitive and selective detection of AMEL gene using an rGO modified glassy carbon electrode to monitor hybridization of target and probe DNA by electrochemical impedance spectroscopy. The biosensor was able to detect as low as 3.2×10^{-21} M with a linear range from 1×10^{-20} to 1×10^{-14} M [58].

3.1.6 Detection of Protein Biomarkers for Disease Diagnosis and Therapy

Immunosensors, an important class of biosensors, have been widely used to detect protein biomarkers, like alpha fetoprotein (AFP), prostate specific antigen (PSA), heat shock protein 70 (HSP70), etc., based on antigen–antibody interaction with high sensitivity and especially excellent specificity [59–61]. Conventional immunosensors use complex label processing steps which are expensive, require time-consuming separations, thereby being unable to meet ever-increasing clinical demands for the rapid detection of biomarkers. To overcome this issue, several novel label-free detection techniques have been reported in literature. For example, Li et al. fabricated an N-doped graphene-based immunosensor for label-free detection of the breast cancer biomarker CA 15-3, wherein the amino group of Anti-CA 15-3 antibody was covalently attached with the carboxylic groups of graphene

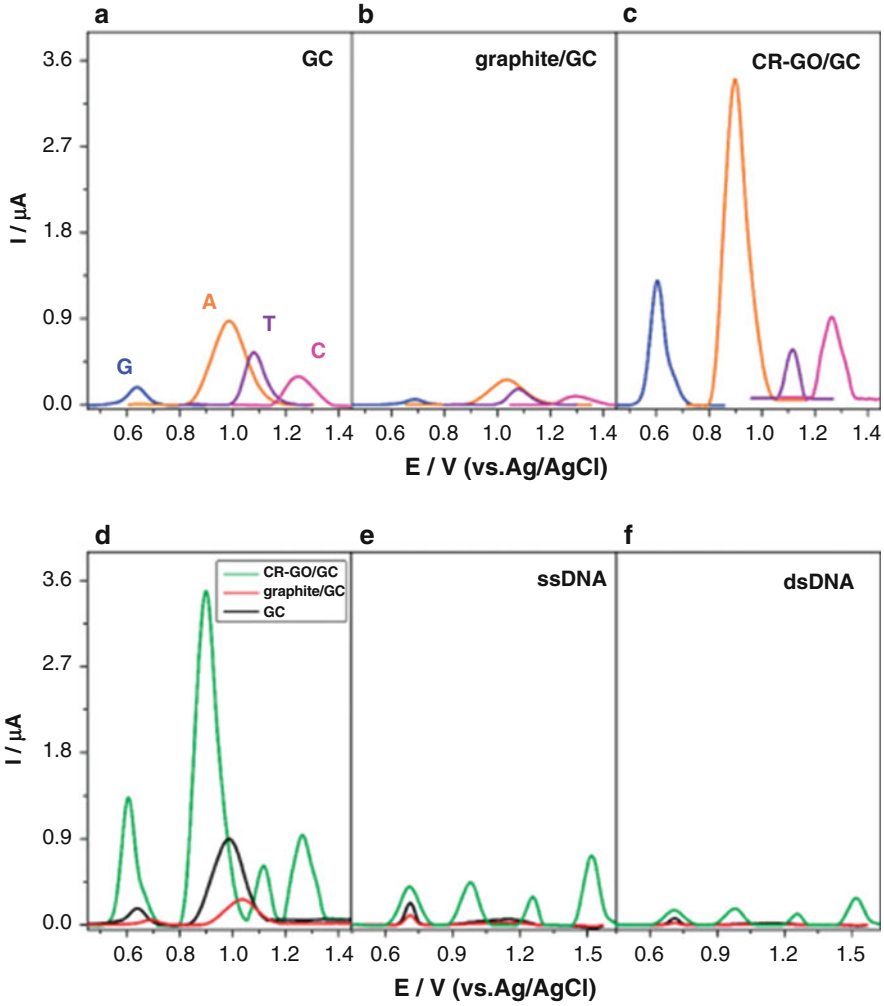

Fig. 8 (**a**) Differential pulse voltammograms (DPVs) at the GCE for G (*blue*), A (*orange*), T (*violet*), and C (*magenta*), respectively. (**b**) DPVs at the graphite/GCE for G (*blue*), A (*orange*), T (*violet*), and C (*magenta*), respectively. (**c**) DPVs at the CR-GO/GCE for G (*blue*), A (*orange*), T (*violet*), and C (*magenta*), respectively. (**d**) DPVs for a mixture of G, A, T, and C at CR-GO/GC (*green*), graphite/GCE (*red*), and GCE (*black*). (**e**) DPVs for ss-DNA at CR-GO/GCE (*green*), graphite/GC (*red*), and GCE (*black*). (**f**) DPVs for ds-DNA at CR-GO/GCE (*green*), graphite/GCE (*red*), and GCE (*black*). Concentrations used for different species (**a**–**f**) G, A, T, C, ss-DNA and ds-DNA: 10 µg/mL in 0.1M pH 7.0 PBS. Reprinted with permission from [57]

surface [62]. The biosensor showed lower limit of detection of 0.012 U/mL in the concentration range of 0.1–20 U/mL with good selectivity, reproducibility, and stability. To check the applicability of biosensor in real samples, it was also used to detect CA 15-3 in serum samples. Singal et al. presented a graphene-Pt

nanoparticles (Pt NP) composite-based impedimetric immunosensor for label-free detection of human cardiac troponin I, cTnI [63]. Monolayer graphene, synthesized using chemical vapor deposition, was decorated with Pt NP through –SH groups of mercaptopropionic acid (MPA) that was covalently attached to the amine groups of interlinker 1-pyrenemethylamine attached to graphene through π–π bonds between graphene and pyrene. Monoclonal antibodies against cTnI were immobilized on Pt NPs through amide bond between the $–NH_2$ groups of anti-cTnI and –COOH groups of MPA. The immunosensor exhibited a linear response to cTnI over the concentration range of 0.01–10 ng/mL with a sensitivity of 80 Ω cm^2 per decade and a limit of detection of 4.2 pg/mL of cTnI. Özcan et al. demonstrated a GO-based immunosensor for label-free determination of tumor marker HSP70 using electrochemical impedance spectroscopy wherein AntiHSP70 was immobilized onto GO surface using covalent bond [64]. Detection was achieved by measuring the charge transfer resistance (R_{ct}) of the electrode where with the increased concentrations of HSP70, R_{ct} increased linearly in the concentration range of 12–144 fg/mL. The biosensor exhibited a limit of detection of 0.765 fg/mL. Furthermore, the developed biosensor was applied to detect HSP70 in human serum sample and these results were compared with the concentrations obtained from the commercial enzyme-linked immunosorbent assay (ELISA) techniques. The insignificant variation in the concentration obtained from those two methods ensured the reliability of the biosensor in practical applications. Liu et al. reported a ferrocene functionalized GO-AuNPs composite-based immunosensor for label-free detection of cTnI using square wave voltammetry (SWV) as shown in Fig. 9 [65]. In Fig. 9b, the relative current corresponds to the changes in current with the concentration of cTnI. The biosensor showed excellent stability, selectivity, reproducibility, and lower detection limit of 0.05 ng/mL in the concentration range of cTnI from 0.05 to 3 ng/mL.

Graphene and GO-based biosensors have been used extensively for the detection of other important biomolecules like dopamine, ascorbic acid, uric acid, other saccharides (e.g., fructose, sucrose, and maltose), hemoproteins, cyclin A_2, etc. [66]. Describing each of them is beyond the scope of this chapter.

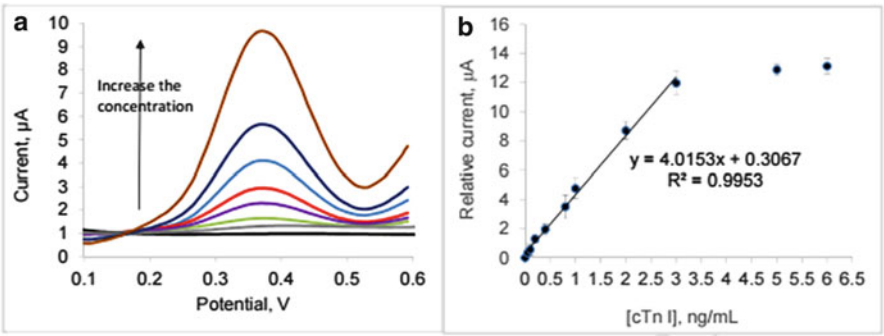

Fig. 9 (**a**) Square wave voltammograms of ferrocene functionalized GO-AuNPs composite-based biosensor towards successive addition of cTnI; (**b**) corresponding calibration curve of immunosensor. Reprinted with permission from [65]

3.2 *Environmental Monitoring Applications*

With the rapid industrialization and globalization, environmental pollutions are becoming increasingly serious. Large quantities of chemicals used in industry, agriculture, and daily life are discharged into the environment. A large number of these chemicals are toxic, carcinogenic, and long-existed in the environment and easily entered into the food chain, which have threatened heavily the environment and human health. In order to protect the ecological environment and human health, it is important to develop simple, highly sensitive, cost-effective sensors for constant monitoring and determination of the environmental pollutants. Most common techniques used for detection of pollutants include liquid and gas chromatography, capillary electrophoresis, flow injection analysis, etc. In spite of their high sensitivity and selectivity, these techniques are expensive, require sophisticated instrumentation and time-consuming sample pretreatments, thereby being unsuitable for in situ and continuous measurements [67]. As a result, biosensors, a class of chemical sensors, have attracted wide attention for detection of pollutants owing to their high sensitivity, low cost, portability, faster response, and ability to detect in in situ condition [4]. The properties of larger specific surface area, faster charge transfer, superior biocompatibility, and bio-stability pave the way for the easy fabrication and testing of graphene and its derivatives, like GO and rGO-based biosensors for constant monitoring and detection of environmental pollutants [68].

3.2.1 Detection of Heavy Metal Ions

Elements with atomic mass greater than 63.5 and specific gravity higher than 5 g cm^{-3} are categorized as heavy metals (e.g., lead (Pb), cadmium (Cd), and mercury (Hg)) [69]. Heavy metals are introduced into the environment from anthropogenic activities such as wastes of metallurgical industries (e.g., mining, automotive, battery, and electric cable manufacturing industries) [4, 9]. Accurate detection and quantification of these heavy metals are of prime importance due to their toxicity, environmental persistence, and carcinogenic effects in the skin, bones, lungs, liver, kidney, central nervous system, etc. [69].

Wen et al. demonstrated a graphene-based biosensor for detection of lead (Pb^{2+}) ions with high sensitivity, lower limit of detection limit ~0.02 nM and high selectivity, using a Pb^{2+} dependent DNAzyme as the recognition element [70]. This Pb^{2+}-dependent DNAzyme is a double stranded DNA comprising of an enzymatic strand and a thiolated substrate strand. Graphene was functionalized with gold nanoparticles to immobilize DNAzyme molecules by forming covalent bonds. Upon Pb^{2+} ions exposure, Pb^{2+} ions facilitated cleavage of the DNAzyme. As a result, the enzymatic strand and the un-thiolated portion of the substrate strand diffused away, leaving the thiolated fragment of the substrate strand on the AuNP. The detection of lead ions was achieved directly from the shifting of Dirac point to positive voltages at higher concentrations of Pb^{2+} ions as shown in Fig. 10.

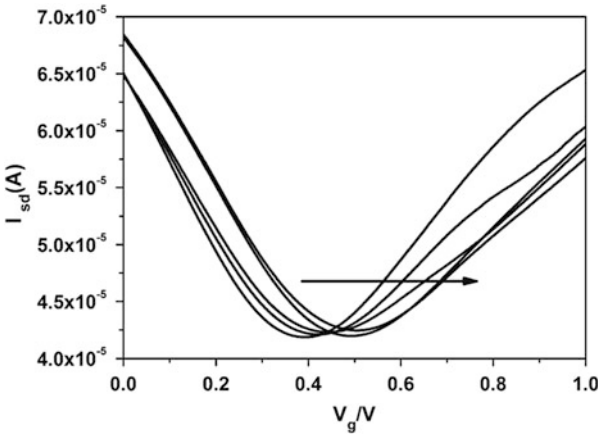

Fig. 10 Transfer characteristics of graphene-based biosensor reacted at different concentrations of Pb^{2+} ions (0, 0.1, 1, 10, and 100 nM). Reprinted with permission from [70]

Sudibya et al. reported micro-patterned rGO film-based biosensor for the detection of heavy metal ions, like Hg^{2+} and Cd^{2+} ions, wherein metallothionein type II protein (MT-II) was functionalized on the surface of rGO films via the pyrene linker to bind metal ions with high affinity [71]. Upon metal ions exposure, a significant conformational change of MT altered the interaction between the MT and rGO channel, which resulted in the conductance change in rGO-FET (field-effect transistor)-based biosensors. Figure 11a exhibits the real-time current response of the rGO-FET-based biosensor towards successive addition of Hg^{2+} ions where Fig. 11b, c shows the calibration curves with the normalized change in drain current ($\Delta I/I$) for varying concentrations of (B) Hg^{2+} and (C) Cd^{2+} ions at a drain voltage, $V_{ds} = 0.4$ V, and at different gate voltages, respectively. The biosensor showed a limit of detection for Hg^{2+} ions of $\sim$1 nM and for Cd^{2+} ions of 1 nM with good stability. The MT-II modified rGO-based biosensor was regenerated by washing with acidic buffer (100 mM glycine, pH 2.3) to remove the bound metal ions from MT-II. The biosensor was also subjected to detect metal ions in the lake water collected from Nanyang Lake.

Tan et al. described a chemiresistive aptasensor based on an electrochemically reduced graphene oxide channel functionalized with a mercuric ion selective ss-DNA aptamer for the detection of Hg^{2+} ions in water [72]. The biosensor was demonstrated to detect as low as 0.5 nM Hg^{2+} ions selectively in the presence of other metal ions without any effect of different matrices.

3.2.2 Detection of Pesticides

Pesticides are used widely in agricultural field to increase the crop production by combating pests and to control vector-borne diseases [73]. However, pesticides such as phenolic compounds (e.g., phenol, chlorinated phenols, and nonylphenol) and organophosphates (OPs) (e.g., carbaryl, carbofuran, and malathion) are considered as one of the most hazardous pollutants in the field of environmental

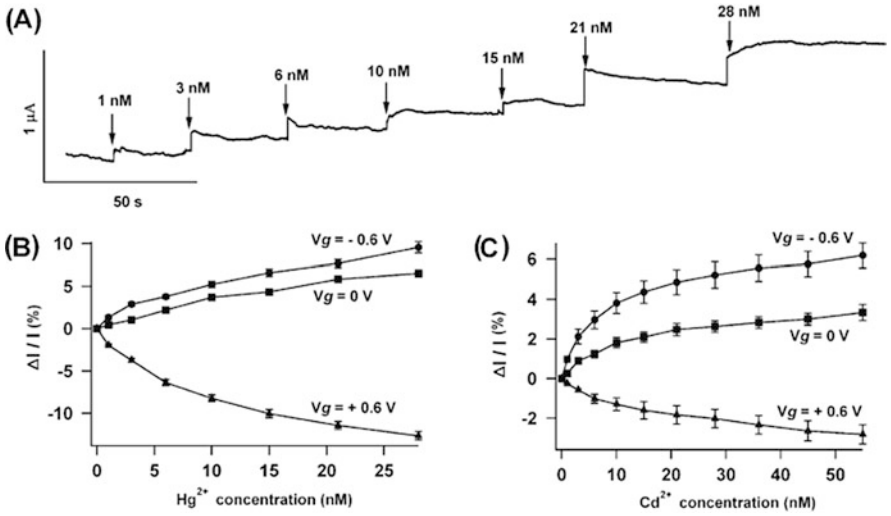

Fig. 11 (**a**) Real-time recording of drain current with the addition of Hg^{2+} ions; (**b**, **c**) calibration curves with the normalized change in drain current ($\Delta I/I$) for varying concentrations of (**b**) Hg^{2+} and (**c**) Cd^{2+} ions at a drain voltage, $V_{ds} = 0.4$ V, and at different gate voltages (0.6, 0 and −0.6 V). Reprinted with permission from [71]

research due to its toxicity, bioaccumulation, highly carcinogenic effects in aquatic organisms, and humans causing damage to lungs, kidney, central nervous system, and human tissues [67, 74, 75]. Therefore, the availability of highly sensitive biosensor for constant monitoring and on-site detection of pesticides in air, soil, and water is of utmost importance.

Zhang et al. developed a partially reduced GO-based biosensor for the determination of phenolic compounds (phenol and *p*-chlorophenol) using DPV [76]. HRP heme-containing protein was immobilized on the surface of the partially rGO modified electrode which oxidized phenolin presence of hydrogen peroxide (0.02 mM). Figure 12 shows DPV curves of the HRP/partially rGO-based biosensor in phosphate buffer recorded during successive addition of phenol. Two peak currents at −0.25 and at 0.27 V were observed in Fig. 12. The presence of peak at −0.25 V indicated the oxidation of phenol whilst another peak at 0.27 V was indexed as the reduction of *o*-quinone, the oxidation product of phenol by HRP. Both peaks were used for the detection of phenol as both peaks increased linearly with all concentrations of phenol. In terms of performance the biosensor exhibited a lower limit of detection (4.4 μM) and high sensitivity (61 μA mM^{-1}) in the phenol concentration range of 0.05–0.1 mM. Similarly, *p*-chlorophenol was detected at the surface of the HRP/partially reduced GO-based biosensor through its oxidation. The biosensor showed a linear response to *p*-chlorophenol at −0.2 V in the concentration range of 1 μM to 0.8 mM. Although the biosensor showed good reusability and stability, selectivity study and detection of phenolic compounds in

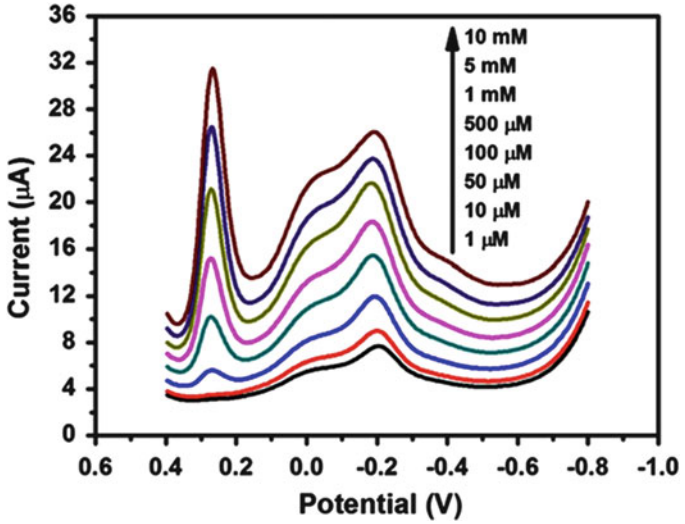

Fig. 12 DPV curves of HRP/partially reduced GO-based biosensor in phosphate buffer recorded during successive addition of phenol. Reprinted with permission from [76]

real samples were not performed to ensure its authenticity and reliability in practical applications.

Zeng et al. reported a graphene-DNA modified biosensor for the detection of nonylphenol (NP) using DPV [77]. The DNA molecule, an array of stacked π electrons, provides faster charge transport to analyte (here, nonylphenol) because of intercalative and electrostatic binding. To achieve enhanced sensitivity and lower limit of detection by combining the synergistic effect of both graphene and DNA, the composite graphene-DNA composite was synthesized and subsequently used for sensing of NP through its oxidation at the surface of this biosensor. The biosensor showed a linear response in the range of concentration from 5×10^{-8} to 4×10^{-6} mol/L with a high sensitivity of 21.99 μA μM^{-1} cm^{-2}, good selectivity and limit of detection of 10 nM. The developed biosensor was also applied to detect NP in water.

Acetylcholinesterase (AChE) is an important enzyme, which catalyzes the breakdown of neurotransmitters such as acetylcholine (ACh) and some other choline esters. The toxicity of OPs is based on inhibition of catalytic activity of AChE [75]. Sensing mechanism for the detection of OPs is based on the inhibition to AChE at the surface of the biosensor. Li et al. developed a porous-reduced GO (prGO)-based amperometric biosensor for the detection of OPs pesticides, wherein AChE was immobilized on prGO [78]. The hydrolysis of acetylthiocholine (ATCl) in PBS yielded thiocholine, which was oxidized by AChE at the surface of the prGO modified GCE. Therefore, the inhibition to AChE was observed by measuring the oxidation current of thiocholine. The sensing performance was optimized by varying the pH of the electrolytic solution and the amount of AChE. pH 7.4 and 5 μL AChE were chosen as the optimal pH value and enzyme amount. With the

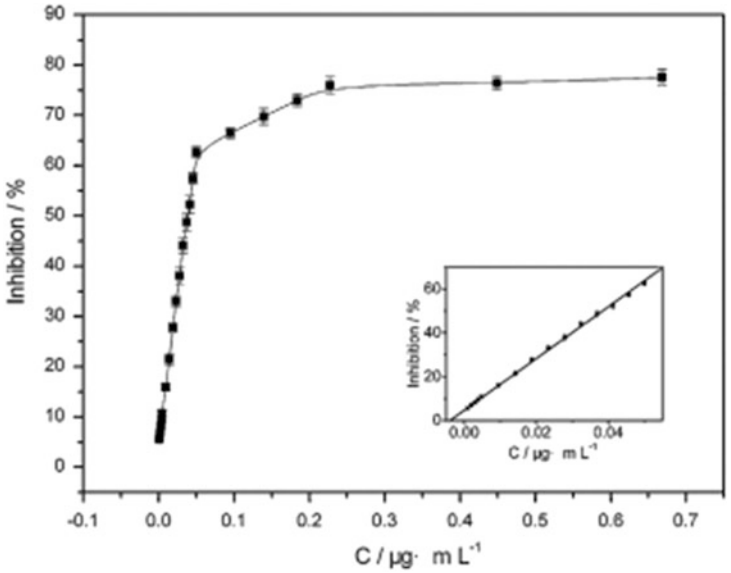

Fig. 13 Calibration plots with the change in inhibition in % for varying concentrations of carbaryl. Reprinted with permission from [78]

increasing concentration of ATCl, the amperometric response increased linearly in the range of 0.72–1.76 mM. The estimated lower value of Michaelis–Menten constant (K_M) of 0.73 mM confirmed excellent enzymatic activity and affinity of immobilized AChE towards ATCl. Furthermore, carbaryl, one type of OPs, was detected based on its inhibition on the immobilized AChE. As shown in Fig. 13, the % of inhibition of carbaryl increased linearly with the increasing concentration of carbaryl in the range from 0.001 to 0.05 μg/mL with good stability, high sensitivity of 1,181.2 ng^{-1} mL, and lower limit of detection of 0.5 ng/mL.

Wang et al. demonstrated self-assembling of AChE on an AuNPs-chemically reduced graphene oxide nanosheets (cr-Gs) hybrid for the detection of the OP paraoxon [79]. As shown in Fig. 14, cr-Gs and AuNPs were formed in situ from GO and chloroauric acid, respectively, in the presence of a water-soluble cationic polyelectrolyte (polydiallyldimethylammonium chloride) (PDDA). The AChE/AuNP/crGs-based biosensor showed excellent stability in the presence of PDDA linker with lower limit of detection of 0.1 pM.

3.2.3 Detection of Other Organic Molecules

Over the past two decades, the environmental pollutions caused by toxic, organic molecules such as explosives and pharmaceuticals have attracted wide attention in the scientific research community due to their adverse effects in humans. These organic molecules are detected by oxidation or reduction at the surface of the electrode.

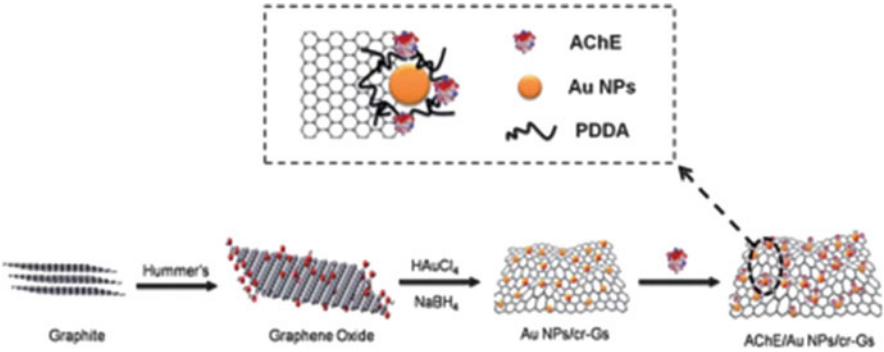

Fig. 14 Schematic illustration of AuNP/cr-Gs hybrid synthesis and AChE/AuNP/cr-Gsnano-assembly generation by using PDDA. Reprinted with permission from [79]

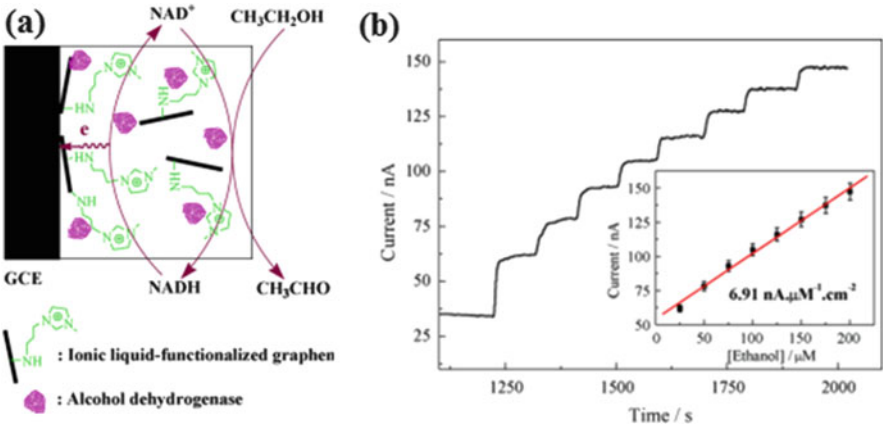

Fig. 15 (**a**) Schematic illustration of ethanol detection using an IL-graphene/chitosan/ADH-based biosensor; (**b**) amperometric response of IL-graphene/chitosan/ADH-based biosensor in 5 mg/mL NAD^+ PBS (0.05M, pH 7.4) towards successive addition of ethanol at a potential of 0.45 V; *inset*: corresponding calibration curve. Reprinted with permission from [82]

Ethanol is a common toxic, flammable, volatile organic compound. Long-time exposure to ethanol can cause several diseases such as central nervous system disorders, allergies, acidosis, pneumonectasis, and even cancer [80, 81]. Therefore, on-site monitoring and detection of liquid ethanol are of great importance. Shan et al. reported on an ionic liquid (IL)-functionalized graphene-chitosan composite as a sensing platform for the detection of ethanol [82]. Graphene was functionalized with IL through an epoxide ring-opening reaction between GO and 1-(3-aminopropyl)-3-methylimidazolium bromide (IL-NH_2) and then, IL-graphene was mixed with chitosan aqueous solution to form an IL-functionalized graphene-chitosan composite. The ethanol detection scheme is presented in Fig. 15a, wherein the enzyme alcohol dehydrogenase (ADH) encapsulated into the IL-functionalized graphene-chitosan

composite film enhanced the electrocatalytic oxidation of ethanol in the presence of NAD. As shown in Fig. 15b, ethanol was detected by measuring the current resulting from oxidation of ethanol at the surface of the biosensor to acetaldehyde with good stability, high sensitivity of 6.91 nA μM^{-1} cm^{-2}, and limit of detection of 5 μM in the range of concentration of 25–200 μM. The biosensor was also subjected to detect ethanol in beer and wine to ensure its applicability for real-time applications.

Trinitrotoluene (TNT) is one of the most commonly used explosives. Owing to its detrimental effects on the environment and human, on-site monitoring and accurate detection of TNT are of prime importance. Guo et al. reported an IL-graphene-based biosensor for the determination of TNT using adsorptive stripping voltammetry (ASV) [83]. The detection was achieved through the reduction of TNT at the surface of the IL-graphene-based biosensor. The IL-graphene sensor exhibited high sensitivity of 351.1 μA mg^{-1} L with a limit of detection of 4 ppb. The biosensor showed satisfactory results while it was also applied in ground water, tap water, and lake water samples to detect TNT. Table 1 summarizes graphene/graphene oxide-based biosensors in the applications of biomedical and environmental monitoring emphasizing their sensing performances such as sensitivity, linear range of detection, and limit of detection (LoD). Biosensors based on graphene and its derivative have been used extensively to detect other environmental pollutants (such as hydroquinone [84], catechol [85], and methyl jasmonate [86]). Describing each of them is, however, beyond the scope of this chapter.

4 Conclusion and Outlook

Graphene shows outstanding electronic, mechanical, thermal, chemical, and optical properties, which pave the way for extensive applications in the field of biomedical and environmental safety and security. To meet the ever growing demands of graphene as a sensing material, its derivative GO is also becoming a promising and alternative sensing platform with its attractive properties, like larger surface area, biocompatibility, ease of chemical modification, water dispersibility, etc. Here, we have discussed different recognition schemes of graphene/GO-based biosensors for the detection of different biomolecules, like protein biomarkers, cholesterol, glucose, urea, etc. and environmental pollutants such as pesticides and heavy metal ions. Although all these biosensors exhibit excellent performances in terms of sensitivity, specificity, stability, reproducibility, and limit of detection, most of these advances are proof-of-concept demonstrations only and limited within lab-based research activities. A lot of critical issues and challenges still need to be addressed. Firstly, the overall performances of graphene/GO-based biosensors depend on the degree of oxidation, surface morphology, defects and number of layers of graphene-based materials. For example, as compared to multilayered graphene, single layer graphene exhibits higher specific surface area, which offers more active sites for surface functionalization or enzyme immobilization, thereby ensuring repeatability in the performance of biosensors.

Table 1 List of graphene/graphene oxide-based biosensors in the field of biomedical and environmental monitoring

	Electrode	Analyte	Technique	Analytical characteristics	Reference
Biomedical applications	1. rGO-GOx/GCE	Glucose	Amperometry	Sensitivity: 1.85 μA mM^{-1} cm^{-2}; linear range: 0.1–27 mM	[43]
	2. ERCGr-GOx/GCE	Glucose	Cyclic voltammetry	Sensitivity: 7 μA mM^{-1} cm^{-2}; linear range: 2–18 mM; LoD: 0.02 mM	[44]
	3. Three-dimensional porous graphene–chitosan/GCE	Glucose	Amperometry	Sensitivity: 11.2 μA mM^{-1} cm^{-2}; linear range: 0.14–7.0 mM; LoD: 17.5 μM	[45]
	4. GO-GOx/Pt[a]	Glucose	Amperometry	Sensitivity: 8 mA M^{-1} cm^{-2}	[46]
	5. SLGnP-TPA-HRPcomposite film/GCE	H_2O_2	Amperometry	LoD: 0.1 μM	[48]
	6. Au-GS-HRP-CS/GCE	H_2O_2	Amperometry	Linear range: 5–5.3 mM; LoD: 1.7 μM	[49]
	7. GO-SH-AuNP-ChOx/Gr	Cholesterol	Amperometry	Sensitivity: 273 mA mM^{-1} cm^{-2}; linear range: 0.05–11.45 mM; LoD: 0.2 nM	[50]
	8. Graphene-Pt NPs /GCE	Cholesterol	Amperometry	Sensitivity: 2.07 ± 0.1 μA μM^{-1} cm^{-2}; LoD: 0.2 μM	[51]
	9. MLG-urease-GLDH/ITO[a]	Urea	Cyclic voltammetry	Sensitivity: 5.43 μA mg^{-1} dL cm^{-2}; linear range: 10–100 mg/dL; LoD: 3.9 mg/dL	[53]
	10. GnPs-urease/SPE[a]	Urea	Current-voltage (I-V) characteristics	Sensitivity: 33 μA $(mg/mL)^{-1}$; linear range: 0.1–0.8 mg/mL	[54]
	11. c-rGO/GCE	Four bases of DNA (A,T,C,G), ss-DNA and ds-DNA	DPV	–	[57]
	12. rGO/GCE	AMEL	EIS[a]	Linear range: 1×10^{-20} to 1×10^{-14} M; LoD: 3.2×10^{-21} M	[58]
	13. N-doped graphene-anti-CA 15-3 antibody/GCE	CA 15-3	DPV	Linear range: 0.1–20 U/mL; LoD: 0.012 U/mL	[62]

	14. Graphene-Pt NPs/GCE	cTnI	EIS[a]	Sensitivity: 80 Ω cm^2/decade; linear range: 0.01–10 ng/mL; LoD: 4.2 pg/mL	[63]
	15. GO-anti HSP70/GCE	HSP70	EIS[a]	Linear range: 12–144 fg/mL; LoD: 0.765 fg/mL	[64]
	16. Ferrocene functionalized GO-AuNPs/GCE	cTnI	Square wave voltammetry	Linear range: 0.05–3 ng/mL; LoD: 0.05 ng/mL	[65]
Environmental monitoring	1. Graphene-DNAzyme-based FET sensor	Pb^{2+}	Current-voltage (I-V) characteristics	LoD: ~0.02 nM	[70]
	2. rGO-based FET sensor	Hg^{2+} and Cd^{2+}	Potentiometry	LoD for Hg^{2+} ions: ~1 nM and LoD for Cd^{2+} ions: 1 nM	[71]
	3. rGO-based chemiresistive sensor	Hg^{2+}	Potentiometry	LoD: 0.5 nM	[72]
	4. Partially rGO-HRP/GCE	Phenol	DPV	Sensitivity: 61 μA/mM; linear range: 0.05–0.1 mM; LoD: 4.4 μM	[76]
	5. Graphene-DNA/GCE	Nonyl-phenol	DPV	Sensitivity: 21.99 μA μM^{-1} cm^{-2}; linear range: 5×10^{-8} to 4×10^{-6} mol/L; LoD: 10 nM	[77]
	6. prGO-AChE/GCE	OPs	Amperometry	Sensitivity: 1,181.20 ng^{-1} mL; linear range: 0.001–0.05 μg/mL LoD: 0.5 ng/mL	[78]
	7. AuNPscr-Gs-AChE/GCE	Paraoxon	Amperometry	LoD: 0.1 pM	[79]
	8. IL–graphene–chitosan/GCE	Ethanol	Amperometry	Sensitivity: 6.91 nA μM^{-1} cm^{-2}; linear range: 25–200 μM; LoD: 5 μM	[82]
	9. IL–graphene/GCE	TNT	Adsorptive stripping voltammetry	Sensitivity: 351.1 μA mg^{-1} L; LoD: 4 ppb	[83]

[a]*EIS* electrochemical impedance spectroscopy, *Pt* platinum, *ITO* indium tin oxide, *SPE* screen-printed electrode

Secondly, nitrogen doping is also an efficient strategy to improve the surface and electronic properties of pristine graphene. Nitrogen doping in single layered graphene induces a shift in Fermi level, thus lowering the density of states near the Fermi level. One of the reasons why realization of graphene-based devices has been challenging is because of its lack of a band gap. But suppression of the density of states opens up the band gap between conduction and valence band in nitrogen doped graphene, thereby improving the performances of graphene-based sensing devices. Nonetheless, the mass production of CVD grown single layered graphene still remains a major challenge because of its high costs. Hence, a dedicated research efforts need to be developed for the mass production of single layered graphene. Thirdly, more attention should be paid to assess biocompatibility and long-term toxicity of graphene-based nanomaterials. Fourthly, considerable work needs to be done to the use of graphene hybrids (graphene-based materials-metal NPs/metal oxides/polymers) in biosensors, which helps to achieve higher sensing performance combining the synergistic effects of both materials. Finally, to make graphene/GO-based biosensors commercialized, integration of this biosensing platform into device level is required which is still in infancy. Ongoing research to tackle these challenges to enable mass fabrication of graphene/GO-based biosensors with low costs wherein sample pretreatment and incubation steps can be performed on the same platform where the detection of analyte takes place shows enormous potential. It is only a matter of time before these issues are successfully addressed/resolved and reproducible, facile, and scalable preparation of graphene/GO-based sensors can be easily realized.

Acknowledgments AM thanks the National Science Foundation (Nos. 1265044 and 1606181), U.S. Department of Agriculture (2014-67021-21589) and W. Ruel Johnson Chair in Environmental Engineering for financial support. RS and SB thank Parikshit Sahatiya, Ph.D. student I.I.T. Hyderabad, for his assistance with proofreading and providing insightful comments.

References

1. Celik N, Balachandran W, Manivannan N (2015) Graphene-based biosensors: methods, analysis and future perspectives. IET Circuits Devices Syst 9(6):434–445
2. Dong H, Dong C, Ren T, Li Y, Shi D (2014) Surface-engineered graphene-based nanomaterials for drug delivery. J Biomed Nanotechnol 10(9):2086–2106
3. Viswanathan S, Narayanan TN, Aran K, Fink KD, Paredes J, Ajayan PM, Demirci U (2015) Graphene–protein field effect biosensors: glucose sensing. Mater Today 18(9):513–522
4. Ramnani P, Saucedo NM, Mulchandani A (2016) Carbon nanomaterial-based electrochemical biosensors for label-free sensing of environmental pollutants. Chemosphere 143:85–98
5. Pumera M (2011) Graphene in biosensing. Mater Today 14(7):308–315
6. Doria G, Conde J, Veigas B, Giestas L, Almeida C, Assunção M, Baptista PV (2012) Noble metal nanoparticles for biosensing applications. Sensors 12(2):1657–1687
7. Solanki PR, Kaushik A, Agrawal VV, Malhotra BD (2011) Nanostructured metal oxide-based biosensors. NPG Asia Mater 3(1):17–24
8. Badhulika S, Terse-Thakoor T, Villarreal C, Mulchandani A (2015) Graphene hybrids: synthesis strategies and applications in sensors and sensitized solar cells. Front Chem 3:38

9. Perreault F, de Faria AF, Elimelech M (2015) Environmental applications of graphene-based nanomaterials. Chem Soc Rev 44(16):5861–5896
10. Geim AK (2011) Random walk to graphene (nobel Lecture). Angew Chem Int Ed 50 (31):6966–6985
11. Avouris P, Dimitrakopoulos C (2012) Graphene: synthesis and applications. Mater Today 15 (3):86–97
12. Pei S, Cheng HM (2012) The reduction of graphene oxide. Carbon 50(9):3210–3228
13. Hummers Jr WS, Offeman RE (1958) Preparation of graphitic oxide. J Am Chem Soc 80 (6):1339–1339
14. Botas C, Álvarez P, Blanco P, Granda M, Blanco C, Santamaría R, Romasanta LJ, Verdejo R, López-Manchado MA, Menéndez R (2013) Graphene materials with different structures prepared from the same graphite by the Hummers and Brodie methods. Carbon 65:156–164
15. Park S, Ruoff RS (2009) Chemical methods for the production of graphenes. Nat Nanotechnol 4(4):217–224
16. Neto AC, Guinea F, Peres NM, Novoselov KS, Geim AK (2009) The electronic properties of graphene. Rev Mod Phys 81(1):109
17. Zhu Y, Murali S, Cai W, Li X, Suk JW, Potts JR, Ruoff RS (2010) Graphene and graphene oxide: synthesis, properties, and applications. Adv Mater 22(35):3906–3924
18. Balandin AA (2011) Thermal properties of graphene and nanostructured carbon materials. Nat Mater 10(8):569–581
19. Fuhrer MS, Lau CN, MacDonald AH (2010) Graphene: materially better carbon. MRS Bull 35 (4):289–295
20. Liu Y, Dong X, Chen P (2012) Biological and chemical sensors based on graphene materials. Chem Soc Rev 41(6):2283–2307
21. Chan CY, Guo J, Sun C, Tsang MK, Tian F, Hao J, Chen S, Yang M (2015) A reduced graphene oxide-Au based electrochemical biosensor for ultrasensitive detection of enzymatic activity of botulinum neurotoxin A. Sensors Actuators B Chem 220:131–137
22. Schwierz F (2010) Graphene transistors. Nat Nanotechnol 5(7):487–496
23. Nurunnabi M, Parvez K, Nafiujjaman M, Revuri V, Khan HA, Feng X, Lee YK (2015) Bioapplication of graphene oxide derivatives: drug/gene delivery, imaging, polymeric modification, toxicology, therapeutics and challenges. RSC Adv 5(52):42141–42161
24. Wan Y, Wang Y, Wu J, Zhang D (2010) Graphene oxide sheet-mediated silver enhancement for application to electrochemical biosensors. Anal Chem 83(3):648–653
25. Georgakilas V, Otyepka M, Bourlinos AB, Chandra V, Kim N, Kemp KC, Hobza P, Zboril R, Kim KS (2012) Functionalization of graphene: covalent and non-covalent approaches, derivatives and applications. Chem Rev 112(11):6156–6214
26. Tran TT, Mulchandani A (2016) Carbon nanotubes and graphene nano field-effect transistor-based biosensors. TrAC Trends Anal Chem 79:222–232
27. Sinitskii A, Dimiev A, Corley DA, Fursina AA, Kosynkin DV, Tour JM (2010) Kinetics of diazonium functionalization of chemically converted graphene nanoribbons. ACS Nano 4 (4):1949–1954
28. Liu H, Ryu S, Chen Z, Steigerwald ML, Nuckolls C, Brus LE (2009) Photochemical reactivity of graphene. J Am Chem Soc 131(47):17099–17101
29. Georgakilas V, Bourlinos AB, Zboril R, Steriotis TA, Dallas P, Stubos AK, Trapalis C (2010) Organic functionalisation of graphenes. Chem Commun 46(10):1766–1768
30. He H, Gao C (2010) General approach to individually dispersed, highly soluble, and conductive graphene nanosheets functionalized by nitrene chemistry. Chem Mater 22(17):5054–5064
31. Su Q, Pang S, Alijani V, Li C, Feng X, Müllen K (2009) Composites of graphene with large aromatic molecules. Adv Mater 21(31):3191–3195
32. Liang Y, Wu D, Feng X, Müllen K (2009) Dispersion of graphene sheets in organic solvent supported by ionic interactions. Adv Mater 21(17):1679–1683

33. Watcharotone S, Dikin DA, Stankovich S, Piner R, Jung I, Dommett GH, Evmenenko G, Wu SE, Chen SF, Liu CP, Nguyen ST (2007) Graphene-silica composite thin films as transparent conductors. Nano Lett 7(7):1888–1892
34. Verdejo R, Barroso-Bujans F, Rodriguez-Perez MA, de Saja JA, Lopez-Manchado MA (2008) Functionalized graphene sheet filled silicone foam nanocomposites. J Mater Chem 18 (19):2221–2226
35. Liu Y, Zhou J, Zhang X, Liu Z, Wan X, Tian J, Wang T, Chen Y (2009) Synthesis, characterization and optical limiting property of covalently oligothiophene-functionalized graphene material. Carbon 47(13):3113–3121
36. Kim KS, Tarakeshwar P, Lee JY (2000) Molecular clusters of π-systems: theoretical studies of structures, spectra, and origin of interaction energies. Chem Rev 100(11):4145–4186
37. Riley KE, Pitoňák M, Jurecka P, Hobza P (2010) Stabilization and structure calculations for noncovalent interactions in extended molecular systems based on wave function and density functional theories. Chem Rev 110(9):5023–5063
38. Sreeprasad TS, Berry V (2013) How do the electrical properties of graphene change with its functionalization? Small 9(3):341–350
39. Li Y, Bai H, Liu Q, Bao J, Han M, Dai Z (2010) A nonenzymatic cholesterol sensor constructed by using porous tubular silver nanoparticles. Biosens Bioelectron 25 (10):2356–2360
40. Ansari AA, Kaushik A, Solanki PR, Malhotra BD (2009) Electrochemical cholesterol sensor based on tin oxide-chitosan nanobiocomposite film. Electroanalysis 21(8):965–972
41. Wulfkuhle JD, Liotta LA, Petricoin EF (2003) Proteomic applications for the early detection of cancer. Nat Rev Cancer 3(4):267–275
42. Badhulika S, Paul RK, Terse T, Mulchandani A (2014) Nonenzymatic glucose sensor based on platinum nanoflowers decorated multiwalled carbon nanotubes-graphene hybrid electrode. Electroanalysis 26(1):103–108
43. Unnikrishnan B, Palanisamy S, Chen SM (2013) A simple electrochemical approach to fabricate a glucose biosensor based on graphene–glucose oxidase biocomposite. Biosens Bioelectron 39(1):70–75
44. Liang B, Fang L, Yang G, Hu Y, Guo X, Ye X (2013) Direct electron transfer glucose biosensor based on glucose oxidase self-assembled on electrochemically reduced carboxyl graphene. Biosens Bioelectron 43:131–136
45. Qian L, Lu L (2014) Three dimensional porous graphene–chitosan composites from ice-induced assembly for direct electron transfer and electrocatalysis of glucose oxidase. RSC Adv 4(72):38273–38280
46. Liu Y, Yu D, Zeng C, Miao Z, Dai L (2010) Biocompatible graphene oxide-based glucose biosensors. Langmuir 26(9):6158–6160
47. Enomoto J, Matharu Z, Revzin A (2013) Electrochemical biosensors for on-chip detection of oxidative stress from cells. Methods Enzymol 526:107–121
48. Lu Q, Dong X, Li LJ, Hu X (2010) Direct electrochemistry-based hydrogen peroxide biosensor formed from single-layer graphene nanoplatelet–enzyme composite film. Talanta 82 (4):1344–1348
49. Zhou K, Zhu Y, Yang X, Luo J, Li C, Luan S (2010) A novel hydrogen peroxide biosensor based on Au–graphene–HRP–chitosan biocomposites. Electrochim Acta 55(9):3055–3060
50. Nandini S, Nalini S, Reddy MM, Suresh GS, Melo JS, Niranjana P, Shanmugam S (2016) Synthesis of one-dimensional gold nanostructures and the electrochemical application of the nanohybrid containing functionalized graphene oxide for cholesterol biosensing. Bioelectrochemistry 110:79–90
51. Dey RS, Raj CR (2010) Development of an amperometric cholesterol biosensor based on graphene-Pt nanoparticle hybrid material. J Phys Chem C 114(49):21427–21433
52. Sha R, Komori K, Badhulika S (2017) Graphene–Polyaniline composite based ultra-sensitive electrochemical sensor for non-enzymatic detection of urea. Electrochim Acta 233:44–51

53. Srivastava RK, Srivastava S, Narayanan TN, Malhotra BD, Vajtai R, Ajayan PM, Srivastava A (2011) Functionalized multilayered graphene platform for urea sensor. ACS Nano 6 (1):168–175
54. Kumar V, Chopra A, Arora S, Yadav S, Kumar S, Kaur I (2015) Amperometric sensing of urea using edge activated graphene nanoplatelets. RSC Adv 5(18):13278–13284
55. Odenthal KJ, Gooding JJ (2007) An introduction to electrochemical DNA biosensors. Analyst 132(7):603–610
56. Ghosh I, Stains CI, Ooi AT, Segal DJ (2006) Direct detection of double-stranded DNA: molecular methods and applications for DNA diagnostics. Mol BioSyst 2(11):551–560
57. Zhou M, Zhai Y, Dong S (2009) Electrochemical sensing and biosensing platform based on chemically reduced graphene oxide. Anal Chem 81(14):5603–5613
58. Benvidi A, Rajabzadeh N, Mazloum-Ardakani M, Heidari MM, Mulchandani A (2014) Simple and label-free electrochemical impedance Amelogenin gene hybridization biosensing based on reduced graphene oxide. Biosens Bioelectron 58:145–152
59. Luppa PB, Sokoll LJ, Chan DW (2001) Immunosensors – principles and applications to clinical chemistry. Clin Chim Acta 314(1):1–26
60. Lin J, Ju H (2005) Electrochemical and chemiluminescent immunosensors for tumor markers. Biosens Bioelectron 20(8):1461–1470
61. Okuno J, Maehashi K, Kerman K, Takamura Y, Matsumoto K, Tamiya E (2007) Label-free immunosensor for prostate-specific antigen based on single-walled carbon nanotube array-modified microelectrodes. Biosens Bioelectron 22(9):2377–2381
62. Li H, He J, Li S, Turner AP (2013) Electrochemical immunosensor with N-doped graphene-modified electrode for label-free detection of the breast cancer biomarker CA 15-3. Biosens Bioelectron 43:25–29
63. Singal S, Srivastava AK, Biradar AM, Rajesh MA (2014) Pt nanoparticles-chemical vapor deposited graphene composite based immunosensor for the detection of human cardiac troponin I. Sensors Actuators B 205:363–370
64. Özcan B, Sezgintürk MK (2016) Graphene oxide based electrochemical label free immunosensor for rapid and highly sensitive determination of tumor marker HSP70. Talanta 160:367–374
65. Liu G, Qi M, Zhang Y, Cao C, Goldys EM (2016) Nanocomposites of gold nanoparticles and graphene oxide towards a stable label-free electrochemical immunosensor for detection of cardiac marker troponin-I. Anal Chim Acta 909:1–8
66. Fang Y, Wang E (2013) Electrochemical biosensors on platforms of graphene. Chem Commun 49(83):9526–9539
67. Sha R, Puttapati SK, Srikanth VV, Badhulika S (2017) Ultra-sensitive phenol sensor based on overcoming surface fouling of reduced graphene oxide-zinc oxide composite electrode. J Electroanal Chem 785:26–32
68. Zhang Y, Zhao H, Wu Z, Xue Y, Zhang X, He Y, Li X, Yuan Z (2013) A novel graphene-DNA biosensor for selective detection of mercury ions. Biosens Bioelectron 48:180–187
69. Saidur MR, Aziz AA, Basirun WJ (2017) Recent advances in DNA-based electrochemical biosensors for heavy metal ion detection: a review. Biosens Bioelectron 90:125–139
70. Wen Y, Li FY, Dong X, Zhang J, Xiong Q, Chen P (2013) The electrical detection of lead ions using gold-nanoparticle- and DNAzyme-functionalized graphene device. Adv Healthc Mater 2 (2):271–274
71. Sudibya HG, He Q, Zhang H, Chen P (2011) Electrical detection of metal ions using field-effect transistors based on micropatterned reduced graphene oxide films. ACS Nano 5 (3):1990–1994
72. Tan F, Cong L, Saucedo NM, Gao J, Li X, Mulchandani A (2016) An electrochemically reduced graphene oxide chemiresistive sensor for sensitive detection of Hg^{2+} in water samples. J Hazard Mater 320:226–233
73. Aktar W, Sengupta D, Chowdhury A (2009) Impact of pesticides use in agriculture: their benefits and hazards. Interdiscip Toxicol 2(1):1–12

74. Gan T, Lv Z, Sun J, Shi Z, Liu Y (2016) Preparation of graphene oxide-wrapped carbon sphere@silver spheres for high performance chlorinated phenols sensor. J Hazard Mater 302:188–197
75. Pundir CS, Chauhan N (2012) Acetylcholinesterase inhibition-based biosensors for pesticide determination: a review. Anal Biochem 429(1):19–31
76. Zhang Y, Zhang J, Wu H, Guo S, Zhang J (2012) Glass carbon electrode modified with horseradish peroxidase immobilized on partially reduced graphene oxide for detecting phenolic compounds. J Electroanal Chem 681:49–55
77. Zeng L, Zhang A, Zhu X, Zhang C, Liang Y, Nan J (2013) Electrochemical determination of nonylphenol using differential pulse voltammetry based on a graphene–DNA-modified glassy carbon electrode. J Electroanal Chem 703:153–157
78. Li Y, Bai Y, Han G, Li M (2013) Porous-reduced graphene oxide for fabricating an amperometric acetylcholinesterase biosensor. Sensors Actuators B Chem 185:706–712
79. Wang Y, Zhang S, Du D, Shao Y, Li Z, Wang J, Engelhard MH, Li J, Lin Y (2011) Self-assembly of acetylcholinesterase on a gold nanoparticles–graphene nanosheet hybrid for organophosphate pesticide detection using polyelectrolyte as a linker. J Mater Chem 21 (14):5319–5325
80. Liang S, Zhu J, Ding J, Bi H, Yao P, Han Q, Wang X (2015) Deposition of cocoon-like ZnO on graphene sheets for improving gas-sensing properties to ethanol. Appl Surf Sci 357:1593–1600
81. Harraz FA, Ismail AA, Ibrahim AA, Al-Sayari SA, Al-Assiri MS (2015) Highly sensitive ethanol chemical sensor based on nanostructured SnO_2 doped ZnO modified glassy carbon electrode. Chem Phys Lett 639:238–242
82. Shan C, Yang H, Han D, Zhang Q, Ivaska A, Niu L (2010) Electrochemical determination of NADH and ethanol based on ionic liquid-functionalized graphene. Biosens Bioelectron 25 (6):1504–1508
83. Guo S, Wen D, Zhai Y, Dong S, Wang E (2011) Ionic liquid–graphene hybrid nanosheets as an enhanced material for electrochemical determination of trinitrotoluene. Biosens Bioelectron 26(8):3475–3481
84. Zhou XH, Liu LH, Bai X, Shi HC (2013) A reduced graphene oxide based biosensor for high-sensitive detection of phenols in water samples. Sensors Actuators B Chem 181:661–667
85. Sethuraman V, Muthuraja P, Raj JA, Manisankar P (2016) A highly sensitive electrochemical biosensor for catechol using conducting polymer reduced graphene oxide–metal oxide enzyme modified electrode. Biosens Bioelectron 84:112–119
86. Sun J, Wu Z, Hu D, Shi Z, Lv Z (2015) Preparation of reduced grapheneoxide–poly (safranine T) film via one-step polymerization for electrochemical determination of methyl jasmonate. Fullerenes, Nanotubes, Carbon Nanostruct 23(8):701–708

Label-Free MIP Sensors for Protein Biomarkers

Katharina J. Jetzschmann, Xiaorong Zhang, Aysu Yarman, Ulla Wollenberger, and Frieder W. Scheller

Abstract Molecularly imprinted polymers (MIPs) have been prepared mostly for low-molecular-weight biomarkers and drugs but also for a spectrum of proteins. As compared with antibodies, MIPs have higher chemical and thermal stability, and they can be regenerated for repeated measurements. Electrochemical methods dominate the read-out of MIP sensors. Many protein MIPs have been tested in artificial urine or spiked semi-synthetic plasma, and point-of-care detection of marker proteins e.g. for cardiac, cancer, Alzheimer's disease or virus infections is the prospective aim.

In the following chapter, the preparation and analytical performance of a broad spectrum of MIP sensors for protein biomarker are presented. The examples are grouped according to the respective diseases. For the majority of biomarkers, different approaches of sensor preparation and signal read-out can be compared.

Keywords Biomimetic sensors, Electropolymerization, Molecularly imprinted polymers, Protein biomarkers, Protein imprinting

Contents

K. J. Jetzschmann (✉), X. Zhang, U. Wollenberger, and F. W. Scheller (✉)
Institute for Biochemistry and Biology, University of Potsdam, Karl-Liebknecht-Strasse 25-26, Potsdam 14476, Germany
e-mail: jetzschm@uni-potsdam.de; fschell@uni-potsdam.de

A. Yarman
Institute for Biochemistry and Biology, University of Potsdam, Karl-Liebknecht-Strasse 25-26, Potsdam 14476, Germany

Faculty of Science, Molecular Biotechnology, Turkish-German University, Sahinkaya Cad. No. 86, Beykoz, Istanbul 34820, Turkey

M. J. Schöning, A. Poghossian (eds.), *Label-Free Biosensing: Advanced Materials, Devices and Applications*, Springer Series on Chemical Sensors and Biosensors (2018) 16: 291–322
DOI 10.1007/5346_2017_3, © Springer International Publishing AG 2017,
Published online: 11 June 2017

1 Introduction

According to the National Institute of Health, a biological marker or biomarker is "a characteristic that is objectively measured and evaluated as an indicator of normal biological processes, pathogenic processes, or pharmacologic responses to a therapeutic intervention" [1]. They can be found in body fluids or tissues and come in various forms, ranging from mutated deoxyribonucleic acid (DNA) and ribonucleic acid (RNA), metabolites, hormones or lipids to whole cells, organs or even physiological states.

This chapter focuses on proteins, one of the most common types of biomarkers. In contrast to nucleic acid-based biomarkers, they hold higher information value due to post-translational modifications, post-transcriptional alteration in consequence of physiological changes and – in case of enzymes – physiological effects on activity levels. They are of particular interest for early-stage disease detection to allow the most effective therapeutic outcome (e.g. cancer, cardiovascular or neurodegenerative disorders), but their detection can be particularly difficult as they are usually found in very low concentration and in complex media. Protein biomarker analysis has therefore to fulfil certain requirements: (1) high sensitivity to detect trace levels in presence of large excess of interfering proteins; (2) high selectivity to outbalance consequences of diagnostic errors, like unnecessary surgery or psychological impact; (3) reasonable sample size and accessibility with least invasivity necessary (e.g. based on blood or urine); and (4) convenient handling and affordability of measurement equipment for application in clinical daily routine [2–5].

Among protein detection assays established in disease diagnosis and monitoring, the enzyme-linked immunosorbent assay (ELISA) remains the most commonly applied technology [6–8]. In ELISA, an immobilized antibody specifically captures the target protein which is then sandwiched by a second antibody carrying a catalytically active, signal-generating unit. This powerful methodology allows detection and differentiation of many protein biomarkers, but development with regard to improved selectively, sensitivity and multiplexing is still ongoing to realize its full potential [9–11].

Biomimetic recognition elements – inspired from biology but usually superior with regard to stability, reusability and cost-effectivity – represent an alternative to antibody-based detection of proteinous biomarkers. Selective receptors in the form of fully synthetic polymers – so-called molecularly imprinted polymers – have traditionally been developed for low-molecular-weight substances according to the

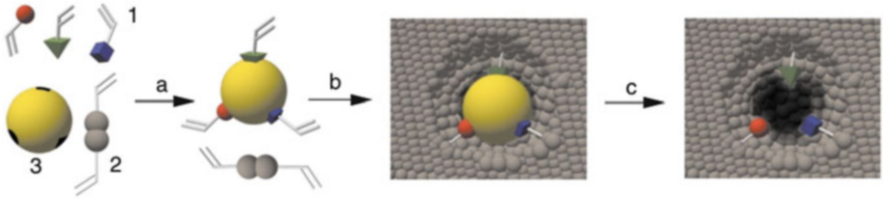

Fig. 1 General scheme of the molecular imprinting technique. 1: Functional monomers, 2: cross-linker, 3: template; a: pre-polymerization complex formation, b: polymerization, c: template removal. (Reprinted with permission [21])

early concepts of Wulff, Shea and Mosbach [12–14]. In order to gain an imprinted material with cavities complementary to the analyte (the template) in size and arrangement of functionalities, one or more functional monomers are polymerized in presence of the template that subsequently has to be removed from the polymeric matrix (see Fig. 1) [15–17].

Interaction of the template with the functional monomers in the pre-polymerization mixture can be of non-covalent (self-assembly approach) or covalent (pre-organized approach) nature effecting the heterogeneity of the resulting binding sites, specificity and binding affinity [12, 14, 18–20].

Because of their great potential in medical diagnostics, MIPs for proteins are nowadays stepping into focus. It is, however, important to note that the imprinting of proteins is considerably more challenging than of low-molecular-weight compounds due to their large size and complex structure. In addition, it was concluded that selectivity of protein target binding is more related to the shape of the cavity than to the interaction of their functional groups with the target [22, 23]. Since their first presentation in 1985, extensive research on MIPs for proteins started about 20 years ago, but publications on the topic make up only ca. 10% of all literature on molecularly imprinted polymers [19, 24–34].

1.1 MIPs for Proteins

As indicated above, classical bulk imprinting methods that fit for low-molecular-weight compounds are usually not appropriate for structurally complex macromolecular templates due to the high probability of entrapment and restricted accessibility of the imprinted pocket. Early examples include hydrogels based on acrylamide or agarose with low density of cross-linking and large pores that have been taken over from chromatography to develop specific sorbents for proteins as precursors of MIPs [35–41].

Another approach that maintains the high degree of cross-linking overcomes the problems of restricted template removal and slow mass transfer. The MIP structure is formed either by generating the binding sites on the surface of micro- or nanoparticles which are deposited onto the sensor in the next step or in thin polymer

films directly on the transducer (surface imprinting). In the latter approach, the thickness of the MIP layer should be comparable with the hydrodynamic radius of the protein for partial embedding of the template in the polymer. This will allow effective removal and rebinding of the target analyte. However, in this approach the number of binding sites is limited by the available surface area of the polymer.

The following methods have been developed for surface imprinting of proteins:

Particle-Based MIPs

1. Micro- or nano-MIPs were synthesized by emulsion or precipitation polymerization of acrylamide-based monomers in mixture with the template for high surface/volume ratio, creating binding sites mainly on the surface of the particle (see Fig. 2) [42–45].
2. Various supporting materials were employed for the preparation of surface-imprinted core-shell nanoparticles with additional features, like fluorescence or magnetism. Here, emulsion or precipitation polymerization, grafting or the self-polymerization of dopamine have been applied (see Fig. 3) [46–57].
3. When the target is immobilized with a uniform orientation before the deposition of the MIP film, increased homogeneity of binding sites with enhanced specificity of rebinding can be achieved. Solid-phase synthesis uses functionalized beads (e.g. from glass) for binding of the pre-oriented template. Thermoresponsive MIP nanoparticles are further synthesized allowing a temperature-dependent

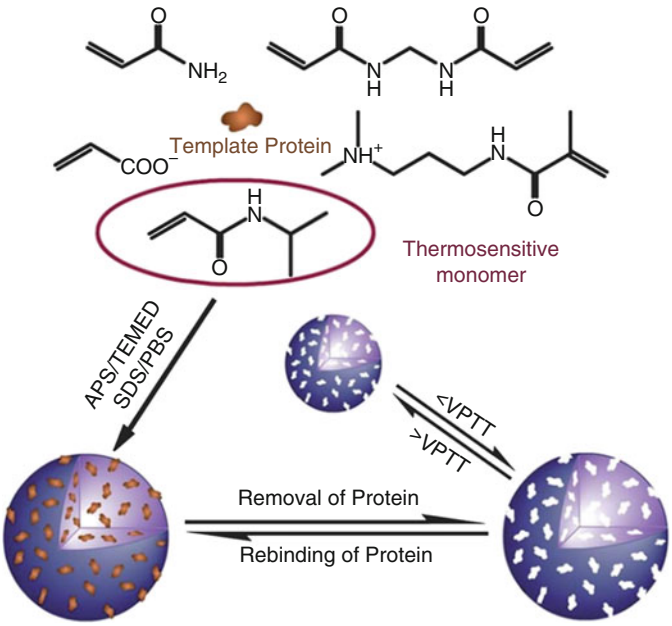

Fig. 2 Schematic representation for the preparation of molecularly imprinted nanospheres by mini-emulsion polymerization. (Reprinted with permission [44])

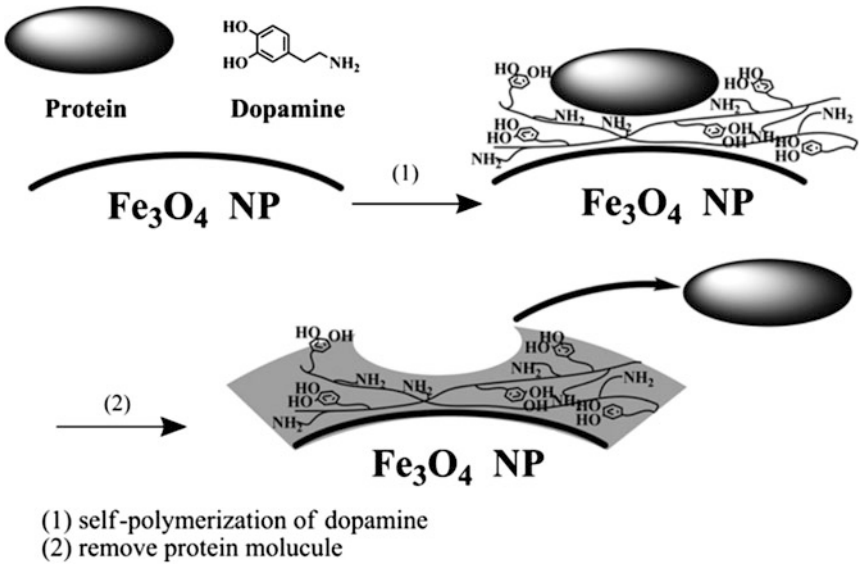

Fig. 3 Schematic protocol for the preparation of surface-imprinted core-shell nanoparticles by self-polymerization of dopamine. (Reprinted with permission [48])

affinity separation from the support (see Fig. 4). The resulting nanoparticles possess dissociation constants in the nanomolar range and enhanced homogeneity of binding sites [58–61]. Alternative strategies employ covalent attachment of the template on the MIP-supporting beads [62–64].

MIP Thin Films Deposited Directly on the Transducer

1. Radicalic polymerization of a template-monomer mixture or of the monomer after template adsorption triggered by a chemical initiator, electrochemical oxidation of the monomer or the self-polymerization by ambient oxygen is the simplest method for the creation of ultrathin MIP layers on top of planar or nanostructured transducers (see Fig. 5) [65–79]. Utilization of monomers that are known to strongly interact with defined sites of the protein molecule, e.g. boronic acid derivatives for glycoproteins, increases both the specificity and affinity of the MIP [80–84].
2. Adsorption/immobilization of the protein on a sacrificial or removable support followed by the synthesis of a soft polymer layer creates stamp-like surface patterns after removal of the support (micro-contact imprinting, see Fig. 6) [66, 85–93].
3. Covalent or non-covalent oriented template immobilization by (specific) anchors on the transducer prior to the formation of ultrathin polymer layers was first demonstrated using metal ion coordination between the monomer and surface-exposed histidine residues (see Fig. 7) [34, 94]. Later on, boronic acids were

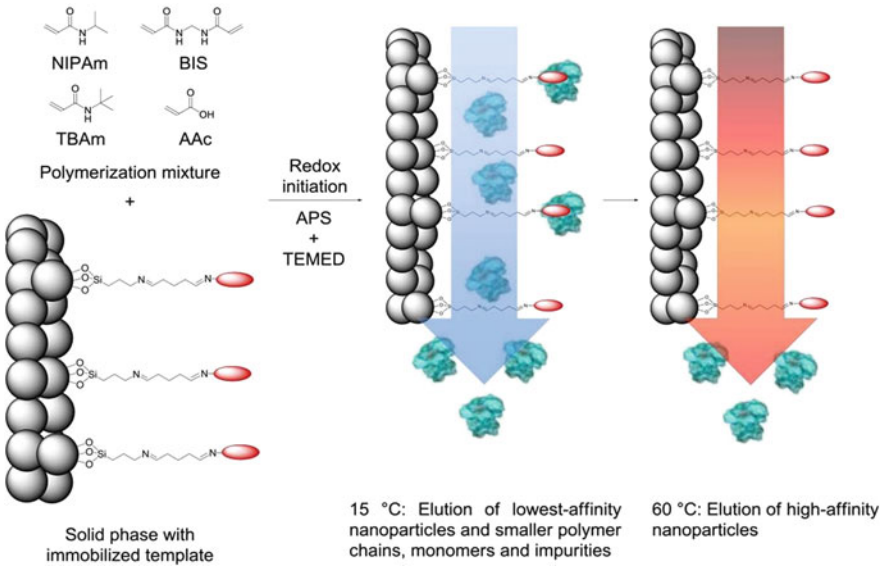

Fig. 4 Schematic illustration of the solid-phase synthesis of thermoresponsive MIP nanoparticles. (Reprinted with permission [59])

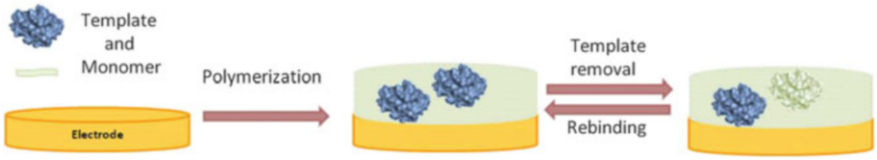

Fig. 5 Surface imprinting technique for the synthesis of MIP films by polymerization of a template-monomer mixture. (Adapted with permission from [34])

applied for the capture of glycoproteins, specific inhibitors or substrates for the recognition of enzymes and specific aptamers, e.g. for the detection of a biomarker [95–104].

4. MIP nanosphere lithography was introduced as a variant of the micro-contact method for site-directed imprinting. Here, the template is orientedly fixed to nanobeads; thus, highly uniform cavities are generated [105].
5. The epitope or fragment approach typically uses an exposed protein fragment as the template for the preparation of MIPs capable of recognizing the entire protein (see Fig. 8). This is usually a short, linear peptide, e.g. originating from the protein termini, but can also be a larger fragment such as the Fab fragment for a MIP towards human immunoglobulin G [106–111].

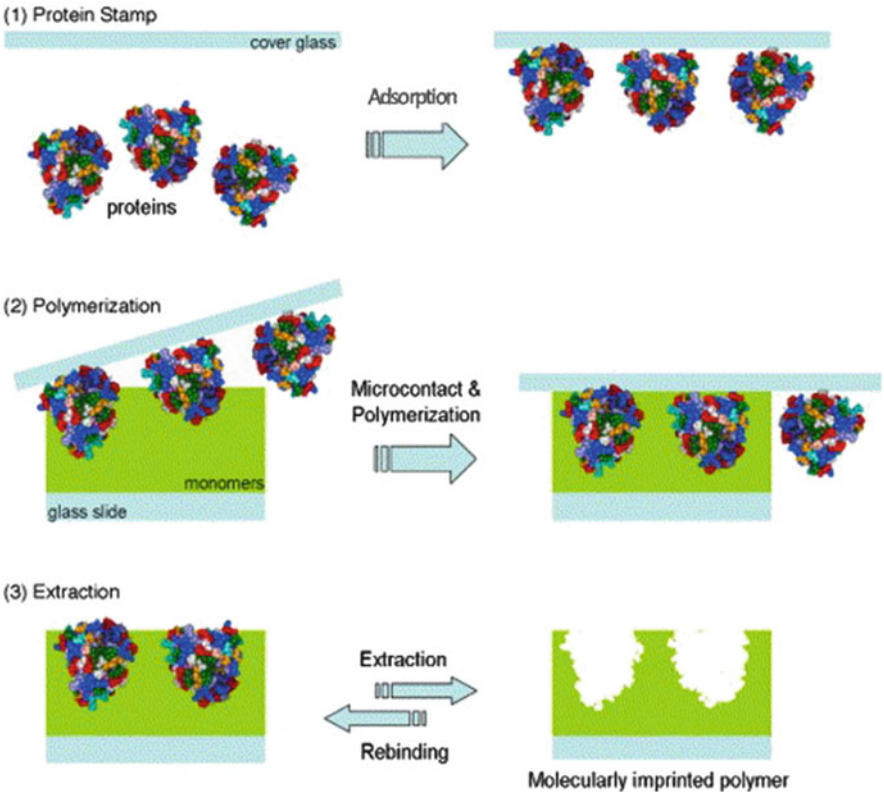

Fig. 6 Schematic representation of the micro-contact imprinting method. (Adapted with permission [89])

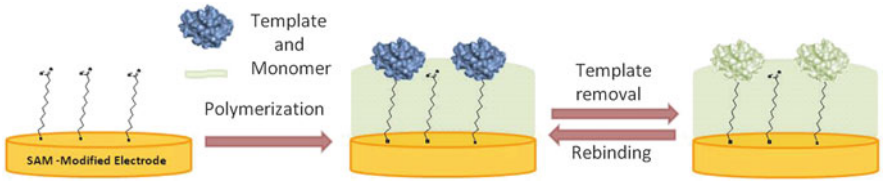

Fig. 7 Surface imprinting technique for the synthesis of MIP films by oriented immobilization of the protein onto a preassembled anchor layer prior to polymerization. (Adapted with permission from [34])

1.2 MIP-Sensor Configurations

Effective signal transfer of analyte recognition by the MIP to the transducer requires close proximity of both sensor components. Concordantly, MIP sensors for proteins mostly apply surface-imprinted layers which were deposited directly on

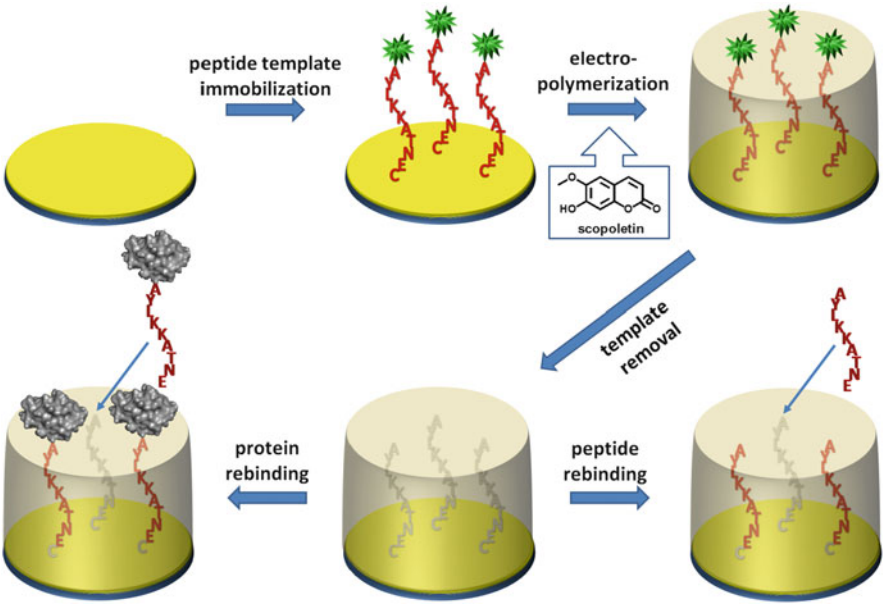

Fig. 8 Schematic representation of the epitope-imprinting approach for a C-terminal-derived nonapeptide. (Reprinted with permission [110])

the transducer surface. For label-free signal generation, the following sensor formats have been adapted from DNA chips and immunosensors: (1) Changes in mass, refractive index, thickness or fluorescence of the recognition layer upon binding of the protein to the MIP can be assessed by quartz crystal microbalance (QCM), surface acoustic wave (SAW) or surface plasmon resonance (SPR) measurements [55, 57, 66, 72, 92, 101, 103, 105, 111, 112]. (2) Surface techniques, like Raman and Fourier transform infrared spectroscopy (FTIR), transmission electron microscopy (TEM) or atomic force microscopy (AFM), allow direct indication of the bound protein template in the MIP film [56, 67, 75, 113–115]. (3) Electroactive (e.g. enzymes) or intrinsically fluorescent proteins can be addressed by measurements of direct electron transfer (DET) or enzymatic activity upon MIP binding, e.g. by amperometry or differential pulse voltammetry (DPV) or by fluorescence spectroscopy [69, 77, 78, 96, 102, 116]. (4) Electrochemical characterization of redox marker permeability can give indirect evidence of protein binding to the MIP layer. It is assumed that the release of the template from the MIP leads to an increase of redox marker accessibility towards the underlying electrode, whilst binding of the target protein to the empty cavities results in a concentration-dependent signal suppression. Usually cyclic voltammetry (CV), square wave voltammetry (SWV) or electrochemical impedance spectroscopy (EIS) are applied in combination with redox markers like ferrocyanide or ferrocene carboxylic acid [67, 70, 71, 73–76, 79, 98, 99, 104, 117, 118].

2 MIPs for Biomarkers

In the following chapter, the preparation and analytical performance of a broad spectrum of MIP sensors for protein biomarkers are presented. The examples are grouped according to the respective diseases. For the majority of biomarkers, different approaches of sensor preparation and signal read-out can be compared. Application of electrochemical methods for the read-out of protein MIPs is dominating [119].

2.1 Cancer Markers

2.1.1 Prostate Cancer Markers

Prostate-specific antigen (PSA) is a 30–33 kDa serine protease which is secreted by the prostate gland. As elevated levels in men point to prostate cancer, PSA is still the most commonly used biomarker for screening and monitoring the effectiveness of treatment [120–122].

For the preparation of a PSA-MIP, the target was bound to a thiolated DNA aptamer which was chemisorbed on the surface of a clean gold electrode [104]. Subsequently, polydopamine was deposited by electropolymerization around the preformed aptamer-PSA complex using cyclic voltammetry. The template was removed by washing the apta-MIP with a solution containing 5% acetic acid and 5% sodium dodecyl sulphate (SDS). Rebinding of the target was indicated by electrochemical impedance spectroscopy (EIS) in 10 mM ferri-/ferrocyanide-containing 10 mM phosphate-buffered saline (PBS) solution. The apta-MIP sensor showed in the semi-logarithmic concentration dependence a linear measuring range from 100 pg mL^{-1} to 100 ng mL^{-1} of PSA with a limit of detection of 1 pg mL^{-1}. This value is threefold lower than for the aptamer alone, suggesting that the MIP layer contributed to the PSA binding by partially entrapping the protein in the imprinted cavities. Furthermore, the apta-MIP sensor showed low cross-reactivity with the homologous protein human kallikrein 2 and low response to human serum albumin (HSA).

A solid-contact PSA-selective electrode was prepared by dispersing chemically modified graphene oxide in a polyvinyl chloride (PVC)-containing tetrahydrofuran solution [115]. In the first step, PSA was bound to graphene oxide which was activated with *N*-hydroxysuccinimide (NHS) and *N*-ethyl-*N*-(3-dimethylaminopropyl) carbodiimide hydrochloride (EDAC). The MIP formation around the covalently bound PSA was performed by radicalic polymerization of the functional monomer acrylamide in the presence of the cross-linker *N*,*N*-methylenebis(acrylamide) (NMAA). The template PSA was removed from the resulting MIP particles by the action of trypsin. The solid-contact MIP sensor was prepared by casting the PVC-MIP mixture on the surface of the electrode which was made up of a graphite-epoxy resin

body. The potentiometric response showed a linear dependence on the PSA concentration between 2.0 and 89.0 ng mL^{-1} (5.8 pM–2.6 nM) with a lower limit of detection of 58 pM. The authors claim that 5×10^7 ng mL^{-1} of bovine serum albumin (BSA) or 1.5×10^7 ng mL^{-1} Hb was tolerated by the device.

Annexin A3 (ANXA3) is another biomarker for prostate cancer. Rebelo et al. developed a sensor for ANXA3 by electrochemical bulk polymerization of caffeic acid on a carbon screen-printed electrode (SPE) [73]. Binding of the target was indicated by evaluating the SWV signal of the redox marker ferricyanide. The authors report successful application in ANXA3-spiked urine samples and a limit of detection (LOD) of 0.09 ng mL^{-1}.

The same group developed a similar MIP sensor for microseminoprotein-beta which is a 94 amino acid peptide (10.7 kDa) [74]. Its concentration is decreased in men with prostate cancer. The MIP is deposited on the surface of a carbon SPE of caffeic acid after the interaction of the target with dopamine. Rebinding of the target gave a semi-logarithmic dependency of the ferricyanide signal in the range of 0.5–100 ng mL^{-1}.

2.1.2 Ovarian and Breast Cancer Antigens

The epithelial ovarian cancer antigen (CA 125) is the standard tumour marker for monitoring ovarian cancer with a normal level in blood below 35 U mL^{-1}. This glycoprotein has a molecular weight of ca. 200 kDa, a diameter of 10 nm and is found on the surface of ovarian cancer cells [123–125].

For preparing MIPs for CA 125, the target protein was adsorbed at three-dimensional gold nanoelectrodes followed by the polymerization of phenol by cyclic voltammetry and removal of the template by development in a solution containing 1% acetic acid and 3% sodium dodecyl sulphate [70]. Removal and rebinding of the template were evaluated by differential pulse voltammetry and electrochemical impedance spectroscopy in ferrocyanide-containing PBS. The percentage of the peak current depended sigmoidal on the logarithm of CA 125 concentration in the range of 1–400 U mL^{-1} with a linear section between 10 and 100 U mL^{-1}. The authors claim absence of significant interferences in the CA 125 determination in serum in spite of pronounced effect of relevant HSA concentrations.

The cancer marker CA 15-3 (>400 kDa) is routinely used for monitoring the treatment of patients with advanced breast cancer [126, 127]. A voltammetric MIP sensor for CA 15-3 was developed based on the electropolymerization of 2-aminophenol around the template adsorbed at the surface of a screen-printed gold electrode [79]. The imprinted protein was removed by incubation in 0.5 M oxalic acid, and the rebinding was characterized by CV measurements using the redox probe ferri-/ferrocyanide. The authors conclude that this sensor could be applied in point-of-care analysis.

2.1.3 Human Papillomavirus-Derived E7 Protein

The human papillomavirus-derived E7 protein has been identified as one of the major viral oncoproteins of human papillomavirus (HPV)-initiated cervical carcinoma [128–130].

The polyphenol-based ultrasensitive label-free MIP nanosensor presented for ferritin (see Sect. 2.3.4) was adapted for the human papillomavirus-derived E7 protein. The ferricyanide signal of the MIP was evaluated by electrochemical impedance spectroscopy and allowed the indication of the E7 protein in subpicogram-per-litre levels. Importantly, the similar E6 protein did not generate a comparable signal [67].

2.1.4 Cancerogenic Embryonic Antigen

Cancerogenic embryonic antigen (CEA) is an established biomarker which is currently applied to follow the progression of colorectal cancer. It is an immunoglobulin which binds via a glycosyl phosphatidylinositol to the cell membrane [131, 132].

A CEA-MIP was prepared on the surface of a silver SPE by electropolymerizing phenol in the presence of the protein target [75]. The presence of the protein after electropolymerization was confirmed by FTIR studies and Raman spectroscopy. The template was enzymatically digested by treatment of the MIP with proteinase K. All steps of MIP preparation and of rebinding were characterized by CV and EIS in a solution containing hexaammineruthenium(III) chloride as a redox probe. The current response depended linearly on the logarithm of CEA concentration between 0.05 and 1.25 pg mL^{-1}.

2.2 Markers for Myocardial Infarction

2.2.1 Cardiac Troponin T

Cardiac troponins are released from injured muscle cells into the blood within 2–4 h after cardiac ischemia without overlap with skeletal troponins. Troponin T, a variant of troponin with a molecular weight of 37 kDa, is the commonly accepted biomarker for cardiac infarction [133, 134].

Tiwari et al. developed an ultrasensitive MIP sensor for human cardiac troponin T that is based on the electropolymerization of *o*-phenylenediamine (*o*-PD) in presence of the target protein on a gold electrode [71]. The target was removed by washing the electrode with alkaline ethanol at elevated temperature. The decrease in peak currents of the redox probe ferri-/ferrocyanide after rebinding showed two linear sections in a logarithmic concentration scale. The authors

conclude from these findings that the sensor has a linear concentration dependence over the range 0.009–0.8 ng mL^{-1} and a high affinity to the target.

Recently, another ultrasensitive MIP sensor for troponin T has been developed based on a nano-molecularly imprinted polymer which is assembled on a reduced graphene oxide SPE [76]. The MIP layer was prepared by electropolymerizing a mixture of pyrrole and carboxylated pyrrole in the presence of the protein by CV and subsequent template removal with oxalic acid. The relative decrease of the peaks in differential pulse voltammetry for ferricyanide after rebinding of troponin depends linearly on the protein concentration in the region from 0.001 to 0.1 ng mL^{-1}. From the concentration dependence, an imprinting factor of approximately 3 and a K_D of 0.73 pM can be derived. The authors claim that the new MIP sensor can discriminate between sera of non-myocardial and infarcted subjects.

2.2.2 Myoglobin

Myoglobin (Mb) is a globular heme protein with a molecular weight of 17 kDa which is the oxygen carrier in the skeletal muscles and in the heart. After myocardial infarction it is released into the blood; thus, its concentration rises from the normal level of 100–200 ng mL^{-1} to 500–2,000 ng mL^{-1}. The blood concentration of Mb allows the diagnosis after 1–5 h after infarction.

Sales and co-workers published two papers on MIPs for Mb: The target was covalently bound at the surface of a gold screen-printed electrode via a cysteamine-glutaraldehyde spacer [98]. The MIP was formed by persulphate-initiated polymerization of acrylamide and *N*,*N*′-methylenebisacrylamide on top of the SPE. The template was removed by incubation of the MIP in oxalic acid, and the rebinding was visualized by EIS and SWV measurements in ferri-/ferrocyanide-containing solutions. The charge transfer resistance (R_{ct}) depended linearly on the Mb concentration between 9 and 36 μg mL^{-1}, whilst the decrease of the SWV peaks exhibited a linear dependence on the target concentration from 9 to 36 μg mL^{-1}. The authors report that the MIP sensor was successfully applied to determine Mb in spiked urine samples.

In a modification of the Mb-MIP, the target was bound to a thiomalic acid SAM on the gold SPE followed by the binding of charged labels to the immobilized protein [99]. In order to modulate the electrostatic interactions in the MIP cavities, a polymer layer around the protein was formed from charged monomers followed by the polymerization of neutral acrylamides. In the next step, the template was removed by enzymatic cleavage of the protein by proteinase K. Evaluation of the current decrease of the ferricyanide signal according to a Langmuir isotherm gave a K_d value of 3 μM. This MIP sensor was tested in Mb-spiked diluted serum. The authors found a recovery within 94 and 97% in the concentration range from 0.6 to 19 μg mL^{-1} and a standard deviation of 5.8%.

The MIP for Mb developed by Shumyanseva et al. is based on the electropolymerization of a solution containing the target protein and *o*-PD on QCM chips or graphite SPEs [77, 78]. Contrary to the indirect measurement of

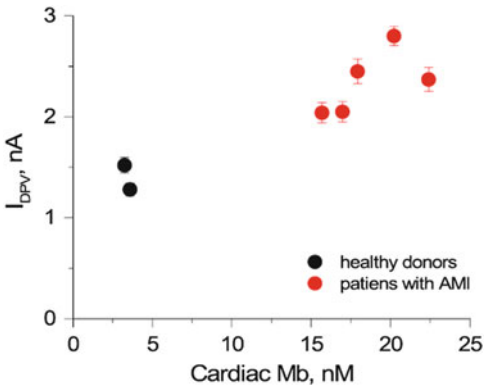

Fig. 9 MIP-assisted discrimination of cardiac Mb in plasma samples of healthy donors and patients with AMI. The MIP sensor shows increasing response with increasing cardiac Mb concentration as can be found in patients with AMI. (Reprinted with permission [78])

rebinding by low-molecular redox probes (as used for the Mb-MIP above), the electrocatalytic reduction of oxygen was indicated by SWV or CV measurements. This process is based on the direct electron transfer between the redox-active group of the protein and the underlying electrode and visualizes the MIP-bound target molecules. MIPs based on the DET of the protein target have been previously described for haemoglobin and cytochrome *c* [69, 96]. The MIP sensor shows a linear measuring range between 1 and 10 nM with a detection limit of 0.5 nM (9 ng mL^{-1}). The imprinting factor is 2–4. The sensor discriminated the plasma samples of healthy donors and of patients with acute myocardial infarction (AMI) (see Fig. 9).

2.2.3 Trypsin

Trypsin (E.C.3.4.21.4) is produced in the pancreas and catalyses the digestion of proteins by cleaving the peptide chain on the C-terminal side of arginine and lysine. Its activity can be measured in the diagnosis of pancreatitis and pancreatic cancer [135–137].

A MIP sensor for trypsin was prepared using micro-contact imprinting: The target was covalently bound to a glass cover slip, and this protein stamp was pressed on a gold electrode which was covered with a layer of polytyramine [93]. The MIP layer was formed around the trypsin molecules by radicalic polymerization of a mixture of acrylamide derivatives. Finally, in order to form an insulating cover on the electrode, pinholes were closed by incubation in 1-dodecanol. Glycine-HCl of pH 2.5 was used to remove the template and rebinding was characterized by capacitance measurements using the current pulse method. The rebinding of the protein resulted in a decrease of the capacitance (probably by the displacement of the counter ions). The measuring signal depended linearly on the logarithm of trypsin concentration between 0.1 pM and 0.1 μM with a limit of detection of 0.3 pM. The sensor showed excellent selectivity vs. chymotrypsin but interference to

cytochrome *c*. Interestingly, the enzyme bound to the imprinted polymer retained its activity as indicated by the digestion of a coloured peptide.

2.3 Further MIPs for Biomarkers

2.3.1 Glycated Haemoglobin: A Long-Term Diabetes Marker

At elevated blood sugar concentrations, the glucose reacts in the red blood cells with the amino group of N-terminal valine of the haemoglobin ß-chains to glycated haemoglobin (HbA_{1c}). As the life span of the red blood cells is approximately 120 days, the quantification of HbA_{1c} serves as an important index of diabetes control. The clinically relevant measuring range extends from 100 to 500 µM [138–140].

MIPs for the determination of glycated haemoglobin are based on two different approaches: (1) The N-terminal fructosyl valine which is formed by proteolysis of the glycated ß-chain by proteinase K is used as the target for bulk imprinting. Sode et al. applied methylvaline as the target analogue, polyvinylimidazole as functional monomer and phenazine methosulphate as the mediator in an amperometric sensor [141]. Our group developed a MIP thermistor with a column containing a bulk polymer which was imprinted by the fructosyl valine-boronic acid ester [142]. Chuang et al. described a potentiometric sensor for fructosyl valine which combines the analyte recognition by a poly-aminophenylboronic acid layer and the signal generation by an indium-doped tin oxide (ITO) electrode [143]. (2) Piletsky's group grafted microtiter plate wells with MIPs for both non-glycated Hb (Hb_o) and HbA_{1c} by persulphate-initiated polymerization of aminophenylboronic acid in the presence of the respective protein [80]. The pseudo-peroxidatic activity was used for characterizing the rebinding of the proteins. The HbA_{1c}-MIP showed almost three times stronger affinity for its target as compared with that for Hb_o.

2.3.2 C-Reactive Protein: A Marker for Infections

C-reactive protein (CRP) is a homopentamer of five identical non-covalently bound subunits, each bearing a binding site for phosphocholine (PC). For healthy persons the CRP level in blood is normally below 1 mg L^{-1}. It increases upon inflammation to values as high as 100 mg L^{-1}. For patients with bacterial infections, autoimmune diseases and cancer, it is even higher. For cardiovascular risk the CRP level is between 1 and 5 mg L^{-1}. CRP has been used as a general marker for health [144, 145]. Current methods for CRP determination use mostly immunological techniques.

Artificial CRP receptors have been developed which use the high affinity between CRP and PC. For this reason PC-conjugated surface-active polymerizable molecules have been prepared and integrated into supported lipid monolayers

[146]. By using 3(4)-vinylbenzyl-12-phosphorylcholine dodecanoate, a MIP for CRP was prepared at the oil-water interface by photopolymerization. The rebinding was measured by applying a HRP-conjugated CRP antibody. The bound CRP was displaced by addition of free PC into the solution. An imprinting factor of 6.9 was obtained, and the MIP showed good selectivity to the template CRP as compared with other serum proteins. However, the low mechanical stability and the need of a detection antibody are marked disadvantages.

A MIP for CRP has been prepared by micro-contact imprinting using *O*-(-4-nitrophenylphosphoryl)choline – an analogue of PC – as the template. The imprinting factor for CRP was almost three and the binding of the target four times stronger than for human serum albumin [86].

2.3.3 Acetylcholine Esterase: A Potential Biomarker in Alzheimer's Disease

The causes of Alzheimer's disease (AD), the most common form of dementia, are still not fully uncovered, and no cure exists. It has been reported that the progression of AD is accompanied by an alteration in acetylcholinesterase (AChE) activity and a change in the glycosylation pattern [147, 148].

A hybrid MIP was presented as a first step towards a sensor system that could effectively detect and discriminate different AChE species and simultaneously determine the enzymatic activity [102]. As a model template for human AChE which mostly exists as a tetramer in the brain, the tetrameric enzyme from *Electrophorus electricus* (280 kDa) was chosen in this study, sharing 88.5% sequence similarity.

The enzyme was orientedly immobilized on top of a self-assembled monolayer terminated by the reversible ligand propidium (Prop-SAM) that was reported to bind via the peripheral anionic site (PAS) [149]. After electrosynthesis of a negatively charged ultrathin imprinted cover layer consisting of a carboxylate-modified derivative of 3,4-propylenedioxythiophene, the resulting MIP enabled detection of AChE via its retained enzymatic activity. Competitive analyses with ligands of the PAS side (propidium and amyloid-β peptide 42) indicated that AChE binding to the Prop-SAM/MIP hybrid is dominated by the interaction of the PAS with the propidium moiety, resulting in comparable affinity constants on the surface and in solution. On the other hand, the imprinted polymer layer acts as a shape-specific filter by permitting full access to the propidium layer and effectively suppressing the binding of other negatively charged proteins (BSA and urease) which strongly bound to the solely Prop-SAM. This synergism of the hybrid system with signal generation exclusively by the AChE provides the prerequisite to enable application in complex protein-containing samples, like cerebrospinal fluid (see Fig. 10).

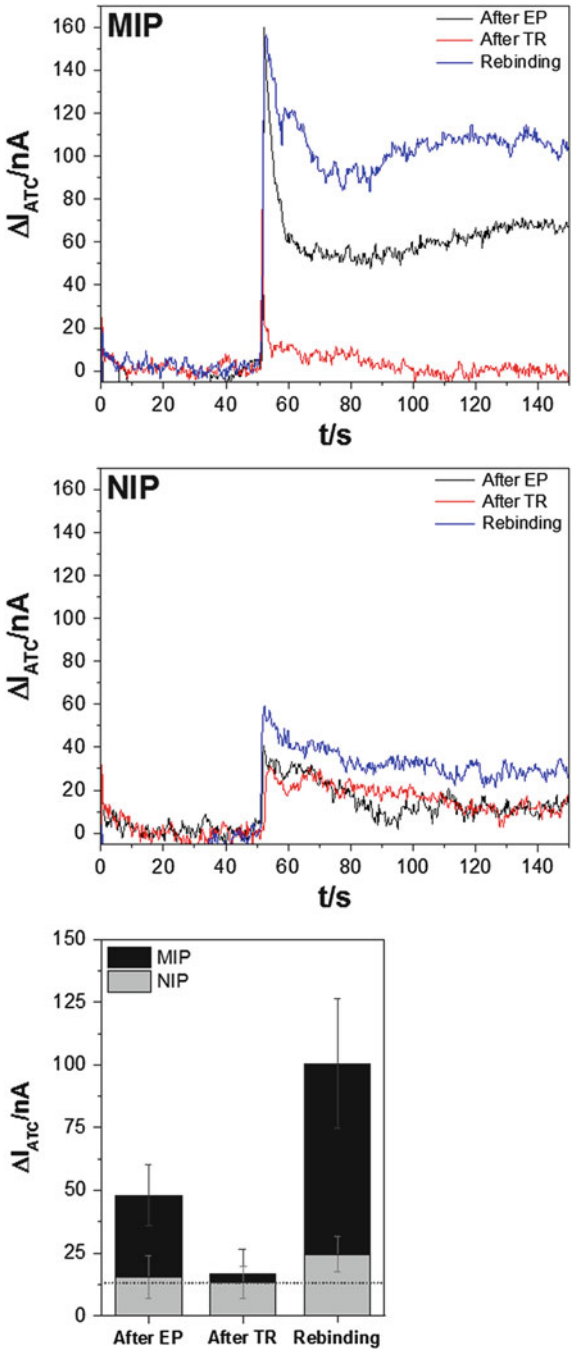

Fig. 10 Rebinding capacity of MIP and NIP sensors for AChE. *Left* and *middle*: Time-current curve of a representative electrode, modified once with a MIP (*left*) and once with a NIP (*middle*)

2.3.4 Ferritin: A Marker for Iron Storage and Inflammation

The major function of the 450 kDa multimeric ferritin is the intracellular storage of iron, and thus its level is a marker of iron deficiency or overload [150]. In serum (normal cut-off 12–15 μg L^{-1}), ferritin serves mainly as a marker for cell damage and is also altered in acute phase reactions and therefore used as an inflammatory biomarker [151, 152]. Britt et al. were the first to prepare a two-dimensional imprint against the biomarker ferritin [153, 154]. The protein was adsorbed in a multicomponent self-assembled ternary lipid film at the air/water interface. Protein-specific binding sides were introduced to the monolayer as local charge patterns by reorganization of the lipid monolayer according to the surface charge of ferritin. Due to transfer of the mixed films prepared in presence and absence of ferritin to hydrophobically modified QCM substrates, the reorientation was stopped, and increased rebinding of the target to the imprinted films could be detected. These cavities were further visualized by AFM and could not be detected in the blank films. For investigation of selectivity, ferritin-imprinted films were incubated with bovine serum albumin, showing only low binding.

Cai et al. created an ultrasensitive label-free nanosensor for ferritin composed of carbon nanotube arrays that were exclusively imprinted on their tips with a non-conducting polyphenol nanocoating [67]. The thickness of the polyphenol film (13 nm) was determined by transmission electron microscopy to be comparable to the dimensions of the template. Based on electrochemical impedance spectroscopy, the sensor detected ferritin with subpicogram-per-litre sensitivity and good selectivity towards BSA.

In 2013, Bosserdt et al. introduced microelectrospotting for the design of microarray-based sensor platforms for multiplexed protein detection using ferritin as proof-of-principle candidate [72]. Non-conductive nanolayers of scopoletin were deposited from a monomer-template mixture on top of gold surface plasmon resonance chips and allowed label-free imaging of removal and rebinding kinetics in real time. This sensor setup might be, besides medical application, very useful for future protein MIP design allowing high throughput synthesis and testing of the established materials.

Recently, Patra et al. prepared a surface-imprinted MIP for ferritin based on silver/cadmium sulphide core-shell nanoparticles for dual optical and electrochemical read-out [55]. After capping with a vinyl derivative of cysteine, polymerization was enabled by mixing of the nanoparticles with the template and monomer ethylene glycol dimethylacrylate (EGDMA) before the addition of the initiator ($CuCl_2$ and bipyridyl). This mixture was drop-coated onto vinyl silane modified

Fig. 10 (continued) layer after electropolymerization (EP), template removal (TR) and incubation with AChE to detect rebinding. (*Right*) Comparison of the average oxidation currents for acetylthiocholine of MIP and NIP sensors. The *dotted line* indicates the value of spontaneous unspecific hydrolysis of the substrate. (Adapted from [174])

pencil graphite electrodes, and the obtained sensors allowed detection of ferritin in the microgram-per-litre range indicated by electrochemical (CV, EIS, DPV, chronocoulometry) and spectroscopic (fluorescence) means. Testing of this ferritin sensor with real samples using blood serum of five women and men led to satisfying recoveries.

2.3.5 Transferrin: A Marker for Alcohol Abuse

Transferrin is an iron-transport glycoprotein with a molecular weight of 74 kDa consisting of two homologous domains, each bearing one single iron-binding site [155]. It exists in several isoforms according to its number of terminal sialic acid residues. Isoforms lacking one or two of these residues are collectively referred to as carbohydrate-deficient transferrin (CDT) and have clinical relevance as alcoholism biomarkers for screening and disease monitoring, as their plasma level usually increases due to chronic heavy alcohol abuse [156]. The physiological concentration in human plasma is around 2,500 mg L^{-1} [157].

As one of the first MIPs for a protein, Glad et al. introduced in 1985 a transferrin-imprinted polymer on porous silica support that addressed surface-exposed glycans [19]. A mixture of silanes including a boronate-based monomer led to a polysiloxane MIP showing affinity for transferrin.

Following this route, the group of Liu introduced UV-initiated photolithographic molecular imprinting based on boronate affinity as a general approach for the imprinting of glycoproteins [84]. The complete imprinting process was carried out within 3 h using 4-vinylphenylboronic acid as the only functional monomer and polyethylene glycol diacrylate as cross-linker. After mixing with the template at basic pH to favour its affinity binding to the boronate, the obtained pre-polymer solution was transferred onto the surface of a masked solid substrate to create macroporous molecularly imprinted arrays. Due to exposure to UV light, thin polymer layers were deposited in extremely short time which is assumed to prevent conformational changes of the template. Removal of the mask and the template resulted in sensors that were able to detect transferrin with exceptional selectivity as analysed by matrix-assisted laser desorption ionization time-of-flight mass spectrometry (MALDI-TOF MS). The approach was further developed as Wang et al. proposed in 2014 to use the boronic acid moiety as an affinity anchor for oriented covalent immobilization of the template prior surface imprinting [100]. Thin hydrophilic layers of dopamine and *m*-aminophenylboronic acid were prepared by in-water self-copolymerization. Inclusion of dopamine into the polymer network significantly reduced the number of unreacted boronic acid groups and thereby the unspecific binding. The template could be removed by incubation in acidic solution and sodium dodecyl sulphate. The obtained sensor could specifically detect transferrin in a complex real sample of human serum containing interfering proteins, like human serum albumin and immunoglobulin G, but also smaller competitive substances such as sugars.

An approach for hierarchical imprinting of transferrin was developed by Li et al. [51]. Before imprinting inside porous silica beads employing a mixture of 1,4-bis (acryloyl)piperazine, methacrylamide, methacrylic acid, ammonium sulphate and polyoxyethylenesorbitan monolaurate, the template was immobilized by non-covalent absorption. Polymerization was executed, and subsequent etching of the silica matrix resulted in surface-exposed imprinted cavities. The polymer beads recognized transferrin within 10 min and possessed a binding capacity of 6.3 mg of protein per gram of imprinted material. Good selectivity was detected towards interfering proteins (ribonuclease B, cytochrome *c* and β-lactoglobulin).

Recently, a plasmonic MIP nanosensor for transferrin has been prepared by self-polymerizing dopamine around the protein which was attached on the surface of gold nanorods [56]. The template was removed using 10% SDS solution, and rebinding was quantified by surface-enhanced Raman scattering. The authors determined a limit of detection of 10 nM, and the imprinting factor was almost 4. The cross-reactivity towards HSA and lysozyme was about 25%.

2.3.6 HIV-1-Related Glycoprotein 41

The human immunodeficiency virus type 1 (HIV-1)-related protein (glycoprotein 41, gp41) is a parameter for characterizing the progression of HIV-1 disease. It consists of 613 amino acids and is involved in the fusion of the virus with the infected cell [158–161].

Lu et al. developed a QCM-based sensor by using the epitope approach [111]. A mixture of dopamine and the C-terminal peptide of gP41 consisting of 35 residues (579–613) was deposited by self-polymerization on the surface of the QCM electrode. In contrast to the original concept of epitope imprinting which applied the target immobilized on a surface, this procedure generates cavities with random images of the target. Nevertheless, the holoprotein gp41 was recognized by the epitope-imprinted MIP layer which resulted in a linear dependence of the frequency shift between 5 and 200 ng mL^{-1} with a lower limit of detection of 2 ng mL^{-1}. The K_d value for gp41 was calculated to be 3.17 nM. The authors found a recovery for gp41 in spiked urine samples in the range of 87–94% and claim the applicability in real samples.

2.3.7 Procalcitonin: A Sepsis Marker

Procalcitonin is a protein with a molecular weight of 13 kDa which has a typical concentration of 0.1 ng mL^{-1} in the blood of healthy persons. Its concentration can rise over 100 ng mL^{-1} for bacterial sepsis. Therefore, it is a promising biomarker for the identification of the origin and severity of sepsis [162–164].

The target procalcitonin was first bound onto a (3-aminopropyl)triethoxysilane-activated glass slide, which was later on contacted with the gold electrode of a SPR chip. The MIP was formed by polymerizing 2-hydroxyethyl methacrylate (HEMA)

as the functional monomer and EGDMA as the cross-linker around the template molecules [92]. After the polymerization the glass slide was removed, and the micro-contact imprinted polymer film on the SPR chip was washed with 1M NaOH solution. The resonance signal of the SPR sensor depended linearly on the target concentration in the region between 20 and 1,000 ng mL^{-1}. Based on a low cross-reactivity, the MIP sensor showed a good correlation to a standard ELISA in simulated blood plasma.

2.3.8 Immunoglobulin G: Indicator of the Immune Status

Immunoglobulin G (IgG) is a y-shaped tetrameric glycoprotein with a molecular weight of 150 kDa consisting of two identical subunits made up from four peptide chains (two identical heavy and light chains, respectively). The arms of the IgG molecule containing the antigen binding sites are called Fab. It is found in blood and other body fluids, and it recognizes and neutralizes foreign molecules and particles by forming immuno-complexes. The immune system of vertebrates has a variability of 10^{12} different species in four heavy chain subclasses [165, 166].

Denizli pioneered the development of MIPs for the recognition of IgG. They applied the Fab fragment of IgG as the target of a SPR-based MIP sensor [109]. HEMA and EGDMA were used as functional monomer and cross-linker, respectively, to synthesize the imprinted nanofilm. This Fab-imprinted polymer layer was able to bind both the template and the IgG molecule. The concentration dependence for IgG has two linear sections in the semi-logarithmic plot between 0 and 1 mg mL^{-1} and between 0.1 and 1 mg mL^{-1}, which are interpreted by the authors on the basis of different modes of IgG binding. The low cross-reactivity of the MIP allowed for IgG measurements in 20,000 times diluted human serum samples (see Fig. 11).

IgG was imprinted as the holoprotein by Öpik's group [97, 103]. IgG was covalently immobilized by a linker of 4-thio aminophenol and (3,3′-dithiobis (sulfosuccinimidyl propionate)) via a cleavable disulphide bond to the surface of a gold electrode of a QCM chip. The polymer film was formed by electrodeposition of an almost 17 nm thin film of polydopamine around the template. This MIP sensor had an imprinting factor of (only) 1.66 and a binding constant of 296 nM.

Recently, quantum-dots-encoded microbeads were covered with a poly-dopamine layer by self-polymerization in the presence of IgG [57]. Binding of the target to these core-shell particles covered with the MIP layer generated a fluorescence signal which was almost twice as high as for HSA.

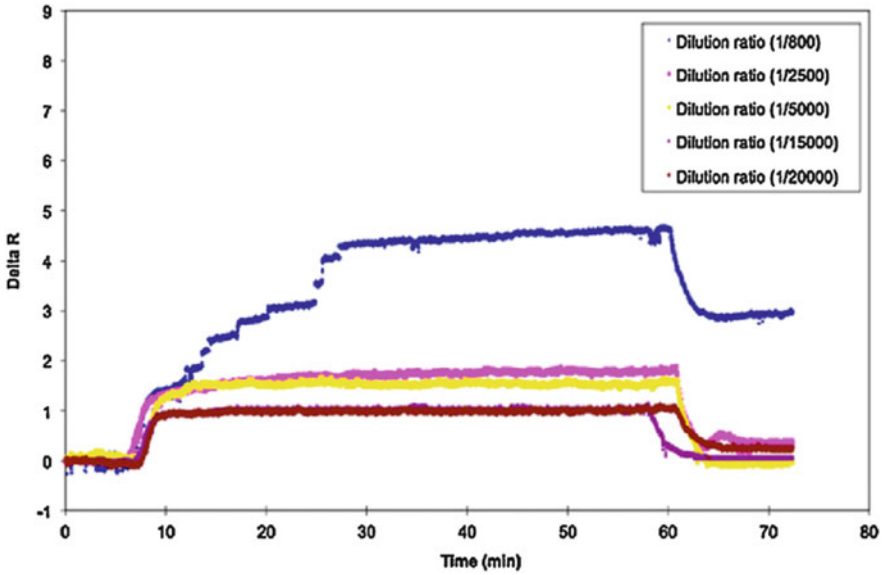

Fig. 11 Detection of IgG by a Fab-imprinted SPR chip from diluted human plasma. With increasing dilution ratio, the response of the sensor decreased. The lowest applied concentration of IgG that could be detected by the MIP sensor was approximately 0.64 g/mL (in 20,000 times diluted human plasma). (Reprinted with permission [109])

3 Conclusions

As compared with antibodies, MIPs have been prepared only for a restricted spectrum of proteins. Almost half of the papers still use haemoglobin, serum albumins and avidin as model templates. Point-of-care detection of marker proteins for cardiac, cancer, Alzheimer's disease or virus infections is the prospective aim. Many protein MIPs have been tested in artificial urine or spiked semi-synthetic plasma. In spite of several reports claiming close to routine applicability, MIPs need still substantial improvements of the operational parameters.

The most important parameters characterizing the performance of all affinity sensors are the affinity and selectivity of the recognition element towards the target analyte which determine the dynamic concentration range including the limit of detection and the cross-reactivity. Low-molecular-weight targets are usually completely embedded in the MIP matrix (bulk imprinting); thus, strong interactions with the surrounding polymer ensure target binding with high affinities. The film thickness of surface-imprinted protein MIPs is typically smaller than the diameter of the target molecule; thus, interaction with the polymer is restricted to a fraction of the macromolecular target and affinity constants for non-covalent MIPs could hardly reach the sub-nanomolar region. Furthermore, physicochemical investigations of the pre-polymerization mixture and target binding as well as quantum

chemical modelling showed that selectivity is more related to the shape than to the interaction of functional groups in the cavities and on the target [22, 23].

Non-specific binding of the protein target to the non-imprinted part of the MIP layer can falsify the measured results. For SPR and QCM, the signal reflects overall changes of mass or refractive index of the recognition layer, which can be induced not only by the target but also by non-specific adsorption or changes of the polymer layer, i.e. swelling or shrinking. Changes in the ionic strength of the measuring medium can influence the electrostatic interactions; therefore, its control is essential [72]. Inclusion of antifouling groups during polymerization or after template removal has been proven to suppress the non-specific interactions [167].

The evaluation of changes in permeability of the nano- and microporous ultrathin MIP layer seems to cause specific problems. As listed in this chapter, application of redox markers for the read-out of protein MIPs is dominating and has been used for a large spectrum of MIP sensors. In these studies the permeation of a redox probe, e.g. mostly ferri-/ferrocyanide, through the MIP film is monitored by cyclic voltammetry, differential pulse voltammetry or impedance spectroscopy. It is plausible that formation of cavities by removal of the template and refilling of these binding sites can change the electrochemical signals of the redox probe. Obviously, this method is very helpful to characterize the different steps of MIP preparation. However, several problems arise in the quantitative evaluation of the analyte concentration using this method: A disadvantage is that at low target concentrations, minute decreases in the current are to be detected in a large base current. Crucial problems are caused by the spontaneous adsorption of the protein target at the electrode surface and changes of the polymer structure by the rebinding [168]. Both processes will overlay the effect of the target binding to the MIP. Using this method, lower limits of detection in the picomolar range or even lower and measuring ranges over more than four decades of target concentration (for both low- and high-molecular-weight targets) have been reported. An explanation for these results may be that the detection scheme resembles to that of ion channel sensors with semi-logarithmic concentration dependence and dynamic range over several orders of magnitude [169].

The measurement of direct effects caused by target binding to the MIP sensor, like FTIR and Raman spectroscopy, direct electron transfer of electro-active target proteins or the activity of biocatalysts seems more straightforward than the application of redox markers [96, 170].

As compared with antibodies, MIPs have higher chemical and thermal stability, and they can be regenerated for repeated measurements. Further advantages are the simultaneous recognition of different targets in multi-target MIPs [171]. Monomolecular nanoparticle MIPs offer an effective alternative to ultrathin MIP films [172]. Further progress is expected by the spatial combination of an aptamer with a MIP for summing up the affinity and specificity of both components [104]. In addition, integration of nanoparticles and of graphene structures has been demonstrated to boost the analytical performance [173]. Following this route, MIPs will become useful compliments for antibodies and enzymes in bioanalysis.

Acknowledgements The authors gratefully acknowledge financial support from the Deutsche Forschungsgemeinschaft (DFG) within the framework of the German Excellence Initiative UniCat (EXC 314), ERA-Chemistry (2014, 61133) and Turkish-German University Scientific Research Projects Commission under the grant No. 2016BF0011 for financial support.

References

1. Atkinson AJJ, Colburn WA, DeGruttola VG, DeMets DL, Downing GJ, Hoth DF, Oates JA, Peck CC, Schooley RT, Spilker BA, Woodcock J, Zeger SL (2001) Biomarkers and surrogate endpoints: preferred definitions and conceptual framework. Clin Pharmacol Ther 69:89–95
2. Ingvarsson J, Wingren C, Carlsson A, Ellmark P, Wahren B, Engström G, Harmenberg U, Krogh M, Peterson C, Borrebaeck CAK (2008) Detection of pancreatic cancer using antibody microarray-based serum protein profiling. Proteomics 8:2211–2219
3. Darmanis S, Nong RY, Hammond M, Gu J, Alderborn A, Vänelid J, Siegbahn A, Gustafsdottir S, Ericsson O, Landegren U, Kamali-Moghaddam M (2010) Sensitive plasma protein analysis by microparticle-based proximity ligation assays. Mol Cell Proteomics 9: 327–335
4. Powers AD, Palecek SP (2012) Protein analytical assays for diagnosing, monitoring, and choosing treatment for cancer patients. J Healthcare Eng 3:503–534
5. Visintin I, Feng Z, Longton G, Ward DC, Alvero AB, Lai Y, Tenthorey J, Leiser A, Flores-Saaib R, Yu H, Azori M, Rutherford T, Schwartz PE, Mor G (2008) Diagnostic markers for early detection of ovarian cancer. Clin Cancer Res 14:1065–1072
6. Engvall E, Perlmann P (1971) Enzyme-linked immunosorbent assay (ELISA) quantitative assay of immunoglobulin G. Immunochemistry 8:871–874
7. Van Weemen BK, Schuurs AHWM (1971) Immunoassay using antigen-enzyme conjugates. FEBS Lett 15:232–236
8. Lequin R (2005) Enzyme immunoassay (EIA)/enzyme-linked immunosorbent assay (ELISA). Clin Chem 51:2415–2418
9. Huang RP (2001) Simultaneous detection of multiple proteins with an array-based enzyme-linked immunosorbent assay (ELISA) and enhanced chemiluminescence (ECL). Clin Chem Lab Med 39:209–214
10. Rissin DM, Kan CW, Campbell TG, Howes SC, Fournier DR, Song L, Piech T, Patel PP, Chang L, Rivnak AJ, Ferrell EP, Randall JD, Provuncher GK, Walt DR, Duffy DC (2010) Single-molecule enzyme-linked immunosorbent assay detects serum proteins at subfemtomolar concentrations. Nat Biotechnol 28:595–599
11. Li C, Yang Y, Wu D, Li T, Yin Y, Li G (2016) Improvement of enzyme-linked immunosorbent assay for the multicolor detection of biomarkers. Chem Sci 7:3011–3016
12. Wulff G, Sarhan A (1972) Use of polymers with enzyme-analogous structures for resolution of racemates. Angew Chem Int Ed 11:341–344
13. Shea K, Thompson E (1980) Template synthesis of macromolecules. Synthesis and chemistry of functionalized macroporous poly (divinylbenzene). Am Chem Soc 102:3148–3156
14. Arshady R, Mosbach K (1981) Synthesis of substrate selective polymers by host guest polymerization. Macromol Chem Phys 182:687–692
15. Mosbach K (1994) Molecular imprinting. Trends Biochem Sci 19:9–14
16. Haupt K, Mosbach K (1998) Plastic antibodies: developments and applications. Trends Biotechnol 16:468–475
17. Haupt K (2003) Molecularly imprinted polymers: the next generation. Anal Chem 75: 376A–383A

18. Wulff G, Grobe-Einsler R, Vesper W, Sarhan A (1977) Enzyme-analogue built polymers, 4. On the synthesis of polymers containing chiral cavities and their use for the resolution of racemates. Makromol Chem 178:2799–2816
19. Glad M, Norrlöw O, Sellergren B, Siegbahn N, Mosbach K (1985) Use of silane monomers for molecular imprinting and enzyme entrapment in polysiloxane-coated porous silica. J Chromatogr A 347:11–23
20. Norrlöw O, Glad M, Mosbach K (1984) Acrylic polymer preparations containing recognition sites obtained by imprinting with substrates. J Chromatogr A 299:29–41
21. Haupt K (2003) Imprinted polymers-tailor-made mimics of antibodies and receptors. Chem Commun 2003:171–178
22. Dorkó Z, Szakolczai A, Tamás B, Verbíc T, Horvai G (2016) A novel interpretation of noncovalent molecularly imprinting. In: 9th international conference on molecular imprinting, Lund, Sweden, O-16
23. Dorkó Z, Szakolczai A, Verbic T, Horvai G (2015) Binding capacity of molecularly imprinted polymers and their nonimprinted analogs. J Sep Sci 38:4240–4247
24. Alexander C, Andersson HS, Andersson LI, Ansell RJ, Kirsch N, Nicholls IA, O'Mahony J, Whitcombe MJ (2006) Molecular imprinting science and technology: a survey of the literature for the years up to and including 2003. J Mol Recognit 19:106–180
25. Turner NW, Jeans CW, Brain KR, Allender CJ, Hlady V, Britt DW (2006) From 3D to 2D: a review of the molecular imprinting of proteins. Biotechnol Prog 22:1474–1489
26. Hansen DE (2007) Recent developments in the molecular imprinting of proteins. Biomaterials 28:4178–4191
27. Janiak DS, Kofinas P (2007) Molecular imprinting of peptides and proteins in aqueous media. Anal Bioanal Chem 389:399–404
28. Takeuchi T, Hishiya T (2008) Molecular imprinting of proteins emerging as a tool for protein recognition. Org Biomol Chem 6:2459–2467
29. Whitcombe MJ, Chianella I, Larcombe L, Piletsky SA, Noble J, Porter R, Horgan A (2011) The rational development of molecularly imprinted polymer-based sensors for protein detection. Chem Soc Rev 40:1547–1571
30. Yang K, Zhang L, Liang Z, Zhang Y (2012) Protein-imprinted materials: rational design, application and challenges. Anal Bioanal Chem 403:2173–2183
31. Whitcombe MJ, Kirsch N, Nicholls IA (2014) Molecular imprinting science and technology: a survey of the literature for the years 2004–2011. J Mol Recognit 27:297–410
32. Li S, Cao S, Whitcombe MJ, Piletsky SA (2014) Size matters: challenges in imprinting macromolecules. Prog Polym Sci 39:145–163
33. Erdőssy J, Horváth V, Yarman A, Scheller FW, Gyurcsányi RE (2016) Electrosynthesized molecularly imprinted polymers for protein recognition. TrAC Trends Anal Chem 79: 179–190
34. Menger M, Yarman A, Erdőssy J, Yildiz HB, Gyurcsányi RE, Scheller FW (2016) MIPs and aptamers for recognition of proteins in biomimetic sensing. Biosensors 6:35
35. Liao J-L, Wang Y, Hjertén S (1996) A novel support with artificially created recognition for the selective removal of proteins and for affinity chromatography. Chromatographia 42:259–262
36. Hjertén S, Liao J-L, Nakazato K, Wang Y, Zamaratskaia G, Zhang H-X (1997) Gels mimicking antibodies in their selective recognition of proteins. Chromatographia 44:227–234
37. Tong D, Heényi C, Bikádi Z, Gao J-P, Hjertén S (2001) Some studies of the chromatographic properties of gels ("artificial antibodies/receptors") for selective adsorption of proteins. Chromatographia 54:7–14
38. Ou SH, Wu MC, Chou TC, Liu CC (2004) Polyacrylamide gels with electrostatic functional groups for the molecular imprinting of lysozyme. Anal Chim Acta 504:163–166
39. Rezeli M, Kilár F, Hjertén S (2006) Monolithic beds of artificial gel antibodies. J Chromatogr A 1109:100–102

40. Takátsy A, Kilár A, Kilár F, Hjertén S (2006) Universal method for synthesis of artificial gel antibodies by the imprinting approach combined with a unique electrophoresis technique for detection of minute structural differences of proteins, viruses, and cells (bacteria): Ia. Gel antibodies against proteins (transferrins). J Sep Sci 29:2802–2809
41. Takátsy A, Végvári Á, Hjertén S, Kilár F (2007) Universal method for synthesis of artificial gel antibodies by the imprinting approach combined with a unique electrophoresis technique for detection of minute structural differences of proteins, viruses and cells (bacteria). Ib. Gel antibodies against proteins (hemoglobins). Electrophoresis 28:2345–2350
42. Vaihinger D, Landfester K, Kräuter I, Brunner H, Tovar GEM (2002) Molecularly imprinted polymer nanospheres as synthetic affinity receptors obtained by miniemulsion polymerisation. Macromol Chem Phys 203:1965–1973
43. Tan CJ, Tong YW (2007) Preparation of superparamagnetic ribonuclease A surface-imprinted submicrometer particles for protein recognition in aqueous media. Anal Chem 79:299–306
44. Pan G, Guo Q, Cao C, Yang H, Li B (2013) Thermo-responsive molecularly imprinted nanogels for specific recognition and controlled release of proteins. Soft Matter 9:3840–3850
45. Pluhar B, Mizaikoff B (2015) Advanced evaluation strategies for protein-imprinted polymer nanobeads. Macromol Biosci 15:1507–1511
46. Burow M, Minoura N (1996) Molecular imprinting: synthesis of polymer particles with antibody-like binding characteristics for glucose oxidase. Biochem Biophys Res Commun 227:419–422
47. Li L, He X, Chen L, Zhang Y (2009) Preparation of novel bovine hemoglobin surface-imprinted polystyrene nanoparticles with magnetic susceptibility. Sci China Ser B Chem 52: 1402–1411
48. Zhou W-H, Lu C-H, Guo X-C, Chen F-R, Yang H-H, Wang X-R (2010) Mussel-inspired molecularly imprinted polymer coating superparamagnetic nanoparticles for protein recognition. J Mater Chem 20:880–883
49. He H, Fu G, Wang Y, Chai Z, Jiang Y, Chen Z (2010) Imprinting of protein over silica nanoparticles via surface graft copolymerization using low monomer concentration. Biosens Bioelectron 26:760–765
50. Zhang M, Zhang X, He X, Chen L, Zhang Y (2012) A self-assembled polydopamine film on the surface of magnetic nanoparticles for specific capture of protein. Nanoscale 4:3141–3147
51. Li Q, Yang K, Liu J, Zhang L, Liang Z, Zhang Y (2013) Transferrin recognition based on a protein imprinted material prepared by hierarchical imprinting technique. Microchim Acta 180:1379–1386
52. Nematollahzadeh A, Shojaei A, Abdekhodaie MJ, Sellergren B (2013) Molecularly imprinted polydopamine nano-layer on the pore surface of porous particles for protein capture in HPLC column. J Colloid Interface Sci 404:117–126
53. Xia Z, Lin Z, Xiao Y, Wang L, Zheng J, Yang H, Chen G (2013) Facile synthesis of polydopamine-coated molecularly imprinted silica nanoparticles for protein recognition and separation. Biosens Bioelectron 47:120–126
54. Li W, Sun Y, Yang C, Yan X, Guo H, Fu G (2015) Fabrication of surface protein-imprinted nanoparticles using a metal chelating monomer via aqueous precipitation polymerization. ACS Appl Mater Interfaces 7:27188–27196
55. Patra S, Roy E, Madhuri R, Sharma PK (2015) An imprinted Ag@CdS core shell nanoparticle based optical-electrochemical dual probe for trace level recognition of ferritin. Biosens Bioelectron 63:301–310
56. Lv Y, Qin Y, Svec F, Tan T (2016) Molecularly imprinted plasmonic nanosensor for selective SERS detection of protein biomarkers. Biosens Bioelectron 80:433–441
57. Liu Y, Liu L, He Y, He Q, Ma H (2016) Quantum-dots-encoded-microbeads based molecularly imprinted polymer. Biosens Bioelectron 77:886–893
58. Ambrosini S, Beyazit S, Haupt K, Tse Sum Bui B (2013) Solid-phase synthesis of molecularly imprinted nanoparticles for protein recognition. Chem Commun 49:6746–6748

59. Poma A, Guerreiro A, Caygill S, Moczko E, Piletsky S (2014) Automatic reactor for solid-phase synthesis of molecularly imprinted polymeric nanoparticles (MIP NPs) in water. RSC Adv 4:4203–4206
60. Xu J, Ambrosini S, Tamahkar E, Rossi C, Haupt K, Tse Sum Bui B (2016) Toward a universal method for preparing molecularly imprinted polymer nanoparticles with antibody-like affinity for proteins. Biomacromolecules 17:345–353
61. Canfarotta F, Poma A, Guerreiro A, Piletsky S (2016) Solid-phase synthesis of molecularly imprinted nanoparticles. Nat Protoc 11:443–455
62. Shiomi T, Matsui M, Mizukami F, Sakaguchi K (2005) A method for the molecular imprinting of hemoglobin on silica surfaces using silanes. Biomaterials 26:5564–5571
63. Bonini F, Piletsky S, Turner APF, Speghini A, Bossi A (2007) Surface imprinted beads for the recognition of human serum albumin. Biosens Bioelectron 22:2322–2328
64. Tan CJ, Chua HG, Ker KH, Tong Yen W (2008) Preparation of bovine serum albumin surface-imprinted submicrometer particles with magnetic susceptibility through core-shell miniemulsion polymerization. Anal Chem 80:683–692
65. Matsunaga T, Hishiya T, Takeuchi T (2007) Surface plasmon resonance sensor for lysozyme based on molecularly imprinted thin films. Anal Chim Acta 591:63–67
66. Menaker A, Syritski V, Reut J, Öpik A, Horváth V, Gyurcsányi RE (2009) Electrosynthesized surface-imprinted conducting polymer microrods for selective protein recognition. Adv Mater 21:2271–2275
67. Cai D, Ren L, Zhao H, Xu C, Zhang L, Yu Y, Wang H, Lan Y, Roberts MF, Chuang JH, Naughton MJ, Ren Z, Chiles TC (2010) A molecular-imprint nanosensor for ultrasensitive detection of proteins. Nat Nanotechnol 5:597–601
68. Lee M-H, Thomas JL, Tseng H-Y, Lin W-C, Liu B-D, Lin H-Y (2011) Sensing of digestive proteins in saliva with a molecularly imprinted poly(ethylene-co-vinyl alcohol) thin film coated quartz crystal microbalance sensor. ACS Appl Mater Interfaces 3:3064–3071
69. Reddy SM, Sette G, Phan Q (2011) Electrochemical probing of selective haemoglobin binding in hydrogel-based molecularly imprinted polymers. Electrochim Acta 56:9203–9208
70. Viswanathan S, Rani C, Ribeiro S, Delerue-Matos C (2012) Molecular imprinted nano-electrodes for ultra sensitive detection of ovarian cancer marker. Biosens Bioelectron 33: 179–183
71. Karimian N, Vagin M, Zavar MHA, Chamsaz M, Turner APF, Tiwari A (2013) An ultrasensitive molecularly-imprinted human cardiac troponin sensor. Biosens Bioelectron 50:492–498
72. Bosserdt M, Erdőssy J, Lautner G, Witt J, Köhler K, Gajovic-Eichelmann N, Yarman A, Wittstock G, Scheller FW, Gyurcsányi RE (2015) Microelectrospotting as a new method for electrosynthesis of surface-imprinted polymer microarrays for protein recognition. Biosens Bioelectron 73:123–129
73. Rebelo TSCR, Pereira CM, Sales MGF, Noronha JP, Silva F (2016) Protein imprinted material electrochemical sensor for determination of Annexin A3 in biological samples. Electrochim Acta 190:887–893
74. Rebelo TSCR, Pereira CM, Sales MGF, Noronha JP, Silva F (2016) Protein imprinted materials designed with charged binding sites on screen-printed electrode for microseminoprotein-beta determination in biological samples. Sensors Actuators B Chem 223:846–852
75. Moreira FTC, Ferreira MJMS, Puga JRT, Sales MGF (2016) Screen-printed electrode produced by printed-circuit board technology. Application to cancer biomarker detection by means of plastic antibody as sensing material. Sensors Actuators B Chem 223:927–935
76. Silva BVM, Rodríguez BAG, Sales GF, Sotomayor MDPT, Dutra RF (2016) An ultrasensitive human cardiac troponin T graphene screen-printed electrode based on electropolymerized-molecularly imprinted conducting polymer. Biosens Bioelectron 77: 978–985

77. Shumyantseva VV, Bulko TV, Sigolaeva LV, Kuzikov AV, Archakov AI (2016) Electrochemical analysis of myoglobin based on electropolymerized molecularly imprinted polymer poly-o-phenylenediamine and carbon nanotubes/screen printed electrode. Dokl Biochem Biophys 468:213–216
78. Shumyantseva VV, Bulko TV, Sigolaeva LV, Kuzikov AV, Archakov AI (2016) Electrosynthesis and binding properties of molecularly imprinted poly-o-phenylenediamine for selective recognition and direct electrochemical detection of myoglobin. Biosens Bioelectron 86:330–336
79. Pacheco JPG, Silva MSV, Freitas M, Nouws HPA, Delerue-Matos C (2016) Molecularly imprinted electrochemical sensor for the point-of-care detection of a breast cancer biomarker (CA 15-3). In: 9th international conference on molecular imprinting, Lund, Sweden, P2–45
80. Bossi A, Piletsky SA, Piletska EV, Righetti PG, Turner APF (2001) Surface-grafted molecularly imprinted polymers for protein recognition. Anal Chem 73:5281–5286
81. Rick J, Chou T-C (2005) Imprinting unique motifs formed from protein–protein associations. Anal Chim Acta 542:26–31
82. Rick J, Chou TC (2006) Using protein templates to direct the formation of thin-film polymer surfaces. Biosens Bioelectron 22:544–549
83. Turner NW, Liu X, Piletsky SA, Hlady V, Britt DW (2007) Recognition of conformational changes in beta-lactoglobulin by molecularly imprinted thin films. Biomacromolecules 8: 2781–2787
84. Li L, Lu Y, Bie Z, Chen H-Y, Liu Z (2013) Photolithographic boronate affinity molecular imprinting: a general and facile approach for glycoprotein imprinting. Angew Chem Int Ed 52:7451–7454
85. Ratner BD, Shi H, Tsai W-B, Garrison MD, Ferrari S (1999) Template-imprinted nanostructured surfaces for protein recognition. Nature 398:593–597
86. Chou PC, Rick J, Chou TC (2005) C-reactive protein thin-film molecularly imprinted polymers formed using a micro-contact approach. Anal Chim Acta 542:20–25
87. Hayden O, Lieberzeit PA, Blaas D, Dickert FL (2006) Artificial antibodies for bioanalyte detection – sensing viruses and proteins. Adv Funct Mater 16:1269–1278
88. Li Y, Yang HH, You QH, Zhuang ZX, Wang XR (2006) Protein recognition via surface molecularly imprinted polymer nanowires. Anal Chem 78:317–320
89. Lin HY, Hsu CY, Thomas JL, Wang SE, Chen HC, Chou TC (2006) The microcontact imprinting of proteins: the effect of cross-linking monomers for lysozyme, ribonuclease A and myoglobin. Biosens Bioelectron 22:534–543
90. Lin H-Y, Rick J, Chou T-C (2007) Optimizing the formulation of a myoglobin molecularly imprinted thin-film polymer – formed using a micro-contact imprinting method. Biosens Bioelectron 22:3293–3301
91. Kryscio DR, Peppas NA (2012) Surface imprinted thin polymer film systems with selective recognition for bovine serum albumin. Anal Chim Acta 718:109–115
92. Sener G, Ozgur E, Rad AY, Uzun L, Say R, Denizli A (2013) Rapid real-time detection of procalcitonin using a microcontact imprinted surface plasmon resonance biosensor. Analyst 138:6422–6428
93. Ertürk G, Hedström M, Mattiasson B (2016) A sensitive and real-time assay of trypsin by using molecular imprinting-based capacitive biosensor. Biosens Bioelectron 86:557–565
94. Kempe M, Glad M, Mosbach K (1995) An approach towards surface imprinting using the enzyme ribonuclease A. J Mol Recognit 8:35–39
95. Liu S, Bakovic L, Chen A (2006) Specific binding of glycoproteins with poly(aniline boronic acid) thin film. J Electroanal Chem 591:210–216
96. Bosserdt M, Gajovic-Eichelman N, Scheller FW (2013) Modulation of direct electron transfer of cytochrome c by use of a molecularly imprinted thin film. Anal Bioanal Chem 405:6437–6444

97. Tretjakov A, Syritski V, Reut J, Boroznjak R, Volobujeva O, Öpik A (2013) Surface molecularly imprinted polydopamine films for recognition of immunoglobulin G. Microchim Acta 180:1433–1442
98. Moreira FTC, Dutra RAF, Noronha JPC, Fernandes JCS, Sales MGF (2013) Novel biosensing device for point-of-care applications with plastic antibodies grown on Au-screen printed electrodes. Sensors Actuators B Chem 182:733–740
99. Moreira FTC, Sharma S, Dutra RAF, Noronha JPC, Cass AEG, Sales MGF (2013) Smart plastic antibody material (SPAM) tailored on disposable screen printed electrodes for protein recognition: application to myoglobin detection. Biosens Bioelectron 45:237–244
100. Wang S, Ye J, Bie Z, Liu Z (2014) Affinity-tunable specific recognition of glycoproteins via boronate affinity-based controllable oriented surface imprinting. Chem Sci 5:1135–1140
101. Dechtrirat D, Gajovic-Eichelmann N, Bier FF, Scheller FW (2014) Hybrid material for protein sensing based on electrosynthesized MIP on a mannose terminated self-assembled monolayer. Adv Funct Mater 24:2233–2239
102. Jetzschmann KJ, Jágerszki G, Dechtrirat D, Yarman A, Gajovic-Eichelmann N, Gilsing H-D, Schulz B, Gyurcsányi RE, Scheller FW (2015) Vectorially imprinted hybrid nanofilm for acetylcholinesterase recognition. Adv Funct Mater 25:5178–5183
103. Tretjakov A, Syritski V, Reut J, Boroznjak R, Öpik A (2016) Molecularly imprinted polymer film interfaced with surface acoustic wave technology as a sensing platform for label-free protein detection. Anal Chim Acta 902:182–188
104. Jolly P, Tamboli V, Harniman RL, Estrela P, Allender CJ, Bowen JL (2016) Aptamer-MIP hybrid receptor for highly sensitive electrochemical detection of prostate specific antigen. Biosens Bioelectron 75:188–195
105. Bognár J, Szucs J, Dorkõ Z, Horváth V, Gyurcsányi RE (2013) Nanosphere lithography as a versatile method to generate surface-imprinted polymer films for selective protein recognition. Adv Funct Mater 23:4703–4709
106. Rachkov A, Minoura N (2000) Recognition of oxytocin and oxytocin-related peptides in aqueous media using a molecularly imprinted polymer synthesized by the epitope approach. J Chromatogr A 889:111–118
107. Tai DF, Lin CY, Wu TZ, Chen LK (2005) Recognition of dengue virus protein using epitope-mediated molecularly imprinted film. Anal Chem 77:5140–5143
108. Nishino H, Huang CS, Shea KJ (2006) Selective protein capture by epitope imprinting. Angew Chem Int Ed 45:2393–2396
109. Ertürk G, Uzun L, Tümer MA, Say R, Denizli A (2011) Fab fragments imprinted SPR biosensor for real-time human immunoglobulin G detection. Biosens Bioelectron 28:97–104
110. Dechtrirat D, Jetzschmann KJ, Stöcklein WFM, Scheller FW, Gajovic-Eichelmann N (2012) Protein rebinding to a surface-confined imprint. Adv Funct Mater 22:5231–5237
111. Lu CH, Zhang Y, Tang SF, Fang ZB, Yang HH, Chen X, Chen GN (2012) Sensing HIV related protein using epitope imprinted hydrophilic polymer coated quartz crystal microbalance. Biosens Bioelectron 31:439–444
112. Lautner G, Kaev J, Reut J, Öpik A, Rappich J, Syritski V, Gyurcsányi RE (2011) Selective artificial receptors based on micropatterned surface-imprinted polymers for label-free detection of proteins by SPR imaging. Adv Funct Mater 21:591–597
113. El Kirat K, Bartkowski M, Haupt K (2009) Probing the recognition specificity of a protein molecularly imprinted polymer using force spectroscopy. Biosens Bioelectron 24:2618–2624
114. Moreira FTC, Sharma S, Dutra RAF, Noronha JPC, Cass AEG, Sales MGF (2014) Protein-responsive polymers for point-of-care detection of cardiac biomarker. Sensors Actuators B Chem 196:123–132
115. Rebelo TSCR, Santos C, Costa-Rodrigues J, Fernandes MH, Noronha JP, Sales MGF (2014) Novel prostate specific antigen plastic antibody designed with charged binding sites for an improved protein binding and its application in a biosensor of potentiometric transduction. Electrochim Acta 132:142–150

116. Zhao W, Chen Z, Xue B, Sun L, Luo A (2011) A biomimetic sensor for fast lysozyme detection. Adv Mater Res 239–242:283–287
117. Karimian N, Turner APF, Tiwari A (2014) Electrochemical evaluation of troponin T imprinted polymer receptor. Biosens Bioelectron 59:160–165
118. Cieplak M, Szwabinska K, Sosnowska M, Chandra BKC, Borowicz P, Noworyta K, D'Souza F, Kutner W (2015) Selective electrochemical sensing of human serum albumin by semi-covalent molecular imprinting. Biosens Bioelectron 74:960–966
119. Piletsky SA, Turner APF (2002) Electrochemical sensors based on molecularly imprinted polymers. Electroanalysis 14:317–323
120. Heidenreich A, Bastian P, Bellmunt J, Bolla M, Joniau S, Van Der Kwast T, Mason M, Matveev V, Wiegel T, Zattoni F, Mottet N (2014) JEAU guidelines on prostate cancer. Part 1: Screening, diagnosis, and local treatment with curative intent – update 2013. Eur Urol 65: 124–137
121. Heidenreich A, Bastian PJ, Bellmunt J, Bolla M, Joniau S, Van Der Kwast T, Mason M, Matveev V, Wiegel T, Zattoni F, Mottet N (2014) EAU guidelines on prostate cancer. Part II: Treatment of advanced, relapsing, and castration-resistant prostate cancer. Eur Urol 65:467–479
122. Hayes JH, Barry MJ (2014) Screening for prostate cancer with the prostate-specific antigen test. JAMA 311:1143–1149
123. Berek JS, Bast RC (1995) Ovarian cancer screening. The use of serial complementary tumor markers to improve sensitivity and specificity for early detection. Cancer 76:2092–2096
124. Peng NJ, Liou WS, Liu RS, Hu C, Tsay DG, Liu CB (2011) Early detection of recurrent ovarian cancer in patients with low-level increases in serum CA-125 levels by 2-[F-18]fluoro-2-deoxy-D-glucose-positron emission tomography/computed tomography. Cancer Biother Radiopharm 26:175–181
125. Comamala M, Pinard M, Thériault C, Matte I, Albert A, Boivin M, Beaudin J, Piché A, Rancourt C (2011) Downregulation of cell surface CA125/MUC16 induces epithelial-to-mesenchymal transition and restores EGFR signalling in NIH:OVCAR3 ovarian carcinoma cells. Br J Cancer 104:989–999
126. Coveney EC, Geraghty JG, Sherry F, McDermott EW, Fennelly JJ, O'Higgins NJ, Duffy MJ (1995) The clinical value of CEA and CA 15-3 in breast cancer management. Int J Biol Markers 10:35–41
127. Duffy MJ, Shering S, Sherry F, McDermott E, O'Higgins N (2000) CA 15-3: a prognostic marker in breast cancer. Int J Biol Markers 15:330–333
128. zur Hausen H (1999) Immortalization of human cells and their malignant conversion by high risk human papillomavirus genotypes. Semin Cancer Biol 9:405–411
129. zur Hausen H (2002) Papillomaviruses and cancer: from basic studies to clinical application. Nat Rev Cancer 2:342–350
130. DeFilippis RA, Goodwin EC, Wu L, DiMaio D (2003) Endogenous human papillomavirus E6 and E7 proteins differentially regulate proliferation, senescence, and apoptosis in HeLa cervical carcinoma cells. J Virol 77:1551–1563
131. Søreide K, Nedrebø BS, Knapp JC, Glomsaker TB, Søreide JA, Kørner H (2009) Evolving molecular classification by genomic and proteomic biomarkers in colorectal cancer: potential implications for the surgical oncologist. Surg Oncol 18:31–50
132. Tanaka T, Tanaka M, Tanaka T, Ishigamori R (2010) Biomarkers for colorectal cancer. Int J Mol Sci 11:3209–3225
133. O'Gara PT, Kushner FG, Ascheim DD, Casey DE, Chung MK, de Lemos JA, Ettinger SM, Fang JC, Fesmire FM, Franklin BA, Granger CB, Krumholz HM, Linderbaum JA, Morrow DA, Newby LK, Ornato JP, Ou N, Radford MJ, Tamis-Holland JE, Tommaso CL, Tracy CM, Woo YJ, Zhao DX (2013) 2013 ACCF/AHA guideline for the management of ST-elevation myocardial infarction: executive summary. J Am Coll Cardiol 61:485–510
134. Roffi M, Patrono C, Collet J-P, Mueller C, Valgimigli M, Andreotti F, Bax JJ, Borger MA, Brotons C, Chew DP, Gencer B, Hasenfuss G, Kjeldsen K, Lancellotti P, Landmesser U, Mehilli J, Mukherjee D, Storey RF, Windecker S (2016) 2015 ESC guidelines for the

management of acute coronary syndromes in patients presenting without persistent ST-segment elevation. Eur Heart J 37:267–315
135. Goldberg DM (2000) Proteases in the evaluation of pancreatic function and pancreatic disease. Clin Chim Acta 291:201–221
136. Hirota M, Ohmuraya M, Baba H (2006) The role of trypsin, trypsin inhibitor, and trypsin receptor in the onset and aggravation of pancreatitis. J Gastroenterol 41:832–836
137. Sarkar FH, Banerjee S, Li Y (2007) Pancreatic cancer: pathogenesis, prevention and treatment. Toxicol Appl Pharmacol 224:326–336
138. Reinauer H, Home PD, Kanagasabapathy AS, Heuck C-C (2002) Use of glycated haemoglobin (HbA1c) in the diagnosis of diabetes mellitus. In: Laboratory diagnosis and monitoring of diabetes mellitus. World Health Organization, Geneva, pp. 1–25
139. International Expert Committee, T. I. E (2009) International Expert Committee report on the role of the A1C assay in the diagnosis of diabetes. Diabetes Care 32:1327–1334
140. Malkani S, Mordes JP (2011) Implications of using hemoglobin A1C for diagnosing diabetes mellitus. Am J Med 124:395–401
141. Sode K, Ohta S, Yanai Y, Yamazaki T (2003) Construction of a molecular imprinting catalyst using target analogue template and its application for an amperometric fructosylamine sensor. Biosens Bioelectron 18:1485–1490
142. Rajkumar R, Warsinke A, Möhwald H, Scheller F, Katterle M (2007) Development of fructosyl valine binding polymers by covalent imprinting. Biosens Bioelectron 22:3318–3325
143. Chuang SW, Rick J, Chou TC (2009) Electrochemical characterisation of a conductive polymer molecularly imprinted with an Amadori compound. Biosens Bioelectron 24:3170–3173
144. Yeh ETH, Willerson JT (2003) Coming of age of C-reactive protein. Circulation 107:370–371
145. Pepys MB, Hirschfield GM, Tennent GA, Gallimore JR, Kahan MC, Bellotti V, Hawkins PN, Myers RM, Smith MD, Polara A, Cobb AJA, Ley SV, Aquilina JA, Robinson CV, Sharif I, Gray GA, Sabin CA, Jenvey MC, Kolstoe SE, Thompson D, Wood SP (2006) Targeting C-reactive protein for the treatment of cardiovascular disease. Nature 440:1217–1221
146. Kim E, Kim H-C, Lee SG, Lee SJ, Go T-J, Baek CS, Jeong SW (2011) C-reactive protein-directed immobilization of phosphocholine ligands on a solid surface. Chem Commun 47:11900–11902
147. Saez-Valero J, Barquero MS, Marcos A, McLean CA, Small DH (2000) Altered glycosylation of acetylcholinesterase in lumbar cerebrospinal fluid of patients with Alzheimer's disease. J Neurol Neurosurg Psychiatry 69:664–667
148. Carvajal FJ, Inestrosa NC (2011) Interactions of AChE with Aβ aggregates in Alzheimer's brain: therapeutic relevance of IDN 5706. Front Mol Neurosci 4:19
149. Halámek J, Teller C, Žeravík J, Fournier D, Makower A, Scheller FW (2006) Characterization of binding of cholinesterases to surface immobilized ligands. Anal Lett 39:1491–1502
150. Arosio P, Ingrassia R, Cavadini PF (2009) A family of molecules for iron storage, antioxidation and more. Biochim Biophys Acta, Gen Subj 1790:589–599
151. Beard JL, Murray-Kolb LE, Rosales FJ, Solomons NW, Angelilli ML (2006) Interpretation of serum ferritin concentrations as indicators of total-body iron stores in survey populations: the role of biomarkers for the acute phase response. Am J Clin Nutr 84:1498–1505
152. Kell DB, Pretorius E (2014) Serum ferritin is an important inflammatory disease marker, as it is mainly a leakage product from damaged cells. Metallomics 6:748–773
153. Dhruv H, Pepalla R, Taveras M, Britt DW (2006) Protein insertion and patterning of PEG bearing Langmuir monolayers. Biotechnol Prog 22:150–155
154. Turner NW, Wright BE, Hlady V, Britt DW (2007) Formation of protein molecular imprints within Langmuir monolayers: a quartz crystal microbalance study. J Colloid Interface Sci 308:71–80
155. Legrand D, Mazurier J, Montreuil J, Spik G (1988) Structure and spatial conformation of the iron-binding sites of transferrins. Biochimie 70:1185–1195
156. Arndt T (2001) Carbohydrate-deficient transferrin as a marker of chronic alcohol abuse: a critical review of preanalysis, analysis, and interpretation. Clin Chem 47:13–27

157. Welch S (1992) Transferrin structure and iron binding. In: Transferrin: the iron carrier, 1st edn. CRC Press, Florida, pp. 64–65
158. Chan DC, Chutkowski CT, Kim PS (1998) Evidence that a prominent cavity in the coiled coil of HIV type 1 gp41 is an attractive drug target. Med Sci 95:15613–15617
159. Contreras LM, Aranda FJ, Gavilanes F, González-Ros JM, Villalain J (2001) Structure and interaction with membrane model systems of a peptide derived from the major epitope region of HIV protein gp41: implications on viral fusion mechanism. Biochemistry 40:3196–3207
160. Dwyer JJ, Hasan A, Wilson KL, White JM, Matthews TJ, Delmedico MK (2003) The hydrophobic pocket contributes to the structural stability of the N-terminal coiled coil of HIV gp41 but is not required for six-helix bundle formation. Biochemistry 42:4945–4953
161. Burton DR, Desrosiers RC, Doms RW, Koff WC, Kwong PD, Moore JP, Nabel GJ, Sodroski J, Wilson IA, Wyatt RT (2004) HIV vaccine design and the neutralizing antibody problem. Nat Immunol 5:233–236
162. Gerard Y, Hober D, Assicot M, Alfandari S, Ajana F, Bourez JM, Chidiac C, Mouton Y, Bohuon C, Wattre P (1997) Procalcitonin as a marker of bacterial sepsis in patients infected with HIV-1. J Infect 35:41–46
163. Han YY, Doughty LA, Kofos D, Sasser H, Carcillo JA (2003) Procalcitonin is persistently increased among children with poor outcome from bacterial sepsis. Pediatr Crit Care Med 4: 21–25
164. Becker KL, Snider R, Nylen ES (2008) Procalcitonin assay in systemic inflammation, infection, and sepsis: clinical utility and limitations. Crit Care Med 36:941–952
165. Schur PH (1987) IgG subclasses: a review. Ann Allergy 58:89–96. 99
166. Meulenbroek AJ (1996) Human IgG subclasses: useful diagnostic markers for immunocompetence, 2nd edn. CLB, Amsterdam, pp. 1–52
167. Li X, Zhang B, Tian L, Li W, Zhang H, Zhang Q (2015) Improvement of recognition specificity of surface protein-imprinted magnetic microspheres by reducing nonspecific adsorption of competitors using 2-methacryloyloxyethyl phosphorylcholine. Sensors Actuators B Chem 208:559–568
168. Yoshimi Y, Ohdaira R, Iiyama C, Sakai K (2001) Gate effect of thin layer of molecularly-imprinted poly(methacrylic acid-co-ethyleneglycol dimethacrylate). Sensors Actuators B Chem 73:49–53
169. Lindner E, Umezawa Y (2008) Performance evaluation criteria for preparation and measurement of macro- and microfabricated ion-selective electrodes (IUPAC technical report). Pure Appl Chem 80:85–104
170. Peng L, Yarman A, Jetzschmann KJ, Jeoung J-H, Schad D, Dobbek H, Wollenberger U, Scheller FW (2016) Molecularly imprinted electropolymer for a hexameric heme protein with direct electron transfer and peroxide electrocatalysis. Sensors 16:272
171. Madikizela LM, Chimuka L (2016) Synthesis, characterization, adsorption and selectivity studies of a multi-template molecularly imprinted polymer. In: 9th international conference on molecular imprinting, Lund, Sweden, P2–P25
172. Wulff G, Liu J (2012) Design of biomimetic catalysts by molecular imprinting in synthetic polymers: the role of transition state stabilization. Acc Chem Res 45:239–247
173. Yarman A, Turner APF, Scheller FW (2014) 6-Electropolymers for (nano-)imprinted biomimetic biosensors. In: Nanosensors for chemical and biological applications, 1st edn. Woodhead Publishing, Amsterdam, pp. 125–149
174. Jetzschmann KJ (2013) Ein oberflächengeprägtes polymer für die molekulare erkennung von acetylcholinesterase. MSc thesis, University of Potsdam

Biomimetic Recognition for Acoustic Sensing in Liquids

Christoph Jungmann and Peter A. Lieberzeit

Abstract Biomimetic strategies aim at mimicking properties of natural materials or compounds within synthetic matrices. Among those, receptors synthesized for the highly selective recognition of analytes have attracted special interest, because man-made structures have several advantages over natural ones: they are usually more cost-effective, rugged, and stable on the long-term scale. So far, three different approaches have proven most useful for chemical sensors: aptamers, molecularly imprinted polymers (MIPs), and self-assembled monolayers (SAMs). This chapter reviews some of the most recent strategies to combine biomimetic receptors with mass-sensitive sensors.

Keywords Aptamers, Bioanalyte detection, Biomimetic recognition, Mass-sensitive sensors, Molecularly imprinted polymers, Self-assembled monolayers

Contents

C. Jungmann and P. A. Lieberzeit (✉)
Faculty for Chemistry, Department of Physical Chemistry, University of Vienna, Waehringer Strasse 42, A-1090 Vienna, Austria
e-mail: Peter.Lieberzeit@univie.ac.at

M. J. Schöning, A. Poghossian (eds.), *Label-Free Biosensing: Advanced Materials, Devices and Applications*, Springer Series on Chemical Sensors and Biosensors (2018) 16: 323–344
DOI 10.1007/5346_2017_6, © Springer International Publishing AG 2017,
Published online: 9 July 2017

1 Introduction

Relying on biologically active materials for the detection of analytes, biosensors have enjoyed great success in the past decades, both in the advancement of analytical sensing as well as in the commercial sector. The first and arguably most prominent example of a biosensor took shape and form in the amperometric glucose sensor developed by Clark and Lyons [1]. While a large portion of available biosensors still makes use of biological receptors [2], efforts are being made to develop artificial systems capable of mimicking the action of their biological counterparts [3, 4]. Furthermore, biomimetic structures promise to be more cost-efficient and chemically robust thus enhancing their overall applicability. Combining them with label-free transducers such as acoustic resonators opens up vast possibilities which are yet to be exploited to their fullest. Herein, we show an overview on what has been achieved in the past years as well as provide an indication of the potential of biomimetic sensor design.

1.1 Biomimetics

Biomimetics, biomimicry, and bionics are all terms first coined in the middle of the twentieth century denoting the practice of exploiting phenomena found in nature for the use in man-made technology and machinery. By definition, they directly imply what has been a longstanding practice: Drawing inspiration and experience from analyzing, understanding as well as improving upon established biological structures. In fact, it may be argued that from the very beginning human technological advances have been directly influenced by nature itself. As such, biomimetics lie at the interface between biology and technology [5].

Since the blossom of the field of biomimetic research in the 1970s, it has transcended the boundaries of biology and crossed over into other fields such as engineering and chemistry leading to inventions including dye-sensitized solar cells [6], synthetic muscles [7], and materials with self-cleaning properties [8]. A well-known case of biomimetics making their way into everyday life, the development of Velcro was directly inspired by the adhesive properties of burrs. Since its introduction, Velcro has become a widespread feature among clothing and shoes. Another modern example of biomimicry and biomimetic design in science is the use of virus particles for the fabrication of large tubular or fiber-like structures. Due to the resilient nature of these creations, they might see use in a wider range of applications including the role of drug carriers [9].

Biomimetic structures and materials have also come to make a large impact on sensor technology leading to developments including electronic tongues and noses as well as a plethora of other systems making use of recognition materials inspired by nature such as dolphin-based sonar devices, artificial electrolocation devices as well as artificial ommatidia arrays [10].

1.2 Biosensors and Biomimetic Sensors

By and large, a biosensor can be understood as a device comprised of a biological recognition site, often times also referred to as a biological receptor, as well as a transducing element transforming the change of one of the receptor's properties into an electric signal. As such, biosensors are targeted towards biological species including antibodies, proteins and enzymes, nucleic acids, cells as well as unicellular organisms. Depending on the field of application, sensors are expected to fulfill a plethora of requirements including but not limited to high sensitivity and specificity, ease of use as well as being robust, mobile, and affordable [11].

Generally speaking, biosensors can be classified into two very distinctive categories: Labeled sensors which take their name from the so-called labels which are used to differentiate an analyte from the surrounding background as well as label-free sensors. Some of the most popular established labeled techniques include, among others, fluorescence, chemiluminescence, and radiolabeling.

While these methods in general feature high sensitivity and a highly stable measuring signal, they are not without their flaws: Among the commonly associated disadvantages of labeled techniques is the need for sample preparation which in turn may result in sample loss. The labels used to mark analytes may also be sensitive to chemical conditions and/or exposure to light (fluorescence-labeling) and cause issues in regard to storage, handling, and disposal (radiolabeling). Other techniques are based on irreversible reactions that only allow for one-off measurement (chemiluminescence).

In stark contrast to their labeled competitors, label-free techniques do not necessitate chemical modification of the sample and may offer detection of a wider range of analytes with relatively little need for adaptation. Label-free biosensors can be separated into two basic categories based on the mode of signal transduction employed. Nonoptical label-free sensors, for example, include systems working off of acoustic wave, electrochemical, or microcalorimetric setups. Optics-based label-free biosensors, on the other hand, are dominated by refraction-based setups in general and surface plasmon resonance (SPR) as well as waveguides in particular. Other optical transducers which are gaining popularity include interferometers, porous materials as well as photonic crystals.

Biomimetic chemosensors extend the scope of biosensors by replacing the biological recognition element in the latter by a synthetic matrix that mimics the binding properties of a biomolecule or biospecies. One can expect that using such synthetic, engineered receptor layers increases ruggedness of the systems as well as makes the resulting sensors more compatible with (industrial) production processes. The main focus of this chapter will be put on acoustic devices coated with such biomimetic materials, and their adaptation and use as platforms in a wide range of sensor applications for the label-free detection of biological species as well as the biomimetic strategies employed in the creation of the bio-receptor sensing layers used.

2 Acoustic Signal Transduction

Acoustic sensors, also known as mass-sensitive devices, belong to a family of transducers exploiting the piezoelectric effect, first discovered in the nineteenth century. By now, oscillators have become a mainstay of modern electronics due to their high frequency stability finding use as clock generators in electronic devices including clocks as well as microprocessors. Their working principle was initially observed and studied on tourmaline crystals. Several other piezoelectric materials are known including, but not limited to, gallium orthophosphate, lead zirconate titanate as well as α-quartz. The piezoelectric effect itself can be explained as follows: Piezoelectricity in crystalline systems only occurs when certain conditions are met including the presence of an anisotropic axis as well as the absence of an inversion center. The ends of an anisotropic axis are not interchangeable: Rotation around an axis positioned perpendicularly to it results in a different configuration than the original one. Directed deformation of the crystal structure along or perpendicular to the anisotropic axis translates into the buildup of dipole moments which, summarized over the entirety of the structure, form a potential. Being a fully reversible process, this in turn means that the opposite case is equally true: Applying voltage leads to mechanical deformation of the crystal. In the case of alternating voltage, this results in a periodic oscillation of the material. This phenomenon is also known as the inverse piezoelectric effect (Fig. 1).

In most cases, sensor responses of acoustic devices are based on recording the frequency shifts resulting from mass deposition on the respective electrode surfaces. Another less often used mode comprises of monitoring energy dissipation through viscous damping which lends itself well for the study of binding kinetics. The interplay between mass loading and resonance frequency was first described in 1959 by Günter Sauerbrey via the equation of the same name [13]:

$$\Delta f = -\frac{2f_0^2}{\sqrt{\rho_q \mu_q}} \frac{\Delta m}{A}$$

Here, Δf denotes the frequency shift, f_0 the fundamental frequency of the device, ρ_q and μ_q the density and the shear modulus of (AT-cut) quartz, respectively, Δm the mass change, and A the electrode area. Although strictly speaking only valid for gas-phase measurements, certain modifications can be made to the Sauerbrey equation extending its applicability to the liquid medium. The most commonly used adaptation for measurements in a Newtonian liquid was published by Kanazawa and Gordon in 1985 [14]:

$$\Delta f = -f_0^{\frac{3}{2}} \left(\frac{\eta \rho}{\pi \mu_q \rho_q} \right)^{\frac{1}{2}}$$

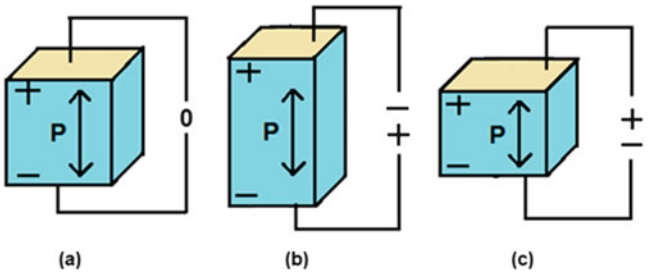

Fig. 1 Illustration of the inverse piezoelectric effect and the resulting mechanical deformation induced by application of a voltage (image adapted from Vatansever et al. [12]). (**a**) denotes the polarized medium; (**b**) applied voltage has the opposite polarity, as material: elongation; (**c**) applied voltage polarized in the same way as material: compression

In addition to the factors known from the Sauerbrey equation, here η and ρ (denoting viscosity and density of the liquid, respectively) also play a role. As a result, mass-sensitive devices have become versatile tools for the measurement of trace amounts of analyte in both liquid and gas phase, typically achieving detection limits reaching down into the low picogram range [15]. Popular acoustic-based systems include the quartz crystal microbalance (QCM), surface acoustic wave (SAW) devices as well as (micro-)cantilevers which will be the main focus of this book chapter.

2.1 Quartz Crystal Microbalance

QCMs consist of flat quartz disks fitted with electrode structures on both sides which serve the dual purpose of conducting the voltage necessary to excite the resonator as well as that of electrical readout of the resonance frequency (Fig. 2). Although QCM in principle can be run in different oscillation modes, for practical reasons thickness shear mode is usually the preferred choice: It is relatively insensitive towards density and temperature effects and usually exhibits the lowest damping. Hence, it can host a range of different recognition materials, such as thin films/coatings, or particles. The wave seen in Fig. 2 symbolizes oscillation within the liquid above the device surface.

As laid out by the Sauerbrey equation, the resonance frequency of a QCM is inversely proportional to its thickness with higher frequencies generally leading to larger sensor effects and thus increased sensitivity. It has to be kept in mind, however, that sensitivity increases proportionally to the square of the resonance frequency. There are also practical limitations in regard to the frequencies attainable with QCMs before the substrates become too thin and thus too mechanically fragile to handle. Quartz crystal resonators are most commonly operated at resonance frequencies spanning from 5 to 20 MHz which, based on the Sauerbrey equation, translates into a well

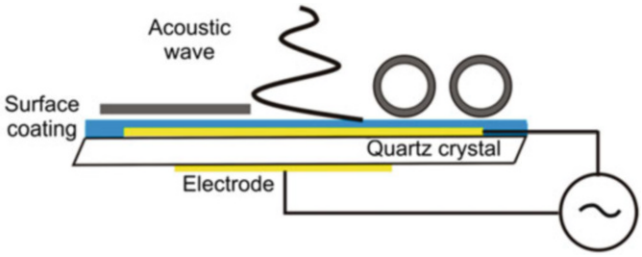

Fig. 2 Schematic representation of a quartz crystal microbalance (QCM) fitted with electrodes on both sides as well as a thin sensing layer on its upper surface (image adapted from Konradi et al. [16]). The *gray line* on the left-hand side denotes a thin layer, and the *two circles* deposited particles

manageable substrate thickness of 334 and 84 μm, respectively. While the odd paper exists that reports the use of 30 MHz (56 μm) [17] or even 40 MHz (42 μm) [18] resonators, these usually require either special treatment of the quartz substrates or specialized equipment as well as careful handling making them impractical in their use. A viable strategy for increasing resonator frequency while retaining sufficient mechanical stability is to change the material of the transducer. Gallium arsenide, among others, has been used to replace quartz due to its higher fracture strength and better machinability [19]. Depending on the requirements of their application, quartz crystal resonators can be fitted with multiple electrodes on one substrate [20, 21]. Each electrode may then be coated with a different chemical layer allowing for simultaneous monitoring of different analytes or for the introduction of an internal reference to the measurement setup [22].

2.2 Surface Acoustic Wave Devices

Based on the sheer number of relevant publications, SAWs are the most popular acoustic transducers. In the 5-year period spanning from 2012 to 2016, around 1,700 publications on SAW sensors have been reported (search keyword: surface acoustic wave sensor) while for QCM and cantilevers the numbers drop to just around 1,000 and 400, respectively (search keywords: quartz crystal microbalance sensor; dynamic cantilever sensor) (data from Scopus: February 2017). Similarly to QCMs, they are manufactured from piezoelectric material, but usually manufactured into rectangular rather than cylindrical shape. Typically, a SAW substrate features a set of two electrodes of interdigitated structure at opposite ends for excitation and readout which are commonly referred to as input and output transducers. Figure 3 sketches such a device. As it is symmetrical, the operating circuit defines which of the two interdigital structures (marked in blue/red) acts as input and output, respectively.

The oscillations, which are generated by applying a voltage, are confined to within just one wavelength of the surface of the resonator, hence the name, and can

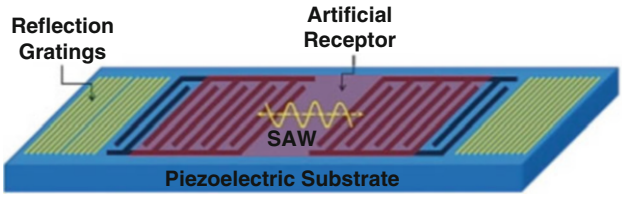

Fig. 3 Graphical depiction of a surface acoustic wave (SAW) resonator (image adapted from Afzal et al. [23])

reach frequencies in the high MHz to low GHz region. This in part makes for the exceptional sensitivity of this particular type of transducer. SAW devices can be distinguished by the kind of surface wave generated, including shear wave (SH-SAW), Love wave, and Rayleigh wave (RSAW)-type sensors. Of these, only shear wave and the so-called shear transverse wave (STW) resonators can be operated in liquid phase due to the inhibitory damping taking place on other types of SAW resonators. For the use as a bioanalytical tool, the electrodes are coated with the respective receptor material. Interactions of the latter and the analyte are then measured by monitoring the shift in resonance frequency encountered. Due to their versatile nature, SAWs have found use in many sensor applications [23, 24].

2.3 Cantilevers

More prominently associated with topological measurement techniques, such as atomic force microscopy (AFM), cantilevers have made their appearance in biosensor applications. The two modes of action most relevant for their use as transducers include static and dynamic measurement (Fig. 4).

In case of static measuring, cantilevers are usually employed in arrays consisting of several tips of which only some are coated with the receptor material while the remainder is used for referencing [26, 27]. Molecular recognition of the analyte on the part of the receptor results in stress-induced static bending of the cantilever which ultimately can be readout via optical beam deflection, interferometry, or capacitance measurement. In dynamic mode, the cantilever is brought to its resonance frequency through external excitation. Similarly to QCM and SAW, adsorption of analyte on the receptor layer causes a shift in resonance frequency which in turn allows the calculation of the adsorbed mass via the Sauerbrey equation. Of these two operating modes only dynamic measuring is of acoustic nature [28]. The most commonly used materials for cantilevers include silicon and silicon nitride. For the use as acoustic transducers, however, they are usually enhanced with thin layers of piezoelectric material in order to allow the cantilevers to resonate.

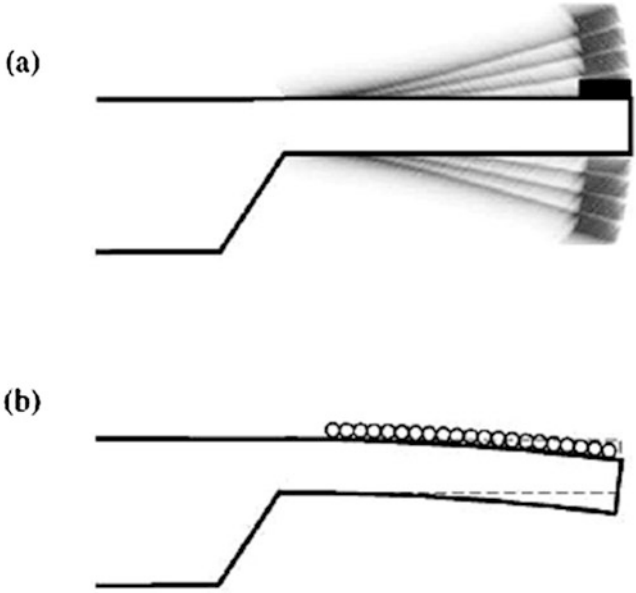

Fig. 4 Cantilevers in dynamic (**a**) and static (**b**) measurement mode (image adapted from Battiston et al. [25] with permission. Copyright: Elsevier BV). The *black square* in (**a**) represents mass loading on the receptor of the cantilever. Part (**b**) shows analyte species deposited on the entire cantilever surface

3 Biomimetic Receptors

As already previously mentioned, the field of sensing biological species faces a constant challenge of designing new, innovative ways of detecting analytes of interest. Besides straightforward copies of biological systems, vast efforts have been made in the past decades to devise and improve artificial structures that mimic their biological counterparts. Ideally, they provide similar binding characteristics and selectivity profiles as natural systems, while eliminating or improving upon some of the major issues linked to biological systems, such as low chemical stability and high costs. One strategy in the pursuit of achieving these goals is referred to as supramolecular chemistry. A hot topic in chemistry, it is focused on assemblies of molecules and the synthesis of molecular networks of defined size, shape, surface, and hierarchy [29]. As such, the concepts of self-assembly as well as host–guest chemistry play a seminal role in creating materials with purpose-built structures and properties. In the scope of this book chapter, three different approaches to creating biomimetic sensing layers will be presented in detail. These include aptamers, molecularly imprinted polymers (MIPs) as well as self-assembled monolayers (SAMs) and their respective use in modern sensor designs.

3.1 Aptamers

The term aptamer is used to describe both short, single-strained oligonucleotides as well as peptides capable of binding to a specific molecule. Analytical targets for aptamers include small molecules [30], proteins [31], amino acids [32], virus particles [33], whole cells [34], as well as unicellular organisms [35]. Their dissociation constants typically lie in the pico- to nanomolar range generally making them comparable to antibodies. This particularly high specificity and binding strength is a result of the 3D structure of the aptamer which is able to wrap itself around its binding partner in what is known as "adaptive binding." Besides the steric fit electrostatic attraction, hydrogen bonds and base stacking are the most important contributors to aptamer–target interaction [36].

Aptamers are artificially crafted in a process commonly known as in vitro selection or alternatively SELEX (i.e., systematic evolution of ligands by exponential enrichment) (Fig. 5). During that process, the respective target compounds are first exposed to a large random oligonucleotide library. Bound nucleotides are then isolated, amplified, and subjected to the next selection process. In the course of several rounds, hence aptamers exhibiting high affinity towards the target are selected while the rest is eliminated ending up with a mixture consisting of just a handful of highly selective oligonucleotides/peptides. Aptamers possess several key advantages over competing antibodies by offering higher stability as well as lower immunogenicity.

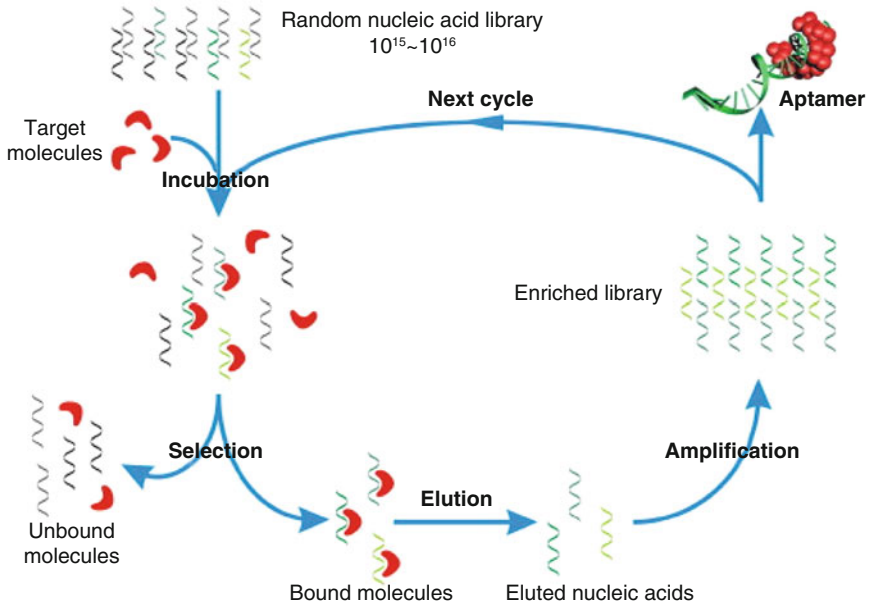

Fig. 5 Schematic representation of the systematic evolution of ligands by exponential enrichment (SELEX) aptamer crafting process (image adapted with permission from Song et al. [37], copyright: Elsevier BV)

Being manufactured through chemical synthesis rather than biological expression also translates to lower costs and allows for the detection of a wider range of biological targets, since aptamers can quickly be custom-tailored for a specific task [38].

3.1.1 Sensor Applications

Despite their relative novelty as biomimetic receptors in biosensor applications, aptamers to date have been combined with a wide selection of transducers including electrochemical, optical, and acoustic readouts resulting in a plethora of analytical sensor systems. One of the first combinations of aptamers and acoustic-based transducers materialized as early as 2002: A sensor system detecting IgE [39], an antibody vital to the defense against parasites which also plays a significant role in the acquirement of certain hypersensitivities. The ability of the synthesized aptamers to selectively bind the analyte was directly compared to anti-IgE antibodies. In conclusion, it was noted that both receptors exhibited a limit of detection (LOD) of 0.5 nmol/L. The linear concentration range in case of the aptamer-based sensor was found to span up to roughly 10 mg/mL. Combined with the ability of regenerating the bio-sensitive layer and the generally higher stability, this puts aptamers well ahead of their competition. Another early application includes the mass-sensitive detection of thrombin, a coagulation factor found in vertebrates, via QCM [40]. Concentrations of thrombin are an indicator for the presence of a blood clot. Thus, its real-time monitoring could help prevent strokes in clinical patients. Thrombin has also been identified as a supporting factor for the progression of atherosclerosis. The LOD of the sensor system was found to be in the 1 nmol/L range while the dynamic range reached up to 140 nmol/L and spanned a frequency shift of 200 Hz [37, 41].

A more recent example of aptamer-based acoustic sensors includes a system specially designed for the detection of cytochrome c, a heme protein found in mitochondria and deeply involved with the electron transport chain [42]. It also plays a role in the initiation of apoptosis. In case the permeability of the mitochondrial membrane is compromised, cytochrome c is released into the cytosol where it promotes cell death as part of a signal cascade. In the course of the study, three different aptamers were tested and immobilized on top of a gold-plated QCM. These included 40-length (apt 40), 61-length (apt 61), and 76-length (apt 76) sequence aptamers. Of these, only apt 76 was found to specifically bind towards the target in the chosen concentration range. The LOD of the aptamer-modified thickness shear resonators was noted to be around 0.5 nmol/L. Furthermore, recovery of cytochrome c in spiked samples of human plasma was found to be as much as 92% at a concentration of just 1 nmol/L. Yet another study showcased the use of aptamers in conjunction with QCMs for the detection of adenosine-5-′-triphosphate (ATP) via both frequency and dissipative monitoring [43]. Its analytical relevance is based on its involvement in a number of biological processes including, but not limited to, signal transduction, energy transfer, and muscle contraction. The system allows for real-time determination of ATP concentration

and shows limited cross-selectivity towards the similar nucleotide guanosine-5-′-triphosphate (GTP) which makes it a viable alternative to existing techniques in medical and hygiene monitoring focusing on ATP.

SAW resonators have also found their way into aptamer-based sensor systems [44]. One of the first applications of its kind featured an array consisting of five sensing elements on a single substrate allowing selective real-time, quantitative determination of both thrombin and HIV-1 Rev, a protein associated with HIV-1 viral expression. As such, it has significant diagnostic value as it serves the purpose of indicating disease progression [45]. The LOD for both analytes was found to be in the region of 75 pg/cm^2 and thus significantly lower than comparable early QCM-based aptamer sensors. As it is the case with similar applications, adapting the aptamer sensing layer may enable detection of various other biologically relevant analytes.

Among the more recent examples is a system for the detection of human breast cancer cells making use of a 2 × 3 array [46]. The MCF-7 cells used as target are a type of circulating tumor cells (CTC) which act as indicators for tumor metastasis. The detection of CTCs in blood samples can help monitor a patient's health status as well as allow for more individual modification of the respective cancer therapy. The sensor itself was found to exhibit appreciable sensitivity towards the target with an LOD of 32 cells/mL and a linear range spreading from 10^2 up to 10^7 cells/mL. It is hoped to expand the applicability of the sensor to a wider range of CTCs by adjusting the aptamers according to the specific requirements. In a different case, aptamers were combined with a love-wave sensor, the latter being a specialized type of SAW resonator [47]. The measurement principle is based on horizontally polarized waves which travel along the surface of the substrate and are disturbed by the immobilized bio-receptor interacting with the analyte. In the application outlined, the system was designed to detect prostate specific antigen (PSA) which is a clinically relevant biomarker in the diagnosis and monitoring of prostate cancer. The sensor was shown to exhibit an LOD of 10 ng/mL, which the authors hope to further improve upon by the introduction of signal amplification.

Combinations of micro-cantilevers with aptamer-based bio-receptors are relatively rare and split between resonance and stress-bending modes in favor of the latter. One true acoustic cantilever application featuring custom-tailored aptamers is targeted towards the hepatitis C virus (HCV) helicase, a popular protein model used to study the working mechanisms of helicases. By achieving sensor effects at concentrations as low as 100 pg/mL, the system demonstrates the viability of label-free, low-cost cantilever sensors for the detection of small-scale proteins in real-life samples [48].

3.2 Molecularly Imprinted Polymers

Molecular imprinting is a strategy for creating cavities of the same size and shape as that of a so-called template inside a highly cross-linked polymer system. In the course of imprinting, the polymer arranges around the template in a process of self-organization

both sterically as well as in regard to the orientation of its functional groups. After polymerization, the template is then extracted leaving behind adapted cavities which can selectively reincorporate the respective analyte (Fig. 6). In principle, the interaction of the template and imprinted polymer can be compared to the lock and key model used to explain the action between enzymes and the corresponding substrates. The use of this technique leads to fully synthetic affinity-based receptors which can stand in as low-cost alternatives for their more sensitive biological counterparts.

First commercial use of the practice included the fabrication of silica-based filter materials for use in industrial extraction processes. Since then, molecular imprinting has expanded into the field of polymer chemistry [50] thus allowing for more sophisticated applications such as that of chiral selectors in chromatography [51], as synthetic enzymes in reaction catalysis [52], as well as artificial receptors for use in sensor systems [53]. Even though the concept of molecular imprinting dates back to the 1930s [54], it was not until the groups of Klaus Mosbach and Günter Wulff independently published papers in the early to mid-1990s proposing the use of MIPs as artificial recognition structures [55, 56] that specific interest in the field rose dramatically. Since then, MIPs have been used to create sensor applications for a wide range of analytically relevant targets including small molecules [57, 58], peptides [59, 60], viruses [61, 62], cells, and bacteria [63, 64]. While a highly interesting subject, MIPs are still facing issues hindering their use in commercial applications. Among

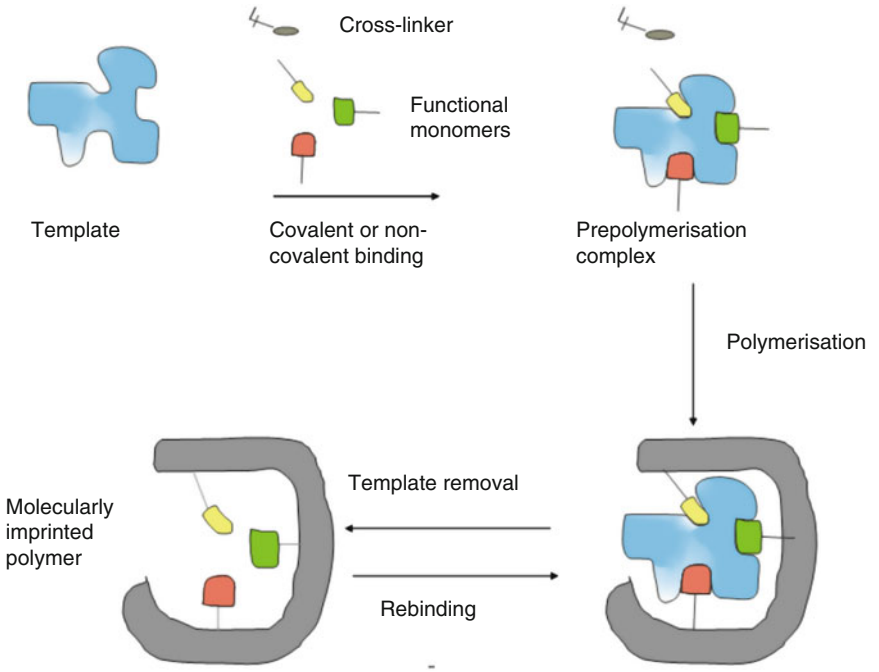

Fig. 6 Workflow schematic for the molecular imprinting of a polymer (image adapted from Menger et al. [49])

the prime concerns are batch-to-batch reproducibility as well as the time-consuming nature of the imprinting step in production as compared to comparable lithographic processes.

Generally speaking, two major types of imprints can be distinguished. Bulk imprinting denotes the practice of directly mixing the template with the prepolymer solution containing the monomers, cross-linking agent, and initiator. Due to the statistic distribution of the template in solution, the cavities are generated within the three-dimensional bulk of the fully polymerized material. This particular approach is preferred when aiming to imprint small molecules: Having recognition sites all over the bulk leads to strongly increased sensitivity of the respective sensors, because binding is not limited to a monolayer on the outer polymer surface. However, this type of MIP faces the challenge of limited accessibility of the majority of binding sites in the polymer bulk thus leading to diffusion-controlled binding processes and limited accessibility of binding sites located deep within the matrix.

Alternatively, surface imprinting can be used to create imprint sites located at or close to the surface of the polymer layer. This is ensured by keeping the polymer layer's thickness in the order of the hydrodynamic radius of the analyte. Surface imprinting is often employed for larger analytes including proteins, viruses, cells, and bacteria where diffusion of the analyte into the polymer bulk would prove to be a severely limiting factor. A drawback of surface imprinting is the much smaller number of binding sites created in the process resulting from the restriction to a near two-dimensional area as opposed to the entire bulk. On the other hand, surface imprinting allows maximum control in terms of localization and special density of the binding sites. Another imprint type worth mentioning is microcontact imprinting, also referred to as stamp imprinting. In this particular case, the template is immobilized on the surface of a suitable substrate, such as glass or silicon. After deposition of the prepolymer onto the desired target, the stamp is then brought into direct contact with it. After the polymer has hardened, the stamp is then carefully removed ideally leaving behind a large number of binding sites on the surface of the polymer layer. Bringing the stamp and prepolymer into sufficiently close contact can be an issue with this type of imprint as well as the removal of the stamp after polymer hardening due to adhesive forces [65, 66].

3.2.1 Sensor Applications

Acoustic devices as transducers make up just a small share in the field of MIP-based label-free biosensor research, the vast majority relying on optical or electrochemical readouts instead. The first particular mention of a piezoelectric MIP sensor in the literature in 1996 [67] described a SAW device for measuring in the gas phase capable of detecting trace amounts of halogenated as well as aromatic hydrocarbons. Since then, the amount of publications released on the topic per year has steadily been increasing demonstrating a substantial rise in interest. Another example for MIP detection of volatile organic compounds (VOCs) in gas phase via acoustic signal transduction is provided by Matsuguchi and Uno [68]. They observed that preparing

copolymers from methyl methacrylate and divinyl benzene in one of the two solvents, toluene or p-xylene, resulted in hardened polymers which showed an increased uptake capacity of the respective solvent used during their synthesis. The sensor effects encountered during gas-phase measurements were generally found to be reversible but the time it took for the sensor to reach saturation was noted to reach up into the 1 h range which limits its usefulness severely. More recently, a similar sensor system capable of detecting VOCs but based on a love-wave transducer has also been reported [69]. The template of interest used for imprinting of the acrylamide-based polymer was adenosine monophosphate (AMP). However, it was noticed that the sensor showed marked sensitivity towards the two VOCs toluene and ethanol. Gas-phase measurements of the system revealed the MIP generally showing appreciable response for both components with sensor effects on average being 3–4 times higher than the non-imprinted polymer (NIP). Using the AMP-imprinted sensor, it was also possible to discern the two organic solvents via their sorption kinetics, ethanol reaching a steady state faster than toluene.

A large number of acoustic sensors using MIP imprints of small molecules have been reported in the past [70]. Caffeine, a xanthine derivative and arguably the most widely consumed psychoactive substance in the world, is the target of choice for a number of publications in MIP research [71, 72]. One of the first reported sensors using a combination of imprinted polymer and acoustic transducer can be found dating back to 1999 [73]. The system was found to exhibit high sensitivity with a detection limit of $5*10^{-9}$ M and a dynamic range spanning from $5*10^{-9}$ M to $1*10^{-4}$ M. Sensor effects of the imprinted polymers were compared to reference sensors featuring non-imprinted versions of the same polymer further confirming the successful imprint of caffeine. Selectivity was also investigated by testing against the functional derivative theophylline showing significantly higher response for caffeine. In a much more recent study, a caffeine-selective MIP was electrochemically synthesized from polypyrrole and directly deposited on QCMs [72]. The use of a custom-built flow-through cell allowed for continuous measurements and the determination of the kinetics of the relevant association/dissociation processes. As a result, it was possible to also evaluate the difference in binding equilibrium of caffeine, theophylline, and the MIP.

Other possible uses of MIP-coated acoustic sensor devices include the monitoring of water resources. Besides more obvious contaminants, antibiotics have garnered great analytical interest due to their extensive use in aquatic cultures and the pharmaceutical industry [74]. One particular study reports a SAW-based sensor system for the sensitive detection of flumequine (FLU) which is among the most heavily used antibiotics in fish farming [75]. The transducer itself was coated with imprinted polypyrrole via electropolymerization within a 10^{-2} M solution of FLU. Measurements were carried out recording the phase shift between input and output in degrees rather than the oscillation frequency. A decrease in phase shift can be interpreted as a result of FLU adsorption on the sensor layer and vice versa. The detection limit of the sensor was determined to be 1 μM with a phase sensitivity of 9.4°/mM. Selectivity of the system was tested by measuring against levofloxacin, an antibiotic belonging to the same group of fluoroquinolones, such as FLU. It was noted that injection of

levofloxacin resulted in no significant sensor response thereby proving the high selectivity towards the FLU template. In a different study, a microcantilever-based device was used to detect ciprofloxacin (CPX), another synthetic antibiotic and pharmaceutical contaminant, in aqueous solution. Mass-sensitive measurements of the target were carried out by means of a dip-and-dry methodology and revealed a detection limit of 0.8 μM as well as a sensitivity of 2.6 Hz/pg. Other analytes relevant in regard to safeguarding of quality and safety of water supplies include endocrine disruptors [76], hormones [77] as well as bacteria [78].

While initially MIPs were almost exclusively targeted towards small molecules, their applicability has since then been expanded towards larger analytes including, among others, proteins [79]. In the course of the last decade, specifically the interest in MIPs capable of selectively binding proteins has increased dramatically. Currently around one tenth of all publications covering MIP are protein related (roughly 330 out of 3,400 reported publications in the time frame of 2012–2016; data taken from Scopus: February 2017). A general limitation in regard to protein MIP is the restriction to aqueous polymerization conditions due to the limited chemical stability of the target. This presents the added challenge of achieving sufficient interaction between MIP and protein target as hydrogen bonds in aqueous solution alone are insufficient and electrostatic attraction is best avoided in order to ensure that nonspecific interactions with charged particles in solution are excluded [49].

Aside from its vital function as oxygen-transporting protein in the respiratory circuit of vertebrates, hemoglobin takes up a special role in protein MIP research due to its overall abundance in the literature. One of the first publications reporting the successful imprinting of polymers using proteins including hemoglobin, albeit not bearing relation to acoustic sensors, was presented in 2001 by Bossi et al. [80]. The study in question served as proof of viability for the imprinting of proteins as well as highlighted the advantages of using MIP for protein recognition including the relative ease of preparing MIP, and their chemical stability and capability of recognizing and differentiating between small and large proteins. While a large portion of the reported hemoglobin MIP sensors make use of electrochemical signal transduction, some can also be found to be based on acoustic transducers. One such study investigated the capabilities of three different acrylamide polymers in regard to being imprinting with and selectively binding to different proteins including bovine hemoglobin (BHb), bovine serum albumin (BSA), myoglobin (Mb) as well as lysozyme (Lyz) and trypsin (Tryp) [81]. It could be shown that selectivity of the imprinted polymers is closely related to their relative hydrophilicity. Of the polymers tested, the one based on N-hydroxymethylacrylamide (NHMA) in particular showed the highest MIP-to-NIP sensor response ratio across the board and was found to be the best fit for the imprinting of BHb. Selectivity of the respective BHb-MIP thin film on QCM was tested by measuring against BSA due to the latter's comparable mass (64.5 vs 66 kDa) and size with sensor effects being in favor of BHb by a factor of roughly 3–4.

Another interesting, related study covers the development of a QCM sensor with MIP thin film imprinted with bilirubin, a by-product of the metabolization of hemoglobin in the liver [82]. Pathologic changes in the breakdown of bilirubin may lead

to discoloration of tissue including the skin. Hence, bilirubin takes up the role of a clinical indicator for liver disorders. The 4-vinylpyridine based MIP was tested in a concentration range spanning from 0.45 to 11 mg/dL exhibiting linear dependency of its sensor signals on analyte concentration. In order to determine selectivity, the bilirubin-imprinted QCM sensor was measured against biliverdin, a close structural analog of near identical molecular mass and structure. It was noted that even at the highest concentration tested (13 mg/dL) biliverdin caused a sensor response of less than 50 Hz as opposed to little over 250 Hz in case of bilirubin at a comparable concentration (11 mg/dL). Furthermore, the MIP sensor was coupled with a flow-injection analysis (FIA) system allowing for fully automated sample analysis including sample loading, unloading, and regeneration steps.

Further developments of acoustic MIP sensors targeted on clinically relevant analytes include a receptor–ligand binding assay featuring the dopamine D1 receptor (D1R) [83]. A member of the family of catecholamines, dopamine serves the function of a neurotransmitter as well as chemical messenger and is thus linked to a number of neurological disorders including Parkinson's disease. The study in question showed that MIPs can be used to estimate the strength of receptor–ligand binding as well as differentiate between free receptor sites, receptors having bound dopamine as well as receptors having bound the antagonist. As such, it presents an innovative approach in the field of ligand-binding assays. Low-density lipoprotein (LDL) constitutes another clinically relevant analyte as increased concentrations have been proven to be indicative of coronary heart diseases. LDL-imprinted polymer layers on QCM have been shown to exhibit high sensitivity towards the template protein at concentrations down to the single digit mg/dL region [84]. Furthermore, the sensors displayed excellent selectivity towards LDL in the presence of other lipoproteins such as high-density lipoprotein (HDL) as well as very-low-density lipoprotein (VLDL) with selectivity factors of 20 and higher in favor of LDL (Fig. 7).

Living organisms have also been the subject of MIP-related sensor studies. Among others, successful imprints of yeast cells have been reported on QCM allowing to differentiate between different growth stages including single and duplex cells depending on the template used during imprinting [85]. Experiments performed on a multichannel sensor system within the same study proved that monitoring of yeast development is indeed viable. Another well-studied microorganism, *Escherichia coli*, has been imprinted on polymer coated QCMs resulting in sensors capable of selective and reversible detection in liquid phase [86]. The reported devices even made it possible to discriminate between different serotypes of the same bacteria while displaying high robustness as well as being easily regenerable.

Other analyte targets prominently featured in the MIP-related literature include histamine [87, 88], immunoglobulins [89, 90], albumins [91], a group of globular proteins typical for the blood of vertebrates, erythrocytes [92], as well as avidin [93], a glycoprotein found in avian eggs.

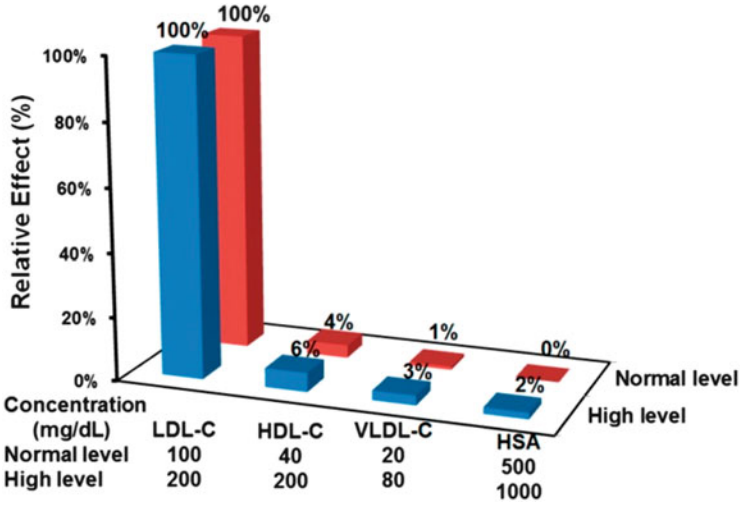

Fig. 7 Selectivity of the low-density lipoprotein (LDL)-MIP towards different lipoproteins (image adapted with permission from Chunta et al. [84], Copyright (2016) American Chemical Society)

3.3 Self-Assembled Monolayers

Self-assembled monolayers, or SAMs for short, are generally understood as molecular assemblies that form on the surface of a suitable substrate through a self-organized adsorption process. The basis of SAMs typically consists of amphiphilic, surface-active compounds featuring a terminally functionalized alkyl group as hydrophobic tail as well as a hydrophilic, polar head (Fig. 8). The formation of SAMs may take anywhere from a few minutes to several hours and is primarily driven by molecular interactions including covalent bonding between reactive groups found on the substrate and the SAM molecules as well as non-covalent interaction between the hydrophobic tails of the latter.

The exact composition of a SAM is chosen based on the planned application as well as the nature of the substrate target used for SAM deposition. Depending on the choice of the head group, which acts as the molecular anchor, different types of SAMs can be differentiated including fatty acids, organosilicon as well as organosulfur compounds. Examples of self-assembly in nature are abundant. Ranging from protein folding over to the double stranded helical structure of desoxy ribonucleic acid – DNA, the lipid bilayer of cell membranes as well as viruses assembling into fibrils and particles, the role of self-assembly is vital to many of the biological processes and structures that make life possible in the first place [95]. The commercial application of SAMs currently is primarily revolving around surface coatings of components in order to purposefully modify their properties according to demand. SAMs see widespread use in the field of solid-state technology among others being used for the functionalization of nanostructures.

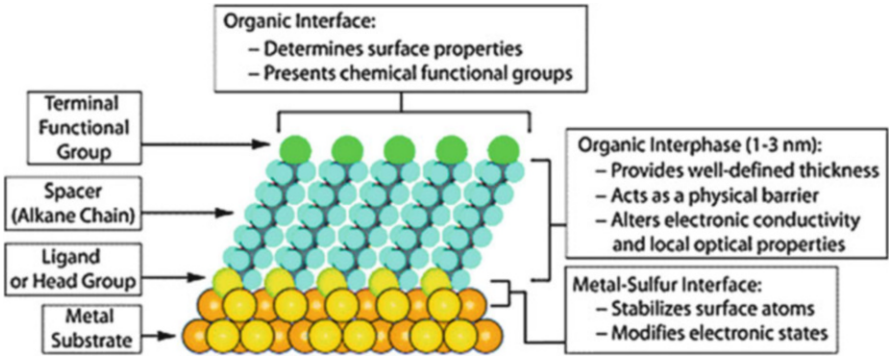

Fig. 8 Schematic representation of the structure of a self-assembled monolayer (SAM) (image adapted with permission from Love et al. [94] Copyright (2005) American Chemical Society)

3.3.1 Sensor Applications

One of the first publications regarding the use of a SAM as recognition material on a chemical sensor reported the selective detection of diisopropyl methylphosphonate (DIMP), a by-product in the synthesis of sarin gas [96], via a composite layer. In detail, a SAM based on 11-mercaptoundecanoic acid (MUA) was deposited on the gold electrodes of a SAW transducer exploiting the high affinity between gold and thiol groups. The terminally positioned carboxyl groups of MUA serve as electrostatic anchors for copper(II) ions which themselves act as binding sites for organophosphonates such as DIMP. Acoustic sensor measurements were carried out by subjecting the SAW device to nitrogen vapor saturated with different amounts of analyte. In conclusion, the system was noted for its high sensitivity allowing detection of organophosphonates in the ppb range, the reversibility of sensor effects, and general durability.

In a different study, a piezoelectric cantilever was used to investigate the difference in adsorption of human serum albumin (HSA) onto SAMs featuring different terminal functional groups [97]. Three different SAMs were tested all based on a C_{11}-thiol but sporting terminally positioned methyl (CH_3), carboxyl (COOH), and hydroxyl (OH) groups, respectively. The cantilever setup was specifically chosen over other acoustic transducers for its high sensitivity and the fact that research regarding protein detection had already been carried out earlier using a similar setup by the same group. As was expected based on publications researching the same field, albeit using different signal transduction methods, it was found that the methyl-substituted SAM showed the highest amount of adsorption followed by the carboxyl SAM. The least amount of adsorption was observed in case of the hydroxyl SAM. Besides investigation of the HSA adsorption, the setup allowed for continuous monitoring of the SAM deposition on the gold-coated cantilever.

Another publication highlighted the suitability of using *N*-acetyl glucosamine (GlcNAc)-based SAMs as recognition elements for the detection of wheat germ agglutinin (WGA), a lectin protein performing a protective function in wheat. The same system was successfully used in parallel to detect different influenza virus

strains due to the fact that GlcNAc is part of the virus target during the infection step [98]. Immobilization of GlcNAc on QCM gold electrodes was accomplished by letting it react in a two-step synthesis with *p*-nitrophenol and cysteine. The composite was then able to bind to the gold surface via the S–H bonds introduced by cysteine. GlcNAc monolayers prepared this way have displayed appreciable sensor responses in mass-sensitive measurements when subjected to WGA. Furthermore, it was possible to prove their viability as receptors for the detection of viruses.

SAMs have also been successfully used to detect large biological species including *E. coli* bacteria [99]. Due to the strong affinity exhibited by type 1 fimbria appendages found on *E. coli* towards mannose, a representative of the aldohexose group of carbohydrates, the latter was used as the basis of a covalently linked self-assembled recognition layer on QCM. Direct bacterial detection was found to not be without its limitations, however, as the binding between *E. coli* and mannose lacks rigidity and allows for water to slip in between the bacteria and the transducer surface which may negatively affect transducer oscillation during measurements. In order to improve contacting between the bacteria and the mannose layer concanavalin A (Con A), a lectin protein capable of binding to carbohydrates found on both the bacteria as well as the SAM was added. Compared to the pure mannose SAM, the lectin-modified sensor was found to have a much wider linear range reaching from 10^2 to 10^7 cells/mL. It therefore compares favorably with similar sensors making use of immobilized antibodies for the purpose of microorganism detection.

In many other sensor applications, SAMs play a secondary role serving the dual-purpose of acting as a covalent linker between the actual receptor, most often a biological species, and the transducer surface as well as providing a protective antifouling layer for the latter.

4 Conclusion

Mimicking biological structures has opened up a vast number of possibilities to design novel sensors, prominently including acoustic transducers. Biomimetic receptors are already rivaling their biological counterparts in terms of both sensitivity and LOD while clearly surpassing them in several other areas including reversibility of the sensor effects as well as their robustness, reusability, and associated long-term costs. Despite all of these merits, the use of artificial sensing materials has thus far been focusing on the academic sector. A successful breakthrough on the commercial market is still to be awaited.

References

1. Clark LC, Lyons C (1962) Ann N Y Acad Sci 102:29–45
2. Mirsky VM (2013) Ultrathin electrochemical chemo-and biosensors: technology and performance, vol 2. Springer, Berlin

3. Piletsky SA, Whitcombe MJ (2012) Designing receptors for the next generation of biosensors, vol 12. Springer, Berlin
4. Tuantranont A (2013) Springer Ser Chem Sens Biosens 14
5. Bensaude-Vincent B, Newman WR (2007) The artificial and the natural: an evolving polarity. MIT Press, Cambridge, MA
6. McConnell R (2002) Renew Sust Energ Rev 6:271–293
7. Shahinpoor M, Bar-Cohen Y, Simpson J, Smith J (1998) Smart Mater Struct 7:R15
8. Bhushan B, Jung YC (2011) Prog Mater Sci 56:1–108
9. Douglas T, Young M (1999) Adv Mater 11:679–681
10. Lenau T, Stroble J, Stone R, Watkins S (2009) Sens Rev 29:112–119
11. Guilbault GG, Pravda M, Kreuzer M, O'Sullivan C (2004) Anal Lett 37:1481–1496
12. Vatansever D, Siores E, Shah T (2012) Global warming – impacts and future perspective, p 263
13. Sauerbrey G (1959) Z Physik 155:206–222
14. Kanazawa KK, Gordon JG (1985) Anal Chem 57:1770–1771
15. Saluz H-P, Köhler M, Mejevaia T (2012) Microsystem technology: a powerful tool for biomolecular studies. Birkhäuser, Basel
16. Konradi R, Textor M, Reimhult E (2012) Biosensors 2:341–376
17. Muñoz-Aguirre S, López-Casique A, Alcántara-Iniesta S, Castillo-Mixcóatl J, Beltrán-Pérez G, Muñoz-Aguirre N (2014) Sensor Mater 26:131–136
18. Boy J, Tavernier H, Vacheret X, Laroche T, Clairet A (2011) Frequency control and the European frequency and time forum (FCS), 2011 joint conference of the IEEE international, IEEE, pp 1–5
19. Lacour V, Bienaime A, Manceau J-F, Leblois T, Dubowski J (2014) European frequency and time forum (EFTF), 2014, IEEE, pp 163–166
20. Jin X, Huang Y, Mason A, Zeng X (2008) Anal Chem 81:595–603
21. Dickert FL, Lieberzeit PA, Achatz P, Palfinger C, Fassnauer M, Schmid E, Werther W, Horner G (2004) Analyst 129:432–437
22. Dickert FL, Hayden O, Bindeus R, Mann K-J, Blaas D, Waigmann E (2004) Anal Bioanal Chem 378:1929–1934
23. Afzal A, Iqbal N, Mujahid A, Schirhagl R (2013) Anal Chim Acta 787:36–49
24. Voinova MV (2009) J Sens 2009
25. Battiston F, Ramseyer J-P, Lang H, Baller M, Gerber C, Gimzewski J, Meyer E, Güntherodt H-J (2001) Sensors Actuators B Chem 77:122–131
26. Lang HP, Hegner M, Gerber C (2005) Mater Today 8:30–36
27. Braun T, Ghatkesar MK, Backmann N, Grange W, Boulanger P, Letellier L, Lang H-P, Bietsch A, Gerber C, Hegner M (2009) Nat Nanotechnol 4:179–185
28. Chaudhary M, Gupta A (2009) Def Sci J 59:634
29. Dickert FL (2014) Sensors 14:22525–22531
30. Ellington AD, Szostak JW (1992) Nature 355:850
31. Green LS, Jellinek D, Jenison R, Östman A, Heldin C-H, Janjic N (1996) Biochemistry 35:14413–14424
32. Famulok M (1994) J Am Chem Soc 116:1698–1706
33. Nitsche A, Kurth A, Dunkhorst A, Pänke O, Sielaff H, Junge W, Muth D, Scheller F, Stöcklein W, Dahmen C (2007) BMC Biotechnol 7:48
34. Xiao Z, Shangguan D, Cao Z, Fang X, Tan W (2008) Chem Eur J 14:1769–1775
35. Tang Z, Parekh P, Turner P, Moyer RW, Tan W (2009) Clin Chem 55:813–822
36. Xiao Y, Lubin AA, Heeger AJ, Plaxco KW (2005) Angew Chem 117:5592–5595
37. Song S, Wang L, Li J, Fan C, Zhao J (2008) TrAC Trends Anal Chem 27:108–117
38. Lee JH, Jin H-E, Desai MS, Ren S, Kim S, Lee S-W (2015) Nanoscale 7:18379–18391
39. Liss M, Petersen B, Wolf H, Prohaska E (2002) Anal Chem 74:4488–4495
40. Hianik T, Ostatná V, Zajacová Z, Stoikova E, Evtugyn G (2005) Bioorg Med Chem Lett 15:291–295
41. Strehlitz B, Nikolaus N, Stoltenburg R (2008) Sensors 8:4296–4307
42. Voinova MV, Syrkin ES (2009) Ele Com Eng 13

43. Özalp VC (2011) Analyst 136:5046–5050
44. Famulok M, Mayer G (2011) Acc Chem Res 44:1349–1358
45. Schlensog MD, Gronewold TM, Tewes M, Famulok M, Quandt E (2004) Sensors Actuators B Chem 101:308–315
46. Chang K, Pi Y, Lu W, Wang F, Pan F, Li F, Jia S, Shi J, Deng S, Chen M (2014) Biosens Bioelectron 60:318–324
47. Zhang F, Li S, Cao K, Wang P, Su Y, Zhu X, Wan Y (2015) Sensors 15:13839–13850
48. Hwang KS, Lee S-M, Eom K, Lee JH, Lee Y-S, Park JH, Yoon DS, Kim TS (2007) Biosens Bioelectron 23:459–465
49. Menger M, Yarman A, Erdőssy J, Yildiz HB, Gyurcsányi RE, Scheller FW (2016) Biosensors 6:35
50. Wulff G, Sarhan A (1972) Angewandte Chemie-International Edition, vol 11. Wiley, Berlin, p 341
51. Maier NM, Lindner W (2007) Anal Bioanal Chem 389:377–397
52. Wulff G (2002) Chem Rev 102:1–28
53. Haupt K, Mosbach K (2000) Chem Rev 100:2495–2504
54. Polyakov M (1931) Zhur Fiz Khim 2:799–805
55. Vlatakis G, Andersson LI, Müller R, Mosbach K (1993) Nature 361:645–647
56. Wulff G (1995) Angew Chem Int Ed Engl 34:1812–1832
57. Theodoridis G, Manesiotis P (2002) J Chromatogr A 948:163–169
58. Tan Y, Yin J, Liang C, Peng H, Nie L, Yao S (2001) Bioelectrochemistry 53:141–148
59. Haupt K (2010) Nat Mater 9:612–614
60. Bossi A, Bonini F, Turner A, Piletsky S (2007) Biosens Bioelectron 22:1131–1137
61. Tai D-F, Lin C-Y, Wu T-Z, Huang J-H, Shu P-Y (2006) Clin Chem 52:1486–1491
62. Lu C-H, Zhang Y, Tang S-F, Fang Z-B, Yang H-H, Chen X, Chen G-N (2012) Biosens Bioelectron 31:439–444
63. Dickert FL, Hayden O, Halikias KP (2001) Analyst 126:766–771
64. Dickert F, Hayden O (2002) Anal Chem 74:1302–1306
65. Tiwari A, Uzun L (2016) Advanced molecularly imprinting materials. Wiley, Hoboken, NJ
66. Hussain M (2016) UK J Pharmaceut Biosci 4:121–132
67. Fischerauer G, Dickert F, Forth P, Knauer U (1996) Ultrasonics symposium, 1996. Proceedings, 1996 IEEE, vol 1, pp 439–442
68. Matsuguchi M, Uno T (2006) Sensors Actuators B Chem 113:94–99
69. Hallil H, Aouled NO, Plano B, Delépée R, Agrofoglio L, Dejous C, Rebière D (2014) J Integr Circuits Syst 9:118–122
70. Avila M, Zougagh M, Rios A, Escarpa A (2008) TrAC Trends Anal Chem 27:54–65
71. Ebarvia BS, Binag CA, Sevilla F III (2004) Anal Bioanal Chem 378:1331–1337
72. Ratautaite V, Plausinaitis D, Baleviciute I, Mikoliunaite L, Ramanaviciene A, Ramanavicius A (2015) Sensors Actuators B Chem 212:63–71
73. Liang C, Peng H, Bao X, Nie L, Yao S (1999) Analyst 124:1781–1785
74. Ayankojo AG, Tretjakov A, Reut J, Boroznjak R, Öpik A, Rappich J, Furchner A, Hinrichs K, Syritski V (2016) Anal Chem 88:1476–1484
75. Ktari N, Fourati N, Zerrouki C, Ruan M, Nassoko D, Seydou M, Yaakoubi N, Chehimi M, Kalfat R (2015) Procedia Eng 120:998–1002
76. Rodriguez-Mozaz S, Marco M-P, de Alda MJL, Barceló D (2004) Anal Bioanal Chem 378:588–598
77. Percival C, Stanley S, Braithwaite A, Newton M, McHale G (2002) Analyst 127:1024–1026
78. Queiros RB, de-los-santos-Alvarez N, Noronha JP, Sales MGF (2013) Sensors Actuators B Chem 181:766–772
79. Ambrosini S, Beyazit S, Haupt K, Bui BTS (2013) Chem Commun 49:6746–6748
80. Bossi A, Piletsky SA, Piletska EV, Righetti PG, Turner AP (2001) Anal Chem 73:5281–5286
81. EL-Sharif HF, Aizawa H, Reddy SM (2015) Sensors Actuators B Chem 206:239–245
82. Wu A-H, Syu M-J (2006) Biosens Bioelectron 21:2345–2353
83. Naklua W, Suedee R, Lieberzeit PA (2016) Biosens Bioelectron 81:117–124

84. Chunta S, Suedee R, Lieberzeit PA (2015) Anal Chem 88:1419–1425
85. Seidler K, Polreichová M, Lieberzeit PA, Dickert FL (2009) Sensors 9:8146–8157
86. Samardzic R, Sussitz HF, Jongkon N, Lieberzeit PA (2014) Sens Lett 12:1152–1155
87. Horemans F, Alenus J, Bongaers E, Weustenraed A, Thoelen R, Duchateau J, Lutsen L, Vanderzande D, Wagner P, Cleij T (2010) Sensors Actuators B Chem 148:392–398
88. Bongaers E, Alenus J, Horemans F, Weustenraed A, Lutsen L, Vanderzande D, Cleij T, Troost F, Brummer RJ, Wagner P (2010) Phys Status Solidi A 207:837–843
89. Tretjakov A, Syritski V, Reut J, Boroznjak R, Oepik A (2016) Anal Chim Acta 902:182–188
90. Diltemiz SE, Hür D, Keçili R, Ersöz A, Say R (2013) Analyst 138:1558–1563
91. Lin T-Y, Hu C-H, Chou T-C (2004) Biosens Bioelectron 20:75–81
92. Seifner A, Lieberzeit P, Jungbauer C, Dickert FL (2009) Anal Chim Acta 651:215–219
93. Bognár J, Szűcs J, Dorkó Z, Horváth V, Gyurcsányi RE (2013) Adv Funct Mater 23:4703–4709
94. Love JC, Estroff LA, Kriebel JK, Nuzzo RG, Whitesides GM (2005) Chem Rev 105:1103–1170
95. Mendes AC, Baran ET, Reis RL, Azevedo HS (2013) Wiley Interdiscip Rev Nanomed Nanobiotechnol 5:582–612
96. Kepley LJ, Crooks RM, Ricco AJ (1992) Anal Chem 64:3191–3193
97. Campbell GA, Mutharasan R (2006) Anal Chem 78:2328–2334
98. Wangchareansak T, Sangma C, Ngernmeesri P, Thitithanyanont A, Lieberzeit PA (2013) Anal Bioanal Chem 405:6471–6478
99. Shen Z, Huang M, Xiao C, Zhang Y, Zeng X, Wang PG (2007) Anal Chem 79:2312–2319

Enzyme Logic Systems: Biomedical and Forensic Biosensor Applications

Evgeny Katz, Joseph Wang, Jan Halámek, and Lenka Halámková

Abstract We offer an overview of recent advances in biosensors based on the biocomputing concept. Novel biosensors digitally process multiple biochemical signals through Boolean logic networks of coupled biomolecular reactions and produce output in the form of YES/NO response. Compared to traditional single-analyte sensing devices, the biocomputing approach enables high-fidelity multi-analyte biosensing, particularly beneficial for biomedical applications. Multi-signal digital biosensors thus promise advances in rapid diagnosis and treatment of diseases by processing complex patterns of physiological biomarkers. Specifically, they can provide timely detection and alert to medical emergencies, along with an immediate therapeutic intervention. Application of the biocomputing concept has been successfully demonstrated for systems performing logic analysis of biomarkers corresponding to different injuries, particularly exemplified for liver injury. Wide-ranging applications of multi-analyte digital biosensors in medicine, environmental monitoring, forensic analysis, and homeland security are anticipated.

Keywords Biocomputing, Biomedical application, Biosensor, Enzyme logic, Forensic analysis, Injury biomarkers, Logic gate

E. Katz (✉)
Department of Chemistry and Biomolecular Science, Clarkson University, Potsdam, NY 13699, USA
e-mail: ekatz@clarkson.edu

J. Wang
Department of NanoEngineering, University of California San Diego, La Jolla, CA 92093, USA
e-mail: josephwang@ucsd.edu

J. Halámek and L. Halámková
Department of Chemistry, University at Albany, SUNY, Albany, NY 12222, USA
e-mail: jhalamek@albany.edu

M. J. Schöning, A. Poghossian (eds.), *Label-Free Biosensing: Advanced Materials, Devices and Applications*, Springer Series on Chemical Sensors and Biosensors (2018) 16: 345–382
DOI 10.1007/5346_2017_4, © Springer International Publishing AG 2017,
Published online: 9 July 2017

Contents

1 Introduction: Bioanalytical Applications of Enzyme Logic Systems

Biosensors, from the very first prototype pioneered by Clark [1] in 1962 to sophisticated modern devices [2], are all based on the same general concept – a biomolecular reaction with analyte species followed by transduction of a chemical signal to an electronic one. Suitable biomolecular reactions can be based on enzyme-catalyzed processes [3] or biorecognition/bioaffinity events [4] using immune-specific [5], DNA (deoxyribonucleic acid)-specific [6], or bioreceptor-specific [7] interactions. The major advantage of all these processes is the high specificity in the biorecognition of a single selected analyte. The results of the biochemical reactions are usually transduced to electronic signals by electrochemical [8], optical [9], or other [10] physical means. The entire biosensor assembly includes a biosensing interface integrated with an electronic transduction instrument, a power supply, and an electronic (usually computerized) signal-processing unit, Fig. 1A. Usually, the output signal is linearly proportional to the analyte concentration and can be characterized by its dynamic concentration range, where the linear dependence on the analyte concentration is preserved, and selectivity (being independent on various interfering species). Typically, a biosensor provides quantitative information on the concentration of a single analyte, e.g., glucose [11]. Many different bioanalytical assays, e.g., enzyme-linked immunosorbent assay (ELISA) [12], while relying on different recognition events, function in a similar manner. Sometimes the differences between biosensors and bioanalytical assays are merely technical, e.g., when the biomolecular reaction is not fully integrated with the transduction interface of the instrument converting the chemical signal to electronic one.

Simultaneous analysis of several different species is carried out by biosensor or bioassay arrays. Such arrays generate signals from multiple analytical channels working in parallel, each channel providing quantitative information on one specific analyte [13]. The resulting signals can then be processed by a computer, Fig. 1B. In “field” situations when extensive use of computers or human involvement is not practical, drawing quantitative conclusions from the results obtained by

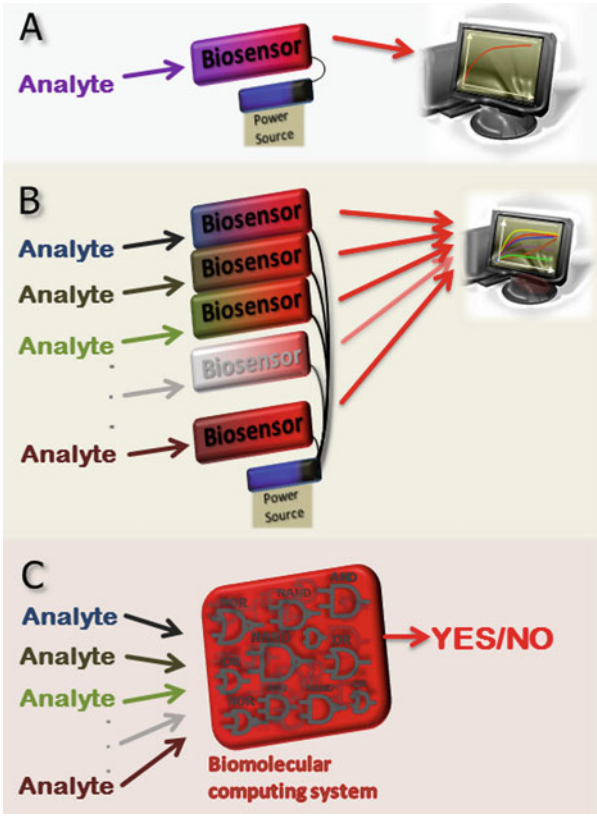

Fig. 1 Different approaches to biosensing: (**A**) a single-analyte biosensor; (**B**) an array of parallel biosensors for multi-analyte analysis with computer-processed multi-channel signals; (**C**) multi-analyte analysis carried out by a biomolecular logic system with the input signals chemically processed and the final output generated in the binary YES/NO form. (The figure was adopted from [67] with permission.)

multi-channel analysis can be challenging, because the concentrations of different analytes typically span wide ranges of values, and their direct inspection not be definitive. Presently, very few applications generate a bioanalytical result with a qualitative YES/NO conclusion. This format can be useful when there is no need for precise, quantitative measurements, e.g., in a pregnancy test [14], or for detection of chemical weapons on a battlefield [15], when a rapid answer is important. Novel approaches to qualitative analysis providing the final result in the YES/NO form would be beneficial for various end-users and point-of-care applications [16] in medicine, homeland security, or military applications, requiring rapid simultaneous analysis of multiple analyte species.

A successful approach has recently been advanced based on unconventional chemical computing [17], specifically, using recently pioneered biomolecular computing systems [18]. Such biocomputing systems based on proteins/enzymes [19], DNA [20], RNA (ribonucleic acid) [21], DNAzymes [22], and whole cells [23] can perform logic operations processing multiple biochemical input signals. Based on biomolecular systems various Boolean logic operations such as AND, OR, XOR, NOR, NAND, INHIB, XNOR, etc., were realized [18]. Sophisticated networks composed of several concatenated biomolecular logic gates performing complex

logic operations were designed for unconventional computing applications [18]. Particularly rapid progress was recently achieved in the area of enzyme-based biocomputing systems allowing their assembling in the form of concatenated logic networks composed of many gates performing various Boolean logic operations and including non-Boolean elements, such as enzyme-based multiplexer and demultiplexer, amplifier, filter, etc. mimicking their electronic counterparts [19]. Although chemical information processing systems were originally considered exclusively for computational applications [24], it has recently been realized that they have features suitable for analytical/bioanalytical use [25]. These systems can analyze several biochemical signals according to a predesigned "program" and generate a binary "YES/NO" answer without using a computer. Such chemical testing, analogous to a pregnancy test, might be convenient for certain end-user and point-of-care applications, Fig. 1C. Networks with computational steps that involve only biochemical processes [18, 19] are being investigated for new technological capabilities that include multi-input biosensors with new functionalities [25]. New approaches are being explored, allowing to reduce the use of batteries, inorganic leads, and electrical power supply for those stages of information processing that occur during biomedical testing, in implantable devices, and towards fast-decision making steps (e.g., therapeutic intervention). The following sections of the chapter describe how the biomedical analysis can benefit from the use of biomolecular information processing (biocomputing) systems and then illustrate logic systems processing biomarkers signaling for liver injury.

2 Biocomputing Approach to the Analysis of Injury Biomarkers

When a biomedical analysis aimed at recognizing a pathophysiological dysfunction is performed with a biosensor, each specific biomarker should be analyzed separately according to a traditional approach. The search for biomarkers signaling various medical problems has become a very important area of medical research [26]. However, diagnostic conclusions can rarely be based on the analysis of just a single highly specific biomarker. Moreover, biomarkers may appear at low concentrations in a complex mixture with many other biomolecular species of similar structure and properties. For example, neuron-specific enolase is considered as a specific biomarker for traumatic brain injury (TBI) [27]. However, its concentration in physiological fluids is much lower than that of generic enolases with similar biocatalytic properties. Furthermore, elevated levels of the enolase activity might result from some other dysfunctions which are not directly related to TBI [28]. Therefore, even the species which is considered as a biomarker might not be specific enough to draw a reliable biomedical conclusion based on a single-species analysis. A standard solution of the specificity problem has been to analyze a set of less specific biomarkers present simultaneously with overlapping specificity, Fig. 2,

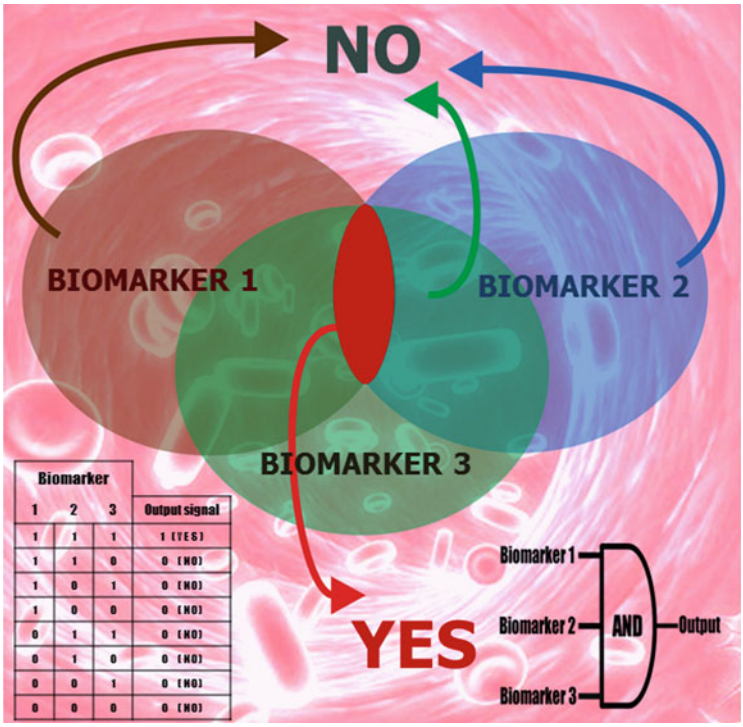

Fig. 2 Simultaneous presence of biomarkers with limited specificity indicates a definitive YES conclusion, schematically represented by the overlapping region in the diagram. In the biochemical computing approach, this conclusion is realized as the output YES (or **1**) of a multi-input AND logic gate, obtained only when all the three inputs are in the ranges corresponding to **1**. The output NO (or **0**) is obtained for all the other combinations of inputs. The "truth table" for such a three-input gate and its logic diagram are also shown. (The figure was adopted from [67] with permission.)

and in the biocomputing approach such analysis is realized via a cascade of biocatalytic reactions.

A biocomputing approach can reduce technical problems in the analysis of highly specific biomarkers by analyzing species appearing at much higher concentrations. For example, glutamate and lactate dehydrogenase analyzed together for their pathophysiologically elevated concentrations could provide an attractive alternative for the challenging analysis of neuron-specific enolase to diagnose TBI [29]. Analysis of several biomarkers, each with limited selectivity, requires a proper design of a logic network for processing of the analyte signals. For example, analysis of two biomarkers for their simultaneous presence requires a biochemical reaction mimicking the Boolean AND logic operation [30]. In case of multiple biomarkers, more sophisticated logic networks composed of several logic gates performing various logic operations might be needed [31]. For example, a multi-enzyme/multi-input logic network composed of many concatenated AND/OR gates

equipped with different biomolecular switches controlling the pathways involved in the input processing was designed for the analysis of different injury biomarkers [31]. These logic operations can be performed as a sequence of biochemical reactions without the use of electronic computers [18, 19]. Both optical and electrochemical transduction modes can be used for detecting the products of such logic operations. Biomedical use of logic gates and sophisticated logic networks is a rather new and undeveloped research area, being advanced in parallel with similar developments, such as logic operations realized with synthetic organic molecules aiming at computational applications [17, 32].

Biomolecular information processing systems have already been successfully applied to analyze protein libraries associated with multiple sclerosis [33]. Biosensor systems for detection of genetic modifications in avian influenza were developed based on the DNA computing principles, involving various oligonucleotide signals being processed by a DNA logic network [34]. Coupling enzyme logic systems with controlled self-assembly of nanoparticles allowed AND/OR logic responses to matrix-metalloproteinases MMP2 and MMP7 [35]. In this study, the enzymes used as the input signals were important cancer biomarkers. MMP2 is over-expressed in many cancers, including breast cancers, and is an indicator of cancer invasiveness, metastasis, and angiogenesis, while MMP7, a protease with broader substrate specificity, is thought to facilitate early stages of mammary carcinoma progression.

The use of input signals with obvious biomedical relevance has represented a significant first step in the development of enzyme logic systems. However, the following important issues have required additional attention: (1) In model studies, the logic **0** values of the input signals were frequently taken as the complete absence of the biomaterial, whereas for practical applications they should be defined as normal physiological concentrations. (2) The logic **1** values of the input signals did not always correspond to the concentrations expected in vivo. Instead they were selected as convenient concentrations which sometimes significantly exceeded pathophysiological levels. (3) Processing of the input signals according to different logic schemes did not always correspond to their diagnostic uses. For example, the proteases MMP2 and MMP7 were applied to activate the AND as well as OR logic gates without justification of the logic operation needed for the appropriate biomedical conclusion [35]. Some of these issues, which are particularly important for practical biomedical applications, were addressed in our recent research. Logic systems for the analysis of biomarkers characteristic of various battlefield injuries, which are important for immediate field-based decision making and therapeutic action (in the absence of hospital facilities), have been developed [31, 36, 37], and then theoretically modeled and optimized [38].

Let us illustrate how logic gates can be optimized for practical biomedical analytical applications and integrated with electronic transducing interfaces amplifying the chemical signal. For this discussion, in order to keep it simple, we will consider only one example system performing a single AND logic operation. The selected example will allow following the development of the system from its biosensoric use to bioactuation and from analysis of model solutions artificially

spiked with biomarkers to the assay of real biological samples containing naturally produced biomarkers. It should be noted, however, that much more sophisticated logic networks composed of many concatenated logic gates and processing more than two input signals were designed for computational and biosensoric applications (the readers can find their examples in the recent reviews [18, 19]).

We consider the system [37] activated by two biomarkers mimicking an AND logic gate and signaling liver injury when the concentrations of both are elevated from the normal to pathophysiological levels. The two inputs are the enzymes alanine transaminase (ALT, E.C. 2.6.1.2) and lactate dehydrogenase (LDH, E.C. 1.1.1.27), which are biomarkers characteristic of liver injury (LI) [39]. It should be noted that each of them alone is not specific enough to indicate LI, however their simultaneous increase in concentration, from normal to pathophysiological levels, provides an unambiguous evidence of LI [40]. Logic **0** and **1** levels of ALT (0.02 and 2 U mL^{-1}) and LDH (0.15 and 1 U mL^{-1}) input signals were selected in order to mimic meaningful circulating levels of these biomarkers under normal and pathophysiological conditions, respectively [39–42]. Based on the sequence of the biochemical reactions, Fig. 3A, the final result, oxidation of NADH (nicotinamide adenine dinucleotide, reduced form) which causes the

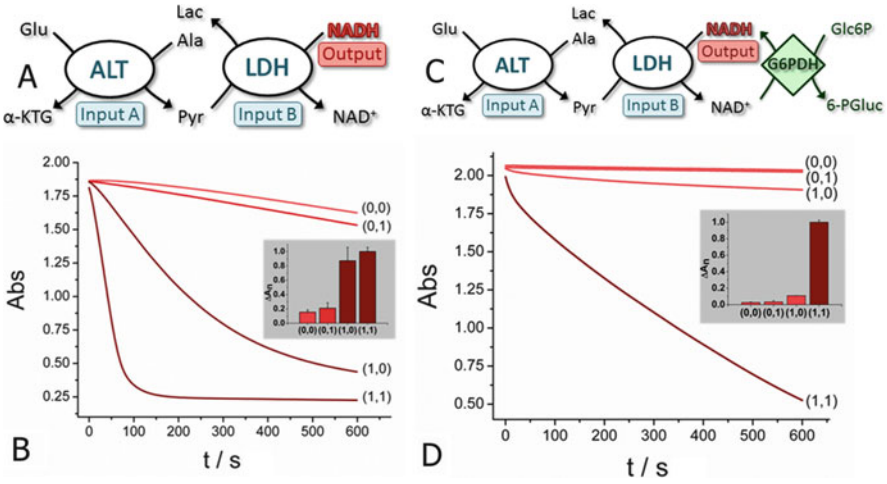

Fig. 3 (**A**) Biocatalytic cascade for analysis of LI, activated by enzymes ALT and LDH as inputs for the AND logic gate. (**B**) Optical absorbance changes corresponding to the decreasing concentration of NADH upon application of different combinations of input signals. The inset shows the normalized output signals measured at 600 s from the reaction initiation. (**C**, **D**) The biocatalytic cascade and absorbance changes for a similar system operating with the added biochemical "filter" partially resetting the output signal, back to nearly its zero level, as long as the filter-activating substrate is not consumed. The inset in (**D**) shows the normalized output signals measured at 600 s with the improved separation between the logic outputs **0** and **1**. The filter enzyme is glucose-6-phosphate dehydrogenase (E.C. 1.1.1.49); the substrate and product in the filter step are D-glucose-6 phosphate and 6-phospho-gluconic acid, respectively. The following abbreviations for products and intermediates are used: Pyr pyruvate, Lac lactate, Glu glutamate, Ala L-alanine, α-KTG α-ketoglutaric acid. (The figure was adopted from [67] with permission.)

decrease in the optical absorbance, Fig. 3B, should be obtained only upon concerted work of the two enzyme biomarker inputs. However, it should be remembered that logic **0** values in their present definition are not the absence of the enzymes, but rather their presence at normal physiological levels. Therefore, the decrease in absorbance is observed not only for the **1**,**1** input combination, but also to some extent for inputs **0**,**0**, **0**,**1** and **1**,**0**, Fig. 3B. When the readout time interval is limited to 50–200 s, the absorbance decrease is measurably larger for the **1**,**1** input combination, defining output **1**. The other three input combinations yield smaller absorbance changes, defining output **0**, Fig. 3B. However, for reaction times exceeding 200 s, which are relevant for recently investigated actuation applications [43], the absorbance decrease for the **1**,**0** input combination becomes comparable with one for **1**,**1** inputs, Fig. 3B. At sufficiently long reaction times, the results for the **1**,**0** and **1**,**1** input combinations will become indistinguishable, and the AND gate will no longer be realized, Fig. 3B, inset.

In order to increase the gap separating output signals **0** and **1**, a "filter" process [44] was added consuming the chemical product NAD^+ (nicotinamide adenine dinucleotide, oxidized form), converting it back to NADH for small input concentrations, Fig. 3C. This has allowed us to achieve high-quality signal separation for times as large as 600 s and beyond, Fig. 3D. It is likely that such "filter" processes can potentially be implemented with any so-called NAD^+-dependent dehydrogenase [45], e.g., glucose dehydrogenase activated by physiological amounts of glucose. However, aiming at the eventual application of our system in a physiological environment, we selected glucose-6-phosphate dehydrogenase (G6PDH, E.C. 1.1.1.49) as the filter-enzyme. It is activated by D-glucose-6 phosphate (Glc6P) which does not interfere with glucose naturally existing in blood, thus allowing tuning the Glc6P concentration independently on the physiological glucose concentration. The filter system works in the following way: In the presence of G6PDH and Glc6P, the biocatalytically produced NAD^+ is converted back to NADH. Thus, absorbance changes are prevented until Glc6P is totally consumed. Only then the depletion of NADH can fully set in, resulting in the absorbance decrease. The delay in the biocatalytic oxidation of NADH is controlled by the amount of the added Glc6P and can be optimized. Comprehensive approach to the filter performance optimization could include detailed analysis of the reactions kinetics [44]. However, a simple experimental optimization might suffice. Addition of the G6PDH-Glc6P filter to the biocatalytic cascade activated by ALT-LDH biomarker inputs, Fig. 3C, has allowed a much better separation of the output signals generated by the system for the **1**,**1** vs. all the other combinations of the inputs, Fig. 3D. However, while improving the binary signal separation, such filtering can decrease the overall signal strength which could be an added source of relative noise [46]. Thus, filtering is useful at sufficiently large times, when the decrease in the absorbance reaches its saturation being relevant for actuation applications [43]. When the output signals were measured at 600 s, the desired system operation corresponding to the high-tolerance AND-logic realization was obtained in the presence of the filter, Fig. 3D, inset. Good-quality separation of the **0** and **1** output signals was found to persist at much larger times as well, up to 3 h.

The robustness of this analytical system has allowed its use in human serum solutions [37].

A system similar to that described in Fig. 3C, but with glucose dehydrogenase (GDH, E.C. 1.1.1.47) as the filter-enzyme, was used for electrochemical transduction/amplification of the signals generated by the AND logic gate activated by ALT and LDH biomarkers [43], Fig. 4. The reaction biocatalyzed by the filter-enzyme

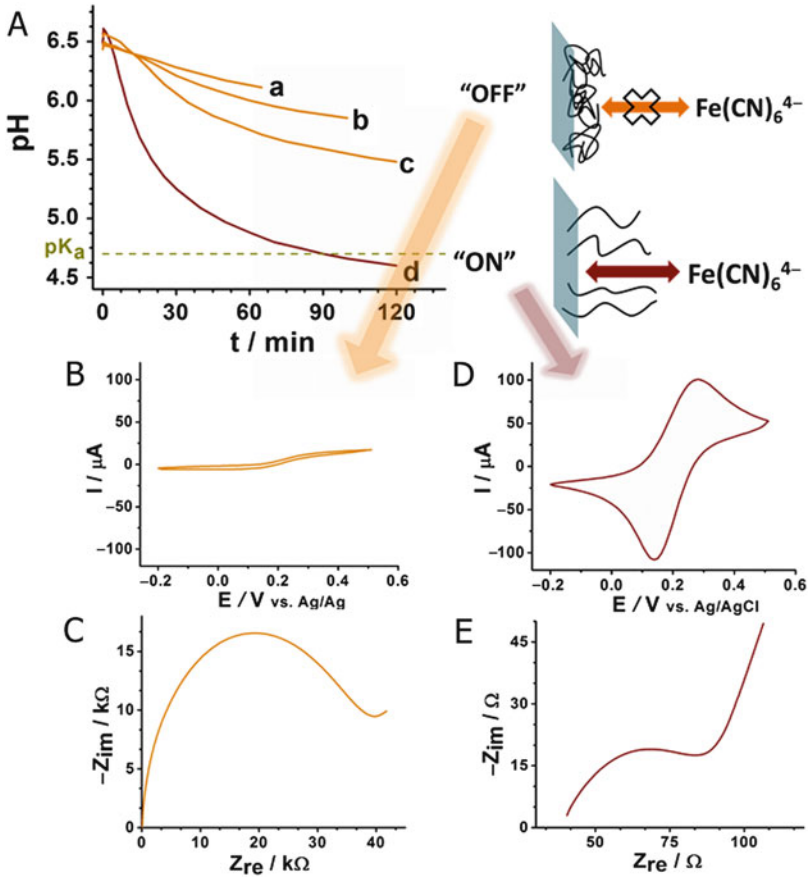

Fig. 4 Electrochemical transduction of the signals generated by the AND logic gate for analysis of LI activated by ALT and LDH input signals: (**A**) pH changes generated in situ by the biocatalytic cascade activated with various combinations of the ALT/LDH signals: (a) **0**,**0**; (b) **0**,**1**; (c) **1**,**0** and (d) **1**,**1**. The *dotted line* corresponds to the pK_a value of the P4VP-brush immobilized on the electrode surface. (**B**, **D**) Cyclic voltammograms, 10 mM $K_4[Fe(CN)_6]$, 100 mV s^{-1}, obtained at the electrode in the OFF and ON states, respectively. (**C**, **E**) Impedance spectra in the form of Nyquist plots (Z_{re} and Z_{im} are real and imaginary parts of the impedance), 10 mM $K_4[Fe(CN)_6]$, bias potential of 0.17 V, obtained at the electrode in the OFF and ON states, respectively. The biocatalytic cascade is the same as in Fig. 3C, but here the filter enzyme is glucose dehydrogenase (GDH, E.C. 1.1.1.47), the substrate and product operating with it are glucose and gluconic acid, respectively. (The figure was adopted from [67] with permission.)

provided improved resolution between the output **0** and **1** signals as described above. In addition, glucose was oxidized in the "filter" biocatalytic step resulting in the formation of gluconic acid and lowering the pH value. A pH-switchable electrode modified with poly(4-vinyl pyridine) (P4VP) was activated for electrochemical reactions only when the solution pH value reached the pK_a of the P4VP polymer brush. In the pH range below pK_a, protonation of the polymer brush produced a swollen state permeable for anionic redox species, Fig. 4A. The pH changes resulting in the electrode activation were achieved only when both biomarker inputs, ALT and LDH, were applied at their **1**,**1** logic values corresponding to the conditions of LI injury. Any other combinations of the input signals (**0**,**0**, **0**,**1** and **1**,**0**) did not produce pH changes reaching the polymer pK_a value and thus did not result in the electrode activation, Fig. 4A. The inactive state of the pH-switchable electrode was characterized by cyclic voltammetry and Faradaic impedance spectroscopy, which demonstrated no peaks and a large electron transfer resistance, respectively, Fig. 4B, C. This is consistent with the properties of the P4VP polymer brush in the neutral (non-protonated) state which is hydrophobic and non-permeable to ionic redox species. The active state of the electrode was obtained only upon application of the **1**,**1** combination of the input signals and showed peaks in the cyclic voltammogram typical for the reversible electrochemical reaction of $[Fe(CN)_6]^{3-}$ redox probe, Fig. 4D, while the impedance spectrum showed the corresponding decrease in the electron transfer resistance, Fig. 4E (note the difference in the impedance scales of the C and E panels). Utilization of a pH-sensitive electrode allowed not only electrochemical transduction of the biochemical output signal generated by the biocatalytic cascade, but also its significant amplification. Small change in the concentration of NAD^+, which is required for glucose oxidation, sufficed for the electrode activation for the redox probe used at a large concentration.

It should be noted that the filter-reaction increasing the separation between the output signal **0** and **1** logic values is critically important for achieving the results described above. In the described systems, ALT and LDH were systematically added to the analyte solutions in four different combinations: **0**,**0**; **0**,**1**; **1**,**0** and **1**,**1**, where **0** and **1** input values corresponded to the normal and pathophysiological concentrations of the biomarkers. The input combinations **0**,**0** and **1**,**1** correspond to the normal physiological and liver-injury conditions, respectively, while the combinations **0**,**1** and **1**,**0** have medical meanings unrelated to the liver injury. In order to analyze performance of the system under real physiological conditions, the samples containing biomarkers should be obtained from biological sources rather than prepared in a laboratory. A well-established previously described [47] model for porcine injury was utilized to obtain samples mimicking physiological conditions of human liver injury. Assuming that porcine samples contain the biomarker concentrations similar to the human physiology [48], they were analyzed for the simultaneous presence of ALT and LDH. Since the biomarkers were not artificially added to the samples, but rather naturally appeared under varying the animal physiological conditions [48], only two major categories of the samples were expected, with **0**,**0** and **1**,**1** logic levels of ALT and LDH for the control and

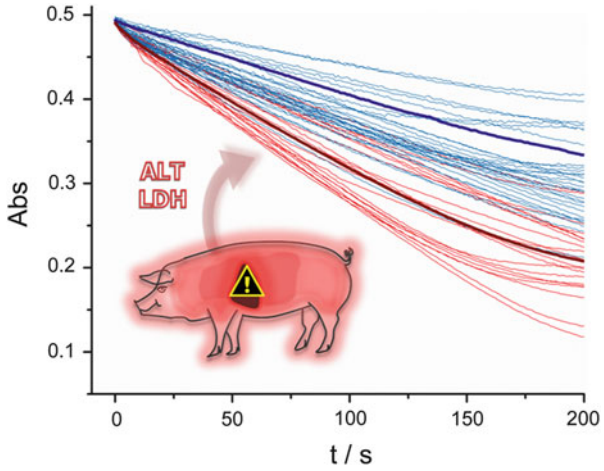

Fig. 5 Absorbance changes corresponding to the consumption of NADH upon operation of the analytical system activated by porcine samples naturally containing ALT and LDH biomarkers. The bottom (*red*) traces correspond to the application of porcine samples from the liver-injured animals, while the top (*blue*) traces correspond to the control group of animals without liver injury. The *individual lines* represent statistic distribution of the biomarker concentrations. *Bold solid curves* show the average responses for both groups. (The figure was adopted from [67] with permission.)

liver-injured groups of animals, respectively. Within these two groups, the porcine samples still had fluctuations in the concentrations of the enzyme biomarkers [48]. This is illustrated in Fig. 5, which shows the time-dependent decrease of NADH absorbance during the reaction of the analytical system with the porcine serum samples. The bottom section of the absorbance decay corresponds to the porcine samples originating from the liver-injured animals (elevated concentrations of the biomarker-enzymes), while the top part was obtained for control animals without the liver injury (with the biomarker-enzymes present at the normal physiological concentrations). These responses are statistically different from each other. The established difference between normal physiological and pathophysiological levels of the biomarkers thus allows distinguishing liver-injured animals from the control group.

3 Biocomputing Applications in Forensic Science

Forensic chemical/biochemical analysis is an essential tool in the criminal justice system, particularly when examining physical evidence to support criminal investigations and subsequent prosecutions [49]. Forensic evidence that is carefully gathered and analyzed can provide important information and potentially lead to the arrest and conviction of a suspect. A biochemistry/molecular biology–based

subarea of forensic analysis, forensic serology, deals with the complex task of gathering information on type of sample, age, origin or gender from biological fluids (blood, saliva, etc.) found at a crime scene [50–54]. If blood or other fluids not belonging to a victim are found at a crime scene, they can be analyzed to provide important information for the investigation. Such data can significantly improve the information pool about possible suspects. Modern forensic serology [55–57] relies on two major methods: immunoassays [57] and DNA [58] /RNA [59] analysis. Compared to the very traditional, rather primitive immunoprecipitation techniques [60] that have been used for dozens of years for blood type determination ("blood typing") [55, 56], DNA analysis is a sophisticated approach that utilizes polymerase chain reaction (PCR), electrophoresis, and blotting techniques, and provides excellent, valuable, and complex results in the field of forensic analysis [58]. Nowadays, DNA-based techniques need to be employed for gathering complex sets of information, like gender, age, or ethnicity from body fluid samples exclusively [61]. "DNA profiling" is used to obtain a DNA "fingerprint" from a biological sample and compares it to profiles obtained from DNA at a crime scene, from an individual, or from profiles stored in a database [62]. Recent developments in this area have allowed for faster apprehension of suspects through comparing newly obtained crime scene samples to those already stored in the database, thus providing links between specific criminals and the crime scene in question. A second application of DNA analysis, "DNA matching" can often be used to either prosecute or release a person, as the blood and other bodily fluids can create a direct link between a violent crime scene and an assailant. However, most of these analyses require sophisticated techniques and complex instrumentation [55]. Thus, current on-site analysis in forensic serology is based entirely on identification of possible samples (e.g., bloodstains) [63] and sample collection, followed by transportation of these samples to specialized laboratories. This introduces time-delay in the investigation procedure and increases the complexity of the investigation itself. Despite the modern trend of designing portable equipment for on-site forensic biochemical analysis [55, 64], including microfluidic [65] and lab-on-a-chip [66] systems, there is an obvious lack of on-site sample detection/characterization technologies, analogous to point-of-care diagnostic approaches, which have become common in medical areas (e.g., diabetes management, pregnancy tests, etc.).

Recent advances in chemical [17] and biochemical [18] unconventional computing, particularly based on enzyme-catalyzed reactions [19], have allowed for formulation of biocatalytic cascades activated by biomarkers characteristic of various pathophysiological conditions (e.g., different injuries) [30, 31, 36]. In general, this approach has resulted in novel bioanalytical methods where combinations of biomolecular inputs result in simple diagnostic conclusions in the binary YES/NO format [25, 67]. Application of this biomedical analysis to forensic investigations can result in novel methods of obtaining information about a crime scene via the analysis of various combinations of biomarkers found in biological samples at a crime scene [68].

3.1 *Biocatalytic Logic Analysis of Biomarkers for Forensic Identification of Ethnicity Between Caucasian and African American*

Biochemical analysis of several biomolecular substances with the approach borrowed from unconventional computing was applied to the analysis of biomarkers characteristic of different ethnic groups [69]. It should be noted that many different biomolecular markers (particularly proteins/enzymes) vary in biofluids depending on ethnic origin [70, 71]. However, the analysis of most of them requires sophisticated proteomic methods and complex instrumentation (e.g., mass-spectroscopy) [72]. Still, some of the enzymes can be analyzed using relatively simple assay procedures. In order to amplify the difference in their analytical discrimination the assay should include two or more analyzed biocatalytic species in the same multi-step biocatalytic cascade. Therefore, the biomarker selection should be based on two criteria: (1) significant difference in the concentrations depending on the sample origin (in the present case depending on the ethnic origin) and (2) inclusion of several (at least two) biomarkers in a single biocatalytic cascade to amplify their effect on the final analytical output signal.

A recently developed biocatalytic assay analyzing simultaneous presence of creatine kinase (CK; E.C. 2.7.3.2) and lactate dehydrogenase (LDH; E.C. 1.1.1.27) was aimed at the recognition of biofluids of different ethnic origins for forensic applications. Knowing the difference in the concentrations of CK and LDH in the blood of healthy adults of two ethnic groups, Caucasian (CA) and African American (AA) [73, 74], and taking into account the distribution pattern, we mimicked the samples of different ethnic origin with the appropriate CK/LDH concentrations. The analysis was performed using a multi-enzyme/multi-step biocatalytic cascade in which the concentration differences in both incorporated enzymes resulted in an amplified difference in the final analytical response. The statistically established analytical results confirmed excellent probability in distinguishing samples of different ethnic origin (CA vs. AA). The standard enzymatic assay routinely used in hospitals for the analysis of CK, performed for comparison, was not able to distinguish the difference between mimicked blood samples of the different ethnic origins. Robustness of the proposed assay was successfully tested on dried/aged serum samples (up to 24 h) in order to mimic a realistic forensic scenario. The results obtained from the model solutions were confirmed by the analysis of real serum samples collected from human subjects of different ethnic origin.

It is well known that CK [75–77] and LDH [41, 78] serum levels can be used as diagnostic tools for various injuries [30, 31, 36] and their concentrations significantly vary for "healthy" and "unhealthy" samples. However, they were not applied to the analysis of "healthy" samples with different ethnic origins prior to our study. One of the reasons for this is because of a relatively small difference in their concentrations depending on the origin, while the person-to-person variation can easily screen the original difference. For example, in reference to this particular study, mean concentrations of CK are 180 U/L and 665 U/L in CA and AA ethnic

groups [73], respectively (note the large difference of 485 U/L), while mean concentrations of LDH differ much less: 152 U/L and 167 U/L in CA and AA groups [74], respectively (the difference of 15 U/L only). In order to solve this problem, both biomarkers (CK and LDH) were included in a single multi-step biocatalytic cascade resulting in amplification of the difference. For illustrating the advantage of this approach, a single CK enzyme-assay [79–81] was applied for comparison.

Figure 6A, B shows the biocatalytic cascades used in the new two-enzyme CK/LDH-assay and single-enzyme CK-assay, respectively. The CK/LDH-assay was experimentally optimized for the best performance, while the CK-assay was used in the standard version recommended by Sigma-Aldrich [82] and commonly used in hospitals [83]. For both analytical procedures we used sets of samples mimicking CK and LDH concentrations in CA and AA groups and then applied statistical analysis to demonstrate and evaluate the difference between the samples mimicking different ethnic (CA and AA) origin.

The CK concentration distribution in human plasma has been previously studied [73] in order to investigate the CK variability in baseline serum and the contribution of ethnicity, gender, and other factors. The study has reported significant ethnic differences in CK levels. The reported data were used in the present study to prepare solutions mimicking CK levels in the blood of different ethnic origins (CA and AA). In order to determine the appropriate concentration values to use in

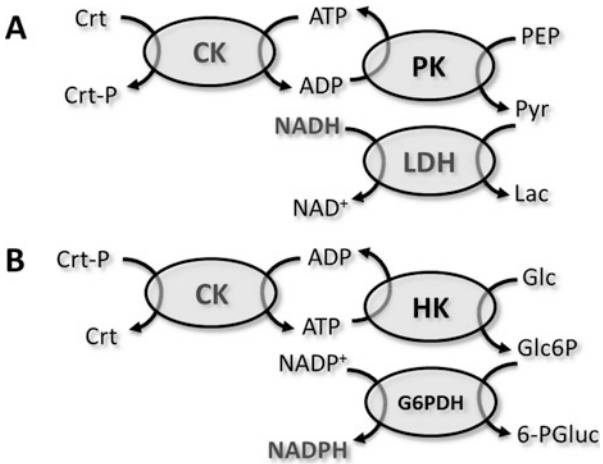

Fig. 6 (**A**) The biocatalytic cascade for the two-enzyme CK/LDH-assay. (**B**) The biocatalytic cascade for the one-enzyme CK-assay. The following abbreviations are used in the scheme: CK creatine kinase, PK pyruvate kinase, LDH lactate dehydrogenase, Crt creatine, Crt-P creatine phosphate, ATP adenosine 5′-triphosphate, ADP adenosine 5′-diphosphate, NAD^+ β-nicotinamide adenine dinucleotide, NADH β-nicotinamide adenine dinucleotide reduced, PEP phospho(enol) pyruvic acid, Pyr pyruvate, Lac lactate, HK hexokinase, G6PDH glucose-6-phosphate dehydrogenase, $NADP^+$ β-nicotinamide adenine dinucleotide phosphate, NADPH β-nicotinamide adenine dinucleotide phosphate reduced, Glc glucose, Glc6P glucose-6-phosphate and 6-PGluc 6-phosphate gluconic acid. (The figure was adopted from [69] with permission.)

our study, we started from the statistical analysis of the available data. The values were not normally distributed, but rather positively skewed and consistent with a log-normal distribution. The parameters of the log-normal distribution were available only for overall CK values, while the distribution parameters estimated from the CA and AA groups came from logarithmic untransformed data. To generate CK concentrations/values for CA and AA groups that arise from the same distribution reported in the CK study, we first corrected only the available parameters from normal distribution to log-normal. Using the standard R-project software [84, 85], we generated random values according to the recalculated parameters for the log-normal distribution of CA ($M_{\log} = 4.37 \pm 1.28$ mU/mL) and AA ($M_{\log} = 5.61 \pm 1.34$ mU/mL) groups based on the CK distribution parameters reported by Deuster et al. [73]. We employed 25 randomly calculated concentrations for each group. The two sets, with identical CK concentrations mimicking the CK distribution in CA and AA groups, were then used in the two-biomarker CK/LDH-assay, Fig. 6A, followed by the single-biomarker CK-assay, Fig. 6B, for comparison. Hence, the two-biomarker enzymatic assay requires variable LDH input. Another set of values (LDH concentrations) characteristic for CA ($M_{\log} = 4.99 \pm 0.21$ mU/mL) and AA ($M_{\log} = 5.09 \pm 0.24$ mU/mL) groups has been generated to follow a log normal distribution. Since the parameters have been reported for a normal distribution [74] they have been recalculated first to follow a log-normal distribution. Since these two biomarkers (CK and LDH) are not associated [86, 87], both sets of CK and LDH values have been randomly paired together by R-project software and these CK-LDH concentration pairings have been used in the analysis of the samples mimicking the distribution of CA and LDH concentrations for the CA and AA groups.

Figures 7 and 8 show the experimental results using the two-enzyme CK/LDH-assay and the single-enzyme CK-assay, respectively, where the CK and LDH concentrations were selected from the values known for the CA and AA ethnic groups with distribution parameters calculated according to the procedure described above. Note that the analytical responses are represented by the decreasing optical absorbance of NADH in the CK/LDH-assay and increasing optical absorbance of NADPH in the CK-assay, respectively, which is consistent with the biocatalytic cascades used in the assays, Fig. 6. To examine the distribution of our output data we prepared histograms, Figs. 9 and 10. Since the input data exhibits a log-normal distribution, this distribution is projected into the output data to some extent and extreme values influence the shape of the distributions in all four plots. Additionally, we superimposed a probability density function (PDF) into our histograms [88]. Since all the distributions are skewed we favored the non-parametric approach over choosing an underlying distribution. The kernel density estimation, which is the most common non-parametric method [89, 90], has been applied.

The presented histograms with the superimposed PDFs show how the output signals for CA and AA groups are distributed, i.e. how their separation will enable

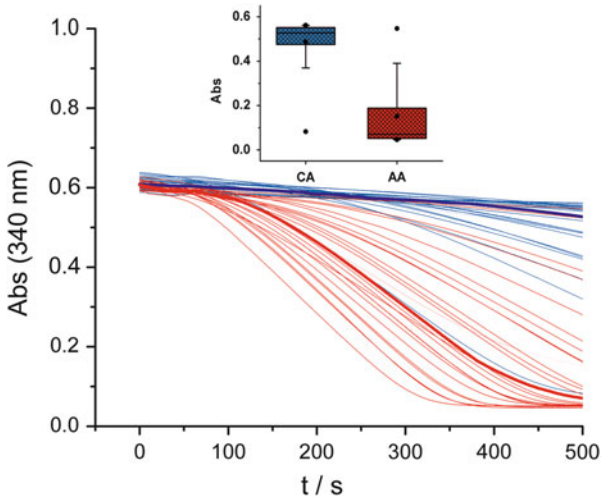

Fig. 7 Absorbance ($\lambda = 340$ nm) corresponding to the consumption of NADH upon operation of the CK/LDH-assay. The bottom (*red*) and top (*blue*) traces correspond to the application of samples with CK and LDH concentrations mimicking AA and CA groups, respectively. *Bold solid curves* show the median responses for both groups. Inset: box and whisker plot of Abs in AA and CA groups. The median value for each group is noted with the *horizontal line* in a box, the boxes represent the range of values from the 25th percentile to the 75th percentile, the ends of the whiskers represent the 5th and 95th percentile of values, and the *dots* are the mean, maximum, and minimum values. (The figure was adopted from [69] with permission.)

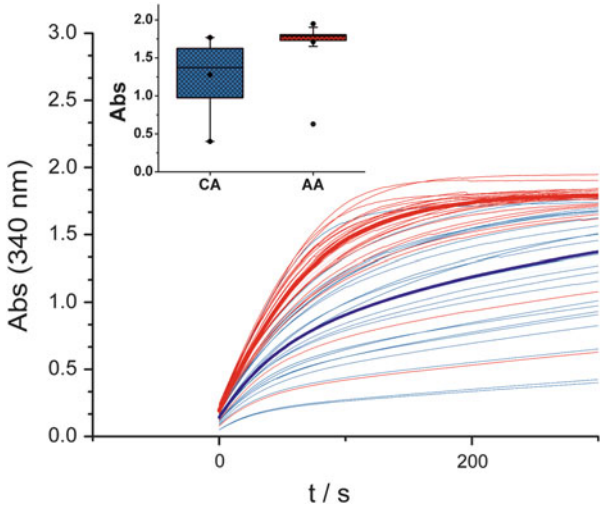

Fig. 8 Absorbance ($\lambda = 340$ nm) corresponding to the production of NADPH upon operation of the CK-assay. The bottom (*blue*) and top (*red*) traces correspond to the application of samples with CK concentrations mimicking CA and AA groups, respectively. *Bold solid curves* show the median responses for both groups. Inset: box and whisker plot of Abs in AA and CA groups. The median value for each group is noted with the *horizontal line* in a box, the boxes represent the range of values from the 25th percentile to the 75th percentile, the ends of the whiskers represent the 5th and 95th percentile of values, and the *dots* are the mean, maximum, and minimum values. (The figure was adopted from [69] with permission.)

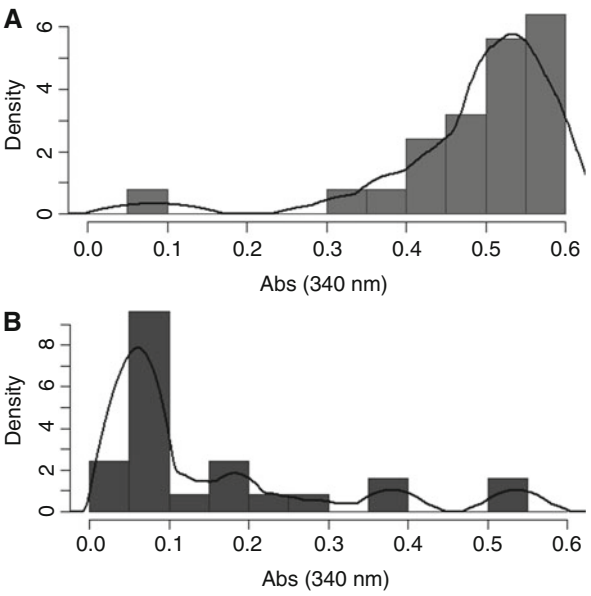

Fig. 9 Density histograms of the output signal (absorbance) obtained for: (**A**) CA group and (**B**) AA group using the CK/LDH-assay (see the biocatalytic cascade shown in Fig. 6A). The histograms were derived from the experimental data shown in Fig. 7. Superimposed is the kernel density curve. (The figure was adopted from [69] with permission.)

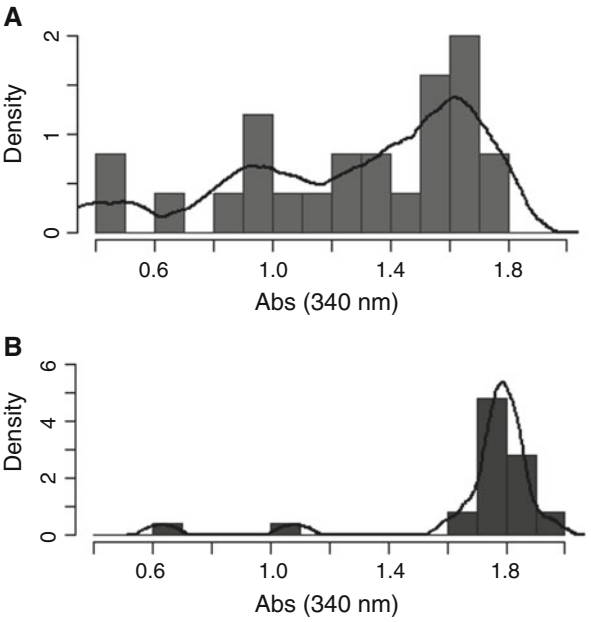

Fig. 10 Density histograms of the output signal (absorbance) obtained for: (**A**) CA group and (**B**) AA group using the CK-assay (see the biocatalytic cascade shown in Fig. 6B). The histograms were derived from the experimental data shown in Fig. 8. Superimposed is the kernel density curve. (The figure was adopted from [69] with permission.)

us to distinguish between these two groups. It is apparent from the illustrated histograms that the two-enzyme (CK/LDH) method performs much better than the standard single-enzyme (CK) method in terms of the overlap between two groups. Also, the two-enzyme CK/LDH-assay achieves better results than the

standard single-enzyme CK-assay in terms of the separation between the distributions [91, 92]. In other words, the separation of the output optical signals was significantly increased when two enzymes were analyzed in the biocatalytic cascade. When the output signal distributions have wide separation, the analytical discrimination between the analyzed CA and AA groups becomes easier. In order to mathematically define the quantitative degree of separation between the two probable distributions over the full set of values metric dissimilarity/similarity measures have been calculated. The Hellinger distance (HD) was used to quantify the dissimilarity between two probability distributions and the Bhattacharyya coefficient (BC) was applied as a measure of the similarity between two probability density functions [91]. A higher value of the BC is associated with more similarity between the histograms. The opposite statement is valid for HD, where a higher value is associated with more dissimilarity between the histograms. For the new two-enzyme CK/LDH-assay the BC and HD values were 0.34 and 0.81, respectively, while the standard single-enzyme CK-assay results in BC and HD equal to 0.83 and 0.41, respectively. An improvement in robustness of the new two-enzyme CK/LDH analytical assay has been demonstrated by its increased ability in distinguishing the difference between CA and AA analyzed groups.

The experiments described above confirmed the capability of the two-enzyme CK/LDH-assay for distinguishing the difference between the CA and AA groups. They were performed in model solutions, however, comprised of an aqueous buffer spiked with the CK and LDH to the concentrations characteristic of the analyzed groups. In real conditions of interest for forensic analysis, the biomarkers should be analyzed in blood stains found at a crime scene. In order to mimic forensic conditions, we performed the analysis in human serum solutions. In the first set of measurements we prepared the samples from serum representing mixed solutions from various donors commercially available from Sigma-Aldrich. Since the samples were mixtures from a number of different donors with averaged concentrations of CK and LDH biomarkers, we used the serum samples as they were to mimic the CA group and dissolved additional amounts of the CK (485 mU/mL) and LDH (15 mU/mL) biomarkers to mimic the AA group to get the concentration difference typical for the AA group vs. CA group. It should be noted that in this set of data the absolute values of the CK and LDH biomarkers might be different from the natural concentrations, but their difference was similar to that between the CA and AA groups. After preparing two sets of samples mimicking the CA and AA groups, the serum samples were dried and preserved at 35°C for different time intervals (up to 24 h), after which the samples were re-dissolved in an aqueous buffer containing the required enzyme substrates and then analyzed according to the two-enzyme CK/LDH-assay, Fig. 6A. The results are shown in Fig. 11, where the zero-time interval corresponds to the analysis of freshly prepared samples without drying and all other time intervals correspond to different aging of the dry serum stains prior to their analysis. Absorbance changes measured in the assay (similar to those shown in Fig. 7 for the model solutions) were normalized to the maximum value

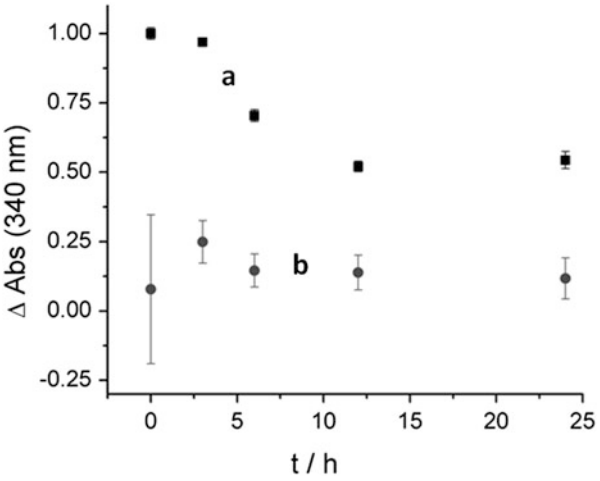

Fig. 11 Absorbance changes (ΔAbs) obtained for the two-enzyme CK/LDH-assay applied to the re-dissolved serum samples mimicking CA (*circles* b) and AA (*squares* a) groups after their drying and aging for different time intervals. The zero-time interval corresponds to the analysis of the freshly prepared samples without drying. The data represent mean values of ΔAbs normalized to the maximum ΔAbs value characteristic of the fresh samples mimicking the AA group; the error bars represent relative standard errors of ΔAbs measurements from five samples. Note that the samples were composed of mixed serum from different donors with added CK and LDH to mimic their concentration difference in the CA and AA groups. (The figure was adopted from [69] with permission.)

characteristic for the fresh samples mimicking the AA group. The assay demonstrated almost unchanged optical responses (meaning the same CK/LDH activity) in the samples mimicking the CA group over the aging time intervals up to 24 h. On the other hand, the samples mimicking the AA group demonstrated somewhat reduced optical changes (attributed to the expected decreasing CK/LDH activity) in the time intervals up to ca. 10 h. After 10 h, the optical responses reached a limit and stayed unchanged until the maximum aging time was applied (24 h). Despite the fact that the gap separating the analyzed CA and AA samples decreased in 10 h of the sample aging by ca. 50%, the analytical responses from the CA and AA groups were perfectly distinguishable, thus confirming the applicability of the proposed analytical method for dry sample stains which are at least 24 h old. In the present preliminary study we did not attempt aging longer than 24 h for the dry samples. It should also be noted that in the preliminary step, we analyzed only the samples with the mean concentration difference without taking into account the natural variability which can potentially screen the difference between the CA and AA groups.

In the next phase of the study, we analyzed serum samples obtained from individual donors with known ethnic origin (CA and AA). The samples were obtained from ProMedDx Specimen Bank (Norton, MA, USA) and were analyzed

using the two-enzyme CK/LDH-assay, Fig. 6A. After obtaining the optical responses (similar to those shown in Fig. 7 for the model solutions), we applied statistical analysis to evaluate the assay sensitivity and specificity for discriminating between samples of different ethnic origin. Receiver operating characteristic (ROC) analysis [93] was used to evaluate the performance of the assay and the possibility of distinguishing between the CA (14 samples) and AA (14 samples) groups of human serum. Using ROC analysis, the best threshold (above which the absorbance changes correspond to the AA group) that yielded the maximum accuracy was determined. The area under the ROC curve (AUC) is a single measure summarizing the overall accuracy of the test. It represents the probability that the diagnostic test will correctly distinguish between the CA and AA samples. The AUC from empirical and smooth ROC curves [94], which expectedly give consistent results in this case (and the corresponding 95% confidence intervals; CI), were estimated for the data obtained with the CK/LDH-assay. The AUC of the empirical ROC curve was estimated by the trapezoidal method of integration, and the corresponding 95% CI was estimated with the method described by DeLong et al. [95]. Smoothed ROC curves were additionally estimated using a non-parametric method. The kernel density function [96] was used to fit a smooth ROC curve to the data points because this method is free of parametric assumptions [97]. This smoothed-curve method outperforms the competing methods when the assumption of a normal distribution is violated. The bandwidth of the kernel function was fixed using the robust method developed by Sheather and Jones [98]. The AUCs of smooth ROC curves were obtained with corresponding 95% CIs computed with 2000 stratified bootstrap replicates as described elsewhere [99]. The AUC was 0.82 (95% CI: 0.64–1.00) from the empirical ROC curve and 0.80 (95% CI: 0.63–0.96) from the smooth ROC curve, Fig. 12, which means that the diagnostic test has an 82% chance of differentiating between CA and AA human serum samples. An absorbance change of 0.103 had the best corresponding sensitivity–specificity pair (the best tradeoff between them), i.e. the most accurate cut-off point for discrimination between CA and AA serum samples (highlighted point in Fig. 12, curve a).

The study performed on the model solutions mimicking CK and LDH biomarker composition in CA and AA groups demonstrated statistically proven recognition of samples with different ethnic origins. It should be noted that only the biocatalytic cascade utilizing both biomarkers CK/LDH allowed for CA and AA differentiation, while the analysis of CK alone was not able to show a statistically meaningful difference between the CA and AA groups. The analytical results obtained for the model solutions were confirmed when real serum samples from donors with known ethnic origins were applied. The developed method was tested on dried and aged serum samples allowing for the recognition of their ethnic origin. This method represents the first attempt to develop an on-field rapid analysis of biological fluids for forensic applications based on multi-enzyme biocatalytic cascades.

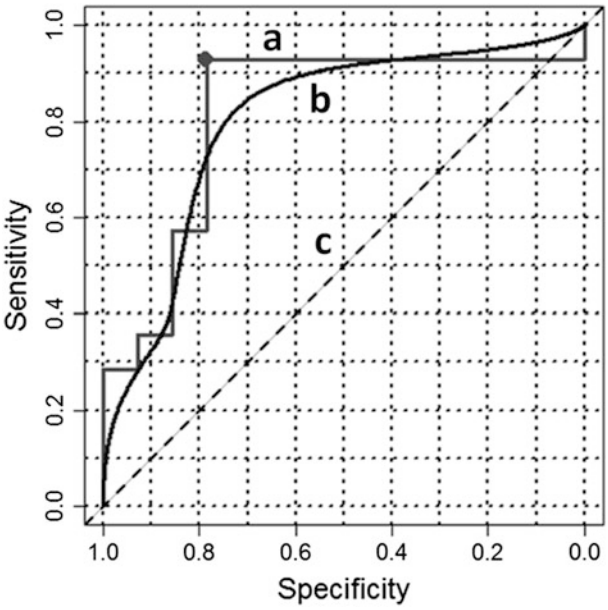

Fig. 12 Receiver operating characteristic (ROC) empirical (a) and smoothed (b) curves for the two-enzyme CK/LDH-assay. Random choice is denoted by the *diagonal line* (line c). The highlighted point on the plot (curve a) corresponds to the best sensitivity–specificity pair (the best tradeoff between them) giving the most accurate cut-off point for discrimination between CA and AA serum samples. Note that samples were serum from individual donors with known ethnic origin. (The figure was adopted from [69] with permission.)

3.2 Biocatalytic Logic Analysis of Biomarkers for Forensic Identification of Gender

The present study reported on the novel analysis of enzyme-biomarkers for forensic identification of gender which can be performed directly at the crime scene [100]. Two enzymes, creatine kinase (CK; E.C. 2.7.3.2) and alanine transaminase (ALT; E.C. 2.6.1.2), were selected for the analysis based on their known difference in concentration levels in blood of healthy adults of male and female groups [73, 101–103]. Mean concentrations of CK are 234 U/L and 122 U/L in male and female groups [73], respectively (note a large difference of 122 U/L), while mean concentrations of ALT differ much less: 32.1 U/L and 22.6 U/L in male and female groups (adapted from the most comprehensive study) [101], respectively (note a difference of 9.5 U/L only). It should be noted that very similar ALT levels in male and female groups were reported in different studies, and were not significantly affected by ethnic origin of donors [102, 103]. CK [30, 31, 36] and ALT [30, 36, 48] blood levels analyzed separately have already been used as diagnostic tools for various injuries because their concentrations significantly vary for physiologically normal and pathophysiological samples. However, they have not been applied prior

to our study for the analysis of "healthy" samples originating from donors of different genders since the difference in the "healthy" samples is much smaller, making the gender recognition more difficult. In our previous study [69] we aimed at the determination of the ethnic origin of the samples, we showed that the small concentration difference of CK cannot be reliably analyzed using the CK-assay in its standard version recommended by Sigma-Aldrich [82] and commonly used in hospitals [83]. Therefore, we re-designed and re-optimized the CK-assay in order to increase the output signal difference, more importantly keeping in mind the ultimate goal of combining the new CK-assay with an ALT-assay in one biocatalytic cascade. In the new CK-assay performed in a 50 mM glycyl-glycine buffer solution, pH 7.95, the biocatalytic reaction of CK was coupled with the biocatalytic action of pyruvate kinase (PK; E.C. 2.7.1.40) to yield pyruvate, followed by NADH oxidation biocatalyzed by lactate dehydrogenase (LDH, E.C. 1.1.1.27), Fig. 6A. The latter biocatalytic reaction was required to convert the pyruvate generation into consumption of NADH in order to produce a readable optical output signal of the CK-assay. The assay solution containing PK (2 U/mL), LDH (1 U/mL), and all required substrates was spiked with CK concentrations corresponding to the enzyme levels expected for male or female groups (234 or 122 U/L, respectively) to activate the biocatalytic process. Figure 13, curves a and b, shows time-dependent decrease of the optical absorbance corresponding to the consumption of NADH over the course of the CK-assay when CK concentrations characteristic of female and male groups were applied. Figure 13, inset b, shows the absorbance changes achieved in 10 min of the enzymatic reactions corresponding to the CK-assay. Then, we combined the CK-PK-LDH biocatalytic cascade with the biocatalytic cascade of ALT-LDH operating in parallel, Fig. 14. Pyruvate production biocatalyzed by the ALT reaction was added to the result of the CK-PK biocatalytic process, thus amplifying the NADH consumption in the terminal step biocatalyzed by LDH. The assay buffer solution containing PK (2 U/mL), LDH (1 U/mL), and all required substrates was spiked with both CK and ALT concentrations corresponding to the enzyme levels expected for male or female groups (234 or 122 U/L for CK and 32.1 or 22.6 U/L for ALT) to activate the biocatalytic process.

Figure 13, curves c and d, shows time-dependent decrease of the optical absorbance corresponding to the consumption of NADH when both biocatalytic cascades, activated by CK and ALT, operated together in parallel. Figure 13, inset a, shows the absorbance changes achieved in 10 min of the enzymatic reactions corresponding to the CK-ALT joint assay. While the ratio of the output signals produced in the presence of biomarker concentrations characteristic of female and male groups was almost the same for the CK-assay and CK-ALT assay, the absolute value of the signal difference was significantly larger when both biomarkers, CK and ALT, were applied with varied concentrations. While using a spectrophotometer does not show much advantage for the assay of CK and ALT in a joint biocatalytic cascade over the single CK-assay (note that the ratio of the "male" and "female" assay outputs is almost the same), the increased absolute difference is important for visual analysis (without optical instruments), which is the ultimate

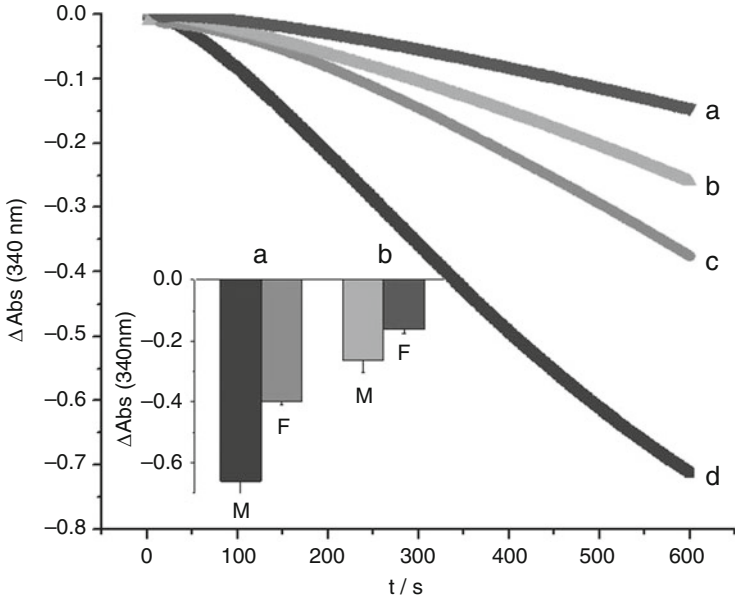

Fig. 13 Time-dependent absorbance changes ($\lambda = 340$ nm) obtained upon running the enzyme assays: (a) CK-assay with the "female" CK concentration, (b) CK-assay with the "male" CK concentration, (c) CK-ALT-assay with the "female" CK and ALT concentrations, (d) CK-ALT-assay with the "male" CK and ALT concentrations. Inset: The bar chart showing the absorbance changing after 10 min of the assay performance: (a) CK-ALT-assay and (b) CK-assay; "M" and "F" bars correspond to the "male" and "female" enzyme concentrations, respectively. The enzymatic assays were performed in a 50 mM glycyl-glycine buffer solution, pH 7.95. (The figure was adopted from [100] with permission.)

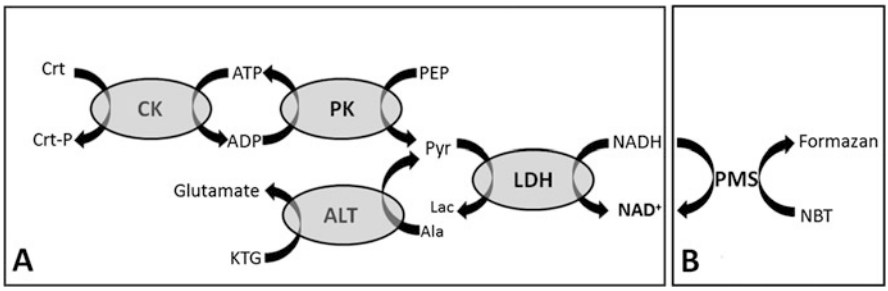

Fig. 14 (**A**) The biocatalytic cascade used for the CK-ALT-assay where CK and ALT were applied jointly as two biomarkers. (**B**) Extension of the CK-ALT-assay for the color production visible by a naked eye. The following abbreviations are used in the scheme: CK creatine kinase, PK pyruvate kinase, LDH lactate dehydrogenase, ALT alanine transaminase, Crt creatine, Crt-P creatine phosphate, ATP adenosine triphosphate, ADP adenosine diphosphate, NAD^+ ß-nicotinamide adenine dinucleotide, NADH ß-nicotinamide adenine dinucleotide reduced, PEP phospho(enol)pyruvic acid, Pyr pyruvate, Lac lactate, KTG α-ketoglutaric acid, NBT nitroblue tetrazolium, PMS phenazine methosulfate. (The figure was adopted from [100] with permission.)

goal for the forensic application. Details of how we modified the assay to incorporate a visualization-enabling component will be discussed further on.

The experiment described above confirmed the applicability of the two-enzyme CK/LDH-assay for distinguishing the difference between the male and female groups. It was performed in model solutions, however, comprised of an aqueous buffer spiked with the CK and LDH to the concentrations characteristic of the analyzed groups. In real conditions of interest for forensic analysis, the biomarkers should be analyzed in blood stains found at a crime scene. In order to mimic forensic conditions, we performed the same analysis in human serum solutions. In the next set of experiments, we realized only the two-enzyme, CK and ALT, assay, Fig. 14A, in human serum solutions. The reacting solution for this assay was prepared in two steps: first the enzyme-biomarkers were dissolved in serum with specific concentrations mimicking "male" and "female" samples; then, the serum was added to the buffer solution containing PK, LDH, and all necessary substrates (similar to the experiments in buffer described above). It should be noted that the commercial Sigma-Aldrich serum samples already included some unknown amounts of CK and ALT; thus, by spiking serum with the CK and ALT concentrations used in the previous set of experiments we only preserved the difference between the "male" and "female" samples. Therefore, the absolute values of the CK and ALT concentrations were not exactly the same as expected for the male and female groups, but, they represented the difference in the mean values of the CK and ALT concentrations in both groups. First, we performed the CK-ALT-assay in a freshly prepared serum-based solution obtaining the output signal (corresponding to the NADH consumption) similar to that of the buffer solution, meaning that numerous biomolecular components present in serum do not affect the assay performance, Fig. 15. Then we spiked serum with CK and ALT ("male" and "female" concentrations), but in the absence of all other components required for the activation of the biocatalytic cascade. These samples, each 0.5 mL, were dried on a glass surface at 35°C under reduced air pressure using a vacuum pump and aged for different time intervals (up to 24 h). After that, the dried samples were re-dissolved in 50 mM glycyl-glycine buffer, pH 7.95, containing PK (2 U/mL), LDH (1 U/mL) and all required substrates to initiate the biocatalytic cascade. The obtained solutions were analyzed according to the CK-ALT-assay procedure described above. The obtained results, Fig. 16, show a clearly distinguishable difference for the "male" and "female" samples after 1 h of aging the samples with decreasing difference after that. Surprisingly, the output signal ratio for the "male"/"female" samples was even larger after 1 h of aging compared to the analysis of freshly prepared solutions (without drying/aging). This phenomenon was reproducible and might originate from different thermal stabilities of the CK and ALT enzymes.

In the last set of the experiments we aimed at visualization of the CK-ALT-assay output signal without use of optical instruments. This was achieved by adding one more reaction step to the biocatalytic cascade, where NADH reduced nitroblue tetrazolium (NBT) to a colored product, formazan dye, in the reaction mediated by phenazine methosulfate (PMS) [104, 105], Fig. 14B. The biocatalytic cascade

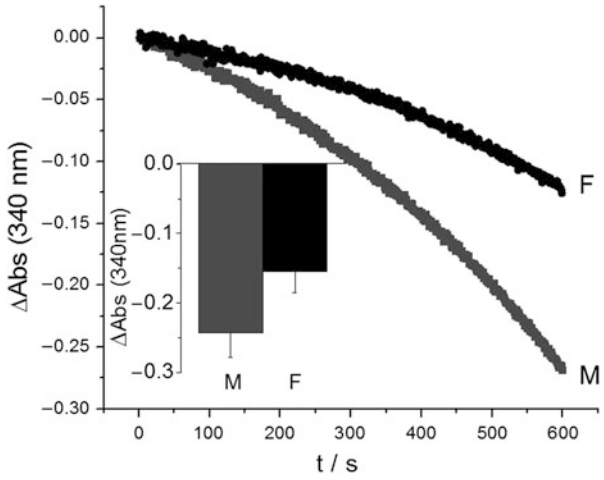

Fig. 15 Time-dependent absorbance changes ($\lambda = 340$ nm) obtained upon running the CK-ALT-assay in human serum (50% v/v) solutions with: (F) the "female" CK and ALT concentrations, (M) the "male" CK and ALT concentrations. Inset: The bar chart showing the absorbance changing after 10 min of the assay performance; "M" and "F" bars correspond to the "male" and "female" enzyme concentrations, respectively. (The figure was adopted from [100] with permission.)

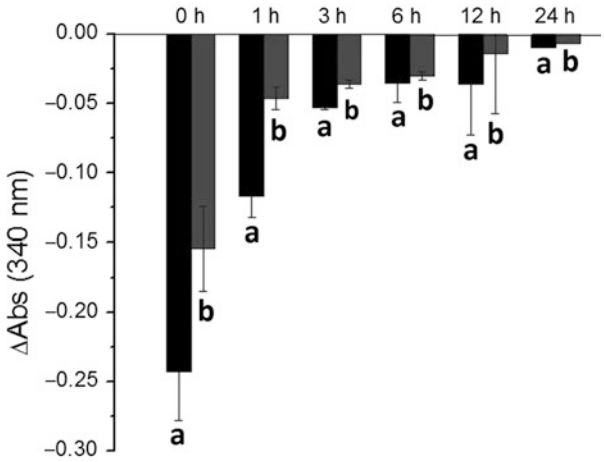

Fig. 16 The bar chart showing absorbance changes ($\lambda = 340$ nm) obtained upon performing CK-ALT-assay for 10 min on serum samples spiked with "male" (a) and "female" (b) CK and ALT concentrations and then after their drying, aging for different time intervals and re-dissolving for the enzyme assay. Note that "0 h" experiment corresponds to the analysis of freshly prepared samples without drying/aging. (The figure was adopted from [100] with permission.)

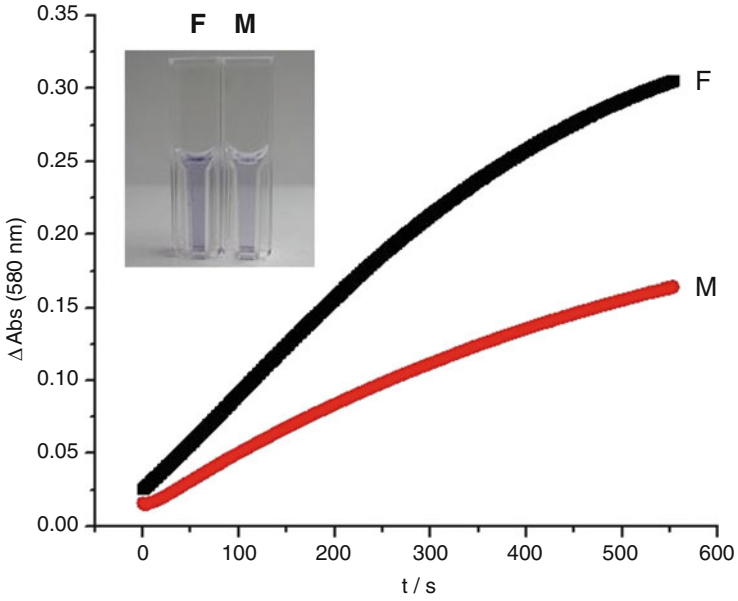

Fig. 17 Time-dependent absorbance changes ($\lambda = 580$ nm) obtained upon performing chemical reaction of NBT and the residual NADH following the CK-ALT-assay performed for 10 min for the serum (50% v/v) solutions spiked with "male" (M) and "female" (F) concentrations of CK and ALT. Inset: Photos of cuvettes with colored solutions obtained for the "male" and "female" samples after CK-ALT-assay extended with the NBT reaction (note that the samples in this experiment were prepared in buffer solutions). *Blue color* in the left cuvette corresponds to the "female" sample. (The figure was adopted from [100] with permission.)

activated by the CK and ALT inputs resulted in the oxidation of NADH to yield NAD^+. The remaining NADH was oxidized to NAD^+ through the catalytic action of PMS, converting NBT to formazan and resulting in the increase of its absorbance detected optically at $\lambda = 580$ nm, Fig. 17. Note that NBT and PMS were added to the assay solutions after completing the biocatalytic reaction, thus the solution spiked with smaller "female" concentrations of CK and ALT contained higher concentration of residual NADH, which resulted in larger production of the formazan dye. Importantly, the difference in the color formation in the presence of the "male" and "female" samples was easily distinguishable by a naked eye where clearly visible blue color corresponded to the "female" sample, Fig. 17, inset.

The study performed on the model solutions mimicking CK and ALT biomarker composition in "male" and "female" groups demonstrated significant difference upon performing the CK-ALT-assay. The developed method was tested on dried and aged serum samples allowing for the recognition of the originator's gender. Most important for forensic applications is the reaction with a chromogenic reactant nitroblue tetrazolium which allowed for qualitative discrimination of the "male" and "female" samples with a naked eye, giving promise for designing analytical kits or paper strips for the rapid identification of the originator's gender from a biofluid

sample. This method represents the first attempt to develop an on-field rapid analysis of biological fluids for forensic applications based on multi-enzyme biocatalytic cascades. The approach, borrowed from unconventional enzyme-based computing [18, 19] and originally applied to biomedical analysis [25, 67], demonstrates promising perspectives for novel forensic serology applications.

3.3 Biocatalytic Logic Assay to Determine Age of Blood Sample

A biocatalytic cascade assay was developed to determine the time elapsed from the point a blood sample was left at a crime scene to the point of discovery [106]. Two blood markers, creatine kinase (CK) and alanine transaminase (ALT), were utilized to determine the age of the blood spot based on their respective denaturation rates. The analysis with the proposed bioassay was performed in human serum samples, which underwent the aging process under environmental conditions expected at crime scenes. The concentration of the markers in the sample was based on physiological levels present in healthy adults. These two markers were each inserted into separate biocatalytic cascades that operated in parallel. Both markers have very distinct denaturation rates which would not allow them to be used in a single marker setup, while still providing satisfactory results. However, by parallel tunable monitoring of both markers, it is possible to provide the blood sample age with low temporal error for a prolonged period of time. To mimic a realistic crime scene scenario, the proposed assay was then tested on dried/aged serum samples (up to 5 days old) in environments with different temperatures.

It should be noted that blood is a valuable source of information not only because of its genetic material, but also because of its unique composition of proteins and low molecular compounds. The age of a blood sample left at a crime scene can be a significantly important piece of information for the identification of the donor. For instance, multiple blood spots could be present at a crime scene and there would be no guarantee that every sample is relevant to the case. Some spots may be days, weeks, or even months old; to separately match every sample to an individual would be costly and time-consuming. Estimating the age of a blood spot is, therefore, largely important in identifying blood that is relevant to a crime investigation and ruling out that which is not. Currently, there is a technique available for distinguishing two individuals from overlapping bloodstains [58, 107], and it has also been shown that a crime can be re-constructed by analyzing blood splatter patterns [108, 109] according to their geometry and distribution [110]. However, with no technique to identify how old the samples are, data from such techniques may be completely irrelevant. Despite its importance, techniques to determine blood spot age are crude and underdeveloped.

Due to the degree of denaturation and other changes, blood samples have the potential to provide the time that has elapsed since the blood left the originator's body. Numerous techniques have been suggested for this purpose over the past decades, but, due to the lack of practicality, they have never been applied in real settings [111]. In 1930, the pioneer in this area, Schwarzacher, attempted to find the relationship between the solubility of blood in water and its age [112]. Spectrophotometry analysis was first applied in 1960 by Patterson [113], where he determined that the changing color of a bloodstain is dependent on environmental conditions by recording the bloodstain's reflectance. Later, in 1983, Tsutsumi studied changes in individual proteins present in bloodstains [114]. More recent methods include electron paramagnetic resonance (EPR) [115], high performance liquid chromatography (HPLC) [116], oxygen electrodes [117], RNA degradation [118], near infrared (NIR) spectroscopy [119], and atomic force microscopy (AFM) [120]. Altogether, the vast majority of these techniques require sample preparation and need to be performed in a laboratory setting, preventing direct analysis at the crime scene. In addition to these requirements, these techniques have yet to report any environmental influences that will play a key factor in the decomposition of the sample such as humidity, temperature, or exposure to light.

In the present study [106], we have developed a novel tunable parallel assay of biomarkers for forensic determination of the age of blood samples left at crime scenes. Two protein biomarkers, the enzymes creatine kinase (CK) and alanine transaminase (ALT) [73, 101–103], were used separately in parallel assays to determine the age of bloodstain samples. The mean concentrations of the biomarkers were based on their physiological levels present in a healthy adult, CK (100 mU/mL) and ALT (20 mU/mL) [73, 101–103]. We designed and optimized a biocatalytic cascade where determination of the activity of both biomarkers was followed in two parallel enzymatic cascades, each following the decay of enzymatic activity of a single biomarker. Both biomarker concentrations are tunable by modulation of their respective performances, the time for which the assay can accurately determine the sample age with low temporal error and increased reproducibility can be flexibly prolonged or shortened.

Figure 14A represents the entire biocatalytic cascade (CK/ALT), which measures the enzymatic activities of both blood biomarkers during the aging process. In the proposed cascade, performed in 50 mM glycyl-glycine buffer solution at pH 7.95, the biocatalytic reaction of the CK biomarker was coupled with the consequent reaction catalyzed by pyruvate kinase (PK) to produce adenosine triphosphate (ATP) and pyruvate. In a parallel cascade, the ALT biomarker also produces pyruvate via the deamination of alanine (Ala) with α-ketoglutaric acid (KTG) acting as a co-substrate. The last biocatalytic step is the reduction of pyruvate into lactate by lactate dehydrogenase (LDH), with the simultaneous consumption of NADH, optically readable at 340 nm.

As shown in Fig. 14A, two parallel reactions biocatalyzed by CK and ALT represent two pathways which can be analyzed and optimized independently. This allows for the individual evaluation of the performance of each independent biomarker. To accomplish this, human serum samples spiked with the appropriate

concentrations of biomarkers were placed on a glass surface and underwent an aging process for variable periods of time (from 0 up to 120 h) while incubated at 40°C. The dried human serum samples were re-suspended with water just before measurements were taken. The biocatalytic cascade was activated by mixing the dried samples with the necessary enzymatic cascade substrates, co-substrates, and auxiliary enzymes that were previously dissolved in 50 mM glycyl-glycine buffer (pH 7.95). Afterwards, the samples were immediately subjected to a continuous optical measuring at $\lambda = 340$ nm, in order to monitor the consumption of NADH. The conditions for the subsystems and the entire cascade were identical. In addition, for each measurement taken, a set of three ($n = 3$) human serum samples, containing the biomarkers was analyzed.

As previously indicated, the aging process was followed at a rather high temperature (40°C), which is not expected at most crime scenes, but amplifies the aging effect on the particular biomarkers. Figure 18 shows the real-time response (oxidation of NADH, as shown in Fig. 14A) following the CK biomarker reaction (in the absence of ALT). The bar diagram, Fig. 18, inset, illustrates the decay in time response in which the output signal is plotted as a function of blood sample age. Figure 18 shows a rather fast decay of CK activity which, after 6 h of aging, is reduced to approximately 20% of its original level. This shows that the CK branch of the sensing cascade provides a low error of blood sample age determination, but its overall performance decreases drastically for samples older than 6 h due to the lack of marker activity caused by denaturation. To address this problem and simultaneously improve the tenability of the presented bioanalytical paradigm, ALT was also evaluated as a biomarker.

Figure 19 shows the real-time response of the samples following only ALT (in the absence of CK) incubated at 40°C for up to 120 h. Figure 19, inset, shows that the enzymatic activity of this particular biomarker undergoes a constant decay

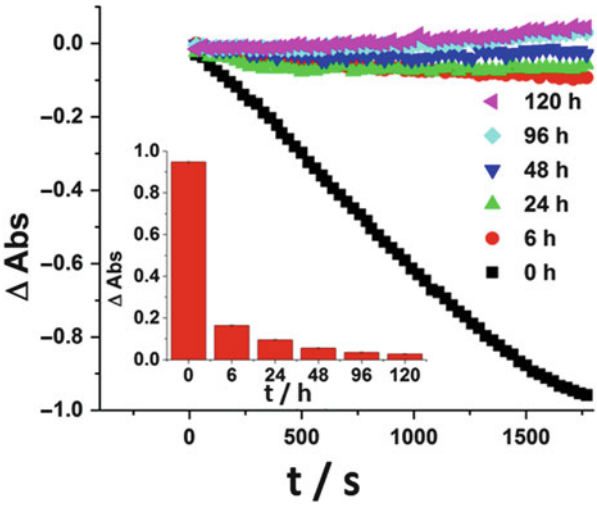

Fig. 18 Change in absorbance ($\lambda = 340$ nm) corresponding to the consumption of NADH upon operation of the CK-biocatalyzed reaction. The traces correspond to samples ($n = 3$) that mimic bloodstains, incubated at 40°C from 0 to 120 h. Inset: Bar-chart representing the change in absorbance at $\lambda = 340$ nm, after 30 min of assay completion. (The figure was adopted from [106] with permission.)

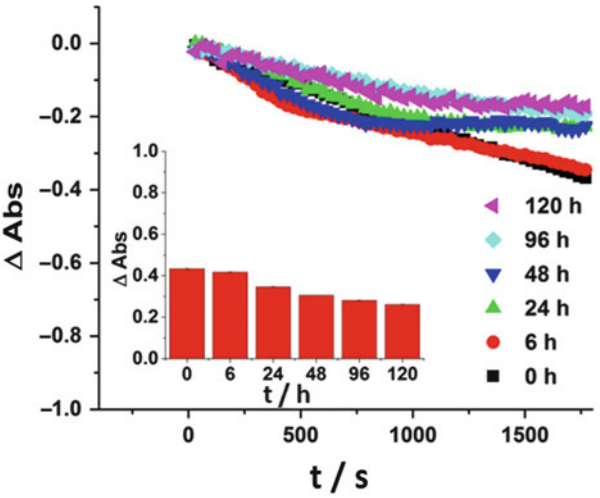

Fig. 19 Change in absorbance ($\lambda = 340$ nm) corresponding to the consumption of NADH upon operation of the ALT-biocatalyzed reaction. The traces correspond to samples ($n = 3$) that mimic bloodstains, incubated at 40°C from 0 to 120 h. Inset: Bar-chart representing the change in absorbance at $\lambda = 340$ nm, after 30 min of assay completion. (The figure was adopted from [106] with permission.)

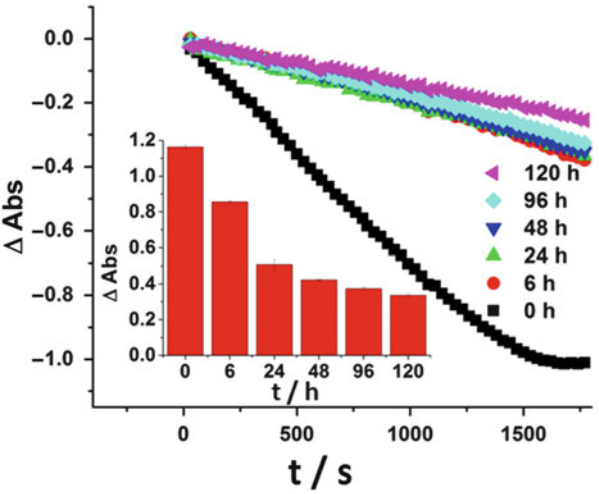

Fig. 20 Change in absorbance ($\lambda = 340$ nm) corresponding to the consumption of NADH upon operation of the CK/ALT-biocatalyzed reactions operating in parallel. The traces correspond to samples ($n = 3$) that mimic bloodstains, incubated at 40°C from 0 to 120 h. Inset: Bar-chart representing the change in absorbance at $\lambda = 340$ nm, after 30 min of assay completion. (The figure was adopted from [106] with permission.)

during the aging process, while more than 50% of the enzymatic activity remains after 120 h. This would allow the determination of the blood sample age even beyond the studied time interval. On the other hand, low decay of the signal in combination with a low signal change overall would result in a high temporal error of the blood sample age determination, which can be a drawback, especially in shorter aging times.

Figure 20 shows an example of real-time responses in which both pathways of the cascade shown in Fig. 14A are simultaneously operating in the presence of CK and ALT. Figure 20, inset, illustrates the overall signal decay. For shorter times, the

dual cascade system offers a significantly better response than a single ALT biomarker output, while at longer aging periods, the cascade is able to provide a more significant output than that of CK alone. Indeed, the CK biomarker provides the major contribution to the signal decay on the short-time periods of the sample aging, while the ALT biomarker is responsible for the signal at longer aging periods. The proposed assay offers parallel analysis of both biomarkers' activity during the aging process and balances both biocatalytic branches between low error and prolonged age determination.

For the proposed CK/ALT-tunable biomarker cascade, the effect of temperature on the aging process was also examined. Human serum samples spiked with the biomarkers underwent an aging process to create an initial database of optical outputs of blood samples subjected to different degradation times and temperatures. The samples were incubated at 18, 25, and 40°C to mimic realistic scenarios that can be encountered in a forensic investigation. The samples were also analyzed for up to 120 h (5 days). Time zero corresponds to the analysis of the freshly prepared sample. The remaining times represent the time that the sample had been incubated at that particular temperature. The samples that were incubated at 18°C, the lowest temperature, predictably show the lowest decomposition decay, while an elevated temperature, such as 40°C, caused faster denaturation, Fig. 21. The difference in optical responses among samples incubated at the same temperature, and among samples that vary in temperature incubation, makes this biocatalytic assay a perfect fit for the forensic investigation setting. These results show the potential of the proposed cascade for a wide range of temperatures. Consequently, when an unknown blood sample is found at a crime scene where the environmental conditions are known, the output signal can be translated to the time the blood sample left the circulatory system.

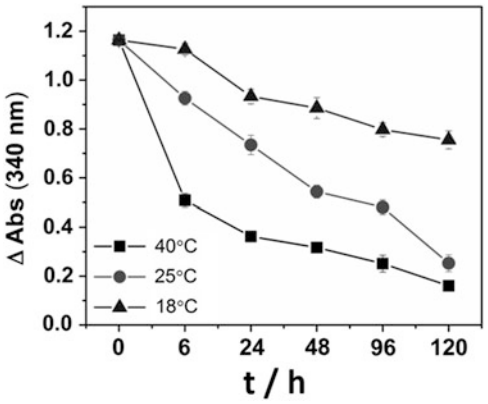

Fig. 21 Absorbance change at $\lambda = 340$ nm, corresponding to the consumption of NADH after the analysis of the samples by the CK/ALT biocatalytic assay. Samples ($n = 3$) were re-suspended after undergoing the aging process under different temperatures: 40, 25, and 18°C, up to 120 h. The time zero corresponds to the freshly prepared samples without drying. (The figure was adopted from [106] with permission.)

This investigation showed that the combination of multiple enzyme biomarkers, such as CK and ALT, can be used as a tool to determine blood spot age at a crime scene. This study also shows the advantage of having two parallel biomarker sensing cascades, operating simultaneously, over a single biomarker cascade as the combination of two biomarkers provides improved information about the sample properties compared to a single biomarker. Due to the differences in the denaturation rates of various biomarkers present in body fluid, a single biomarker assay may not allow for a reliable determination of blood sample age. For instance, biomarkers with high stabilities would continue to provide a signal for long periods of time, but would also cause a high percentage of error in the analysis. Biomarkers that rapidly denature, such as CK, cannot be used for a prolonged period of time, but would provide a lower chance of error. In our parallel assay, we used a combination of both types of biomarkers to provide a "balanced" response. By using the high sensitivity of biomarkers with short half-lives, together with the stability of biomarkers with longer lives, the response was more reliable. This, apart from a prolonged time horizon, also allowed for the "tuning" of the sensing cascade via the optimization of both reaction branches for longer/shorter aging intervals. This approach showed that the multi-biomarker bioanalytic assay paradigm can be successfully used for reliable determination of the age of a biological sample in forensic analysis. Because of its simplicity and robustness, this methodology can be adapted as a component of a forensic field kit, and can potentially be used by trained nonscientific personnel at crime scenes.

4 Conclusions and Perspectives

Applying novel concepts from the area of unconventional computing [24] (specifically from biomolecular computing [18]) to biosensing and bioanalytical assays has resulted in the design of biomolecular systems logically processing several chemical signals and converting them to a single binary output in the format of YES/NO. Information processing in biomolecular systems does not require electronic computers and proceeds at the level of chemical reactions. The "program" for processing chemical inputs can be implemented in the composition of the biomolecular system and can include various logic operations applied in different combinations. The systems exemplified above demonstrated the simplest AND logic applied to two biochemical input signals. However, many other logic operations integrated in various logic circuitries are possible with the use of different enzymes [19] and other biomolecules [20–22], to allow high-fidelity detection of diverse pathophysiological conditions and medical emergencies. The resulting digital biosensors would thus benefit different important fields, ranging from biomedical analysis [25, 67] as well as environmental monitoring and security screening [121], by enabling on-demand immediate intervention or corrective action on the basis of reliable analytical data.

An important challenge in developing this kind of digital multi-signal biosensor system is obtaining a significant difference between the logic **1** and **0** output values (in other words, a well-defined YES/NO answer). One should remember that in case of biomedical applications the input signals appear at their physiological levels, where the logic value **0** may not correspond to the physically zero concentration. Moreover, there might be a relatively small difference in the physical concentrations of the input signals corresponding to the logic **0** and **1**. In order to obtain significant difference in the output signals, the response function should be sigmoid rather than linear [46]. In other words, the system should demonstrate a non-linearity with a sharp transition between the **0** and **1** states. The first steps in this direction have been already done experimentally and analyzed theoretically [44]. However, extensive research effort aimed at designing chemical "filter"--systems similar to the electronic counterparts is needed [122]. The thresholds separating the logic **0** and **1** values could be personally tailored for a given patient by following circulating biomarkers in the physiological liquids. This will be an important step towards future personalized medicine.

Analysis of various biomarkers found in biofluids at a crime scene, particularly based on multi-enzyme biocatalytic reactions, is rapidly progressing toward practical applications. The approach, borrowed from unconventional enzyme-based computing [18, 19] and originally applied to biomedical analysis [25, 67], demonstrates promising perspectives for novel forensic serology applications [123, 124]. Analytical applications for rapid identification of personal characteristics are feasible as the results of this study. New tools (e.g., analytical kits or paper strips) for the rapid identification of biofluid origin are expected based on the present research. Further development in this area will be directed towards incorporation of the methods exemplified above and other similar approaches into portable lateral flow strip-like devices for rapid analysis of biomarkers directly on-site at the crime scene.

Biochemical computing and logic-gate systems based on biomolecules have the potential to revolutionize the field of biosensors. Interfacing biocomputing elements with sensing processes would allow multi-signal analysis followed by biochemical processing of the data, giving a final digital ("YES" or "NO") analytical answer. Such "Yes/No" information allows also direct coupling of the signal processing with signal-responsive materials [43] and chemical actuators [125, 126] to offer a closed-loop "Sense/Act" operation. Biochemical networks can offer robust error-free operation upon appropriate optimization of their components and interconnections. Chemical stability of the biomolecular components will be improved upon their immobilization in signal-responsive materials or at functional interfaces. Further development of this research area requires collaborative efforts of engineers, biochemists, and computer specialists. The ultimate goal of this work will be the design of a microfluidic lab-on-a-chip performing multi-enzyme-catalyzed cascades and operating similarly to an electronic chip by being able to integrate large networks for processing biochemical signals.

References

1. Clark Jr LC, Lyons C (1962) Ann N Y Acad Sci 102:29–45
2. Renneberg R, Lisdat F (eds) (2008) Biosensing for the 21st century. In: Scheper T (series ed) Advances in biochemical engineering/biotechnology. Springer, Berlin
3. Willner I, Katz E (2000) Angew Chem Int Ed 39:1180–1218
4. Leech D (1994) Chem Soc Rev 23:205–213
5. van Emon JM (ed) (2006) Immunoassay and other bioanalytical techniques. CRC Press, Boca Raton
6. Sassolas A, Leca-Bouvier BD, Blum LJ (2008) Chem Rev 108:109–139
7. Zourob M (ed) (2010) Recognition receptors in biosensors. Springer, New York
8. Ronkainen NJ, Halsall HB, Heineman WR (2010) Chem Soc Rev 39:1747–1763
9. Borisov SM, Wolfbeis OS (2008) Chem Rev 108:423–461
10. Steinem C, Janshoff A (eds) (2010) Piezoelectric sensors. In: Wolfbeis OS (series ed) Springer series on chemical sensors and biosensors. Springer, Berlin
11. Wang J (2008) Chem Rev 108:814–825
12. Crowther JR (2010) The ELISA guidebook. Humana Press, New York
13. Schena M (2002) Microarray analysis. Wiley-Liss, Hoboken
14. Ehrenkranz JRL (2002) Epidemiology 13:S15–S18
15. Kumar V, Kaushik MP (2011) Analyst 136:5151–5156
16. Warsinke A (2009) Anal Bioanal Chem 393:1393–1405
17. Katz E (ed) (2012) Molecular and supramolecular information processing: from molecular switches to logic systems. Wiley-VCH, Weinheim. ISBN: 978-3-527-33195-6
18. Katz E (ed) (2012) Biomolecular information processing – from logic systems to smart sensors and actuators. Wiley-VCH, Weinheim. ISBN: 978-3-527-33228-1
19. Katz E, Privman V (2010) Chem Soc Rev 39:1835–1857
20. Stojanovic MN, Stefanovic D (2003) Nat Biotechnol 21:1069–1074
21. Win MN, Smolke CD (2008) Science 322:456–460
22. Stojanovic MN, Mitchell TE, Stefanovic D (2002) J Am Chem Soc 124:3555–3561
23. Li Z, Rosenbaum MA, Venkataraman A, Tam TK, Katz E, Angenent LT (2011) Chem Commun 47:3060–3062
24. Calude CS, Costa JF, Dershowitz N, Freire E, Rozenberg G (eds) (2010) Unconventional computation. Lecture notes in computer science, vol 5715. Springer, Berlin
25. Wang J, Katz E (2010) Anal Bioanal Chem 398:1591–1603
26. Vaidya VS, Bonventre JV (eds) (2010) Biomarkers: in medicine, drug discovery, and environmental health. Wiley, Hoboken
27. Honda M, Tsuruta R, Kaneko T, Kasaoka S, Yagi T, Todani M, Fujita M, Izumi T, Maekawa T (2010) J Trauma – Inj Infect Crit Care 69:104–109
28. Lee S-Y, Choi Y-C, Kim J-H, Kim W-J (2010) J Neurology 257:1708–1712
29. Zhou N, Windmiller JR, Valdés Ramírez G, Zhou M, Halámek J, Katz E, Wang J (2011) Anal Chim Acta 703:94–100
30. Halámek J, Windmiller JR, Zhou J, Chuang M-C, Santhosh P, Strack G, Arugula MA, Chinnapareddy S, Bocharova V, Wang J, Katz E (2010) Analyst 135:2249–2259
31. Halámek J, Bocharova V, Chinnapareddy S, Windmiller JR, Strack G, Chuang M-C, Zhou J, Santhosh P, Ramirez GV, Arugula MA, Wang J, Katz E (2010) Mol Biosyst 6:2554–2560
32. de Silva AP, Uchiyama S (2007) Nat Nanotechnol 2:399–410
33. Margulies D, Hamilton AD (2009) J Am Chem Soc 131:9142–9143
34. May EE, Dolan PL, Crozier PS, Brozik S, Manginell M (2008) IEEE Sensors J 8:1011–1019
35. von Maltzahn G, Harris TJ, Park J-H, Min D-H, Schmidt AJ, Sailor MJ, Bhatia SN (2007) J Am Chem Soc 129:6064–6065
36. Zhou J, Halámek J, Bocharova V, Wang J, Katz E (2011) Talanta 83:955–959
37. Halámek J, Zhou J, Halámková L, Bocharova V, Privman V, Wang J, Katz E (2011) Anal Chem 83:8383–8386

38. Melnikov D, Strack G, Zhou J, Windmiller JR, Halámek J, Bocharova V, Chuang M-C, Santhosh P, Privman V, Wang J, Katz E (2010) J Phys Chem B 114:12166–12174
39. Tan K-K, Bang S-L, Vijayan A, Chiu M-T (2009) Injury 40:978–983
40. Khalili H, Dayyeh BA, Friedman LS (2010) In: Ginès P, Kamath PS, Arroyo V (eds) Clinical gastroenterology: chronic liver failure. Humana Press, New York, pp 47–76
41. Olerud JE, Homer LD, Carroll HW (1976) Arch Intern Med 136:692–697
42. Kratz A, Ferraro M, Sluss PM, Lewandrowski KB (2004) N Engl J Med 351:1548–1563
43. Privman M, Tam TK, Bocharova V, Halámek J, Wang J, Katz E (2011) ACS Appl Mater Interfaces 3:1620–1623
44. Privman V, Halámek J, Arugula MA, Melnikov D, Bocharova V, Katz E (2010) J Phys Chem B 114:14103–14109
45. Beutler E (2008) Blood 111:16–24
46. Privman V (2011) Isr J Chem 51:118–131
47. Lusczek ER, Nelson T, Lexcen D, Witowski NE, Mulier KE, Beilman GJ (2011) Bioanal Biomed 3:38–48
48. Halámková L, Halámek J, Bocharova V, Wolf S, Mulier KE, Beilman G, Wang J, Katz E (2012) Analyst 137:1768–1770
49. Blackledge RD (ed) (2007) Forensic analysis on the cutting edge: new methods for trace evidence analysis. Wiley-Interscience, Hoboken
50. Li R (2008) Forensic biology. CRC Press, Boca Raton
51. Shaler RC (2002) In: Saferstein R (ed) Forensic science handbook. Prentice Hall, Upper Saddle River, pp 529–546
52. Kobilinsky L (ed) (2011) Forensic chemistry handbook. Wiley, Hoboken
53. Sikirzhytski V, Sikirzhytskaya A, Lednev IK (2011) Appl Spectrosc 65:1223–1232
54. Virkler K, Lednev IK (2009) Forensic Sci Intern 193:56–62
55. Virkler K, Lednev IK (2009) Forensic Sci Intern 188:1–17
56. An JH, Shin K-J, Yang WI, Lee HY (2012) BMB Rep 45:545–553
57. Gaensslen RE (1983) Sourcebook in forensic serology, immunology, and biochemistry. U.S. Department of Justice, Washington, DC
58. Elkins KM (2012) Forensic DNA biology: a laboratory manual. Academic Press, Oxford
59. Bauer M (2007) Forensic Sci Int Gen 1:69–74
60. Bonifacino JS, Dell'Angelica EC, Springer TA (2001) Immunoprecipitation. Current protocols in molecular biology. Wiley, New York, pp 1–29
61. Butler JM (2009) Fundamentals of forensic DNA typing. Academic Press, Burlington
62. Donovan EJ, Mccullen RG (eds) (2012) DNA testing and data banking; law, crime and law enforcement. Nova Science, New York
63. James SH, Kish PE, Sutton TP (2005) Principles of bloodstain pattern analysis: theory and practice. CRC Press, Boca Raton
64. Eckenrode A, Bartick EG, Harvey S, Vucelick ME, Wright BW, Huff RA (2001) Forensic Sci Commun 3(4). http://www.fbi.gov/about-us/lab/forensic-science-communications/fsc/oct2001/eknrode.htm
65. Horsman KM, Bienvenue JM, Blasier KR, Landers JP (2007) J Forensic Sci 52:784–799
66. Liu P, Yeung SHI, Crenshaw KA, Crouse CA, Scherer JR, Mathies RA (2008) Forensic Sci Intern Gen 2:301–309
67. Katz E, Wang J, Privman M, Halámek J (2012) Anal Chem 84:5463–5469
68. Katz E, Halámek J (2014) Ann Forensic Res Anal 1:1002
69. Kramer F, Halámková L, Poghossian A, Schöning MJ, Katz E, Halámek J (2013) Analyst 138:6251–6257
70. Xie H-G, Kim RB, Wood AJJ, Stein CM (2001) Ann Rev Pharm Toxicol 41:815–850
71. Kalow W (1982) Clin Pharmacokinet 7:373–400
72. Lovric J (2011) Introducing proteomics: from concepts to sample separation, mass spectrometry and data analysis. Wiley, Hoboken

73. Deuster PA, O'Connor FG, Kenney K, Heled Y, Muldoon S, Contreras-Sesvold C, Campbell WW (2009) Creatine kinase clinical considerations: ethnicity, gender and genetics. Abstract at the conference: RTO-MP-HFM-181 – human performance enhancement for NATO military operations (Science, Technology and Ethics). http://www.cso.nato.int/pubs/rdp.asp?RDP=RTO-MP-HFM-181
74. Samadi N, Cembrowski GS, Chan J (2007) Clin Biochem 40:206–212
75. Okinaka S, Sugita H, Momoi H, Toyokura Y, Kumagai H, Ebashi S, Fujie Y (1959) Trans Am Neurol Assoc 84:62–64
76. Henson JB, Rao RR (1966) Can J Comp Med Vet Sci 30:157–159
77. Kumbhare D, Parkinson W, Dunlop B (2008) J Spinal Disord Tech 21:49–54
78. Kratz A, Ferraro M, Sluss PM, Lewandrowski KB (2004) New Engl J Med 351:1548–1563
79. Rosalki SB, Wilkinson JH (1960) Nature 188:1110–1111
80. Noda L, Nihet T, Morale MF (1960) J Biol Chem 235:2830–2834
81. Forster G, Bernt E, Bergmeyer HU (1974) In: Bergmeyer HU (ed) Methods of enzymatic analysis, 2nd ed., vol 2. Academic Press, New York, pp 789–793
82. Sigma-Aldrich information. http://www.sigmaaldrich.com/etc/medialib/docs/Sigma/General_Information/creatine_phosphokinase.Par.0001.File.tmp/creatine_phosphokinase.pdf
83. Wu AHB (2006) Tietz clinical guide to laboratory tests4th edn. Saunders-Elsevier, St. Louis
84. R Core Team (2012) R: a language and environment for statistical computing. R Foundation for Statistical Computing, Vienna. ISBN: 3-900051-07-0
85. The R project for statistical computing. http://www.R-project.org
86. Hirata RDC, Hirata MH, Strufaldl B, Possik RA, Asai M (1989) Clin Chem 35:1385–1389
87. Rumley AG, Pettigrew AR, Colgan ME, Taylor R, Grant S, Manzie A, Findlay I, Dargie H, Elliott A (1985) Br J Sports Med 19:152–155
88. Walck C (2007) Handbook on statistical distributions for experimentalists. University of Stockholm internal report SUF-PFY/96-01. http://www.stat.rice.edu/dobelman/textfiles/DistributionsHandbook.pdf
89. Rosenblatt M (1956) Ann Math Stat 27:832–837
90. Parzen E (1962) Ann Math Stat 33:1065–1076
91. Basu A, Shioya H, Park C (2011) Statistical inference: the minimum distance approach. CRC Press, Boca Raton. ISBN: 978-1-4200-9965-2
92. Deza MM, Deza E (2009) Dictionary of distances. Springer, Berlin. ISBN: 978-3-642-00233-5
93. Zweig MH, Campbell G (1993) Clin Chem 39:561–577
94. Hanley JE (1988) Med Decis Mak 8:197–203
95. DeLong ER, DeLong DM, Clarke-Pearson DL (1988) Biometrics 44:837–845
96. Zou KH, Hall WJ, Shapiro DE (1997) Stat Med 16:2143–2156
97. Faraggi D, Raiser B (2002) Stat Med 21:3093–3106
98. Sheather SJ, Jones MC (1991) J R Stat Soc B 53:683–690
99. Carpenter J, Bithell J (2000) Stat Med 19:1141–1164
100. Bakshi S, Halámková L, Halámek J, Katz E (2014) Analyst 139:559–563
101. Bilal M, Tariq A, Khan S, Quratulain, Tariq A, Shahid MF, Khan MW, Shah AR, Naveed AK (2011) J Ayub Med Coll Abbottabad 23:70–72
102. Lee JK, Shim JH, Lee HC, Lee SH, Kim KM, Lim Y-S, Chung Y-H, Lee YS, Suh DJ (2010) Hepatology 51:1577–1583
103. Prati D, Taioli E, Zanella A, Torre ED, Butelli S, Vecchio ED, Vianello L, Zanuso F, Mozzi F, Milani S, Conte D, Colombo M, Sirchia G (2002) Ann Intern Med 137:1–9
104. Ponti V, Dianzani MU, Cheeseman K, Slater TF (1978) Chem Biol Interact 23:281–291
105. Dunigan DD, Waters SB, Owen TC (1995) Biotechniques 19:640–649
106. Agudelo J, Huynh C, Halámek J (2015) Analyst 140:1411–1415
107. Sikirzhytskaya A, Sikirzhytski V, McLaughli G, Lednev IK (2013) J Forensic Sci 58:1141–1148
108. Mayntz-Press K, Sims L, Hall A, Ballantyne J (2008) J Forensic Sci 53:342–348

109. Brettell TA, Butler JM, Saferstein R (2005) Anal Chem 77:3839–3860
110. Bevel T, Gardner RM (2012) Bloodstain pattern analysis. With an introduction to crime scene reconstruction. CRC Press, Boca Raton
111. Bremmer RH, de Bruin KG, van Gemert MJ, van Leeuwen TG, Aalders MC (2010) Forensic Sci Int 216:1–11
112. Schwarzacher PD (1930) Am J Police Sci 1:374–380
113. Patterson D (1960) Nature 187:688–689
114. Tsutsumi A, Ishizu H (1983) Jpn J Legal Med 37:770–776
115. Fujita Y, Tsuchiya K, Abe S, Takiguchi Y, Kubo S, Sakurai H (2005) Forensic Sci Int 152:39–43
116. Inoue H, Takabe F, Iwasa M, Maeno Y, Seko Y (1992) Forensic Sci Int 57:7–27
117. Matsuoka T, Taguchi T, Okuda J (1995) Biol Pharm Bull 18:1031–1035
118. Bauer M, Polzin S, Patzelt D (2003) Forensic Sci Int 138:94–103
119. Botonjic-Sehic E, Brown CW, Lamontagne M, Tsaparikos M (2009) Spectroscopy 2:42–48
120. Strasser S, Zink A, Kada G, Hinterdorfer P, Peschel O, Heckl WM, Nerlich AG, Thalhammer S (2007) Forensic Sci Int 170:8–14
121. Chuang M-C, Windmiller JR, Santhosh P, Valdés-Ramírez G, Katz E, Wang J (2011) Chem Commun 47:3087–3089
122. Rafael SP, Vallée-Bélisle A, Fabregas E, Plaxco K, Palleschi G, Francesco Ricci F (2012) Anal Chem 84:1076–1082
123. Katz E, Halámek J, Halámková L, Bakshi S, Agudelo J, Huynh C (2016) Biochemical analysis of biomarkers for forensic applications. In: Katz E (ed) Forensic science: a multidisciplinary approach. Wiley-VCH, Weinheim, pp 151–176
124. Katz E, Halámek J, Bakshi S (2015) J Forensic Legal Invest Sci 1:004
125. Strack G, Bocharova V, Arugula MA, Pita M, Halámek J, Katz E (2010) J Phys Chem Lett 1:839–843
126. Zhou M, Zhou N, Kuralay F, Windmiller JR, Parkhomovsky S, Valdés-Ramírez G, Katz E, Wang J (2012) Angew Chem Int Ed 51:2686–2689

Heat Transfer as a New Sensing Technique for the Label-Free Detection of Biomolecules

Kasper Eersels, Bart van Grinsven, Marloes Peeters, Thomas J. Cleij, and Patrick Wagner

Abstract This chapter focuses on a new thermal sensing technique based on analyzing the heat-transfer resistance of a functionalized solid–liquid interface in time. This method, the so-called heat-transfer method (HTM), was developed by the authors in 2012. In order to monitor the thermal resistance of a functional interface in time, the temperature beneath a functionalized chip is controlled, while the output temperature in the measuring chamber is registered in time. Originally, the method was used for the detection of single-nucleotide polymorphisms (SNPs) in deoxyribonucleic acid (DNA). It was found that upon denaturation of double-stranded DNA, the DNA curled up, leading to an increased surface coverage and hence thermal resistance. This transition from low to high thermal resistance regimes could be employed to pinpoint the melting temperature of the DNA strain under study and thereby identify point mutations. In recent years, HTM has been combined with various synthetic and natural receptors for various applications including the detection of whole cells and microorganisms, neurotransmitters and hormones, and proteins using surface imprinted polymers (SIPs), molecularly imprinted

K. Eersels and P. Wagner (✉)
Soft-Matter Physics and Biophysics Section, Department of Physics and Astronomy, KU Leuven, Celestijnenlaan 200 D, B-3001 Leuven, Belgium
e-mail: kasper.eersels@kuleuven.be; patrickhermann.wagner@kuleuven.be

B. van Grinsven and T. J. Cleij
Maastricht Science Programme, Maastricht University, P.O. Box 616, 6200 MD Maastricht, The Netherlands
e-mail: bart.vangrinsven@maastrichtuniversity.nl; thomas.cleij@maastrichtuniversity.nl

M. Peeters
Faculty of Science and Engineering, School of Science and the Environment, Division of Chemistry and Environmental Science, Manchester Metropolitan University, Chester Street, Manchester M1 5GD, UK
e-mail: m.peeters@mmu.ac.uk

M. J. Schöning, A. Poghossian (eds.), *Label-Free Biosensing: Advanced Materials, Devices and Applications*, Springer Series on Chemical Sensors and Biosensors (2018) 16: 383–408
DOI 10.1007/5346_2017_1, © Springer International Publishing AG 2017,
Published online: 20 April 2017

polymers (MIPs), and aptamers, respectively. This chapter aims at discussing HTM as a sensing technique and its application in bio-analytics in detail and benchmarking it by providing an overview of other thermal sensing principles and their inherent benefits and drawbacks.

Keywords Biosensors, Cell detection, DNA, Heat transfer, Synthetic receptors

Contents

1 Introduction

Traditionally, thermal techniques have been used for diverse biotechnological applications including deoxyribonucleic acid (DNA) melting curve analysis and DNA amplification by polymerase chain reaction (PCR) [1, 2]. However, the application of calorimetric and thermal sensing methods in bio-analytics was considered to be limited due to the requirement of complex and expensive instrumentation, the relatively slow response time, the poor sensitivity, and the interference of nonspecific heating effects [3, 4]. In the 1970s, simple calorimetric devices were combined with the specificity of immobilized enzymes for the detection of urea and glucose [5, 6]. These thermal biosensors offer several advantages in comparison to other sensing platforms including insensitivity to varying optical and ionic properties of the sample under study, simple bulk production, good long-term stability, and reusability of the biocatalyst [7]. In following years, multiple enzyme-based thermal sensor platforms have been developed for the detection of several clinical markers including cholesterol, creatine, and triglycerides [8–10].

Thermal biosensors typically measure the heat that arises from the biochemical reactions or molar enthalpy changes. Historically, enzyme-based thermal biosensors could be roughly divided into two categories. The first-generation sensors were based on a thermistor registering the temperature at the outlet of an enzyme-packed column [6]. Whenever a sample is loaded into the column, the target molecule, if present, will react specifically with the enzyme generating heat that will change the resistance of the thermistor that is compared in real time to the resistance of a reference thermistor [11]. The sensitivity of the device can be increased by coupling a thermistor-based sensor to an automated flow injection analysis unit [12]. Another

important category of thermal biosensors is based on the so-called Seebeck effect. The thermoelectric potentials developed between the ends of two metal or alloy wires are proportional to the temperature difference between both points. Thermocouples [13] and thermopiles [14, 15] use this effect to translate the temperature in a measurable electrical signal. These types of sensors do not require a reference channel, making them easier to miniaturize.

Many biotechnological applications require the simultaneous detection of multiple targets in a single sample. Therefore, multiple technological improvements have been aimed at developing parallel sensor arrays. This can be achieved by creating an array of thin-film thermistors [16] or integrating the temperature-sensitive elements onto a single chip allowing for differential measurements [17, 18]. Due to the advancements in both thin-film and microchip technology, these improvements facilitate miniaturization of the sensors and improve the reproducibility of the sensors. In order to create more versatile sensor platforms, hybrid systems have been developed combining thermal sensing with electrochemical readout techniques [19] and bulk acoustic wave resonators [20].

In addition to enzymatic biosensors, devices have been developed based on other types of bio(mimetic) receptors. Thermal immunosensors have been developed by immobilizing antibodies onto a column, connected to a thermal sensing element [21]. In most cases, the recognition of the antigen by the antibody is indirect and antigen–antibody coupling is usually followed by an enzymatic-labeling step, often coupled to a secondary antibody. Upon addition of the ligand of the enzyme, heat is created proportional to the amount of antigen bound to the surface. Therefore, these types of sensors were named thermometric enzyme-linked immunosorbent assay (TELISA) due to the resemblance to the well-known ELISA technique [22]. Nucleic acids such as DNA [23] and aptamers [24] have also been used as receptor layers in thermal biosensors. Recently, a novel microcalorimetric method was combined with infrared spectroscopy to create a very sensitive sensor application that enables the user to identify single-nucleotide polymorphisms (SNPs) [25]. Due to the limited stability of biological receptors, a lot of research effort has been put into the incorporation of synthetic receptors such as molecularly imprinted polymers (MIPs) into thermal biosensor platforms, leading to more stable and reproducible devices [26, 27].

In 2012, the authors of this chapter introduced a new type of thermal biosensor technique that is based on the analysis of heat transfer through a functionalized chip surface rather than the generation of heat by a biochemical process or change in enthalpy. Initially, the technique, coined the heat-transfer method (HTM), was used to detect SNPs in DNA [28] but the technique was extended towards other biosensing applications and has actually proven to be a very versatile readout methodology [29]. This chapter will provide an overview of the various HTM-based biosensor applications that have been developed over the years and will provide an outlook directing future research.

2 General Sensing Concept

HTM is based on analyzing the transport of thermal energy over the receptor layer. The thermal resistance (R_{th}) at the interface can change due to various effects including DNA hybridization/denaturation, binding of bio-particles to the receptor layer, or phase transitions in lipid vesicle layers. A typical HTM setup is schematically illustrated in Fig. 1. The functional interface, which can be any type of receptor layer, is applied onto a solid chip. The chip can be made of virtually any heat conducting material, ensuring that the heat flux is focused through the functional interface. The thermal current is provided by a power resistor and passes through a copper block, serving as a heat provider or heat sink. The temperature of the copper block, T_1, is measured by a thermocouple and actively steered by a proportional-integral-derivative (PID) controller, controlling the power produced by the resistor. The functional interface is exposed to the analyte under study by means of a flow cell that is connected to a tubing system, allowing automated sample administration and flushing using a syringe-driven or peristaltic flow pump. The temperature of the liquid inside this flow cell, T_2, is measured in time by a second thermocouple. The values of both T_1 and T_2 are registered by a thermocouple card; the PID controller uses the T_1 data to adjust the voltage over the resistor, which is also registered by the software. From these data, the thermal resistance R_{th} (°C/W) can be approximated by the ratio of the temperature difference $\Delta T = T_1 - T_2$ and the input power P according to $R_{th} = \Delta T/P$ [28]. Current research is focused on deriving a more exact calculation of the thermal resistance from the experimental data as the current approximation neglects the fact that only a small portion of the heating power P transfers through the functional interface.

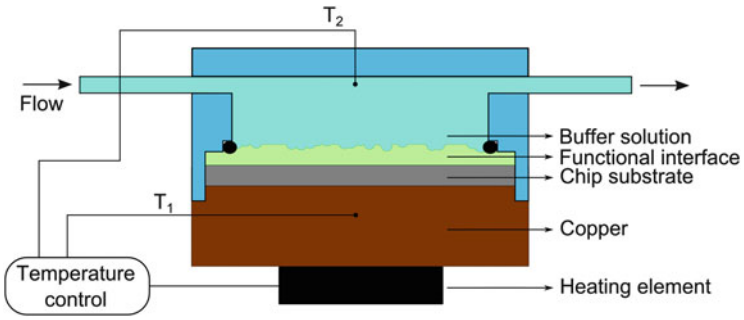

Fig. 1 Schematic representation of the HTM sensing concept. The measuring chip, coated with a functional layer, is connected mechanically to a copper block, heated by a power resistor (P). The temperature of this heat sink, T_1, is registered and actively steered by a temperature-control unit (TCU). The temperature of the liquid inside the flow cell, T_2, is monitored in time by a second thermocouple. In this way, the thermal resistance of the solid–liquid interface can be derived as $R_{th} = T_1 - T_2/P$. Changes occurring at the functional layer can influence the heat transport through the chip and hence the heat-transfer resistance of the solid–liquid interface. Reproduced, with permission, from van Grinsven et al. [28]. Copyright 2012 American Chemical Society

3 Detection of Single-Nucleotide Polymorphisms in DNA

The first HTM-based biosensor application was introduced in 2012 in the context of DNA mutation analysis [28]. Gold standard DNA mutation analysis tools include sophisticated molecular techniques which are generally quite sensitive but typically involve fluorescent labeling, DNA isolation, amplification, and expensive instrumentation and are lacking real-time kinetic information [30]. The potential of HTM to serve as an alternative for these techniques was examined by coating a silicon chip with a 300 nm nanocrystalline diamond (NCD). The NCD layer was functionalized by covalently attaching 29-mers double-stranded DNA (ds-DNA) via the 1-Ethyl-3-(3-dimethylaminopropyl)carbodiimide (EDC) coupling route. The probe strand was linked to the diamond through stable C–C bonds in a "head-on" configuration, while the target strand was allowed to hybridize or denature without steric hindrance as can be seen in Fig. 2a. Since the 29-mer total length of the ds-DNA fragments (10 nm) is well below the persistence length for ds-DNA (50 nm), they will behave as "stiff rods." The surface coverage of these rods was experimentally determined at 35% by X-ray photoelectron spectroscopy, which allows a large part of the thermal energy to pass freely through the nonfunctionalized areas of the NCD (Fig. 2b). However, some of the heat dissipates along the ds-DNA eventually inducing denaturation. The resulting ss-probe DNA fragments have a total length of 12.24 nm which is well above the persistence length of ss-DNA (1.48 nm), inducing the probe DNA to curl up in an irregular shape with a Flory radius of 2.46 nm, increasing the surface coverage to 150%, leading to a higher thermal resistance of the functional interface (Fig. 2c).

The effect described above was used for the detection of SNPs in DNA. The results of these experiments are shown in Fig. 3. The red curve illustrates that the thermal resistance of a nonfunctionalized diamond chip, exposed to phosphate buffered saline

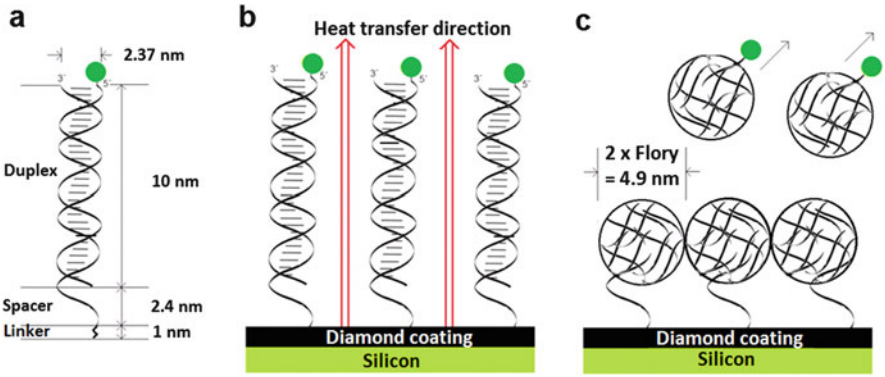

Fig. 2 (**a**) Schematic illustration of DNA duplexes with labeled target strands. (**b**) Heat-transfer path through a molecular DNA brush. (**c**) Upon denaturation, the probe DNA curls up in irregular structures, characterized by the Flory radius, thereby blocking heat transfer at the solid–liquid interface. Adapted, with permission, from van Grinsven et al. [28]. Copyright 2012 American Chemical Society

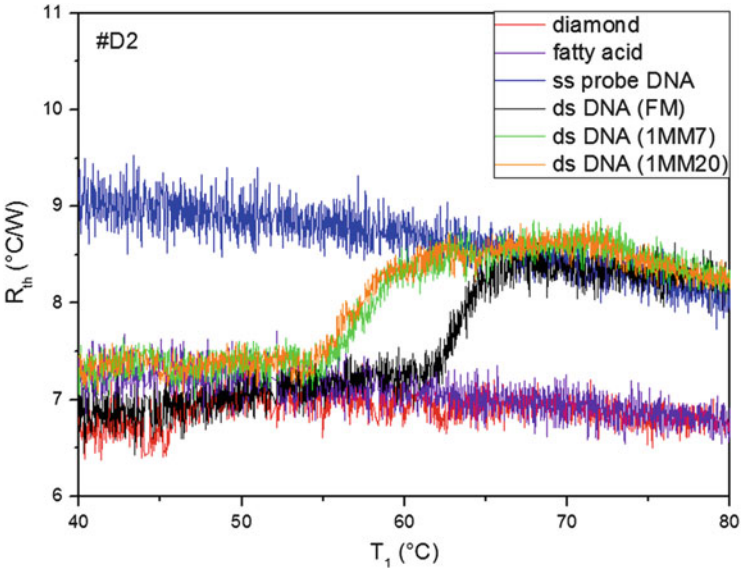

Fig. 3 Heat-transfer resistance R_{th} as a function of temperature. The unmodified (*red curve*) and fatty-acid modified electrode (*purple curve*) have a widely constant R_{th}. In the configuration with attached ss-DNA (*blue curve*), the heat-transfer resistance has notably increased due to an efficient thermal insulation by the DNA fragments. The R_{th} of full-match ds-DNA (*green curve*) is comparable to the non-modified surface at low temperatures and switches to the ss-DNA behavior upon denaturation with a midpoint. Repeating the experiment DNA duplexes containing a mismatch at position 7 (*green curve*) or position 20 (*orange curve*) results in a clear shift of $T_{midpoint}$ to lower temperatures. Adapted, with permission, from van Grinsven et al. [28]. Copyright 2012 American Chemical Society

(PBS) solution, remained fairly constant over a wide temperature range (red curve). Attachment of the fatty-acid cross-linker did not result in a measurable change in R_{th} (purple curve). Attachment of ss-DNA results in an increase of the thermal resistance that slowly decreases at increasing temperatures (blue curve). Hybridizing the ss-probe DNA to either a complementary strand (black curve) or a strand containing a mismatch (green and orange curve) results in a signal that is in range with the signal for ds-stranded DNA. At a certain temperature, the melting temperature, an upward jump in thermal resistance can clearly be observed as the DNA transits the ds- to the ss-state. The midpoint of each temperature curve: $63.0 \pm 0.1°C$ (black line), $57.6 \pm 0.1°C$ (green line), and $56.8 \pm 0.1°C$ (orange line) can be used to discriminate between complementary DNA fragments and fragments containing a cytosine–cytosine mismatch located at different positions. These findings can be explained by the fact that an SNP in the target fragment leads to a decreased stability of the resulting duplex, leading to a shift of the melting temperature towards the lower temperature regime.

The possibility of using HTM for DNA mutation analysis was further studied in 2013 demonstrating that the platform can be used to differentiate between sequence

polymorphisms of the same gene in a simultaneous analysis [31]. These findings illustrate that HTM might offer a user-friendly alternative to parallel techniques such as microarrays. An additional study revealed that it is possible to use the technique to estimate the mutated fraction of a gene under study by simultaneous analysis of full-match and mismatch sequences [32]. These findings eventually lead to a first clinical test for the HTM-based DNA mutation analysis tool in 2014 [33]. The technology was used to detect mutations in phenylketonuria (PKU)-related exons in patient samples, confirming that HTM has the potential for implementation in various diagnostic fields. These experiments also reveal that when the ds-DNA fragment exceeds the persistence length (ca. 150 base pairs), the technique cannot be used anymore. In addition to this drawback, the high amount of noise on the signal and the price of the diamond-coated samples could also be a limitation when aiming at a commercial application.

In this context, the HTM-based DNA analysis principle was studied using low-cost, electrically insulating sapphire chips [34]. These chips were functionalized with (3-aminopropyl) triethoxysilane (APTES) and succinic anhydride, allowing to attach DNA through the EDC route. The thermal conduction and DNA denaturation effect in these sapphire chips were compared to the results obtained in a similar experiment on the diamond-coated silicon chips (Fig. 4). The signal-to-noise ratio appears to be improved by almost a factor of three when using synthetic sapphire. This effect can

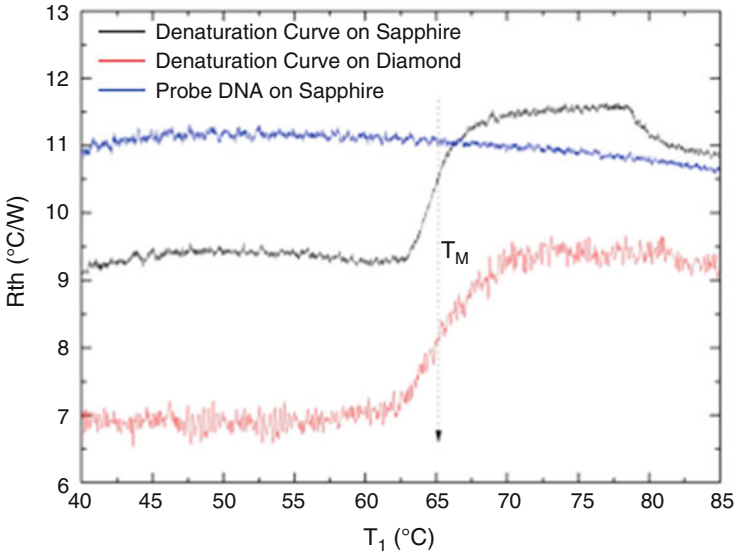

Fig. 4 Temperature-dependent thermal resistance data showing the denaturation of ds-DNA on a diamond-coated silicon (*red curve*) and a synthetic sapphire (*black curve*) chip. For comparison, a similar experiment was conducted on a sapphire chip coated with ss-DNA (*blue curve*). The resulting profile illustrates that the noise on the thermal resistance is substantially lower in the experiment using a sapphire chip, allowing for a more accurate determination of the melting temperature. Adapted, with permission, from Murib et al. [34]. Copyright 2016 Elsevier

be explained by the fact that there is no internal interface inside the chip and sapphire has a higher heat capacity than silicon and diamond. The resulting thermal mass will therefore be higher, making the sapphire chip less susceptible for temperature fluctuations. In turn, this allows for a more accurate determination of the melting temperature, making the device more sensitive.

4 Detection of Small Organic Molecules with Molecularly Imprinted Polymers

MIPs are synthetic receptors that are sometimes referred to as "antibody mimics" [35]. Similar to natural antibodies, they possess a high affinity for their template molecule but have the advantages of low-cost, superior chemical and thermal stability, and possibility to tailor the MIP to its target. The potential of HTM for the detection of small organic molecules with MIP-based sensor platforms was demonstrated for the first time in 2013. MIP particles were prepared by bulk polymerization and then applied onto aluminum chips that were pre-coated with a polyphenylenevinylene adhesive layer [36]. After gentle heating of the sample, the particles sink into the adhesive layer where they remain entrapped after subsequent cooling. These polymer-functionalized electrodes were mounted into the HTM setup and the thermal resistance was measured in buffer solutions with increasing neurotransmitter concentrations. An increase in the thermal resistance was observed, which can be qualitatively explained by the "pore-blocking model" (Fig. 5) [36]. The response in thermal resistance is then used to quantify the amount of neurotransmitter in the sample.

With this approach, detection limits in the order of 50 nM in buffered solutions were determined for the neurotransmitters serotonin, histamine, and L-nicotine. The sensor platform was able to discriminate between histamine and histidine, a competitor molecule similar in size and structure, illustrating the specificity of the sensor (Fig. 6). Additionally, in a reference measurement using non-imprinted polymer (NIP) beads as synthetic receptors, the sensor does not respond to a solution containing target or analogue. This proves that the observed effect for the MIP is not the result of a change in the thermal conductivity of the liquid inside the measuring chamber.

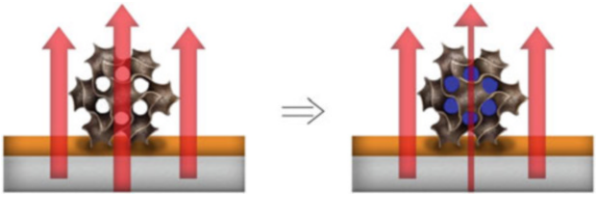

Fig. 5 Schematic representation of the MIP-based small molecule detection principle using HTM. When the template, represented as *blue dots*, binds to the MIP layer, heat transfer is blocked in a certain direction and this leads to a measurable increase of the overall thermal resistance. Adapted with permission from Peeters et al. [36]. Copyright 2013 Springer

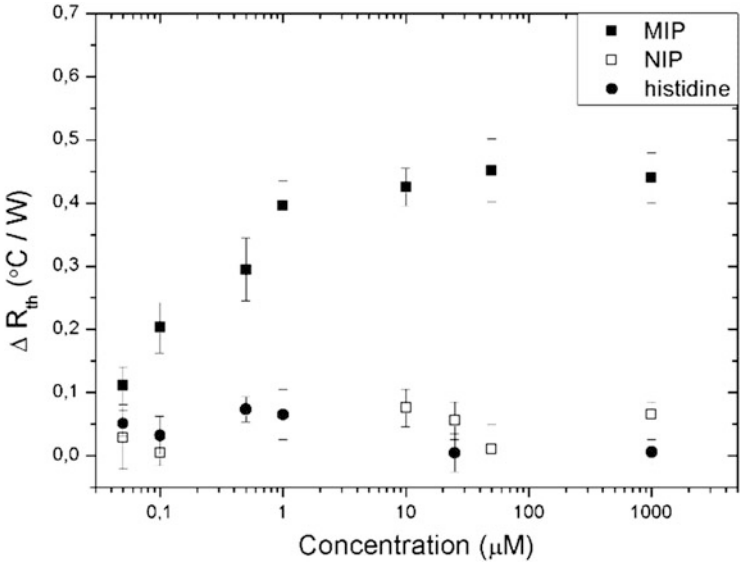

Fig. 6 Dose–response curve for an MIP imprinted with histamine. MIP and NIP are exposed to increasing concentrations of histamine (target) and histidine (analogue). The specificity of the platform is proven by the fact that the sensor does not respond to histidine, while the NIP response illustrates that the observations are not the result of a change in thermal conductivity of the liquid inside the measuring chamber. Adapted, with permission, from Peeters et al. [36]. Copyright 2013 Springer

In a follow-up study on this research, the limit-of-detection (LoD) was brought down by a factor of two by optimizing the settings of the feedback loop of the temperature-control system [37]. Further improvements were made by introducing a novel method for selectively functionalizing parts of the electrode, which made it possible to cover the electrode with MIP particles imprinted with different molecules. In this way, the authors could measure three different neurotransmitters simultaneously using an MIP-based parallelized array [38].

The described functionalization method is not commercially viable since it requires the use of an additional adhesive layer, stamping of MIP microparticles, and a preparation time of at least 20 min per sample. In order to address this, a new concept was introduced that is based on Screen-Printed Electrodes (SPEs); these electrodes are cost-effective, highly reproducible, and can be prepared in bulk quantities [39]. Particles were mixed with the screen-printing ink and printed onto SPEs, which is a simple and fast (1 min/sample) preparation method [40]. As a proof-of-concept, MIPs for dopamine were synthesized and integrated into SPEs with a 30% ratio of particles vs. ink. Measurements performed with HTM improved the LoD with an order of magnitude compared to traditional cyclic voltammetry (0.35 vs. 4.7 μM) in buffer [40]. In addition, it was possible to measure spiked concentrations of dopamine in banana fluid (Fig. 7).

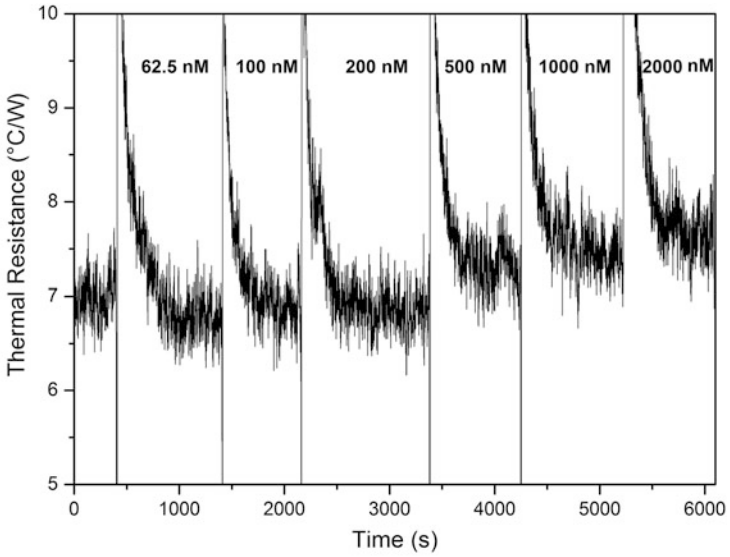

Fig. 7 Thermal resistance in time for an MIP stabilized in banana fluid (homogenized with a blender) to which spiked solutions of dopamine in banana fluid were added. In each addition step, the fluid inside the measuring chamber was replaced entirely by flushing with an excess volume of banana fluid. In this way, the concentration of dopamine was gradually increased (62.5, 100, 200, 500, 1,000, and 2,000 nM). From 500 nM on, a significant effect was observed. Adapted with permission from Peeters et al. [40]. Copyright 2016 Multidisciplinary Digital Publishing Institute

Screen printing of MIP layers onto electrodes is a sensor development technique that has a high commercial potential for large-scale application in clinical and bioanalytical settings due to its simplicity, low-cost nature, and portability of the setup. These types of devices are suitable for routine, on-site screening in diverse areas including health and care, environmental analysis, and food and water screening. New research opportunities include printing the receptor layers on sustainable alternatives to traditional electrode materials such as paper or organic polymer foils. These materials are both biocompatible and flexible and can therefore be used in biomedical devices such as catheters or implants which would allow for in vivo detection of relevant molecules.

5 Cell and Pathogen Detection

The possible use of HTM for diagnostic applications based on specific cell detection was explored in 2013 [41]. Synthetic cell receptors, known as surface imprinted polymers (SIPs), were chosen because of their ability to specifically and selectively recognize their target in addition to their superior stability and low-cost synthesis procedure [42]. The SIPs were made using the stamping approach. This straightforward, elegant

strategy consists of stamping the template cells into a semi-cured polyurethane layer. Upon cross-linking of the layer, the template cells are removed, leaving a pattern of micron-sized imprints behind on the surface of the polymer-coated chip. In Fig. 8, a typical SIP layer is shown. This layer was imprinted with MCF-7 cells, a breast cancer cell line that typically has a spherical shape with a diameter of ±20 μm. From the optical image of the SIP (Fig. 8a), it can be concluded that the horizontal dimensions of the template are transferred into the SIP layer. Both the spherical shape and the size of the MCF-7 cells are retained. The topographic analysis of an imprint, shown in Fig. 8b, reveals that the vertical dimensions of the template are not retained in the SIP. The imprint is only 600 nm deep, which can be considered shallow in comparison to the dimensions of the cell. However, this is crucial for the selectivity of the SIP: cells that fit the dimensions of an imprint can fit within the microcavities but can be easily washed out if the morphological match is not supplemented by a functional match, created during imprinting.

The detection principle is shown in Fig. 9. The thermal resistance of the interface is determined by the thickness of the polyurethane layer. Therefore, the microcavities should have a lower R_{th} in comparison to the thicker non-imprinted parts of the SIP layer and will act as preferential heat channels. However, when a cell binds to the receptor layer, they will replace the water that was previously inside the cavities. As it was recently shown that the phospholipid bilayers surrounding a cell have a lower thermal conductivity than water [43], cell rebinding will result in an increase of the R_{th} of the interfacial layer, resulting in a drop in T_2.

This effect was exploited for the specific detection of cancer cells in phosphate buffer. It was analyzed whether it was possible to discriminate between breast cancer cells (MCF-7 cells), immortalized leukemic T-lymphocytes (Jurkat cells), and a mixed population of healthy blood cells (peripheral blood mononuclear cells or PBMCs). The results, summarized in Fig. 10, reveal that exposing an MCF-7 SIP to a solution of target cells will lead to an increase in the thermal resistance of the interface (Fig. 10a,

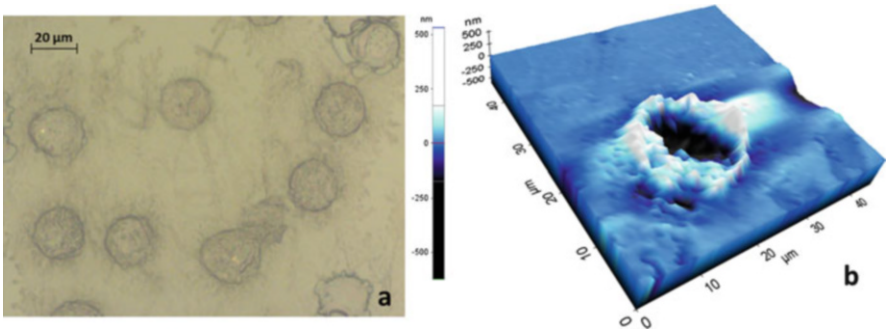

Fig. 8 (**a**) Optical analysis of SIP layer imprinted with MCF-7 cells, indicating that the lateral dimensions, i.e., the size and shape, of the template are preserved, (**b**) the topographic study of the layer by atomic force microscopy (AFM) illustrates that the vertical dimensions are not transferred to the SIP layer given the imprint depth of only ±600 nm. Adapted with permission from Eersels et al. [41]. Copyright 2013 American Chemical Society

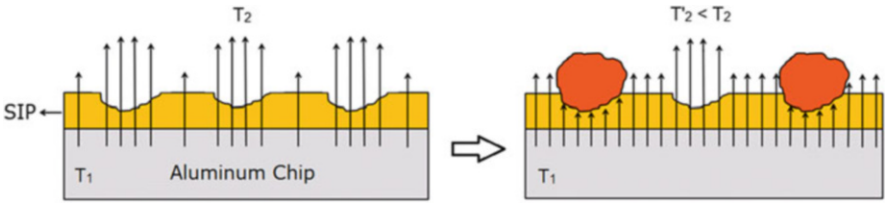

Fig. 9 Schematic representation of the SIP-based cell detection principle using HTM. As the thermal resistance of the extracted SIP (*left*) will be mainly determined by the thickness of the insulating polyurethane layer, the microcavities will form preferential heat channels. When cells bind into these cavities, they will block the heat flow through the cavities, thereby increasing the thermal resistance of the solid–liquid interface. The HTM device will keep the temperature of the copper heat provider, underneath the sample, constant. The temperature in the liquid measuring chamber, T_2, will increase upon binding of the cells to the layer. Adapted, with permission, from Eersels et al. [41]. Copyright 2013 American Chemical Society

black curve). In addition, a small degree of cross-selectivity is observed when Jurkat cells bind to the SIP (red curve), while the sensor does not respond to a solution of PBMCs (blue curve). After applying two consecutive flushing steps, in which the flow cell is rinsed with buffer at flow rates of 2.5 and 0.25 mL min^{-1}, respectively, the signal returns to baseline for the competitor but not the target cells. This indicates that the nonspecifically bound competitor cells can be washed out of the microcavities due to the shear forces provided by flushing. On the other hand, the target cells adhere tightly to the SIP layer due to their specific interaction with the microcavities. As a result, they cannot be removed from the layer by flushing with buffer. The precise origin of this selective binding mechanism is the topic of ongoing research.

Similar experiments were performed on SIPs imprinted with Jurkat cells (Fig. 10b) and PBMCs (Fig. 10c). Moderate degrees of cross-selectivity were observed when: (1) MCF-7 and PBMCs attached to Jurkat SIPs and (2) a PBMC SIP was exposed to a solution of Jurkat cells. It was possible to revert the signal to baseline by flushing the flow cell with buffer, thereby removing the competitor cells from the SIP. In both cases, the washing steps had no effect on the signal for the experiment with target cells complementary to the imprints.

These results illustrate the potential of the device for diagnostic cell detection applications such as the specific detection of circulating tumor cells (CTCs) in blood samples. The gold standard techniques for CTC detection are usually based on specialized flow cytometry techniques. Although these methods require expensive training and both operating and data analysis require some training, they are very sensitive, allowing to detect cells at concentrations below 10 cells mL^{-1}. HTM could offer a low-cost, user-friendly, and label-free alternative that can be used on-site but the LoD (10^4 cells mL^{-1}) needs to be improved dramatically in terms of CTC detection.

The selectivity and sensitivity limit of the methodology was examined in 2014. The previous experiments illustrate that it is possible to discriminate between morphologically similar cells. However, the cell types under study differed significantly in terms of the distribution of functional groups. Therefore, Chinese hamster ovarian (CHO) cells were induced to express the MUC1 protein, a transmembrane protein

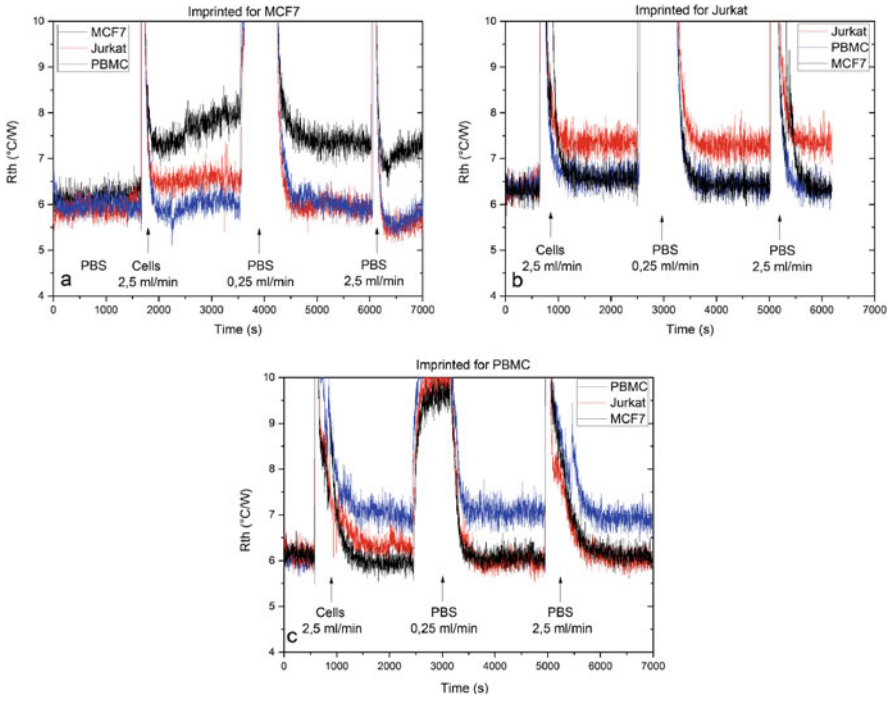

Fig. 10 (**a**) Time-dependent profile of the heat-transfer resistance for an SIP imprinted with MCF-7 cells in response to MCF-7 cells (*black curve*), Jurkat cells (*red curve*), and PBMCs (*blue curve*). (**b**) Thermal response of a Jurkat-imprinted SIP towards Jurkat, PBMC, and MCF-7 cells. (**c**) Thermal resistance profile of a PBMC SIP in response to PBMCs, Jurkat, and MCF-7 cells. The *color codes* are identical in all graphs. Mild rinsing of the flow cell with cell-free PBS suppresses the cross-selective response observed when exposing an SIP to a solution of competitor cells for all SIPs and cell types under study. Adapted, with permission, from Eersels et al. [41]. Copyright 2013 American Chemical Society

that is normally absent in these cells [44]. Furthermore, by incubating the MUC1-expressing cells with a differential amount of carbohydrates, it was possible to tune the degree of glycosylation on the MUC1 protein of these cells. The platform was used to discriminate between these morphologically identical cell lines and proved to be capable of distinguishing between cells based on the presence or absence of sugar moieties on their transmembrane proteins. However, slight differences in the glycosylation pattern of the MUC1 protein did not induce a different binding behavior and therefore could not be identified by the sensor, illustrating its limit-of-selectivity. Additionally, the LoD of the device was boosted by the development of a gradual enrichment approach that enables the user to identify target cells in concentrations as low as 10^4 cells mL^{-1} in the presence of a hundredfold excess of competitor cells. Although these results hold up well to other biosensor platforms, CTC detection still requires the LoD to be improved by three or four orders of magnitude.

In this light, other applications that do not require a very high degree of sensitivity were explored. In 2015, the device was used as a novel assay for monitoring the quality of cell lines in a cell culture lab [45]. Cross-contamination and spontaneous mutations arising from over-passaging or improper handling of cell cultures pose a serious threat for cell biologists as the fidelity of their scientific results depends largely on the integrity of the cell lines in culture. However, most cell analysis platforms are slow and require sophisticated machinery. Therefore, cell biologists monitor the quality of their cell cultures visually. As many negative effects of culturing cells for a prolonged period of time do not necessarily result in phenotypic changes, cell culture suppliers simply recommend to limit the number of passages. With the advent of short tandem repeat (STR) DNA profiling, a lot of progress has been made in this field [46]. This low-cost technique allows the user to analyze a given number of alleles of the cells they have in culture. The obtained profile can be compared to that in a database to assess the quality of the cell culture. However, this technique is typically slow, involves fluorescent labeling, and is confined to a separate, readout platform. Therefore, the technique is not suitable for routine analysis of cell cultures on a weekly basis. To determine whether the SIP-based thermal sensor platform could be a fast and user-friendly alternative in this context, an experiment was designed using the adherently growing breast cancer cell line, ZR-75-1. These cells were cultured in the presence of a faster growing, descendant cell line that was created involuntarily by cross-contamination in a previous experiment. SIPs were imprinted with ZR-75-1 cell lines and the cells were cultured for 30 passages. At regular time intervals, a sample of the cell culture was analyzed with the sensor. The results of this experiment are shown in Fig. 11. At low passage numbers, addition of a sample of the cell culture results in an irreversible increase of the thermal resistance at the functional interface, indicating that the ZR-75-1 cells adhere tightly to the SIP layer. Starting from passage 18, a decrease in the relative response becomes apparent. This indicates that some of the cells can be washed out of the layer as they bind less tightly to the SIP layer. The effect becomes more pronounced as the number of passages increases which implies that a cross-contamination with the faster growing cell line probably occurred. These findings were confirmed by STR DNA profiling [45].

Another interesting application for the sensor was demonstrated recently in terms of bacterial identification and viability testing [47]. In a first series of experiments, the concept of HTM-based bacterial sensing was introduced (Fig. 12) and it illustrates that it is possible to distinguish between viable and dead *Escherichia coli* cells (Fig. 12a) as well as specifically identifying gram-negative (*E. coli*) and gram-positive (*Staphylococcus aureus*) bacterial strains (Fig. 12b). Additionally, it was possible to detect *E. coli* cells at concentrations down to 10^4 colony forming units (CFUs) mL^{-1} in the presence of a hundredfold excess of *S. aureus*.

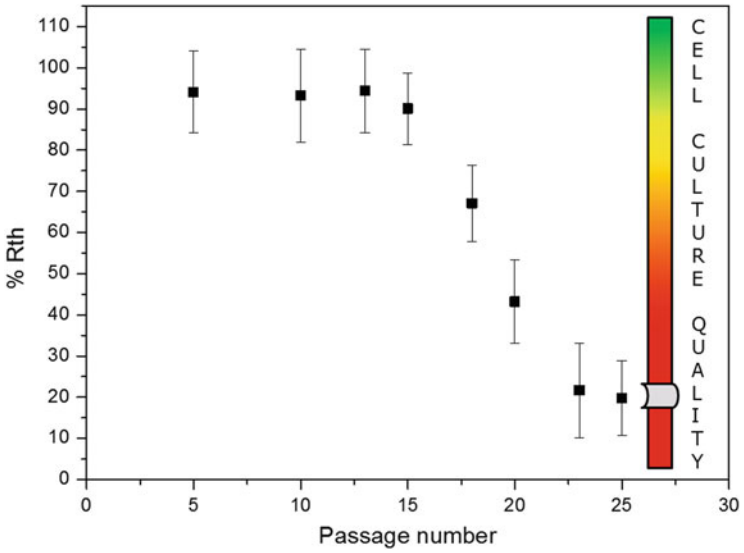

Fig. 11 Time-dependent thermal resistance data illustrating the potential of the SIP-based thermal sensing for cell culture quality assay. At low passage numbers, addition of a sample of the cell culture results in a large sensor response. Upon the introduction of a cross-contamination (passage 17), the signal drops. This effect gets more pronounced at increasing passage numbers. Adapted with permission from Eersels et al. [45]. Copyright 2015 American Chemical Society

6 Phase Transition Study on Supported Lipid Vesicle Layers

In addition to biosensing, HTM was also used for the detection of phase transitions in lipid membranes [48]. Experimental data on transition effects in lipid vesicles are mainly focused on dispersed vesicles and often restricted to molecular simulations [49]. With HTM, it was possible to study the phase transition behavior in these layers without the need for fluorescent labeling, which would change the transition behavior. Lipid vesicle layers were created on silica chips covered by a hydrogenated NCD coating. The thermal resistance of these functionalized chips at a solid–liquid interface was analyzed over time. Dipalmitoylphosphatidylcholine (DPPC) was chosen as a model lipid because of its rich phase behavior in an experimentally accessible temperature range. The "main phase transition," i.e., the transition from the ripple to the liquid disorder phase, takes place around 41°C [50]. Small unilamellar vesicles (SUVs) were formed by power sonication of a DPPC vesicle dispersion in 4-(2-hydroxyethyl)-1-piperazineethanesulfonic acid (HEPES) buffer. Phase transitions in these SUVs can be induced by heating and cooling the chip as shown in Fig. 13, leading to a change in the order of the lipid vesicle layer, thereby changing the thermal resistance of the interface.

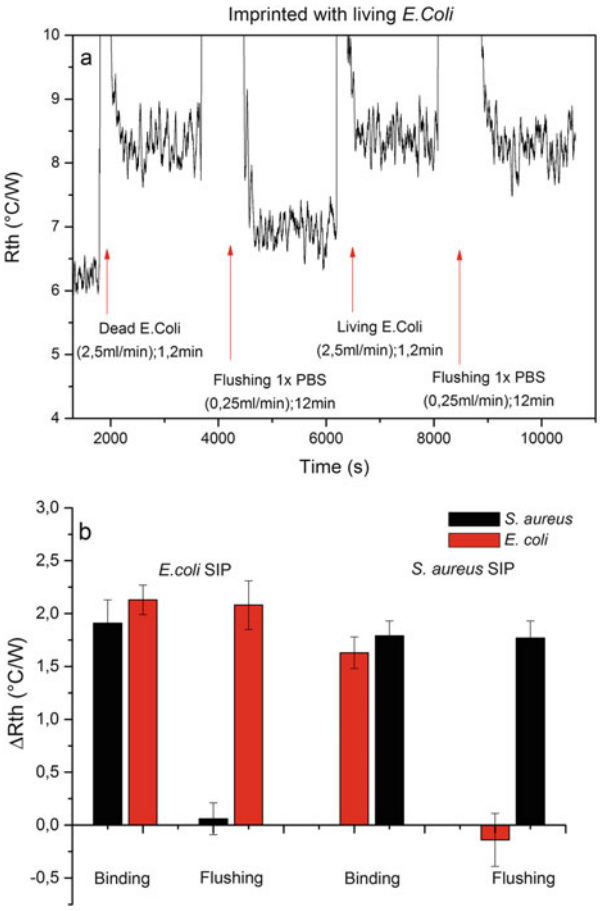

Fig. 12 (**a**) Time-dependent data illustrating the setup's potential for bacterial viability testing. (**b**) Bacterial identification experiment illustrating the possibility for discriminating between gram-negative and gram-positive bacterial strains. Adapted, with permission, from van Grinsven et al. [47]. Copyright 2016 American Chemical Society

Prior to the phase transition study, a control experiment was performed in HEPES buffer by applying a heating and cooling run, sweeping the temperature from 25°C to 60°C and back at a rate of 0.2°C min^{-1}. Next, a suspension of SUVs was injected into the measuring chamber at 25°C, well below the literature value for the main phase transition. After an hour of incubation time, the temperature was increased to 60°C at a rate of 0.2°C min^{-1}, after which the flow cell was flushed with HEPES buffer to remove any weakly or non-bound vesicles from the chip surface. After a cooling run at the same rate, an additional cooling and heating cycle was performed at a rate of 0.3°C min^{-1}, followed by a final heating run at 0.2°C min^{-1}. The resulting temperature profile for the liquid inside the flow cell, T_2, presented in Fig. 14a, shows an increase in thermal resistance at a copper temperature of 41°C, which corresponds well with the value for the main phase transition temperature obtained with other experimental techniques, such as microcalorimetry, for the study of vesicles in dispersion [50]. The hysteresis observed between heating and cooling further confirms the

hypothesis that these R_{th} jumps can be related to a first-order transition in the lipid vesicle layer from the ripple to the liquid disordered state.

The loss of order upon heating can be explained by a temperature-induced increase in the lateral mobility of the alkyl chains and appears to be endothermic as heat is absorbed by the disordered layer, leading to an increase of the interfacial thermal resistance. On the other hand, the transition from the liquid disordered phase to the ripple phase upon cooling is accompanied by a decrease in thermal resistance as the oriental order of the lipid chains enhances thermal conductivity at the interface. However, the contribution of a calorimetric effect, reflecting a first-order transition that influences the thermal resistance, cannot be ruled out.

When subtracting the baseline contribution of a blank substrate exposed to buffer, an effective difference R_{th}* can be obtained. These data, shown in Fig. 15b, agree with molecular dynamics simulations, indicating that the heat conduction mainly takes place across the vesicle layer [49].

These experiments demonstrate that HTM can also be used to study structural phase transitions in soft condensed matter and, in this case, provides an alternative to calorimetry for the detection of phase transitions in lipid vesicles. This opens up possibilities for future research including the study of more complex lipid mixtures to monitor lipid raft formation or the formation of lipid bilayers and self-assembled monolayers (SAMs) on chemically modified substrates, which might be interesting in terms of biosensing.

7 Protein Detection

An interesting HTM-based approach to detect the peanut allergen Ara h1 was introduced in 2015 [51]. This application is highly relevant for the food industry as Ara h1 is responsible for >90% of anaphylactic shock cases [52]. Previous research has demonstrated that it is possible to detect Ara h1 using aptamers [53]. These receptors were immobilized on measuring chips using a simple three-step process. First, gold electrodes are functionalized with a thiol SAM onto which amino-terminated aptamers are coupled. Finally, the electrodes are incubated into a solution containing bovine serum albumin (BSA) in order to prevent nonspecific binding to the surface. This receptor

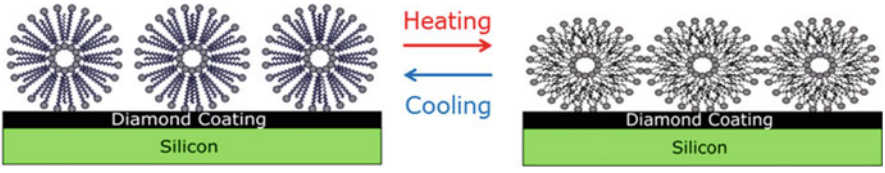

Fig. 13 Schematic representation of the lipid vesicle layer. Phase transitions are induced by heating and cooling of the substrate, and changing the surface coverage and the thermal resistance of the solid–liquid interface. Adapted with permission from Losada-Pérez et al. [48]. Copyright 2014 Wiley-VCH Verlag GmbH & Co. KGaA

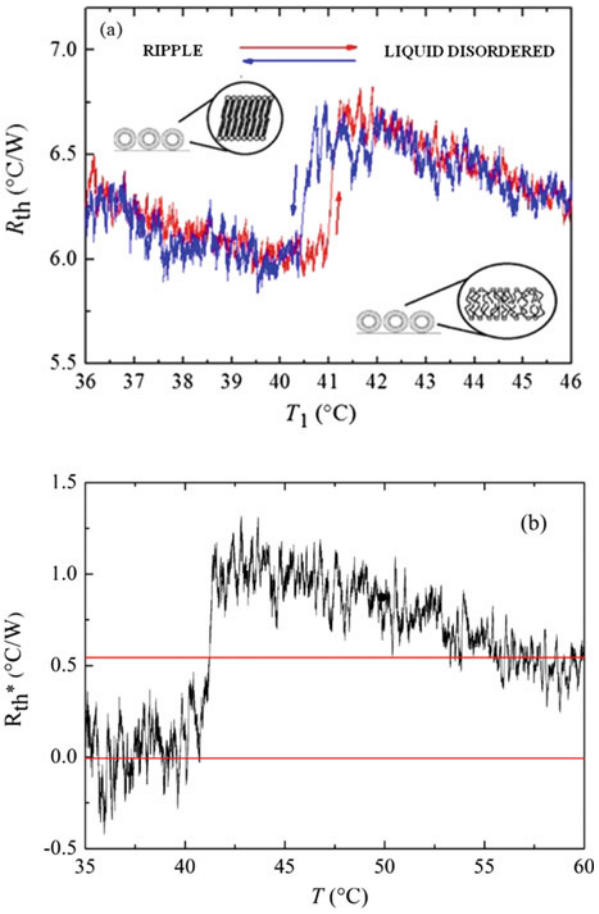

Fig. 14 (**a**) Temperature profile of the interfacial thermal resistance in response to main phase transitions in a supported DPCC vesicle layer adsorbed on an NCD-coated silicon chip. The *arrows* indicate the sequence of the run: heating (*red solid line*) and cooling (*blue solid line*). (**b**) Temperature profile of the effective thermal resistance R_{th}*, calculated as R_{th}* = R_{th} (DPPC + HEPES buffer) − R_{th} (HEPES buffer). *Solid red lines*: plateaus of R_{th}* values at temperatures away from the main phase transition. Adapted with permission from Losada-Pérez et al. [48]. Copyright 2014 Wiley-VCH Verlag GmbH & Co. KGaA

layer design is compatible with electrochemical, thermal, and gravimetric detection and is the result of a spontaneous process. However, it has to be noted that the formation of thiol SAM layers is specific for gold and platinum electrodes and this method is not directly transferable to other metal or nonmetal electrodes.

This method was used to functionalize gold HTM chips with aptamers for the peanut allergen Ara h1. Its attachment was confirmed by analysis with the Quartz Crystal Microbalance (QCM) and AFM images. HTM measurements were performed in buffer solutions (pH 8.4) to force the aptamers into a straight and rigid configuration prior to binding of the peanut allergen. This fixation of the structure has proven to be essential for achieving low detection limits with optical measurement techniques in previous work [53]. After stabilization of the aptamer-functionalized gold electrodes, a stepwise increase in the thermal resistance was observed at increasing allergen concentrations (Fig. 15).

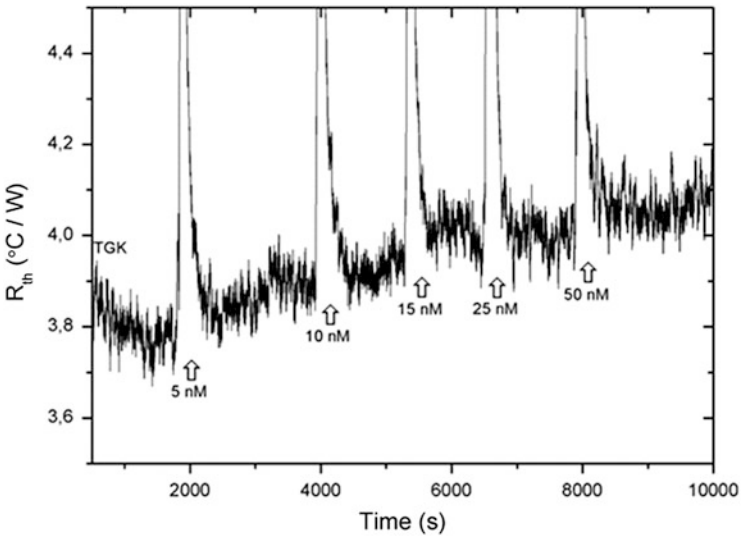

Fig. 15 The thermal resistance (R_{th}) in time for a gold chip functionalized with aptamers and a BSA coating with repellent properties. The R_{th} gradually increases at increasing concentrations of peanut allergen Ara h1. Reproduced with permission from Burks et al. [51]. Copyright 2015 American Chemical Society

Protein capturing by the aptamer resulted in a conformational change that added an additional degree of freedom at the solid–liquid interface and thereby increased the overall thermal resistance. This effect on the thermal resistance was not seen on gold functionalized with solely the BSA overcoating (without presence of the template), which demonstrated the specificity of the sensor platform. An LoD was established in the low nanomolar regime, which is in line with results previously obtained using aptamers combined with electrochemical methods. To demonstrate a first proof-of-application, a peanut butter enriched matrix spiked with Ara h1 was measured with HTM and QCM. Food samples are challenging and complex, which is not in the least due to their viscosity, and the results indicate the potential of the sensing platform to cope with challenging analytes. However, this research has not been extended to other aptamer–protein couples yet and general applicability of this biosensor remains to be proven. Although LoD values of sensors based on antibodies are in the picomolar range and exhibit superior sensitivity [54], it is worth noting that they do have significant drawbacks and are not able to compete with aptamers in terms of their price, shelf-life, stability, and reusability.

8 Thermal Wave Transport Analysis

Although HTM has proven to be a very versatile technique, the major drawback associated with its use in biosensor applications is the high level of noise on the power over the heater and therefore the thermal resistance signal. As the sensitivity of the device is inversely proportional to the noise on the measurement signal, the LoD of the methodology is adversely influenced by the high noise levels on the power. In addition, the method requires stabilization of the signal upon each addition step, resulting in relatively long response times. Therefore, a similar thermal readout technique was developed based on monitoring the propagation of a thermal wave through a functional interface. This method, thermal wave transfer analysis (TWTA), was combined with MIPs deposited on SPEs, synthesized as described in the section on small molecule detection, for the detection of dopamine in banana juice [40]. The concept is illustrated in Fig. 16.

In TWTA, a thermal wave rather than a constant thermal current is created by the TCU and applied onto the heat sink. The thermal wave, with an offset temperature of 37°C and an amplitude of ±0.1°C, propagates through the SPE surface and eventually reaches the liquid flow cell where the T_2 thermocouple registers the transmitted wave. Whenever the target molecules bind within the MIP immobilized on the SPE, the resulting increased thermal resistance at the interface will damp the transmission of the wave, resulting in a delay in the phase ($\varphi \neq \varphi'$) and a decrease in amplitude ($\alpha \neq \alpha'$) of the transmitted thermal wave in comparison to the baseline signal, measured in buffer solution or the non-spiked analyte under study.

In a dopamine detection experiment, comparing the performance of TWTA and HTM, it was shown that TWTA appears to be slightly more sensitive but, more importantly, also allows to reduce the measurement time to less than 5 min. In addition, the effect size was increased by nearly a factor of two [36]. Therefore, the sensor setup was used to detect dopamine in banana juice. To assess the potential of TWTA for dopamine detection in food samples, commercially available bananas were ground, centrifuged, and filtered to obtain a clear liquid. These samples were spiked with various concentrations of dopamine and analyzed using TWTA. Measurable effects were observed starting at concentrations of 500 nM as can be seen in Fig. 17.

9 Conclusions

HTM has proven to be a versatile and promising biosensing tool over the past 5 years. The combination of a fast, user-friendly, label-free, and low-cost transducer technique and the specificity of both biological and synthetic receptors has led to numerous applications including DNA mutation analysis and the detection of various targets ranging from low-molecular weight compounds to macromolecular entities such as proteins, bacteria, and mammalian cells. The platform has even been used for phase transition

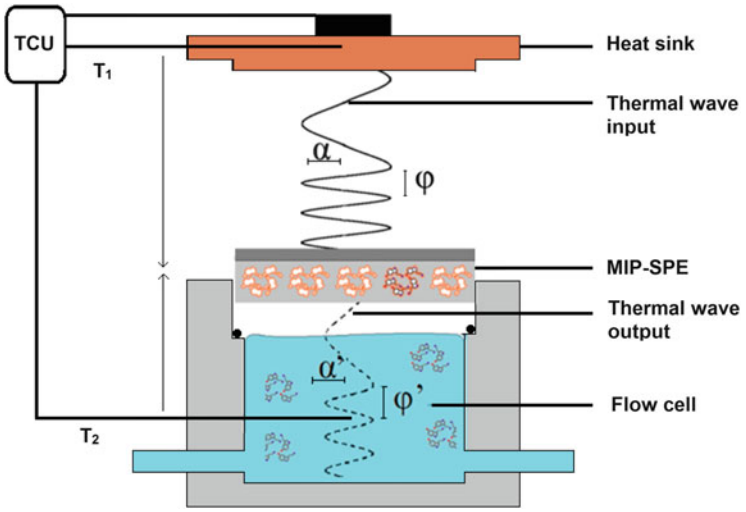

Fig. 16 Schematic representation of the TWTA concept. The temperature-control unit (TCU) generates a thermal wave (phase φ) that is transmitted through a functional interface, in this containing an MIP-SPE. The transmitted wave and corresponding phase φ' are recorded in the flow cell. Adapted, with permission, from Peeters et al. [40]. Copyright 2016 Multidisciplinary Digital Publishing Institute

studies in lipid vesicles, illustrating its application in fundamental scientific studies. Currently, the high amount of noise on the measurement signal limits the sensitivity of the system and therefore its application in, e.g., CTC detection. However, the achievable LODs for small molecule, cell, pathogen, and protein detection indicate that HTM can compete with many classical biosensing readout principles including non-Faradaic impedance spectroscopy. Given the fact that the technique has only been introduced 4 years ago, this is a huge success.

Future research opportunities are focused on exploring receptor–target binding mechanisms, thermal transport effects, and improving the sensitivity of the measurement technique. To this extent, a first improvement was achieved by introducing TWTA. For comparison reasons, HTM can be considered as the thermal equivalent of a direct current electrochemical readout principle, whereas TWTA could be compared to an alternating current method, allowing for faster response times and an improved sensitivity. On the other hand, HTM offers the benefit of straightforward data processing and interpretation. Both techniques are advantageous over other readout methods as they require minimal instrumentation, can be combined with electrical insulating chip material (e.g., sapphire), and are performant in nonconducting liquids such as ethanol. Finally, both HTM and TWTA have been combined with classical readout techniques such as impedance spectroscopy or fluorescence spectroscopy to provide additional information about the analyte under study.

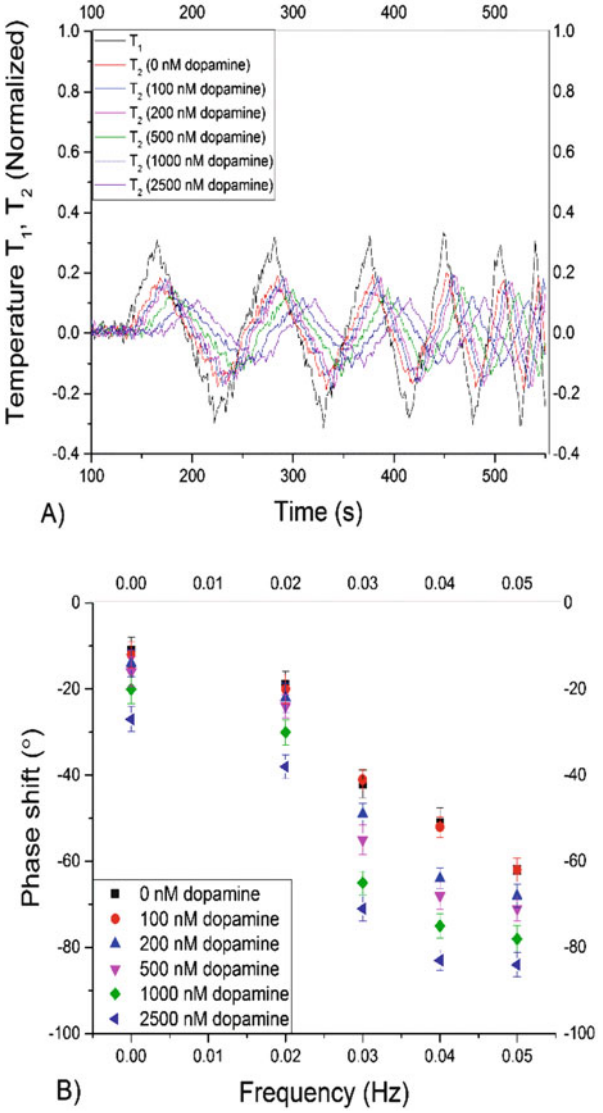

Fig. 17 (**a**) Time-dependent TWTA analysis of an MIP-SPE exposed to banana juice spiked with increasing concentrations of dopamine. (**b**) Frequency-dependent phase shift analysis. A concentration-dependent phase shift is visible. Adapted, with permission, from Peeters et al. [40]. Copyright 2016 Multidisciplinary Digital Publishing Institute

References

1. Ansevin AT, Vizard DL, Brown BW et al (1976) High-resolution thermal denaturation of DNA. Theoretical and practical considerations for the resolution of thermal subtransitions. Biopolymers 15:153–174
2. Saiki R, Scharf S, Faloona F et al (1985) Enzymatic amplification of beta-globin genomic sequences and restriction site analysis for diagnosis of sickle cell anemia. Science 230:1350–1354

3. Spink C, Wads SI (1976) Calorimetry as an analytical tool in biochemistry and biology. Methods Biochem Anal 23:1–159
4. Lammers F, Scheper T (1999) Thermal biosensors in biotechnology. In: Scheper T (ed) Advances in biochemical engineering/biotechnology, vol 64. Springer-Verlag, Berlin Heidelberg, pp 36–64
5. Bowers LD, Carr PW (1976) Immobilized-enzyme flow-enthalpimetric analyzer: application to glucose determination by direct phosphorylation catalyzed by hexokinase. Clin Chem 22:1427–1433
6. Danielsson B, Gadd K, Mattiasson B et al (1976) Determination of urea with an enzyme thermistor using immobilized urease. Anal Lett 9:987–1001
7. Danielsson B, Mosbach K (1988) Enzyme thermistors. Methods Enzymol 137:181
8. Danielsson B, Bülow L, Lowe CR et al (1981) Evaluation of the enzyme thermistor as a specific detector for chromatographic procedures. Anal Biochem 117:84–93
9. Lammers F, Scheper T (1997) On-line monitoring of enzyme catalyzed biotransformations with biosensors. Enzyme Microb Technol 20:432–436
10. Satoh I, Danielsson B, Mosbach K (1981) Triglyceride determination with use of an enzyme thermistor. Anal Chim Acta 131:255–262
11. Xie B, Danielsson B, Norberg P et al (1992) Development of a thermal micro-biosensor fabricated on a silicon chip. Sens Actuators B Chem 6:127–130
12. Bhand SG, Soundararajan S, Surugiu-Wärnmark I et al (2010) Fructose-selective calorimetric biosensor in flow injection analysis. Anal Chim Acta 668:13–18
13. Bjarnason B, Johansson P, Johansson G (1998) A novel thermal biosensor: evaluation for determination of urea in serum. Anal Chim Acta 372:341–348
14. Bataillard P, Steffgen E, Haemmerli S et al (1993) An integrated silicon thermopile as biosensor for the thermal monitoring of glucose, urea and penicillin. Biosens Bioelectron 8:89–98
15. Xie B, Mecklenburg M, Danielsson B et al (1994) Microbiosensor based on an integrated thermopile. Anal Chim Acta 299:165–170
16. Urban G, Kamper H, Jachimowicz A et al (1991) The construction of microcalorimetric biosensors by use of high resolution thin-film thermistors. Biosens Bioelectron 6:275–280
17. Maskow T, Lerchner J, Peitzsch M et al (2006) Chip calorimetry for the monitoring of whole cell biotransformation. J Biotechnol 122:431–442
18. Vermeir S, Nicolaï BM, Verboven P et al (2007) Microplate differential calorimetric biosensor for ascorbic acid analysis in food and pharmaceuticals. Anal Chem 79:6119–6127
19. Xie B, Tang X, Wollenberger U et al (1997) Hybrid biosensor for simultaneous electrochemical and thermometric detection. Anal Lett 30:2141–2158
20. Lai SVH, Kao P, Tadigadapa S (2011) Thermal biosensors from micromachined bulk acoustic wave resonators. Procedia Engin 25:1381–1384
21. Brandes W, Maschke HE, Scheper T (1993) Specific flow injection sandwich binding assay for IgG using protein A and a fusion protein. Anal Chem 65:3368–3371
22. Mecklenburg M, Lindbladh C, Hongshan L et al (1993) Enzymatic amplification of a flow-injected thermometric enzyme-linked immunoassay for human insulin. Anal Biochem 212:388–393
23. Wang L, Sipe DM, Xu Y (2008) A MEMS thermal biosensor for metabolic monitoring applications. J Microelectromech Syst 17:318–327
24. Paul P, Hossain M, Kumar GS (2011) Calorimetric and thermal analysis studies on the binding of phenothiazinium dye thionine with DNA polynucleotides. J Chem Thermodyn 43:1036–1043
25. Lee D, Hwang KS, Kim S (2014) Rapid discrimination of DNA strands using an opto-calorimetric microcantilever sensor. Lab Chip 14:4659–4664
26. Lettau K, Waskinke A, Katterle M et al (2006) A bifunctional molecularly imprinted polymer (MIP): analysis of binding and catalysis by a thermistor. Angew Chem Int Ed Engl 45:6986–6990
27. Rajkumar R, Katterle M, Warsinke A et al (2008) Thermometric MIP sensor for fructosyl valine. Biosens Bioelectron 23:1195–1199
28. van Grinsven B, Vanden Bon N, Strauven H et al (2012) Heat-transfer resistance at solid-liquid interfaces: a tool for the detection of single-nucleotide polymorphisms in DNA. ACS Nano 6:2712–2721

29. van Grinsven B, Eersels K, Peeters M et al (2014) The heat-transfer method: a versatile low-cost, label-free, fast, and user-friendly readout platform for biosensor applications. ACS Appl Mater Interfaces 6:13309–13318
30. Fodde R, Losekoot M (1994) Mutation detection by denaturing gradient gel electrophoresis (DGGE). Hum Mutat 3:83–94
31. Bers K, van Grinsven B, Vandenryt T et al (2013) Implementing heat transfer resistivity as a key element in a nanocrystalline diamond based single nucleotide polymorphism detection array. Diam Relat Mater 38:45–51
32. Cornelis P, Vandenryt T, Wackers G et al (2014) Heat transfer resistance as a tool to quantify hybridization efficiency of DNA on a nanocrystalline diamond surface. Diam Relat Mater 48:32–36
33. Vanden Bon N, van Grinsven B, Murib MS et al (2014) Heat-transfer-based detection of SNPs in the PAH gene of PKU patients. Int J Nanomedicine 9:1629–1640
34. Murib MS, Yeap WS, Eurlings Y et al (2016) Heat-transfer based characterization of DNA on synthetic sapphire chips. Sens Actuators B Chem 230:260–271
35. Ye L, Haupt K (2004) Molecularly imprinted polymers as antibody and receptor mimics for assays, sensors and drug discovery. Anal Bioanal Chem 378:1887–1897
36. Peeters M, Csipai P, Geerets B et al (2013) Heat-transfer-based detection of L-nicotine, histamine, and serotonin using molecularly imprinted polymers as biomimetic receptors. Anal Bioanal Chem 405:6453–6460
37. Geerets B, Peeters M, van Grinsven B et al (2013) Optimizing the thermal read-out technique for MIP-based biomimetic sensors: towards nanomolar detection limits. Sensors (Basel) 13:9148–9159
38. Wackers G, Vandenryt T, Cornelis P et al (2014) Array formatting of the heat-transfer method (HTM) for the detection of small organic molecules by molecularly imprinted polymers. Sensors (Basel) 14:11016–11030
39. Metters JP, Kadara RO, Banks CE (2011) New directions in screen printed electroanalytical sensors: an over-view of recent developments. Analyst 136:1067–1076
40. Peeters M, van Grinsven B, Foster CW et al (2016) Introducing thermal wave transport analysis (TWTA): a thermal technique for dopamine detection by screen-printed electrodes functionalized with molecularly imprinted polymer (MIP) particles. Molecules 21:552
41. Eersels K, van Grinsven B, Ethirajan A et al (2013) Selective identification of macrophages and cancer cells based on thermal transport through surface-imprinted polymer layers. ACS Appl Mater Interfaces 5:7258–7267
42. Eersels K, Lieberzeit P, Wagner P (2016) A review on synthetic receptors for bioparticle detection created by surface-imprinting techniques – from principles to applications. ACS Sens 1:1171–1187
43. Nakano T, Kikugawa G, Ohara TA (2010) A molecular dynamics study on heat conduction characteristics in DPPC lipid bilayer. J Chem Phys 133:154705
44. Bers K, Eersels K, van Grinsven B et al (2014) Heat-transfer resistance measurement method (HTM)-based cell detection at trace levels using a progressive enrichment approach with highly selective cell-binding surface imprints. Langmuir 30:3631–3639
45. Eersels K, van Grinsven B, Khorshid M et al (2015) Heat-transfer-method-based cell culture quality assay through cell detection by surface imprinted polymers. Langmuir 31:2043–2050
46. Reid Y, Storts D, Riss T et al (2004) Authentic authentication of human cell lines by STR DNA profiling analysis. In: Gall-Edd N, Arkin M (eds) Assay guidance manual. Eli Lilly & Company and the National Center for Advancing Translational Sciences, Bethesda, pp 1–52
47. van Grinsven B, Eersels K, Akkermans O et al (2016) Label-free detection of Escherichia coli based on thermal transport through surface imprinted polymers. ACS Sens 1:1140–1147
48. Losada-Pérez P, Jiménez-Monroy KL, van Grinsven B et al (2014) Phase transitions in lipid vesicles detected by a complementary set of methods: heat-transfer measurements, adiabatic scanning calorimetry and dissipation-mode quartz crystal microbalance. Phys Status Solidi A 211:1377–1388

49. Privalov PL (1980) Scanning microcalorimeters for studying macromolecules. Pure Appl Chem 52:479–497
50. Zammit U, Marinelli M, Mercuri F et al (2010) Analysis of the order character of the R(II)-R(I) and the R(I)-R(V) rotator phase transitions in alkanes by photopyroelectric calorimetry. J Phys Chem B 114:8134–8139
51. Peeters M, van Grinsven B, Cleij TJ et al (2015) Label-free protein detection based on the heat-transfer method – a case study with the peanut allergen Ara h 1 and aptamer-based synthetic receptors. ACS Appl Mater Interfaces 7:10316–10323
52. Burks A, Shin D, Cockrell G et al (1997) Mapping and mutational analysis of the IgE-binding epitopes on Ara h 1, a legume vicilin protein and a major allergen in peanut hypersensitivity. Eur J Biochem 245:334–339
53. Tran DT, Knez K, Janssen KPF et al (2013) Selection of aptamers against Ara h 1 protein for FOSPR biosensing of peanut allergens in food matrices. Biosens Bioelectron 43:245–251
54. Das BK, Tlili C, Badhulika S et al (2011) Single-walled carbon nanotubes chemiresistor aptasensors for small molecules: picomolar level detection of adenosine triphosphate. Chem Commun (Camb) 47:3793–3795

Toward Ultrasensitive Surface Plasmon Resonance Sensors

Vitali Scherbahn, Shavkat Nizamov, and Vladimir M. Mirsky

Abstract Despite the history of application of surface plasmon resonance (SPR) for chemo- and biosensing being over 30 years long, the development of this technique is still in progress.

This review is focused on the technological aspects of further improvement of analytical performance of SPR transducers based on Kretschmann configuration. We describe basic measurement configurations, their improvements and optimizations, and their drawbacks and limitations. An importance of referencing in SPR sensors is highlighted. The referencing approaches are classified into the following domains: (1) macroscopic spatially separated referencing, (2) self-referencing based on micro-patterning, (3) in-place referencing, (4) spatiotemporal referencing, and (5) electrochemically assisted referencing. The underlying principles of these approaches, examples of their implementation, and resulting improvements of sensor performance are described. Finally, an analysis of SPR data and an extraction of affinity properties are discussed.

Keywords Self-referencing, Surface plasmon resonance, Surface plasmon resonance microscopy

Contents

V. Scherbahn, S. Nizamov, and V. M. Mirsky (✉)
Department of Nanobiotechnology, Institute of Biotechnology, Brandenburg University of Technology Cottbus-Senftenberg, Senftenberg, Germany
e-mail: mirsky@b-tu.de

M. J. Schöning, A. Poghossian (eds.), *Label-Free Biosensing: Advanced Materials, Devices and Applications*, Springer Series on Chemical Sensors and Biosensors (2018) 16: 409–448
DOI 10.1007/5346_2017_21,
Published online: 9 March 2018

1 Introduction

Affinity sensors form one of the main classes of chemical sensors. We were not able to find an exact definition of this type of sensors neither in IUPAC nor in other chemical literature. However, based on general logic of this commonly used term, it can be defined as a type of chemical sensor whose output signal is proportional to the concentration of analyte bound to the receptor layer. The story of affinity sensors is almost a century long, and it was probably started with the first attempts to use optical techniques (e.g., interferometry [1] or electrochemical methods [2]) to study adsorption processes. The next important step in establishing the concept of affinity sensing was an implementation of quartz microbalance [3, 4] – in combination with intensive development of semiconductor electronics, a whole measurement system was realized as a compact device. Namely, based on the quartz microbalance (in some cases, the term quartz crystal microbalance is also used), the main application fields of affinity sensors, such as affinity biosensors (immunosensors) or gas sensors, were formulated. The next important step in the development of affinity sensors was the implementation of surface plasmon resonance (SPR). At the beginning of the 1980s, the Swedish group [5] suggested to apply this physical phenomenon for chemical sensing. After this pioneer work, the first commercial SPR sensor was developed by the Swedish company Pharmacia at the end of the 1980s; later, this part of the company was separated into Biacore and then purchased by GE Healthcare [6, 7]. Further development occurred extremely fast. Before the pioneer work, the resonance of surface plasmons was known as a sophisticated physical effect only. Just 10–15 years later, the abbreviation “SPR” became well known not only to physicists but also to chemists and biologists, while the method of SPR was established as a powerful instrument for real-time label-free investigation of interactions of (bio)molecules in biochemistry, pharmacology, supramolecular chemistry, and other fields of science and technology. Currently, over 20 different companies offer such devices.

During the last 20 years, a few thousands of papers on implementation of the SPR technology were published. In the same time, the method was further

developed and optimized. The current chapter is focused on the development of technological aspects of SPR. We skip numerous applications of this technique; the readers interested in these aspects are referred to recent books [8, 9] and numerous reviews [10–14]. Our consideration is limited by the so-called Kretschmann configuration [15], which is very convenient for routine analytical applications and belongs to the most used one.

2 Basic Measurement Configuration

The underlying physical principles of SPR are described in [8, 16, 17]. In the Kretschmann configuration, which is most frequently used in SPR instruments, the SPR effect is simply observed as a frustration of the total internal reflection of *p*-polarized light from a thin metallic layer deposited on the surface of a glass prism. This effect occurs due to the coupling of impinging light to the collective oscillations of electrons (surface plasmons) on the surface of the highly conducting metallic layer (e.g., silver or gold). Oscillations of surface plasmons generate an electromagnetic wave that penetrates to both sides of this surface. The intensity of this electromagnetic wave decays exponentially; thus, it is called an evanescent wave. At resonance conditions, the incident light is almost completely coupled to the surface plasmons, thus achieving a manifold increase in the intensity of the evanescent wave. Small changes in the refractive index within the penetration depth of the evanescent wave change resonance conditions. This provides a way to make extremely sensitive measurements of adsorption of any species onto the resonant surface: just a few angstrom change in the mean thickness of the adsorbed layer leads to a measurable signal.

In such instruments the *p*-polarized light beam is reflected from the thin metallic layer deposited on the surface of the glass prism (Fig. 1a). The reflectivity (ratio of reflected and incident light intensities) in this case depends on the coupling condition of incident light to surface plasmons:

$$k_x = \frac{2\pi}{\lambda}\sqrt{\frac{\varepsilon_1\varepsilon_2}{\varepsilon_1+\varepsilon_2}} = \frac{2\pi}{\lambda}\sqrt{\varepsilon_0}\sin\theta, \quad \text{or}: \quad \sqrt{\frac{\varepsilon_1\varepsilon_2}{\varepsilon_1+\varepsilon_2}} = \sqrt{\varepsilon_0}\sin\theta \tag{1}$$

where k_x is the wavenumber, λ is the free-space wavelength of incident light, θ is its incidence angle, and ε_0, ε_1, and ε_2 are complex dielectric permittivities of the glass, metal film, and aqueous solution, correspondingly.

The plot of the reflectivity of SPR biosensor versus incidence angle (and/or wavelength) shows a strongly pronounced dip. The exact position and shape of the reflectivity dip, caused by SPR, depend only on ε_2 if other parameters (ε_1, ε_0, and θ) are kept constant. Thus, the SPR curve provides information on the dielectric permittivity (correspondingly, on refractive index n using the $\varepsilon = n^2$ relation) near to the exposed metal surface (Fig. 1a). An example of such dependency of SPR curve is shown in Fig. 1. The SPR biosensor consists of a 50 nm gold layer deposited on the coupling glass prism exposed to the pure water. For a better

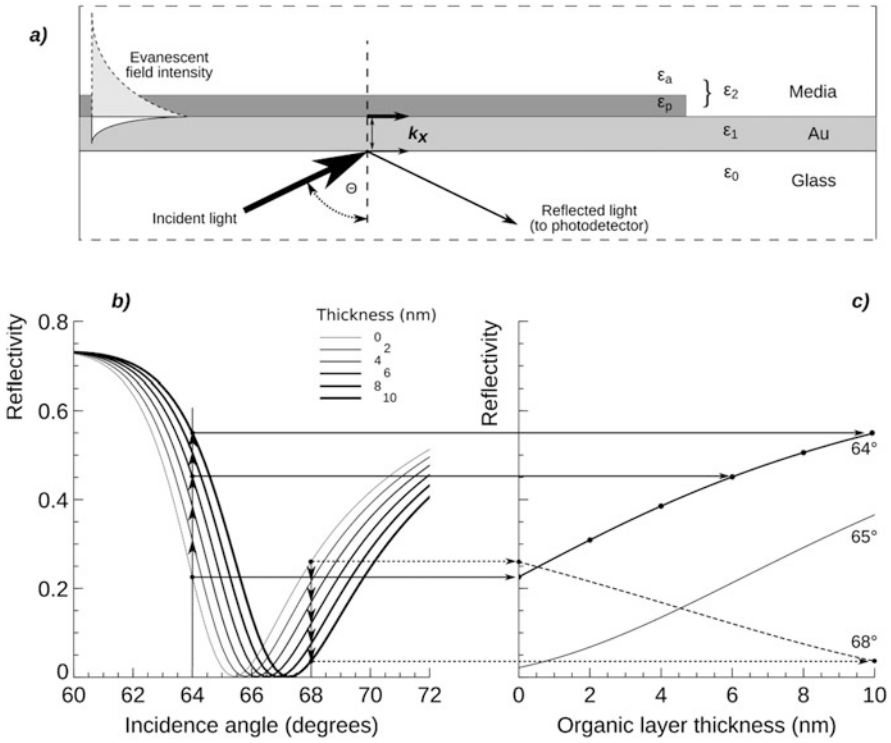

Fig. 1 Kretschmann configuration for SPR measurement (**a**), SPR curves calculated for different thickness of organic layer on the metallic surface (**b**) and corresponding reflectivity changes measured at fixed incidence angle (64, 65, or 68°) (**c**). Parameters for the calculation: metallic layer consists of 2 nm Cr and 50 nm Au (refractive indices: Cr, 3.105 + 3.327i; Au, 0.168 + 3.138i); glass, refractive index 1.615; wavelength, 650 nm; organic layer, refractive index 1.49; thickness of the organic layer, 0, 2, 4, 6, 8, or 10 nm. The organic layer is contacting with water at 22°C (refractive index 1.3317) (Reproduced from [18])

adhesion of gold to the glass surface, a 2 nm thick chromium adhesive layer is considered. This layer was also taken into account in the calculations of the SPR effect; however, its influence on this effect is minor.

In case of deposition of a thin organic layer on the gold surface, the refractive index near the gold surface is not homogenous. To account for inhomogeneous distribution of the refractive index near the gold surface ($\varepsilon_2 = f(z)$, where z is distance from the surface), the concept of effective refractive index n_{eff} is useful [19]:

$$n_{\text{eff}} = \frac{2}{z_2} \int n_2(z) \times \exp(-2z/z_2) dz \tag{2}$$

where $n_2(z)$ is the distribution of refractive index in aqueous media defined by the refractive index of adsorbed layer (n_p) and bulk aqueous solution (n_a) and z_2 is the penetration depth of the evanescent wave into the aqueous media.

In Fig. 1b, SPR curves were calculated for an organic layer with refractive index 1.49, which is close to that of proteins [20–22]. The deposition of a thin organic layer on the gold surface increases the effective refractive index and the whole SPR curve shifts to the right. This shift characterizes the thickness and the refractive index of the organic layer. This is the main idea of SPR application in chemo- and biosensors: the high sensitivity of the resonance shift to minor changes of refractive index near the resonant layer (within the substantial penetration of the evanescent wave) allows one to use it as a highly sensitive refractometric transducer to detect binding of analyte to the sensor surface (Fig. 2) as a change of the effective refractive index Δn_{eff}.

It follows from Eq. (1) that at constant optical properties (refractive index) of participating media, the SPR effect is determined by the incidence angle of impinging light. However, most materials have a dispersion of refractive index whose value is dependent on the wavelength ($n = n(\lambda)$). Thus, the SPR effect is dependent on the wavelength of the impinging light as well. Correspondingly, there are three prime approaches to realize a sensor based on SPR:

1. Fixing the wavelength of incident light and measuring the angular dependence of SPR reflectivity (the full SPR curve or just the angle of SPR dip, also known as an angular interrogation)
2. Fixing the incidence angle and measuring the wavelength dependence (SPR spectra, wavelength interrogation)
3. Fixing both the incidence angle and wavelength, measuring the intensity (or phase) of the reflected light

The first approach is based on the fixation of the wavelength and on the measurement of the position of the SPR minimum (SPR angle) by variation of the incidence angle. This requires measurements at some angle range around the resonance angle. Namely, this approach was realized in the first commercial SPR device from Biacore and later in the SPR micromodule Spreeta developed by Texas Instruments. To exclude the necessity to use moveable parts, the angle dependence

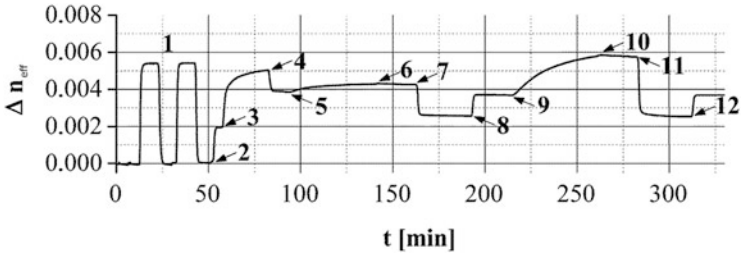

Fig. 2 Typical SPR sensogram denoting the change of the effective refractive index (Δn_{eff}): (1) sensor calibration by subsequent injections of water and 600 mM NaCl in water. Next steps: (2) running buffer, (3) covalent coupling of human serum albumin (HSA), (4) running buffer, (5) monoclonal anti-HSA antibody, (6) running buffer, (7) elution buffer, (8) running buffer, (9) polyclonal anti-HSA, (10) running buffer, (11) elution buffer, (12) running buffer (Reproduced from [23])

was measured for a divergent (or convergent) light beam using a linear array of photodiodes (the principle is described at www.biacore.com or in [24]). Using a rotating prism (it was realized in the device of Biosuplar) leads to lower sensitivity but allows one to extend the angle range. From the angle dependence of reflectivity, the resonance angle is determined as the angle of minimal reflectivity. The angle shift due to the adsorption characterizes the thickness of the adsorbed layer (Fig. 1b).

In the second approach (wavelength interrogation), the dispersion of the dielectric permittivities leading to the wavelength dependence of SPR is exploited. The main contribution into this dependence is provided by the dispersion of metals, which can be described by the Drude model. By measuring the wavelength dependence of the reflected light at fixed incidence angle, the SPR effect can be measured as a dip in the reflection spectra. The position of this dip (its wavelength) characterizes the adsorption.

Either approach is practically effective for measuring a single or few SPR signals. For the high-throughput application of SPR sensors, however, simultaneous measuring of many SPR signals is essential. An efficient way of implementing this is by imaging of the SPR sensor surface. Since implementation of angular or wavelength interrogation for SPR imaging is difficult, in this case, the third approach is mainly used. In the third approach, both wavelength and angle of the incident light are fixed, and the intensity (in more advanced instruments – the phase) of the reflected light is measured. Such a case is shown in Fig. 1c where the light with a wavelength of 650 nm is incident at an angle of 64°, and due to an increase in the thickness of the organic layer, the SPR curve shifts to the right resulting in an increase in the reflected light intensity. If the incidence angle is larger than the resonance angle (Fig. 1c, 68° curve), the sensor response becomes negative: an increase in the thickness of the organic layer results in a decrease in the reflected light intensity. All three approaches to measure SPR are well presented in scientific literature [8, 9, 13]. The features of the approach based on the variation of angle or on simultaneous measurements at different angles were analyzed in [5, 25]. The measurements based on the variation of wavelength at fixed incidence angle were discussed in [26–28]. This approach provides a high sensitivity at higher wavelengths, when the resonance is sharper; therefore it is often used in the near-infrared range [29, 30]. The approach based on the measurement of light intensity provides the simplest realization: such a device does need neither a spectrometer nor precise mechanical parts. At the same time, focusing of the image of the SPR sensor area on the image sensor (camera) enables an important extension of SPR technology – SPR imaging (SPRi) or SPR microscopy (SPRM) [31] (Fig. 3). The difference between these terms is only the magnification and lateral resolution. SPRi is mainly applied for characterization of homogenous films where a high magnification and/or resolution is not required [32]. The simultaneous real-time imaging of the entire sensor surface in SPRM/SPRi has a lot of advantages, e.g., it provides a development of high-throughput, multiplexed, or self-referencing sensors [32–34], while their low lateral optical resolution is outweighed by extremely high sensitivity in transversal direction. Due to these features, SPRi is now widely

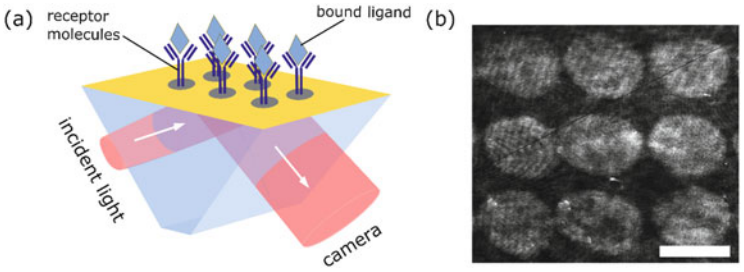

Fig. 3 (**a**) Schematic of a sensor array in a SPR-imaging setup. (**b**) Integral SPR image of a 3 × 3 sensor array: bright spots denote the interaction of ligands with receptors bound to the surface. Scale bar is 200 μm

used in surface science and in bioanalytical chemistry, particularly in chemo- and biosensing. The immobilization of capturing entities or ligands is usually carried out off-line by spotting of the selective ligands in a microarray format [35], as can be seen in Fig. 3. The binding of analytes leads to a change of the spot intensity that correlates with the amount of bound analyte. Examples of such applications are described in [36].

3 Main Factors Limiting the Performance of SPR-Based Sensors

As shown by Eqs. (1) and (2), SPR sensors are based on the transducing of effective refractive index (n_{eff}) of adjacent media into the optical response. Therefore, a SPR sensor can be used for measuring both physical and chemical effects that influence the refractive index within the penetration of the evanescent wave. This fact also explains the versatility and the wide application field of SPR sensors, as well as the fact that SPR sensors are inherently non-specific to the measured process. Therefore, the development of affinity chemo- and biosensors, where the sensor surface is specifically modified to detect an analyte, only partially solves the problem of the signal specificity. As the evanescent field penetrates into the background much beyond the receptor–analyte layer, the detected signal may also include changes in refractive index due to fluctuations, e.g., by temperature, composition of the background solution, inhomogeneous distribution of the analyte concentration in the background solution, or unspecific adsorption of other compounds. In addition, the measurement setup may also have mechanical drifts (influencing, e.g., the actual incidence angle), temperature drifts (causing, e.g., the change of refractive index of substrate and plasmonic layer on it), wavelength and/or polarization fluctuation of the light source, noise of the detector itself, etc. Therefore, the resulting SPR signal contains contribution from both useful signal (e.g., due to specific adsorption of analyte) and undesired noise. Correspondingly, the

applicability of SPR sensor for a particular case is determined by the value of the signal-to-noise ratio (SNR). Therefore, the improvement of SPR sensors can be roughly divided into two directions: (1) increasing of the useful signal or SNR and (2) separation of the contributions of the surface layer (the layer of receptor and adsorbed analyte) and that of the bulk effect (effect of the background solution).

The first goal is mainly achieved by optimization of the receptor layer, metallic resonant layer, and instrumentation, as well as by development of new measurement configurations. The second goal is achieved by introduction of internal referencing into SPR sensing. Both aspects will be discussed in the next sections.

4 Increase of the Signal Magnitude and Signal-to-Noise Ratio

4.1 Optimization of the Receptor Layer

First reports on application of SPR for chemical sensing and biosensing [5, 37] were performed using a silver resonant layer to investigate just physical adsorption. However, the further development of this technique was highly favored by the discovery of an extremely strong gold–thiol bond [38], which has resulted into intensive development of technology of self-assembled monolayers [39–42]. The interaction of thiolates with such metals, like gold or silver (as well as nickel, copper, mercury, and few others), leads to the formation of a bond with an energy of ~50 kJ/mol [39, 42]. This value is essentially higher than the typical energy of a hydrogen bond but is still few times lower than the typical energy of a covalent bond (~400 kJ/mol). The formation of self-assembled monolayers (SAM) by thiolated compounds on metallic surfaces has provided a solution for the long-term problem of biomolecule immobilization on metallic surfaces. The technology is well compatible with industrial needs. An expelling of non-thiolated compounds presented at much higher concentrations [43] decreases the requirements to surface purity. Therefore, since the middle of the 1990s, the typical approach of immobilization of biomolecules on gold surface (or silver; other metals are used very seldom) has been based on the following steps: (1) deposition of a SAM of ω-functionalized (typically – carboxy-functionalized (–COOH)) alkylthiol and (2) chemical conjugation of biomolecules to the functionalized groups of the SAM.

Numerous literature data demonstrate the possibility to use almost any type of thiolated molecules for the formation of SAM [39, 44–49]. However, from the thermodynamic point of view, a monomolecular layer (even with a high but finite binding energy to the surface) cannot be in equilibrium with a liquid containing a zero concentration of such molecules – it would lead to an infinitely high gradient of chemical potentials between the deposited layer and the volume phase. Therefore, one can expect only a strong suppression of kinetics of spontaneous desorption. This apparent stability is expected to increase with increasing of the energy of

these molecules in the liquid phase. The spontaneous desorption can be simply measured using monitoring of the electrode capacitance [40] or radioactive approaches [50]. For –COOH alkylthiols, the desorption rate becomes impossible to be measured by capacitive monitoring during 1,000 min incubation if the length of the hydrophobic chain of these molecules reaches 15 methylene groups. Assuming an about 25 times ratio between electric capacities of coated and uncoated electrode and a ~0.5% sensitivity of the measurement, one obtains a desorption rate below 1 molecule from 10^6 molecules per second. The stability can be also improved by the cross-linkage of thiol molecules by immobilized proteins [40]. Another approach to improve the stability of the gold–thiol bond is based on the application of thiol compounds with two [51] or more [52, 53] thiol groups; in this case, the water solubility of the compound is essentially less important and even well-soluble thiolates form very stable monolayers.

Chemical conjugation of receptor molecules to the functional group of formerly deposited SAM can be performed by different techniques [47, 54–56]. One of the mostly used techniques providing a well-reproducible and highly effective immobilization is to form a peptide bond between the –COOH group of the SAM and the primary $–NH_2$ group of the biomolecule. This approach includes an activation of the –COOH group by water-soluble 1-ethyl-3-(3-dimethylaminopropyl)carbodiimide (EDC) [57–60] followed by the reaction with the $–NH_2$ group. EDC is sometimes used in a mixture with an additional activating reagent, *N*-hydroxysuccinimide (NHS) [59, 61], which catalytically affects the reaction. To the immobilization approaches established during the last two decades also belong the "click" chemistry [62, 63] and the oriented immobilization of antibodies through their preliminary oxidized sugar group [64]. However, due to a rather complicate chemistry and expensive reagents, the application of these techniques is still relatively limited.

The development of technologies of SAM-based immobilization of biomolecules, which occurred in the same time as the introduction of SPR technology, was an extremely important promoting factor for the fast development and expansion of this type of affinity sensing. On the other hand, the progress in surface chemistry provided a possibility to make a precise design of the sensor surface and to realize conditions for maximal efficiency of SPR measurements. It was performed by introduction of three-dimensional receptor layers.

The typical size of protein molecules is 3–10 nm, but the penetration depth of the evanescent wave into aqueous phase is ~150 nm for 600 nm wavelength of the incident light increasing slightly superlinear till a penetration depth of ~ 750 nm for 1,100 nm wavelength of the incident light [65]. Therefore, in measurements of monomolecular protein layers at 650 nm, their contribution into the effective refractive index is only a few percent. Correspondingly, the SPR signal is dominated by the refractive index of the media, and the effect of protein layers is relatively lower. This was a motivation to immobilize receptors into three-dimensional matrix of hydrogel with a thickness of about 100 nm [6, 24, 66]. However, due to the necessity to provide a diffusion of the analyte through this hydrogel, it should be very porous. Moreover, the randomly immobilized receptor molecules are at some distance from the SPR sensor surface, thus decreasing their impact on

the effective refractive index. However, already at the concentration of receptors equivalent to 1.5 monolayers, the overall SPR signal is larger than for the dense monolayer directly on the sensor surface [6]. Therefore, the implementation of this approach allows one to increase the SPR effect for several times due to the binding of analyte with the immobilized receptor [6].

4.2 Optimization of the Resonant Layer

Two metals are mainly used in resonant layers for chemical sensors based on SPR – gold and silver. Only recently, aluminum also gained attention due to its plasmonic properties in the blue range [67]. Gold is chemically much more stable than silver. On the other side, silver provides lower absorption losses in the visible and near-infrared optical ranges; hence, it possesses a narrower resonance curve providing a higher SNR of SPR-based chemical sensors. To combine the advantages of both metals, a new structure of resonant metallic film based on bimetallic silver/gold (Ag/Au) layers was suggested (Fig. 4): a layer consisting mainly of silver but with a thin protective gold layer on the surface. An implementation of this idea for Ag/Au bimetallic layers with the ratio of thicknesses of 3:1 resulted in about 40% improvement of the SNR (Fig. 4a) [68]. This result was reproduced in [69]. It was also observed that thinner silver layers possess a high surface roughness limiting the sensor performance. The stability of the surface layer was so high that the authors have applied this sensor for electrochemical measurements; surprisingly, such sensors with immobilized receptors demonstrated a much higher improvement of SNR of up to 2.7. Later, bimetallic Au/Ag resonant layers were applied for sensitivity improvements in the experiments by the Biacore 3,000 device [70]. The chips were stable during six cycles of measurements and regeneration.

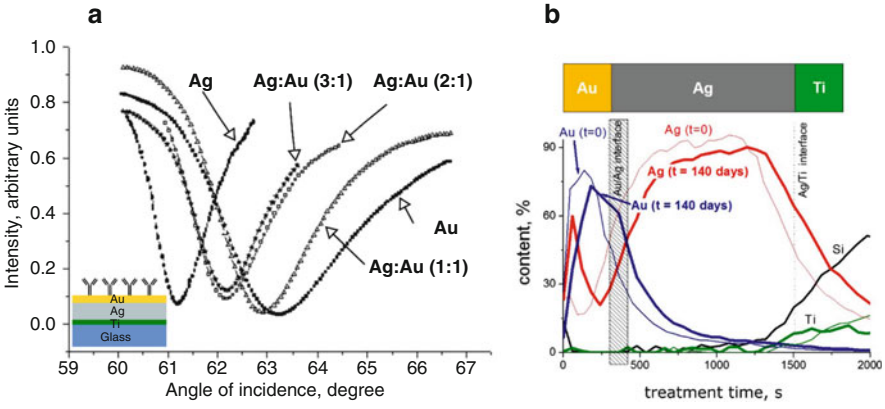

Fig. 4 Bimetallic silver/gold (Ag/Au) resonant layers provide a more sharp surface plasmon resonance than gold solely (**a**) and are stable for at least 140 days at room temperature (**b**)

The sensitivity of SPR sensors based on bimetallic layers of gold with silver, aluminum, and copper was analyzed in [71]. It was shown that bimetallic Au/Ag resonant layers also increase the sensitivity of another type of SPR – long-range SPR [72]. Long-range SPR is observed when a thin layer with low refractive index is deposited between glass prism and metallic resonant layer [73, 74]. This leads to a large increase of the penetration depth of evanescent wave and to a higher amplification of the magnitude of this wave. In this case, a substitution of the gold layer, separated from the glass prism by a 500–650 nm thick layer of magnesium fluoride, by a silver/gold bilayer resulted in a more sharp resonance [72].

The gold layer deposited on the surface of silver layer not only protects the silver layer against oxidative damage but also participates in the formation of resonant media for surface plasmons. However, it is not necessary, and instead of gold, other chemically inert materials can be used. An interesting result was obtained in [75]: a deposition of 15–25 nm of titanium dioxide (TiO_2) on the surface of a silver resonant layer not only protects silver against oxidation but also increases the sensor sensitivity to changes of the refractive index for over ten times.

Discussions about Au/Ag bimetallic layers often lead to criticism because of an expected very limited temporal stability: a mutual diffusion of metallic atoms can lead to the formation of mixed metallic layer with poor chemical stability. However, an investigation of metal distribution performed by layer-by-layer laser ablation after 140 days storage at room temperature (the data were generously provided by Dr. A. Zybin) demonstrated that despite the measurable diffusion of silver atoms to the gold surface, the layered structure of the sample was still preserved (Fig. 4b).

There is a distinctly defined optimal thickness of the gold layer for defined refractive index of glass, resonant metal and dielectric phase near to the gold surface (e.g., water). Any deviation from the optimal geometry of layers leads to the less pronounced resonance. It was shown that even so small change of the root-mean-square (RMS) roughness as its increase from 1.31 to 1.40 nm results in a decrease in sensor performance [76]. On the other hand, a formation of structures of the size comparable with the wavelength affects (like in nanostructured SPR sensors) the geometry of the evanescent wave. Considering a formation of these structures as an increase of roughness, one can expect less pronounced resonance peaks. In the same time, the change of the layer geometry due to formation of surface structures leads to the gradual change of the evanescent field from planar to spherical geometry resulting in a decrease of the penetration depth. Correspondingly, the influence of the adsorbed layer is amplified; the influence of the bulk phase on the SPR signal is attenuated. Such effect of SNR improvement was observed in [77, 78]. In contrary, in [79] only about 20% increase of sensitivity was observed. The increase of sensitivity for some types of columnar resonant films was studied experimentally and theoretically in [80, 81]. Notably, a raise of the microscopic area due to formation of different micro- and nanostructures increases possible number of immobilized receptor molecules.

A formation of nano- and microstructured resonant layers in a perspective may be a way for improvement of SPR sensors. However, it is a step into the direction of chemosensors based on localized SPR [82, 83] or terahertz metamaterials [84]; such sensing principles are out of scope of this chapter.

4.3 Optimization of the Incidence Angle

In the approach with the fixed wavelength and incidence angle, the strongest SPR response (caused by a shift of the resonance curve) is observed when the incidence angle corresponds to the steepest part of the SPR curve. At such condition, the sensitivity (defined as $s = dR/dn$, where R is the reflectivity and n is the refractive index) exhibits its maximal value. Usually, SPR measurements are performed at this angle [85, 86]: it provides the best detection limit if the noise is independent on the reflectivity. This may be the case if the noise level is determined by digitalization of the photodetector current. However, in the better-designed devices, the noise is additionally determined by other factors, which lead to its dependence on the incidence angle. In particular, this is the case when a shot noise or fluctuations of the laser intensity are the main noise sources. Therefore, the noise dependence of the reflected intensity on the incidence angle should be taken into account for optimization of the detection limit. Such analysis was performed in [25]. The results of theoretical analysis demonstrate that for the case of shot noise, the value $\frac{dR/dn}{\sqrt{R}}$ should be optimized instead of dR/dn (Fig. 5). For detectors based on the charged coupled devices (CCD) at optimal light intensity or if the noise is limited by fluctuations of irradiation source, the value of $\frac{dR/dn}{R}$ should be optimized. These predictions were confirmed by experimental data [25].

Current fabrication technologies of gold-coated glasses for SPR applications cannot provide an exact thickness of resonant layer and its perfect smoothness. Therefore, even though SPR conditions are matched, the SPR reflectivity is not zero as it could be theoretically. In practice, some residual reflectivity is observed instead. Therefore, an enhancement of the SNR by optimization of the incidence angle requires measurements of the relative sensitivity versus the incidence angle for each gold-coated glass substrate. This is time-consuming and can hardly be

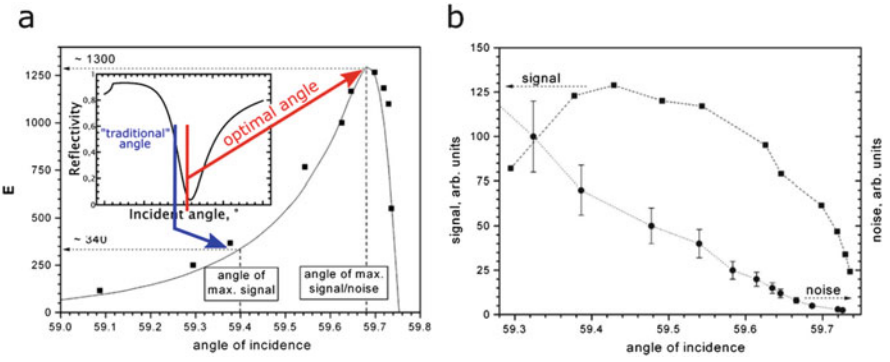

Fig. 5 (**a**) Relative SPR sensitivity E in dependence on the reflection angle. Inset: resonance curve showing the measurement at "traditional" angle of incidence and in the optimized case. (**b**) SPR signal (squares) and corresponding noise (circles) measured in dependence on the angle of incidence (Reproduced from [25])

realized. However, taking into account that dR/dn is proportional to $dR/d\theta$, an optimization of angle (for the case of CCD noise or fluctuations of light intensity) can be obtained from the angle dependence of reflectivity as a maximum of the absolute value of $\frac{dR/d\theta}{R}$. In analogy, for the shot noise, the value $\frac{dR/d\theta}{\sqrt{R}}$ can be optimized as well. The measurements of the angle dependencies are provided by many commercial SPR devices. The analysis of this dependence calculated from experimental data (using Biosuplar-321 SPR spectrometer, $\lambda = 650$ nm, 50 nm Au on glass with $n = 1.6$) shows the value of the optimal angle to be ~0.2° before the resonance angle for negligible residual reflectivity and ~0.6° before the resonance angle for 9% residual reflectivity.

The application of this optimization resulted in an improvement of the SNR for ~2 times for CCD detection or for ~3.5 times for photodiode detection in comparison with the measurements at maximal sensitivity. However, the calibration curve (SPR response dR versus dn change of effective refractive index) at the angle of enhanced detection power deviates more from linear dependency compared to such calibration curve at traditional incidence angle. For most of SPR applications, such deviation is tolerable and can be corrected by calibration. The developed approach was further applied for numerous applications including the detection of nanoparticles by wide-field SPR microscopy [87–91].

4.4 Instrumental Improvement of SPR Sensitivity

A number of techniques for improvement of SPR sensitivity are based on the development of new measurement technologies without any modification of the resonant or receptor layers. Some of them, which include a referencing relative to the bulk phase, form a large and special group of SPR techniques and will be discussed in the next section. A drastic improvement of SPR sensitivity can be achieved by measuring the phase shift of the reflected light [92–97]; however, this requires complicated, often environment-susceptible, optical setups. Along with that, without further complication of measurement principle, the high sensitivity leads to a small measurement range. For these reasons, in practical applications, the intensity-sensitive SPR sensors have found much wider adoption than phase-sensitive ones.

An improvement of sensitivity was reached by using a bi-cell photodetector [98]: a small shift in the position of SPR minimum angle is detected as the differential signal of this photodetector. A normalization of the differential signal to the sum of the photodiode signals allowed one to exclude an influence of ambient light.

Several methods based on modulation techniques were suggested. The method based on small modulation of the incidence angle by a piezo-electrical actuator was reported in [99]. At resonance conditions, the reflectance signal detected by a lock-in amplifier equals to zero. The resonance shifts are measured as a deviation

from zero or through a feedback signal, which adjusts the angle of incidence to match resonance conditions changed due to the sorption. Another modulation-based approach was realized by means of a tuneable acousto-optical filter [100].

Zybin et al. suggested a modulation based on using two lasers with different wavelengths [101]. This idea was implemented by using the wavelength modulation without moving instrumental components. Unlike spectroscopic scanning of the wavelength, in the double-wavelength approach, only two laser beams with different wavelengths irradiate in parallel to the same surface area [101]. Illumination conditions are chosen so that for given SPR conditions, the corresponding photodetector currents are equal (Fig. 6). However, the shift of SPR conditions will destroy this balance and result into an alternative current (AC) signal at the photodiode. Hence, the AC signal value was used to characterize the SPR shift and, consequently, the adsorption processes. Such referencing allows compensating not only the effect of ambient and/or scattered light but also of possible change in the resonance width. Later, this approach was extended for imaging [102]. A detection limit of $\Delta n \sim 2 \times 10^{-6}$ was achieved. However, this double-wavelength approach was realized exploiting lasers with very close wavelengths – 785 nm and 830 nm leading to similar penetration depths of their evanescent waves: ~340 nm and ~380 nm, correspondingly [65]. The small difference between the penetration depths did not allow one to apply this approach for referencing to separate bulk and volume effects; therefore, it was performed by traditional macroscopic spatial referencing (Sect. 5.1).

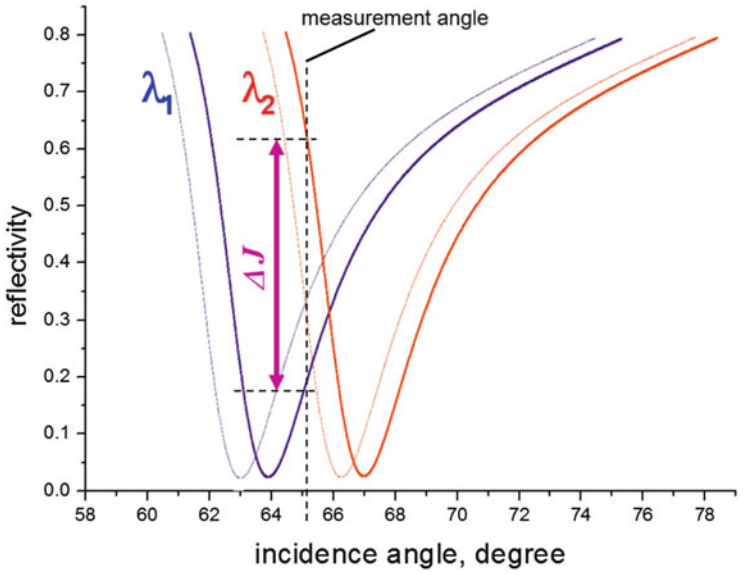

Fig. 6 Differential SPR measurement at two wavelengths. The measurement point corresponds to the negative and positive slopes of the shorter (λ_1) and longer (λ_2) wavelengths, correspondingly

5 Self-Referencing in SPR Measurements

As the SPR signal is sensitive to the change of refractive index within the entire evanescent field, changes of refractive index due to both specific molecular binding to the surface and bulk refractive index cannot be distinguished. To minimize such effects, a typical SPR measurement is performed as a differential one. Practical realization of such measurements can be very different and includes (1) macroscopic spatially separated referencing, (2) self-referencing based on micro-patterning, (3) in-place referencing, (4) spatiotemporal referencing, and (5) electrochemically assisted referencing.

5.1 Macroscopic Spatially Separated Referencing

This type of referencing is based on the measurement of a differential signal between a macroscopic sensing spot, coated by a selective receptor to the analyte, and a macroscopic referencing spot, coated by a compound of similar chemical nature but not possessing so strong affinity to the analyte. This type of referencing belongs to the mostly studied and is described in detail in SPR literature [8, 103, 104]. It was realized in different configurations [105, 106] by using completely independent sensing and referencing channels or by deposition of a thin additional layer on the half of the prism leading to the formation of two SPR dips at different angles or wavelengths [103, 107]. In such systems, a gap between two SPR dips can be measured to characterize the adsorption process mainly occurring on the sensing spot and neglecting other effects happening on both reference and sensing spots.

Due to simple implementation, an efficiency good enough for many practical applications and straightforward data analysis, the macroscopic spatially separated referencing is the mostly used approach. It is well compatible with SPR imaging (in fact, SPR imaging allows one to use this approach in most effective and unambiguous way).

However, the value of the uncompensated signal in systems with a macroscopic mean distance between sensing and referencing spots remains relatively high. If a SPR device is well designed, and the contribution of the instrumental noise (e.g., shot noise) is minimized, it is a typical case that the signal due to noise and drift is caused by micro-fluctuations of temperature between sensing and referencing spots. The temperature dependence of the refractive index of water is about 100 micro-refractive index units (μRIU) per 1K° [108]. Therefore, to achieve a measurement resolution of 0.1 μRIU with SNR $>$ 3, the temperature fluctuations between the sensing and referencing spots should be within 0.0003°C. This can be hardly achieved in usual laboratory conditions. The large gap between experimentally reached sensitivity and its theoretical limit was discussed in many publications [18, 34, 65, 109], and the temperature fluctuations were supposed to be one of the main reasons for this difference. In such case, no further improvement of optical or

electrical components of the measurement system can provide any essential improvement of the detection limit. Additionally, artifacts may be caused by inhomogeneities of other parameters, such as fluctuations of analyte concentration or pressure caused by micro-turbulences of analyte flow near the resonant surface.

5.2 *Self-Referencing Based on Micro-patterning*

The common feature of this approach is determined by numerous referencing and sensing spots distributed over the sensor surface (Fig. 7) instead of a single macroscopic referencing spot. The signals obtained on a large number of miniaturized referencing and sensing spots are subtracted from each other. Thus, a decrease of the effective values of temperature difference (as well as of difference of pressure, reagent concentrations, reagent flow rates, and other parameters) to the level of their differences between two closely positioned miniaturized sensing and referencing spots is achieved, yet the total surface area of these spots remains macroscopic. Therefore, noise and signal drifts caused by such local gradients are suppressed significantly, while the large total area of sensing and referencing spots enables measurements with low level of the shot noise. In case of the fixed total sensor area, a simple mathematical analysis [34] demonstrates the SNR to be inverse-proportional to the number of pairs of sensing and referencing spots. The use of several patterning procedures (μ-contact printing [110] or photolithography [111]) allows one to fabricate μm-sized surface patterns. The experimental test confirmed the expected linear dependence between the mean distance between the

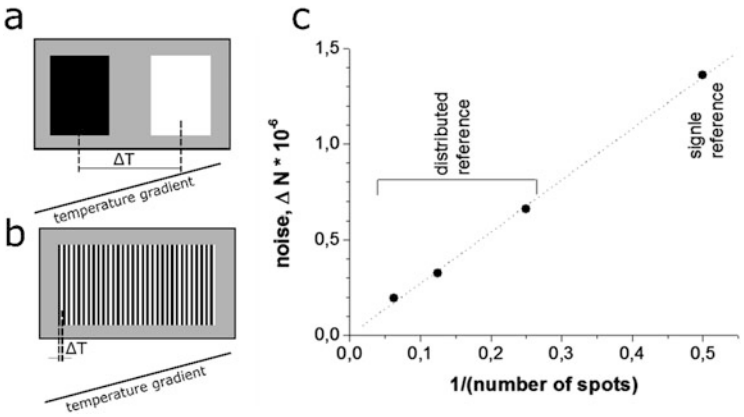

Fig. 7 Principle of distributed sensing and referencing spots and experimental validation: instead of single sensing (black) and referencing (white) spots (**a**), numerous miniaturized referencing spots placed between miniaturized sensing spots are used (**b**). Experimental confirmation of SNR to be inverse-proportional to the number of pairs with sensing and referencing spots (**c**) (Reproduced from [34])

sensing and referencing spots and the noise level. Using this technique, an over ten times suppression of noise was demonstrated. The level of the baseline noise of 0.3 μRIU was achieved without any temperature stabilization. A strong suppression of the influence of temperature fluctuations was demonstrated. An extrapolation of the dependence (Fig. 7) to the zero value corresponds to the noise limit for an infinite increase of the number of pairs of sensing and referencing spots. Therefore, one can expect that further increase of the number of sensing and referencing spots will lead to further essential decrease of the signal noise.

Similar results can be achieved by using the diffraction-based SPR, when the signal is read in the diffraction maximum of the grating formed by strips of sensing and referencing spots [112, 113]. In contrast to [34], the subtraction of the optical intensity from sensing and referencing spots is performed not by image analysis and subsequent processing, but purely optically, using light interference. An analyte binding leads to the formation of a dynamic biological grating, a process that could be followed by the change of the diffraction intensity.

Another approach for optical subtraction of SPR signals from sensing and referencing spots does not require any defined structure on the surface and can be realized using most commercial SPR devices [18]. When roughly a half of the area is used as the sensing area while its optical thickness is different from that of the referencing area, an integral measurement of the intensity of the reflected light over such a patterned surface near the summary resonance conditions exhibits self-referencing properties (Fig. 8). An over tenfold suppression of the effect caused by the variation of the bulk refractive index was observed (Fig. 9).

5.3 In-Place Self-Referencing

5.3.1 Dual-Wavelength SPR

Spatially allocated sensing and referencing spots enable a simple and efficient self-referencing in SPR sensors. However, the formation of spots with distinctly different surface properties requires additional efforts and sacrifices a substantial amount of surface area just for referencing. One possibility to develop self-referencing SPR sensors without using separate referencing channels is based on double-wavelength technique. Unlike using two close wavelengths with similar penetration depth of evanescent wave [101], the Penetration Difference Self-Referencing SPR (PDSR-SPR) approach uses two wavelengths (658 nm and 980 nm) with several times differing penetration depths. The rather high difference in the penetration depth of evanescent waves can be applied to separate contributions of surface layer and bulk solution into the measured values of refractive index [65]. The principle of PDSR-SPR is shown in Fig. 10, but practically it was also realized using only a single lock-in measurement channel. The suppression of the effect of the bulk refractive index was studied by addition of sodium chloride (NaCl) (Fig. 10d). While NaCl solutions of various concentrations showed significant change of the refractive

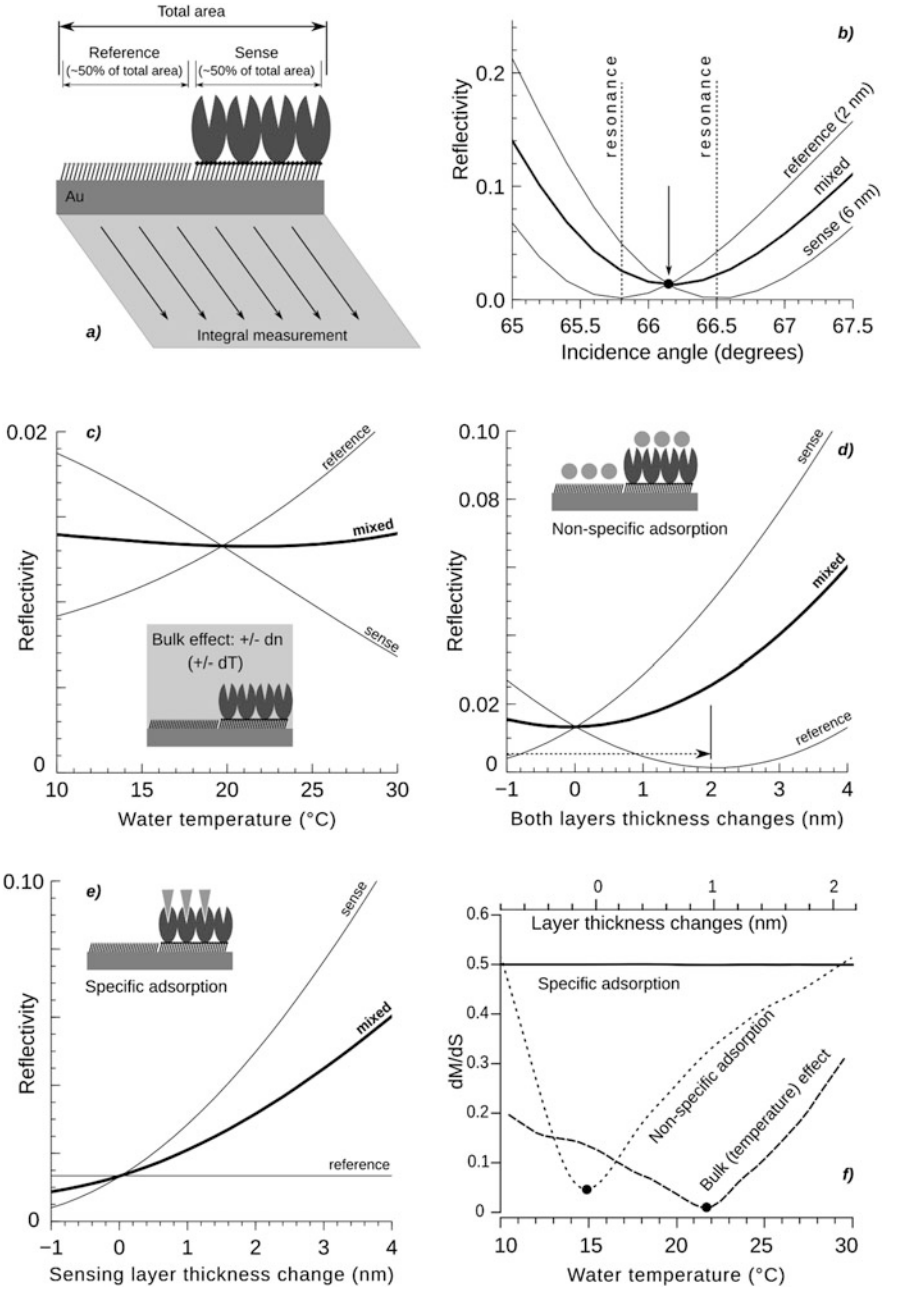

Fig. 8 Principle of internal referencing based on integral measurements of light intensity reflected by arbitrarily distributed sensing and referencing spots. Calculated SPR signals for the mixed surface with arbitrary pattern including 50% of sensing area and 50% of referencing area (**a**) are shown in the panel (**b**) for separated referencing and sensing areas as well as for their mixture.

index at each wavelength separately, the double-beam differentiated signal showed a suppression of this bulk change in the refractive index for ~35 times. In the same time, the signal due to albumin binding to immobilized antibodies was only slightly decreased (Fig. 10e). Therefore, the PDSR-SPR is sensitive only to surface processes, while conventional SPR is also sensitive to the changes of the refractive index in the bulk solution.

Beyond self-referencing purposes, an excitation of SPR at two wavelengths with largely differing penetration depths can be used to separate the determination of the thickness and refractive index of adsorbate layers [114] and for determination of changes in the structure of adsorbate layers [115].

5.3.2 Referencing by Using Simultaneous Excitation of Long- and Short-Range SPR

The penetration depth of surface plasmons in the case of conventional SPR is mainly determined by the wavelength of the incident light. Therefore, to excite two surface plasmon waves with differing penetration depth of evanescent wave, two light sources with largely differing wavelengths are used. However, this results inevitably into an additional complexity of the measurement system. Therefore, to excite two surface plasmon waves with largely different penetration depths, the application of two plasmon modes was suggested instead of two wavelengths [73, 74, 116]. In this approach, a simultaneous excitation of long- and short-range surface plasmons is performed. It requires an additional layer of low refractive index material (typically, Teflon was used) between the coupling glass substrate and the resonant layer. The evanescent field caused by long surface plasmon modes penetrates more deeply into the dielectric medium, whereas the penetration depth of the short-range plasmon mode is similar to that of the conventional SPR. As a result, the change of the refractive index, e.g., due to surface binding, influences the propagation constant of the short-range mode much stronger than that of the long-range mode. This is the key point allowing one measurements in the self-referencing regime. As these plasmons possess different propagation constants, two reflectivity minima are obtained which can be also used for self-referencing. Sensing experiments carried out with a classical avidin–streptavidin binding in addition to glycerol have shown a clear suppression of the bulk refractive index [74].

Fig. 8 (continued) Temperature variation leads to the signals at both sensing and referencing spots, but its influence is essentially compensated when detected integrally at the mixed area (**c**). SPR signal corresponding to non-specific adsorption is also suppressed manifold, (**d**) while the signal corresponding to specific adsorption is only twice attenuated (**e**). A quantitative efficiency of self-referencing is indicated in (**f**); dM/dS indicates the ratio of integral signal change in the mixed area to the signal change in the sensing area. Specific and non-specific adsorptions correspond to the upper *x*-axis; the bulk (temperature) effect corresponds to the lower *x*-axis (Reproduced from [18])

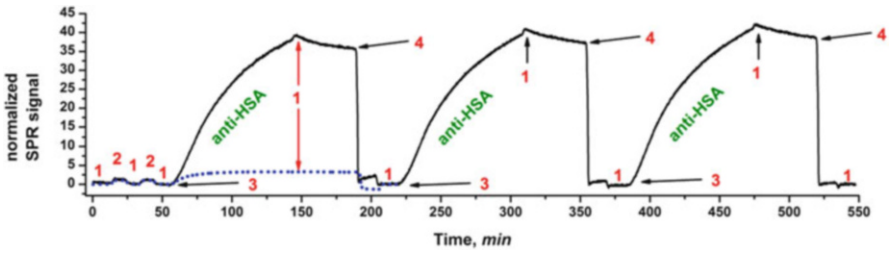

Fig. 9 Comparison of SPR effects by conventional measurements at homogeneous sensor surface (dotted line) and at the surface with 40% of referencing spots measured as the light intensity at SPR minima for the whole surface. Both curves were normalized to the response on addition of salt (calibration). Additions: 1, PBS; 2, PBS containing 100 mM NaCl additionally; 3, antibodies to HSA; 4, PBS (Reproduced from [18])

Therefore, in-place referencing using surface plasmon waves with differing penetration depths of evanescent waves is inherently well suited for distinguishing surface and bulk effects.

5.4 Spatiotemporal Referencing

Surface plasmon microscopy introduced by Rothenhausler and Knoll [31] has become a highly attractive high-throughput technology for bioanalytical purposes [33]. However, due to the low magnification and mediocre lateral resolution (partly due to the large propagation length of surface plasmons), it considers the adsorbates on the SPR sensor surface as homogenous films or islands [32]. For this reason, the approach is mainly known as SPR imaging (SPRi). Using a regular SPRi, an imaging of single binding molecules or nanoparticles is practically impossible: the image changes are too weak and averaged over the large surface. This drawback led to a gap in the research concerning the application of SPRi to detect and to visualize single nano-objects.

At the same time, the task of detection, quantification, and characterization of nanoparticles of different origin counts to actual challenges in such fields as analytical science, including food and environmental safety, bioanalytics, and medical diagnostics [117, 118]. There were many attempts to study adsorption of nanoparticles using conventional SPR (e.g., [23, 119]); however, they do not consider nanoparticles individually.

Only with the development of higher-magnification SPR microscopy (SPRM), this drawback was successfully overcome: it became possible to apply SPRM for detection, visualization, and characterization of single nano-objects down to 20 nm size. A visualization of optical signals from single biological and engineered nano-objects by means of SPRM technology in various implementations was reported in [87, 120, 121]. Despite distinct differences in the measurement layout of novel

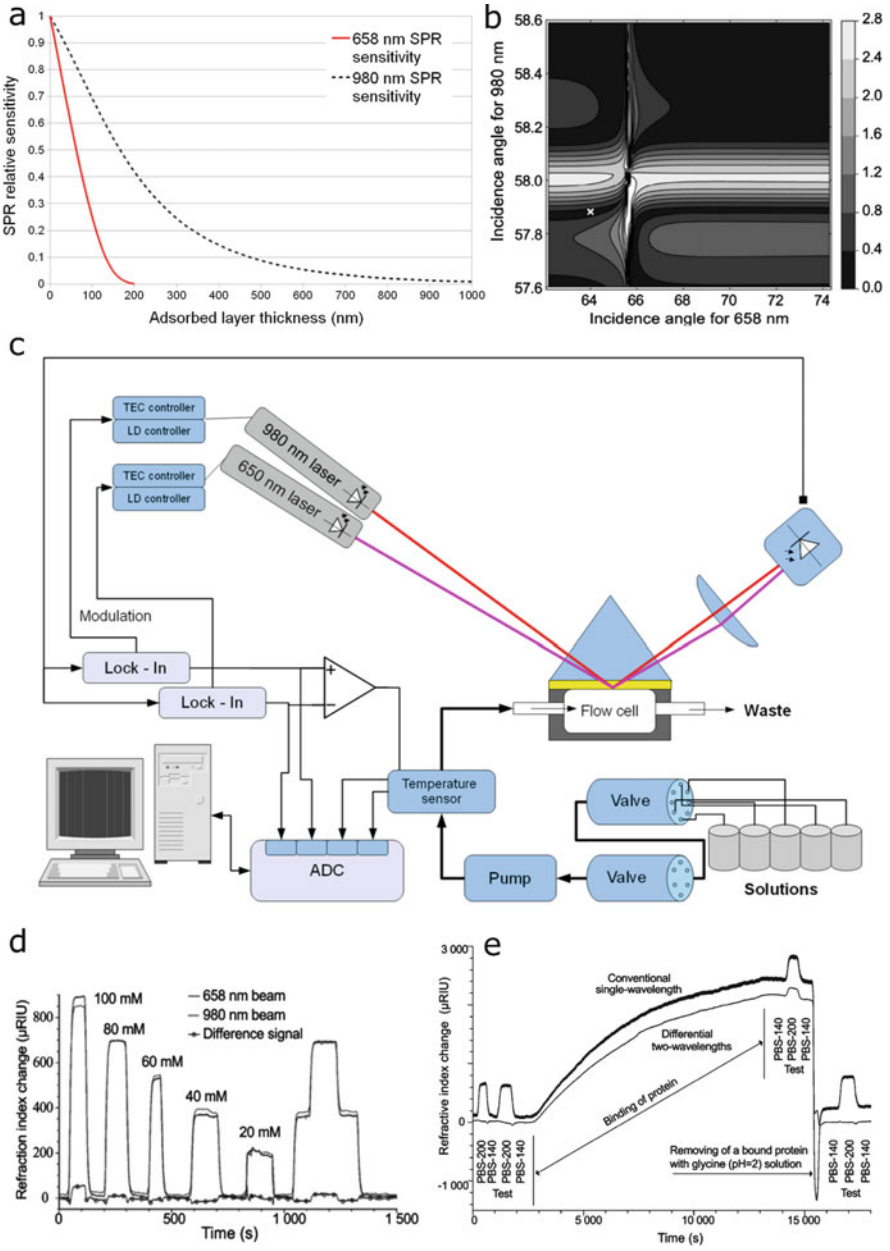

Fig. 10 Principle, implementation, and test of the Penetration Difference Self-Referencing SPR (PDSR-SPR). Comparison of contribution of layer thickness to sensitivity of SPR at 658 nm and 980 nm (**a**), optimization of measurement conditions by numerical simulation (**b**), simplified setup of the PDSR-SPR (**c**) and its test: suppression of the bulk refractive index changes, induced by addition of NaCl solutions (**d**) and detection of protein (albumin) binding using conventional single-wave SPR and PDSR-SPR (**e**) (Reproduced from [65])

SPRM setups [90, 91, 122–124], they share a common feature – the application of a spatiotemporal referencing for processing obtained images. In such referencing, two SPRM images, taken at different times, are compared to reveal the minute image changes occurred within this time. Therefore, despite the image of single nanoparticles being hardly recognized in raw SPRM image, its adsorption can be visualized as spatially and temporally localized image changes. Thus, the adsorption position of nanoparticle is referenced spatially to its local vicinity, and both areas are also self-referenced temporally.

Originally, an averaged SPRM image in the absence of adsorbing nanoparticles was considered for referencing: this averaged background image was subtracted from each subsequent SPRM image to obtain a differential image showing only the difference in the image intensity (static image referencing) [87]. However, since the plasmonic image of a single nanoparticle is much larger than its physical size, the nanoparticle images accumulate in the differential SPRM image and start overlapping already at low surface coverage. Besides, the SPRM image background changes slowly over the time due to some drifts in the measurement system. To overcome this issue, instead of static referencing, a dynamic referencing was introduced advantageously [90, 122, 125]. In dynamic referencing, two SPRM frames with a small temporal lag are compared (Fig. 11). To calculate the difference between two SPRM images, their ratio is considered; this allows one an additional internal referencing to the intensity of the incident light [90, 122].

Using a micro-patterned sensor surface, similar to those applied for spatial referencing, a selective adsorption of charged nanoparticles to the surface which was patterned with oppositely charged SAM (Fig. 12A) was achieved [91]. The direct detection and visualization of adsorption of single nanoparticles to the differently functionalized sensor surfaces (Fig. 12B) enable ultrasensitive and

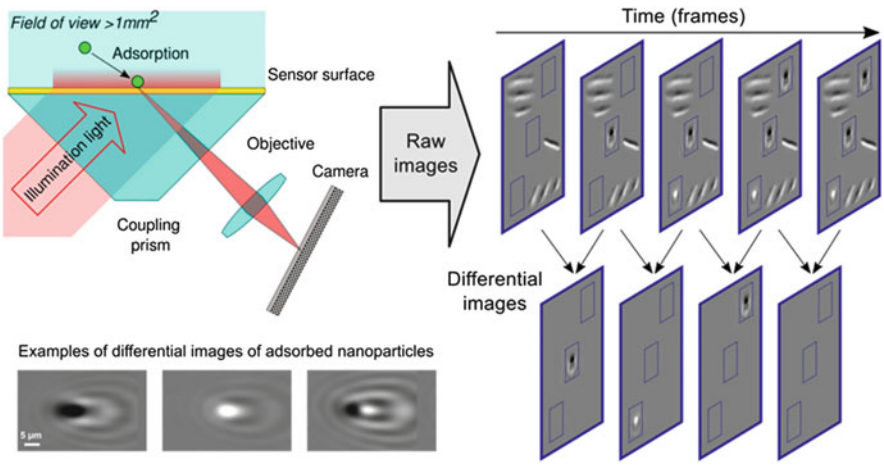

Fig. 11 Schematic of spatiotemporal referencing: detection of single adsorbing nanoparticles using SPR microscopy (Reproduced from [90])

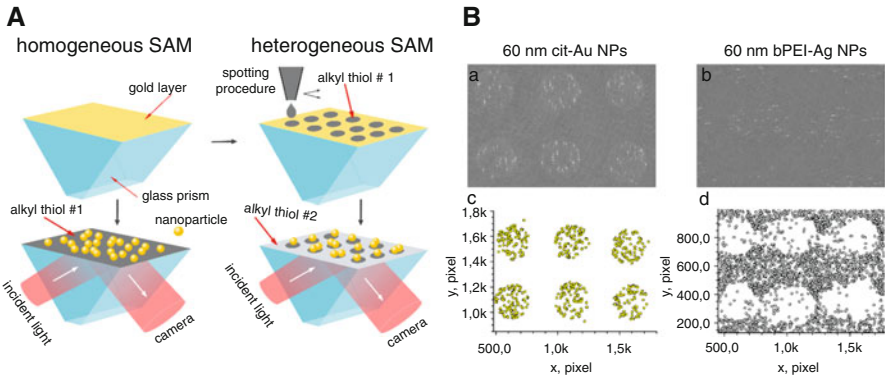

Fig. 12 Schematic of the coating procedure of a SPRM sensor surface (**A**). Homogeneous, non-structured SAM (**A**, left panel) and heterogeneous, structured SAM (**A**, right panel). Close-up visualization of selective adsorption of negatively charged citrate-stabilized gold nanoparticles (cit-Au NPs) (**B**, left panel) and positively charged branched polyethylenimine-coated silver nanoparticles (bPEI-Ag NPs) (**B**, right panel) on structured SAM by spots with C11-N-$(CH_3)_3^+$ Cl^- (120–130 µm spot diameter) and C10-COOH-coated area in-between. Differential SPRM images (a, b). Topologic visualization of single nanoparticles adsorbed within 90 s (c, d) as a close-up with ~0.3 mm^2 (initial visible area, ~1.3 mm^2) (Reproduced from [91])

unambiguous characterization of this type of interfacial reaction and bear an immense potential to develop ultrasensitive bioanalytical assays.

Since the adsorption of a single nanoparticle can be detected and visualized by spatiotemporal referencing in SPRM, the limit of detection is determined by the collision (adsorption) frequency of nanoparticles with sensor surface. Therefore, it depends predominantly on the measurement time and on the diffusion conditions of nanoparticles. Corresponding to Fick's diffusion law, the detection limit is as well dependent on the imaged sensor surface [90]. SPRM with a relatively large visible surface (1.3–1.5 mm^2, the largest described in the literature up to date) shows a detection limit better than 10^6 NPs/mL (~1.6 fM) or ~0.3 ppb with a measurement time of few minutes [89, 90]. This can be further improved by increasing the measurement time or the visible sensor area.

The short review of recent results shows that the spatiotemporal referencing being realized in SPRM extended the application area of SPR sensors into the quantitative analytics of suspensions of particles of subwavelength size. The detected SPRM images of adsorbing nanoparticles are dependent on their size and composition. Being able to suppress matrix effects, hence, it is suitable for complex media samples. The approach can be applied for detection and analysis of metallic, metal oxide, or plastic nanoparticles, protein nanoparticles and nanoparticle–drug conjugates developed for drug delivery, liposomes, exosomes, viruses, bacteria, and many other artificial and natural particles. The detailed review of this technique is presented in [90, 91, 123, 124], as well as in [126].

5.5 *Electrochemically Assisted Referencing*

5.5.1 Ionic Referencing

In most cases concerning SPRi or SPRM sensing, the sensor surface requires a functionalization to attach receptors to the metal layer. Receptor immobilization to the metallic sensor surface is often performed first by deposition of SAMs of thiolated compounds with functional groups followed by coupling with different receptors (antibodies, antigens, DNA, aptamers, etc.) [42]. The formation of an array-like patterned sensor surface can be performed at the level of SAM as well. However, the signal difference between spots coated by thiolates differing mainly by terminal functional group is usually so small that this difference cannot be reliably detected by SPRM. Thus, complications in preparation, monitoring, and quality control of the sensor array are expected. On the other side, a determination of the position of sensing and referencing spots is a prerequisite for most applications of sensor arrays and/or referencing techniques [34]. But the effects of small changes in the thicknesses of the adsorbate layer on the gold surface due to SAM deposition can be easily overwhelmed by the inhomogeneity of the glass substrate, gold layer, and illumination or by other factors that influence the resonance conditions.

An effective and reliable approach for visualization of spots with different surface properties was developed [127]. The approach is easily applicable in each SPR-imaging system. It is based on the fact that the distribution of ions near the surface is determined by their interaction with the surface (Fig. 13a). Applying electrolyte solutions with very different contribution of anions and cations into the total refractive index of solutions, the difference in surface properties over the whole sensor area can be visualized. As the difference of the optical length of two functionalized coatings is too small to be visualized, no structure in the raw image is recognizable (Fig. 13b). Since the sensor surface is patterned by different types of SAM, e.g., with $–NH_2$ and –COOH terminal groups, such surface areas possess opposite pH-dependent surface charges. This effect leads to different distribution of counterions in the diffuse layer. To reveal this difference and, thus, the position of the different areas, raw SPRM images gathered for all electrolyte solutions (including buffer) were mutually referenced to each other. For the referencing, the pixel-to-pixel ratio of images [128] was taken. The histograms of ratio images were calculated after contrast stretching and presented as a matrix (Fig. 13b).

The differences in physical adsorption of ions to differently functionalized surfaces can be exploited similarly. For this purpose, two arrays of spots were deposited – the first one with OH and the second with NH_2 terminal groups; the rest part of the surface was coated by –COOH-terminated SAM. To be distinguishable in topology, the –OH and $–NH_2$ spots were formed in lines with a pitch 250 and 300 μm, correspondingly; afterward, ionic solutions, e.g., sodium salicylate, were perfused. However, as can be seen in Fig. 13c, upper left, only –OH spots can be observed. To visualize both types of spots, consequent flushing by solutions containing different electrolytes was performed. The surface areas with $–NH_2$

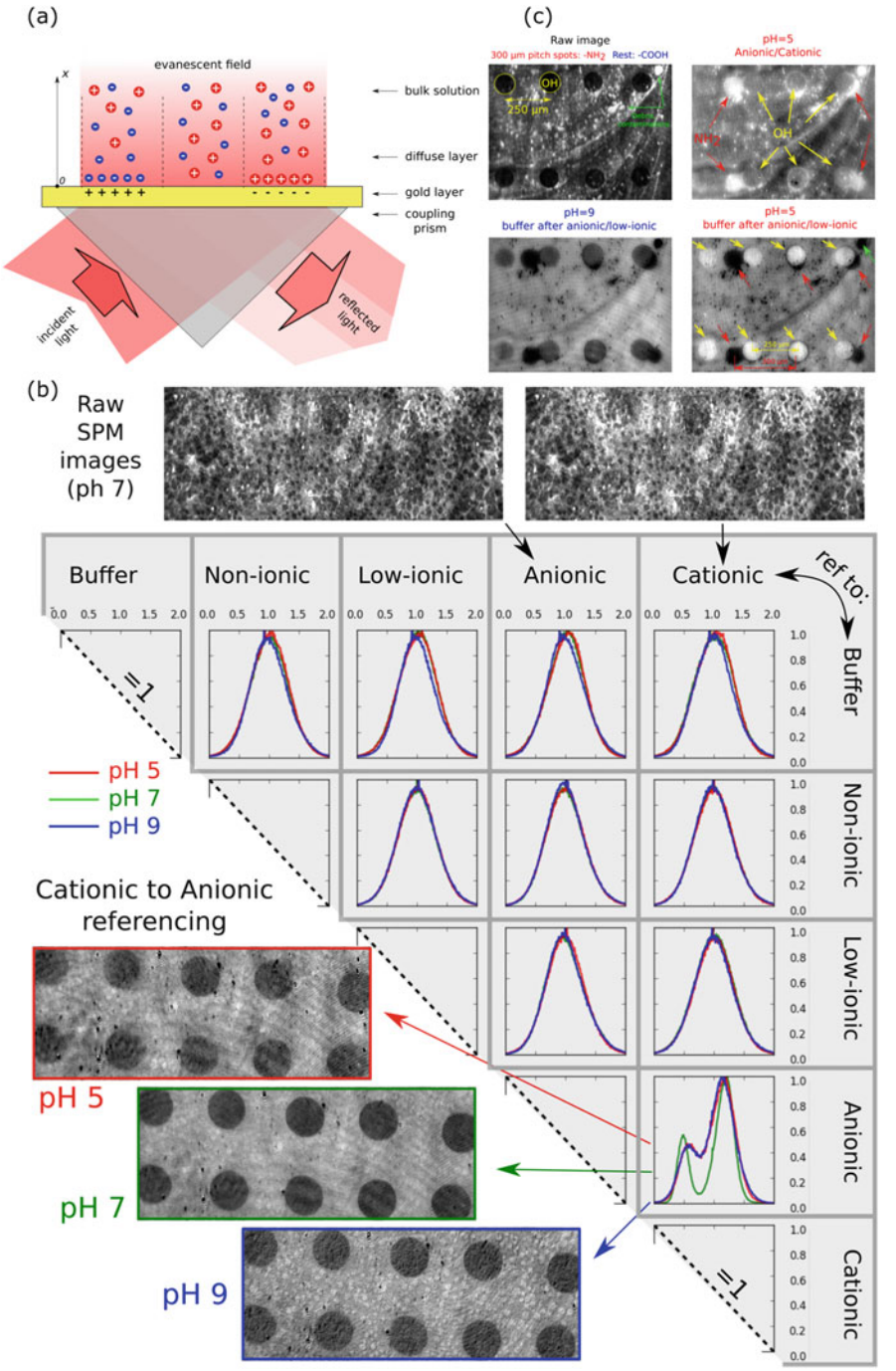

Fig. 13 (**a**) SPR response is influenced by redistribution of ions near the charged surface. Notably, the thickness of the diffuse layer at concentrations above 10 µM is less than the penetration depth

terminal groups, being not recognizable in raw SPRM images, can be visualized using ionic referencing (Fig. 13, upper right panel). It can be also observed that –OH spots overlap fully or partially with $–NH_2$ spots; however, this is not clearly visible because of low contrast between –OH spots and –COOH area. The distinct visualization of all types of coatings was achieved by taking SPRM images in buffer after injection of sodium salicylate as the reference. Indeed, the –OH and $–NH_2$ spots are visualized in contrast to the rest surface and also in contrast to each other (Fig. 13c, bottom line). The interaction between salicylate ions and the three SAM areas ($–NH_2$, –COOH, and –OH) seems to be at different level, thus enabling a visualization of these differently coated surface areas.

5.5.2 Electrochemically Assisted Spatiotemporal Referencing

The principle of spatiotemporal referencing can be complemented by other analytical techniques. A combination of wide-field SPRM with in situ electrochemical analysis was reported [89]. This approach enables characterization of adsorbed nanoparticles in relation to size and material. The method was demonstrated for silver and copper nanoparticles, using gold nanoparticles as a negative control. The measurement was performed in three steps. First, nanoparticles adsorbed to the sensor surface at cathodic potential (to prevent their oxidation). Adsorbing nanoparticles were detected and counted, and their adsorption positions were determined. Then, unbound nanoparticles were eluted from the measurement cell. Finally, the electrical potential of the gold electrode (SPRM sensor surface) was scanned toward anodic direction. At some potential, which depends on the material and size of nanoparticle, their disappearance due to electrochemical oxidation onto ions was detected. It is to expect that adsorption of nanoparticles to the sensor surface and their further disappearance by electrochemical oxidation and dissolution are denoted by differential SPRM images at the same place, with the same shape but opposite intensity (similar to photopositive and photonegative) (Fig. 14a). This can be quantified by the regression coefficient (RC) between images taken at the moment of adsorption of nanoparticle with SPRM differential image at the same place any other time. Therefore, the adsorption and desorption images of the same nanoparticle have a RC close to -1, whereas at any other time RC is close to zero. When the potential is swept to the anodic direction, the RCs for each adsorbed nanoparticle were determined. The value of the electrode potential at which these nanoparticles dissolve and disappear provides information on their chemical composition and size (Fig. 14b). Simultaneous analysis of different nanoparticles is also possible (Fig. 14c).

Fig. 13 (continued) of the evanescent wave. (**b**) Raw SPRM images are shown in the upper line. Ionic referencing using pixel-to-pixel ratio of images measured in two solutions is indicated as the column and row of the corresponding cell of the table. All images are intensity-normalized. The curves indicate normalized intensity histograms. (**c**) Gold surface coated by deposition of two overlapped arrays of spots of –OH- and $–NH_2$-terminated SAM. The rest surface was coated by –COOH-terminated SAM (Reproduced from [127])

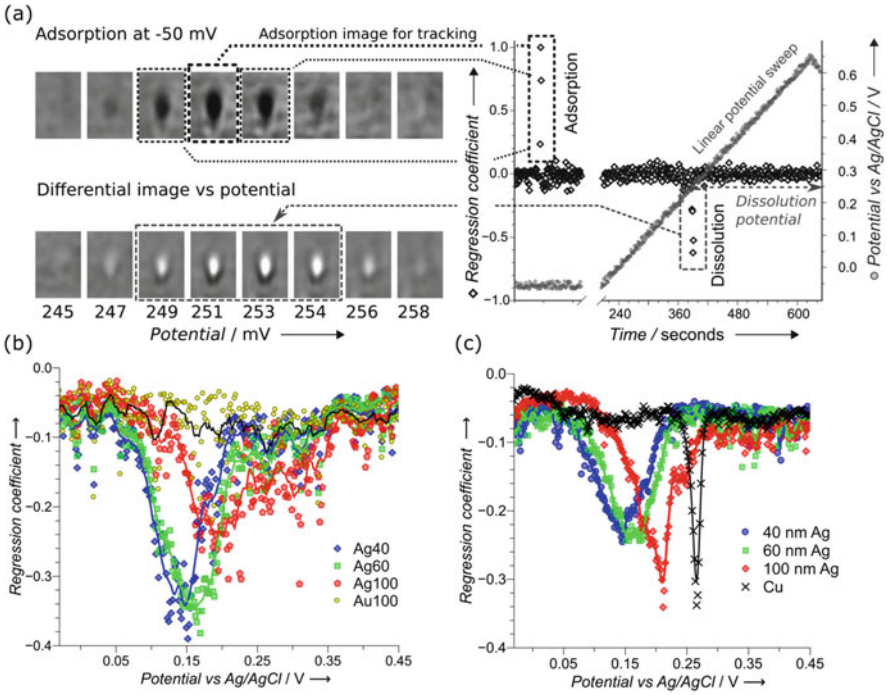

Fig. 14 Determination of electrical potential of electrochemically driven dissolution of a single nanoparticle using differential SPRM (**a**) and the same analysis performed for all nanoparticles adsorbed on the electrode surface (**b**, **c**). Differential images corresponding to adsorption (**a**, top left) and dissolution (**a**, bottom left) of the same nanoparticle and corresponding changes in the regression coefficient (**a**, right). (Reproduced from [89])

SPR technology is also well compatible with other analytical techniques, for example, with fluorescence [129], surface-enhanced Raman scattering (SERS) [130], or electrochemical impedance spectroscopy [131, 132]. One can expect a development of new combinations of SPR with other analytical techniques as well as an introduction of new referencing schemes to further improve the analytical performance.

6 Evaluation of Affinity Properties from SPR Measurements

Transducers of affinity sensors (e.g., SPR transducers) provide information on the surface concentration of analytes bound to the immobilized receptors. For practical needs, volume concentrations of analytes are required. Therefore, it is important to have a relation between volume concentration of an analyte and its surface

concentration that can be then used as a calibration curve. In physical chemistry, such relations are known as adsorption isotherms. A quantitative description of these isotherms provides a mathematical base for interpolation and extrapolation of the calibration curve, which is important for analytical applications, as well as allows one a quantitative characterization of receptors and a better understanding of binding processes [133].

6.1 Measurements in Quasi-equilibrium Conditions

Using a formal kinetics approach to describe binding of an analyte (ligand) (A) to a receptor (binding sites) (B), which leads to the reversible formation of an analyte–receptor complex AB

$$A + B \leftrightarrow AB, \tag{3}$$

we obtain equal reaction rates for the formation and dissociation of the analyte–receptor complex in equilibrium state:

$$k_{\text{ads}} \cdot c_A\left(1 - \theta_{\text{eq}}\right) = k_{\text{des}} \cdot \theta_{\text{eq}} \tag{4}$$

Therefore:

$$\theta_{\text{eq}} = \frac{c_A K}{1 + c_A K} \tag{5}$$

where $K = k_{\text{ads}}/k_{\text{des}}$, c_A is the concentration of analyte, θ is the fraction of occupied binding sites (and correspondingly, $(1 - \theta)$ is the fraction of not occupied binding sites), the subscript index eq means an equilibrium value, and k_{ads} and k_{des} are kinetic association and dissociation constants. These constants are sometimes referred in literature also as the kinetic constants of adsorption/desorption and binding/dissociation. The value K is defined as the binding (or association or adsorption) constant. Equation (4) is often written as:

$$\theta_{\text{eq}} = \frac{c_A}{c_A + c_{1/2}} \tag{6}$$

where $c_{1/2} = 1/K$; a substitution shows that this value corresponds to the concentration at which 50% of binding sites are occupied. The obtained Eq. (5) is well known as the Langmuir adsorption isotherm. This model assumes that (1) all binding sites are equivalent, (2) the ability of an analyte molecule to bind to a binding site is independent of the occupation of neighboring sites, (3) the number of binding sites is limited, and (4) there is an equilibrium between bound molecules and free molecules in aqueous environment. For low analyte concentrations ($c_A\, K \ll 1$), this equation is linearized: $\theta = c_A\, K$ (Henry adsorption isotherm). It corresponds to binding at low surface coverage.

The Langmuir model is valid for the most cases of analyte–receptor binding in affinity sensors. However, numerous cases of deviation from this model were reported, too. A non-homogeneity of binding sites is a typical case for the receptors formed by molecularly imprinted polymerization [134, 135] or by using of polyclonal antibodies. For the small number of receptor types (e.g., two or three with strongly different binding constants), Eq. (5) can be replaced by a sum of such terms with corresponding weight coefficients. For exponential distribution of energy of the binding sites, the Freundlich adsorption isotherm $\theta = A \sqrt[B]{c_A}$ (where A and B are some parameters) can be applied. Other cases of non-homogeneity are seldom.

The non-homogeneity of binding sites leads to serious practical problems in analytical applications of such sensors. Thus, the sensor behavior depends strongly on the initial occupation of the receptor layer, and a non-complete desorption of analyte cannot be taken into account just as a decrease of the total number of binding sites leading to a proportional attenuation of the formerly obtained binding curve.

An influence of the analyte to receptor binding on the neighboring binding sites can be observed for binding of large analyte molecules to the densely placed receptor molecules or for analytes possessing a trend for aggregation. The mostly used model for such cases is the Frumkin isotherm:

$$Kc_A = \frac{\theta}{1-\theta}\exp(-2a\theta) \tag{7}$$

The interaction is described by the parameter a, which is positive for attraction and negative for repulsion between adsorbed species. For $a = 0$ the Frumkin isotherm coincides with the Langmuir isotherm.

According to our definition of affinity sensors (see the first paragraph of this chapter), the signal of affinity sensors S is proportional to their surface coverage θ (i.e., $S = \alpha\,\theta$, where the constant coefficient α depends on the particular type of transducer, amplification factor during signal processing, etc.); therefore, for the binding that obeys the Langmuir isotherm, we get:

$$S = \alpha\frac{c_A K}{1 + c_A K} \tag{8}$$

The binding constant K can be extracted from experimental data by direct nonlinear fitting using Eq. (8). Another approach is based on linearization of this dependence in a double-reciprocal plot (Lineweaver–Burk plot); linear extrapolation to zero values of abscissa and ordinate gives the values of $1/\alpha$ and $-1/K$, correspondingly. In the case of two or three types of binding sites differing in the binding constant, such linearization may give one or two breaking points allowing one to make such analysis differently for each type of binding sites. The binding constant can be also obtained from data plot the logarithmic concentration scale (Fig. 15b): the reciprocal binding constant corresponds to the concentration at the symmetry point of the curve.

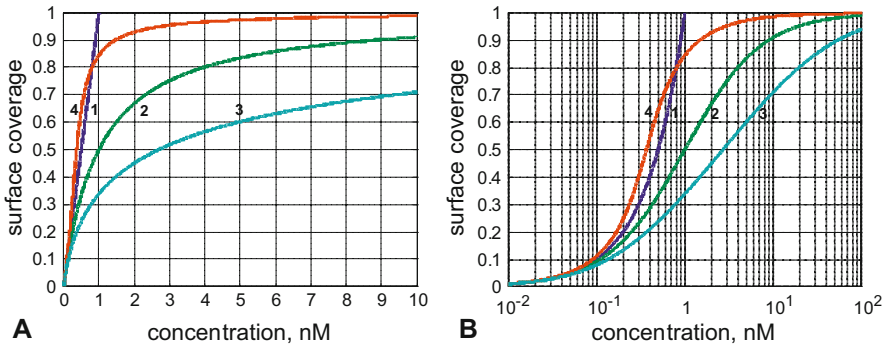

Fig. 15 Simulated binding curves according to the models of Henry (curve 1), Langmuir (curve 2), and Frumkin (curves 3 and 4) for attraction ($a = +1$, curve 4) and repulsion ($a = -1$, curve 3) of adsorbed molecules at linear (**a**) and logarithmic plot (**b**) concentration scale. Binding constant in all the curves is 1/(1 nM)

The value of the Gibbs free energy of the binding reaction is mathematically connected with the value of binding constant and can be calculated as:

$$\Delta G^0 = -RT \ln K \tag{9}$$

It is to note that the value K in this thermodynamic equation characterizes the ratio of activities of corresponding species and must be a dimensionless value. By application of usual approximations of activities by concentrations, the concentration values should be converted into dimensionless ones by normalization to 1 mol/L.

6.2 *Kinetic Measurements*

SPR sensors provide a unique possibility for sensitive monitoring of an analyte–receptor binding in real time. The measured response kinetics allows much more detailed analysis of kinetic and thermodynamic characteristics of the binding reaction. Kinetic measurements can be performed much faster than the measurements in quasi-equilibrium conditions.

The process of analyte binding to the corresponding receptor includes two kinetic steps: (1) analyte diffusion to the sensor surface and (2) analyte–receptor binding. The analysis of kinetic measurements is based on the following assumptions: (1) the kinetic-limiting step of the whole process is the binding, and (2) the binding can be described by the Langmuir isotherm (i.e., all above-discussed assumptions for the Langmuir adsorption model are valid).

Based on the formal kinetics, the adsorption rate $\frac{d\theta(t)}{dt}$ can be described as an algebraic sum of the rates of adsorption and desorption:

$$\frac{d\theta(t)}{dt} = k_{\text{ads}}(1 - \theta(t))c_A - k_{\text{des}}\theta(t) \tag{10}$$

Therefore, the signal kinetics $S(t) = \alpha\theta(t)$ obeys the dependence:

$$\frac{dS(t)}{dt} = - \; S(t)\,k_S + \alpha\, k_{\text{ads}}\, c_A \tag{11}$$

$$\text{with :} \quad k_S = k_{\text{ads}} c_A + k_{\text{des}}. \tag{12}$$

Equation (12) has the following solution:

$$S(t) = [1 - \exp(-k_S t)]\, S_{\text{eq}}, \tag{13}$$

where the value S_{eq} is the surface coverage in equilibrium described by Eq. (5).

A desorption kinetics observed after replacement of the analyte solution by the solution without analyte can be obtained from Eqs. (11), (12), and (13) by substitution $k_{\text{ads}} = 0$ with initial condition $S(0) = S_{\max}$:

$$S(t) = S_{\max} \exp(-k_{\text{des}} t) \tag{14}$$

The value k_S is an apparent kinetic constant of adsorption which can be obtained from experimental data. Paradoxically, the desorption constant is one of the components positively contributing into the apparent kinetic adsorption constant (Eq. (12)). The linear dependence of k_s on ligand concentration allows one to obtain the values of k_{ads} and k_{des}. The value k_s can be obtained by exponential fitting of adsorption kinetics with Eq. (13). Instead of nonlinear fitting, the dependence of $\frac{dS(t)}{dt}$ vs. $S(t)$ can be analyzed: a linearity of this dependence verifies the exponential character of the signal kinetics, while its slope gives the value k_s. The desorption rate constant k_{des} can be also extracted from fitting of desorption kinetics with Eq. (14). This provides a principal possibility to get kinetic constants of adsorption and desorption and to estimate binding constants from a single experiment. However, desorption kinetics for many receptors is very slow, and k_{ads} cannot be measured directly. Data that are more reliable are obtained by repetition of the measurements at different concentrations and by analysis of the concentration dependence of k_S according to Eq. (12). The values of k_{ads} and k_{des} obtained from kinetic measurements can be used for calculation of the binding constant K. Numerous investigations demonstrated that the values of binding constants obtained from kinetic and equilibrium measurements are almost identical.

Non-equilibrium measurements allow one not only to get quantitative analysis of receptor properties but also to improve selectivity and reduce or even eliminate a relative contribution of interferences to the sensor signal. Such approach was described in [136]. If the kinetic constant of the analyte desorption is higher than that of interfering species, an analysis during an initial part of adsorption stage

provides an increase in selectivity which is equal to the ratio of the respective kinetic constants. If the desorption of the analyte is slower than that of the interfering species, one can reach a considerable improvement of selectivity performing analysis after partial desorption of species bond to the sensor surface. A quantitative value of this selectivity improvement depends on the kinetic desorption constants being limited by acceptable attenuation of the sensor signal due to desorption of the analyte.

6.3 Analysis of Temperature Dependencies

Analysis of temperature dependencies of responses of SPR sensors on analyte injections provides more detailed data on affinity properties. A substitution $\Delta G = \Delta H - T\Delta S$ in Eq. (9) leads to the van't Hoff relationship:

$$\ln K = \frac{1}{R}\left(\Delta S^0 - \frac{\Delta H^0}{T}\right) \tag{15}$$

Here, the slope of the dependence of the logarithm of the equilibrium constant on reciprocal temperature gives the value of the reaction enthalpy, while an extrapolation to zero value of the reciprocal temperature gives the value of the reaction entropy; the superscript 0 indicates the standard values. A deviation of this dependence was explained by contribution of temperature-dependent heat capacity [137] which can be also determined from temperature dependence (however, numerical simulation demonstrated that typical values of experimental errors make such analysis very uncertain [138]).

Temperature dependencies of the kinetic constants of binding (k_{ads}) and dissociation (k_{des}) allow one to obtain the values of activation energies for binding and dissociation, $E_{a,\text{ads}}$ and $E_{a,\text{des}}$. The transition-state theory developed by Eyring and coauthors [139] gives the following equation for the kinetic constant of binding:

$$k_{\text{ads}} = \frac{\kappa k_B T}{h} \exp\left(-\Delta H^{\#0}_{\text{ads}}/RT\right) \exp\left(\Delta S^{\#0}_{\text{ads}}/R\right) \tag{16}$$

where the superscript # indicates the corresponding thermodynamic potential of activation process, k_B and h are the Boltzmann and Planck constants, and κ is the transmission factor, which is considered to be between 0.5 and 1. A linearization in the coordinates $\ln(k/T)$ vs. $1/T$ (Eyring plots) and an assumption on the value of the transmission factor κ (usually, as $\kappa = 1$) allow one to extract the values of standard activation enthalpies and entropies.

Finally, we have to discuss the risk of misinterpretation during data analysis. In the case of measurements in quasi-equilibrium conditions, it is not easy to estimate the "distance" from equilibrium. Usually, such measurements are performed by subsequent additions of increasing analyte concentrations, and the signals are read

in ~30 min when no visible change of the signal magnitude is observed. An absence of equilibria leads to a systematic error in data analysis. In the case of kinetic measurements, it is not a rare case, especially for receptor layers with three-dimensional matrix, when the binding is limited by diffusion. In this case, the here described simple approach cannot be applied. Ignoring of this fact and a mechanistic application of the analysis based on the Langmuir model to diffusion-limited processes leads to giant errors in the determination of k_{ads} and k_{des} and may lead to considerable errors in determination of binding constants. Therefore, it is important to distinguish diffusion and reaction control of the binding process. A deviation of the binding kinetics from mono-exponential dependence (or nonlinear dependence of k_s vs. ligand concentration) may indicate on diffusion limitation; however, a quality of this analysis depends strongly on the SNR. For diffusion-controlled processes, the adsorption rate depends on the solution viscosity; a modification of the viscosity can be performed by addition of sugar, glycerol, or other compounds. To exclude a chemical influence of the viscosity modifier on the binding process, one can prove that the effect does not depend on the chemical nature of this compound. Another approach to distinguish diffusion and reaction kinetics is based on the variation of thickness of the diffusion boundary layer; it can be realized by variation of the flow rate [140–143]. A risk of misinterpretation of temperature dependencies of equilibrium and kinetic data is also very high. Critical analysis of many aspects of this approach is discussed in [138, 144].

A more detailed description of data analysis is presented in [133] and in numerous literature on application of affinity sensors.

7 Conclusion

The introduction of SPR sensors ~30 years ago has revolutionized the landmark of label-free bio- and chemosensors. SPR sensing was almost immediately commercialized and adopted in science, industry, medicine, and pharmacy. The major milestone in the development of SPR sensors – its implementation in imaging format (SPRi or SPRM) – is also dated by those times. However, the development of SPR sensors has never stopped. Since then, SPR and SPR-imaging sensors have been evolving and maturing in all regards. This chapter summarized some efforts in the instrumental and methodological development of SPR sensors. Improvement of the plasmonic sensor itself and of the measurement methodology was described. One of the most important methodological advances in SPR sensors is the application of self-referencing in order to increase SNR and to distinguish surface and bulk effects in SPR signals. Due to the versatility of SPR-sensing aspects and limited space, not all relevant developments in the field of SPR sensors could be described here. Nevertheless, the progress is self-evident. The overview of SPR development shows many new ideas emerging on the base of SPR effect. SPR was started once as a tool to study large-area protein films; nowadays, SPR is able to detect and characterize single biological and engineered nanoparticles at sub-femtomolar

concentrations. Detection of single proteins or DNA molecules can be expected very soon. Combination with many other analytical techniques (e.g., electrochemical, surface-enhanced Raman scattering, mass spectrometry, chromatography) is being suggested to further extend the application area and capabilities of SPR. Therefore, SPR sensors are highly competitive and, more importantly, have a large potential for further development.

References

1. Bartell FE, Sloan CK (1929) An interferometric investigation of adsorption by pure carbon from non-aqueous binary systems. J Am Chem Soc 584:1637–1643
2. Damaskin BB, Petrii OA, Batrakov VV (1972) Adsorption of organic compounds on electrodes. Plenum Press, New York
3. Sauerbrey G (1959) Verwendung von schwingquarzen zur wägung dünner schichten und zur mikrowägung. Z Phys 155:206–222
4. King WH (1964) Piezoelectric sorption detector. Anal Chem 36:1735–1739
5. Liedberg B, Nylander C, Lunström I (1983) Surface plasmon resonance for gas detection and biosensing. Sensors Actuators 4:299–304
6. Lofas S, Malmqvist M, Ronnberg I, Stenberg E, Liedberg B, Lundstrom I (1991) Bioanalysis with surface plasmon resonance. Sensors Actuators B Chem 5:79–84
7. Liedberg B, Nylander C, Lundström I (1995) Biosensing with surface plasmon resonance - how it all started. Biosens Bioelectron 10:1–9
8. Homola J (2006) Surface plasmon resonance based sensors. Springer, Berlin
9. Schasfoort RBM, Tudos AJ (2008) Handbook of surface plasmon resonance. The Royal Society of Chemistry, London
10. Homola J (2003) Present and future of surface plasmon resonance biosensors. Anal Bioanal Chem 377:528–539
11. Safina G (2012) Application of surface plasmon resonance for the detection of carbohydrates, glycoconjugates, and measurement of the carbohydrate-specific interactions: a comparison with conventional analytical techniques. A critical review. Anal Chim Acta 712:9–29
12. Hoa XD, Kirk AG, Tabrizian M (2007) Towards integrated and sensitive surface plasmon resonance biosensors: a review of recent progress. Biosens Bioelectron 23:151–160
13. Homola J, Yee SS, Gauglitz G (1999) Surface plasmon resonance sensors: review. Sensors Actuators B Chem 54:3–15
14. Puiu M, Bala C (2016) SPR and SPR imaging: recent trends in developing nanodevices for detection and real-time monitoring of biomolecular events. Sensors 16:870
15. Kretschmann E, Raether H (1968) Radiative decay of non-radiative surface plasmons excited by light. Z Naturforsch 23:2135–2136
16. Boardman AD (1982) Electromagnetic surface modes. Wiley, Chichester
17. Raether H (1988) Surface plasmons on smooth and rough surfaces and on gratings. Springer, Berlin
18. Nizamov S, Scherbahn V, Mirsky VM (2015) Self-referencing SPR-sensor based on integral measurements of light intensity reflected by arbitrarily distributed sensing and referencing spots. Sensors Actuators B Chem 207:740–747
19. Jung LS, Campbell CT, Chinowsky TM, Mar MN, Yee SS (1998) Quantitative interpretation of the response of surface plasmon resonance sensors to adsorbed films. Langmuir 14:5636–5648
20. Mcmeekin TL, Wilensky M, Groves ML (1962) Refractive indices of proteins in relation to amino acid composition and specific volume. Biochem Biophys Res Commun 7:151–156

21. Barer R, Tkaczyk S (1954) Refractive index of concentrated protein solutions. Nature 173:821–822
22. Vörös J (2004) The density and refractive index of adsorbing protein layers. Biophys J 87:553–561
23. Klemm F, Johnson R, Mirsky VM (2015) Binding of protein nanoparticles to immobilized receptors. Sensors Actuators B Chem 208:616–621
24. Liedberg B, Lundström I, Stenberg E (1993) Principles of biosensing with an extended coupling matrix and surface plasmon resonance. Sensors Actuators B Chem 11:63–72
25. Zybin A, Boecker D, Mirsky VM, Niemax K (2007) Enhancement of the detection power of surface plasmon resonance measurements by optimization of the reflection angle. Anal Chem 79:4233–4236
26. Akimoto T, Sasaki S, Ikebukuro K, Karube I (2000) Effect of incident angle of light on sensitivity and detection limit for layers of antibody with surface plasmon resonance spectroscopy. Biosens Bioelectron 15:355–362
27. Eum NS, Kim DE, Yeom SH, Kang BH, Kim KJ, Park CS, Kang SW (2009) Variable wavelength surface plasmon resonance (SPR) in biosensing. Biosystems 98:51–55
28. Akimoto T, Wada S, Karube I (2008) A surface plasmon resonance probe without optical fibers as a portable sensing device. Anal Chim Acta 610:119–124
29. Nelson BP, Frutos AG, Brockman JM, Corn RM (1999) Near-infrared surface plasmon resonance measurements of ultrathin films. Anal Chem 71:3928–3934
30. Frutos AG, Weibel SC, Corn RM (1999) Near-infrared surface plasmon resonance measurements of ultrathin films. 2. Fourier transform SPR spectroscopy. Anal Chem 71:3935–3940
31. Rothenhausler B, Knoll W (1988) Surface plasmon microscopy. Nature 332:615–617
32. Brockman JM, Nelson BP, Corn RM (2000) Surface plasmon resonance imaging measurements of ultrathin organic films. Annu Rev Phys Chem 51:41–63
33. Campbell CT, Kim G (2007) SPR microscopy and its applications to high-throughput analyses of biomolecular binding events and their kinetics. Biomaterials 28:2380–2392
34. Boecker D, Zybin A, Niemax K, Grunwald C, Mirsky VM (2008) Noise reduction by multiple referencing in surface plasmon resonance imaging. Rev Sci Instrum 79:2–8
35. Berger CEH, Beumer TAM, Kooyman RPH, Greve J (1998) Surface plasmon resonance multisensing. Anal Chem 70:703–706
36. Guo X (2012) Surface plasmon resonance based biosensor technique: a review. J Biophotonics 5:483–501
37. Nylander C, Liedberg B, Lind T (1982) Gas detection by means of surface plasmon resonance. Sensors Actuators 3:79–88
38. Nuzzo RG, Allara DL (1983) Adsorption of bifunctional organic disulfides on gold surfaces. J Am Chem Soc 105:4481–4483
39. Ulman A (1996) Formation and structure of self-assembled monolayers. Chem Rev 96:1533–1554
40. Riepl M, Mirsky VM, Novotny I, Tvarozek V, Rehacek V, Wolfbeis OS (1999) Optimization of capacitive affinity sensors: drift suppression and signal amplification. Anal Chim Acta 392:77–84
41. Mirsky VM (2002) New electroanalytical applications of self-assembled monolayers. TrAC Trends Anal Chem 21:439–450
42. Love JC, Estroff LA, Kriebel JK, Nuzzo RG, Whitesides GM (2005) Self-assembled monolayers of thiolates on metals as a form of nanotechnology. Chem Rev 105:1103–1169
43. Hirsch T, Shaporenko A, Mirsky VM, Zharnikov M (2007) Monomolecular films of phthalocyanines: formation, characterization, and expelling by alkanethiols. Langmuir 23:4373–4377
44. Stewart A, Zheng S, McCourt MR, Bell SEJ (2012) Controlling assembly of mixed thiol monolayers on silver nanoparticles to tune their surface properties. ACS Nano 6:3718–3726
45. Crooks RM, Ricco AJ (1998) New organic materials suitable for use in chemical sensor arrays. Acc Chem Res 31:219–227

46. Glebe U, Baio JE, Árnadóttir L, Siemeling U, Weidner T (2013) Molecular suction pads: self-assembled monolayers of subphthalocyaninatoboron complexes [BCl{Subpc'(SR)6}] on gold. ChemPhysChem 14:1155–1160
47. Ferretti S, Paynter S, Russell DA, Sapsford KE, Richardson DJ (2000) Self-assembled monolayers: a versatile tool for the formulation of bio-surfaces. TrAC Trends Anal Chem 19:530–540
48. Faucheux N, Schweiss R, Lützow K, Werner C, Groth T (2004) Self-assembled monolayers with different terminating groups as model substrates for cell adhesion studies. Biomaterials 25:2721–2730
49. Ostuni E, Yan L, Whitesides GM (1999) The interaction of proteins and cells with self-assembled monolayers of alkanethiolates on gold and silver. Colloids Surf B Biointerfaces 15:3–30
50. Schlenoff JB, Li M, Ly H (1995) Stability and self-exchange in alkanethiol monolayers. J Am Chem Soc 117:12528–12536
51. Noh J, Kato HS, Kawai M, Hara M (2002) Surface and adsorption structures of dialkyl sulfide self-assembled monolayers on Au(111). J Phys Chem B 106:13268–13272
52. Phares N, White RJ, Plaxco KW (2009) Improving the stability and sensing of electrochemical biosensors by employing trithiol-anchoring groups in a six-carbon self-assembled monolayer. Anal Chem 81:1095–1100
53. Li Z, Jin R, Mirkin CA, Letsinger RL (2002) Multiple thiol-anchor capped DNA-gold nanoparticle conjugates. Nucleic Acids Res 30:1558–1562
54. Hermanson GT (2013) Bioconjugate techniques.3rd edn. Academic Press, Boston
55. Chaki NK, Vijayamohanan K (2002) Self-assembled monolayers as a tunable platform for biosensor applications. Biosens Bioelectron 17:1–12
56. Gooding JJJ, Hibbert DBB (1999) The application of alkanethiol self-assembled monolayers to enzyme electrodes. TrAC Trends Anal Chem 18:525–533
57. Wrobel N, Schinkinger M, Mirsky VM (2002) A novel ultraviolet assay for testing side reactions of carbodiimides. Anal Biochem 305:135–138
58. Yamada H, Imoto T, Fujita K, Okazaki K, Motomura M (1981) Selective modification of aspartic acid-101 in lysozyme by carbodiimide reaction. Biochemistry 20:4836–4842
59. Pei Z, Anderson H, Myrskog A, Dunér G, Ingemarsson B, Aastrup T (2010) Optimizing immobilization on two-dimensional carboxyl surface: pH dependence of antibody orientation and antigen binding capacity. Anal Biochem 398:161–168
60. Wrobel N, Deininger W, Hegemann P, Mirsky VM (2003) Covalent immobilization of oligonucleotides on electrodes. Colloids Surf B Biointerfaces 32:157–162
61. Johnsson B, Löfås S, Lindquist G (1991) Immobilization of proteins to a carboxymethyldextran-modified gold surface for biospecific interaction analysis in surface plasmon resonance sensors. Anal Biochem 198:268–277
62. Kolb HC, Finn MG, Sharpless KB (2001) Click chemistry: diverse chemical function from a few good reactions. Angew Chem Int Ed 40:2004–2021
63. Mehlich J, Ravoo BJ (2011) Click chemistry by microcontact printing on self-assembled monolayers: a structure–reactivity study by fluorescence microscopy. Org Biomol Chem 9:4108–4415
64. Fleminger G, Hadas E, Wolf T, Solomon B (1990) Oriented immobilization of periodate-oxidized monoclonal antibodies on amino and hydrazide derivatives of Eupergit C. Appl Biochem Biotechnol 23:123–137
65. Nizamov S, Mirsky VM (2011) Self-referencing SPR-biosensors based on penetration difference of evanescent waves. Biosens Bioelectron 28:263–269
66. Fägerstam LG, Frostell-Karlsson Å, Karlsson R, Persson B, Rönnberg I (1992) Biospecific interaction analysis using surface plasmon resonance detection applied to kinetic, binding site and concentration analysis. J Chromatogr A 597:397–410
67. Knight MW, King NS, Liu L, Everitt HO, Nordlander P, Halas NJ (2014) Aluminum for plasmonics. ACS Nano 8:834–840

68. Zynio SA, Samoylov AV, Surovtseva ER, Mirsky VM, Shirshov YM (2002) Bimetallic layers increase sensitivity of affinity sensors based on surface plasmon resonance. Sensors 2:62–70
69. Zhai P, Guo J, Xiang J, Zhou F (2007) Electrochemical surface plasmon resonance spectroscopy at bilayered silver/gold films. J Phys Chem C 111:981–986
70. Chen Y, Zheng RS, Zhang DG, Lu YH, Wang P, Ming H, Luo ZF, Kan Q (2011) Bimetallic chips for a surface plasmon resonance instrument. Appl Opt 50:387–391
71. Nesterenko DV, Saif-Ur-Rehman, Sekkat Z (2012) Surface plasmon sensing with different metals in single and double layer configurations. Appl Opt 51:6673–6682
72. Zekriti M, Nesterenko DV, Sekkat Z (2015) Long-range surface plasmons supported by a bilayer metallic structure for sensing applications. Appl Opt 54:2151–2157
73. Slavík R, Homola J, Vaisocherová H (2006) Advanced biosensing using simultaneous excitation of short and long range surface plasmons. Meas Sci Technol 17:932–938
74. Hastings JT, Guo J, Keathley PD, Kumaresh PB, Wei Y, Law S, Bachas LG (2007) Optimal self-referenced sensing using long- and short- range surface plasmons. Opt Express 15:17661–17672
75. El-Gohary SH, Choi M, Kim YL, Byun KM (2016) Dispersion curve engineering of TiO2/silver hybrid substrates for enhanced surface plasmon resonance detection. Sensors 16:1442–1452
76. Chen X, Jiang K (2010) Effect of aging on optical properties of bimetallic sensor chips. Opt Express 18:1105–1112
77. Genslein C, Hausler P, Kirchner E-M, Bierl R, Baeumner AJ, Hirsch T (2017) Detection of small molecules with surface plasmon resonance by synergistic plasmonic effects of nanostructured surfaces and graphene. Proc SPIE 10080:100800F
78. Genslein C, Hausler P, Kirchner EM, Bierl R, Baeumner AJ, Hirsch T (2016) Graphene-enhanced plasmonic nanohole arrays for environmental sensing in aqueous samples. Beilstein J Nanotechnol 7:1564–1573
79. Pang K, Dong W, Zhang B, Zhan S, Wang X (2015) Sensitivity-enhanced and noise-reduced surface plasmon resonance sensing with microwell chips. Meas Sci Technol 26:8pp
80. Shalabney A, Abdulhalim I (2010) Electromagnetic fields distribution in multilayer thin film structures and the origin of sensitivity enhancement in surface plasmon resonance sensors. Sensors Actuators A Phys 159:24–32
81. Shalabney A, Khare C, Rauschenbach B, Abdulhalim I (2011) Sensitivity of surface plasmon resonance sensors based on metallic columnar thin films in the spectral and angular interrogations. Sensors Actuators B Chem 159:201–212
82. Vaskevich A, Rubinstein I (2008) Localized surface plasmon resonance (LSPR) spectroscopy in biosensing. Part four. Handbook of biosensors and biochips. Wiley, Chichester, p 26
83. Kedem O, Tesler AB, Vaskevich A, Rubinstein I (2011) Sensitivity and optimization of localized surface plasmon resonance transducers. ACS Nano 5:748–760
84. Drexler C, Shishkanova TV, Lange C, Danilov SN, Weiss D, Ganichev SD, Mirsky VM (2014) Terahertz split-ring metamaterials as transducers for chemical sensors based on conducting polymers: a feasibility study with sensing of acidic and basic gases using polyaniline chemosensitive layer. Microchim Acta 181:1857–1862
85. Shumaker-Parry J, Campbell C (2004) Quantitative methods for spatially resolved adsorption/desorption measurements in real time by surface plasmon resonance microscopy. Anal Chem 76:918–929
86. Nelson BP, Grimsrud TE, Liles MR, Goodman RM, Corn RM (2001) Surface plasmon resonance imaging measurements of DNA and RNA hybridization adsorption onto DNA microarrays. Anal Chem 73:1–7
87. Zybin A, Kuritsyn YA, Gurevich EL, Temchura VV, Überla K, Niemax K (2010) Real-time detection of single immobilized nanoparticles by surface plasmon resonance imaging. Plasmonics 5:31–35

88. Zybin A, Shpacovitch V, Skolnik J, Hergenröder R (2016) Optimal conditions for SPR-imaging of nano-objects. Sensors Actuators B Chem 239:338–342
89. Nizamov S, Kasian O, Mirsky VM (2016) Individual detection and electrochemically assisted identification of adsorbed nanoparticles by using surface plasmon microscopy. Angew Chem Int Ed 55:1–6
90. Nizamov S, Scherbahn V, Mirsky VM (2016) Detection and quantification of single engineered nanoparticles in complex samples using template matching in wide-field surface plasmon microscopy. Anal Chem 88:10206–10214
91. Scherbahn V, Nizamov S, Mirsky VM (2016) Plasmonic detection and visualization of directed adsorption of charged single nanoparticles to patterned surfaces. Microchim Acta 183:2837–2845
92. Grigorenko AN, Beloglazov AA, Nikitin PI, Kuhne C, Steiner G, Salzer R (2000) Dark-field surface plasmon resonance microscopy. Opt Commun 174:151–155
93. Kabashin AV, Nikitin PI (1997) Interferometer based on a surface-plasmon resonance for sensor applications. Quantum Electron 27:653–655
94. Nikitin PI, Grigorenko AN, Beloglazov A, Valeiko MV, Savchuk AI, Savchuk OA, Steiner G, Kuhne C, Huebner A, Salzer R (2000) Surface plasmon resonance interferometry for micro-array biosensing. Sensors Actuators A Phys 85:189–193
95. Nelson SG, Johnston KS, Yee SS (1996) High sensitivity surface plasmon resonance sensor based on phase detection. Sensors Actuators B Chem 35:187–191
96. Piliarik M, Vaisocherová H, Homola J (2005) A new surface plasmon resonance sensor for high-throughput screening applications. Biosens Bioelectron 20:2104–2110
97. Kashif M, Bakar A, Arsad N, Shaari S (2014) Development of phase detection schemes based on surface plasmon resonance using interferometry. Sensors 14:15914–15938
98. Tao NJ, Boussaad S, Huang WL, Arechabaleta RA, D'Agnese J (1999) High resolution surface plasmon resonance spectroscopy. Rev Sci Instrum 70:4656–4660
99. Berger CEH, Greve J (2000) Differential SPR immunosensing. Sensors Actuators B Chem 63:103–108
100. Jory MJ, Bradberry GW, Cann PS, Sambles JR (1995) A surface-plasmon-based optical sensor using acousto-optics. Meas Sci Technol 6:1193–1200
101. Zybin A, Grunwald C, Mirsky VM, Kuhlmann J, Wolfbeis OS, Niemax K (2005) Double-wavelength technique for surface plasmon resonance measurements: basic concept and applications for single sensors and two-dimensional sensor arrays. Anal Chem 77:2393–2399
102. Boecker D, Zybin A, Horvatic V, Grunwald C, Niemax K (2007) Differential surface plasmon resonance imaging for high-throughput bioanalyses. Anal Chem 79:702–709
103. Boozer C, Yu Q, Chen S, Lee C-Y, Homola J, Yee SS, Jiang S (2003) Surface functionalization for self-referencing surface plasmon resonance (SPR) biosensors by multi-step self-assembly. Sensors Actuators B Chem 90:22–30
104. Eddings MA, Eckman JW, Arana CA, Papalia GA, Connolly JE, Gale BK, Myszka DG (2009) "Spot and hop": internal referencing for surface plasmon resonance imaging using a three-dimensional microfluidic flow cell array. Anal Biochem 385:309–313
105. Sigal GB, Mrksich M, Whitesides GM (1997) Using surface plasmon resonance spectroscopy to measure the association of detergents with self-assembled monolayers of hexadecanethiolate on gold. Langmuir 13:2749–2755
106. O'Brien II MJ, Brueck SRJ, Perez-Luna VH, Tender LM, Lopez GP (1999) SPR biosensors: simultaneously removing thermal and bulk-composition effects. Biosens Bioelectron 14:145–154
107. Homola J, Lu HB, Yee SS (1999) Dual-channel surface plasmon resonance sensor with spectral discrimination of sensing channels using dielectric overlayer. Electron Lett 35:1105–1106
108. Lide DR (1971) Handbook of chemistry and physics. CRC Press, Boca Raton

109. Grassi JH, Georgiadis RM (1999) Temperature-dependent refractive index determination from critical angle measurements: implications for quantitative SPR sensing. Anal Chem 71:4392–4396
110. Kaufmann T, Ravoo BJ (2010) Stamps, inks and substrates: polymers in microcontact printing. Polym Chem 1:371–387
111. Pimpin A, Srituravanich W (2012) Review on micro- and nanolithography techniques and their applications. Eng J 16:37–55
112. Yu F, Tian S, Yao D, Knoll W (2004) Surface plasmon enhanced diffraction for label-free biosensing. Anal Chem 76:3530–3535
113. Yu F, Knoll W (2004) Immunosensor with self-referencing based on surface plasmon diffraction. Anal Chem 76:1971–1975
114. Peterlinz KA, Georgiadis R (1996) In situ kinetics of self-assembly by surface plasmon resonance spectroscopy. Langmuir 12:4731–4740
115. Zacher T, Wischerhoff E (2002) Real-time two-wavelength surface plasmon resonance as a tool for the vertical resolution of binding processes in biosensing hydrogels. Langmuir 18:1748–1759
116. Slavík R, Homola J (2006) Simultaneous excitation of long and short range surface plasmons in an asymmetric structure. Opt Commun 259:507–512
117. Medina C, Santos-Martinez MJ, Radomski A, Corrigan OI, Radomski MW (2007) Nanoparticles: pharmacological and toxicological significance. Br J Pharmacol 150:552–558
118. Hoet PH, Brüske-Hohlfeld I, Salata OV (2004) Nanoparticles – known and unknown health risks. J Nanobiotechnol 2:12
119. Raz SR, Leontaridou M, Bremer MGEG, Peters R, Weigel S (2012) Development of surface plasmon resonance-based sensor for detection of silver nanoparticles in food and the environment. Anal Bioanal Chem 403:2843–2850
120. Wang S, Shan X, Patel U, Huang X, Lu J, Li J, Tao N (2010) Label-free imaging, detection, and mass measurement of single viruses by surface plasmon resonance. PNAS 107:16028–16032
121. Halpern AR, Wood JB, Wang Y, Corn RM (2014) Single-nanoparticle near infrared surface plasmon resonance microscopy for real-time measurements of DNA hybridization adsorption. ACS Nano 8:1022–1030
122. Sidorenko I, Nizamov S, Hergenröder R, Zybin A, Kuzmichev A, Kiwull B, Niessner R, Mirsky VM (2016) Computer assisted detection and quantification of single adsorbing nanoparticles by differential surface plasmon microscopy. Microchim Acta 183:101–109
123. Nizamov S, Scherbahn V, Mirsky VM (2017) Advanced wide-field surface plasmon microscopy of single adsorbing nanoparticles. Proc SPIE 10231:102312F
124. Nizamov S, Scherbahn V, Mirsky VM (2017) Wide-field surface plasmon microscopy of nano- and microparticles: features, benchmarking, limitations, and bioanalytical applications. Proc SPIE 10231:1023108
125. Gurevich EL, Temchura VV, Überla K, Zybin A (2011) Analytical features of particle counting sensor based on plasmon assisted microscopy of nano objects. Sensors Actuators B Chem 160:1210–1215
126. Nizamov S, Mirsky VM (2018) Wide-field surface plasmon resonance microscopy for in-situ characterization of nanoparticle suspensions. In: Kumar CSSR (ed) In-situ characterization techniques for nanomaterials. Springer, Berlin. https://doi.org/10.1007/978-3-662-56322-9_3
127. Nizamov S, Scherbahn V, Mirsky VM (2017) Ionic referencing in surface plasmon microscopy: visualization of the difference in surface properties of patterned monomolecular layers. Anal Chem 89:3873–3878
128. Radke RJ, Andra S, Al-Kofahi O, Roysam B (2005) Image change detection algorithms: a systematic survey. IEEE Trans Image Process 14:294–307
129. Yu F, Yao D, Knoll W (2003) Surface plasmon field-enhanced fluorescence spectroscopy studies of the interaction between an antibody and its surface-coupled antigen. Anal Chem 75:2610–2617

130. Mao L, Yuan R, Chai Y, Zhuo Y, Xiang Y (2011) Signal-enhancer molecules encapsulated liposome as a valuable sensing and amplification platform combining the aptasensor for ultrasensitive ECL immunoassay. Biosens Bioelectron 26:4204–4028
131. Terrettaz S, Stora T, Duschl C, Vogel H (1993) Protein binding to supported lipid membranes: investigation of the cholera toxin-ganglioside interaction by simultaneous impedance spectroscopy and surface plasmon resonance. Langmuir 9:1361–1369
132. Patskovsky S, Latendresse V, Dallaire A-M, Doré-Mathieu L, Meunier M (2014) Combined surface plasmon resonance and impedance spectroscopy systems for biosensing. Analyst 139:596–602
133. Mirsky VM (2011) Quantitative characterization of affinity properties of immobilized receptors. Artificial receptors for chemical sensors. Willey, Weinheim, p 486
134. Umpleby RJ, Baxter SC, Chen Y, Shah RN, Shimizu KD (2001) Characterization of molecularly imprinted polymers with the Langmuir - Freundlich isotherm. Anal Chem 73:4584–4591
135. Kim H, Kaczmarski K, Guiochon G (2006) Thermodynamic analysis of the heterogenous binding sites of molecularly imprinted polymers. J Chromatogr A 1101:136–152
136. Mirsky VM (2001) Affinity sensors in non-equilibrium conditions: highly selective chemosensing by means of low selective chemosensors. Sensors 1:13–17
137. Naghibi H, Tamura A, Sturtevant JM (1995) Significant discrepancies between van't Hoff and calorimetric enthalpies. PNAS 92:5597–5599
138. Zhurkov A, Karlsson R (2007) Statistical aspects of van't Hoff analysis: a simulation study. J Mol Recognit 20:379–385
139. Wynne-Jones WFK, Eyring H (1935) The absolute rate of reactions in condensed phases. J Chem Phys 3:492–502
140. Glaser RW (1993) Antigen-antibody binding and mass transport by convection and diffusion to a surface: a two dimensional computer model of binding and dissociation kinetics. Anal Biochem 213:152–161
141. Lok BK, Cheng YL, Robertson CR (1983) Total internal reflection fluorescence: a technique for examining interactions of macromolecules with solid surfaces. J Colloid Interface Sci 91:87–103
142. Svitel J, Boukari H, Van Ryk D, Willson RC, Schuck P (2007) Probing the functional heterogeneity of surface binding sites by analysis of experimental binding traces and the effect of mass transport limitation. Biophys J 92:1742–1758
143. Filippov LK, Filippova NL (1997) Adsorption kinetics of polyelectrolytes on planar surfaces under flow conditions. J Colloid Interface Sci 189:1–16
144. Winzor DJ, Jackson CM (2006) Interpretation of the temperature dependence of equilibrium and rate constants. J Mol Recognit 19:389–407

Biomagnetic Sensing

Hans-Joachim Krause and Hui Dong

Abstract Biomagnetic sensing is a particularly valuable measurement technique because it is noninvasive in nature. Moving ions responsible for the electric activity of cells give rise to a magnetic field surrounding the current flow. Biomagnetic measurements denote the purely passive recording of this magnetic field outside the human body. The challenge is to record these extremely small magnetic fields in the presence of magnetic disturbance fields from the environment. Superconducting Quantum Interference Devices (SQUIDs), the most sensitive magnetic field sensors known to date, are used to measure the minute biomagnetic fields originating from the human heart or brain, in conjunction with attenuation of disturbances from the environment by passive shielding and/or active gradiometric suppression. Magnetic resonance imaging (MRI) is a well-established technique based on exposing the subject to a strong magnetic field, thus allowing to non-destructively measure the distribution of hydrogen atoms within the body. Low-field magnetic resonance imaging (LF-MRI) is a novel measurement technique requiring more than 1,000-fold lower magnetic fields than conventional MRI, thus allowing to perform imaging with much simpler instrumentation in the presence of metals. Recent experiments yielded promising results with respect to distinction of healthy from malignant tissue. Recently, combinatorial devices allowing to simultaneously

H.-J. Krause (✉)
Institute of Complex Systems, Bioelectronics (ICS-8), Forschungszentrum Jülich, Peter Grünberg Institute (PGI-8), 52425 Jülich, Germany
e-mail: h.-j.krause@fz-juelich.de

H. Dong
State Key Laboratory of Functional Materials for Informatics, Shanghai Institute of Microsystem and Information Technology (SIMIT), Chinese Academy of Sciences (CAS), Shanghai 200050, China

CAS Center for ExcelleNce in Superconducting Electronics (CENSE), Shanghai 200050, China

M. J. Schöning, A. Poghossian (eds.), *Label-Free Biosensing: Advanced Materials, Devices and Applications*, Springer Series on Chemical Sensors and Biosensors (2018) 16: 449–474
DOI 10.1007/5346_2017_13, © Springer International Publishing AG 2017,
Published online: 10 August 2017

record biomagnetic signals and perform magnetic resonance imaging of the anatomy of the human body source are developed to facilitate the determination of the biomagnetic sources by solving the three-dimensional magnetic inverse problem.

Keywords Biomagnetism, Magnetic immunoassay, Magnetic resonance imaging, Magnetocardiography, Magnetoencephalography, SQUID

Contents

1 Introduction

Almost 200 years ago, Oersted discovered that the flow of electrical currents produces a magnetic field that encircles the current. Inside all animate beings and plants, ions move inside and outside of living cells, as well as from cell to cell. These moving charge carriers give rise to a magnetic field inside and in the vicinity of the creatures. Due to the fact that these natural currents in animals and humans are very small, the ensuing magnetic field is extremely weak. In almost all cases, this so-called biomagnetic field is much smaller than the magnetic field from other environmental sources, such as the earth's magnetic field and the field from man-made sources such as power lines, electric appliances, and moving steel objects. Therefore, it is indispensable to shield these environmental disturbance fields in order to be able to record minute biomagnetic fields. In many cases the fields are so small that they can hardly be measured even with the most sensitive magnetic field sensors known to date.

The strongest contributions to the magnetic field intrinsically generated by human beings are from the heart, the so-called magnetocardiogram (MCG), from muscles (magnetomyogram), and from the brain, the magnetoencephalogram (MEG). Biomagnetic measurements denote the contact-free registration of this magnetic field emitted from the body of the human or animal subject. This measurement is entirely noninvasive and purely passive. No excitation whatsoever

is incident on the subject; just the magnetic field generated by the ongoing electrical action currents is recorded at one or more positions outside the body. Due to the non-magnetic properties of almost all tissue types, the magnetic field is practically unaffected by the intermediate tissue between source current and measurement location. In particular, the varying electrical conductivities of the different types of tissue between source and sensor do not influence the magnetic field, whereas they do influence the voltages during electrocardiogram (ECG) recordings. Therefore, finding a solution to the inverse problem for noninvasive 3D localization of intracardiac sources is much easier when using MCG data as compared to ECG recordings.

2 Superconducting Quantum Interference Devices

A SQUID consists of a superconducting loop with one or two Josephson junctions. It combines the effects of quantization of magnetic flux in units of the magnetic flux quantum $\Phi_0 = 2.07 \times 10^{-15}$ Vs and the dependence of the supercurrent circulating in the loop on the magnetic flux threading the loop. The SQUID is an extremely sensitive converter of magnetic flux to output voltage. With a feedback electronics that compensates the measured flux with counter-flux to maintain a stable operating point, the device can be used as a linear null detector. SQUIDs are capable of resolving better than 10^{-6} of Φ_0, which makes them the most sensitive sensors of magnetic flux known to date. Typical readout electronics offer a frequency range extending from direct current (dc) to MHz with a dynamic range of 120 dB or more. In the case of SQUIDs fabricated from conventional, low-temperature (low-T_c) superconductors, operation is usually done at the boiling temperature of liquid helium ($T = 4.2$ K) whereas high-temperature superconductor (high-T_c) SQUIDs are used in liquid nitrogen at 77 K. A comprehensive coverage of SQUIDs can be found in [1].

The most common type of SQUID is the dc SQUID schematically shown in Fig. 1a. It contains two Josephson junctions connected in parallel to a bias current source by a superconducting loop of inductance L_s. The voltage drop across the junctions is measured. When external magnetic flux Φ_e threads the SQUID loop, the

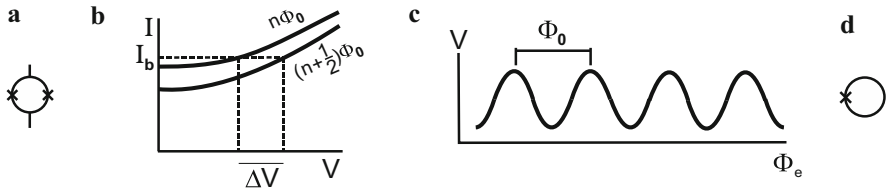

Fig. 1 (**a**) dc SQUID, consisting of a superconducting loop with two Josephson junctions marked by *crosses*, (**b**) *I–V* curve for integer and half-integer flux quantum threading the SQUID loop, (**c**) *V–Φ* curve, (**d**) rf SQUID, consisting of a superconducting loop with one Josephson junction

ensuing circulating current $I = -\Phi_e/L_s$ in the ring adds to the bias in one junction while subtracting in the other. With increasing Φ_e, junction phases are switching alternately, and the current I is reversing direction at each $\Phi = \Phi_0/2$. Consequently, the current-voltage (I–V) curve measured across the junctions is alternating between two extreme traces: the upper one corresponding to integer flux quantum, $\Phi = n\Phi_0$ ($n = 0, 1, 2, 3, \ldots$), and the lower one corresponding to half integer flux quantum, $(n + ½)\Phi_0$, as shown in Fig. 1b. The voltage V across a dc SQUID is thus a periodic function of Φ_e with the period of Φ_0, see Fig. 1c. The ultimate flux sensitivity is limited by thermal and $1/f$ low-frequency flux noise components which originate in the SQUID itself and in the feedback electronics. Usually, the intrinsic dc SQUID noise is larger than that of the electronics and thus determines the resolution.

Another relatively common SQUID type is the radio-frequency (rf) SQUID, schematically shown in Fig. 1d. It contains only one Josephson junction in the loop which is inductively coupled to a resonant LC circuit which applies an rf bias current to the SQUID. Similarly as in case of the dc SQUID, the voltage across the resonant circuit is a periodic function of the magnetic flux threading the loop. At low-T_c, the ultimate sensitivity of dc SQUIDs is better than that of rf SQUIDs. At higher operation temperature, this advantage is less predominant. The advantage of rf SQUIDs over dc SQUIDs is that they do not require galvanic contacts to the sensor, making them safe against static discharge.

SQUIDs are flux sensors of unequaled sensitivity. In most magnetometric applications, however, the task is to measure the local intensity of magnetic field $B = \Phi/A$, with A denoting the area over which the flux is collected. To measure very small magnetic fields B, the pickup area A needs to be of the order of mm^2 or even cm^2. Hence, SQUID magnetometers must include flux pickup structures having a sufficiently large effective area, A_{eff}. The low-inductance SQUID loop alone has a very small A_{eff} of the order of 10^{-3} mm^2, which is not sufficient in most cases. For low SQUID noise, its inductance L_s should be as small as possible, but for good field sensitivity, a large A_{eff} yields a large L_s. This conflict can be resolved by collecting the magnetic flux Φ over a larger area and coupling it more or less effectively to the very small SQUID hole. The simplest solution is to make the outer dimensions of the SQUID loop much larger than the loop's hole in order to concentrate into that hole a fraction of the flux expelled from the superconductor due to the Meissner effect. This scheme is called washer SQUID. Much higher effective areas A_{eff} can be obtained using flux transformers. They consist of a pick-up coil, a pair of interconnecting leads, and a multiturn input coil inductively coupled to the SQUID, see Fig. 2a. In order not to deteriorate performance by thermal Johnson noise, the whole flux transformer circuit is superconducting.

In biomagnetic applications, very weak signals from localized sources such as heart or brain have to be measured against a background of magnetic disturbances which are orders of magnitude stronger, but more uniformly distributed in space because they stem from far sources, like power lines or cars. In such cases, the use of gradiometers is an alternative to magnetic shielding. For example, in the simplest case of a single first-order gradient component, two coils having identical areas

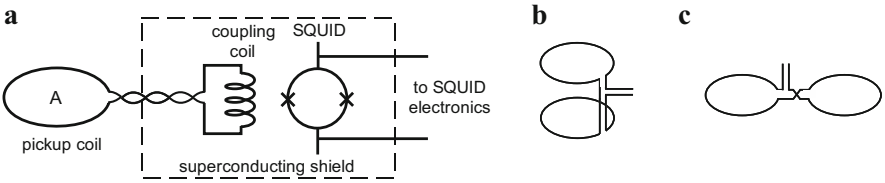

Fig. 2 (**a**) Flux transformer, consisting of a pickup coil and a coupling coil made from superconducting wire, inductively coupled to a SQUID, (**b**) axial gradiometer, consisting of two counter-wound pickup coils above each other, (**c**) planar gradiometer, with counter-wound pickup coils next to each other

A and a spacing *b* called baseline are connected in series-opposite, as shown schematically in Fig. 2b for $\partial B_z/\partial z$ (axial gradiometer) and Fig. 2c for $\partial B_z/\partial x$ (planar gradiometer). Higher-order gradiometers that measure second and higher order spatial gradients of the magnetic field are made similarly using more pickup coils. Planar gradiometers can be fabricated in thin-film technology. However, the axial version involves 3D superconducting wire structures, and thus is feasible only with low-temperature superconductor technology. High-T_c axial gradiometers require the usage of two or more SQUID sensors and electronic subtraction of the SQUID signals.

Low-T_c SQUID sensors are usually fabricated in thin-film niobium technology using magnetron sputtering on oxidized silicon or quartz wafers. The SQUID structure and the junctions are photolithograhically patterned from Nb/AlO_x/Nb trilayers, where the aluminium oxide barrier is formed by thermally oxidizing a nanometer-thin aluminum layer. Additional metallization is used for bonding pads and for fabrication of junction shunts. The insulation between Nb and conducting layers is usually obtained by depositing silicon oxide films and by edge anodization to form an insulating NbO_x oxide. SQUID and input coil of the flux transformer are usually integrated into one monolithic thin-film structure. For biomagnetic applications, the complete magnetometers and gradiometers are often made with 3D Nb-Ti wire-wound pickup coils bonded to Nb pads of the input coil.

High-T_c SQUID sensors are typically fabricated from $YBa_2Cu_3O_{7-x}$ (YBCO) epitaxial thin films deposited on single crystal $SrTiO_3$, MgO or $LaAlO_3$ substrates with surface polished to epitaxial quality. The most popular Josephson junction type is the grain-boundary junction. The grain boundary can, for instance, be formed by depositing YBCO on a bicrystal substrate assembled from two single crystals which are glued together with twisted crystal orientations. Another approach is to etch a ditch into the substrate and to grow the YBCO film across this so-called step edge. The YBCO SQUID structures are patterned by optical photolithography of films followed by argon ion beam or wet-chemical etching.

3 Biomagnetism

The term "biomagnetism" denotes the measurement of the natural magnetic field generated by a living creature due to the movement of electric charge carriers inside the body [2]. Both intra- and extracellular currents, as well as the exchange of ions between cells contribute to the electrical currents inside the body and thus to the magnetic field surrounding the currents [3]. MCG and MEG are the most common biomagnetic modalities. Other electrically active organs are also known to produce detectable magnetic fields. The field of the eye is called magnetooculogram, the field of the stomach is the magnetogastrogram.

3.1 Magnetocardiography

The heart of mammals, in particular the human heart, consists of heart muscle cells, so-called myocardial fibers, arranged as series of cells connected with intercalated discs. These discs act as connectors that allow the electrical excitation to propagate successively from cell to cell [4]. In order to pump blood through the body, all the muscle cells in the atria and in the ventricles have to be excited quasisimultaneously. This is performed by the natural pacemaker, the so-called sinus node, located close to the entry of the vena cava superior into the right atrium. In ECG as well as in MCG, sinus node and atrial depolarization are seen as so-called P wave, following the well-known terminology of Einthoven [5] who named the characteristic ECG peaks using the letters P, Q, R, S, and T. Then, the excitation signal reaches the atrioventricular (AV) node which provides a ~120 ms time delay. The excitation is then distributed from the AV node to both ventricles by means of the His bundle and the Purkinje fibers. The depolarization of the ventricles gives rise to the QRS complex of ECG and MCG signal which is the strongest signal of the heart. A typical adult exhibits a peak-to-peak QRS signal of ~100 pT directly above the chest, see Fig. 3. Electrical excitation leads to synchronous depolarization of the heart muscle cells. After about 200 ms of

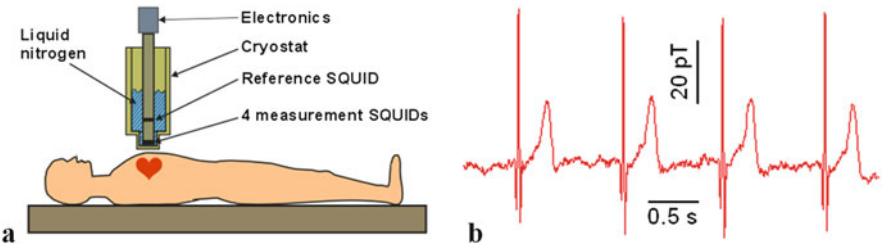

Fig. 3 (**a**) Principle of MCG measurement; (**b**) Typical human MCG measured with high-T_c rf SQUID

refractory period, the heart muscle cells repolarize, leading to the characteristic broad T wave in the signal.

The electrical activity of the human heart by measuring the voltage on the skin of the patient was already measured in the late nineteenth century. In the early 1900s, ECG was fully established [5]. Because the magnetic field associated with the intracorporal electric current of the heard is so small, it took another 60 years until the first magnetic recording of the human heart was performed by Baule and McFee [6] using induction coils. With the invention of the Superconducting Quantum Interference Device (SQUID) in the 1960s [7], sufficiently sensitive magnetometers became available [8], allowing to record MCG with higher quality [9] and eventually leading to a breakthrough in biomagnetic measurements [10].

The first MCG measurements were performed with just one SQUID channel. Single-channel instruments, however, required tedious sequential recordings at different positions above the patient's chest, thus significantly prolonging the measurement time [11]. Therefore, MCG instrumentation was gradually improved from single channel towards multichannel devices [12]. Multichannel SQUID systems for biomagnetic measurements were developed first at Helsinki University [13]. Subsequently, multichannel systems were developed and commercialized by the companies Neuromag (24 channels in 1989), Siemens (37 channels, 1989), Dornier (28 channels, 1990), Philips (62 channels, 1993), and Elekta (99 channels, 2000) [14]. All these systems rely on liquid helium cooling which constitutes a major cost item in their continuous operation.

Another serious drawback that hampered clinical applications was the requirement for expensive and bulky magnetically shielded rooms to suppress environmental disturbance signals. At Helsinki Hospital, MCG was recorded with a SQUID-based gradiometer in a wooden cottage [15]. MCG systems with 9 or 36 channels for unshielded operation were commercialized by CardioMag Imaging Inc. [14].

With the advent of high-T_c superconductors in 1986, SQUIDs made of $YBa_2Cu_3O_{7-x}$ became a promising alternative for biomagnetic measurements. They only require liquid nitrogen as coolant, thus cutting down operating costs to negligible values as compared to helium-cooled systems. However, they do not reach the same sensitivity as their low-T_c counterparts and their production are much less reproducible and reliable. Nevertheless, several high-T_c systems for MCG were realized for shielded [16–18] and unshielded operation [19]. The application of the four-channel system to adult magnetocardiography and to fetal magnetocardiography has been shown in [20]. The system has been utilized for educational purposes in Jülich, measuring the MCG of more than 3,000 high-school students.

Numerous clinical trials have been performed regarding the application of MCG to different heart problems. Applications include the detection of myocardial ischemia [21] and viability [22], coronary artery disease [23–25], arrhythmogenic risk assessment, imaging of arrhythmogenic sites such as the Wolff-Parkinson-White syndrome [26] or ventricular arrhythmia [27].

3.2 Fetal Magnetocardiography

The MCG of an unborn baby in the mother's womb was measured for the first time in 1974 with an unshielded SQUID system [28]. Fetal magnetocardiography (fMCG) is a reliable method for noninvasive study of fetal cardiac electrophysiology from the 20th week of gestation on, especially during the third trimester of pregnancy when the electrically insulating vernix caseosa hampers abdominal recording of fetal ECG [29]. In addition, maternal ECG obscures fetal ECG. Systematic studies on the analysis of cardiac time intervals have been performed in [30]. Other common fetal monitoring techniques such as cardiotocography and echocardiography lack the temporal resolution to extract such information. fMCG has been shown well applicable to the early diagnosis of arrhythmia [31, 32]. For the early detection of congenital heart defects, however, only a few fMCG case reports have been reported [29]. Here, echocardiography appears to be the method of choice. Albeit the sensitivity is not as high as in case of usual helium-cooled SQUIDs, it is possible to record fMCG with high-T_c SQUIDs [33], see Fig. 4. In order to study the electrophysiology, averaging and subtraction of the maternal MCG is needed, in contrast to low-T_c instrumentation that yields sufficient signal-to-noise even in real time.

Once that instrumentation becomes more robust and can operate outside magnetic shielding, it is expected that fMCG finds widespread acceptance because it is the only modality that allows to study the electrophysiology of the fetal heart.

3.3 Magnetoencephalography

Measuring the magnetic field of neuronal brain activity with MEG is more challenging than MCG because the magnetic field of the human brain is about 100-fold smaller than that of the heart [34]. The electrical ion currents flowing in the human head tissue give rise to a magnetic field that can be observed outside the skull. The currents include both intracellular "impressed" currents by neural activity, and the so-called "volume current" of freely moving ions in the extracellular space. The latter can be modeled as a conductive medium with an electrical conductivity

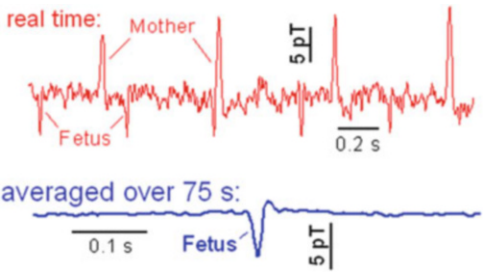

Fig. 4 Typical real-time fetal MCG signal, measured with high-T_c rf SQUID, and fetal signal averaged over 75 s

depending on the type of tissue, i.e. white matter, gray matter, etc. The total magnetic field is determined by a summation over all current elements in the whole head according to Biot-Savart's law. To a good approximation, the magnetic field generated by the impressed currents is orthogonal to the scalp surface, whereas the contribution from the volume currents is tangential to it [35]. Thus, the contribution of volume currents can be neglected in the most common measurement configuration that registers just the magnetic field component orthogonal to the scalp. In the case of pyramidal neurons with an open-field structure [2], predominantly consisting of a single dendrite and one long axon, the small current flowing in the dendrite due to membrane depolarization after neurotransmitter intake at the synapse can be modeled as a current dipole with a field $B \propto 1/r^3$, where r denotes the distance. This current dipole contributes to the magnetic field. A typical current dipole of one post-synaptic dendrite has a magnetic moment of 2×10^{-15} Am, which gives rise to a magnetic field contribution of 3×10^{-19} T at a distance of 5 cm [35]. The summation of current dipoles from the pyramidal neurons is orthogonal to the scalp surface and results in a detectable biomagnetic signal. Considering a magnetic field resolution of typical MEG instrumentation of a few fT/$\sqrt{\text{Hz}}$, it becomes obvious that approximately 50,000 synchronously firing neurons are needed to obtain a measureable signal.

The so-called "action potential" (AP) contribution to the brain's magnetic field is obtained from the depolarization current flowing along an axon, followed by a repolarization current restoring the rest state potential. Thus, the AP consists of a pair of current dipoles with opposing directions, a current quadrupole, which yield a field $B \propto 1/r^4$ that is about tenfold smaller than that of a dipole because it decays more with distance.

Multichannel MEG instrumentation has been developed and commercialized by a number of companies, including the Magnes systems from 4-D Neuroimaging (formerly BTi) with up to 248 channels, the CTF MEG systems from VSM MedTech with up to 275 channels, the Elekta Neuromag systems with up to 306 channels, and the ARGOS systems from Advanced Technologies Biomagnetics with up to 495 channels [14]. In order to accommodate as many SQUIDs as possible as close to the scalp as possible, these systems are equipped with helmet-shaped cryostats. The systems have been designed for everyday clinical use operated by technicians. They include computer-controlled equipment for visual, auditory, and tactile stimulation of neuronal activity. Some systems allow to simultaneously record electroencephalograms (EEG).

Detailed studies of the normal function of the primary sensory and motor system were performed, thus establishing a basis to assess dysfunctions later. Techniques to evoke somatosensory activity include electric, tactile, and laser stimulation to the skin, preferably of the peripheral nerve at the wrist. It was found that the first cortical component about 20 ms after stimulation (called N20) is completely exogenous and not affected by attention. The functional analysis of the auditory cortex was performed by sine-wave tones of different frequencies and duration and localization of the tonotopic organization of the cortex. Stimulation of the visual system was done by pattern reversal, flashes and moving stimuli. Primary answers

as well as entrainment of the alpha rhythm were studied. Examinations of the movement-evoked magnetic field include both self-paced and externally paced movements, preferably of the fingers. Synchronization mechanisms for control of movements were also studied.

A big challenge to MEG and other brain imaging modalities is the identification of higher cognitive functions because neuronal networks exhibit a high spatial and temporal complexity and a great individual variability. The idea is that certain brain regions are responsible for certain tasks.

MEG studies yielded significant contributions to the revelation of brain processes in reception and processing of speech signals. For instance, a specific electrophysiological component has been identified about 150 ms after the onset of a critical word [36]. A second peak named N400 at around 400 ms is correlated to lexical-semantic integration [37]. With respect to the recognition of written language, several relevant areas such as Broca's and Wernicke's area were localized, demonstrating the usefulness of MEG for presurgical planning [38]. By manipulating the expectancy of the final words of a sentence, semantic processing of words on the sentence level during reading was investigated and found to be also related to the N400 peak [39]. Music is perceived differently than speech, albeit there are similarities [40]. Especially the response to harmonic violations is fast and can be localized near the primary auditory cortex [41].

A fundamental question in neuroscience is how the brain groups different sensory inputs such as sound pitch, timbre and volume, color and intensity of light, and olfactory stimuli, to form recognizable objects. With support from MEG studies, the assumption was made that synchronous oscillations in the so-called γ band at around 40 Hz play a role in the process. A review on this so-called binding process is given in [42]. Nonoscillatory magnetic brain responses have also been studied with respect to feature binding and object recognition [43].

Another important field of brain research involves the study of motor actions. Preparation, control, and execution of movements involve transient, slow, and oscillatory magnetic activity in both primary sensory-motor and higher cognitive areas. The role of the so-called magnetic μ-rhythms for the preparation and execution of movements was investigated by means of event-related spectral power changes [44].

MCG is clinically used for evaluating normal and abnormal brain functions, and for the localization of cortical sources. Currently, the localization of epileptic discharges and presurgical brain mapping represent the most common clinical applications [45, 46]. For presurgical evaluation in patients with intractable focal epilepsy, MEG is medically necessary to localize areas of epileptic activity. There is a need to measure small epileptic discharges with bigger background brain activity. Other diagnostic applications remain in the research stage.

Normal spontaneous brain activity of EEG and MEG consists of various frequency bands. Alpha waves (8–13 Hz) are dominant when the subject is awake, beta waves (>13 Hz) are seen during wakefulness and light sleep. Theta (4–7 Hz) and delta (<4 Hz) rhythms are usually observed during sleep, but they may also appear due to brain tumors and ischemia. The source of the spontaneous activity,

both normal and abnormal, spreads over the bilateral cerebral cortices, so that separation of each generator is hardly possible with EEG. The higher spatial resolution of MEG may help to localize abnormally slow waves [47, 48] due to structural brain lesions. Ischemia of the brain can also be detected with MEG. Stenotic lesions of the internal carotid artery system sometimes yield an oscillatory signal at 6–8 Hz in the temporo-parietal area [49].

It has been successfully shown that MEG is even feasible with high-T_c SQUID instrumentation. By comparison with the result obtained from a commercial 248 channel whole-head MEG system, it was demonstrated that the sources of auditory evoked responses can be localized with similar precision using a single high-T_c dc SQUID magnetometer operating at 77 K [50]. However, a long way of development is still needed until nitrogen-cooled SQUID systems will have matured to be suitable for routine MEG recordings.

Today, there are more than 130 MEG systems installed worldwide, which is a relatively small number as compared to the approximately 36,000 MRI machines. The application of MEG is still mainly focused on research, i.e. all the different aspects of brain activity listed above. Routine clinical applications are still scarce. In order to fully establish MEG in clinical practice, the reliability of source estimation needs improvement. Inversion software should be improved, in particular for multiple source estimation to overcome the nonuniqueness of the electromagnetic inverse problem. For clinical research, a validation of the source estimation accuracy of MEG by fusion with other imaging modalities is needed. MEG has excellent time resolution but is not perfect with respect to localization accuracy. Therefore, a combination with low field MRI as an anatomical imaging modality becomes particularly promising for future work (see Sect. 5 on hybrid biomagnetism).

4 Magnetic Resonance Imaging

Magnetic resonance imaging (MRI) is a powerful and probably the most versatile medical imaging modality for the human body [51, 52]. This technique is developed from nuclear magnetic resonance (NMR) [53]. The MR signal originates from the nuclei with nonzero spin, and protons are conventionally most commonly imaged because of widely distribution in human body fluids, proteins, lipids, glucose, etc. In a static magnetic field B_0 along z direction, an energy difference $\Delta E = \gamma \hbar B_0$ occurs dependent on if the spin is aligned parallel or antiparallel to the field, with γ denoting the gyromagnetic ratio (in case of proton: $\gamma/2\pi = 42.58$ MHz/T) and $\hbar$ being Planck's constant h divided by 2π. The populations of parallel and antiparallel spins are nearly equal. For example, at $B_0 = 1$ T, the ratio between the two types of spins is approximately 1.000007. The net equilibrium magnetization of the spin system can be expressed as $M_0 = \rho \gamma^2 \hbar^2 B_0/(4k_B T)$, in which ρ is the spin density and T the temperature.

The imaging of nuclei is realized by applying linear three-dimensional magnetic field gradients $\boldsymbol{G} \equiv \frac{\partial B_z}{\partial x}\hat{\boldsymbol{x}} + \frac{\partial B_z}{\partial y}\hat{\boldsymbol{y}} + \frac{\partial B_z}{\partial z}\hat{\boldsymbol{z}}$. Each component is generated by special coils and can be controlled separately. The gradients $\boldsymbol{G}$ will encode the precession frequency (or phase) by the spatial position of the proton. By applying specific pulse sequences and a spatial Fourier transform, three-dimensional images can be acquired.

Certain nuclei (commonly hydrogen) can absorb and emit rf energy. The application of an rf pulse causes the protons to precess about B_0 at their Larmor frequency $f_L = (\gamma/2\pi)B_0$. During the precession, M_0 undergoes two relaxation processes. The longitudinal relaxation, characterized by the relaxation time T_1, reflects the interaction between spin and nearby lattice with energy exchange which causes the longitudinal magnetization back to equilibrium. The transverse relaxation, characterized by the relaxation time T_2, describes the dephasing process of net magnetization in the transverse plane. There is no energy lost in the transverse relaxation process, and $T_2 \leq T_1$. In tissues, T_2 and T_1 are both field-strength dependent, and they may range from tens of milliseconds to about one second. The T_1 (or T_2) weighted MRI images may show the diseased tissues like tumors by different image contrasts because these malignant tissues usually exhibit different relaxation times from the normal tissues.

4.1 High-Field MRI

In conventional MRI technique, a Faraday coil oriented perpendicularly to B_0 is used to transfer the precession of magnetization to the voltage output, according to the Faraday's law of electromagnetic induction. The induced electromotive force V is proportional to the rate of change of flux in the detection coil, namely $V \propto \frac{\mathrm{d}M}{\mathrm{d}t} \propto 2\pi f_L B_0 \propto B_0^2$. The signal-to-noise ratio (SNR) is one of the key parameters for MR images. The fact that the signal output is proportional to the square of B_0 resulted in the continuous pursuit of increasing B_0 field strength, from the millitesla to the Tesla range, during MRI history.

The NMR phenomenon was observed independently by Purcell group [54] and Bloch group [55] in 1946. In 1966, Ernst introduced the pulsed Fourier transform into NMR, which pioneered the MRI technique [56]. Seven year later, Paul Lauterbur acquired the first MR image [57]. In 1977, Peter Mansfield proposed the Echo Planar Imaging (EPI) technique which significantly accelerated the scan time and made the real-time clinical scanning become possible [58]. In 1980s, the full-body MRI scanners were developed rapidly and the MRI industry became blooming. MRI produces high-quality images of the human body with good tissue contrast and has proven to be a versatile tool for biological research and medical applications. Nowadays, there are more than 36,000 MRI machines working in hospitals, universities, and research institutes for a multitude of medical

applications including diagnosing and studying the central nervous system, like brain and spinal cord, joint disease, and organs, like liver and pancreas. Further prominent application examples include functional magnetic resonance imaging (fMRI) [59, 60], flow imaging (MRI angiography) [61, 62], diffusion-weighted imaging [63, 64], and magnetic resonance spectroscopy (MRS) [65]. Besides the most commonly used proton MRI, the X-nuclei MRI, which images different nuclei (e.g., ^{17}O, ^{19}F, ^{23}Na, ^{31}P, ^{35}Cl), may provide complementary information to proton MRI in physiological processes [66].

fMRI is well suited for brain function analysis. Neural activity causes increased metabolic activity and blood flow in the adjacent vessels to feed the activity. As the metabolic activity takes oxygen from the diamagnetic hemoglobin, the amount of unoxygenated paramagnetic hemoglobin is increased, thus locally affecting the MRI signal [67]. This method called blood oxygen level dependence (BOLD) has various medical applications to identify brain pathologies. The association of neural activity with BOLD has been established recently [68].

4.2 Low-Field MRI

At present the typical field strengths of clinical MRI systems are 1.5 and 3.0 T, usually produced by superconducting magnets, resulting in expensive, large, and complex systems. In the decades since the discovery of NMR phenomena, people have been working on low-field (LF) NMR and MRI at microtesla range, the same order of magnitude as earth's magnetic field (about 50 μT). Since the B_0 field strength is reduced by four orders of magnitude, the detection sensitivity of the Faraday coil can no longer meet the requirements of the imaging SNR. In order to increase SNR, there are two common methods. First, SQUIDs are used as detectors instead of Faraday coils. The SQUID with a sensitivity of up to 10^{-15} T/$\sqrt{\text{Hz}}$ is one of the most sensitive magnetic field sensors, and its sensitivity is independent of frequency [69]. Alternatively, the introduction of pre-polarization will increase the initial macroscopic magnetization of the sample and finally improve SNR. In this technique, a strong magnetic field pulse (B_p) is applied to pre-polarize the sample, and then the MRI signal is detected in the B_0 field.

In addition, the entire system can be housed in a magnetically or conductively shielded room. The external magnetic field noise in the signal frequency bandwidth will be attenuated and the SNR can be improved. However, the rapid switch-off of B_p – typically in 10 ms – to avoid significant decay of the magnetization before signal acquisition induces transient eddy currents in nearby conducting objects, most notably the walls of the shielded room, see Fig. 5. The resultant inhomogeneous magnetic-field transient may both seriously distort the spin dynamics of the sample and exceed the dynamic range of the SQUID readout electronics, and must be greatly reduced before one can begin image encoding and acquisition.

We developed the so-called dynamical cancellation (DynaCan) technique to suppress adverse, pulse-induced transient eddy currents [70]. DynaCan exploits

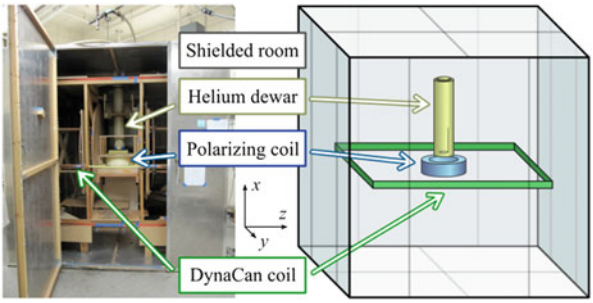

Fig. 5 Aluminium shielded room containing the liquid-helium dewar, the B_p coil and the DynaCan coil

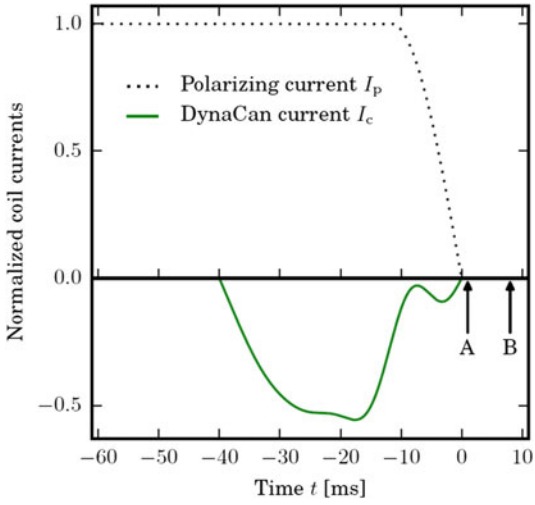

Fig. 6 Dynamical cancellation waveform I_c and end of pre-polarizing pulse I_p; the currents are normalized to the amplitude of I_p. *Arrows* indicate logic switching instants for (*A*) opening relays in the B_p and DynaCan coil circuits and (*B*) beginning data acquisition

the fact that eddy currents are typically a superposition of modes that decay exponentially with their individual time constants. Different time constants correspond to different spatial eddy-current patterns. An additionally pulsed magnetic-field waveform with features at corresponding time scales thus allows selective coupling to the dynamics of the individual patterns (Fig. 6). This cancellation pulse is provided by a current fed into a separate coil, spatially larger than the B_p coil, during the later part and turn-off of the polarizing pulse. The computationally determined DynaCan current waveform is designed to drive the eddy currents to zero at the precise moment that the polarizing field becomes zero. With DynaCan we demonstrated a reduction of the eddy-current fields by 99% (Fig. 7).

Although the shielded room may provide a magnetically quiet environment for LF-MRI system, it makes the system immobile and increases its cost. An unshielded, portable, and inexpensive LF-MRI system is attractive for, e.g., routine examination in underdeveloped countries, and remote sites. We began building unshielded systems in an urban laboratory environment in 2008 [71]. A 7-channel unshielded system was implemented by Espy et al. in 2015 [72].

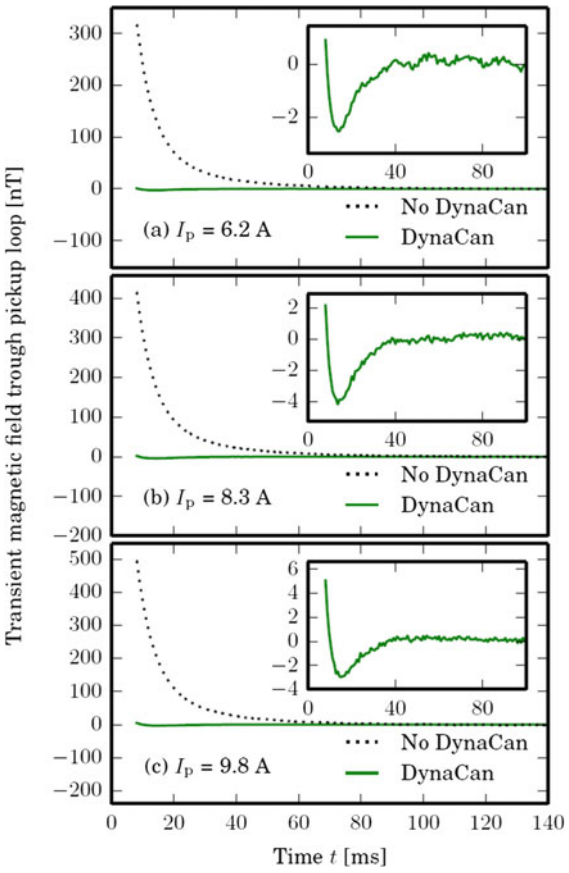

Fig. 7 Magnetic-field transients at the center of the room without (*black dashed line*) and with DynaCan (*green solid line*, also in *insets*) for three different B_p currents I_p: (**a**) 6.2 A, (**b**) 8.3 A, and (**c**) 9.8 A. Oscillations in the *inset* to (**a**) are residual 60 Hz interference

Magnetic field fluctuations in an unshielded urban laboratory can reach hundreds of nT per minute during noisy daytime, but usually drop down to only a few nT at night. The field fluctuation causes the signal Larmor frequency to drift randomly for several Hz during the unshielded LF-NMR/MRI measurements, thus seriously spoiling the averaging effect and causing imaging artifacts [73]. An effective active compensation technique was developed, based on spatial correlation of the low-frequency magnetic field fluctuation to stabilize the B_0 field [74]. A full-tensor environmental gradient field compensation was suggested for cancelling the spatial gradients from the environment [75]. With these noise suppression techniques, a four-channel LF-MRI system for parallel imaging [76] achieved a spatial resolution better than 2.5 mm × 2.5 mm × 5 mm in vegetable imaging (Fig. 8).

SQUID-based LF-MRI has been demonstrated to have many advantages [77], such as:

1. No superconducting magnet is needed because B_0 is very low. This greatly reduces system complexity and cost, so it is possible to easily develop an open and mobile low-cost medical system.

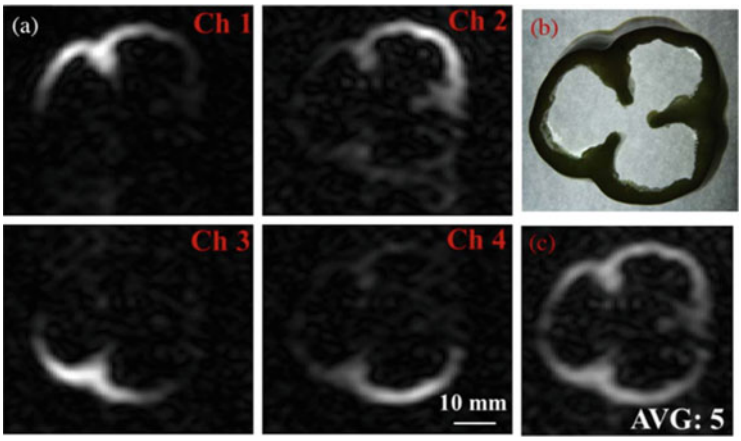

Fig. 8 (**a**) Two-dimensional MR images of pepper sample for each channel of the low-T_c SQUID-based second-order gradiometer system, (**b**) photograph of the pepper slice, (**c**) reconstructed MR image from the four images of (**a**) using the weighted superposition method. The average number of times was 5

2. The enhanced intrinsic longitudinal relaxation times (T_1) of different soft tissues at low field can be used to distinguish cancerous and normal tissues, e.g. prostate cancer, breast cancer, etc., which have poor specificities in high-field MRI [78–80].
3. High-field MRI images cannot be acquired if the patient has a pacemaker, screws, or other metallic implants in the body, because the susceptibility difference between metal and tissue may lead to a local field inhomogeneity proportional to B_0 strength and gives rise to image distortion. By lowering the B_0 field to microtesla range, this effect becomes negligible [81]. In addition, these objects are exposed to strong magnetic forces that might hurt the patient.
4. Hybrid imaging by combing MEG with LF-MRI may provide functional and anatomical information of brain simultaneously, see the following Sect. 5.
5. The relaxation dispersion behavior reflects the B_0 field dependence of the relaxation times (typically T_1). Because of technical constraints in commercial machines, the frequency range of traditional relaxation dispersion curves obtained by fast field cycling technique usually starts from 10 kHz (234 μT) to several MHz [82]. Therefore, people developed the spin-locking technique to measure the $T_{1\rho}$ relaxation dispersion in the rotating frame at low spin-lock field to gain useful information on the composition of macromolecules, like proton exchange between water and macromolecules [83]. However, the heat produced by the spin-lock pulse usually makes the $T_{1\rho}$ technique prohibitive for human study. The LF-MRI technique enables direct T_1 and T_2 dispersion measurement at all frequencies below 10 kHz without heating problem. Inglis et al. showed in vivo human brain images at LF with distinguishable components, like brain tissue, scalp, blood, and cerebrospinal fluid [84]. In order to determine whether LF-MRI has further potential advantages for in vivo human brain imaging, a quantitative comparison was made between relaxation dispersion in postmortem

pig brain measured at ultra-low fields and spin-locking at 7 T [85]. It was found that LF-MRI may offer distinct, quantitative advantages for human brain imaging, while simultaneously avoiding the severe heating limitation imposed on high-field spin-locking.

5 Hybrid Biomagnetism and Magnetic Resonance Imaging

The temporal resolution of MEG, typically 1 ms, is much better than fMRI, but a drawback of magnetic neuroimaging is the fact that the three-dimensional inverse problem is ill-posed. Helmholtz showed more than 150 years ago that it is impossible to uniquely determine the current distribution inside a conductor from a measurement of the magnetic field in its surroundings. Therefore, MEG is not perfect with respect to localization accuracy of the source. If, however, a priori information on the shape and on the conductivity of the conductor is available, the ill-posedness of the problem can be overcome. If MRI and MEG measurements are performed in different systems, data migration from one system to the other is a big challenge. In addition, geometrical positioning errors cannot be avoided. Typically, MEG/MRI co-registration errors may reach the order of 5–10 mm in the cortex. The spatial resolution is less precise for sources in the deep brain region. Since MRI and MEG signals can be distinctly separated in the frequency domain, co-registration of both modalities is feasible. Because of simultaneous measurement, positioning errors are completely avoided. Furthermore, the combination of MEG with LF-MRI no longer requires moving the patient and reduces the total system cost. Several groups combined LF-MRI with MEG.

The Los Alamos group first demonstrated the possibility of simultaneous measurement of MEG and MRI using their homemade seven-channel low-T_c SQUID system [86]. It allows three-dimensional matching of LF-MRI images and MEG data with better accuracy than that of traditional subsequent MEG and MRI registration. They also suggested that parallel imaging of LF-MRI with hundreds of SQUID channels would significantly reduce the system noise. The total imaging time would be accelerated, which finally would make the hybrid MEG/MRI system more reliable and efficient for clinical diagnosis [87]. Subsequently, the Finnish group developed a combined MEG/MRI using a commercial whole-head 306-channel MEG machine [88]. Great efforts are made to optimize the sensors, the pulse sequences, and the reconstruction methods.

6 Magnetic Resonance Imaging of Neural Activity

The magnetic field generated by neuronal activity adds to the magnetic field imposed on the human body for MR imaging. In case of LF-MRI, this local distortion of the imaging field on the order of hundreds of picotesla may affect

spin dynamics because it slightly changes the imaging field in the microtesla range. This local field change may lead to a detectable change in the NMR signal. This modality is called direct neuronal imaging (DNI) [89] or neuronal current imaging (NCI) [90]. Sustained neuronal activity characterized by a local quasi-static magnetic field change can be observed as a change of the local spin-precession frequency. Fast neuronal activity may act as a tipping pulse, the so-called AC or resonant effect in NCI [91].

Using a priori information on anatomical structure and on the electrical conductivity of the different tissues in the brain may considerably improve the accuracy of source localization. MRI allows to measure the electric current density in an object by observing how the associated magnetic field affects the spin precession. This so-called current-density imaging (CDI) modality has been shown to be feasible with externally impressed current [92]. It has been shown that conductivity imaging can be done in a standard MRI system without applying a current just by post-processing analysis of the phase distribution of the imaging rf pulse [93]. Evaluation of the magnitude allows to perform permittivity imaging [94]. However, conductivity imaging is usually done in standard high-field MRI systems, leading to a measurement of the electrical properties in the upper MHz range [95], whereas for MEG inversion, a knowledge of these quantities at sub-kHz frequencies is needed. For CDI of static currents, rotation of the object is usually needed because CDI measures only the change of the MRI main field component. The magnetization is rotated adiabatically, thus overcoming the requirement for object rotation [96]. A zero-field encoding protocol was recently published which allows to perform static CDI measurements without applying any MRI fields [97]. The obtained distribution map of conductivity and permittivity of the brain does already yield information on possible pathogenic tissue. If the knowledge of the cortical anatomy obtained with MRI and the conductivity distribution from CDI is put in to the calculation of the sources of neural signals from the field, the ill-posed inverse problem is expected to become uniquely solvable.

7 Magnetic Immunoassays

Magnetic nanoparticles (MNP) are becoming increasingly popular for manipulation and examination of biological samples. MNP consisting of magnetite (Fe_3O_4) or maghemite (Fe_2O_3) are particularly favorable because of their biocompatibility. MNP are usually superparamagnetic, i.e. their magnetism is vanishing if no external magnetic field is present. Often, they are coated with a biocompatible surfactant, e.g. dextran or streptavidin. They can be used for sample preparation, e.g. for nucleic acid filtration [98] because they can be moved in a magnetic gradient field and thus be used for extraction and sorting. In addition, their magnetic field can be detected by a sensitive magnetometer. Thus, MNP are particularly attractive in biochemistry because they can be used both as a handle and as a marker. Albeit biomagnetic sensing using MNP markers is not a label-free technique, magnetic

immunoassays are briefly covered in this chapter because the method is versatile and sensitive.

Immunoassays employ the highly specific interaction between antigens and antibodies in conjunction with labels or markers for the detection and quantification of specific biomolecules. Typically, fluorophores, enzymes, or radioactive compounds are used as labels. However, the detection range of fluorescence markers is restricted, the sensitivity of enzyme techniques is limited and radioactive markers pose radiation hazards. Magnetic bioassays have therefore been identified as a very promising alternative [99, 100].

For measuring the magnetic response of MNP with respect to a magnetic excitation field, three magnetic detection techniques are employed:

1. Susceptometry [101] involves lock-in detection of the response to a magnetic excitation at a frequency f_0. In case of monodispersed particles, their concentration in a test volume can be quantitatively determined. In addition, the hydrodynamic size parameters of MNP can be determined [102]. If the particle sizes follow a lognormal distribution, the mean hydrodynamic radius and its standard deviation can be determined from the measured complex magnetic susceptibility [103]. Therefore, the size enhancement due to biocompatible surface coating and subsequent functionalization and analyte binding can be measured [104]. A key disadvantage of the susceptometry technique is its lack of selectivity. In case of low concentrations of biomolecules and consequently low concentrations of magnetic marker particles, the resultant susceptibility of the solution is hard to discern from the parasitic susceptibility of the sample container, of the reagents, and of the laboratory environment.
2. Relaxometry [105] is based on recording the time transient of the magnetic response of the particles during the off-time of a pulsed excitation field. By analyzing the relaxation time of the particle's magnetization, a distinction between the Néel relaxation of bound particles and the Brownian relaxation of unbound carriers is feasible [106], since the reorientation of the magnetization vector inside the magnetic core is significantly slower than the Brownian relaxation of particles in solution. It is possible to obtain information on the size distribution of the magnetic cores of nanoparticles, especially on the mean value and the standard deviation of the core diameter of the magnetic crystallites. The technique allows to monitor binding kinetics [107]. Since the relaxometric magnetic field signals are typically very small, the technique usually requires the use of ultra-sensitive SQUIDs as magnetic field sensors. On samples with higher particle concentration, relaxometry can also be measured with fluxgate sensors [108].
3. The frequency mixing technique [109] probes the nonlinear magnetization curve of superparamagnets. Upon magnetic excitation at two distinct frequencies f_1 and f_2 incident on the sample, the response signal generated at a frequency representing a linear combination $m{\cdot}f_1 + n{\cdot}f_2$ is detected. The appearance of these components is highly specific to the nonlinearity of the magnetization curve of the particles. With this magnetic measurement technique, a magnetic

immunoassay for detection of tetanus toxoid was developed. Coaxial coils provided magnetic excitation fields at two distinct frequencies $f_1 = 49.38$ kHz and $f_2 = 61$ Hz incident on the sample. By means of a differential pickup coil, the response signal of the sample inside the coil at a frequency $f_1 + 2 \cdot f_2$ was detected. This mixing component was chosen since it is maximum for vanishing static offset field. Prior to the measurement, primary antibodies were immobilized on a polyethylene filter (Abicap from Senova, Weimar). Then, 500 µL sample was added. When the sample passed the filter, 500 µL of secondary antibody solution (anti-h-IgG biotinylated in PBS) and 500 µL magnetic bead solution (fluidMAG-Streptavidin 200 nm from chemicell, Berlin) were added and rinsed with 750 µL PBS. Figure 9 shows the measured signals of different tetanus immunoassay samples as a function of the concentration of the analyte. At low concentrations of the analyte, unspecific binding of MNP and the thermal noise of the detection coil determines the detection limit. At high concentrations, saturation occurs because nearly all available binding sites in the filter are occupied. Numerous magnetic immunoassays have been demonstrated [110–112] which usually yielded a better sensitivity than conventional immunoassays.

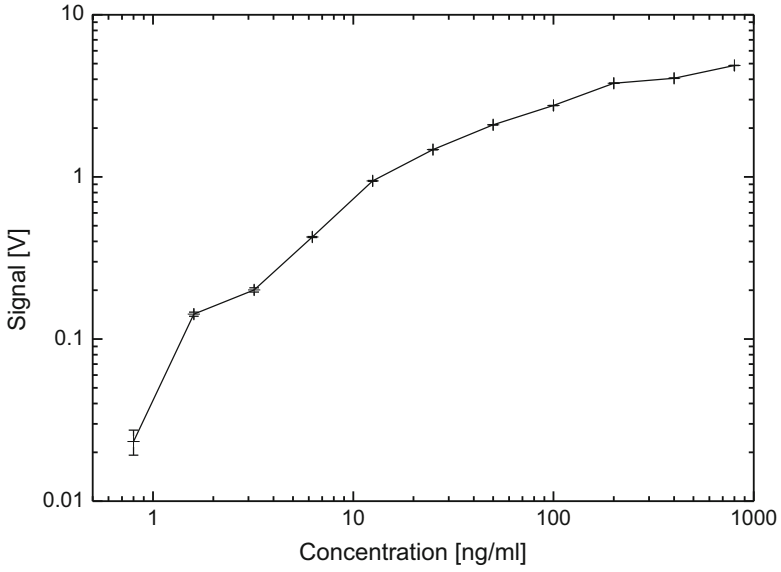

Fig. 9 Calibration curve of a magnetic tetanus immunoassay

8 Conclusion and Perspectives

Biomagnetic measurements of the magnetic field surrounding the human body, generated by the electrophysiological processes of life in the body, have developed continuously over the past decades. The evolution of supersensitive SQUID technology has led to the development of multichannel systems with hundreds of sensor channels for recording MCG and MEG. They provide unique images of heart and brain activity on a millisecond time scale. Increasing computational power and the fusion of data obtained with different imaging modalities has led to unique solutions of the inverse problem of electromagnetism and thus opened up a new window into the human body. Numerous clinical diagnostic applications of MCG, MEG, and LF-MRI have been already demonstrated. LF-MRI allows more broadly applicable, less dangerous, and eventually cheaper instrumentation than its well-established high field counterpart. In addition, promising first results with respect to distinction between malignant and healthy tissue have been obtained. The fusion of these techniques, in conjunction with the novel imaging modalities NCI and CDI, is expected to lead to added diagnostic value as compared to the sum of the individual techniques. Major obstacles are the need for heavy magnetic shielding and for liquid helium coolant, both of which account for a major fraction of the cost of procurement and operation. Recently, flexible shielding solutions adapted to the specific requirements of the location are being offered at affordable cost. As high-T_c SQUIDs are becoming increasingly sensitive and reliable, they might establish as an alternative in MCG instrumentation where sensitivity is not as critical as for MEG. Due to its noninvasive and almost passive nature, biomagnetic sensing is expected to become increasingly important in the near future, both in scientific research and in clinical diagnostics.

References

1. Clarke J, Braginski AI (eds) (2004) The SQUID handbook, Vol. I Fundamentals and technology of SQUIDs and SQUID systems. Wiley, Weinheim
2. Andrä W, Nowak H (eds) (2007) Magnetism in medicine, 2nd edn. Wiley, Weinheim
3. Malmivuo J, Plonsey R (1995) Bioelectromagnetism, principles and applications of bioelectric and biomagnetic fields. Oxford University Press, New York
4. Erné SN, Lehmann J (1996) Magnetocardiography, an introduction. In: Weinstock H (ed) SQUID sensors: fundamentals, fabrication and applications. Kluwer, Dordrecht, pp 395–412
5. Einthoven W (1902) Galvanometrische registratie van het menschelijk electrocardiogram. Herinneringsbudendedl Professor S.S. Rosenstein. Eduard Ijdo, Leiden, pp 101–1077
6. Baule GM, McFee R (1963) Detection of the magnetic field of the heart. Am Heart J 55:95–96
7. Jaklevic RC, Lambe J, Silver AH, Mercereau JE (1964) Quantum interference effects in Josephson tunneling. Phys Rev Lett 12:159–160
8. Zimmerman JE, Thiene P, Harding JT (1970) Design and operation of stable rf-biased superconducting point-contact quantum devices, and a note on the properties of perfectly clean metal contacts. J Appl Phys 41:1572–1580

9. Cohen D, Edelsack EA, Zimmerman JE (1970) Magnetocardiograms taken inside a shielded room with a superconducting point-contact magnetometer. Appl Phys Lett 16:278–280
10. Nowak H (2015) SQUIDs in biomagnetism. In: Seidel P (ed) Applied superconductivity. Wiley, Weinheim
11. Stroink G, Hailer B, van Leeuwen P (2007) Cardiomagnetism. In: Andrä W, Nowak H (eds) Magnetism in medicine, 2nd edn. Wiley, Weinheim, pp 164–209
12. Fenici R, Brisinda D, Sorbo AR, Venuti A (2012) MCG instrumentation and application. In: Rogalla H, Kes PH (eds) 100 years of superconductivity. CRC Press, Boca Raton, pp 582–602
13. Ilmoniemi RJ, Hari R, Reinikainen K (1984) A four-channel SQUID magnetometer for brain research. Electroencephalogr Clin Neurophysiol 58:467–473
14. Nowak H (2007) Biomagnetic instrumentation. In: Andrä W, Nowak H (eds) Magnetism in medicine, 2nd edn. Wiley, Weinheim, pp 101–163
15. Saarinen M, Karp PJ, Katila TE, Siltanen P (1974) The magnetocardiogram in cardiac disorders. Cardiovasc Res 8:820–834
16. Dilorio MS, Yang KY, Yoshizumi S (1995) Biomagnetic measurements using low-noise integrated SQUID magnetometers operating in liquid nitrogen. Appl Phys Lett 67:1926–1928
17. Itozaki H, Tanaka S, Toyoda H, Hirano T, Haruta Y, Nomura M, Saijou T, Kado H (1996) A multi-channel high-Tc SQUID system and its applications. Supercond Sci Technol 9: A38–A41
18. David B, Grundler D, Krey S, Doormann V, Eckard R, Krumme JP, Rabe G, Dössel O (1996) High-Tc-SQUID magnetometers for biomagnetic measurements. Supercond Sci Technol 9: A96–A99
19. Zhang Y, Wolters N, Schubert J, Lomparski D, Banzet M, Panaitov G, Krause HJ, Mück M, Braginski AI (2003) HTS SQUID gradiometer using substrate resonators operating in unshielded environment – a portable MCG system. IEEE Trans Appl Supercond 13:389–392
20. Zhang Y, Wolters N, Lomparski D, Zander W, Banzet M, Schubert J, Krause HJ, van Leeuwen P (2005) Multi-channel HTS rf SQUID gradiometer system recording fetal and adult magnetocardiograms. IEEE Trans Appl Supercond 15:631–634
21. Tolstrup K, Madsen BE, Ruiz JA, Greenwood SD, Camacho J, Siegel RJ, Gertzen HC, Park JW, Smars PA (2006) Non-invasive resting magnetocardiographic imaging for the rapid detection of ischemia in subjects presenting with chest pain. Cardiology 106:270–276
22. Morguet AJ, Behrens S, Kosch O, Lange C, Zabel M, Selbig D, Munz DL, Schultheiss HP, Koch H (2004) Myocardial viability evaluation using magnetocardiography in patients with coronary artery disease. Coron Artery Dis 15:155–162
23. Park JW, Leithäuser B, Vrsansky M, Jung F (2008) Dobutamine stress magnetocardiography for the detection of significant coronary artery stenoses – a prospective study in comparison with simultaneous 12-lead electrocardiography. Clin Hemorheol Microcirc 39:21–32
24. Kwong JSW, Leithäuser B, Park JW, Yu CM (2013) Diagnostic value of magneto-cardiography in coronary artery disease and cardiac arrhythmias: a review of clinical data. Int J Cardiol 167:1835–1842
25. Shin ES, Lam YY, Her AY, Brachmann J, Jung F, Park JW (2017) Incremental diagnostic value of combined quantitative and qualitative parameters of magnetocardiography to detect coronary artery disease. Int J Cardiol 228:948–952
26. Fenici RR, Masselli M, Lopez L, Sabetta F (1985) High resolution magnetocardiography: electrophysiological and clinical findings. Med Biol Eng Comput 23:1475–1478
27. Brisinda D, Fenici R (2007) Noninvasive classification of ventricular preexcitation with unshielded magnetocardiography and transesophageal atrial pacing and follow-up. Pacing Clin Electrophysiol 30(Suppl 1):S151–S155
28. Kariniemi V, Ahopelto J, Karp PJ, Katila TE (1974) The fetal magnetocardiogram. J Perinat Med 2:214–216
29. Schneider U, Schleussner E (2007) Fetal magnetography. In: Andrä W, Nowak H (eds) Magnetism in medicine, 2nd edn. Wiley, Weinheim, pp 268–290

30. Stinstra J, Golbach E, van Leeuwen P, Lange S, Menendez T, Moshage W, Schleussner E, Kaehler C, Horigome H, Shigemitsu S, Peters MJ (2002) Multicentre study of fetal cardiac time intervals using magnetocardiography. Br J Obstet Gynaecol 109:1235–1243
31. van Leeuwen P, Hailer P, Bader W, Geissler J, Trowitsch E, Grönemeyer D (1999) Magnetocardiography in the diagnosis of fetal arrhythmia. Br J Obstet Gynaecol 106:1200–1208
32. Srinivasan S, Strasburger J (2008) Overview of fetal arrythmias. Curr Opin Pediatr 20:522–531
33. Zhang Y, Wolters N, Lomparski D, Zander W, Banzet M, Schubert J, Krause HJ, Geue D, van Leeuwen P (2006) Foetal magnetocardiography with a multi-channel HTS rf SQUID gradiometer. Supercond Sci Technol 19:S266–S270
34. Knösche TR, Nakasato N, Eiselt M, Haueisen J (2007) Neuromagnetism. In: Andrä W, Nowak H (eds) Magnetism in medicine, 2nd edn. Wiley, Weinheim, pp 210–267
35. Del Gratta C, Della Penna S, Pizzella V, Romani GL (2012) Medical applications of magnetoencephalography. In: Rogalla H, Kes PH (eds) 100 years of superconductivity. CRC Press, Boca Raton, pp 562–581
36. Gross J, Ioannides AA, Dammers J, Maess B, Friederici AD, Mollergartner HJ (1998) Magnetic field tomography analysis of continuous speech. Brain Topogr 10:273–281
37. Kutas M, Hillyard SA (1980) Reading senseless sentences: brain potentials reflecting semantic incongruity. Science 207:203–205
38. Kober H, Moller M, Nimsky C, Vieth J, Fahlbusch R, Ganslandt O (2001) New approach to localize speech relevant brain areas and hemispheric dominance using spatially filtered magnetoencephalography. Hum Brain Mapp 14:236–250
39. Halgren E, Dhond RP, Christensen N, van Petten C, Marinkovic K, Lewine JD, Dale AM (2002) N400-like magnetoencephalography responses modulated by semantic context, word frequency, and lexical class in sentences. NeuroImage 17:1101–1116
40. Neuhaus C, Knösche TR, Friederici AD (2006) Effects of musical expertise and boundary markers on phrase perception in music. J Cogn Neurosci 18:472–493
41. Kuriki S, Isahai N, Ohtsuka A (2005) Spatiotemporal characteristics of the neural activities processing consonant/dissonant tones in melody. Exp Brain Res 162:46–55
42. Herrmann CS, Munk MHJ, Engel AK (2004) Cognitive functions of gamma band activity: memory match and utilization. Trends Cogn Sci 8:347–355
43. Okusa T, Kakigi R, Osaka N (2000) Cortical activity related to cue-invariant shape perception in humans. Neuroscience 98:615–624
44. Feige B, Kristeva-Feige R, Rossi S, Pizzella V, Rossini PM (1996) Neuromagnetic study of movement-related changes in rhythmic brain activity. Brain Res 734:252–260
45. Nakasato N, Yoshimoro T (2000) Somatosensory, auditory and visual evoked magnetic fields in patients with brain diseases. J Clin Neurophysiol 17:201–211
46. Knowlton RC, Shih J (2004) Magnetoencephalography in epilepsy. Epilepsia 45:61–71
47. Vieth J, Kober H, Weise E, Daun A, Moeger A, Friedrich S, Pongratz H (1992) Functional 3D localization of cerebrovascular accidents by magneto-encephalography (MEG). Neurol Res 14:132–134
48. Qiao F, Kuroda S, Kamada K, Houkin K, Iwasaki Y (2003) Source local-ization of the re-build up phenomenon in pediatric moyamoya disease – a dipole distribution analysis using MEG and SPECT. Childs Nerv Syst 19:760–764
49. Seki S, Nakasato N, Ohtomo S, Kanno A, Shimizu H, Tominaga T (2005) Neuromagnetic measurement of unilateral temporo-parietal theta rhythm in patients with internal carotid artery occlusive disease. NeuroImage 25:502–510
50. Dammers J, Chocholacs H, Eich E, Boers F, Faley MI, Dunin-Borkowski RE, Shah NJ (2014) Source localization of brain activity using helium-free interferometer. Appl Phys Lett 104:213705
51. Callaghan PT (1991) Principles of nuclear magnetic resonance microscopy. Clarendon Press, Oxford

52. Haacke EM, Brown RW, Thompson MR, Venkatesan R (1999) Magnetic resonance imaging physical principles and sequence design. Wiley, New York
53. Abragam A (1961) The principle of nuclear magnetism. Oxford University Press, London
54. Purcell EM, Torrey H, Pound RV (1946) Resonance absorption by nuclear magnetic moments in a solid. Phys Rev 69:37–38
55. Bloch F, Hansen WW, Packard M (1946) Nuclear induction. Phys Rev 69:127
56. Ernst RR, Anderson WA (1966) Application of Fourier transform spectroscopy to magnetic resonance. Rev Sci Instrum 37:93–102
57. Lauterbur PC (1973) Image formation by induced local interactions: examples employing nuclear magnetic resonance. Nature 242:190–191
58. Mansfield P (1977) Multi-planar image formation using NMR spin echoes. J Phys C 10: L55–L58
59. Huettel SA, Song AW, McCarthy G (2009) Functional magnetic resonance imaging, 2nd edn. Sinauer Associates, Sunderland
60. Li X (2014) Functional magnetic resonance imaging processing. Springer, Dordrecht
61. Dumoulin CL, Souza SP, Walker MF, Wagle W (1989) Three-dimensional phase contrast angiography. Magn Reson Med 9:139–149
62. Nishimura DG (1990) Time-of-flight MR angiography. Magn Reson Med 14:194–201
63. Koh DM, Collins DJ (2007) Diffusion-weighted MRI in the body: applications and challenges in oncology. Am J Roentgenol 188:1622–1635
64. Le Bihan D, Mangin JF, Poupon C, Clark CA, Pappata S, Molko N, Chabriat H (2001) Diffusion tensor imaging: concepts and applications. J Magn Reson Imaging 13:534–546
65. Matson GB, Weiner MW (1992) Spectroscopy. In: Stark DD, Bradley WG (eds) Magnetic resonance imaging. Mosby Yearbook, St. Louis, pp 438–477
66. Konstandin S, Schad LR (2014) 30 years of sodium/X-nuclei magnetic resonance imaging. Magn Reson Mater Phys 27:1–4
67. Ogawa S, Tank DW, Menon R, Ellermann JM, Kim SG, Merkle H, Ugurbil K (1992) Intrinsic signal changes accompanying sensory stimulation: functional brain mapping with magnetic resonance imaging. Proc Natl Acad Sci U S A 89:5951–5955
68. Lee JH, Durand R, Gradinaru V, Zhang F, Goshen I, Kim DS, Fenno LE, Ramakrishnan C, Deisseroth K (2010) Global and local fMRI signals driven by neurons defined optogenetically by type and wiring. Nature 465:788–792
69. Clarke J (2011) Ultralow field NMR and MRI. In: Rogalla H, Kes PH (eds) 100 years of superconductivity. CRC Press, Boca Raton, pp 610–619
70. Zevenhoven KCJ, Dong H, Ilmoniemi RJ, Clarke J (2015) Dynamical cancellation of pulse-induced transients in a metallic shielded room for ultra-low-field magnetic resonance imaging. Appl Phys Lett 106:034101
71. Dong H, Wang Y, Zhang L, Sun Y, Xie X (2008) Detection of proton NMR signal in the earth's magnetic field at an urban laboratory environment without shielding. Supercond Sci Technol 20:115009
72. Espy MA, Magnelind PE, Matlashov AN, Newman SG, Sandin HJ, Schultz LJ, Sedillo R, Urbaitis AV, Volegov PL (2015) Progress toward a deployable SQUID-based ultra-low field MRI system for anatomical imaging. IEEE Trans Appl Supercond 25:1601705
73. Liu C, Chang B, Qiu L, Dong H, Qiu Y, Zhang Y, Krause HJ, Offenhäusser A, Xie X (2015) Effect of magnetic field fluctuation on ultra-low field MRI measurements in the unshielded laboratory environment. J Magn Reson 257:8–14
74. Qiu L, Liu C, Dong H, Xu L, Zhang Y, Krause HJ, Xie X (2012) Magnetic field improved ULF-NMR measurement in an unshielded laboratory using a low-Tc SQUID. Phys Procedia 36:388–393
75. Dong H, Qiu L, Shi W, Chang B, Qiu Y, Xu L, Liu C, Zhang Y, Krause HJ, Offenhäusser A, Xie X (2013) Ultra-low field magnetic resonance imaging detection with gradient tensor compensation in urban unshielded environment. Appl Phys Lett 102:102602

76. Liu C, Chang B, Qiu L, Qiu Y, Dong H, Zhang Y, Xie X (2015) Multichannel ULF-MRI study in magnetic unshielded urban laboratory environment. IEEE Trans Appl Supercond 25:1602804
77. Clarke J, Hatridge M, Mößle M (2007) SQUID-detected magnetic resonance imaging in microtesla fields. Annu Rev Biomed Eng 9:389–413
78. Lee SK, Mößle M, Myers W, Kelso N, Trabesinger AH, Pines A, Clarke J (2005) SQUID-detected MRI at 132 μT with T1-weighted contrast established at 10 μT-300 mT. Magn Reson Med 53:9–15
79. Busch S, Hatridge M, Mößle M, Myers W, Wong T, Mück M, Chew K, Kuchinsky K, Simko J, Clarke J (2012) Measurements of T1-relaxation in ex vivo prostate tissue at 132 μT. Magn Reson Med 67:1138–1145
80. Lee SJ, Shim JH, Kim K, Hwang S, Yu KK, Lim S, Han JH, Yim H, Kim JH, Jung YS, Kim KS (2015) T1 relaxation measurement of ex-vivo breast cancer tissues at ultralow magnetic fields. Biomed Res Int 2015:385428
81. Mößle M, Han SI, Myers WR, Lee SK, Kelso N, Hatridge M, Pines A, Clarke J (2006) SQUID-detected microtesla MRI in the presence of metal. J Magn Reson 179:146–151
82. Kimmich R, Anoardo E (2004) Field cycling NMR relaxometry. Prog Nucl Magn Reson Spectrosc 44:257–320
83. Gilani IA, Sepponen R (2016) Quantitative rotating frame relaxometry methods in MRI. NMR Biomed 29:841–861
84. Inglis B, Buckenmaier K, Sangiorgio P, Pedersen AF, Nicols MA, Clarke J (2013) MRI of the human brain at 130 microtesla. Proc Natl Acad Sci U S A 110:19194–19201
85. Dong H, Sm H, Wendland M, You L, Clarke J, Inglis B (2017) Ultralow-field and spin-locking relaxation dispersion in post mortem pig brain. Magn Reson Med. doi:10.1002/mrm.26621
86. Zotev VS, Matlashov AN, Volegov PL, Savukov IM, Espy MA, Mosher JC, Gomez JJ, Kraus RH Jr (2008) Microtesla MRI of the human brain combined with MEG. J Magn Reson 194:115–120
87. Matlashov AN, Burmistrov E, Magnelind PE, Schultz L, Urbaitis AV, Volegov PL, Yoder J, Espy MA (2012) SQUID-based systems for co-registration of ultra-low field nuclear magnetic resonance images and magnetoencephalography. Physica C 482:19–26
88. Vesanen PT, Nieminen JO, Zevenhoven KCJ, Dabek J, Parkkonen LT, Zhdanov AV, Luomahaara J, Hassel J, Penttilä J, Simola J, Ahonen AI, Mäkelä JP, Ilmoniemi RJ (2013) Hybrid ultra-low-field MRI and magnetoencephalography system based on a commercial whole-head neuromagnetometer. Magn Reson Med 69:1795–1804
89. Bodurka J, Bandettini PA (2002) Toward direct mapping of neuronal activity: MRI detection of ultraweak, transient magnetic field changes. Magn Reson Med 47:1052–1058
90. Burghoff M, Albrecht HH, Hartwig S, Hilschenz I, Körber R, Höfner N, Scheer HJ, Voigt J, Trahms L, Curio G (2010) On the feasibility of neurocurrent imaging by low field nuclear magnetic resonance. Appl Phys Lett 96:233701
91. Körber R, Nieminen JO, Höfner N, Jazbinsek V, Scheer HJ, Kim K, Burghoff M (2013) An advanced phantom study assessing the feasibility of neuronal current imaging by ultra-low field NMR. J Magn Reson 237:182–190
92. Oh SH, Lee BI, Woo EJ, Lee SY, Cho MH, Kwon O, Seo JK (2003) Conductivity and current density image reconstruction using harmonic Bz algorithm in magnetic resonance electrical impedance tomography. Phys Med Biol 48:3101–3116
93. Voigt T, Katscher U, Doessel O (2011) Quantitative conductivity and permittivity imaging of the human brain using electric properties tomography. Magn Reson Med 66:456–466
94. Kim DH, Choi N, Gho SM, Shin J, Liu C (2014) Simultaneous imaging of in vivo conductivity and susceptibility. Magn Reson Med 71:1144–1150
95. Woo EJ, Seo JK (2008) Magnetic resonance electrical impedance tomography (MREIT) for high-resolution conductivity imaging. Physiol Meas 29:R1–R26

96. Nieminen JO, Zevenhoven KCJ, Vesanen P, Hsu YC, Ilmoniemi RJ (2014) Current-density imaging using ultra-low-field MRI with adiabatic pulses. Magn Reson Imaging 32:54–59
97. Vesanen P, Nieminen JO, Zevenhoven KCJ, Hsu YC, Ilmoniemi RJ (2014) Current-density imaging using ultra-low-field MRI with zero-field encoding. Magn Reson Imaging 32:766–770
98. Häfeli U, Schütt W, Teller J, Zborowski M (eds) (1997) Scientific and clinical applications of magnetic carriers. Plenum, New York
99. Thanh NTK (ed) (2012) Magnetic nanoparticles – from fabrication to clinical applications. CRC Press and Taylor & Francis Group, Boca Raton
100. Cardoso S, Leitao DC, Dias TM, Valadeiro J, Silva MD, Chicharo A, Silverio V, Gaspar J, Freitas PP (2017) Challenges and trends in magnetic sensor integration with microfluidics for biomedical applications. J Phys D 50:213001
101. Kriz K, Gehrke J, Kriz D (1998) Advancements toward magneto immunoassays. Biosens Bioelectron 13:817–823
102. Payet B, Vincent D, Delaunay L, Noyel G (1998) Influence of particle size distribution on the initial susceptibility of magnetic fluids in the Brown relaxation range. J Magn Magn Mater 186:168–174
103. Ludwig F, Heim E, Schilling M (2009) Characterization of magnetic core-shell nanoparticles by fluxgate magnetorelaxometry, ac susceptibility, transmission electron microscopy and photon correlation spectroscopy – a comparative study. J Magn Magn Mater 321:1644–1647
104. Prieto Astalan A, Jonasson C, Petersson K, Blomgren J, Ilver D, Krozer A, Johansson C (2007) Magnetic response of thermally blocked magnetic nanoparticles in a pulsed magnetic field. J Magn Magn Mater 311:166–170
105. Matz H, Drung D, Hartwig S, Gross H, Kötitz R, Müller W, Vass A, Weitschies W, Trahms L (1998) A SQUID measurement system for immunoassays. Appl Supercond 6:577–583
106. Kötitz R, Fannin PC, Trahms L (1995) Magnetorelaxometry domain study of Brownian and Néel relaxation in ferrofluids. J Magn Magn Mater 149:42–46
107. Eberbeck D, Wiekhorst F, Steinhoff U, Schwarz KO, Kummrow A, Kammel M, Neukammer N, Trahms L (2009) Specific binding of magnetic nanoparticle probes to platelets in whole blood detected by magnetorelaxometry. J Magn Magn Mater 321:1617–1620
108. Ludwig F, Heim E, Schilling M (2007) Characterization of superparamagnetic nanoparticles by analyzing the magnetization and relaxation dynamics using fluxgate magnetometers. J Appl Phys 101:113909
109. Krause HJ, Wolters N, Zhang Y, Offenhäusser A, Miethe P, Meyer MHF, Hartmann M, Keusgen M (2007) Magnetic particle detection by frequency mixing for immunoassay applications. J Magn Magn Mater 311:436–444
110. Meyer MHF, Hartmann M, Krause HJ, Blankenstein G, Müller-Chorus B, Oster J, Miethe P, Keusgen M (2007) CRP determination based on a novel magnetic biosensor. Biosens Bioelectron 22:973–979
111. Hong HB, Krause HJ, Song KB, Choi CJ, Chunga MA, Offenhäusser A (2011) Detection of two different Influenza A viruses using an ELIFA system and a magnetic biosensor. J Immunol Methods 365:95–100
112. Rettcher S, Jungk F, Kühn C, Krause HJ, Nölke G, Commandeur U, Fischer R, Schillberg S, Schröper F (2015) A simple and portable magnetic immunoassay for the rapid detection and sensitive quantification of plant viruses. Appl Environ Microbiol 81:3039–3048

Index

M. J. Schöning, A. Poghossian (eds.), *Label-Free Biosensing: Advanced Materials,* Devices and Applications, Springer Series on Chemical Sensors and Biosensors (2018) 16: 475–480
DOI 10.1007/5346_2017,